



Abánades Lázaro, Isabel (2018) The effect of surface functionalisation on cancer cells internalisation and selective cytotoxicity of zirconium metal organic frameworks. PhD thesis.

<https://theses.gla.ac.uk/9099/>

Copyright and moral rights for this work are retained by the author

A copy can be downloaded for personal non-commercial research or study, without prior permission or charge

This work cannot be reproduced or quoted extensively from without first obtaining permission in writing from the author

The content must not be changed in any way or sold commercially in any format or medium without the formal permission of the author

When referring to this work, full bibliographic details including the author, title, awarding institution and date of the thesis must be given

Enlighten: Theses

<https://theses.gla.ac.uk/>  
[research-enlighten@glasgow.ac.uk](mailto:research-enlighten@glasgow.ac.uk)

# **The Effect of Surface Functionalisation on Cancer Cells Internalisation and Selective Cytotoxicity of Zirconium Metal-Organic Frameworks**

Isabel Abánades Lázaro



University  
of Glasgow

Submitted in fulfilment of the requirements  
for the Degree of Doctor of Philosophy  
School of Chemistry  
University of Glasgow

March 2018

## **Declaration**

This thesis has been written and compiled by the author, Isabel Abánades Lázaro, who has carried out the research at the University of Glasgow between 2014 and 2018 under the supervision of Dr Ross Forgan. Where collaborative results have been included in this thesis the input of others has been acknowledged. Parts of this thesis have been published in peer-reviewed journals and at the start of each chapter reference to the relevant publications is given.

## Abstract

A considerable amount of effort has been directed to develop porous materials as drug delivery systems (DDSs) – one of the most promising emerging applications in healthcare, as most anticancer therapeutics have toxic dose dependence due to a lack of tumour selectivity – as their hierarchical porosity can be used to store and release challenging drugs.

Among them, Metal-Organic Frameworks (MOFs) – emerging hybrid, highly porous crystalline structures – offer several advantages compared to other available DDS, as they combine desirable features from both organic (biocompatibility, e.g. porous polymers) and inorganic (high loadings, e.g. mesoporous silica) porous materials. MOFs are highly amenable to functionalisation, meaning fine control over their physical properties can be achieved, and thus they have experienced tremendous development during the past decade in many applications. Despite surface engineering being advantageous for diverse fields – in biomedicine, it can both improve stability and dispersion, and provide the possibility of targeted carriers, decreasing the immune system recognition – surface functionalization of MOFs is underdeveloped. The multiple synthetic steps – synthesis, drug loading and surface modification – and the lack of orthogonality between them hinder their industrial manufacturing as DDSs.

This thesis focuses on the development of surface functionalisation protocols of Zirconium MOFs, particularly UiO-66, a Zr-terephthalate MOF, the study of their cell internalisation fate and routes and the correlation with their therapeutic activity.

During Chapter 1, an introduction to the use of DDSs in anticancer therapy, followed by examples of the most relevant MOFs from a coordination chemistry point of view, is given, in which zirconium MOFs and their synthesis are highlighted. Particular focus is given to the coordination modulation process, in which monodentate modulators are introduced to the MOFs synthesis to compete with the multidentate linkers during nucleation, enhancing properties such as porosity through the induction of defects. Then, the most relevant examples of surface functionalization of Zr MOFs for drug delivery are discussed with respect to the effects on properties such as colloidal dispersion in aqueous solvents, physiological stability, and drug release kinetics.

In Chapter 2 different functionalised modulators (i.e. *p*-functionalised benzoic acids, folic acid or biotin) are introduced to UiO-66 synthesis to obtain surface-functionalised UiO-66 with the appropriate size for drug delivery by one-pot synthesis. Full characterisation of the materials shows them to be remarkably porous due to the defects formed when modulators attach to available zirconium positions in the pores and on the surfaces of the MOFs. Furthermore, the use of a carboxylate-containing anticancer metabolic target (dichloroacetic acid, DCA) as a

modulator of UiO-66 synthesis is explored, and co-modulated samples, in which both DCA and functionalised modulators are introduced to UiO-66 synthesis, are synthesised and fully characterised, resulting in drug-containing (ca. 20% w/w) surface-functionalised MOFs by one pot syntheses. Importantly, DCA modulation induces a high number of defects, and consequently highly charged nanoparticles which are colloidally stable in aqueous solvents. Particle size control in the DCA modulated synthesis of the UiO family of isorecticular MOFs – including UiO-66 and its bromo, amino and nitro derivatives, and extended structures Zr-Naphthalenedicarboxylate (NDC) and Zr-Biphenyldicarboxylate (BPDC) – is achieved, obtaining ca. 100 nm particles of UiO-66 derivatives and microcrystals of Zr-NDC and Zr-BPDC when  $ZrCl_4$  is the metal precursor, and mesoporous < 20 nm UiO-66 derivatives and ca. 200 nm Zr-NDC and Zr-BPDC when  $ZrOCl_2$  is used as the metal precursor. The high porosity of the DCA modulated samples, due to DCA attachment to the inner and outer surface at defect sites, allows the loading of a second drug, the well-known anticancer drug 5-fluorouracil (5-FU), into the pores of the isorecticular MOFs to create dual DDSs.

Different postsynthetic modes of surface coating, based in both coordination and covalent chemistry, are studied during Chapter 3. The functionalities of the *p*-functionalised benzoic acid modulators, introduced to UiO-66 structure during Chapter 2, are used to covalently attach short-chain alkanes and long-chain polymers to UiO-66 surface through copper-catalysed azide-alkyne cycloaddition. Exhaustive characterisation confirms that the attachment occurs through covalent chemistry and not through surface adhesion or electrostatic forces. Folic acid and biotin, which are introduced to UiO-66 surface as synthetic modulators during Chapter 2, are also introduced to UiO-66 surface postsynthetically. Colloidal dispersion and stability towards phosphates are investigated and compared to bare MOFs, in order to gain insights into the effect of both surface chemistry and mode of attachment on physical properties.

A comprehensive overview of *in vitro* studies of cellular internalisation of zirconium MOFs is given in Chapter 4, focussing on the relevance of the endocytosis internalisation routes, which are strictly correlated with therapeutic efficacy. The postsynthetic surface functionalisation protocols investigated in Chapter 3 are applied to analogous calcein-loaded UiO-66 samples. Calcein is a fluorescent molecule not able to efficiently cross the cell membrane by itself, and hence serves as an ideal probe of MOFs cellular internalisation. Its release from bare and poly(ethylene glycol) coated UiO-66 into phosphate buffered saline at pH 7.4 and 5.5, in order to simulate extracellular and intracellular conditions, is found to be pH responsive (more pronounced at 5.5) for all MOFs, but an ideal decrease in calcein release at pH 7.4 occurs only for PEGylated MOFs. Internalisation of calcein-loaded MOFs by HeLa cervical cancer

cells is studied by fluorescence assisted cell sorting, highlighting the effects of surface chemistry on endocytosis efficiencies and internalisation mechanisms.

A discussion of *in vitro* studies into anticancer drug delivery from Zr MOFs is provided in Chapter 5, alongside a summary of the therapeutic effects of DCA and approaches to enhance its anticancer efficacy. Experimental assessment of the *in vitro* anticancer performance towards MCF-7 breast cancer cells of the DCA-containing MOFs of the UiO family of different sizes (*ca.* 100 nm and <20 nm), synthesised by coordination modulation during Chapter 2, is given. The effect of dual-drug containing MOFs (DCA and 5-FU) is also examined, to investigate the possible synergic effect of the drug combination. Then, the cytotoxicity of bare and surface functionalised, DCA-loaded and empty UiO-66 MOFs is studied at first upon incubation with HeLa cells, for which the cellular routes of internalisation were elucidated in Chapter 4. The most promising MOFs are then tested for selective anticancer activity against a series of cancerous and healthy cells lines, and their macrophage uptake and ROS production is also analysed, to determine the effect of surface functionalization. The selective anticancer cytotoxicity of folate-coated MOFs is attributed to a combination of cancer cell targeting and optimal cell internalisation routes.

To summarise, the one-pot synthesis of drug-loaded, surface functionalised UiO-66 has been successfully performed, resulting in porous, crystalline MOFs with the appropriate size for drug delivery. The use of a carboxylate-containing anticancer metabolic target as a modulator has been explored for the UiO family of isorecticular MOFs, resulting in well-dispersed nanoMOFs with enhanced anticancer activity, into which a second drug can be loaded, enabling the creation of dual DDSs. A series of postsynthetic surface modifications are performed, enabling the study of the MOF's properties (colloidal dispersion, physiological stability and biocompatibility) with respect to their surface chemistry and coating mode, but more importantly providing valuable insights into correlations between surface chemistry, routes of cellular internalisation and therapeutic effect.

## **Acknowledgements**

Living and doing my PhD in Glasgow has been an enjoyable experience. Although being far away from home, being surrounded by great people has made this experience unique and unforgettable.

First, I would like to thank my supervisor, Dr Ross S Forgan, for his help and sympathy during my PhD; His door was open every time I asked for help. I specially appreciate the freedom to choose my own direction, and to design and develop my projects and collaborations, which I believe has made me a better researcher.

I am grateful to the whole Forgan group, past and present members, who have made working in the lab and going on conferences, among many other many adventures enjoyable. I will not forget the longest bicycle ride ever with San Francisco's sun and wind, how Sarah turned the oven on fire and how we were constantly forgetting our posters. I would like to specially thank Dr Ross Marshall, who although our projects were not related, helped me the most and somehow was my mentor during the first years. I would also like to thank the other groups with which we have shared labs.

Thanks to the MSci students, Sabrina Sacca and Connor Wells, with who I have had the pleasure to work. FACs will not be the same without Connor, and I will try my best to reproduce his heart MOF. Also thanks to Ali, who although was not my student, has made me laugh uncountable times about it.

I am very thankful to our collaborators, both in Cambridge (Dr David Fairen-Jimenez, Dr Claudia Orellana-Tavra and Sam Haddad) and in Spain (Dr Victoria del Pozo and Jose Manuel Rodrigo-Muñoz), with who I have learnt many techniques and further develop my research skills. This thesis would not have been the same if I didn't have the opportunity to go there to do biology and learn from them. Thank you very much to Sam, to who I stressed quite a lot when I was aiming to study all the endocytosis pathways and cytotoxicity on HeLa cells in just a month. It was possible just thanks to his help, and to the RSC who funded me to perform the visit.

I would also like to thank the School of Chemistry staff, in special Susan Ganon (cell culture), Andrew Monaghan (TGA and Mass spec) Claire Wilson (PXRD), James Gallagher and Peter Chung (SEM).

I am extremely thankful to my family, who supported me on every step of the way, and made me feel a bit closer every single day. In special to my mum, who made sure I had always all the wonderful food that I might be missing from home, and to my sister, Sandra, for the constant visits and the Scottish summers together, always full of adventures. Working with my younger sister in the lab during 2016 summer was an amazing experience, and although she had enough and went to do law and politics, she made lovely little nanoparticles and stole a smile from me every single day. To my friends, who through visits, travels and skype calls, have always been close despite the kilometres.

Thank you very much to Laura, who I have had the pleasure to live with during the last two years of my PhD and who has certainly made me feel at home, with the morning coffee, the wonderful dinners and chats, company and support. You feel like family to me now.

The EPSRC, University of Glasgow and Royal Society of Chemistry are acknowledged for their financial support.

## Table of Contents

Declaration .....	i
Abstract .....	ii
Acknowledgements .....	v
Table of Abbreviations .....	x
<b>Chapter 1</b> .....	1
Table of Contents .....	2
1.1. The Use of Drug Delivery Systems (DDSs) .....	3
1.2. Metal-Organic Frameworks (MOFs): A Coordination Chemistry Point of View .....	5
1.3. Synthesis of Zr MOFs: Coordination Modulation .....	8
1.4. Metal Organic Frameworks as Carriers for Drug Delivery: Background .....	14
1.5. Surface Modifications of Zr MOFs for Drug Delivery .....	17
1.5.1. Postsynthetic Surface Modifications of Zr MOFs Based on Coordination Chemistry .....	17
1.5.2. Postsynthetic Surface Modifications of Zr MOFs Based on Covalent Chemistry ...	20
1.6. Colloidal Dispersion of Zr MOFs under Simulated Physiological Conditions .....	24
1.7. Stability of Zr MOFs under Simulated Physiological Conditions .....	27
1.8. Drug Release Kinetics of Zr MOFs .....	28
1.9. Biocompatibility of Zr MOFs .....	33
1.10 Conclusions and Future Work .....	35
1.11. References .....	36
<b>Chapter 2</b> .....	43
2.1 Introduction .....	45
2.2 Aims .....	46
2.3 UiO-66 Modulated Synthesis and Characterisation .....	48
2.3.1 The Use of Functionalised Benzoic Acid Derivatives as Modulators .....	49
2.3.2 The Use of Biotin and Folic Acid as Modulators .....	55
2.3.3 The Use of Dichloroacetic acid (DCA) as Modulator .....	63
2.3.4 Co-Modulated Synthesis of DCA-containing, Surface Modified UiO-66 .....	70
2.4. DCA Modulated Synthesis of the UiO Family of Isoreticular MOFs .....	77
2.5. Conclusions and Future Work .....	92
2.6. Experimental .....	93
2.7 References .....	99
<b>Chapter 3</b> .....	102
Table of Contents .....	103
3.1 Introduction .....	104

3.2 Aims .....	105
3.3 UiO-66 Surface FunctionalisationS.....	107
3.3.1 UiO-66-L1 and Ui-66-L2 Postsynthetic Covalent Surface ModificationS .....	107
3.3.1.1. Alkyl-Modified UiO-66: Proof-of-Concept Surface Modifications .....	107
3.3.1.2. UiO-66-L1 Postsynthetic Covalent PEGylation .....	111
3.3.1.3. UiO-66-L1 and UiO-66-L2 Postsynthetic Covalent Polymeric Coating .....	116
3.3.2. Postsynthetic Surface Coordination of UiO-66-L1 .....	122
3.4. The Effect of UiO-66 Surface Chemistry on its Colloidal Dispersion .....	128
3.5. The Effect of Surface Chemistry in UiO-66 Degradation Kinetics.....	140
3.6 Conclusions.....	146
3.7 Experimental .....	147
3.8 References .....	150
<b>Chapter 4</b> .....	153
Table of Contents .....	154
4.1 Introduction to Cellular Internalisation.....	155
4.1.1. Cellular Internalisation of MOFs .....	157
4.2 Aims .....	164
4.3. Postsynthetic Surface Functionalisation of Calcein-Loaded Samples .....	165
4.4 The Effect of PEG Coating on UiO-66 Calcein Release Kinetics .....	169
4.5 Endocytosis Efficacy of MOFs .....	173
4.6 Endocytosis Routes of MOFs .....	175
4.7 Confocal Fluorescence Microscopy .....	181
4.8 Conclusions.....	184
4.9 Experimental .....	186
4.10 References.....	188
<b>Chapter 5</b> .....	191
Table of Contents .....	192
5.1 Introduction.....	193
5.1.1 <i>In vitro</i> Studies of MOFs.....	193
5.1.2 <i>In vivo</i> Studies of MOFs .....	201
5.1.3 Dichloroacetate, a Metabolic Target.....	203
5.2 Aims .....	205
5.3 Therapeutic Efficiency of the DCA@UiO family .....	207
5.3.1 Therapeutic Efficiency of DCA@MOFs .....	207
5.3.2. Therapeutic Efficiency of 5-FU@DCA@MOFs .....	212
5.4. Postsynthetic Surface Functionalisation of DCA-Loaded Samples.....	216
5.5. Therapeutic efficacy of DCA-Loaded, Surface Modified UiO-66.....	222
5.5.1 MOFs Cytotoxicity Towards HeLa Cervix Cancer Cells .....	222

5.5.2. Cytotoxicity Against MCF-7 and HEK293 .....	228
5.5.3. Cytotoxicity of Free Dichloroacetate .....	232
5.6. Immune System Response Towards Surface Modified UiO-66.....	233
5.6.1. Endocytosis Efficiency Towards J774 Macrophage Cells .....	234
5.6.2. Cytotoxicity Against J774 and PBL Cells .....	235
5.6.3. Reactive Oxygen Species Generation in J774 and PBL Cells .....	237
5.7 Conclusions .....	239
5.8 Experimental .....	242
5.9 Refereces .....	244
<b>Chapter 6</b> .....	248
Table of Contents .....	249
6.1 Conclusions .....	250
6.2 References .....	258
<b>Chapter 7</b> .....	260
Table of Contents .....	261
7.1 Modulators' <sup>1</sup> HNMR .....	262
7.2 Kinetic Fitting of Degradation Profiles .....	265
7.3 Kinetic Fitting of Calcein Release Profiles.....	267

## Table of Abbreviations

~	Approximately
3T3	Mouse fibroblast cell line
5-FU	5-Fluorouracil
A2780	Human ovarian carcinoma cell line
A549	Human lung carcinoma cell line
AcOH	Acetic acid
AL	Alendronate
ATP	Adenosine triphosphate
AZT-TP	Azidothymidinetriphosphate
B16F10	Mouse skin melanoma cell line
BET	Brunauer-Emmett-Teller
BDC	Benzenedicarboxylic acid
Biot	Biotin
BODIPY	Boron dipyrromethene
BPDC	Biphenyldicarboxylic acid
BTC	Benzene tricarboxylic acid
C26	Mouse colon carcinoma cell line
ca.	<i>circa</i> (approximately)
CDV	Cidofovir
CM	Coordination modulation
CT26	Murine colon carcinoma cell line
CuAAC	Copper-catalysed azide-alkyne cycloaddition
CytC	Cytochrome c protein
DBCO	Dibenzylcyclooctyne
DCA	Dichloroacetic acid
DDS	Drug delivery system
DFT	Density functional theory
DLS	Dynamic light scattering
DMF	Dimethylformamide

DMSO	Dimethylsulfoxide
DOPA	1,2-dioleoyl-sn-glycero-3-phosphate
DOPC	1,2-dioleoyl-sn-glycero-3-phospho-choline
DOX	Doxorubicin
DUT	Dresden University of Technology
FA	Folic acid
FACS	Fluorescence assisted cell sorting
FDA	Food and Drug Administration
FR	Folate receptor
H2DC-FDA	2',7'-dichlorodihydrofluorescein diacetate
H460	Human lung carcinoma cell line
HCl	Hydrochloric acid
HeLa	Human cervical cancer cell line
Hep	Heparin
His-tags	Histidine residues
HKUST	Hong Kong University of Science and Technology
HRMS	High-resolution mass spectroscopy
I <sub>2</sub> -BDP	Diiodo-substituted BODIPY
IC <sub>50</sub>	Half inhibitory concentration
IR	Infrared
IRMOF	Isorecticular metal-organic framework
<i>J</i>	Dipole-dipole coupling
K	Kelvin
L929	Mouse fibroblast cell line
LD <sub>50</sub>	Lethal dose
M	Moles per litre
<i>m/z</i>	Mass to charge ratio
MCF-7	Human breast carcinoma cell line
MDA-MB-231	Triple negative breast cancer cell line
MeCN	Acetonitrile
MeOH	Methanol

MFC-10A	Breast epithelial cells
mg	Milligram
MIL	Materials of Institut Lavoisier
mL	Millilitre
MTS	(3-(4,5-dimethylthiazol-2-yl)-5-(3-carboxymethoxyphenyl)-2-(4-sulfophenyl)-2H-tetrazolium)
MTT	3-(4,5-dimethylthiazol-2-yl)-2,5-diphenyltetrazolium bromide
MOF	Metal-organic framework
MPS	Mononuclear phagocytic system
MRI	Magnetic resonance imaging
$M_w$	Molecular weight
n/a	Not applicable
NDC	Naphthalenedicarboxylic acid
NHS	<i>N</i> -hydroxysuccinimide
nm	Nanometre
NMOF	Nanoparticulate metal-organic framework
NMR	Nuclear magnetic resonance
NP	Nanoparticle
PBLs	Phospholipid bilayers
PBS	Phosphate buffered saline
PDT	Photodynamic therapy
PET	Positron emission tomography
PEG	Poly(ethylene glycol)
PNIPAM	Poly( <i>N</i> -isopropylacrylamide)
PolyLact	Poly-L-Lactide
PS	Postsynthetically
PSD	Pore size distribution
PSM	Postsynthetic modification
PXRD	Powder X-ray diffraction
QSDFE	Quenched solid density functional theory
ROS	Reactive oxygen species

SA	Surface area
SALE	Solvent assisted ligand exchange
SANS	Small angle neutron scattering
SBU	Secondary building unit
SEM	Scanning electron microscopy
SKOV-3	Human ovarian cancer cell line
SMMC-7721	Human hepatocellular carcinoma cell line
STEM	Scanning tunnelling electron microscopy
TEA	Triethylamine
TGA	Thermogravimetric analysis
TFA	Trifluoroacetic acid
THF	Tetrahydrofuran
TR-SL	Time-resolved light scattering
UiO	Universitetet i Oslo
UCNPs	Upconverting nanoparticles
UV-Vis	Ultraviolet-visible spectroscopy
ZIF-8	Zeolitic Imidazole Framework-8
XPS	X-ray photoelectron spectroscopy

# Chapter 1

## Introduction

**This Chapter is adapted in part from the following publications:**

“Image-Guided Therapy Using Maghemite-MOF Nanovectors”

*Chem*, 3, (2), 2017, 200-202

**I. Abánades Lázaro** and Ross S.Forgan

“Zirconium Metal-Organic Frameworks in Drug Delivery and Biomedicine”

Submitted

**I. Abánades Lázaro** and R. S.Forgan

## Table of Contents

<b>Chapter 1</b> .....	1
Table of Contents .....	2
1.1. The Use of Drug Delivery Systems (DDSs).....	3
1.2. Metal-Organic Frameworks (MOFs): A Coordination Chemistry Point of View .....	5
1.3. Synthesis of Zr MOFs: Coordination Modulation .....	8
1.4. Metal Organic Frameworks as Carriers for Drug Delivery: Background .....	14
1.5. Surface Modifications of Zr MOFs for Drug Delivery .....	17
1.5.1. Postsynthetic Surface Modifications of Zr MOFs Based on Coordination Chemistry .....	17
1.5.2. Postsynthetic Surface Modifications of Zr MOFs Based on Covalent Chemistry....	20
1.6. Colloidal Dispersion of Zr MOFs under Simulated Physiological Conditions .....	24
1.7. Stability of Zr MOFs under Simulated Physiological Conditions .....	27
1.8. Drug Release Kinetics of Zr MOFs .....	28
1.9. Biocompatibility of Zr MOFs.....	33
1.10 Conclusions and Future Work.....	35
1.11. References .....	36

### 1.1. The Use of Drug Delivery Systems (DDSs)

Cancer is the price the human race has to pay as a consequence of our remarkable evolution. It is estimated that between one third and one half of the developed countries population will be diagnosed with cancer at some point of their life. In this context, developing effective and innovative cancer treatment and diagnosis has become a major priority within the scientific community and revolutionary thinking and design of drugs and their delivery systems may lead to more effective treatments and to its final cure.

Cancer cells are so fast growing because their metabolism differs from healthy cells. In some cancer cells, once glucose has been transformed to two molecules of pyruvate, instead of being transformed to acetylCoA (AcCoA) in the cytosol, entering the mitochondria to undergo oxidative phosphorylation and ATP formation during the Krebs cycle, pyruvate is alternatively transformed to lactate in the cytosol, even in the presence of oxygen. This process is known as the Warburg effect.<sup>1-4</sup> Mitochondria are the primary regulators of apoptosis, or cellular suicide, allowing cancer cells to avoid this process, as well as being able to grow in the absence of oxygen.<sup>1-4</sup> Radiation and chemotherapy are well established treatments for cancer, but these often result in healthy cell damage, as most therapeutics have toxic dose dependence due to a lack of tumour selectivity, consequence of the potency required to overcome the high resistance and invasion of cancer tissue.<sup>5-9</sup> Additionally, some tumours have developed resistance to anticancer drugs such as doxorubicin, 5-fluorouracil (5-FU) or cis-platin.<sup>10-13</sup>

With the aim of circumventing these and other problems associated with available therapeutics, nanotechnology offers the possibility of introducing Trojan horses loaded with anti-cancer drugs which are selectively delivered to damaged cells.<sup>14-18</sup> This may be achieved through local accumulation of drugs in the damaged tissue by targeted delivery and controlled release, offering the best way to minimise side effects and toxicity, while maximizing impact of treatment (Figure 1.1 a).<sup>19-22</sup>

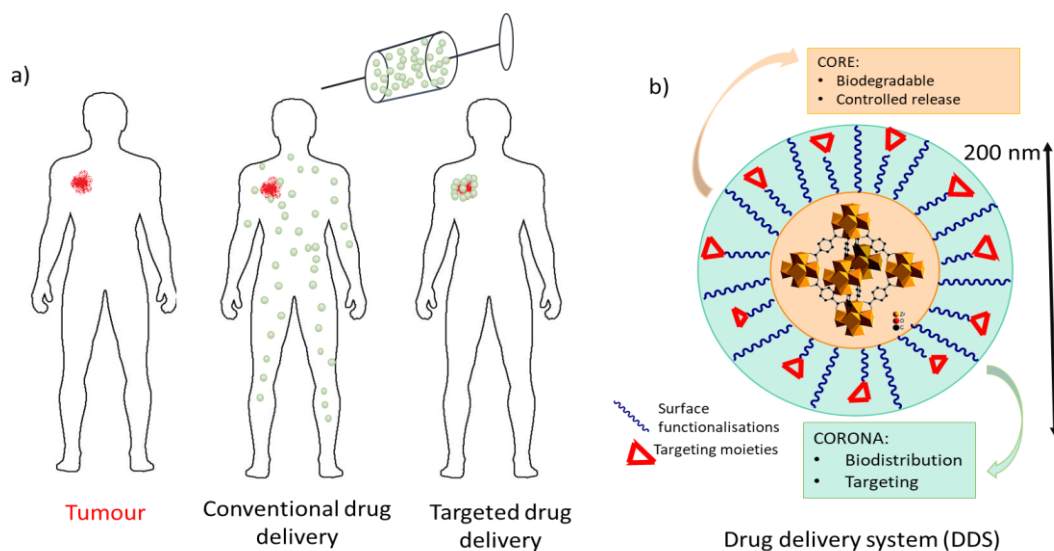


**Figure 1.1.** a) Ideal body distribution of targeted drug delivery compared to conventional drug delivery. b) Composition of a drug delivery system (DDS).

A drug delivery system (DDS) should be designed to avoid any indiscriminate biological interactions, selectively reaching the desired tissue to release the drug at an optimal rate and degrade into non-toxic components while having little to no side effects.

DDSs are generally composed of a core and a corona. The former is designed to control the release of the drugs stored within its pores or covalently attached to its structure, and should be made of pharmacologically degradable material, and the latter, which is responsible for bio distribution and targeting, can be tuned by surface modifications (Figure 1.1 b).<sup>15</sup> In order to test the suitability of the drug delivery process, the drug release should be able to be monitored. Imaging components can be incorporated into the corona by postsynthetic modifications,<sup>23, 24</sup> or in the core as multidentate ligands,<sup>25, 26</sup> metal connecting points (such as  $Gd^{3+}$ ,  $Fe^{3+}$ , and  $Mn^{2+}$ )<sup>27, 28</sup> or stored in the pores.<sup>29, 30</sup>

Cancer cells are known to have enhanced permeability and retention (EPR), thus uptake and accumulation of DDSs are enhanced in cancer over healthy tissue.<sup>31, 32</sup> Cancer cells also contain overexpressed enzymes and receptors on their cell membrane surface, so DDSs can be functionalised with targeting moieties allowing their uptake to be directed to damaged tissue. Hence, DDS have aroused an enormous interest for tailored treatment over the past decade and its approach has been validated in the clinic with the FDA approval.<sup>20</sup>

However, drawbacks such as uncontrollable drug release,<sup>25, 33, 34</sup> usually as a consequence of carrier degradation, or accumulation in the body,<sup>35, 36</sup> often due to macrophage recognition<sup>37, 38</sup> and to low carrier degradation fate,<sup>39, 40</sup> hinder the clinical application of DDSs. Toxicity and biocompatibility are also important factors to take into count when designing a novel DDS,<sup>41-</sup>

<sup>43</sup> together with drug loading capacity and efficient cell internalisation.<sup>44-46</sup> Most available DDSs are purely organic or inorganic, with their own strengths and weaknesses. Purely organic materials such as liposomes, dendrimers or polymers have poor drug payloads compared to purely inorganic materials,<sup>47-49</sup> such as Fe<sub>3</sub>O<sub>4</sub>, Au or silica nanoparticles, but the latter tend to be less biocompatible and easily excreted before reaching their target.<sup>14, 50, 51</sup>

Metal-Organic Frameworks (MOFs) are a new generation of hybrid materials which are promising DDSs candidates. MOFs have properties from organic and inorganic materials, and consequently they have some potential advantages over existing DDSs.<sup>15, 52-57</sup> Owing to their versatile functionality- different reactive groups can be attached to the surface and the linkers can have different functional groups which allow post synthetic modification<sup>58-60</sup>- the drug release kinetics and biological behaviour of MOFs can be modified by post-synthetic modifications.<sup>61-63</sup>

Their properties and cytotoxicity can be tuned through the thoughtful choice of metals and linkers, and they are easily degraded in the body, avoiding side effects from accumulation.<sup>43</sup>

Additionally, due to their remarkable porosity, some of them present exceptional high drug loadings compared to other DDSs.<sup>24</sup>

In summary, the fine control of MOFs' cytotoxicity, drug payload, release and degradation kinetics, cellular internalisation and colloidal stability can be achieved through their structure and surface engineering, making them promising candidates as DDSs and magnetic resonance imaging (MRI) contrast agents.

## **1.2. Metal-Organic Frameworks (MOFs): A Coordination Chemistry Point of View**

Metal-Organic Frameworks (MOFs) are a class of hybrid macromolecules where metal ions or metal clusters, called secondary building units (SBUs), are linked by multidentate spacer ligands through Werner-type coordination chemistry, forming three dimensional, crystalline, porous structures.<sup>64-66</sup> This class of hybrid materials have nearly infinite tunability due to the relatively unlimited choice of metals and organic bridging ligands. Therefore, a tremendous number of MOFs have been reported, and well-studied models such as MOF-5,<sup>67</sup> ZIF-8,<sup>68</sup> (Zeolitic Imidazole Framework-8), the MIL family,<sup>69</sup> (Materials of Institut Lavoisier), or the UiO family, (Universitetet i Oslo),<sup>70</sup> have been a platform for the synthesis of more complex derivative MOFs (Figure 1.2).

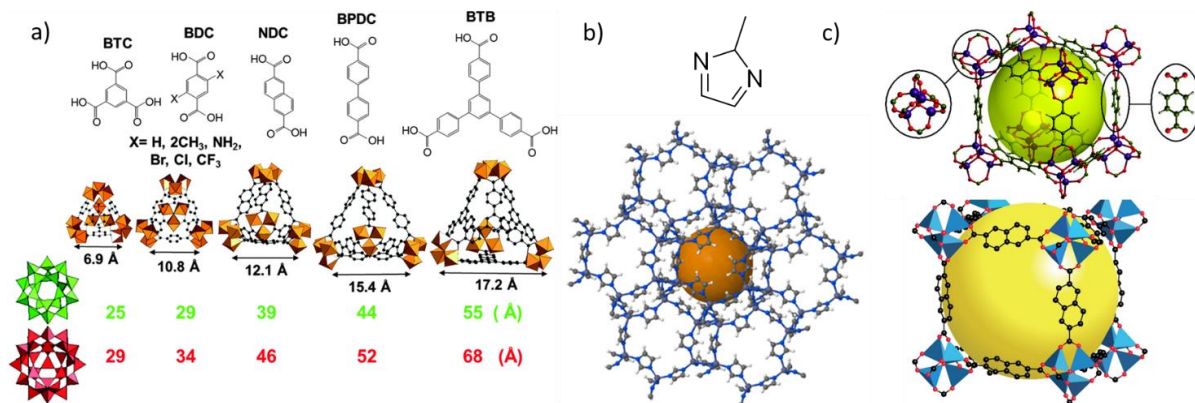


**Figure 1.2.** a) The MIL family, big and small cages (bottom) hybrid supertetrahedra (middle) in functional of the organic linker (top). Iron polyhedra, carbon and oxygen are represented in orange, black and red, respectively.<sup>71</sup> b) ZIF-8 structure, Zn bluish purple, N dark blue, C grey, H white.<sup>72</sup> c) MOF-5 structure where terephthalate ligands link the SBUs (Zn<sub>4</sub>O clusters) (top) and IRMOF-8, analogue of MOF-5, in which extended ligands bridge the SBUs (bottom). The yellow spheres represents the porosity of the framework.<sup>73</sup>

Iron-based MOFs of the MIL family have received widespread attention for healthcare applications due to the low toxicity of iron.<sup>15, 71, 74-76</sup> Particularly, in MIL-101 (iron-terephthalate), which exhibits an extremely large surface area of 5900 cm<sup>2</sup>g<sup>-1</sup>, the SBUs are composed of iron (III) trimers, which are connected together via six terephthalate (1,4-benzenedicarboxylate, BDC) ligands and a  $\mu_3$ -oxo ligand. The SBUs are connected by bdc linkers forming a ‘super tetrahedron’ where the metallic centres have an octahedral environment.<sup>69</sup> The supertetrahedra are arranged forming two highly porous cages with pores of 29 Å and 34 Å diameter. XL analogues of MIL-101 and MIL-100 (Benzene tricarboxylic acid, BTC, as linker) have been synthesised by Horcajada et al (Figure 1.2a).<sup>71</sup>

Zeolitic Imidazole Frameworks (ZIFs) are a class of MOFs that are isomorphic with zeolites. They are composed of tetrahedrally-coordinated transition metal ions, such as Fe, Co, Cu or Zn, connected by imidazole ligands.<sup>77, 78</sup> ZIF-8, illustrated in Figure 1.2b, is composed of Zn ions and 2-methylimidazole ligands, and has a Langmuir surface area of 1,810 m<sup>2</sup>g<sup>-1</sup>, high thermal stability (up to 550°C),<sup>72</sup> and remarkable chemical resistance to boiling alkaline water and organic solvents compared to other MOF structures.<sup>79</sup> Although, due to its acidic instability, ZIF-8 has been studied as an anticancer DDS,<sup>80</sup> its potential cytotoxicity hinders its biomedical applications.<sup>43</sup>

[Zn<sub>4</sub>O(BDC)<sub>3</sub>]<sub>n</sub>, commonly known as MOF-5 or IRMOF-1, (IR stands for isorecticular), is shown in Figure 1.2c. Its structure can be viewed as a derivative of a cube, whose eight corners, Zn<sub>4</sub>O SBUs, are linearly linked by BDC ligands, and it has been widely studied for several applications. Based on the MOF-5 net, IRMOF-10, also known as MOF-10, has the same

topology. It is formed by  $Zn_4O$  nodes linked by 4,4'-biphenyldicarboxylate (BPDC) ligands.<sup>67, 81</sup> IRMOF-16 is also its analogue, possessing *p*-terphenyl-4,4'-dicarboxylate ligands in this case. Logically, the pore size of the series of MOFs increases as the length of the bidentate linkers does.<sup>82</sup>

Zirconium-based MOFs have recently acquired a notable interest as DDS and MRI contrast agents<sup>83</sup> due to their biocompatibility<sup>84</sup> and higher chemical stability compared to late transition metal based MOFs,<sup>85-87</sup> which provides more favourable degradation and drug release kinetics.

The first Zr MOFs were reported by Lillerud et al. in 2008.<sup>70</sup> In the UiO series of isorecticular MOFs, for which UiO-66 was first discovered, the SBUs consist of six zirconium cations forming an octahedron. Each cation is coordinated in a square-antiprismatic geometry by  $\mu_3$ -O,  $\mu_3$ -OH and carboxylate groups. The  $[Zr_6O_4(OH)_4(RCO_2)_{12}]$  octahedral clusters are linked by linear dicarboxylate ligands into extended, highly porous materials with the ideal formula  $[Zr_6O_4(OH)_4(RCO_2)_6]_n$ . These  $Zr_6$  clusters and derivatives serve as secondary building units (SBUs) in the vast majority of Zr MOFs reported to date (Figure 1.3 a).<sup>83, 88-90</sup>

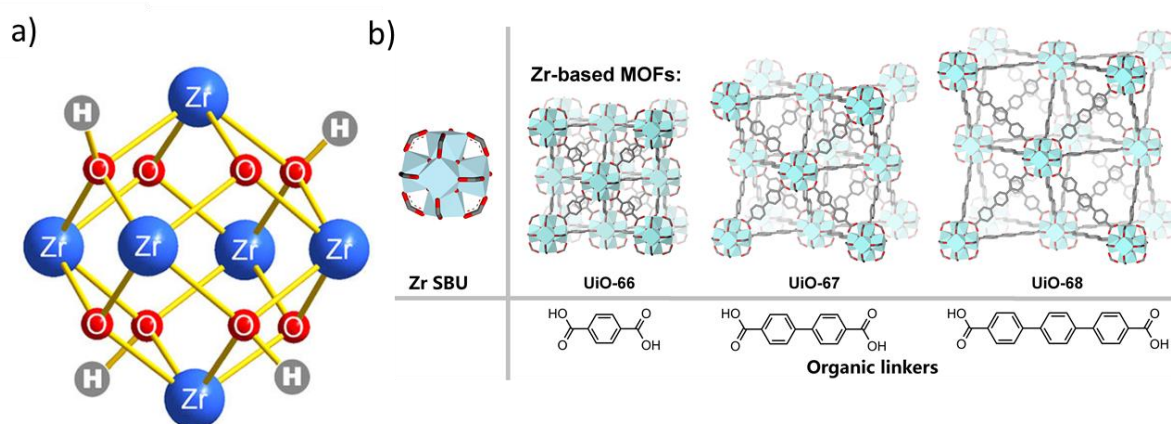


**Figure 1.3.** a) UiO-66 SBU.<sup>91</sup> b) UiO family of isorecticular MOFs with extended linkers in which porosity increases with the length of the organic linker.<sup>92</sup>

The archetypal member of the series, UiO-66, in which the linker is BDC, exhibits a surface area of  $1200 \text{ m}^2\text{g}^{-1}$  and a pore volume of  $0.5 \text{ cc/g}$  when free of defects. Its octahedral and tetrahedral pores have sizes of 11 and  $8 \text{ \AA}$ , respectively, with pore windows of 3 and  $5 \text{ \AA}$ .<sup>70</sup>

A range of ligands have been used to form an isorecticular series, with porosity increasing with ligand length (Figure 1.3 b) until interpenetration occurs with phenylene-bis-ethynylbenzoate linkers.<sup>93, 94</sup> The use of dicarboxylate linkers with anchored pendant functionalities along with the excellent chemical stabilities of the series has allowed various postsynthetic modification (PSM) protocols to be developed.<sup>58, 60, 88, 95</sup>

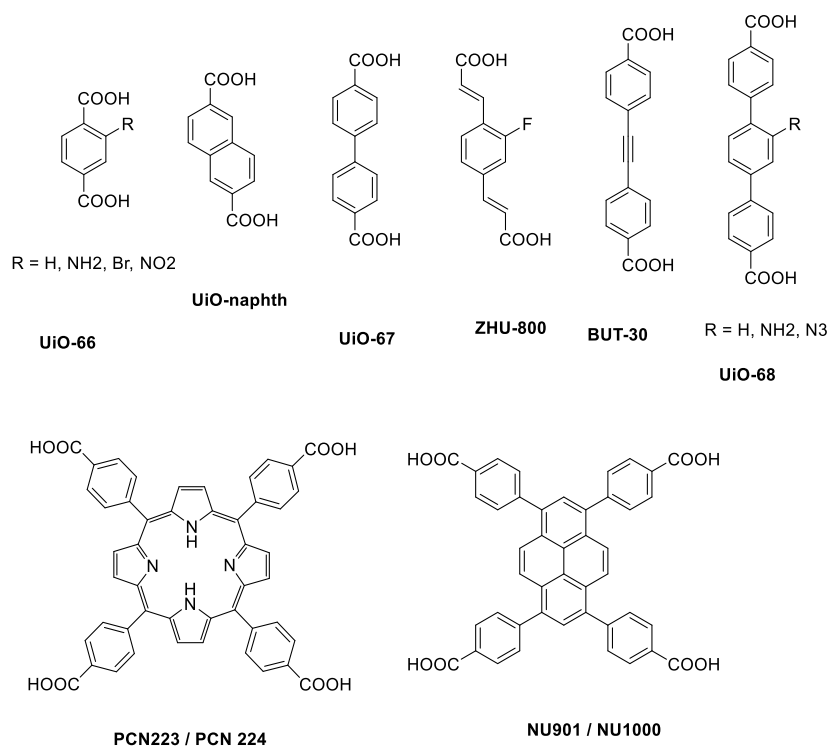


**Figure 1.4.** Zr MOFs linkers discussed during this Chapter.

Zirconium MOFs containing tricarboxylate or tetracarboxylate linkers have been also synthesised. For example, planar tetracarboxylates such as tetrakis(4-carboxyphenyl)porphyrin combined with 6-connected Zr<sub>6</sub> SBUs gives PCN-223 where solvent molecules or modulators cap the free coordination sites, and with 12-connected Zr<sub>6</sub> SBUs gives PCN-224; additives to synthesis tune the formation of the different MOFs.<sup>26, 96</sup> Similarly, the structurally related 1,3,6,8(tetrakis(*p*-benzoate)pyrene) ligand, when linked by 8-connected Zr<sub>6</sub> SBUs, leads to both NU-901 and NU-1000 MOFs.<sup>97</sup>

A wide variety of other Zr MOFs are known, but this thesis is focused on the above examples, shown in Figure 1.4, due to their potential for use in biomedical applications.

### 1.3. Synthesis of Zr MOFs: Coordination Modulation

The synthesis of Zr MOFs is usually carried out under solvothermal conditions,<sup>98-103</sup> although other synthetic routes have also been reported.<sup>83, 98, 104, 105</sup> Solvothermal synthesis is sensitive to several factors, such as pH, concentration, temperature, pressure, reaction time or stoichiometry among others. These parameters can be tuned to adjust the crystallisation process and obtain MOFs of various sizes.

The coordination modulation protocol- first reported by Fisher and co-workers for Zn MOFs<sup>106-</sup> in which monodentate ligands (modulators) with similar chemical functionality to the

multidentate organic linkers are introduced to the synthetic process, has been widely used as a tool to control size and enhance MOFs properties such as crystallinity.<sup>92, 100, 107-109</sup>

Fisher et al studied the modulated synthesis of MOF-5 (Zn-terephthalate) in presence of 4-n-decylbenzoic acid.<sup>106</sup> The particles were synthesized by mixing a pretreated solution containing a molecular precursor providing the SBUs, which causes persistent nucleation and growth, and a solution containing the ligand. Following the process with time-resolved light scattering (TR-SLS) and small angle neutron scattering (SANS) among other techniques, the authors provided rationale insights of MOF-5 coordination modulation process, comparing it with the solvothermal induced process. The crystallization process was affected by the molar ratio of the components, resulting in lower crystallization process when an excess of the building units or modulator was used. SANS and light scattering results showed that the presence of the modulator does not affect the morphology and nature of the final particles in this case.

The addition of monodentate ligands, such as acetic acid, benzoic acid and derivatives among others, influences the coordination equilibrium through competition with the multidentate bridging MOF linkers for the metal clusters coordination sites during the crystallisation process, in some cases favouring the crystal growth of certain crystal faces and enabling the synthesis of alternative morphologies (Figure 1.5).<sup>110</sup>

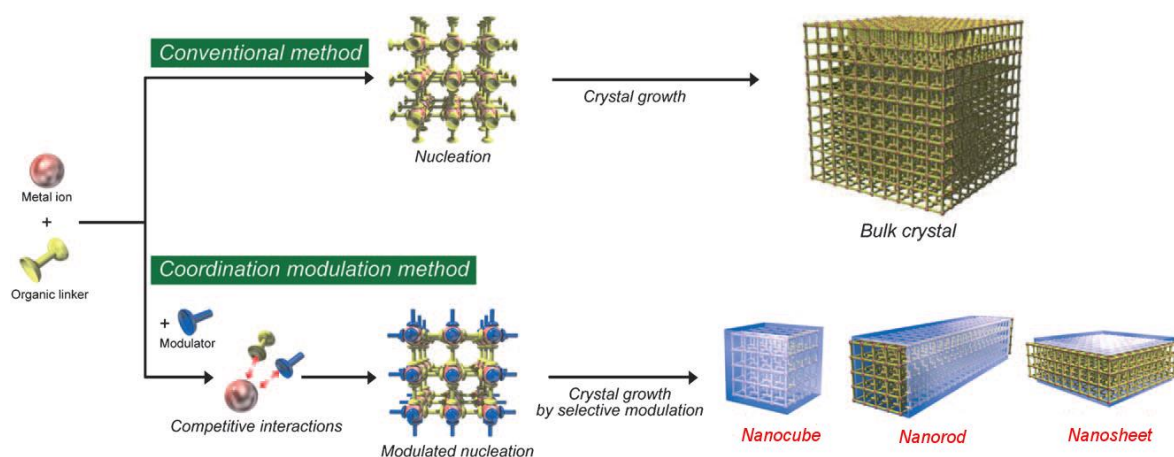


**Figure 1.5.** Comparison of conventional and coordination modulation MOF synthesis. Selective crystal faces modulation results in direct MOF synthesis of different morphologies.<sup>110</sup>

In this process, the monodentate ligands can act in two different ways. On the one hand, if it acts as a crystal growth promoter the size of the crystal will depend on the concentration of the modulator.<sup>102, 111, 112</sup> On the other hand, if it acts as a capping agent, its functionality will be confined to the surface, being permanently coordinated to metal sites and thus inhibiting crystal growth.<sup>107, 113</sup> Therefore, this technique can be wisely used to control not only the particle size of the MOFs<sup>100</sup> - scaling down the size of DDSs to <200 nm is imperative for

intravenous administration in order to ensure circulation through small capillaries without blockage - but also the surface chemistry during the synthetic process (Figure 1.6 a). However, the role and effect of the modulator during synthesis is difficult to predict.<sup>114</sup>

For example, Kitagawa et al reported the acetic acid modulated synthesis of a copper framework  $[\{Cu_2(ndc)_2(dabco)\}_n]$  (ndc=1,4-naphthalene dicarboxylate; dabco=1,4-diazabicyclo[2.2.2]octane).<sup>110</sup> In this anisotropic framework the dicarboxylate ligands link the copper clusters forming two-dimensional lattices, which are further connected by the amine pillar ligands forming a three dimensional framework. It was found that addition of acetic acid resulted in face selective modulation. One of the coordination modes (ndc carboxylate - copper) was inhibited by the capping of acetate groups, while the dabco nitrogen -copper coordination was favored, allowing the formation of nanorods. Lui and Guo studied the effect of both acid-base environment of the reaction medium and the addition of capping agents to a copper-BTC MOF, HKUST-1 (where HKUST-1 stands for Hong Kong University of Science and Technology), synthesis under hydrothermal conditions (water/ethanol) using different modulators: sodium formate, sodium acetate and triethylamine (TEA).<sup>115</sup> The addition of carboxylate salts (capping agents) to the reaction mixture drastically reduced the particle size compared to the unmodulated MOF. For example, upon addition of 1 equivalent of sodium formate the MOF particle size was reduced from 20 micrometers (when unmodulated) to 300 nm, and further decreased as the equivalents of capping agent were increased, until the fourth equivalent, where new peaks appeared in the PXRD diffraction pattern, indicating the formation of a new phase.

Increasing the pH of the reaction mixture leads to faster deprotonation of the linkers. Thus a basic modulator can speed up the crystallization process affecting the nucleation and growth processes through both coordination and deprotonation equilibriums (Figure 1.6 b).<sup>107</sup> HKUST-1, modulated with addition of TEA, which does not have a carboxylate coordination site to act as capping agent, resulted in nano crystals with a size of 200-250 nm, which were packed forming hierarchical octahedral-shape crystals with a diameter of 2.5-3 micrometers.<sup>115</sup>

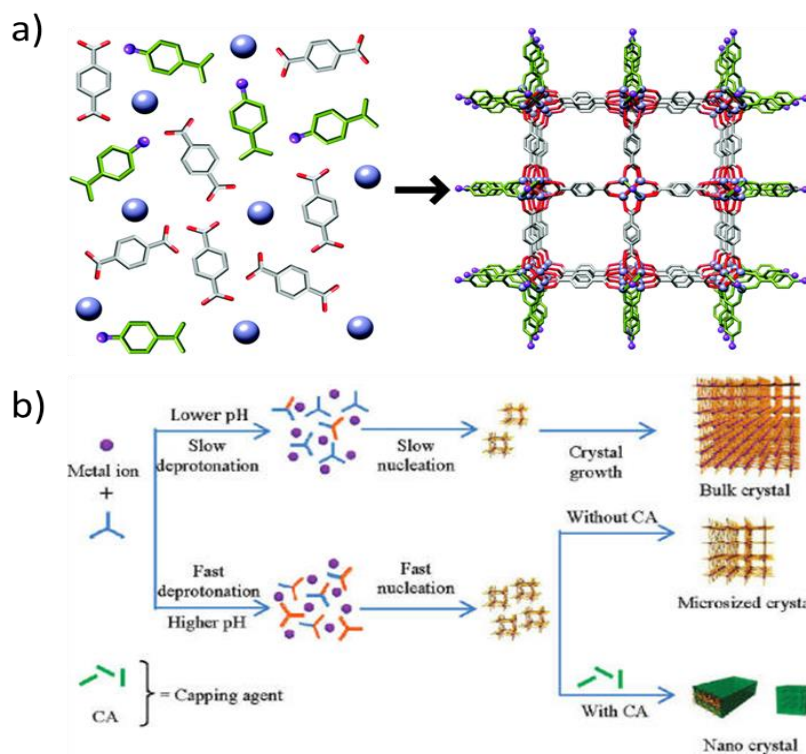


**Figure 1.6.** a) Ideal attachment of functionalised monocarboxylate modulator, inhibiting crystal growth.<sup>61</sup> b) Schematic representation of pH effect in nucleation and crystal growth of MOFs depending of pH and capping agents.<sup>107</sup>

Coordination modulation of Zr-based MOFs has been widely studied, showing different behaviors upon addition of modulators. The first study of Zr MOFs coordination modulation was performed by Behrens *et al.*, who used benzoic acid, acetic acid and water as modulators of Zr MOFs of the UiO family, demonstrating size-control by varying the amount of modulator added.<sup>100</sup> Benzoic acid affected both size and morphology of UiO-67 crystals, enhancing crystallinity and increasing crystallite size with the amount of benzoic acid added during synthesis. The authors attributed the size increase to the in-situ formation of Zr-benzoic acid complexes, which reduce the nucleation rate. In contrast to other carboxylate containing modulators, which act as capping agents,<sup>113</sup> benzoic acid did not get permanently attached to UiO-66 Zr<sub>6</sub> clusters after synthesis, acting as a guest and getting trapped in the MOF pores (Figure 1.7).<sup>100</sup>

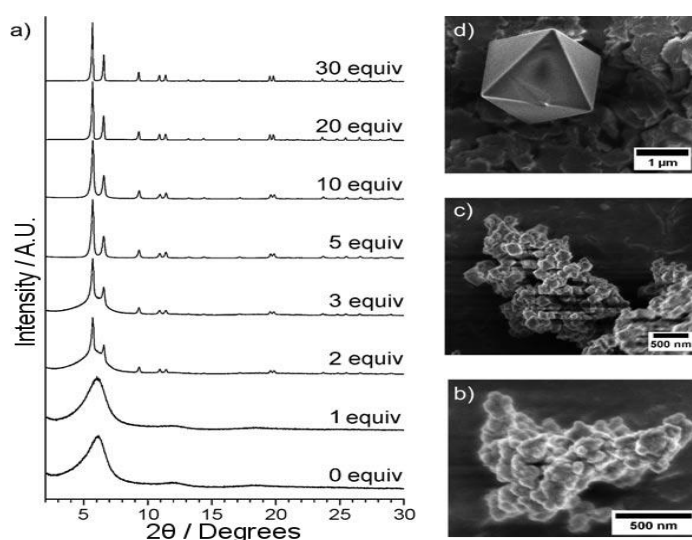


**Figure 1.7.** a) PXRD patterns of UiO-67 modulated with different equivalents of benzoic acid. SEM images of UiO-67 modulated with b) 0, c) 3 and d) 30 equivalents of benzoic acid, showing a transition from amorphous aggregates to individual octahedral micro crystals.<sup>100</sup>

Modulators are known to induce missing linker and missing cluster defects in Zr MOFs by capping SBUs and replacing multidentate ligands throughout the bulk of the material.<sup>92</sup> Despite defects representing a type of structural “imperfection” they can result in improved properties, such as boosting the MOFs porosity. Defects can modify a number of physical properties, including chemical and mechanical stability (Figure 1.8).<sup>103, 108, 116-118</sup>

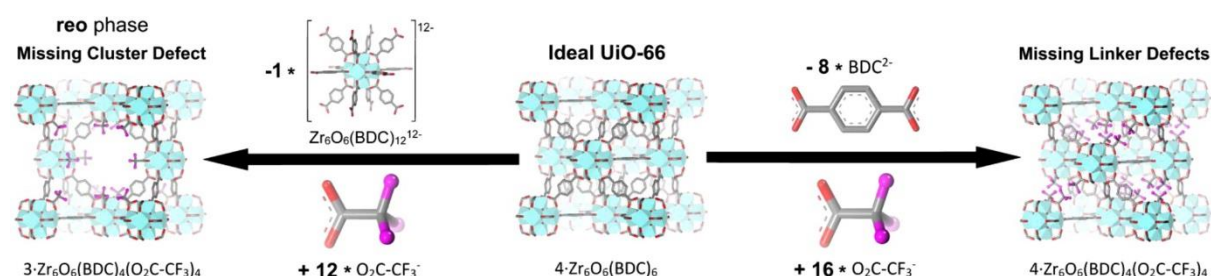


**Figure 1.8.** Schematic representation of ideal and defective (missing linkers or missing clusters) UiO-66 structures. Missing cluster defect yields in the reo topology in which one missing cluster is compensated by 12 trifluoroacetate modulators, while 8 missing linkers are compensated by 16 trifluoroacetate modulators.<sup>92</sup>

The first detailed investigation of missing linker defects was reported by the Zhou group, using acetic acid as a modulator of UiO-66 synthesis.<sup>116</sup> In contrast to HKUST-1 AcOH modulated synthesis,<sup>115</sup> enhanced crystal growth and promoted defects were found upon UiO-66 AcOH modulation.<sup>116</sup> An increase in surface area and pore volumes (ranking from 0.44 cc/g to 0.65 cc/g) was observed as AcOH concentration increased. Interestingly, when the reaction time was increased from one to two days, the pore volume increased to 1 cc/g. Color change was observed as porosity increased, indicating that changes in the electronic band structures were

occurring. Through inelastic neutron scattering experiments, acetate groups were observed, indicating partial incorporation of acetic acid to the MOF structure as a compensation for missing linkers (Figure 1.9).<sup>116</sup>

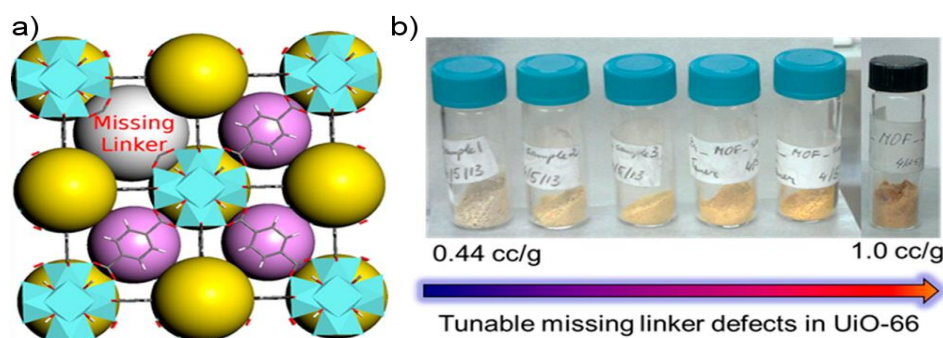


**Figure 1.9.** a) Representation of missing linker defects. b) Color change as missing linker defects increase as a consequence of acetic acid addition.<sup>116</sup>

Similarly, Vermoortele et al reported extremely porous UiO-66 when modulated with trifluoroacetic acid (TFA), with missing linkers compensated by modulators attachment, and used them for catalytic purposes.<sup>119</sup> Farha and co-workers reported the effect of introducing hydrochloric acid to UiO-66 and UiO-67 MOFs synthesis, resulting in highly defective samples with hysteresis loops characteristic of mesoporous materials.<sup>99</sup> Indeed, the MOFs had 4 out of 12 missing linkers, as determined by TGA and N<sub>2</sub> adsorption and desorption measurements among other techniques, resulting in 8-connected nodes instead of 12-connected nodes.

Missing cluster defects were first reported by Goodwin et al, showing that using formic acid as a modulator of UiO-66 synthesis results in nanoregions of missing clusters with 8-connectivity, denominated reo topology, within UiO-66 (Figure 1.8).<sup>116</sup>

Taking into account the wide variety of defects induced by the modulation of UiO-66 using different monocarboxylates as modulators, Lillerud and co-workers performed a detailed coordination modulation study based on the acidity of monocarboxylate modulators- acetic acid ( $pK_a$  4.8), formic acid ( $pK_a$  3.8) difluoroacetic acid ( $pK_a$  1.24) and trifluoroacetic acid ( $pK_a$  0.23)- introduced to UiO-66 synthesis.<sup>92</sup> The authors found an increase in porosity as the concentration of modulator increased, but more importantly as the  $pK_a$  of the modulator decreases, ultimately resulting in mesoporosity when 6 equivalents of TFA are added to the synthetic mixture. The incorporation of formate as compensating ligand for missing linkers was identified in the acid-digested proton nuclear magnetic resonance (<sup>1</sup>HNMR), even when formic acid was not used during synthesis, but coming from DMF hydrolysis during synthesis. Incorporation of the modulators used during synthesis was also observed, more noticeable for lower  $pK_a$  carboxylates. The authors found evidence that missing clusters were the most

predominant defects when monocarboxylates are used as modulators of UiO-66, which are compensated by the attachment of the former (Figure 1.10).<sup>92</sup>

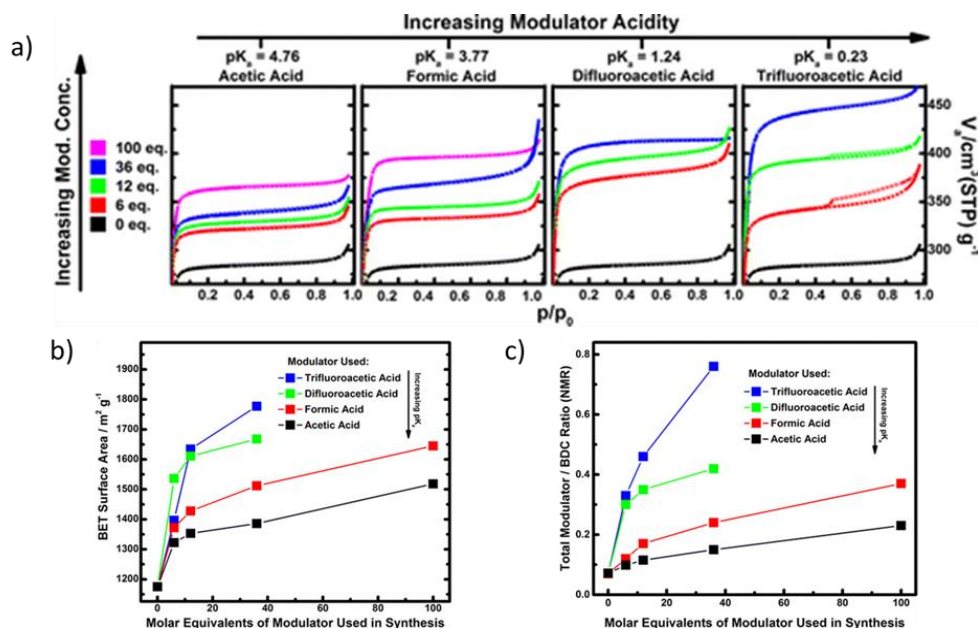


**Figure 1.10.** UiO-66 a) nitrogen adsorption and desorption isotherms b) surface area c) incorporation of modulator - depending on modulators'  $pK_a$  and the number of equivalents of modulator added during UiO-66.<sup>92</sup>

Importantly for healthcare applications, Mirkin et al have found that the  $pK_a$  of the modulator also affects the colloidal stability of the MOF as a consequence of the defects induced through modulator attachment, generating highly charged nanoparticles (measured by zeta potential), which when dispersed in a solvent suffer from higher repulsion between each other (See section 1.6).<sup>120</sup>

In summary, the coordination modulation protocol can be used to tune size, crystallinity, porosity, surface chemistry and colloidal stability of MOFs among other properties. It is clear that more acidic monocarboxylates have a stronger effect due to the higher competition for the metal clusters coordination sites, yielding in highly porous (defective), and consequently, colloidal stable nanoMOFs. Since modulators attachment to the Zr clusters is also governed by their  $pK_a$ , one-pot synthesis surface functionalisation could be achieved by coordination modulation.

#### 1.4. Metal Organic Frameworks as Carriers for Drug Delivery: Background

Since 2006, when Ferey and co-workers reported the first study of iron-based MOFs for applications in biomedicine,<sup>55</sup> a tremendous amount of work has been developed towards MOFs various potential uses in healthcare.<sup>121</sup> Iron MOFs are probably the most widely studied

MOFs for healthcare applications to date; this is largely due to iron being well tolerated by the body, with rat oral lethal dose 50% (LD<sub>50</sub>) of 30 gkg<sup>-1</sup>, while their high porosity enables very large drug loadings.<sup>15, 34</sup>

The MIL family has raised special interest for healthcare applications and a remarkable amount of high quality research has been focused on their biological applications.<sup>15, 74, 75, 122</sup> Antivirals such as azidothymidinetriphosphate (AZT-TP) and cidofovir (CDV) have been trapped into MIL-101(Fe) and MIL-101-(Fe)-NH<sub>2</sub> with remarkable high loadings (> 40 % w/w).<sup>15</sup> This could be explained due to the fact that the open metal sites have high affinity for the phosphates presents in the CDV and AZT-TP, as Doxorubicin loadings, which does not have phosphate groups, were remarkably lower (ca. 10 % w/w). On the other hand, NMOFs with smaller pores, such as MIL-53 and MIL-88A, have smaller drug payloads (<1 % w/w) due to the fact that the molecules do not have access to the pore, likely staying on the surface.<sup>15</sup>

Lin and co-workers synthesised MIL-101(Fe)-NH<sub>2</sub>, Fe<sub>3</sub>-(μ<sub>3</sub>-O)Cl(H<sub>2</sub>O)<sub>2</sub>(BDC)<sub>3</sub> and an analogue containing a mixture of BDC (82.6%) and 2-aminoterephthalic acid (NH<sub>2</sub>-BDC) (17.4%).<sup>57</sup> The pendant amino functionality was used to covalently attach a fluorescent dye (boron dipyrromethene, BODIPY) or a cisplatin prodrug through amide formation. BODIPY and cis-platin release under simulated physiological conditions was shown to be fast, suggesting MOF instability. Thus, silica coating was used to enhance their stability and to satisfactorily slow down the drug release. To selectively direct the MOFs uptake to cancer cells, a targeting peptide for angiogenic tumours, c(RGDfK) was postsynthetically attached to the silica shell (Figure 1.11).<sup>57</sup>

This example highlights the importance of MOF design and post-synthetic functionalisation for drug delivery applications, and it proves the high potential of selected NMOFs to selectively deliver contrasts agents and anticancer drugs to cancer cells. However, silica coating has cytotoxic disadvantages,<sup>36, 123</sup> and its in vivo potential is truncated by their rapid excretion.<sup>14,</sup>

50

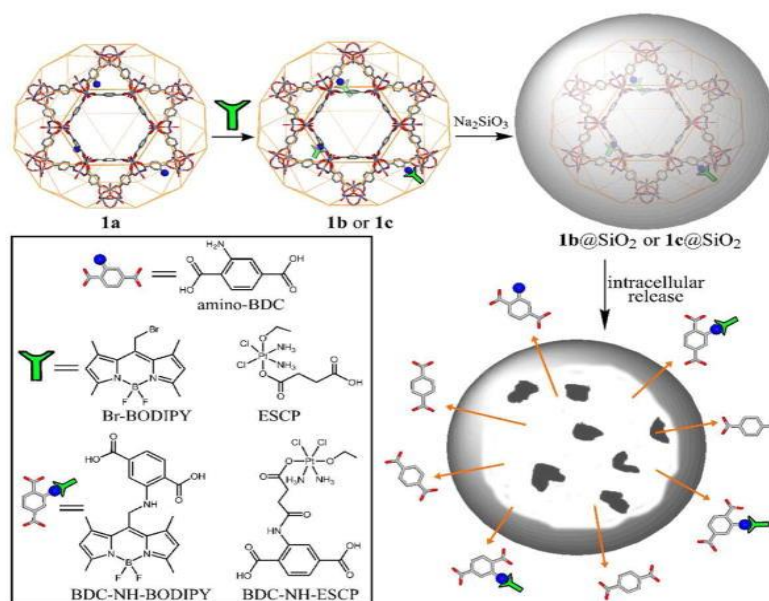


**Figure 1.11.** Schematic representation of MIL-101-NH<sub>2</sub> post-synthetic modifications for drug delivery.<sup>57</sup>

Zirconium-based MOFs have recently acquired a notable interest for biomedical applications, as Zirconium is a biocompatible metal: the human body typically contains about 300 mg of Zirconium, and the recommended daily ingestion is 3.5 mg per day. The lethal dose (LD<sub>50</sub>) of zirconyl acetate in rats, as determined by *in vivo* experiments, has been found to be 4.1 g kg<sup>-1</sup>, which is comparable to iron.<sup>84</sup> Additionally, the hard Lewis acid/base coordination nature of Zr-carboxylate bonds makes them more chemically and mechanically stable than iron, and other MOFs.<sup>86, 87, 90, 96, 108, 124</sup>

For example, core-shell iron oxide-MOF nanoparticles have been proposed as dual anti-cancer therapeutics and MRI contrast agents.<sup>125</sup> Fe<sub>3</sub>O<sub>4</sub>@UiO-66-NH<sub>2</sub> core (150 nm)-shell (2, 25, 50 nm) nanoparticles were synthesised through growth of UiO-66-NH<sub>2</sub> on Fe<sub>3</sub>O<sub>4</sub> surface, which was terminated with carboxylic acid groups. The core-shell NMOFs exhibited strong superparamagnetic behaviour, suggesting their use as optimal T<sub>2</sub>-contrast agents retaining the core iron oxides properties, only with minor decrease in saturation magnetisation from 69.7 emu/g to 51.6 emu/g, consequence of the MOF coating. Fe<sub>3</sub>O<sub>4</sub>@UiO-66-NH<sub>2</sub> has high transverse relaxivity ( $r_2$ ) of 255.9 Mms<sup>-1</sup>,<sup>125</sup> considerably higher than some clinical Fe-based T<sub>2</sub>-weighed contrast agents.<sup>126</sup>

Examples of Zr MOFs for healthcare applications are emerging in the literature and will be further discussed during the course of this Chapter.

## 1.5. Surface Modifications of Zr MOFs for Drug Delivery

The surface chemistry of a given DDS governs its interaction with the media, improving stability and dispersion, and providing the possibility of targeted carriers. As such, surface modifications are of great interest for the development of efficient DDSs, however, the multiple synthetic steps – synthesis, drug loading and surface modification – and the requirement for orthogonality between them, can hinder the efficient manufacture of DDSs. Surface modification of MOFs can be performed during synthesis, by the coordination modulation (CM) protocol, or postsynthetically (PS). Postsynthetic surface modification can be categorised into (i) coordinative PSM, whereby the coordination chemistry of metal clusters at the particle surface is used to attach functionality, for example by surface ligand exchange, or (ii) covalent PSM, usually performed using the linker functionality as a platform for further reactions, such as click chemistry.<sup>60, 61</sup>

### 1.5.1. Postsynthetic Surface Modifications of Zr MOFs Based on Coordination Chemistry

Zirconium SBUs are susceptible to nucleophilic attack. Hence zirconium MOFs can be functionalised through coordination to Zr<sub>6</sub> SBUs, and thus nucleophilic functional groups such as carboxylates,<sup>127</sup> phosphates,<sup>26</sup> and imidazoles,<sup>128</sup> among others have been used to confine functionalities to the surfaces of Zr MOFs directly through coordination to the unsaturated Zr positions available on the surface (Table 1.1). This type of PSM typically requires size selectivity in order to address only the outer MOF surface, as if the reagents can penetrate the porosity, the inner surface of the MOF can also be functionalised during the process. The new functionality may coordinate to unsaturated Zr SBUs or displace surface linkers in a process previously termed surface ligand exchange.

The solvent-assisted ligands exchange (SALE) protocol has been used to introduce linkers to MOFs structures that were not able to be successfully formed during one-pot synthesis. For example, Wang *et al.* have shown that a carboxyl-functionalised diiodo-substituted BODIPY (I<sub>2</sub>-BDP) can be postsynthetically incorporated onto the surfaces of UiO-66, by heating the two in DMF at 65 °C for 24 h, without compromising the topology or porosity of the crystal.<sup>23</sup> The optical properties of the BODIPY functionality led to the MOF being studied for photodynamic therapy (PDT) and thus it was termed UiO-PDT. Comprehensive characterisation showed that the content of I<sub>2</sub>-BDP in the 70 nm nanoparticles of UiO-66-PDT was around 30% w/w, with the measured BET surface area of 1422 m<sup>2</sup>g<sup>-1</sup> confirming the anchoring of I<sub>2</sub>-BDP at the external surfaces rather than loaded in the pores. Park *et al.* have taken a similar approach to attach two different surface molecules – a porphyrin and a dithienylethene – to UiO-66

nanoparticles in a range of ratios.<sup>129</sup> Again, these optically active conjugate materials were assessed for PDT.

**Table 1.1.** Literature examples of Zirconium MOFs functionalised by postsynthetic surface coordination.

MOF	Surface coating	Surface modification	Drugs	Name during the review	Enhanced properties
UiO-66	BODIPY	SALE	Linker singlet oxygen generation	UiO-PDT <sup>23</sup>	Singlet oxygen generation Cell internalisation
UiO-66	Flavin mononucleotide (FMN)	PS Phosphate coordination	Alendronate (AL) 51.4 % w/w	AL-UiO-66-FMN <sup>24</sup>	pH-responsive drug release Cytotoxicity
UiO-66 UiO-67 BUT-30	1,2-dioleoyl-sn-glycero-3-phosphate(L-DOPA)	PS Phosphate coordination	-	DOPA-UiO-66 DOPA-UiO-67 DOPA-BUT-30 <sup>130</sup>	Dispersion
UiO-68-NH <sub>2</sub>	SiRNA	PS Phosphate coordination	Cis-platin (12.3 % w/w)	SiRNA@UiO-Cis <sup>131</sup>	Dispersion Cell uptake Gene silencing Overcome cis-platin resistance
PCN-223	Phospholipid bilayers (PBLs) DOPC/DOPC	PS Phosphate coordination/ Self-assembly	Linker singlet oxygen generation	PCN-223@DOPC PCN-223@DOPC/DOPC <sup>26</sup>	Stability towards PO <sub>4</sub> <sup>3-</sup> Dispersion Intracellular bio stability
Zr-fumarate	Histagged peptides	PS imidazole coordination	Pro-apoptosis peptides	Zr-fum-peptide <sup>128</sup>	Cell uptake Cytotoxic effect
PCN-224	Folic acid (FA)	PS coordination	Linker singlet oxygen generation	PCN-224-FA <sup>127</sup>	Drug release Cell uptake Therapeutic efficiency

In 2014, Lin<sup>131</sup> and Shi<sup>24</sup> independently reported the use of phosphate groups to coordinate biomolecules to the available zirconium clusters on the surfaces of MOFs. Shi et al took advantage of the phosphate affinity for the Zr SBUs of UiO-66 to attach the amino-biphosphonate Alendronate (AL) for the treatment of bone cancer.<sup>24</sup> The resultant MOF, AL-UiO-66, had very high drug loadings (51.4% w/w) compared to previously reported DDS (37 w/w %). The sample was fully characterised and showed a drastic decrease in porosity after loading, while FT-IR spectra showed appearance of shifted AL characteristic vibration bands and new signals attributed to P-O-Zr stretching. The combination of the results suggests that AL was coordinated to the Zr positions in the outer and inner surface of the MOF, which was confirmed by O1s XPS spectrum of the materials, explaining the high drug payloads as a consequence of the high affinity of Zr clusters for AL. The authors also functionalised UiO-66 surface with fluorescent molecules of flavin mononucleotide (the phosphorylated form of vitamin B2) using the same principle, thus forming UiO-66-FMN, which was used to explore intracellular imaging. The difference in size of flavin mononucleotide compared to alendronate ensured that the flavin was confined to the surface as it could not penetrate the pores.<sup>24</sup>

Lin and co-workers studied the attachment of small interfering RNA (siRNA), through the phosphate groups present on its backbone, to the  $Zr^{4+}$  cations present on UiO-68-NH<sub>2</sub> surface, after loading the pores with a cis-platin prodrug. The authors further used this highly specialised MOF named **siRNA-UiO-Cis** for siRNA and cis-platin co-delivery. (Figure 1.12)<sup>131</sup>

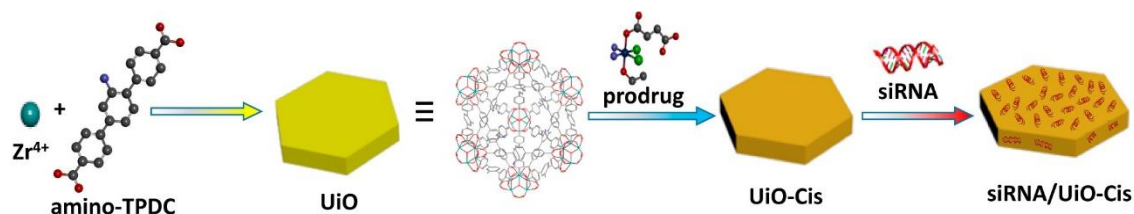


**Figure 1.12.** Schematic representation of siRNA-UiO-Cis synthesis and drug loading.<sup>131</sup>

Later, in 2015, Mirkin and co-workers studied the use of phosphate coordinating groups in order to functionalise the surface of three different zirconium MOFs, UiO-66, UiO-67 and BUT-30 (in which (4,4'-ethylene-1,2-diyl)dibenzoic acid is the MOF linker), with a phospholipid through PSM.<sup>130</sup> Importantly, in this isorecticular family of MOFs the density of zirconium clusters present in the surface decreases as the length of organic linker increases, and thus the content of 1,2-dioleoyl-sn-glycero-3-phosphate (DOPA), determined by ICP-MS, was higher for DOPA-UiO-66 and lower for DOPA-BUT-30. Similarly, the surface selectivity of the functionalisation, driven by the size of the DOPA units, was confirmed when smaller DOPA-functionalised nanoparticles of each MOFs, in which the surface to bulk ratio is higher, had higher DOPA content. In other words, it was found that DOPA density correlates with the density of metal nodes in the outer surface. The samples were fully characterised, showing that after DOPA functionalisation the MOFs maintained their porosity, with FT-IR shifts again suggesting Zr-O-P coordination.<sup>130</sup>

This protocol was later extended by Mirkin *et al.* into a general procedure for functionalising Zr MOFs with oligonucleotides through phosphate coordination.<sup>132</sup> A number of Zr MOFs with different topologies and connectivity were examined, and a correlation was again found between surface SBU density and surface oligonucleotide coverage. The connectivity of the Zr SBU also mediates surface coverage; MOFs with more highly connected clusters have more surface defects due to coordinative unsaturation, allowing greater binding of surface phosphates.<sup>132</sup>

More recently, the zirconium-phosphonate interaction has been exploited for the synthesis of Zr-based MOFs grafted by phospholipid bilayers (PBLs). In this case, a porphyrin MOF, PCN-223, was postsynthetically coated with 1,2-dioleoyl-sn-glycero-3-phospho-choline (DOPC) in order to create a monolayer via coordination Zr-O-P, forming nanoPCN-223@DOPC, which was further coated with cholesterol and DOPC, creating a hydrophobic system in which coated

MOFs and DOPC chains further self-assemble into supported MOFs-PBLs, so called nanoPCN-223@DOPC/DOPC (Figure 1.13).<sup>26</sup> The formation of PBLs was confirmed by negative staining with uranyl acetate, due to strong interaction between phosphate and uranyl groups, among other characterisation techniques, such as FT-IR spectroscopy, Zeta potential measurement and X-ray photoelectron spectroscopy (XPS).

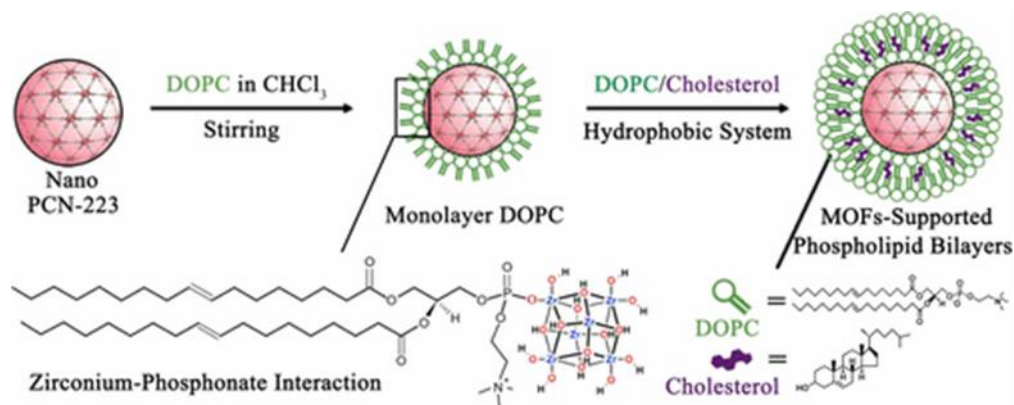


**Figure 1.13.** Representation of nanoPCN-223@DOPC and nanoPCN-223@DOPC/DOPC synthesis.<sup>26</sup>

Beside phosphate groups, the use of imidazole coordinating agents has recently been reported for the bio applications of a Zr-fumarate MOF.<sup>128</sup> Once more, the use of a Lewis base, in this case the imidazole groups present in the histidine residues (His-tags) of several peptide sequences, was used to address Zr-MOFs surface with bio molecules. It was proved that the higher the number of histidine residues in the peptide, the higher the binding to the MOF and thus the authors used a series of peptides containing 6 histidine residues (H<sub>6</sub>-Tags) to coat Zr-fumarate surface to further study their bio applications.

### 1.5.2. Postsynthetic Surface Modifications of Zr MOFs Based on Covalent Chemistry

Surface functionalisation can also be achieved through covalent postsynthetic modification, through chemical transformation of pendant functionalised groups present in the organic linkers of MOFs. In 2010, the amino group of UiO-66-NH<sub>2</sub>, in which terephthalic acid is substituted by 2-aminoterephthalic acid during synthesis, was first used for PSM.<sup>88, 89</sup> The amino group was reacted with a series of anhydrides and the conversion was monitored by <sup>1</sup>HNMR spectroscopy of acid digested samples. It was proved that higher conversion rates were obtained for smaller anhydrides, as a consequence of reaction with amino groups present in the core of the structure, while larger anhydrides were limited to functionalisation at the surface, a consequence of the size selectivity of the process to achieve only outer surface functionalisation. Since then, the amino functionality has been widely used for PSM for a variety of applications, including drug delivery (Table 1.2).

**Table 1.2.** Literature examples of Zirconium MOFs functionalised by covalent PSM

MOF	Surface coating	Surface modification protocol	Drugs	Name during the review	Enhanced properties
UiO-66-NH <sub>2</sub>	PNIPAM-NHS <sup>72</sup>	PS Succinimide ester amide coupling	Resorufin Caffeine Procainamide	UiO-66-PNIPAM <sup>133</sup>	On-off temperature release
UiO-66-N <sub>3</sub>	DABCO-DNA <sup>75</sup>	PS click chemistry	-	UiO-66-DNA conjugate <sup>134</sup>	Stability and dispersion
Zr <sup>89</sup> UiO-66	Pyrene-derived PEG (py-PEGA-PEG) with maleimide residue Targetic peptide (F3)	Pi-pi interaction Peptide conjugated to maleimide through cysteine residue	Doxorubicine (DOX)	DOX@ <sup>89</sup> Zr-UiO-66-py-PGA-PEG-F3 <sup>135</sup>	pH –responsive drug release Cell uptake Positron emission tomography (PET)
UiO-68-N <sub>3</sub>	DNA conjugates -Cytosine-rich sequence -C-rich seq +nucleolin binding aptamer (AS1411)	DABCO copper free click chemistry	DOX Mehtylen blue Rhodamine 6G	UiO-68-N <sub>3</sub> -DNA-C UiO-68-N <sub>3</sub> -DNA-C – AS1411 <sup>30</sup>	pH responsive drug release Anti-cancer targeting
UiO-68-N <sub>3</sub>	1. Nucleobase acting as substrate 2. DNAzyme	1. Copper free click chemistry 2. Enzyme-substrate binding	DOX	UiO-68-N <sub>3</sub> -DNAzyme <sup>30</sup>	Metal-ion responsive drug release Anti-cancer targeting

For example, poly(*N*-isopropylacrylamide) (PNIPAM) chains have been attached to the amino groups present in UiO-66-NH<sub>2</sub> through amide coupling with polymer chains terminated with activated *N*-hydroxysuccinimide (NHS) esters, forming the surface functionalised UiO-66-PNIPAM (Figure 1.14).<sup>133</sup>

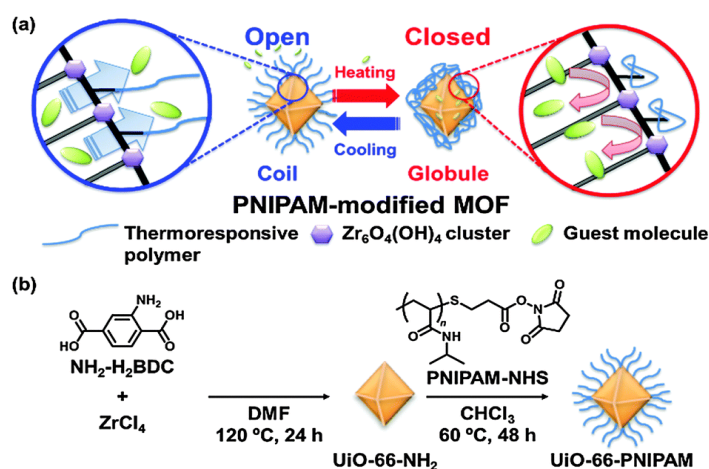


**Figure 1.14.** (a) Scheme of controlled release using UiO-66-PNIPAM, based on PNIPAM thermo-responsive behaviour (open and close forms). (b) Schematic representation of UiO-66-NH<sub>2</sub> PSM, leading to UiO-66-PNIPAM formation.<sup>133</sup>

In 2014, Mirkin *et al.* synthesised a UiO-66 analogue containing an azide group on its linker, UiO-66-N<sub>3</sub>, and subsequently covalently attached dibenzylcyclooctyne (DBCO) functionalised DNA to the MOF through copper-free strained-alkyne click chemistry (Figure.1.15).<sup>134</sup> Through radio labelling, the authors confirmed that PSM occurs only on the outer surface, as expected due to size-selectivity.

Recently, Willner and co-workers have reported the synthesis of UiO-68-NH<sub>2</sub>, and its postsynthetic transformation to UiO-68-N<sub>3</sub>.<sup>30</sup> The NMOF was loaded with an anti-cancer drug Doxorubicin (DOX) or with fluorescent dyes, and subsequently, the azide functionality was reacted with various DBCO-functionalised DNA moieties through postsynthetic copper-free click chemistry. Sequential addition of a single oligonucleotide strand on the MOF surface followed by hybridisation with complementary strands allowed a diverse range of surface functionality, including pH-responsive sequences, aptamers, and DNAzymes.<sup>30</sup>

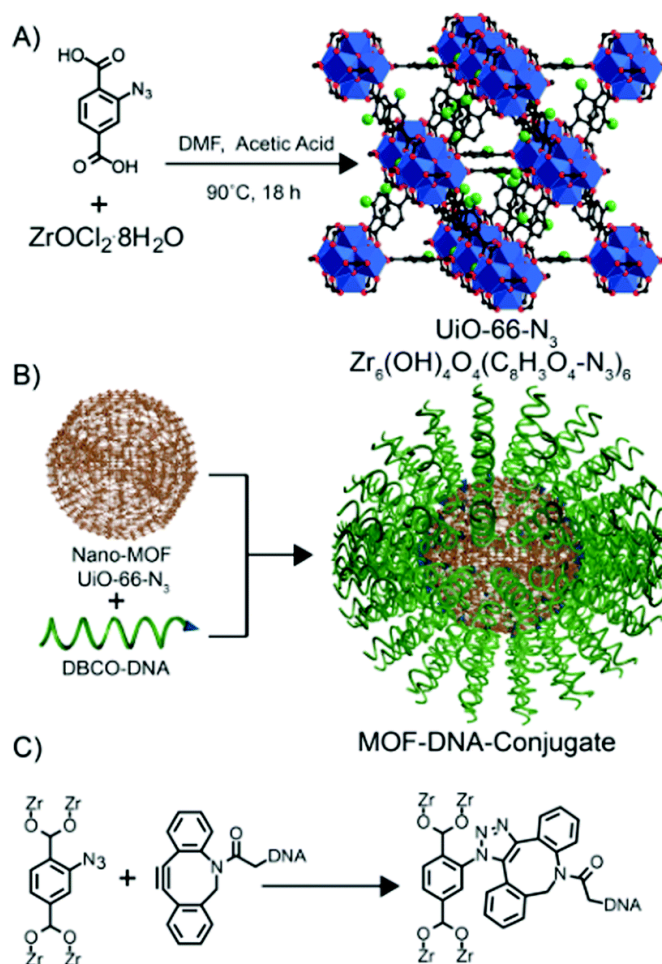


**Figure 1.15.** (a) Synthesis of UiO-66-N<sub>3</sub> (Zr<sub>6</sub>O<sub>4</sub>OH<sub>4</sub>(C<sub>8</sub>H<sub>3</sub>O<sub>4</sub>-N<sub>3</sub>)<sub>6</sub>) nanoparticles. (b) DNA functionalization of UiO-66-N<sub>3</sub> nanoparticles, utilizing DNA functionalized with dibenzylcyclooctyne (DBCO). (c) Strain promoted click reaction between a metal-organic framework (MOF) strut and DNA. Zirconium atoms = blue; oxygen atoms = red; carbon atoms = black; azide groups = green. Hydrogen atoms are omitted for clarity.<sup>134</sup>

Controlled supramolecular interactions can also be used to surface modify MOFs. Hong *et al.* reported the synthesis of a radioactive version of UiO-66 ( $^{89}\text{Zr}$ -UiO-66), which they further functionalised with pyrene-derived PEG (PY-PGA-PEG) through  $\pi$ - $\pi$  stacking interactions with the organic linkers of UiO-66 structure.<sup>135</sup> The py-derived PEG chains also contained a maleimide residue, which was used to further functionalise the MOF with a nucleolin-targeting peptide (F3) through postsynthetic modification with one of its cysteine residues. The authors found that the PEG units, due to their flexible structure, were partially blocking the porosity of the MOF, as a consequence of  $\pi$ - $\pi$  stacking with organic linkers present inside the structure. The authors postulated that to control the distribution of PEG on the MOF's surface, covalent attachment might be needed.<sup>135</sup>

Other approaches, such as liposome encapsulation<sup>136</sup> or silica coating and subsequent surface functionalisation based on reactions with silica siloxane groups,<sup>63, 137</sup> have also been reported for other MOF systems. Although silica coating provides further MOF stability under simulated physiological conditions, higher cytotoxic effects and a higher accumulation in the body in the body are usually drawbacks of this approach. To the best of my knowledge, this approach has not been used for the surface functionalisations of zirconium MOFs, possibly because their water stability is higher than for other MOF systems.

A combination of the coordination, covalent, and supramolecular approaches has also been used to functionalise PCN224.<sup>138</sup> The amino acid  $\text{N}\alpha,\text{N}\alpha$ -bis(carboxymethyl)-L-lysine was attached to the surface by coordination of its three carboxylates, followed by covalent amide conjugation with a bifunctional linker with an activated NHS ester and a DBCO unit. Subsequent copper-free click chemistry allowed conjugation of azide-modified DNA, complementary strands of which were attached to lanthanide-based upconverting nanoparticles (UCNPs). Complementary base-pair recognition resulted in the formation of MOF-UCNP composites.

In summary, a wide range of surface modifications, either through coordination or through covalent chemistry, have been performed on Zr MOFs in order to enhance their properties as DDSs, such as colloidal dispersion, physiological stability and biodistribution among others. The vast majority of the surface modifications are performed postsynthetically, using bulky surface reagents to avoid inner surface modifications. Among the different coordinating groups, it is more likely that those with a higher affinity to Zr, related to a lower  $\text{p}K_{\text{a}}$ , will create stronger bonds with the zirconium clusters, which might protect the MOFs surface from degradation and improve their colloidal dispersion to a higher extent.

## 1.6. Colloidal Dispersion of Zr MOFs under Simulated Physiological Conditions

To ensure the safe and efficient use of MOFs in medicinal applications, they must be stable towards aggregation and hydrolysis in aqueous solvents. Good water dispersion is vital for *in vivo* treatment, as blood is an aqueous, phosphate-containing fluid, and aggregation could result in harmful capillarity blockage.

It is important to take into account that the ultimate aggregation that NMOFs will suffer in the blood current is difficult to predict. *In vitro* studies using phosphate buffered saline (PBS) or water as dispersants have been widely used in order to evaluate their behaviour in aqueous media, as well as the effect of the presence of phosphates on their colloidal stability. Other dispersants, such as growth media, serum, or PBS spiked with diverse proteins, have been exploited to study the presence of blood containing proteins in the dispersion of NMOFs.<sup>74-76</sup>

Fairen-Jimenez et al have recently studied the colloidal stability of the UiO family of zirconium MOFs in PBS and growth media.<sup>139, 140</sup> It was found that all MOFs highly aggregate in PBS, whereas no major aggregation was found when dispersed in growth media, possibly as a consequence of the formation of a protein corona on the NMOFs' surface. This phenomena has also been proved for other MOF systems.<sup>74, 76</sup>

Surface modifications are known to play a crucial role in the hydrolytic stability and colloidal dispersion of MOFs and DDSs in general, as they govern the interactions with the media in which DSS are dispersed. For example, UiO-66-N<sub>3</sub> nanoparticles in water aggregate quickly upon NaCl addition, however, UiO-66-N<sub>3</sub>-DNA conjugated nanoparticles are colloidally stable in aqueous solutions of up to 0.4 M NaCl, possibly due to the steric and electrostatic barriers provided by the DNA surface coating.<sup>134</sup> UiO-66-Cis was found to be colloidal stable by DLS measurements, and minor increase in the hydrodynamic diameter was found for siRNA@UiO-Cis, which the authors attribute to siRNA coating.<sup>131</sup>

Surface modification with the phospholipid L-DOPA can even enable the dispersion of hydrophilic Zr MOFs (UiO-66, UiO-67 and BUT-30) in low polarity media such as CHCl<sub>3</sub>. Thus, UiO-66-DOPA, UiO-67-DOPA and BUT-30-DOPA migrated from the aqueous to the organic phase upon liquid-liquid extraction (Figure 1.16 a).<sup>130</sup>

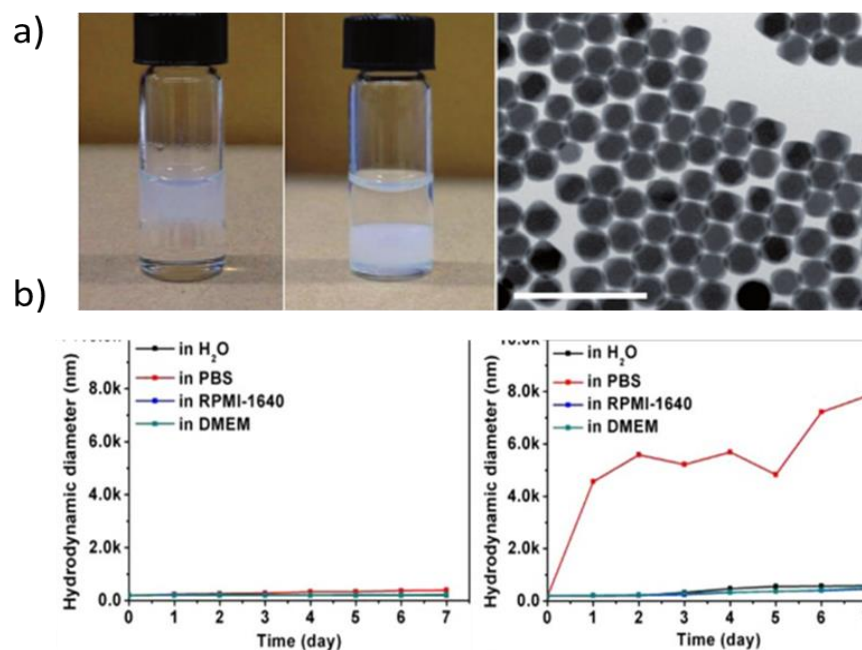


**Figure 1.16.** a) UiO-66 and UiO-66-DOPA suspended in an aqueous phase and after being transferred to a chloroform phase after DOPA functionalization. SEM image of drop-casted colloiddally stable UiO-66-DOPA in CHCl<sub>3</sub>. Scale bar: 1 μm.<sup>130</sup> b) Aggregative behaviour of PCN223 before (right) and after PBLs coating (left).<sup>26</sup>

The colloidal stability and dispersion of bare PCN-223 nanoparticles, nanoPCN-223@DOPC and nanoPCN-223@DOPC/DOPC was assessed in a series of solvents, such as water, PBS and biological growth media RPMI-1640 and DMEM. The hydrodynamic size of bare nanoPCN-223 drastically increased with time in water, and more importantly in PBS. PCN-223@DOPC was found to be highly hydrophobic, aggregating in water, possibly due to the acyl chains of DOPC, but the MOFs coated with phospholipid bilayers did not significantly aggregate in water or PBS over a period of 7 days, highlighting the power of surface modifications (Figure 1.16 b).<sup>26</sup>

Hong and co-workers found slight changes on aggregative behaviour when UiO-66 was dispersed in water before and after supramolecular py-PGA-PEG functionalisation. The hydrodynamic diameter of UiO-66 (ca. 220 nm) was slightly higher than the size observed by SEM, and relatively increased for UiO-66-py-PGA-PEG-F3 (ca.250 nm). These results suggest that, although many factors are involved in MOFs aggregative behaviour, surface functionalisation through covalent attachment might be more efficient at enhancing colloidal stability of UiO-66 than using  $\pi$ - $\pi$  interactions, possibly due to the higher stability of the coating using the former protocol.<sup>135</sup>

Mirkin and co-workers have recently reported that the monocarboxylic acid modulator used during UiO-66 synthesis plays a crucial role in the MOFs polydispersity.<sup>120</sup> Modulators with

lower  $pK_a$  values are more likely to be deprotonated during synthesis, and so increased competition with the organic linker for the zirconium positions induces the formation of defects. These defects increase the surface charge (measured by zeta potentials), hence increasing the repulsion between nanoparticles and enhancing their colloidal stability. UiO-66 samples modulated by formic acid (FA,  $pK_a = 3.77$ ), dichloroacetic acid (DCA,  $pK_a = 1.36$ ) and trifluoroacetic acid (TFA,  $pK_a = 0.23$ ) were colloidally stable in water, as determined by DLS, and did not show any aggregation by scanning tunnelling electron microscopy (STEM). In contrast, when acetic acid (AcOH,  $pK_a = 4.76$ ) is used as a modulator for the synthesis of UiO-66 (the BDC linker has a first  $pK_a$  of 3.51 and a second of 4.82) the resultant particles were considerably aggregated (Figure 1.17).<sup>120</sup>

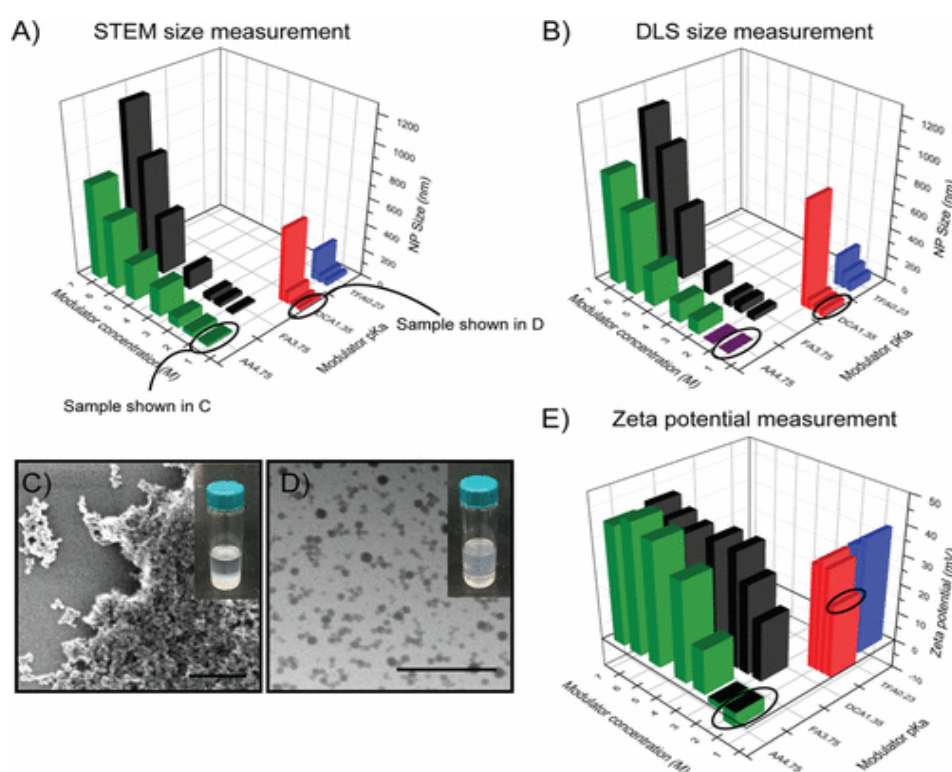


**Figure 1.17.** Overall results of colloidal stability of UiO-66 as a function of modulator acidity ( $pK_a$ ) and molar concentration. Formic acid FA (black), Acetic acid AA (green), dichloroacetic acid DCA (red), and TFA (blue). A) STEM size measurement (B) DLS size measurement, where the purple region in B corresponds to highly aggregated samples where particle size cannot be determined by DLS. C) and D) STEM image and digital photographs of UiO-66 dispersed in  $H_2O$  synthesized with UiO-Acetic acid and (D) dichloroacetic acid (0.58 M) respectively (Scale bars C = 200 nm and D = 500 nm), showing the difference in aggregation. (E) Zeta potential measurements.<sup>120</sup>

Thus, based on the results available in the literature, it is evident that the use of a low  $pK_a$  modulator during MOFs synthesis highly enhances their colloidal dispersion, while high improvements are also found through surface modifications.

### 1.7. Stability of Zr MOFs under Simulated Physiological Conditions

As zirconium, among other metals, has a greater affinity for phosphates than for carboxylates, phosphates present in the body can also attack the zirconium positions, inducing degradation and thus resulting in uncontrollable release of the drug.<sup>85</sup> Hence, MOFs degradation kinetics have been widely studied in PBS.

It is well-known that the stability of MOFs towards phosphates depends on many factors, but clearly surface coating is one of the most important, as it can shelter metal clusters from phosphate attack. Compared to the amount of work that has been performed to determine and to enhance the drug release kinetics of Zr MOFs (see Section 1.8), there are few studies in the literature that discuss the degradation kinetics of the Zr MOFs, despite the fact that the drug release might be a consequence of carrier degradation. Monitoring linker release by UV/Vis spectroscopy yields more detailed real-time information than *ex situ* diffraction techniques, and has shown that UiO-66 degrades rapidly in PBS.

Although initial degradation could yield in burst drug release, final degradation of a DDS is of vital importance, as otherwise long-term accumulation of the DDS could induce unwanted side effects and toxicity.

Fairen-Jimenez *et al.* revealed rapid degradation of benzoic acid modulated UiO-66 in PBS, releasing 80% of the bdc linker during the first hour, but not in water, where less than 10% of the linker was released after 7 days.<sup>139</sup> The samples were characterised after different exposure times in PBS, confirming the formation of a phosphate corona by FT-IR spectroscopy, a consequence of phosphate attacking the Zr units and displacing the bdc linkers. Similar high degradation rates in PBS were found for other members of the UiO-66 isorecticular series, which could result in unwanted uncontrollable release of drugs.

Coating PCN-223 with phospholipid bilayers (PBLs) drastically improved the resistance of this zirconium MOF towards phosphates.<sup>26</sup> The authors measured the stability of bare MOF, nanoPCN-223@DOPC and nanoPCN-223@DOPC/DOPC towards various chemicals, finding that both mono- and bi-layer coated nanoparticles were stable towards common cations and anions, as well as in serum. The sensitivity of Zr MOFs towards phosphate was illustrated by the rapid corrosion and linker release displayed by bare nanoPCN-223 in PBS, for which 90% of the linker was released in the first hour of PBS exposure, while PCN-223 coated with PBLs releases less than 3% of the organic linker after 7 days in PBS, strongly suggesting that PBLs act as a barrier to block phosphate attack (Figure 1.18).<sup>26</sup>

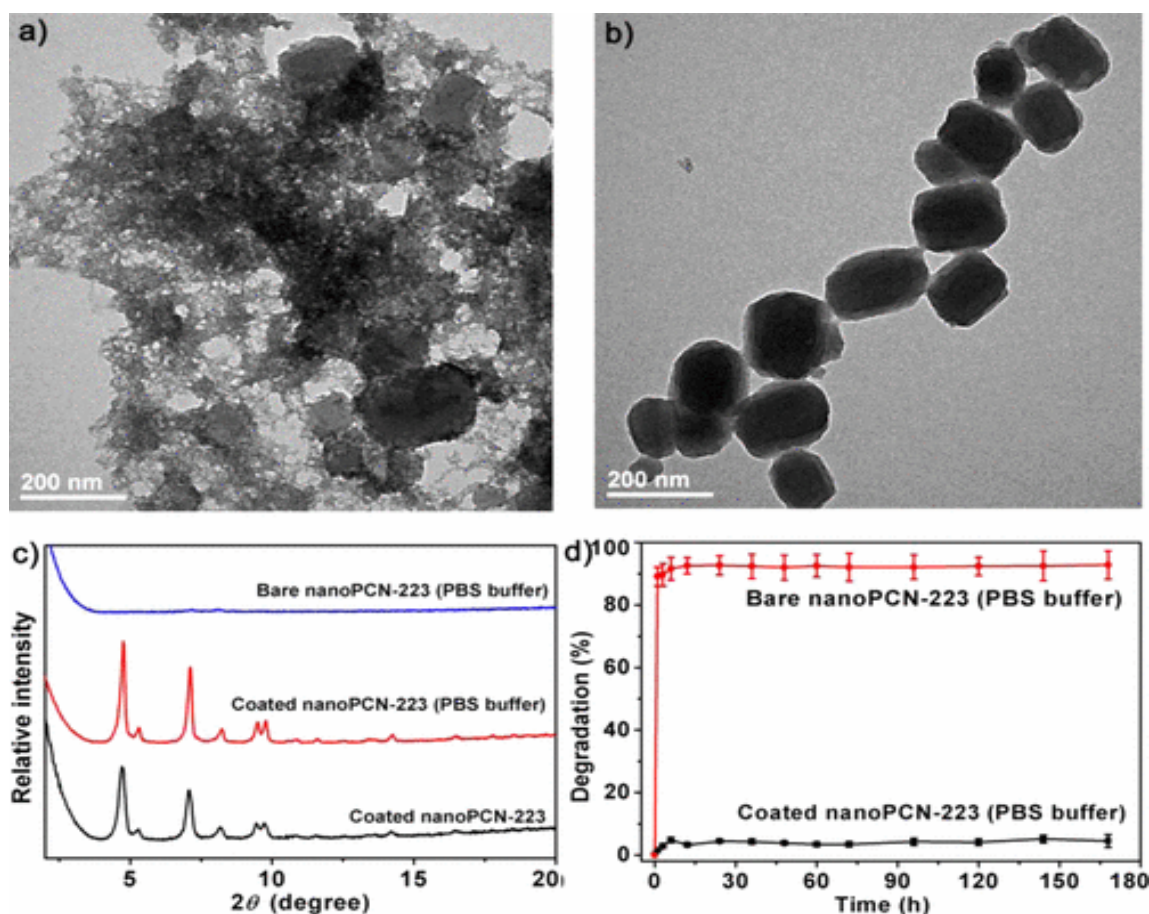


**Figure 1.18.** Enhanced phosphate stability of TEM images of (a) bare nanoPCN-223 and (b) PBLs coated nanoPCN-223 particles in PBS solution with 2-day incubation time. (c) Powder XRD patterns for coated nanoPCN-223. d) Degradation profiles of bare and PBLs coated PCN-223 in PBS buffer. <sup>26</sup>

### 1.8. Drug Release Kinetics of Zr MOFs

For DDSs to be effective, premature release of therapeutic cargo should be minimised, allowing the drug to travel to the location of the disease within the body before delivering the payload. For MOFs, release of cargo can occur by diffusion out of the pores or through degradation of the MOF itself, with unwanted early release – the so-called “burst release” phenomenon – a major issue to overcome.<sup>33</sup> If the guest molecules are partially located on the MOF surface premature release is also likely to be observed. The chemical stability and ease of functionalisation of Zr MOFs has facilitated the development of many strategies to allow controlled or even stimuli-responsive release.

As hydrolytic stability is implicit in control of cargo release, similar strategies to those discussed above have been employed overcome burst release in Zr MOFs. Attaching cargo to the surfaces and defect sites of Zr MOFs by coordination provides the possibility of pH or phosphate induced cleavage and release. For example, Lachelt and co-workers studied the

release of fluorescent peptides, attached to Zr-fumarate surfaces using His-tag imidazole coordination, into HEPES buffered glucose (HBG) at different pH values over 24 h by photometric determination.<sup>128</sup> HBG does not contain phosphates, so the role of pH can be assessed independently. At pH 7.4 the coating was stable, while at pH 5 the peptide was partially released, and at pH 3 was completely cleaved from the surface of Zr-fum. Although imidazole ions present in histidine residues have  $pK_a$  values around 6, and thus detachment at pH 5 due to imidazole protonation would be expected to be more pronounced, the authors suggest that incomplete detachment could be due to the lowered  $pK_a$  value when His-tags are attached to the zirconium units. The coordination of the drug alendronate through its phosphate groups to UiO-66 resulted in pH responsive drug release from UiO-66-AL, which released 43% of AL in PBS at pH 7.4 over 60 hours, and 59% of AL under the same conditions but at pH 5.5.<sup>24</sup>

Physically modifying drug-loaded MOFs to sterically protect the surface from hydrolysis is also an effective approach to control drug release. Fairen-Jimenez *et al.* have applied an amorphisation approach to trap calcein, a fluorescent model drug molecule, within UiO-66 by grinding. Full release of calcein from amorphous UiO-66 took 30 days rather than 2 days for crystalline UiO-66.<sup>29</sup> The release of Diclofenac sodium (DS) from ZFU-800, a member of the isorecticular UiO-66 series linked by 3,3'-(2-fluoro-1,4-phenylene)diacrylic acid, was monitored in PBS by Jian *et al.* DS payloads of 59% w/w were obtained, and its release in PBS (pH 7.4) at 37 °C displayed a burst effect, with an immediate 10% release, followed by full release over two days.<sup>141</sup> The effect of pressure on the drug release kinetics was investigated by applying different pressures (10 MPa and 30 MPa) to drug loaded samples for one minute, compacting the MOFs into slices, which were further broken for the drug release experiments. Interestingly, the sample was still crystalline after the process. The authors observed a 2.5 fold decrease in the release rates for the lowest pressure, maintaining the release up to 5 days, and when the highest pressure was applied, the release was prolonged to 8 days, with no burst release for either sample. Whilst bulk crystallinity was maintained, pressure-induced amorphisation at particle surfaces could sufficiently block pores and slow down release.

Thermal amorphisation has also been used to prolong the drug release times of NU-1000 and NU-901.<sup>25</sup> These zirconium MOFs have remarkably high storage capacities – with calcein loadings of 41.6% w/w and 37.0% w/w, respectively – due to their high porosity ( $S_{BET} = 2320$  and  $2500 \text{ m}^2\text{g}^{-1}$ , respectively), but their larger pore cavities can at the same time result in rapid drug release. Calcein was confirmed to be located in the pores, as the loaded samples had drastically reduced porosities. Temperature treatment (180°C) was performed in order to collapse the structure and to hinder calcein release through the pore cavity. In contrast to the mechanical amorphisation protocols performed on the UiO-66 family, although the intensity of

the Bragg peaks had decreased, they could still be observed clearly in the PXRD pattern, indicating only partial structure collapse. (Figure 1.19)

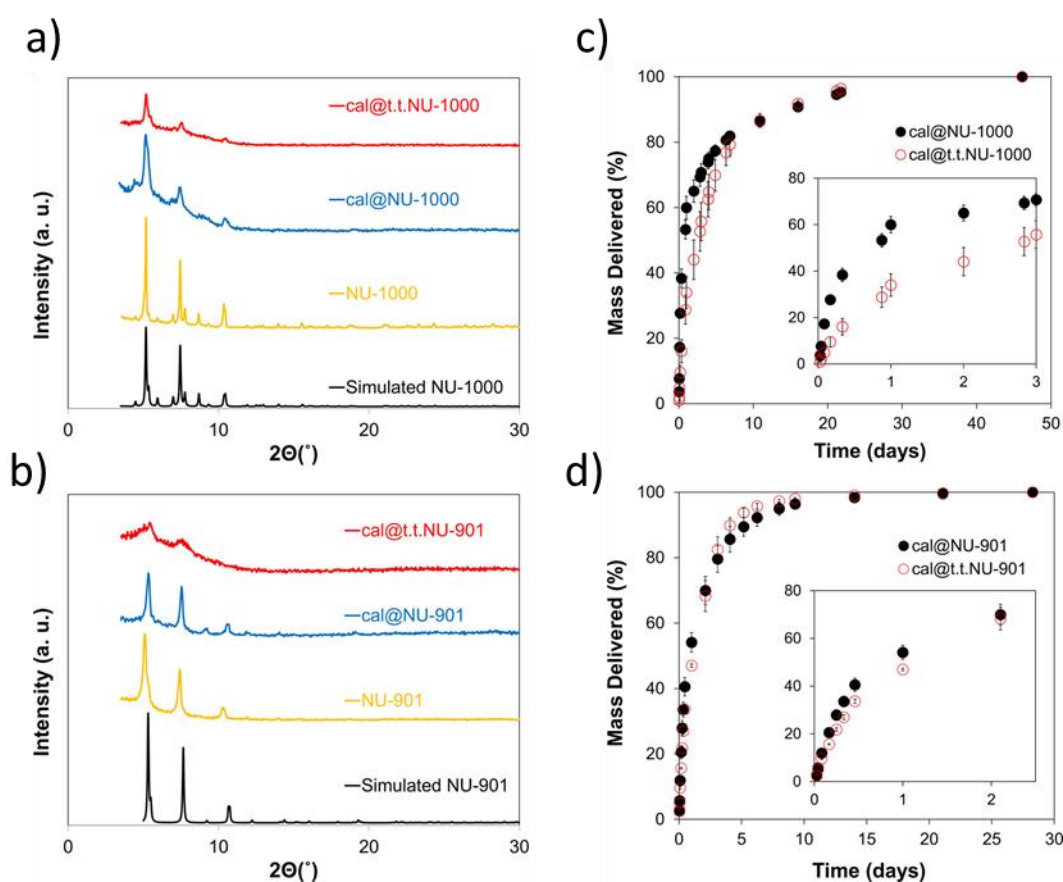


**Figure 1.19.** Effect of temperature treatment in NU-1000 and NU-901 drug release kinetics. a) and b) PXRD patterns. c) and d) Drug release profiles in PBS.<sup>25</sup>

The effect of thermal treatment on the drug release kinetics was clear; after 4 hours cal@NU-1000 had released ~28% of its calcein, but after thermal treatment only 10% was released in the same time period. The release kinetics were slowed to the 7<sup>th</sup> day, when the profiles for thermally amorphised and pristine calcein-loaded NU-1000 overlap at around 80% release, and continue to release the full amount up to 7 weeks. On the other hand, only a minor effect on calcein release kinetics was found upon thermal treatment of NU-901.<sup>25</sup>

Incorporation of surface functionality can also block the release of cargo molecules. PNIPAM is thermosensitive polymer, which adopts a closed, globular mode at higher temperatures, and opens to a coil formation at lower temperatures. Thus, Kokado and Sada reported the on-off thermoresponsive release of three different molecules – resorufin, caffeine and procainamide – from UiO-66-PNIPAM in water.<sup>133</sup>

The release kinetics at 25°C were slightly improved compared to the precursor UiO-66-NH<sub>2</sub>, which released ca. 95% of resorufin after few hours. Drug release from the PNIPAM-

functionalised MOF was pronounced at 25 °C, when the polymer is in its open coil form, exhibiting a burst release of more than 50% of the different molecules in the first few hours and 80-90% release after 1 day. The release kinetics were remarkably reduced at 40 °C, with an initial release of only 10-20 % of the cargo molecules in the first hours and no subsequent release. As the drugs were loaded after PSM, the small amount of drug released initially at 40 °C could be a consequence of minor surface drug location. By changing the temperature during the course of the drug release experiment, UiO-66-PNIPAM drug release was switched on and off by external stimuli. It is important to point out that this temperature responsive behaviour was only achieved when the degree of PNIPAM coating was high enough to ensure significant surface coverage, as UiO-66-PNIPAM with 4.2% w/w PNIPAM did not present thermoresponsive behaviour (Figure 1.20).<sup>133</sup>

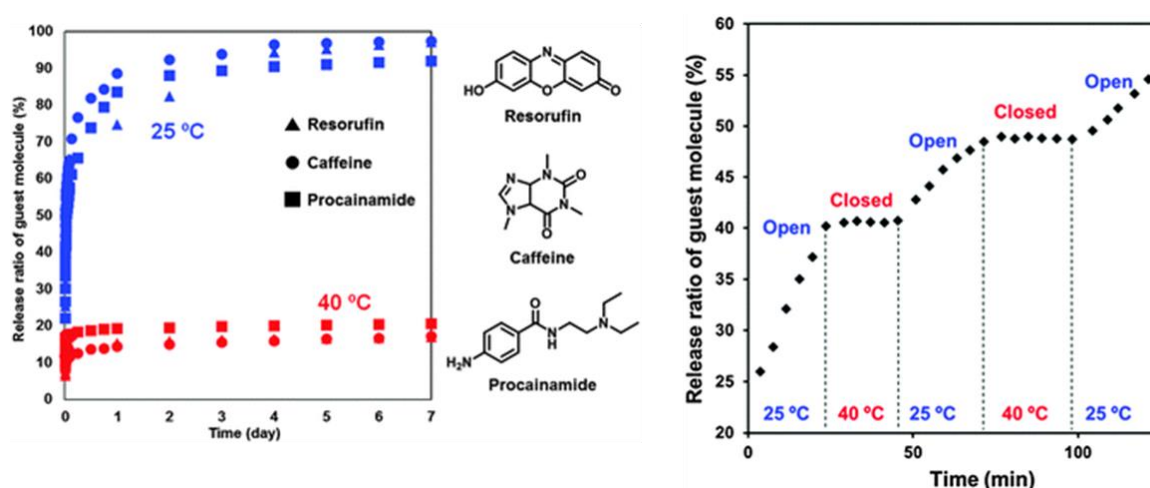


**Figure 1.20.** Release behaviour of guest molecules (resorufin, caffeine, procainamide) from UiO-66-PNIPAM in water at 25 °C and 40 °C for seven days. Stepwise release-and-halt behaviour of resorufin from UiO-66-PNIPAM in water by temperature variation. The release ratio was determined from the absorbance at 572 nm.<sup>133</sup>

Willner et al studied the reorganisation of DNA on the surface of UiO-68 in response to pH and metal ions as mechanisms for the release of doxorubicin and several dyes.<sup>30</sup> To induce pH responsive release, cytosine-rich DNA sequences were attached to the MOF surface, and the authors attributed the enhanced release of the molecules into PBS at pH 5 compared to that at pH 7.4 to the reorganisation of the cytosine-rich DNA into an i-motif structure that allowed cargo to be released, rather than linker protonation and structure decomposition. Metal ion ( $Mg^{2+}$  and  $Pb^{2+}$ ) responsive release was probed by attaching “DNAzyme” sequences through hybridisation with surface sequences. Upon metal-ion binding, these DNAzymes are released from the MOF and should result in uncapping and release of trapped cargo. The doxorubicin-loaded MOF was further functionalised with a DNA containing both an  $Mg^{2+}$  dependent DNAzyme sequence and an adenosine triphosphate (ATP) aptamer unit, based

on the fact that ATP concentrations are higher in cancerous cells than in healthy ones. Release was only slightly enhanced upon increase of  $Mg^{2+}$ , but a two-fold increase was promoted through cooperation of  $Mg^{2+}$  and ATP addition. It should be noted that the phosphate units of ATP may also become involved with coordination to the  $Zr_6$  SBUs at the surface of the MOF.<sup>30</sup>

The stability of  $Fe_3O_4@UiO-66-NH_2$  core-shell NPs has been investigated at different pHs (4.0, 5.0, 6.0, 7.4, 8.0) finding no significant changes in the crystallinity (PXRD) or morphology (SEM) of the samples.<sup>125</sup> DOX was loaded into the core-shell  $Fe_3O_4@UiO-66-NH_2$  by stirring in PBS during 24 hours. DOX loading capability increases as the thickness of MOF shell does. Surprisingly, DOX loadings as high as 66.3 w/w % were achieved. DOX fluorescent quenching upon  $Fe_3O_4@UiO-66-NH_2$  addition strongly suggested interaction between the MOF and DOX. The authors suggested  $\pi$ - $\pi$  stacking, hydrogen bonding between DOX atoms and UiO-66- $NH_2$  amino group, and attachment to the available Zr positions through DOX carboxylic group, being later confirmed through UV-Vis and X-ray photoelectron spectroscopy.  $DOX@Fe_3O_4@UiO-66-NH_2$  DOX release was investigated at various pHs (4.0, 5.0, 6.0, 7.4), finding a pH dependence with no burst release, only releasing a ca. 40 % of DOX at pH 4.0 after 45 days.<sup>125</sup>

In general, all zirconium MOFs have pH responsive drug release as a consequence of hydrolysis, which is favourable for anti-cancer treatment, as the cytoplasm of cancer cells is more acidic than for healthy cells. If we compare the release kinetics of different drugs from UiO-66, it comes to mind that drugs attached to the Zr clusters (such as Alendronate)<sup>24</sup> are released with a more favourable rate than drug stored in the pores (such as caffeine or resorufin).<sup>133</sup> The importance of surface coating is obvious and has different effects depending on its nature. For example, surface coatings which can compete with phosphates during degradation highly enhance the stability of the samples through coordination equilibrium, and protecting polymers attached to the NMOFs surface also sterically protect them from degradation, although to a lower extent, as once the coating has been displaced, degradation occurs at a normal rate. Protocols to collapse NMOFs porosity around loaded molecules – such as mechanical amorphisation, temperature treatment, or applied pressure – have also induced more desirable release fates, although their effect in colloidal stability is not pronounced, indicating that surface coatings are more suitable to enhance both stability and dispersion. Thus, an appropriate strategy could be to perform surface coating after amorphisation.

## 1.9. Biocompatibility of Zr MOFs

The therapeutic efficiency of any DDS is strictly correlated to its ability to cross the cell membrane and successfully deliver the drug to the various cell compartments.<sup>44, 45, 142</sup> Both cell internalisation rates and routes are of crucial importance for efficiency OF drug delivery, as well as low toxicity of the DDS and its counter parts.<sup>42, 43</sup> Importantly, the DDS should avoid immune system recognition, and thus not be internalised by immune system cells such as macrophages.<sup>143, 144</sup> Hence, surface modifications to enable targeting and thus avoid immune system recognition while enhancing dispersion, stability and drug release kinetics – which are imperative for efficient DDS- are of great importance with the ultimate aim of enhancing NMOFs therapeutic efficiency.

Nanoparticle's cellular internalisation depends on many factors, including size, morphology and surface chemistry among others,<sup>45, 142, 145, 146</sup> and attempts have been made to enhance uptake and also control the endocytosis mechanisms of MOFs.<sup>140, 147</sup> Nanoparticles are generally internalised by cells through active transport such as endocytosis, including clathrin-mediated,<sup>148, 149</sup> caveolae-mediated,<sup>150, 151</sup> non-mediated endocytosis, and macropinocytosis.<sup>152</sup> While nanoparticles internalised through clathrin-mediated endocytosis are finally delivered to lysosomes, which can result in degradation and inefficient cytosolic release of the cargo, nanoparticles internalised through caveolae-mediated endocytosis can escape lysosome capture, typically resulting in faster cytosolic release and hence potentially higher therapeutic efficiency.<sup>151</sup> For MOFs, fluorescent linkers or cargo molecules are usually used to monitor endocytosis through confocal microscopy and fluorescence-activated cell sorting (FACS) (See Chapter 4 for full discussion).

*In vitro* cell proliferation experiments, such as MTS, 3-(4,5-dimethylthiazol-2-yl)-5-(3-carboxymethoxyphenyl)-2-(4-sulfophenyl)-2H-tetrazolium), and MTT, (3-(4,5-dimethylthiazol-2-yl)-2,5-diphenyltetrazolium bromide, assays after incubation of cells with the DDSs, are used as key initial evaluators of the effect of factors such as surface modification and drug loading on their therapeutic effect and biocompatibility. These assays are based on the cellular internalisation of certain tetrazolium compounds and their cellular transformation into formazan products. The formazan products have a characteristic absorbance, which is measured by UV-Vis and compared to a control of untreated cells, indicating the metabolic activity of cells with and without treatment, and consequently the cell proliferation.

The biocompatibility and therapeutic efficacy of empty Zr MOFs has been investigated before and after surface modifications (See Chapter 5 for full discussion).<sup>53, 54, 56, 153, 154</sup> For example, the archetypal Zr MOF UiO-66 has been proven not to induce remarkable cytotoxicity in HeLa cervical cancer cells, with a half inhibitory concentration (IC<sub>50</sub>) of  $1.50 \pm 0.15$  mgmL<sup>-1</sup> after 24

hours of exposure.<sup>29</sup> ZJU-800 has been also proved non-cytotoxic in rat neuroblastic pheochromocytoma PC12 cells after incubation with a solution of 0.1 mgmL<sup>-1</sup> of NMOF during 24 hours.<sup>141</sup>

The biocompatibility of bare PCN-223 towards SMMC-7721 (human hepatocellular carcinoma) and HeLa cervix cancer cells was enhanced after PBLs coating, with nanoPCN-223@DOPC/DOPC being non-cytotoxic at concentrations of 0.4 mgmL<sup>-1</sup>, while treatment with the same concentration of bare MOF decreased cell viability to ca. 70%, even though its cell internalisation efficiency is lower than for the coated MOF.<sup>26</sup>

The potential of Zr-fum as DDS was investigated by attaching- through H6-Tag- various pro-apoptotic peptides (Bak, Bad, KLK) and a cytochrome c protein (CytC) to the NMOF surface, which due to their membrane impermeability are not able to efficiently cross the cells membrane by themselves. Thus, a decrease on HeLa cells viability when treated with the NMOFs was considered a consequence of efficient cytosolic release of the attached peptides. The authors compared the effects produced on cells growth to those obtained when incubating cells with free peptide or naked Zr-fumarate during the same period of time, 48 hours. The peptide or protein conjugated MOFs induced remarkably higher cytotoxicity on cells (ca. 40% cells viability) compared with the free peptide (ca. 90%), while naked MOF did not exhibit any cytotoxicity, confirming the high potential of Zr-fumarate as a DDS.<sup>128</sup>

Although a wide variety of *in vitro* and *in vivo* studies of Zr MOFs as anticancer DDSs are present in the literature, and are discussed in Chapter 5, the examples discussed during this section highlight the high potential of Zr MOFs as DDSs, embodied by their efficient cargo release, colloidal stability and cellular internalisation.

A considerable number of *in vivo* studies have been performed with a wide variety of MOFs, showing tumour remission after their intravenous administration. However, the potential of MOFs and other nanocarriers as DDSs is limited by the fact that they often accumulate in the liver and spleen, possibly due to macrophage recognition and internalisation.<sup>52, 135</sup>

As such, from an ethical point of view, the need to find a rationalisation between the effect of the intrinsic characteristics of NMOFs, such as surface chemistry, on their properties (colloidal dispersion and physiological stability), and on their cellular internalisation, which is strictly related to their therapeutic efficacy, is inherently clear, providing if so the possibility of reducing early-stage animal testing while maximizing the potential application of MOFs as DDSs. Thus, finding insights to facilitate the thoughtful design of surface chemistry of MOFs, which should be efficiently internalised by cancer cells while able to avoid the immune system recognition and subsequent accumulation, might reduce unnecessary animal testing.

## 1.10 Conclusions and Future Work

The high potential of Zr MOFs as DDSs has been highlighted in the context of their biocompatibility and amenable functionalisation, which further improves Zr MOFs properties such as colloidal dispersion in aqueous solvents, physiological stability and drug release kinetics. The latter, due to the nature of the metal-linker coordination bond, are sensitive to pH changes, an enormous advantage for anticancer DDSs, given that extracellular pH is ~7.4, and intracellular pH of cancer cells (~5.5) is more acidic than for healthy cells (~6.8).

Examples of Zr MOFs surface functionalisations, subsequent properties and therapeutic effect are constantly emerging in the literature, and many reports have been published during the course of this thesis. However, one-pot functionalisations are still scarce in the literature, and to the best of the author's knowledge, simultaneous surface functionalisation and drug loading during synthesis has not been achieved so far.

This thesis will focus on the development of surface functionalisation protocols of UiO-66, both during synthesis and postsynthetically, the study of the MOFs' properties, and correlation between cellular internalisation fates and routes with their therapeutic efficiency.

The use of carboxylate containing surface reagents and a carboxylate containing anticancer metabolic target (dichloroacetic acid, DCA) as modulators of UiO-66 synthesis will be explored with the aim of obtaining surface-functionalised drug-loaded MOFs by one-pot syntheses, and empty surface-functionalised MOF analogues.

The surface functionalities of certain modulators will be used to postsynthetically modify the MOFs surface through covalent chemistry with protecting polymers. Coordinating surface reagents (e.g the former carboxylate modulators) will be postsynthetically attached to the MOF surface, in order to compare the MOFs properties - colloidal dispersion and stability - depending on both surface coating type (targeting unit, polymers etc) and synthetic mode (e.g coordination modulation of postsynthetically).

Additionally, the DCA modulated synthesis will be applied to the UiO family of isorecticular MOFs (including UiO-66 and its bromo, nitro and amino derivatives, Zr-Naphthalene and UiO-67). DCA has a low  $pK_a$  and hence its attachment to the Zr clusters should be pronounced, inducing defects and a consequent high surface charge, which was found desirable for colloidal dispersion by a separate group<sup>120</sup> during the course of this PhD.

Further discussion of examples of cellular internalisation of MOFs present in the literature will be provided during Chapter 4, and the endocytosis routes and fates of bare and surface functionalised calcein-loaded UiO-66 will be studied in order to find a correlation with their therapeutic efficacy. Rationalisation of literature examples of *in vitro* studies of Zr MOFs with

their properties and cellular internalisation will be provided in Chapter 5. The biocompatibility of the empty surface-functionalised and bare MOFs will be assessed, and the therapeutic efficiency, anticancer selectivity of the DCA-loaded surface functionalised MOFs will be studied in a series of cancerous and healthy cell lines, including a study of the macrophage uptake, cytotoxicity and reactive oxygen species production.

### 1.11. References

1. R. A. Cairns, I. S. Harris and T. W. Mak, *Nature Review Cancer*, 2011, **11**, 85-95.
2. P. P. Hsu and D. M. Sabatini, *Cell*, 2008, **134**, 703-707.
3. G. Kroemer and J. Pouyssegur, *Cancer Cell*, 2008, **13**, 472-482.
4. N. Pavlova and C. B. Thompson, *Cell Metabolism*, 2016, **23**, 27-47.
5. N. Castaing, D. Merlet and J. Cambar, *Toxicology in Vitro*, 1990, **4**, 396-398.
6. J. Poljaková, T. Eckschlager, J. Hřebačková, J. Hraběta and M. Stiborová, *Interdisciplinary Toxicology*, 2008, **1**, 186-189.
7. A. H. Partridge, H. J. Burstein and E. P. Winer, *Journal of the National Cancer Institute*, 2001, **2001**, 135-142.
8. L. Y. Ramirez, S. E. Huestis, T. Yi Yap, S. Zyzanski, D. Drotar and E. Kodish, *Pediatric Blood & Cancer*, 2009, **52**, 497-502.
9. C. C. Sun, D. C. Bodurka, C. B. Weaver, R. Rasu, J. K. Wolf, M. W. Bevers, J. A. Smith, J. T. Wharton and E. B. Rubenstein, *Supportive Care in Cancer*, 2005, **13**, 219-227.
10. L. Galluzzi, L. Senovilla, I. Vitale, J. Michels, I. Martins, O. Kepp, M. Castedo and G. Kroemer, *Oncogene*, 2012, **31**, 1869-1883.
11. C.-W. Lu, S.-C. Lin, C.-W. Chien, S.-C. Lin, C.-T. Lee, B.-W. Lin, J.-C. Lee and S.-J. Tsai, *The American Journal of Pathology*, 2011, **179**, 1405-1414.
12. R. M. Mader, M. Müller and G. G. Steger, *General Pharmacology: The Vascular System*, 1998, **31**, 661-666.
13. H. Akhdar, P. Loyer, C. Rauch, A. Corlu, A. Guillouzo and F. Morel, *European Journal of Cancer*, 2009, **45**, 2219-2227.
14. J. Lu, M. Liong, Z. Li, J. I. Zink and F. Tamanoi, *Small*, 2010, **6**, 1794-1805.
15. P. Horcajada, T. Chalati, C. Serre, B. Gillet, C. Sebrie, T. Baati, J. F. Eubank, D. Hurtaux, P. Clayette, C. Kreuz, J.-S. Chang, Y. K. Hwang, V. Marsaud, P.-N. Bories, L. Cynober, S. Gil, G. Ferey, P. Couvreur and R. Gref, *Nature Materials*, 2010, **9**, 172-178.
16. A. Myc, J. Kukowska-Latallo, P. Cao, B. Swanson, J. Battista, T. Dunham and J. R. Baker, *Anticancer drugs*, 2010, **21**, 186.
17. K. Y. Kim, *Nanomedicine: Nanotechnology, Biology and Medicine*, 2007, **3**, 103-110.
18. M. E. Gindy and R. K. Prud'homme, *Expert Opinion on Drug Delivery*, 2009, **6**, 865-878.
19. L. K. Bogart, G. Pourroy, C. J. Murphy, V. Puentes, T. Pellegrino, D. Rosenblum, D. Peer and R. Levy, *ACS Nano*, 2014, **8**, 3107-3122.
20. D. Peer, J. M. Karp, S. Hong, O. C. Farokhzad, R. Margalit and R. Langer, *Nature Nanotechnology*, 2007, **2**, 751-760.
21. K. Krukiewicz and J. K. Zak, *Materials Science and Engineering: C*, 2016, **62**, 927-942.

22. D. B. Pacardo, F. S. Ligler and Z. Gu, *Nanoscale*, 2015, **7**, 3381-3391.
23. W. Wang, L. Wang, Z. Li and Z. Xie, *Chemical Communications*, 2016, **52**, 5402-5405.
24. X. Zhu, J. Gu, Y. Wang, B. Li, Y. Li, W. Zhao and J. Shi, *Chemical Communications*, 2014, **50**, 8779-8782.
25. M. H. Teplensky, M. Fantham, P. Li, T. C. Wang, J. P. Mehta, L. J. Young, P. Z. Moghadam, J. T. Hupp, O. K. Farha, C. F. Kaminski and D. Fairen-Jimenez, *Journal of the American Chemical Society*, 2017, **139**, 7522-7532.
26. J. Yang, X. Chen, Y. Li, Q. Zhuang, P. Liu and J. Gu, *Chemistry of Materials*, 2017, **29**, 4580-4589.
27. A. Ray Chowdhuri, D. Bhattacharya and S. K. Sahu, *Dalton Transactions*, 2016, **45**, 2963-2973.
28. T.-H. Shin, J.-s. Choi, S. Yun, I.-S. Kim, H.-T. Song, Y. Kim, K. I. Park and J. Cheon, *ACS Nano*, 2014, **8**, 3393-3401.
29. C. Orellana-Tavra, E. F. Baxter, T. Tian, T. D. Bennett, N. K. H. Slater, A. K. Cheetham and D. Fairen-Jimenez, *Chemical Communications*, 2015, **51**, 13878-13881.
30. W.-H. Chen, X. Yu, A. Ceconello, S. Yang Sung, R. Nechushtai and I. Willner, *Chemical Science*, 2017; **8**, 5769–5780.
31. K. Greish, *Methods in Molecular Biology*, 2010, **624**, 25-37.
32. K. Maruyama, *Advanced Drug Delivery Reviews*, 2011, **63**, 161-169.
33. X. Huang and C. S. Brazel, *Journal of Controlled Release*, 2001, **73**, 121-136.
34. D. Cunha, M. Ben Yahia, S. Hall, S. R. Miller, H. Chevreau, E. Elkaïm, G. Maurin, P. Horcajada and C. Serre, *Chemistry of Materials*, 2013, **25**, 2767-2776.
35. G. Jarockyte, E. Daugelaite, M. Stasys, U. Statkute, V. Poderys, T.-C. Tseng, S.-H. Hsu, V. Karabanovas and R. Rotomskis, *International Journal of Molecular Sciences*, 2016, **17**, 1193.
36. Y. Yu, Y. Li, W. Wang, M. Jin, Z. Du, Y. Li, J. Duan, Y. Yu and Z. Sun, *PLoS One*, 2013, **8**, e61346.
37. M. A. Dobrovolskaia and S. E. McNeil, *Nature Nanotechnology*, 2007, **2**, 469-478.
38. J. Xie, C. Xu, N. Kohler, Y. Hou and S. Sun, *Advanced Materials*, 2007, **19**, 3163-3166.
39. K. Kim, M. Yu, X. Zong, J. Chiu, D. Fang, Y.-S. Seo, B. S. Hsiao, B. Chu and M. Hadjiargyrou, *Biomaterials*, 2003, **24**, 4977-4985.
40. W. H. De Jong, W. I. Hagens, P. Krystek, M. C. Burger, A. J. A. M. Sips and R. E. Geertsma, *Biomaterials*, 2008, **29**, 1912-1919.
41. S. Arora, J. M. Rajwade and K. M. Paknikar, *Toxicology and Applied Pharmacology*, 2012, **258**, 151-165.
42. N. Lewinski, V. Colvin and R. Drezek, *Small*, 2008, **4**, 26-49.
43. C. Tamames-Tabar, D. Cunha, E. Imbuluzqueta, F. Ragon, C. Serre, M. J. Blanco-Prieto and P. Horcajada, *Journal of Materials Chemistry B*, 2014, **2**, 262-271.
44. I. Canton and G. Battaglia, *Chemical Society Reviews*, 2012, **41**, 2718-2739.
45. T.-G. Iversen, T. Skotland and K. Sandvig, *Nano Today*, 2011, **6**, 176-185.
46. I. Mellman, *Annual Review of Cell and Developmental Biology*, 1996, **12**, 575-625.
47. J. M. Saul, A. Annapragada, J. V. Natarajan and R. V. Bellamkonda, *Journal of Controlled Release*, 2003, **92**, 49-67.
48. S. Sur, A. C. Fries, K. W. Kinzler, S. Zhou and B. Vogelstein, *Proceedings of the National Academy of Sciences of the United States of America*, 2014, **111**, 2283-2288.
49. M. Javadi, W. G. Pitt, C. M. Tracy, J. R. Barrow, B. M. Willardson, J. M. Hartley and N. H. Tsosie, *Journal of Controlled Release*, 2013, **167**, 92-100.

50. T. Yu, D. Hubbard, A. Ray and H. Ghandehari, *Journal of Controlled Release*, 2012, **163**, 46-54.
51. M. Longmire, P. L. Choyke and H. Kobayashi, *Nanomedicine*, 2008, **3**, 703-717.
52. R. Bian, T. Wang, L. Zhang, L. Li and C. Wang, *Biomaterials Science*, 2015, **3**, 1270-1278.
53. R. C. Huxford, J. D. Rocca and W. Lin, *Current Opinion in Chemical Biology*, 2010, **14**, 262-268.
54. S. Beg, M. Rahman, A. Jain, S. Saini, P. Midoux, C. Pichon, F. J. Ahmad and S. Akhter, *Drug Discovery Today*, 2017, **22**, 625-637.
55. P. Horcajada, C. Serre, M. Vallet-Regí, M. Sebban, F. Taulelle and G. Férey, *Angewandte Chemie International Edition*, 2006, **45**, 5974-5978.
56. J. D. Rocca, D. Liu and W. Lin, *Accounts of Chemical Research*, 2011, **44**, 957-968.
57. K. M. L. Taylor-Pashow, J. D. Rocca, Z. Xie, S. Tran and W. Lin, *Journal of the American Chemical Society*, 2009, **131**, 14261-14263.
58. S. M. Cohen, *Chemical Reviews*, 2012, **112**, 970-1000.
59. Z. Wang and S. M. Cohen, *Chemical Society Reviews*, 2009, **38**, 1315-1329.
60. R. J. Marshall and R. S. Forgan, *European Journal of Inorganic Chemistry*, 2016, **27**, 4310-4331.
61. C. V. McGuire and R. S. Forgan, *Chemical Communications*, 2015, **51**, 5199-5217.
62. D. Zacher, R. Schmid, C. Wöll and R. A. Fischer, *Angewandte Chemie International Edition*, 2011, **50**, 176-199.
63. W. J. Rieter, K. M. L. Taylor and W. Lin, *Journal of the American Chemical Society*, 2007, **129**, 9852-9853.
64. H. Furukawa, K. E. Cordova, M. O'Keeffe and O. M. Yaghi, *Science*, 2013, **341**.
65. O. M. Yaghi and H. Li, *Journal of the American Chemical Society*, 1995, **117**, 10401-10402.
66. P. Z. Moghadam, A. Li, S. B. Wiggin, A. Tao, A. G. P. Maloney, P. A. Wood, S. C. Ward and D. Fairen-Jimenez, *Chemistry of Materials*, 2017, **29**, 2618-2625.
67. O. M. Yaghi, M. O'Keeffe, N. W. Ockwig, H. K. Chae, M. Eddaoudi and J. Kim, *Nature*, 2003, **423**, 705-714.
68. Y. Pan, Y. Liu, G. Zeng, L. Zhao and Z. Lai, *Chemical Communications*, 2011, **47**, 2071-2073.
69. G. Férey, C. Serre, C. Mellot-Draznieks, F. Millange, S. Surblé, J. Dutour and I. Margiolaki, *Angewandte Chemie International Edition*, 2004, **43**, 6296-6301.
70. J. H. Cavka, S. Jakobsen, U. Olsbye, N. Guillou, C. Lamberti, S. Bordiga and K. P. Lillerud, *Journal of the American Chemical Society*, 2008, **130**, 13850-13851.
71. P. Horcajada, H. Chevreau, D. Heurtaux, F. Benyettou, F. Salles, T. Devic, A. Garcia-Marquez, C. Yu, H. Lavrard, C. L. Dutson, E. Magnier, G. Maurin, E. Elkaim and C. Serre, *Chemical Communications*, 2014, **50**, 6872-6874.
72. Y.-R. Lee, M.-S. Jang, H.-Y. Cho, H.-J. Kwon, S. Kim and W.-S. Ahn, *Chemical Engineering Journal*, 2015, **271**, 276-280.
73. Y. Sun and H.-C. Zhou, *Science and Technology of Advanced Materials*, 2015, **16**, 054202-054213.
74. E. Bellido, T. Hidalgo, M. V. Lozano, M. Guillevic, R. Simón-Vázquez, M. J. Santander-Ortega, Á. González-Fernández, C. Serre, M. J. Alonso and P. Horcajada, *Advanced Healthcare Materials*, 2015, **4**, 1246-1257.

75. S. Sene, M. T. Marcos-Almaraz, N. Menguy, J. Scola, J. Volatron, R. Rouland, J.-M. Grenèche, S. Miraux, C. Menet, N. Guillou, F. Gazeau, C. Serre, P. Horcajada and N. Steunou, *Chem*, 2017, **3**, 303-322.
76. E. Bellido, M. Guillevic, T. Hidalgo, M. J. Santander-Ortega, C. Serre and P. Horcajada, *Langmuir*, 2014, **30**, 5911-5920.
77. J. Cravillon, R. Nayuk, S. Springer, A. Feldhoff, K. Huber and M. Wiebcke, *Chemistry of Materials*, 2011, **23**, 2130-2141.
78. J. Yao, M. He and H. Wang, *CrystEngComm*, 2015, **17**, 4970-4976.
79. X. Liu, Y. Li, Y. Ban, Y. Peng, H. Jin, H. Bux, L. Xu, J. Caro and W. Yang, *Chemical Communications*, 2013, **49**, 9140-9142.
80. C.-Y. Sun, C. Qin, X.-L. Wang, G.-S. Yang, K.-Z. Shao, Y.-Q. Lan, Z.-M. Su, P. Huang, C.-G. Wang and E.-B. Wang, *Dalton Transactions*, 2012, **41**, 6906-6909.
81. D. J. Tranchemontagne, J. R. Hunt and O. M. Yaghi, *Tetrahedron*, 2008, **64**, 8553-8557.
82. H. Li, M. Eddaoudi, M. O'Keeffe and O. M. Yaghi, *Nature*, 1999, **402**, 276.
83. Y. Bai, Y. Dou, L.-H. Xie, W. Rutledge, J.-R. Li and H.-C. Zhou, *Chemical Society Reviews*, 2016, **45**, 2327-2367.
84. *The MAK-Collection for Occupational Health and Safety*, 2002.
85. J. B. DeCoste, G. W. Peterson, H. Jasuja, T. G. Glover, Y.-g. Huang and K. S. Walton, *Journal of Materials Chemistry A*, 2013, **1**, 5642-5650.
86. J. E. Mondloch, M. J. Katz, N. Planas, D. Semrouni, L. Gagliardi, J. T. Hupp and O. K. Farha, *Chemical Communications*, 2014, **50**, 8944-8946.
87. H.-L. Jiang, D. Feng, K. Wang, Z.-Y. Gu, Z. Wei, Y.-P. Chen and H.-C. Zhou, *Journal of the American Chemical Society*, 2013, **135**, 13934-13938.
88. S. J. Garibay and S. M. Cohen, *Chemical Communications*, 2010, **46**, 7700-7702.
89. M. Kandiah, M. H. Nilsen, S. Usseglio, S. Jakobsen, U. Olsbye, M. Tilset, C. Larabi, E. A. Quadrelli, F. Bonino and K. P. Lillerud, *Chemistry of Materials*, 2010, **22**, 6632-6640.
90. D. Feng, W.-C. Chung, Z. Wei, Z.-Y. Gu, H.-L. Jiang, Y.-P. Chen, D. J. Darensbourg and H.-C. Zhou, *Journal of the American Chemical Society*, 2013, **135**, 17105-17110.
91. C. Wang, X. Liu, J. P. Chen and K. Li, *Scientific Reports*, 2015, **5**, 16613.
92. G. C. Shearer, S. Chavan, S. Bordiga, S. Svelle, U. Olsbye and K. P. Lillerud, *Chemistry of Materials*, 2016, **28**, 3749-3761.
93. A. Schaate, P. Roy, T. Preuße, S. J. Lohmeier, A. Godt and P. Behrens, *Chemistry – A European Journal*, 2011, **17**, 9320-9325.
94. J. Lippke, B. Brosent, T. von Zons, E. Virmani, S. Lilienthal, T. Preuße, M. Hülsmann, A. M. Schneider, S. Wuttke, P. Behrens and A. Godt, *Inorganic Chemistry*, 2017, **56**, 748-761.
95. M. Kim and S. M. Cohen, *CrystEngComm*, 2012, **14**, 4096-4104.
96. D. Feng, Z. Y. Gu, J. R. Li, H. L. Jiang, Z. Wei and H. C. Zhou, *Angewandte Chemie International Edition*, 2012, **51**, 10307-10310.
97. J. E. Mondloch, W. Bury, D. Fairen-Jimenez, S. Kwon, E. J. DeMarco, M. H. Weston, A. A. Sarjeant, S. T. Nguyen, P. C. Stair, R. Q. Snurr, O. K. Farha and J. T. Hupp, *Journal of the American Chemical Society*, 2013, **135**, 10294-10297.
98. W. Liang and D. M. D'Alessandro, *Chemical Communications*, 2013, **49**, 3706-3708.
99. M. J. Katz, Z. J. Brown, Y. J. Colon, P. W. Siu, K. A. Scheidt, R. Q. Snurr, J. T. Hupp and O. K. Farha, *Chemical Communications*, 2013, **49**, 9449-9451.
100. A. Schaate, P. Roy, A. Godt, J. Lippke, F. Waltz, M. Wiebcke and P. Behrens, *Chemistry – A European Journal*, 2011, **17**, 6643-6651.

101. G. Wißmann, A. Schaate, S. Lilienthal, I. Bremer, A. M. Schneider and P. Behrens, *Microporous and Mesoporous Materials*, 2012, **152**, 64-70.
102. R. J. Marshall, C. L. Hobday, C. F. Murphie, S. L. Griffin, C. A. Morrison, S. A. Moggach and R. S. Forgan, *Journal of Materials Chemistry A*, 2016, **4**, 6955-6963.
103. M. R. DeStefano, T. Islamoglu, S. J. Garibay, J. T. Hupp and O. K. Farha, *Chemistry of Materials*, 2017, **29**, 1357-1361.
104. N. Stock and S. Biswas, *Chemical Reviews*, 2012, **112**, 933-969.
105. S. Tai, W. Zhang, J. Zhang, G. Luo, Y. Jia, M. Deng and Y. Ling, *Microporous and Mesoporous Materials*, 2016, **220**, 148-154.
106. S. Hermes, T. Witte, T. Hikov, D. Zacher, S. Bahn Müller, G. Langstein, K. Huber and R. A. Fischer, *Journal of the American Chemical Society*, 2007, **129**, 5324-5325.
107. H. Guo, Y. Zhu, S. Wang, S. Su, L. Zhou and H. Zhang, *Chemistry of Materials*, 2012, **24**, 444-450.
108. B. Van de Voorde, I. Stassen, B. Bueken, F. Vermoortele, D. De Vos, R. Ameloot, J.-C. Tan and T. D. Bennett, *Journal of Materials Chemistry A*, 2015, **3**, 1737-1742.
109. R. Makiura, S. Motoyama, Y. Umemura, H. Yamanaka, O. Sakata and H. Kitagawa, *Nature Materials*, 2010, **9**, 565-571.
110. T. Tsuruoka, S. Furukawa, Y. Takashima, K. Yoshida, S. Isoda and S. Kitagawa, *Angewandte Chemie International Edition*, 2009, **48**, 4739-4743.
111. A. Umemura, S. Diring, S. Furukawa, H. Uehara, T. Tsuruoka and S. Kitagawa, *Journal of the American Chemical Society*, 2011, **133**, 15506-15513.
112. J. Zajac, H. Kostrhunova, V. Novohradsky, O. Vrana, R. Raveendran, D. Gibson, J. Kasparkova and V. Brabec, *Journal of Inorganic Biochemistry.*, 2016, **156**, 89-97.
113. T. Rijnaarts, R. Mejia-Ariza, R. J. M. Egberink, W. van Roosmalen and J. Huskens, *Chemistry – A European Journal*, 2015, **21**, 10296-10301.
114. M. Taddei, K. C. Dumbgen, J. A. van Bokhoven and M. Ranocchiari, *Chemical Communications*, 2016, **52**, 6411-6414.
115. F. Wang, H. Guo, Y. Chai, Y. Li and C. Liu, *Microporous and Mesoporous Materials*, 2013, **173**, 181-188.
116. M. J. Cliffe, W. Wan, X. Zou, P. A. Chater, A. K. Kleppe, M. G. Tucker, H. Wilhelm, N. P. Funnell, F. X. Coudert and A. L. Goodwin, *Nature Communications*, 2014, **5**, 4176.
117. C. A. Trickett, K. J. Gagnon, S. Lee, F. Gándara, H.-B. Bürgi and O. M. Yaghi, *Angewandte Chemie*, 2015, **54**, 11162-11167.
118. H. Wu, Y. S. Chua, V. Krungleviciute, M. Tyagi, P. Chen, T. Yildirim and W. Zhou, *Journal of the American Chemical Society*, 2013, **135**, 10525-10532.
119. F. Vermoortele, B. Bueken, G. Le Bars, B. Van de Voorde, M. Vandichel, K. Houthoofd, A. Vimont, M. Daturi, M. Waroquier, V. Van Speybroeck, C. Kirschhock and D. E. De Vos, *Journal of the American Chemical Society*, 2013, **135**, 11465-11468.
120. W. Morris, S. Wang, D. Cho, E. Auyeung, P. Li, O. K. Farha and C. A. Mirkin, *ACS Applied Material Interfaces*, 2017, **9**, 33413-33418.
121. A. Baeza, D. Ruiz-Molina and M. Vallet-Regí, *Expert Opinion on Drug Delivery*, 2017, **14**, 783-796.
122. R. Mejia-Ariza and J. Huskens, *Journal of Materials Chemistry B*, 2016, **4**, 1108-1115.
123. E.-J. Park and K. Park, *Toxicology Letters*, 2009, **184**, 18-25.
124. D. Feng, Z.-Y. Gu, Y.-P. Chen, J. Park, Z. Wei, Y. Sun, M. Bosch, S. Yuan and H.-C. Zhou, *Journal of the American Chemical Society*, 2014, **136**, 17714-17717.
125. H. X. Zhao, Q. Zou, S. K. Sun, C. Yu, X. Zhang, R. J. Li and Y.-Y. Fu, *Chemical Science*, 2016, **7**, 5294-5301.

126. Y. X. Wang, *Quantitative Imaging in Medicine and Surgery*, 2011, **1**, 35-40.
127. J. Park, Q. Jiang, D. Feng, L. Mao and H.-C. Zhou, *Journal of the American Chemical Society*, 2016, **138**, 3518-3525.
128. R. Röder, T. Preiß, P. Hirschle, B. Steinborn, A. Zimpel, M. Höhn, J. O. Rädler, T. Bein, E. Wagner, S. Wuttke and U. Lächelt, *Journal of the American Chemical Society*, 2017, **139**, 2359-2368.
129. J. Park, Q. Jiang, D. Feng and H.-C. Zhou, *Angewandte Chemie*, 2016, **128**, 7304-7309.
130. S. Wang, W. Morris, Y. Liu, C. M. McGuirk, Y. Zhou, J. T. Hupp, O. K. Farha and C. A. Mirkin, *Angewandte Chemie*, 2015, **54**, 14738–14742.
131. C. He, K. Lu, D. Liu and W. Lin, *Journal of the American Chemical Society*, 2014, **136**, 5181-5184.
132. S. Wang, C. M. McGuirk, M. B. Ross, S. Wang, P. Chen, H. Xing, Y. Liu and C. A. Mirkin, *Journal of the American Chemical Society*, 2017, **139**, 9827-9830.
133. S. Nagata, K. Kokado and K. Sada, *Chemical Communications*, 2015, **51**, 8614-8617.
134. W. Morris, W. E. Briley, E. Auyeung, M. D. Cabezas and C. A. Mirkin, *Journal of the American Chemical Society*, 2014, **136**, 7261-7264.
135. D. Chen, D. Yang, C. A. Dougherty, W. Lu, H. Wu, X. He, T. Cai, M. E. Van Dort, B. D. Ross and H. Hong, *ACS Nano*, 2017, **11**, 4315-4327.
136. R. C. Huxford, K. E. deKrafft, W. S. Boyle, D. Liu and W. Lin, *Chemical Science*, 2012, **3**, 198-204.
137. W. J. Rieter, K. M. Pott, K. M. L. Taylor and W. Lin, *Journal of the American Chemical Society*, 2008, **130**, 11584-11585.
138. L. He, M. Brasino, C. Mao, S. Cho, W. Park, A. P. Goodwin and J. N. Cha, *Small*, 2017, **13**, 1700504-1700511.
139. C. Orellana-Tavra, R. J. Marshall, E. F. Baxter, I. A. Lazaro, A. Tao, A. K. Cheetham, R. S. Forgan and D. Fairen-Jimenez, *Journal of Materials Chemistry B*, 2016, **4**, 7697-7707.
140. C. Orellana-Tavra, S. Haddad, R. J. Marshall, I. Abánades Lázaro, G. Boix, I. Imaz, D. Maspoch, R. S. Forgan and D. Fairen-Jimenez, *ACS Applied Materials Interfaces*, 2017, **9**, 35516-35525.
141. K. Jiang, L. Zhang, Q. Hu, D. Zhao, T. Xia, W. Lin, Y. Yang, Y. Cui, Y. Yang and G. Qian, *Journal of Materials Chemistry B*, 2016, **4**, 6398-6401.
142. N. Oh and J. H. Park, *International Journal of Nanomedicine*, 2014, **9**, 51-63.
143. P. R. Taylor, L. Martinez-Pomares, M. Stacey, H. H. Lin, G. D. Brown and S. Gordon, *Annual Review of Immunology*, 2005, **23**, 901-944.
144. E. Duvall, A. H. Wyllie and R. G. Morris, *Immunology*, 1985, **56**, 351-358.
145. H. Gao, W. Shi and L. B. Freund, *Proceedings of the National Academy of Sciences of the United States of America*, 2005, **102**, 9469-9474.
146. J. Rejman, V. Oberle, I. S. Zuhorn and D. Hoekstra, *The Biochemical journal*, 2004, **377**, 159-169.
147. C. Orellana-Tavra, S. A. Mercado and D. Fairen-Jimenez, *Advanced Healthcare Materials*, 2016, **5**, 2261-2270.
148. H. T. McMahon and E. Boucrot, *Nature reviews. Molecular cell biology*, 2011, **12**, 517-533.
149. S. Mayor and R. E. Pagano, *Nature reviews. Molecular cell biology*, 2007, **8**, 603-612.
150. J. Shin and S. N. Abraham, *Immunology*, 2001, **102**, 2-7.

151. A. L. Kiss and E. Botos, *Journal of Cellular and Molecular Medicine*, 2009, **13**, 1228-1237.
152. J. L. Perry, K. G. Reuter, M. P. Kai, K. P. Herlihy, S. W. Jones, J. C. Luft, M. Napier, J. E. Bear and J. M. DeSimone, *Nano Letters*, 2012, **12**, 5304-5310.
153. N. A. Mohamed, R. Davies, P. D. Lickiss, H. Saleem, D. M. Reed, P. M. George, J. S. Wort, G. Freeman, L. M. Gutierrez, D. Morales, B. B. Barba, A. H. Chester, M. H. Yacoub and J. A. Mitchell, *Qatar Foundation Annual Research Conference Proceedings*, 2016, **2016**, HBSP2477.
154. M.-X. Wu and Y.-W. Yang, *Advanced Materials*, 2017, **29**, 1606134.

## Chapter 2

# Coordination Modulation of Zirconium MOFs

**This Chapter is adapted in part from the following publications:**

“Selective Surface PEGylation of UiO-66 Nanoparticles for Enhanced Stability, Cell Uptake and pH Responsive Drug Delivery”

*Chem*, **2017**, 2, 561–578. (DOI: 10.1016/j.chempr.2017.02.005.)

**I. Abánades Lázaro**, S. Haddad, S. Sacca, C. Orellana-Tavra, D. Fairen-Jimenez and R. S. Forgan

“Mechanistic Investigation into the Selective Anticancer Cytotoxicity and Immune System Response of Surface Functionalised, Dichloroacetate-Loaded, UiO-66 Nanoparticles”

*ACS Appl. Mater. Interfaces*, **2018**, 10, 6, 5255-5268 (DOI: 10.1021/acsami.7b17756)

**I. Abánades Lázaro**, S. Haddad, J. Rodrigo-Muñoz, C. Orellana-Tavra, V. del Pozo, D. Fairen-Jimenez, and Ross S. Forgan

“Enhancing Anticancer Cytotoxicity through Bimodal Drug Delivery from Ultrasmall Zr MOF Nanoparticles”

*Chem. Commun.*, **2018**, 54, 2792-2795. (DOI: 10.1039/C7CC09739E)

**I. Abánades Lázaro**, S. Abánades Lázaro and R. S. Forgan.

**Table of Contents**

<b>Chapter 2</b> .....	43
2.1 Introduction.....	45
2.2 Aims .....	46
2.3 UiO-66 Modulated Synthesis and Characterisation.....	48
2.3.1 The Use of Functionalised Benzoic Acid Derivatives as Modulators.....	49
2.3.2 The Use of Biotin and Folic Acid as Modulators .....	55
2.3.3 The Use of Dichloroacetic acid (DCA) as Modulator.....	63
2.3.4 Co-Modulated Synthesis of DCA-containing, Surface Modified UiO-66 .....	70
2.4. DCA Modulated Synthesis of the UiO Family of Isoreticular MOFs .....	77
2.5. Conclusions and Future Work.....	92
2.6. Experimental.....	93
2.7 References .....	99

## 2.1 Introduction

The high drug loading and excellent biocompatibilities of metal-organic frameworks (MOFs) have led to their application as drug delivery systems (DDSs).<sup>1-3</sup> Nanoparticle surface chemistry dominates both biostability and dispersion of DDSs while governing their interactions with biological systems, cellular and/or tissue targeting, and cellular internalisation, leading to a requirement for versatile and reproducible surface functionalisation protocols. Although a considerable amount of work has been performed to modify the bulk structure and internal pore spaces of MOFs,<sup>4-11</sup> only few studies have addressed their external surface chemistry, usually through surface-selective postsynthetic modification protocols designed for specific MOFs and surface substrates.<sup>12-17</sup>

Effective cell internalisation and intracellular drug release are vital characteristics of effective nanoparticulate DDSs.<sup>18-22</sup> Nanoparticles are generally internalised through active transport mechanisms such as endocytosis, however, if they are small enough (<20 nm), nanoparticles can be internalised by passive diffusion, enabling direct release of cargo into the cytosol.<sup>23</sup> Cell internalisation pathways are closely related to both particle size and surface chemistry.<sup>22, 24, 25</sup> It has been recently reported that 50-600 nm nanoparticles of UiO-66, the zirconium 1,4-benzenedicarboxylate (bdc)<sup>26</sup> MOF with ideal formula  $[\text{Zr}_6\text{O}_4(\text{OH})_4(\text{bdc})_6]_n$ , and its -Br, -NO<sub>2</sub>, and -NH<sub>2</sub> functionalised derivatives undergo HeLa cancer cell internalisation primarily through clathrin-mediated endocytosis, while isorecticular MOFs with more hydrophobic, extended linkers, such as 2,6-naphthalenedicarboxylate and 4,4'-biphenyldicarboxylate, are partially internalised through caveolae-mediated endocytosis and release their cargo into the cytosol, thus enhancing therapeutic efficiency.<sup>27</sup>

The size and shape of NMOF particles can be tuned by introducing modulators – monotopic capping agents such as benzoic acid - to their syntheses.<sup>28-33</sup> It is well known that monocarboxylic acid modulators can be attached to Zr MOFs surface and defect sites during synthesis, boosting their porosity.<sup>34-37</sup> Coordination modulation offers the prospect of decorating the external surfaces of MOFs with desirable functionality during the synthetic process, but this remains a challenging process.

## 2.2 Aims

Despite the clear need to develop reproducible and versatile protocols to modify the outer surfaces of MOFs, few studies have addressed this issue so far, and even though it has been reported that drugs can be introduced into MOFs during synthesis, achieving one pot-syntheses to create drug containing nanoparticulate MOFs (NMOFs) with functionalised surface is still a challenging goal.

UiO-66 was chosen as the object of study as it has excellent biocompatibility<sup>38</sup> which, together with its well-characterised structure,<sup>26</sup> ability to cross the cell membrane<sup>39, 40</sup> and pH responsive drug release,<sup>40, 41</sup> makes it a great candidate for nanoparticle-conjugated anti-cancer drug delivery. Additionally, it is well known that monocarboxylic acid functionalised modulators can be attached to its surface and defect sites during synthesis, yielding highly porous nanoparticles.<sup>36, 42, 43</sup>

With this ultimate aim, a protocol to introduce various surface reagents and an anticancer metabolic target (Figure 2.1a) to UiO-66 external surface and defect sites during its synthetic process has been conceived. Functionalised *p*-benzoic acid modulators, *p*-azidomethylbenzoic acid (L1) and *p*-propargyloxybenzoic acid (L2), have been chosen as modulators due to their structural similarities compared to the bdc linker, and the fact that, if attached to the Zr<sub>6</sub> clusters of UiO-66, the desired functionalities should point outwards, resulting in accessible reactive groups as platforms for further postsynthetic modifications on its surface (Figure 2.1b).

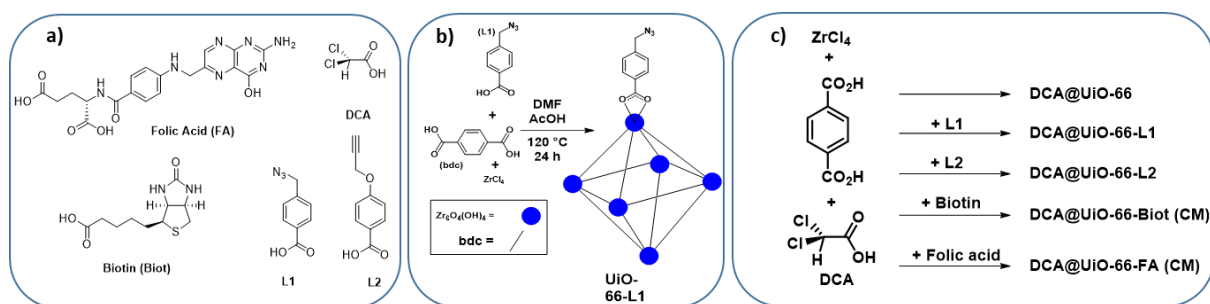


**Figure 2.1.** a). Scope of modulators utilised in UiO-66 modulated synthesis. b) Schematic representation of UiO-66-L1 synthesis, in which modulator L1 gets attached to the Zr<sub>6</sub> clusters on UiO-66 surface during synthesis. c) Synthesis of DCA-loaded, surface modified MOFs obtained through coordination modulation (CM)

Additionally, more complex carboxylate containing molecules such as vitamin B<sub>9</sub> folic acid (FA) and vitamin B<sub>7</sub> biotin (Biot) will be used to modulate UiO-66 synthesis. Particularly, FA has been widely used as a targeting unit for cancer cells, as most of them overexpress the folate receptor (FR) on their cell membrane surface, enhancing and directing the uptake of

the DDSs to cancer cells. In order to study the modulating capability of the selected modulators, the modulated samples were compared with unmodulated or AcOH modulated UiO-66.

Dichloroacetic acid (DCA), a small molecule that inhibits pyruvate kinase dehydrogenase, targeting the metabolism of cancer cells (See section 5.1.3 for full discussion), has been chosen as a modulator of UiO-66, in order to synthesise drug-containing surface functionalised MOFs by one-pot synthesis. The lower  $pK_a$  value (1.36) of dichloroacetic acid means that considerable amounts could be attached to UiO-66 Zr positions at defect sites during synthesis, even in the presence of other functionalised modulators (Figure 2.1c). Additionally, this concept of defect loading of drugs that act as modulators during synthesis could be applied to any therapeutic molecule containing carboxylate groups, such as doxorubicin.

The DCA-modulated protocol will be extended to the UiO series of isorecticular  $Zr_6$  MOFs (Figure 2.2), which includes the use of terephthalic acid, functionalised terephthalic acid derivatives containing bromo, nitro or amino pendant functionalities and extended linkers such as 2,6 naphthalenedicarboxylic acid, and 4,4' biphenyldicarboxylic acid, forming the MOFs UiO-66, DUT-52 and UiO-67 respectively. These MOFs and their linkers do not induce cytotoxicity to HeLa cervix cancer cells for concentrations up to  $1 \text{ mg mL}^{-1}$ .

Different synthetic conditions will be applied with the aim of controlling particle size and obtaining smaller ( $< 20 \text{ nm}$ ) - in order to enable passive diffusion of the drug containing MOFs into cancer cells with the ultimate goal of enhancing their therapeutic efficiency - and bigger (ca.  $100 \text{ nm}$ ) nanoparticles to allow comparison of their cytotoxicity depending on both size and surface chemistry during Chapter 5.

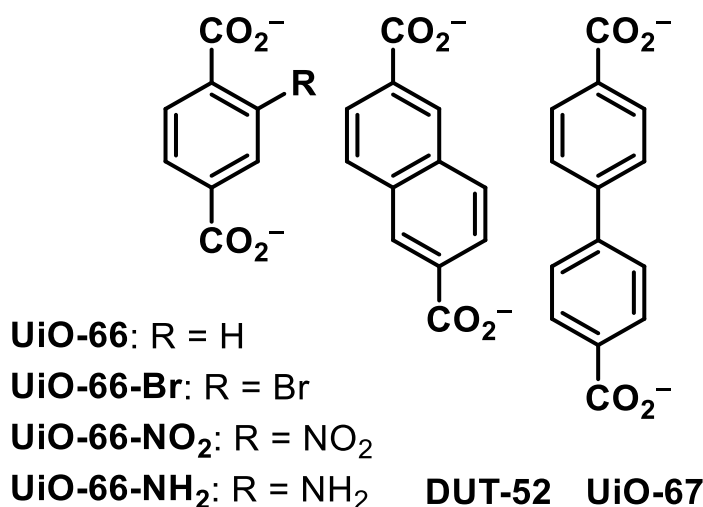


**Figure 2.2.** Structures of linkers used in the preparation of the UiO series of Zr MOFs.

Attaching a small molecule with anticancer activity to MOFs metal clusters, creating defective structures, should allow the possibility of introducing a second drug into the MOF pores for multimodal treatments. For example, cisplatin prodrugs containing axial DCA ligands have been reported to be more effective than cisplatin, and able to overcome cisplatin resistance. Similarly, DCA is known to enhance the anticancer effect of 5-fluorouracil (5-FU) and to reduce resistance. Hence, the smaller DCA@UiO MOFs will be postsynthetically loaded with 5-FU in order to study their cytotoxic activity during Chapter 5.

### **2.3 UiO-66 Modulated Synthesis and Characterisation**

Characterisation of the chemistry at the external surfaces of MOFs is complicated by the surface comprising a small fraction of the bulk material, although general guidelines can be followed. Nuclear magnetic resonance (NMR) spectroscopy of digested samples can give insights into the composition of the sample; the molar ratio of surface components compared to the linker can be estimated based on the intensities of resonances assigned to protons of both the linker and surface reagents, although defectivity hampers efforts to obtain mass fractions of surface functionality. Reactivity of linkers or functionalised modulators can also be assessed. Thermogravimetric analysis (TGA) can provide information on the gravimetric content and nature of the coating. If new mass loss events are observed at a higher temperature than those of free surface reagents, coordinative attachment to the Zr positions rather than simple electrostatic forces or surface adsorption is suggested. Similarly, the shifting of characteristic signals in Fourier transform infrared (FT-IR) spectra resulting from the coordination surface reagents, and/or appearance of new signals corresponding to coordination bonds between Zr and surface reagents, indicate attachment through coordination. Porosity should not be significantly affected by surface functionalisation, although addition of mass at the surfaces may result in lower gravimetric gas uptake and surface areas. If the modified MOF has much lower porosity (or is non-porous), it is an indication that the surface reagents are also coordinated in the inner porosity or simply stored in the pores as guests. Scanning electron microscopy (SEM) may also show the physical effects of surface modification; large polymers may induce “rounding” of particle surfaces. It is important to note that in order to confirm surface coating content and mode, the correlation of a number of techniques is required.

### 2.3.1 The Use of Functionalised Benzoic Acid Derivatives as Modulators

UiO-66 nanoparticles were synthesised via solvothermal conditions<sup>37</sup> (Section 2.6) by adding 1, 3 or 5 equivalents of the desired modulator (L1 or L2) with 7 v/v % acetic acid (AcOH) as co-modulator, yielding in highly crystalline nanoparticles, as confirmed by PXRD (Figure 2.3), with enhanced crystallinity compared to unmodulated or AcOH modulated samples. An unmodulated sample and a sample modulated with 7 v/v % AcOH were synthesised for comparison.

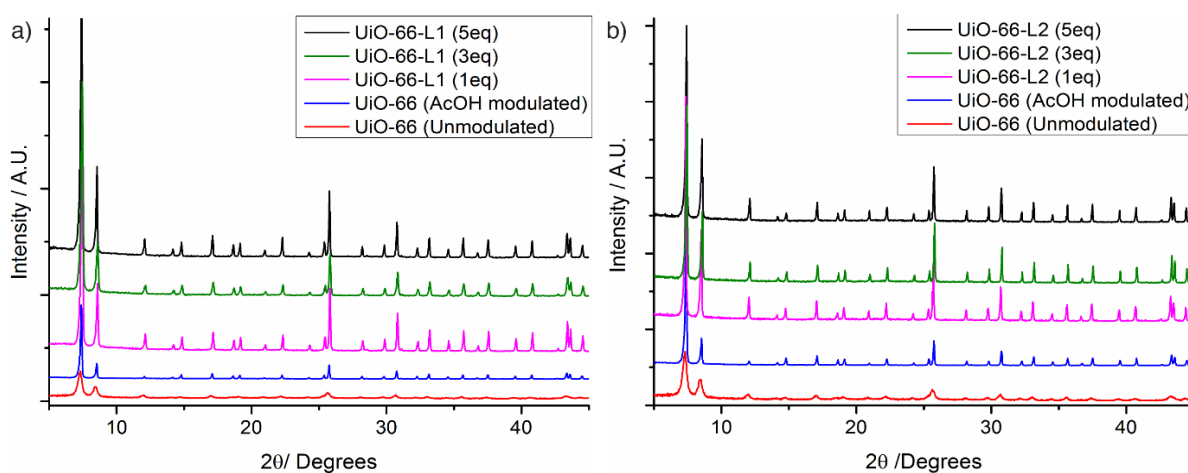


**Figure 2.3.** Stacked PXRD patterns of UiO-66 modulated with a) L1 and b) L2.

The modulator (L1 or L2) content in the UiO-66 samples was calculated using  $^1\text{H}$  NMR spectroscopy of samples digested in  $\text{D}_2\text{SO}_4$  /  $\text{DMSO-}d_6$ . By comparing intensity of one of the aromatic signals of the modulator (d, 2H) to the resonance of the aromatic protons of the bdc linker (s, 4H), it is possible to determine modulator content.

Typical  $^1\text{H}$  NMR spectra are shown in Figure 2.4, which corresponds to UiO-66-L1 (5 eq), and UiO-66-L2 (3 eq). The integral ratios confirm that L1 is present in 13.3% molar ratio when compared to the linker, BDC, and L2 is present in 6.8% molar ratio. In this way, the content of both L1 in UiO-66-L1 and L2 in UiO-66-L2 could be determined (Table 2.1).

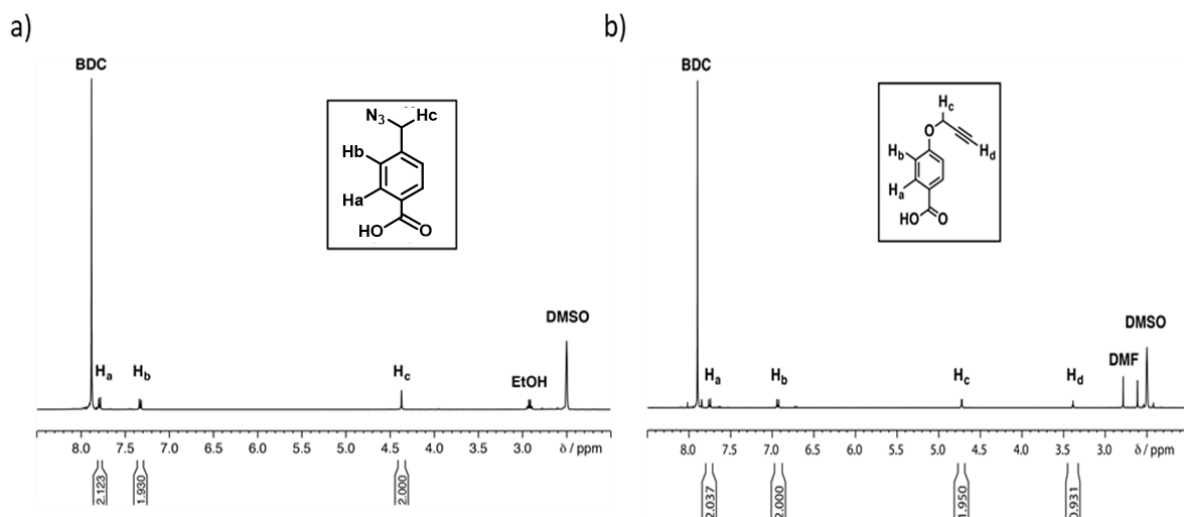


**Figure 2.4.** a)  $^1\text{H}$  NMR spectrum ( $\text{D}_2\text{SO}_4 / \text{DMSO-}d_6$ , 293 K) of UiO-66-L1 (5 eq), showing the presence of the modulator L1. b)  $^1\text{H}$  NMR spectrum ( $\text{D}_2\text{SO}_4 / \text{DMSO-}d_6$ , 293 K) of UiO-66-L2 (3 eq), showing the presence of the modulator L2.

**Table 2.1.** Modulator content in UiO-66 samples determined by  $^1\text{H}$  NMR spectra.

Modulator	L1 (1 eq)	L1 (3 eq)	L1 (5 eq)	L2 (1 eq)	L2 (3 eq)	L2 (5 eq)
Mol % versus bdc	5.6%	8.3%	13.3%	1.2%	6.8%	17.1%

FTIR spectra of the samples revealed an increase in the intensity of the  $\text{N}_3$  vibration band at  $1100 \text{ cm}^{-1}$  as the number of equivalents in UiO-66-L1 syntheses increases, while vibration bands characteristic of C-C triple bonds were observed for UiO-66-L2 (Figure 2.5).

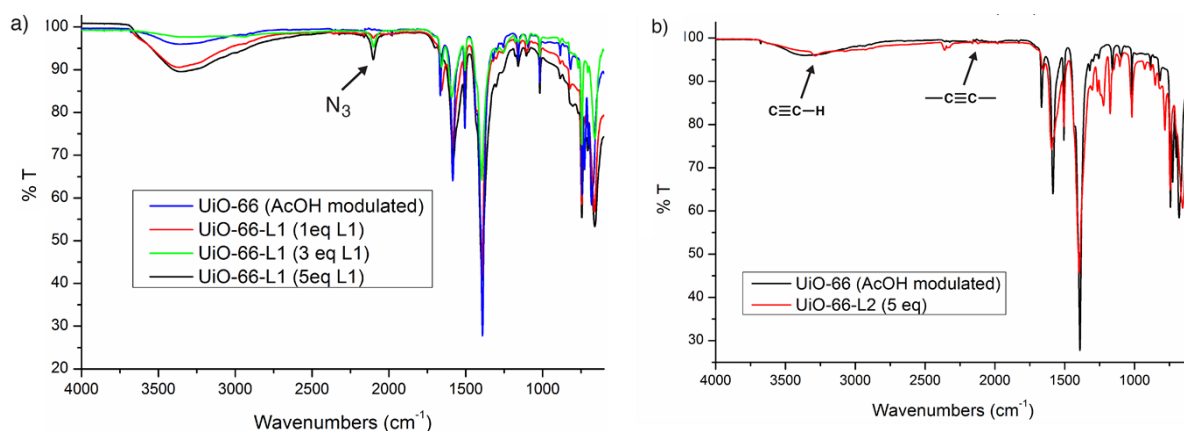


**Figure 2.5.** FTIR spectra of modulated UiO-66 samples showing the presence of functional groups of a) L1 and b) L2 in the synthesised MOF.

The effect of modulator incorporation on particle size was examined by SEM imaging. For UiO-66-AcOH (Figure 2.6), particles were roughly spherical aggregates of very small crystals, with a diameter of around 200 nm.

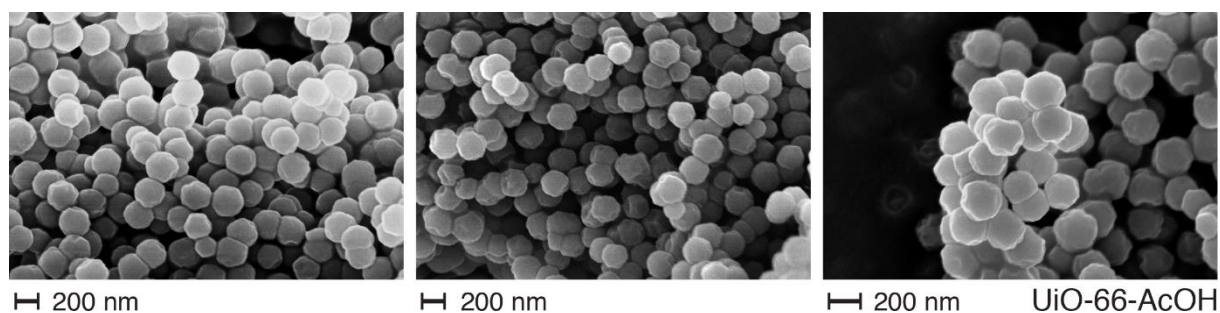


**Figure 2.6.** SEM images of UiO-66-AcOH.

For UiO-66-L1 samples, the morphology is noticeably different, being roughly octahedral crystallites of 100-200 nm in size regardless of the number of equivalents of L1 included in the synthetic mixture (Figure 2.7). UiO-66-L1 synthesised with 5 equivalents of L1 had an average particle size of  $147 \pm 30$  nm, determined by ImageJ software.

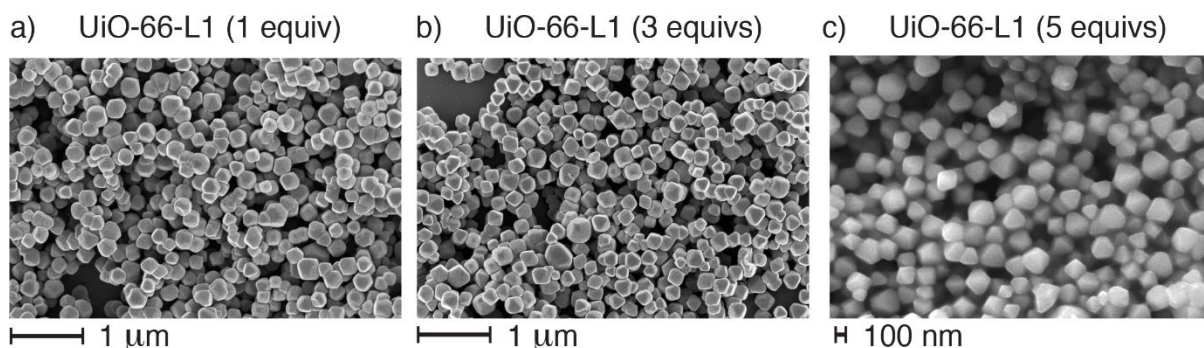


**Figure 2.7.** SEM images of a) UiO-66-L1 (1 equiv), b) UiO-66-L1 (3 equiv), and c) UiO-66-L1 (5 equiv).

In contrast, samples of UiO-66-L2 became larger and more polydisperse as more equivalents of L2 were included in the synthetic mixture (Figure 2.8), reaching sizes of ~600 nm for UiO-66-L2 (5 equiv). UiO-66-L2 (1 equiv) has a reasonable particle size range of around 200-300 nm, but as  $^1\text{H}$  NMR spectroscopic analysis showed very little incorporation of L2, UiO-66-L2 (5 equiv) was used for proof-of-concept surface modification along with UiO-66-L1 (5 equiv) in Chapter 3.

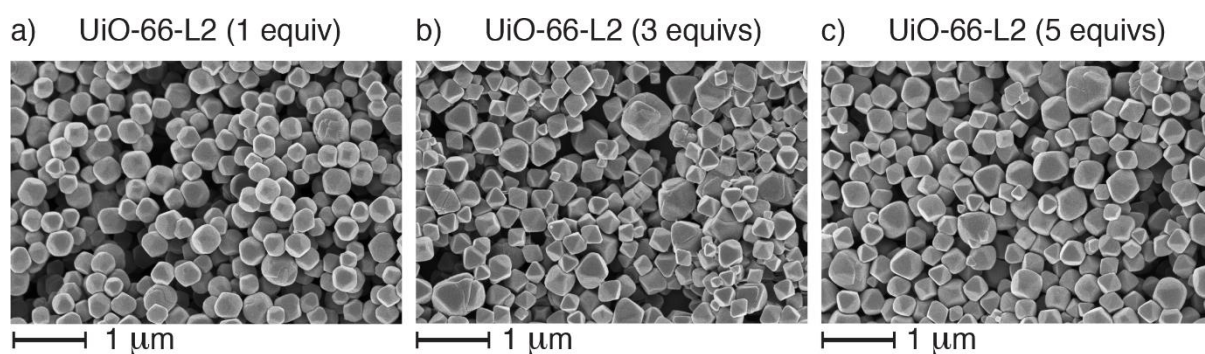


**Figure 2.8.** SEM images of a) UiO-66-L2 (1 equiv), b) UiO-66-L2 (3 equiv), and c) UiO-66-L2 (5 equiv).

The quantities of organic components (either BDC or the modulator) present in UiO-66-L1 and UiO-66-L2 (all subsequent samples synthesised with 5 equivalents of modulator) were calculated by TGA measurements (Figure 2.9) and used for further degradation studies during Chapter 3.

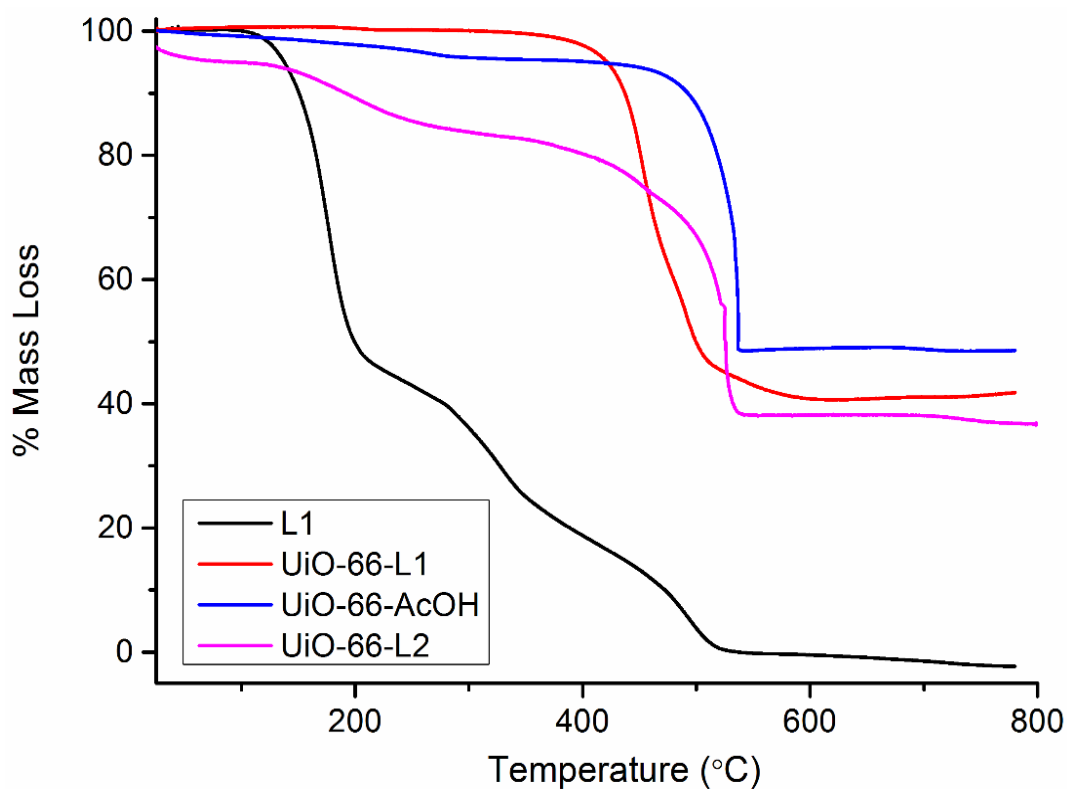


**Figure 2.9.** TGA traces (recorded in air) of UiO-66-L1 and UiO-66-L2, compared to L1 and UiO-66-AcOH.

It has been previously reported that when UiO-66 ( $Zr_6O_4(OH)_4L_6$  theoretical structure) is thermally degraded in air, the first mass loss step at 200-300 °C corresponds to the zirconium clusters losing 2 molecules of water, adopting the  $Zr_6O_6L_6$  molecular formula, then, the ligand decomposition takes place near 500 °C, leaving the residue  $ZrO_2$ .<sup>44</sup> Therefore, by comparing experimental mass loss of the last decomposition step with the weight percent of the linker in the  $[Zr_6O_4(OH)_4L_x]_n$  structure for different values of x, the number of ligands in the structure can be estimated (Table 2.2).

$$Linker\ wt\% = \frac{xL}{Zr_6O_4(OH)_4L_x} * 100$$

**Table 2.2.** Theoretical compositions of different defective UiO-66 samples.

Number of linkers in $Zr_6O_4(OH)_4L_x$	Linker wt%
<b>X=6</b>	59.2 wt%
<b>X=5</b>	54.5 wt%
<b>X=4</b>	49.1 wt%
<b>X=3</b>	42.0 wt%

It can be observed in Figure 2.9 that the last decomposition step of UiO-66-AcOH corresponds to 46.8 wt% of the sample, which matches a material with 2.5 ligands missing, leading the approximate composition  $[Zr_6O_4(OH)_4L_{3.5}]_n$ , with either acetates, chlorides or solvents at defect sites.

When L1 is introduced to the synthetic procedure, the material  $[Zr_6O_4(OH)_4L_x(L1)_y]_n$  shows a similar decomposition profile to UiO-66-AcOH, indicating that L1 degrades together with the linker (BDC) but at a lower temperature, suggesting L1 is incorporated at the surfaces or the particles and at defects. As L1 has a similar molecular weight to the BDC linker the total organic content (BDC and L1) present in the sample has been estimated using the former theoretical calculations. In UiO-66-L1 the last decomposition step corresponds to 59.1% of the total weight of sample, suggesting a full complement of six linkers/modulators in the structure. Therefore, the UiO-66-L1 composition is expected to be close to  $[Zr_6O_4(OH)_4L_{6-x}L1_x]_n$ . UiO-66-L2 shows a more complex degradation profile, in which degradation of the last ligand step corresponds to 46.2 wt%. As its bioapplications, due to particle size, were not further studied (see Chapter 4 and Chapter 5), no in depth analysis of its thermal degradation was performed.

The porosities of the samples were measured by  $N_2$  adsorption isotherms at 77 K, and the adsorption isotherms (Figure 2.10a) yielded the following information:

**UiO-66-AcOH:**  $S_{BET} = 1232 \text{ m}^2\text{g}^{-1}$ ; pore volume =  $0.652 \text{ ccg}^{-1}$ .

**UiO-66-L1:**  $S_{BET} = 1565 \text{ m}^2\text{g}^{-1}$ ; pore volume =  $0.762 \text{ ccg}^{-1}$ .

**UiO-66-L2:**  $S_{BET} = 1420 \text{ m}^2\text{g}^{-1}$ ; pore volume =  $0.702 \text{ ccg}^{-1}$ .

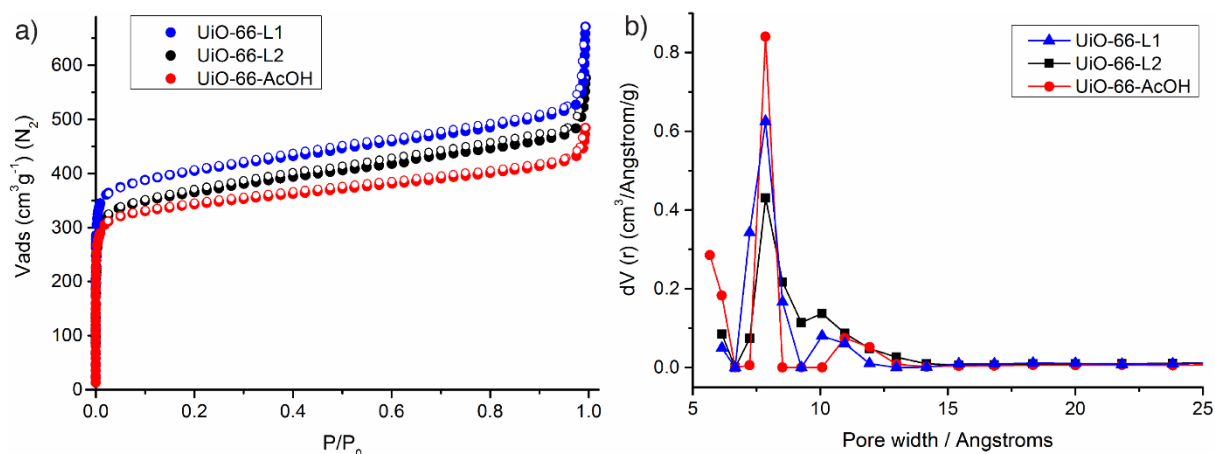


**Figure 2.10.** a) Adsorption and desorption isotherms ( $N_2$ , 77 K) of UiO-66-L1 and UiO-66-L2 modulated samples compared to UiO-66-AcOH. Filled symbols represent adsorption, empty symbols represent desorption. b) Pore size distribution (slit pore,  $N_2$  at 77 K on carbon, QSDFT equilibrium model) of UiO-66-L1 and UiO-66-L2 modulated samples compared to UiO-66-AcOH.

The surface areas for the samples modulated by 5 equivalents of L1 and L2 are enhanced, while the pore size distribution of these modulated samples (Figure 2.10b) is similar to the reported for UiO-66 ( $8 \text{ \AA}$  and  $11 \text{ \AA}$ ).<sup>26</sup> These results, together with the pore volume determination and the surface area of the nanoparticles, unequivocally confirm that the modulators are attached to the surface and defects sites and not stored in the pores of the NMOFs.

### 2.3.2 The Use of Biotin and Folic Acid as Modulators

Four samples were initially prepared by coordination modulation, with biotin and folic acid added during synthesis. The samples are named, taking into account the addition (or not) of acetic acid as a co-modulator during synthesis, UiO-66-FA (CM), UiO-66-Fa-AcOH (CM), UiO-66-Biot (CM), and UiO-66-Biot-AcOH (CM) (Section 2.6). Analysis by PXRD (Figure 2.11) shows that all the samples exhibit characteristic reflections to confirm the formation of UiO-66.<sup>26</sup> When acetic acid (7% v/v) is added to the reaction mixture as a co-modulator, the intensity of the peaks increased. It is notable that UiO-66-FA (CM) has a broad pattern with low intensity, suggesting small particle size or perhaps incorporation of folic acid, which is itself a dicarboxylic acid, into the structure as defects.

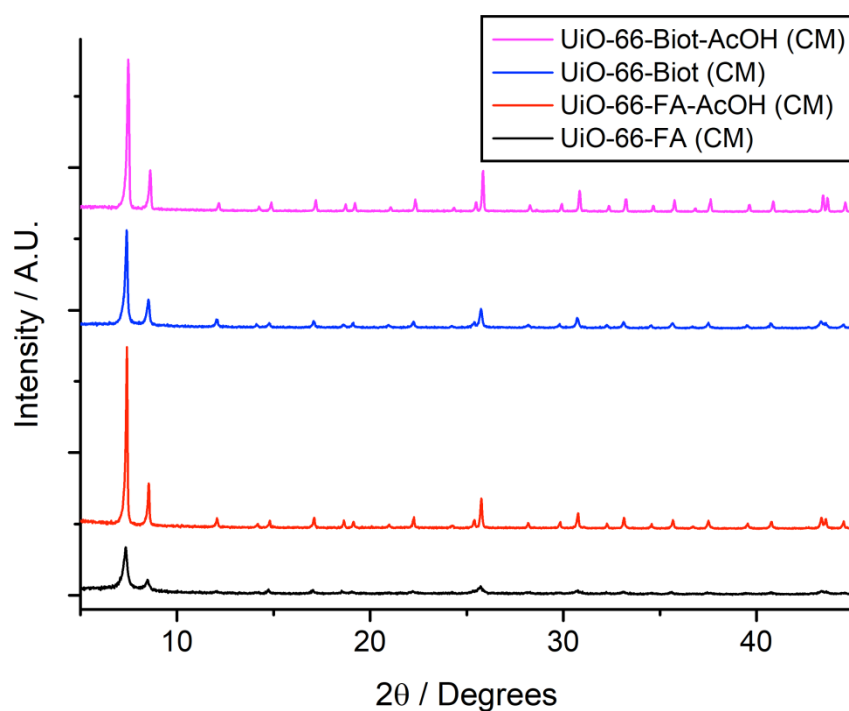


**Figure 2.11.** Stacked PXRD patterns of the surface modified UiO-66 samples prepared by the direct coordination modulation approach.

Due to the strength of the Zr-carboxylate bond, acidification and heating are needed to dissolve the MOFs for  $^1\text{H}$  NMR spectroscopy analysis. Hence, study of the acidified and heated  $^1\text{H}$  NMRs of their surface reagents (folic acid and biotin) is imperative, as the preparation conditions could result in structural composition changes, with different resonance signals and integration ratio than the non-acidified spectra prepared at room temperature. Full characterisation of the surface reagents  $^1\text{H}$  NMRs spectra is given in the appendix, while the MOFs  $^1\text{H}$  NMR spectra are compared to acidified  $^1\text{H}$  NMR of their modulator.

The  $^1\text{H}$  NMR spectra of the modulated samples after acid digestion show the presence of the modulator in all cases. Generally, when acetic acid is added as a co-modulator during synthesis, the quantity of incorporated modulator decreases. This could be explained due to the more acidic pH of the reaction mixture and therefore more gradual deprotonation of the modulators' carboxylic acid groups, or due to competition between the two modulators for the  $\text{Zr}^{4+}$  cations during synthesis.<sup>28</sup> Although the coordination modulation protocol and crystallisation process of these MOFs are still not fully understood, the role of the  $\text{pK}_a$  of the different modulators is thought to play a crucial role.<sup>35, 37</sup>

When only folic acid is used as the modulator in the synthesis of UiO-66-FA (CM), folic acid, which possesses two carboxylic acid groups, is significantly incorporated into the materials, with resonances assigned to folic acid easily identified in the  $^1\text{H}$  NMR spectrum (Figure 2.12) (See appendix for full characterisation of the effect of acid and heating in folic acid  $^1\text{H}$  NMR resonance signals). Analyses based on the intensities of the different resonances of the folic acid alkyl protons (G, H, I, and J) were consistent, and the integral ratios confirm folic acid is present with a 28.0% molar ratio when compared to the bdc linker, while the folic acid content determined by UV-Vis spectra of the digested samples, was 13.6% w/w (Section 2.6)

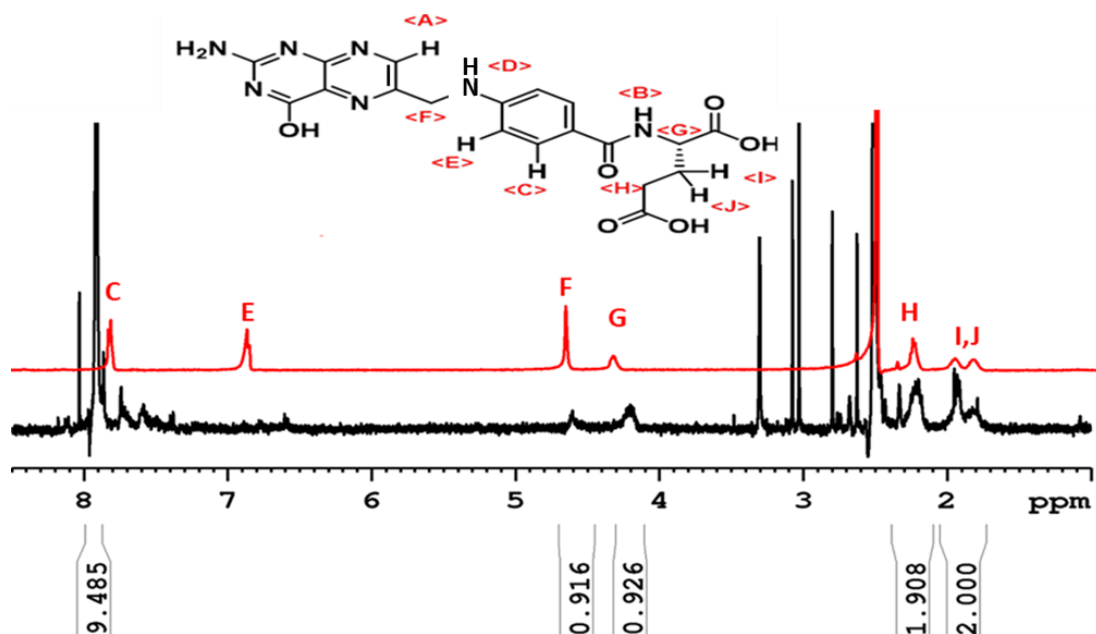


**Figure 2.12.** Stacked partial  $^1\text{H}$  NMR spectra of UiO-66-FA (CM), bottom, and folic acid, top, in  $\text{D}_2\text{SO}_4/\text{DMSO}-d_6$  with signal assignment.

Although still appreciable, folic acid resonances in the  $^1\text{H}$  NMR spectrum of UiO-66-FA-AcOH (CM) have lower intensity, hindering their analysis (Figure 2.13). The lower incorporation when AcOH is added as the co-modulator of the synthesis was expected, and the content of folic acid dropped from 28% molar ratio in UiO-66-FA (CM) to 12% molar ratio in UiO-66-FA-AcOH

(CM), or in other words the incorporation of folic acid decreased by 57% when acetic acid is present, based on  $^1\text{H}$  NMR spectroscopic analysis. The incorporation determined by UV-Vis spectroscopy was 7.0% w/w, around 50% lower than for UiO-66-FA (CM), and in great agreement with the  $^1\text{H}$  NMR spectroscopy results.

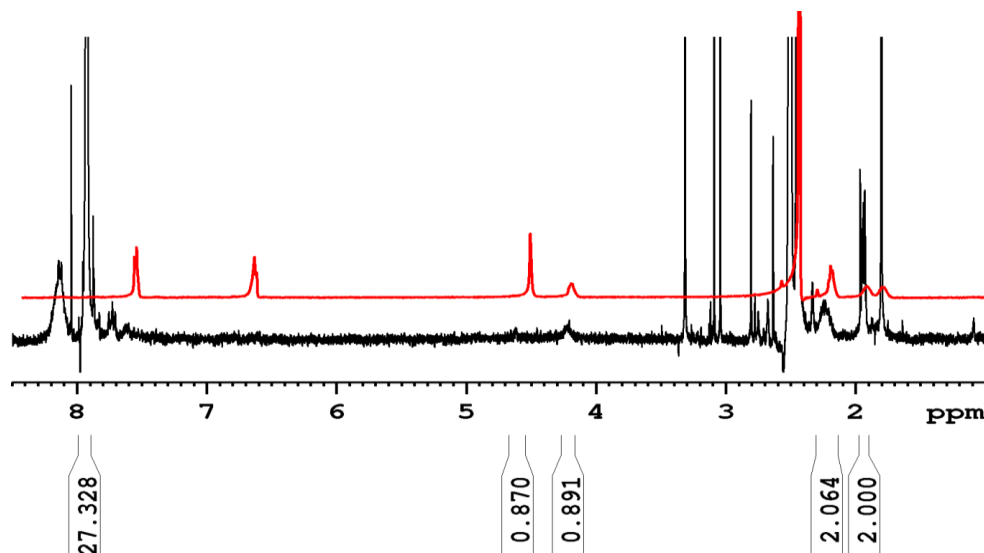


**Figure 2.13.** Stacked partial  $^1\text{H}$  NMR spectra of UiO-66-FA-AcOH (CM), bottom, and folic acid, top, in  $\text{D}_2\text{SO}_4/\text{DMSO}-d_6$ .

The presence of biotin in both UiO-66-Biot (CM) and UiO-66-Biot-AcOH (CM) was also confirmed by  $^1\text{H}$  NMR spectroscopy of the acid-digested samples (Figures 2.14 and 2.15, respectively, See appendix for full biotin acidified  $^1\text{H}$ NMR discussion). Its incorporation was however considerably lower than folic acid, possibly due to the difference in the  $\text{p}K_a$  values of their carboxylic acid groups.<sup>37</sup>

Biotin content was estimated through analysis of alkyl proton resonances; B, C, and D (equivalent for a total of 6H) and A (2H) which were compared to the aromatic resonance for bdc. Integral ratios confirmed the presence of biotin in UiO-66-Biot (CM) in a 7% molar ratio compared to bdc, while UiO-66-Biot-AcOH (CM) shows very little incorporation of biotin, with the resonances observable, but too weak to allow quantification.

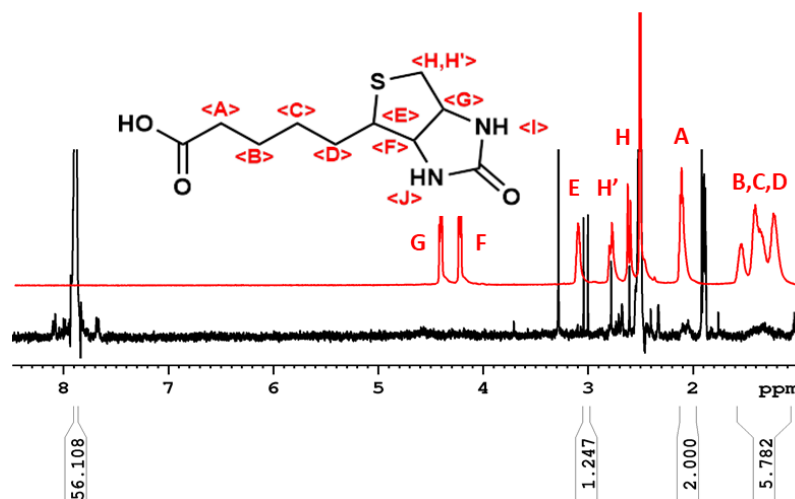


**Figure 2.14.** Stacked partial  $^1\text{H}$  NMR spectra of UiO-66-Biot-AcOH (CM), bottom, and biotin, top, in  $\text{D}_2\text{SO}_4/\text{DMSO-}d_6$  with signal assignment, showing disappearance of resonances for exchangeable N-H protons upon acidification.

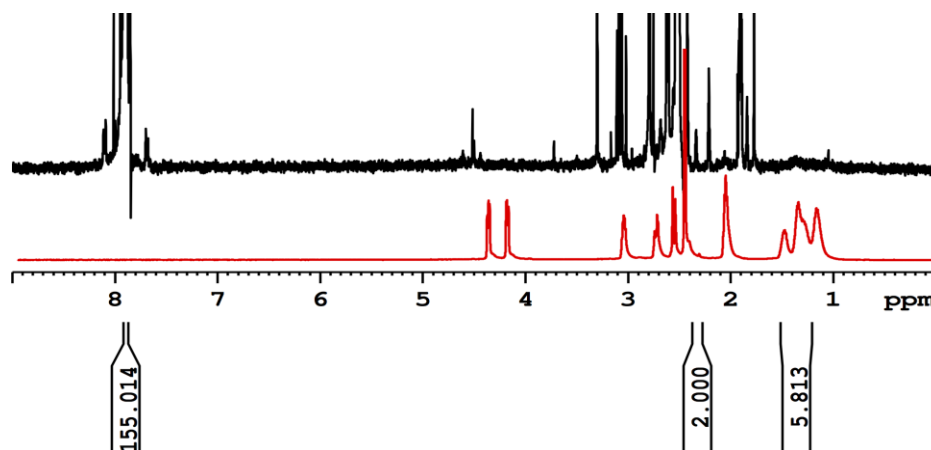


**Figure 2.15.** Stacked partial  $^1\text{H}$  NMR spectra of UiO-66-Biot-AcOH (CM), bottom, and biotin, top, in  $\text{D}_2\text{SO}_4/\text{DMSO-}d_6$ .

While the carboxylic acid groups of the linker bdc have  $pK_a$  values of 3.54 and 4.46, the carboxylic acid groups of folic acid have  $pK_a$  values of 3.5 and 4.3, and the  $pK_a$  of the biotin carboxylic acid is 4.5. The  $pK_a$  values of the linker and the two modulators are close, but folic acid has slightly lower values and also two sites of attachment, possibly explaining why its incorporation is higher.

Different features in the TGA profiles of the modulated samples were observed when compared to unfunctionalised UiO-66 (Figure 2.16).

The folic acid modulated UiO-66 samples showed TGA profiles with additional mass loss features around 300-400°C compared to unfunctionalised UiO-66. These events occur at a higher temperature than for folic acid itself, strongly indicating its attachment to the MOF rather

than being stored in the pores. Due to the gradual thermal degradation of folic acid, quantitative determination of the mass fraction is not possible using TGA. When only folic acid is added as the modulator of UiO-66 synthesis the metal residue at 800 °C is lower than when acetic acid acts as the co-modulator consistent with higher incorporation of folic acid observed in the  $^1\text{H}$  NMR and UV-vis spectra. The linker degradation occurs, although in a more gradual way, at a similar temperature to UiO-66.

When biotin is used as the modulator of UiO-66 synthesis only minor incorporation was observed by  $^1\text{H}$  NMR spectroscopy, decreasing with the addition of AcOH as a co-modulator. Similar TGA profiles to UiO-66 were obtained (Figure 2.16), in which new mass loss events are also observed around 300-450 °C.

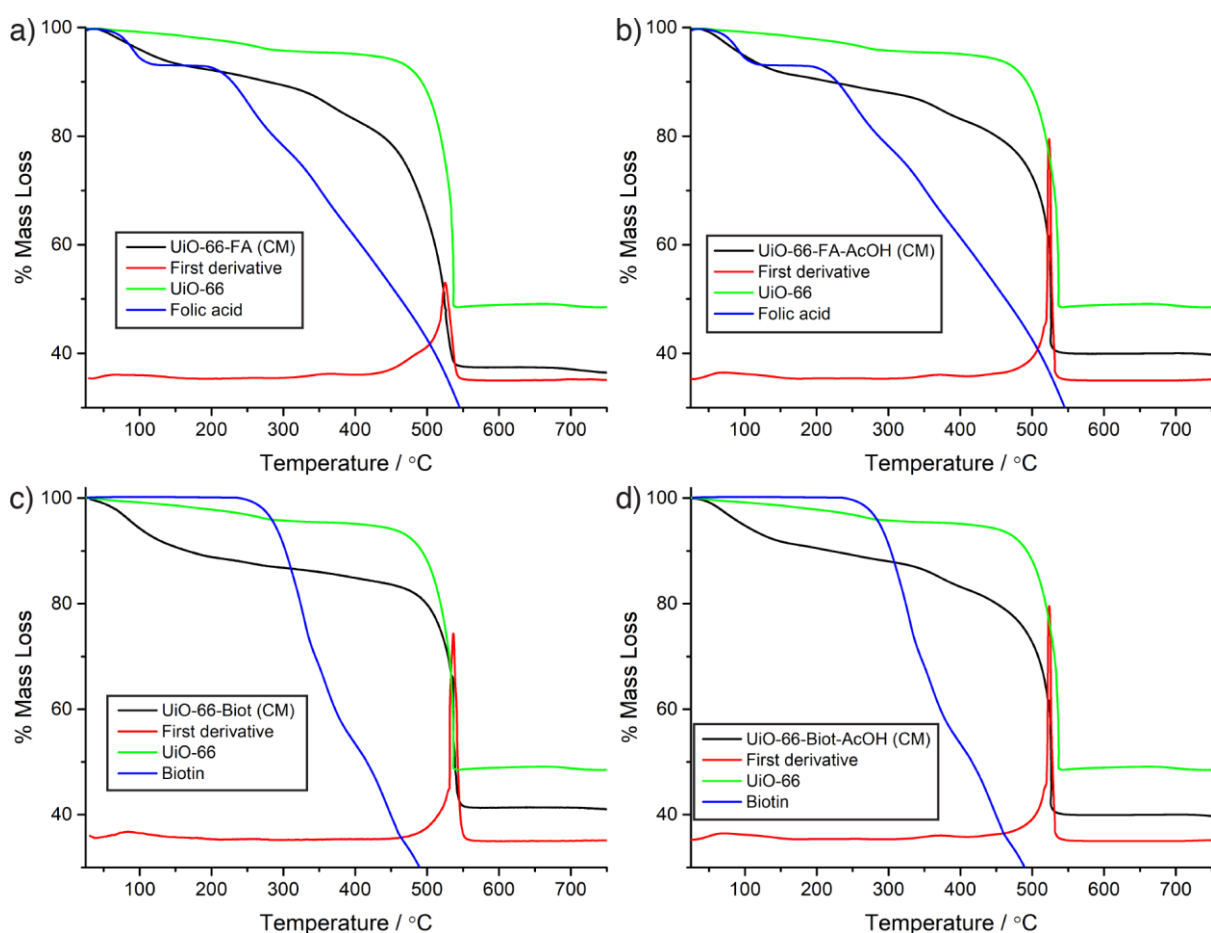


**Figure 2.16.** TGA traces of MOFs surface modified through coordination modulation compared with the surface functionality and unfunctionalised UiO-66, for a) UiO-66-FA (CM), b) UiO-66-FA-AcOH (CM), c) UiO-66-Biot (CM), and d) UiO-66-Biot-AcOH (CM).

The FT-IR spectra of the folic acid modulated samples showed new peaks in the carboxylic acid region ( $1700\text{ cm}^{-1}$ ), matching with a major peak in the FT-IR spectrum of folic acid,

although slightly shifted as a possible consequence of its coordination to the Zr positions (Figure 2.17).

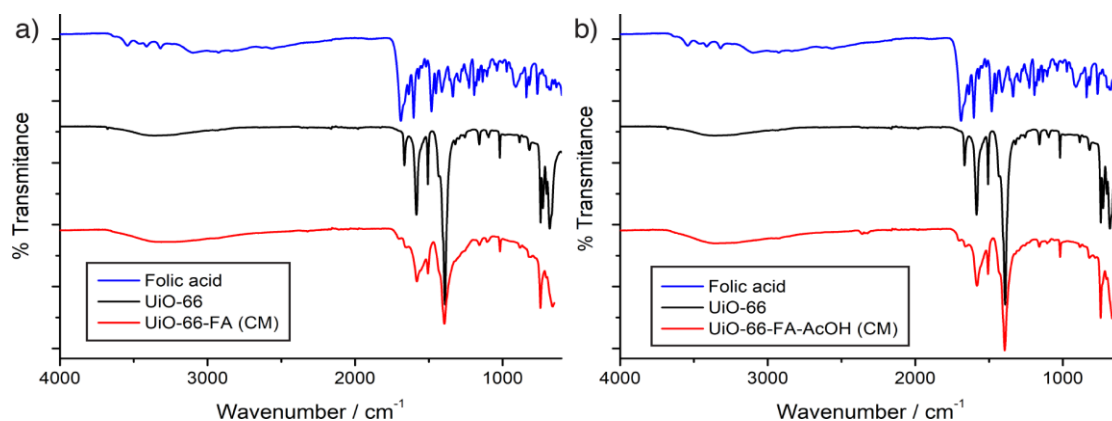


**Figure 2.17.** FT-IR spectra of the folic acid modulated MOFs compared to bare UiO-66 and the surface functionality, for a) UiO-66-FA (CM), and b) UiO-66-FA-AcOH (CM).

When biotin is used as the modulator of UiO-66 synthesis, new characteristic peaks also appear in the same region of the FT-IR spectrum, suggesting coordination and incorporation of biotin into the UiO-66 samples (Figure 2.18).

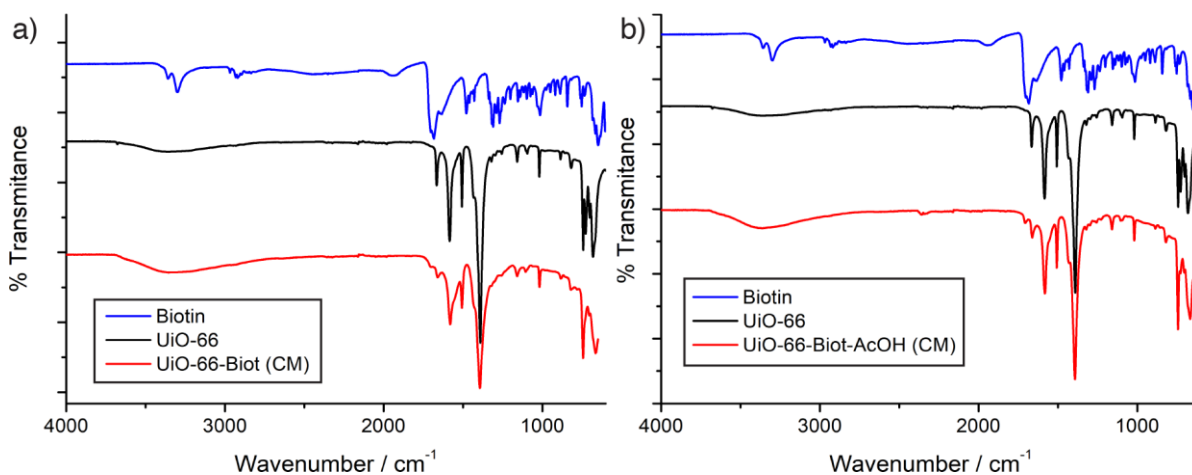


**Figure 2.18.** FT-IR spectra of the biotin modulated MOFs compared to bare UiO-66 and the surface functionality, for a) UiO-66-Biot (CM), and b) UiO-66-Biot-AcOH (CM).

The porosity of the samples was studied using N<sub>2</sub> adsorption and desorption measurements (Figure 2.19). UiO-66-FA (CM) was the only sample with lower porosity compared to UiO-66, but it is also the sample with the highest modulator incorporation and a possibly defective structure, as indicated by the broad PXRD pattern. Folic acid possesses two carboxylic acid groups with a similar arrangement to fumaric acid, which is also capable of forming a UiO-66 topology MOF known as Zr-fumarate.<sup>32</sup> The surface area of UiO-66-FA (CM) is similar to that reported for Zr-fumarate, indicating that folic acid could be partially incorporated as the linker of UiO-66-FA (CM). As folic acid is bigger than UiO-66 pore, its incorporation in the pore

cavities is unlikely. Folic acid incorporation determined by UV-Vis (13.6% w/w), and estimated by  $^1\text{H}$  NMR (28% molar ratio), is considerably large for it to be found only in the outer surface, and it is likely distributed throughout the particles in a defective manner, as indicated by the featureless pore size distribution.

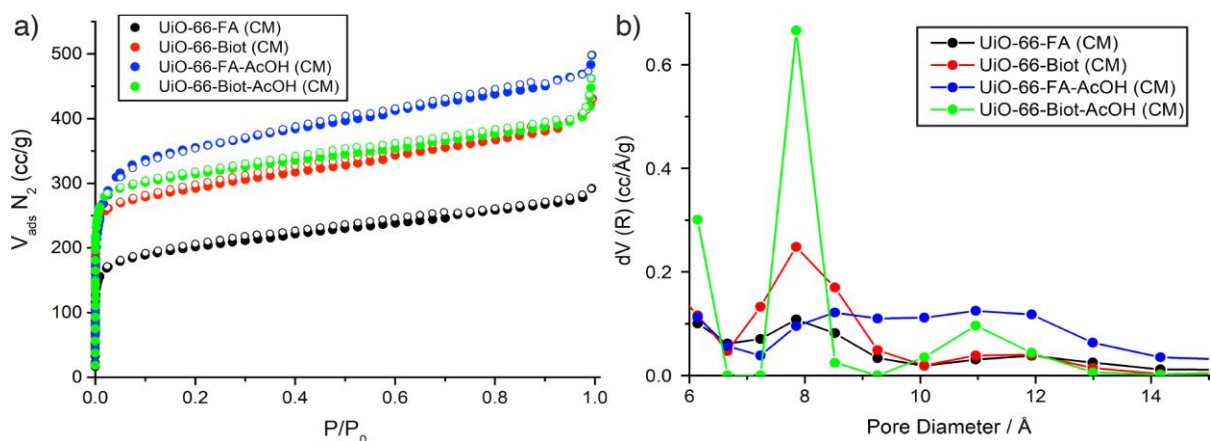


**Figure 2.19.** a)  $\text{N}_2$  adsorption isotherms (77 K) of the MOFs surface modified by coordination modulation. Closed symbols for adsorption, empty symbols for desorption. b) Pore size distributions calculated from the isotherms.

**UiO-66-FA (CM):**  $S_{\text{BET}} = 753 \text{ m}^2\text{g}^{-1}$ ; pore volume=  $0.405 \text{ ccg}^{-1}$

**UiO-66-FA-AcOH (CM):**  $S_{\text{BET}} = 1377 \text{ m}^2\text{g}^{-1}$ ; pore volume=  $0.672 \text{ ccg}^{-1}$

**UiO-66-Biot (CM):**  $S_{\text{BET}} = 1129 \text{ m}^2\text{g}^{-1}$ ; pore volume=  $0.578 \text{ ccg}^{-1}$

**UiO-66-Biot-AcOH (CM):**  $S_{\text{BET}} = 1227 \text{ m}^2\text{g}^{-1}$ ; pore volume=  $0.578 \text{ ccg}^{-1}$

When acetic acid is added as the co-modulator in the synthesis of UiO-66-FA-AcOH, as the amount of incorporated folic acid decreases, so increases the surface area of UiO-66-FA-AcOH (CM). Biotin modulated samples exhibit similar porosity to UiO-66,<sup>26</sup> with slightly higher porosity when AcOH is used as the co-modulator, again suggesting surface attachment and consequent creation of defects.<sup>37, 42, 43, 45</sup>

SEM imaging was used to study the size and morphology of the folic acid and biotin modulated samples (Figure 2.20).

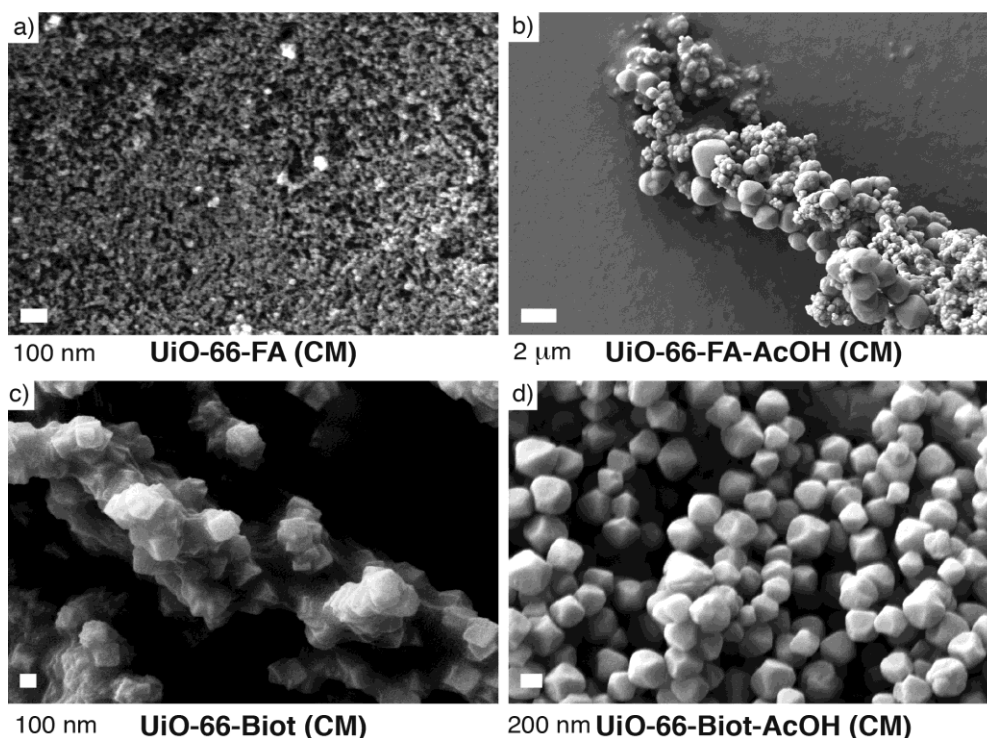


**Figure 2.20.** SEM images of a) UiO-66-FA (CM), b) UiO-66-FA-AcOH (CM), c) UiO-66-Biot (CM), and d) UiO-66-Biot-AcOH (CM).

On the one hand UiO-66-FA (CM) forms very small nanoparticles, thus its size was difficult to determine by SEM. The smaller size when only folic acid is added as the modulator indicates that it acts as a capping agent, with an average size of  $35.9 \pm 13.2$  nm, determined by ImageJ software. On the other hand, when AcOH is the co-modulator, UiO-66-FA-AcOH (CM) particles are not homogeneous in size and different populations can be observed by SEM, one with bigger particles around 2  $\mu$ m and another with small poorly defined nanoparticles. This could be explained once again by competition or pH variability, highlighting the complexity and variability of the coordination modulation process. Therefore, for further drug delivery experiments, UiO-66-FA (CM) was chosen.

The role of the modulator in particle size and morphology is remarkably important when studying the differences between folic acid or biotin modulated samples. UiO-66-Biot (CM) particles consist of small interpenetrated crystallites with an individual size of around 120 nm, growing among each other extensively. When AcOH is also added to the reaction mixture, UiO-66-Biot-AcOH forms individual crystallites of  $157.2 \pm 15.8$  nm with defined edges; for this reason it was chosen for biological testing.

### 2.3.3 The Use of Dichloroacetic acid (DCA) as Modulator

DCA is a pyruvate D-kinase inhibitor,<sup>46-48</sup> which is over expressed in cancerous cells.<sup>49, 50</sup> Its hydrophilic nature hinders its cell uptake;<sup>51</sup> as its cytotoxic effects on cancer cells depend on effective cytosolic release and mitochondrial localisation making it an ideal mechanistic probe molecule for cell uptake.

DCA@UiO-66, DCA@UiO-66-L1 and DCA@UiO-66-L2 were synthesised according to previous methods,<sup>37</sup> using dichloroacetic acid as a modulator in place of acetic acid. The lower  $pK_a$  of dichloroacetic acid compared to acetic acid ensures it is incorporated into the MOFs in significant quantities at defect sites. The samples were obtained as phase pure fine powders with high crystallinity, as confirmed by PXRD (Figure 2.21).

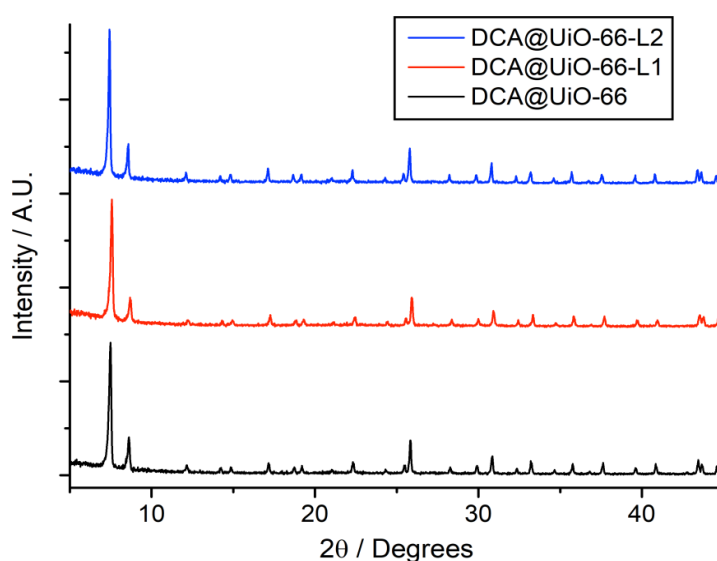


**Figure 2.21.** Stacked PXRD patterns of DCA-loaded UiO-66 samples prepared by coordination modulation.

The presence and quantity of DCA and the functionalised modulators L1 and L2, compared to the ligand bdc, were assessed by  $^1\text{H}$  NMR spectroscopy of samples digested in  $\text{D}_2\text{SO}_4$  /  $\text{DMSO-}d_6$ .

From the  $^1\text{H}$  NMR spectrum of digested DCA@UiO-66-L1 (Figure 2.22 a), the content of functionalised modulator, L1, and DCA was estimated to be 5.7 mol % and 32.4 mol %, respectively, compared to bdc. Similarly, in the  $^1\text{H}$  NMR spectrum of digested DCA@UiO-66-L2 (Figure 2.22 b), the presence of L2 and DCA was confirmed, showing a molar integral ratio of 4.4 mol % and 33.2 mol %, respectively, compared to the bdc linker.

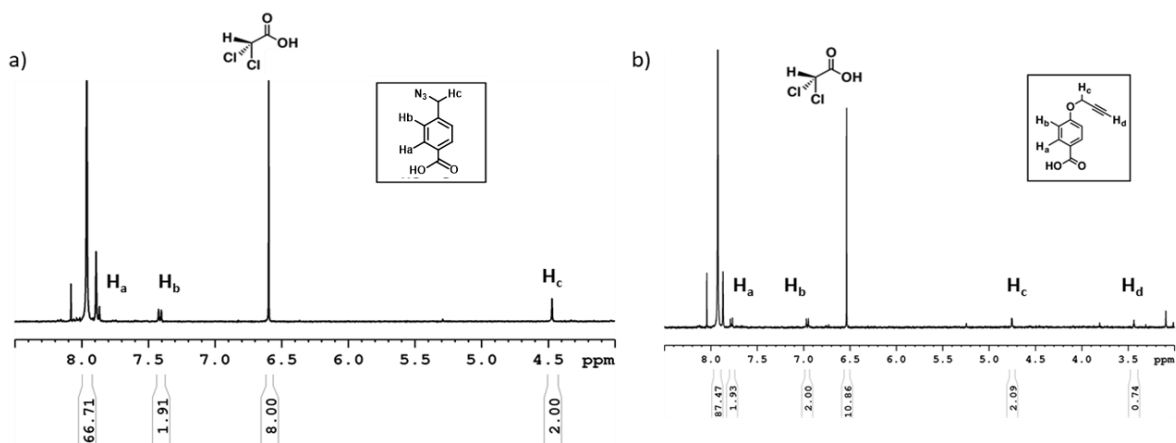


**Figure 2.22.** a)  $^1\text{H}$  NMR spectrum of DCA@UiO-66-L1 digested in  $\text{D}_2\text{SO}_4 / \text{DMSO-}d_6$ . The resonance at  $\delta = 6.6$  ppm corresponds to the  $\text{HOOCCHCl}_2$  proton in DCA. b)  $^1\text{H}$  NMR spectrum of DCA@UiO-66-L2 digested in  $\text{D}_2\text{SO}_4 / \text{DMSO-}d_6$ . The resonance at  $\delta = 6.6$  ppm corresponds to the  $\text{HOOCCHCl}_2$  proton in DCA.

It can be observed that for the two DCA functionalised modulated samples, the modulator content is remarkably lower than when the samples are co-modulated with acetic acid (Section 2.3). The difference in the  $\text{p}K_a$  values of acetic acid (4.8) and dichloroacetic acid (1.4) might explain the different features of the samples when using the same functionalised modulator and either DCA or AcOH as co-modulators.<sup>35, 37</sup> The lower  $\text{p}K_a$  of DCA means that it will be more easily deprotonated in the reaction mixture, and therefore the competition with the functionalised modulators and linker will be higher, resulting in lower incorporation of functionalised modulator. Indeed, the  $\text{p}K_a$  values of benzoic acid derivatives are in general close to the  $\text{p}K_a$  values reported for bdc (3.54 and 4.46).<sup>35</sup> It has also been reported that incorporation of modulator as capping defects in UiO-66 increases as their  $\text{p}K_a$  decreases.<sup>37</sup>

The size of the nanoparticles was analysed by SEM imaging (Figure 2.23) showing that the samples are composed of nanoparticles with regular size.

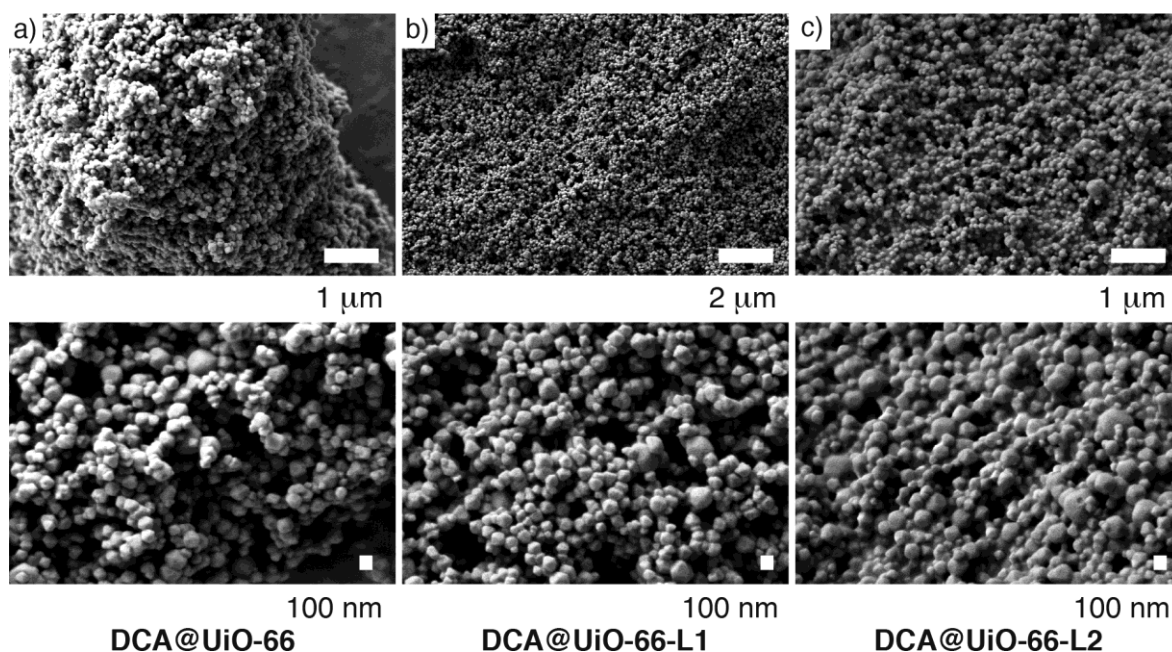


**Figure 2.23.** SEM images at different magnifications of a) DCA@UiO-66, b) DCA@UiO-66-L1, and c) DCA@UiO-66-L2.

The size of the NMOFs differs slightly among the different functionalised modulators used during synthesis. Indeed, when no co-modulator is used, DCA@UiO-66 nanoparticles are typically  $77 \pm 24$  nm in size, and the size is maintained or increased when the functionalised modulators are added, being  $100 \pm 15$  nm for DCA@UiO-66-L1 and  $77 \pm 11$  nm for DCA@UiO-66-L2. The size distributions are also in general more homogeneous when a functionalised co-modulator is present during synthesis.

An additional DCA decomposition step is clearly noticeable in the TGA profiles of the samples (Figure 2.24) at temperatures of around 250-350 °C. Interestingly, this decomposition step when found within the UiO-66 structure generally starts at a higher temperature than the one reported for DCA as a free molecule (194 °C),<sup>52</sup> thus indicating that it is attached to the structure through coordination of its carboxylic acid group to  $Zr_6$  secondary building units.

The mass fraction of DCA can be determined by TGA, as shown in Table 2.3, and is quite similar across the samples. The chlorine atoms of DCA also allow its quantification by inductively coupled plasma mass spectrometry (ICP-MS). The values for DCA loading from ICP-MS (after deduction of the chlorine content of a blank sample of UiO-66 to account for residual chloride from the  $ZrCl_4$  starting material) correlate very well with those from TGA.

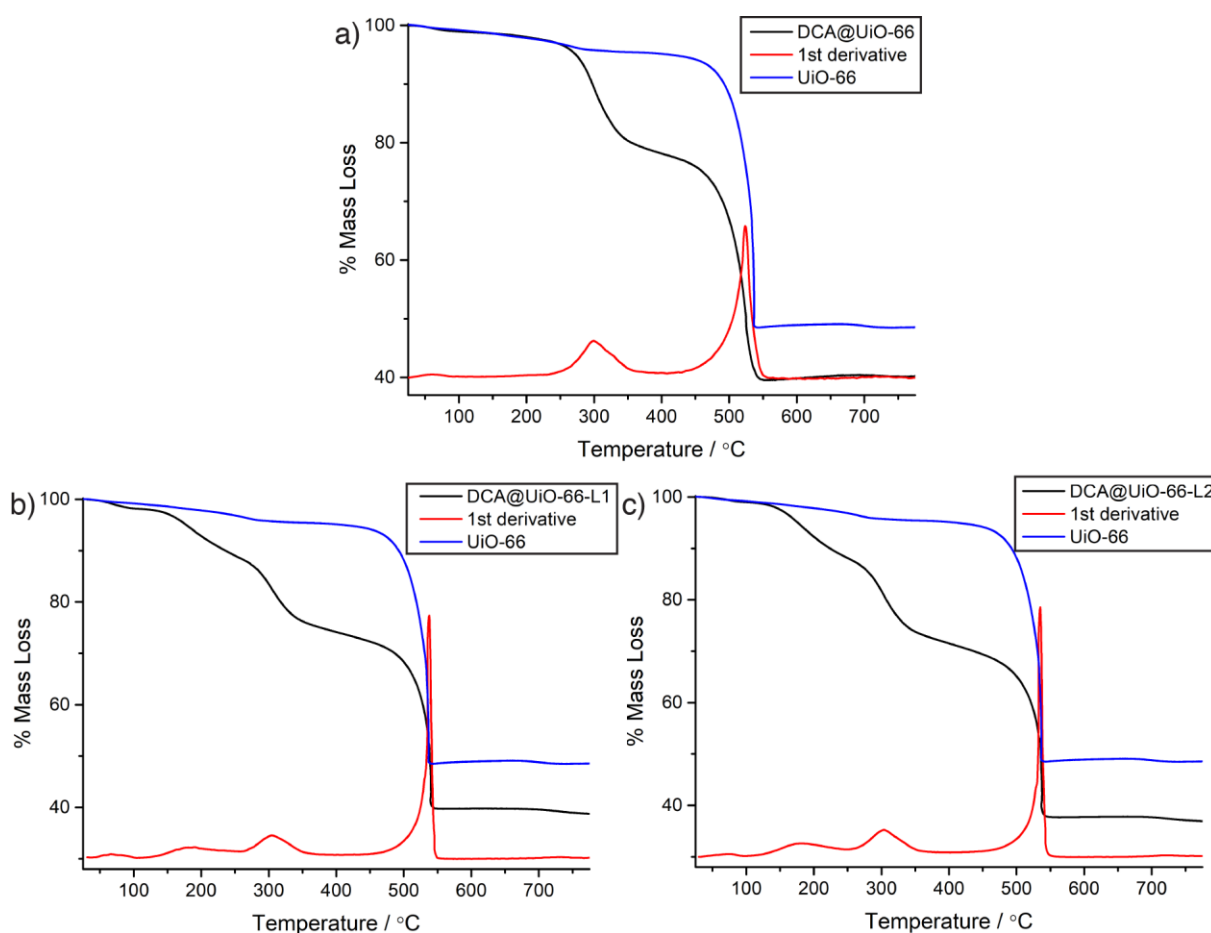


**Figure 2.24.** TGA traces for DCA-modulated MOFs compared to the empty materials for a) DCA@UiO-66, b) DCA@UiO-66-L1, and c) DCA@UiO-66-L2.

**Table 2.3.** TGA residues and DCA loading values from TGA and ICP-MS for the DCA-loaded samples.

Sample	TGA residue at 800°C (% w/w)	DCA content (TGA / ICP) % w/w
DCA@UiO-66	41.3	17.0 / 16.9
DCA@UiO-66-L1	43.7	15.9 / 15.5
DCA@UiO-66-L2	36.6	18.7 / 18.9

FT-IR spectra were collected to monitor the nature of DCA incorporation after coordination modulation (Figure 2.25). Although some of the signals associated with its functional groups are masked by UiO-66 vibration bands, new ones can easily be identified. Firstly the new band around  $1750\text{ cm}^{-1}$ , partially overlapping with UiO-66 carboxylic acid vibration bands, is attributed to the DCA carbonyl stretch. Importantly, it can be observed that in all the UiO-66 samples the signal is shifted to slightly lower values, indicating attachment through the carboxylic acid group of DCA rather than pore storage. Also, the band associated to the C-Cl stretch ( $800\text{ cm}^{-1}$ ) is appreciable with no shifting observed.

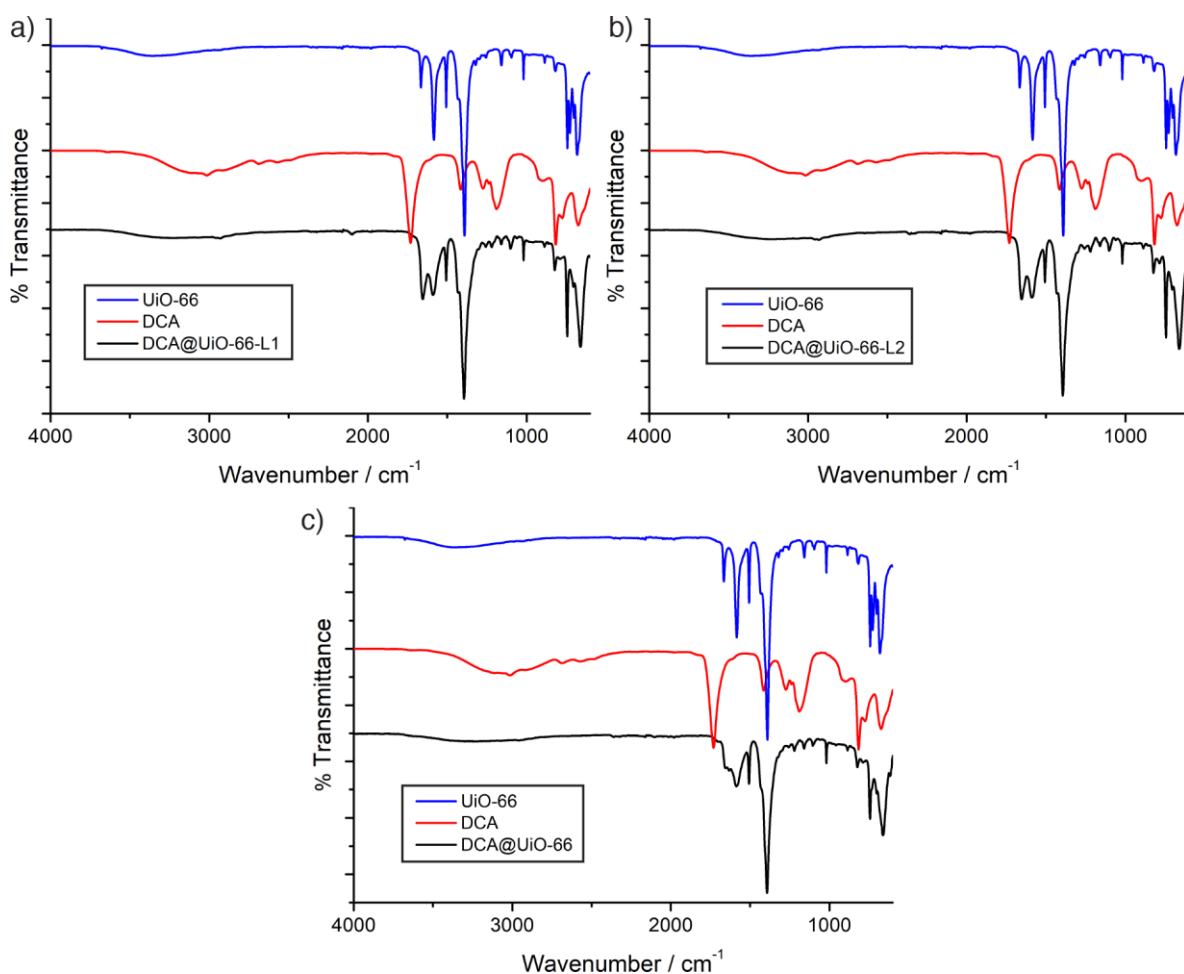


**Figure 2.25.** FT-IR spectra of DCA-loaded MOFs compared to the UiO-66 and DCA, for a) DCA@UiO-66-L1, b) DCA@UiO-66-L2, and c) DCA@UiO-66.

Even though they are of low intensity, due to the relatively small incorporation of functionalised modulator determined by  $^1\text{H}$  NMR spectroscopy, signals associated with the functional groups of the modulators were observed in the FT-IR spectra. For example DCA@UiO-66-L1 exhibits the characteristic azide band ( $2100\text{ cm}^{-1}$ ) of the modulator L1, while DCA@UiO-66-L2 FT-IR shows the alkyne characteristic vibration bands of L2.

Nitrogen adsorption and desorption isotherms were collected at 77 K in order to evaluate the porosity of the samples and ultimately determine DCA location in the structure (Figure 2.26).

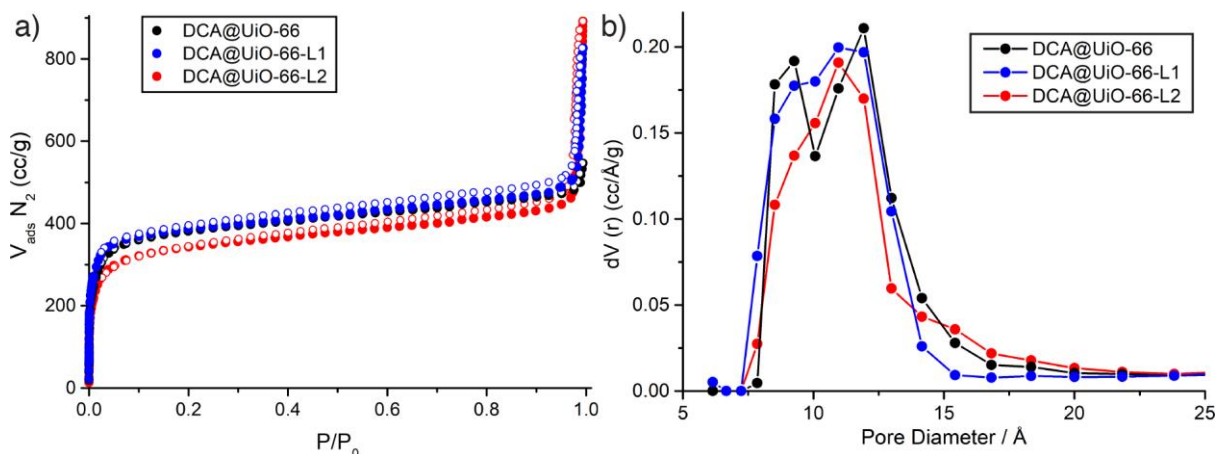


**Figure 2.26.** a)  $N_2$  adsorption isotherms (77 K) of the DCA-loaded MOFs. Closed symbols for adsorption, empty symbols for desorption. b) Pore size distributions calculated from the isotherms.

**DCA@UiO-66:**  $S_{BET} = 1488 \text{ m}^2\text{g}^{-1}$ ; pore volume =  $0.686 \text{ ccg}^{-1}$

**DCA@UiO-66-L1:**  $S_{BET} = 1510 \text{ m}^2\text{g}^{-1}$ ; pore volume =  $0.759 \text{ ccg}^{-1}$

**DCA@UiO-66-L2:**  $S_{BET} = 1299 \text{ m}^2\text{g}^{-1}$ ; pore volume =  $0.701 \text{ ccg}^{-1}$

The samples exhibit higher porosity than defect free UiO-66. Indeed, apart from DCA@UiO-66-L2, which has the lowest surface area, the BET surface areas are around 20% higher than UiO-66 ( $1200 \text{ m}^2\text{g}^{-1}$ ), all of them with pore volumes more than 30% higher than that reported for UiO-66 ( $0.4 \text{ ccg}^{-1}$ ).<sup>26</sup> Additionally, TGA and PXRD were performed after nitrogen uptake, confirming that the high porosity of the samples is not a consequence of DCA desorption during sample activation (heating to  $120 \text{ }^\circ\text{C}$  for 20 h).

The high porosity is therefore a consequence of the defects induced during synthesis due to both DCA and functionalised modulator attachment, as competition with the linker during the nucleation process could lead in incorporation not only in the surface as a capping agent, but also in the core of the structure. As it only possess one site of attachment, this will lead to missing linkers in the structure, and/or missing clusters, and therefore empty space that enhances the overall porosity.<sup>37</sup>

In fact, the pore size distribution of UiO-66 usually shows two main defined pores, octahedral ( $11 \text{ \AA}$ ) and tetrahedral ( $8 \text{ \AA}$ ),<sup>26</sup> while when DCA modulates UiO-66 synthesis, the simulated pore size distribution differs from the expected (Figure 2.26b). All the DCA modulated samples show similar pore size distributions, where bigger pores are observed. This is again a consequence of the attachment of DCA in the core of the structure, deriving on defected samples.

During the course of this investigation, an investigation of the effect of modulator  $pK_a$  on UiO-66 properties was published, including the use of DCA as a modulator.<sup>35</sup> The authors reported that, when using DCA (and other low  $pK_a$  carboxylic acids) as a modulator, the number of defects induced during synthesis results in materials that form stable colloidal dispersions in water, with size distributions very close to those determined by SEM. DLS measurements of our own DCA modulated samples collected in water (Figure 2.27) confirm this, showing stable colloidal dispersions of particles that are initially monodisperse, with the same particle sizes as found by SEM, but with some minor aggregation over time (Section 2.6).

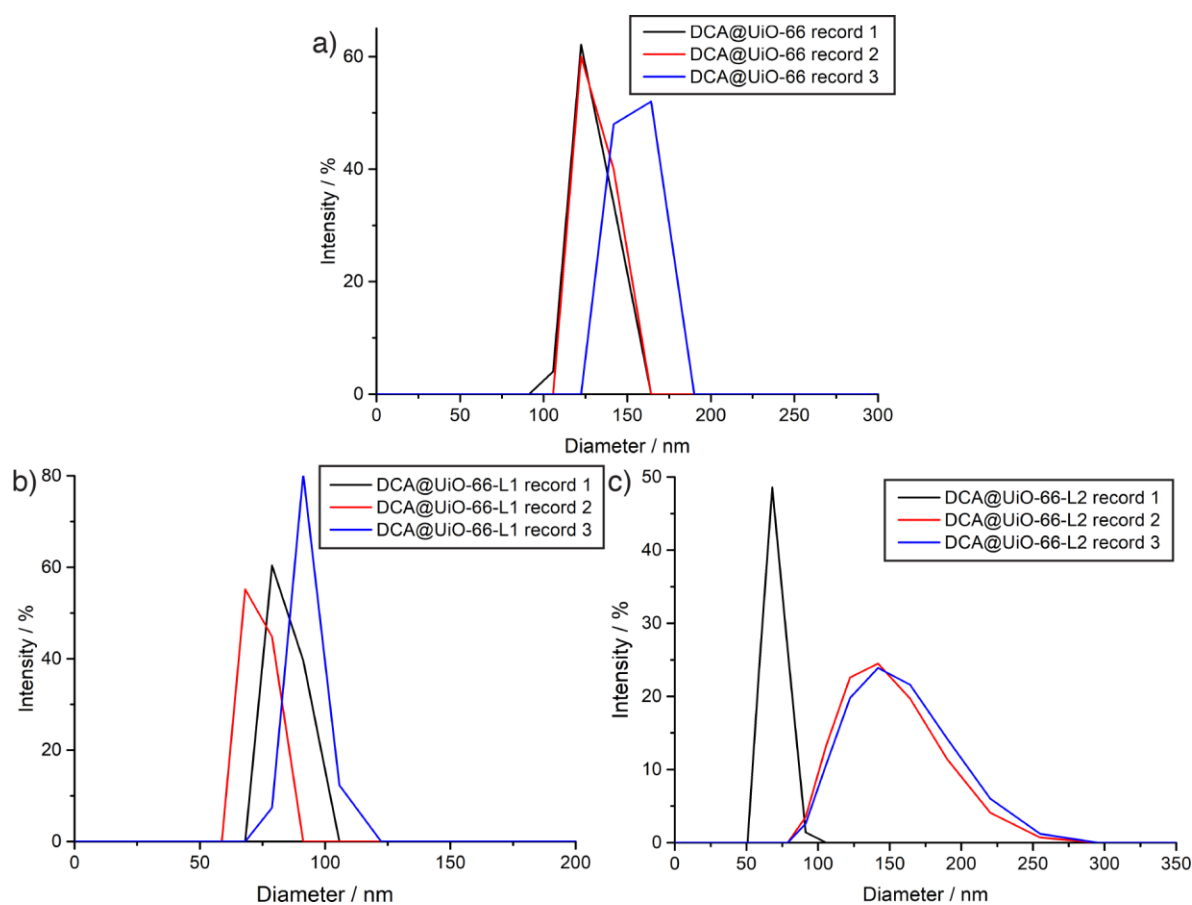


**Figure 2.27.** DLS profiles in water of a) DCA@UiO-66, b) DCA@UiO-66-L1, and c) DCA@UiO-66-L2.

The importance of these findings is based not only on the fact that with only one synthetic step both an anticancer drug and a functionalised modulator can be successfully attached to the UiO-66 structure, yielding highly crystalline and porous nanoparticles with the appropriate size for drug delivery, but also in the fact that this high porosity could potentially be used to store a second drug in the pore, especially interesting for treatments with multiple drugs. Additionally, the fact that DCA is attached rather than stored should ensure no major release of the drug during the following postsynthetic surface modification process (See Chapter 5), and more favourable release kinetics, possibly reducing the burst effect, during drug delivery experiments.

### 2.3.4 Co-Modulated Synthesis of DCA-containing, Surface Modified UiO-66

The coordination modulation protocol using DCA as co-modulator of UiO-66 synthesis was further extended to include the presence of either folic acid or biotin as functionalised modulators, to produce surface-modified, DCA-loaded UiO-66 in a single step.

Different amounts of folic acid and DCA were employed and samples are named based on the molar ratio of each component to bdc added during synthesis: DCA<sub>10</sub>@UiO-66-FA<sub>0.25</sub> (CM) (10 equiv DCA, 0.25 equiv folic acid), and DCA<sub>5</sub>@UiO-66-FA<sub>1</sub> (CM) (5 equiv DCA, 1 equiv folic acid). As previously observed, when adding 10 equivalents of DCA to the reaction mixture, both folic acid and biotin co-modulated samples are highly crystalline and phase pure by PXRD (Figure 2.28). When the equivalents of DCA and folic acid are adjusted to increase folic acid content, DCA<sub>5</sub>@UiO-66-FA<sub>1</sub> (CM) maintains characteristic reflection peaks, but they are broader and with lower intensity, indicating smaller nanoparticles, as with UiO-66-FA (CM) (Section 2.3.2).

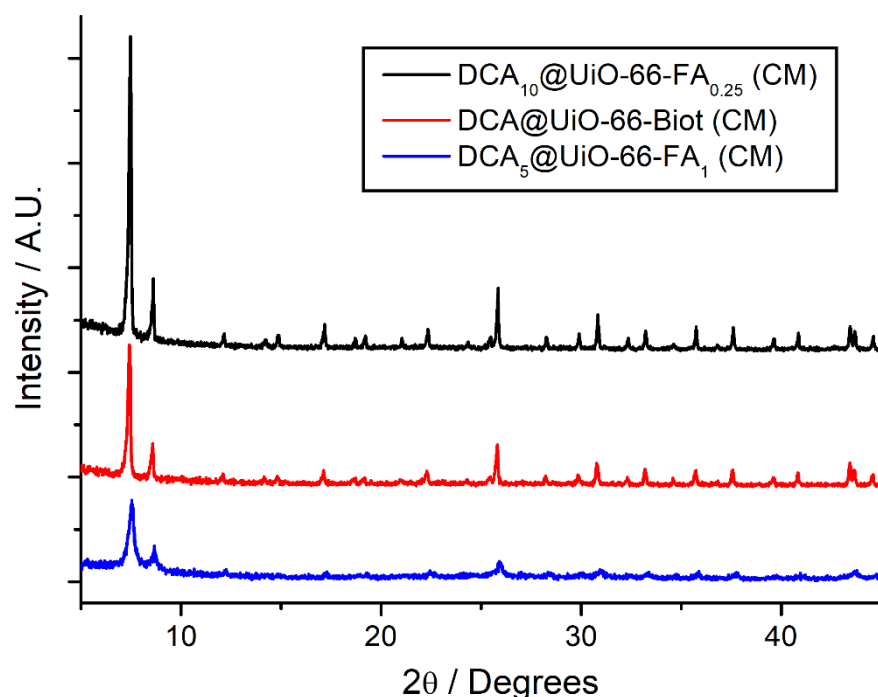


**Figure 2.28.** Stacked PXRD patterns of surface-modified, DCA-loaded UiO-66 prepared in one-pot co-modulated syntheses.

<sup>1</sup>H NMR spectroscopy was used once again to determine the content of the modulators in the acid-digested samples (See appendix for discussion of the modulators' acidified <sup>1</sup>H NMR). The <sup>1</sup>H NMR spectrum of acid-digested DCA<sub>10</sub>@UiO-66-FA<sub>0.25</sub> (CM) enabled determination of most of the characteristic signals of DCA and folic acid (Figure 2.29). While the intensity of

DCA proton resonance at  $\delta = 6.6$  ppm is high and enables easy analysis – 42.6% molar ratio compared to the bdc linker – the intensities of the signals assigned to folic acid are low and the integral ratios are difficult to estimate, but suggest a folic acid content of <5% molar ratio compared to bdc.

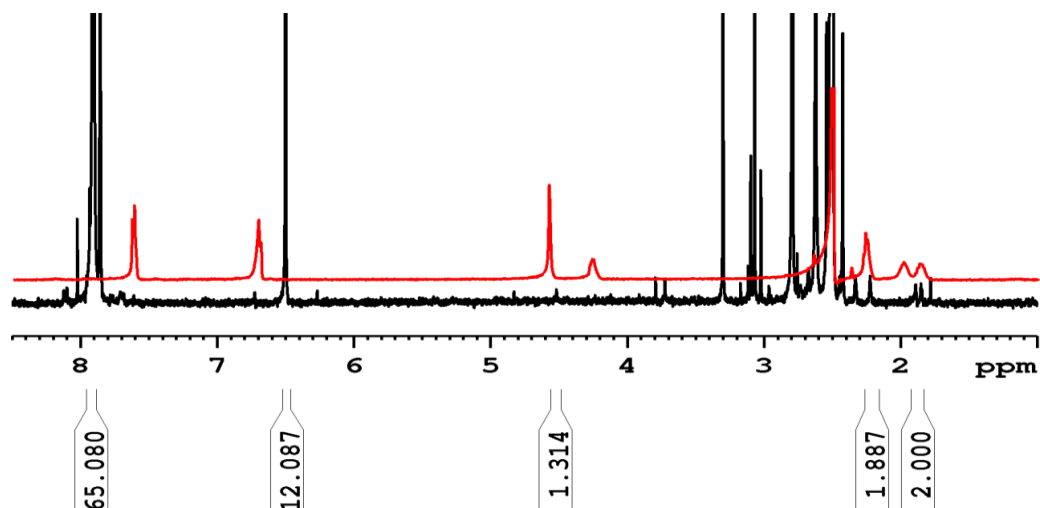


**Figure 2.29.**  $^1\text{H}$  NMR spectrum of  $\text{DCA}_{10}@UiO-66\text{-FA}_{0.25}$  (CM) digested in  $\text{D}_2\text{SO}_4 / \text{DMSO-}d_6$ . The resonance at  $\delta = 6.6$  ppm corresponds to the  $\text{HOOCCHCl}_2$  proton in DCA.

This could be easily explained once again by the difference of the  $pK_a$  values of the two modulators; 1.4 for DCA while 3.5 and 4.3 for the carboxylic acid groups of folic acid. Therefore, the competition between modulators during the nucleation process, together with the higher number of equivalents of DCA added, will enhance incorporation of DCA over folic acid.

Thus, the ratio of DCA: FA was adjusted during synthesis in order to increase folic acid content in the sample. As expected, the  $^1\text{H}$  NMR spectrum acid-digested of  $\text{DCA}_5@UiO-66\text{-FA}_1$  (CM) (Figure 2.30) showed an increased content of folic acid, and accordingly, a relatively smaller incorporation of DCA.

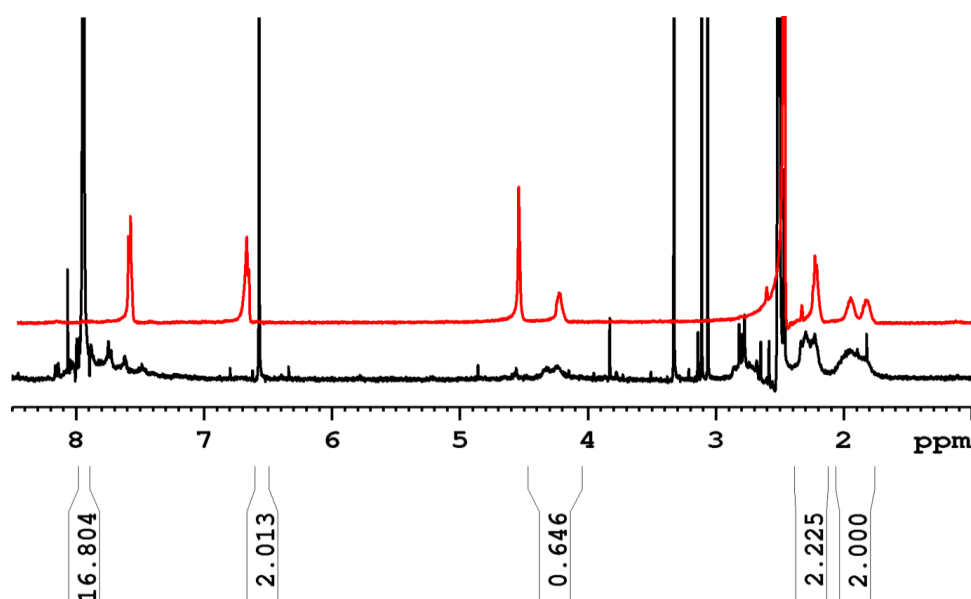


**Figure 2.30.** <sup>1</sup>H NMR spectrum of DCA<sub>5</sub>@UiO-66-FA<sub>1</sub> (CM) digested in D<sub>2</sub>SO<sub>4</sub> / DMSO-*d*<sub>6</sub>. The resonance at  $\delta = 6.6$  ppm corresponds to the HOCC $\underline{H}$ Cl<sub>2</sub> proton in DCA.

The DCA content was estimated to be 32.4 mol % compared to bdc, while analysis of the resonances assigned to the alkyl protons of folic acid confirmed ~15-20 mol % incorporation of folic acid. Folic acid content in the samples was further determined by UV-Vis spectroscopy of the digested samples, as described previously, being 3.6% *w/w* for DCA<sub>10</sub>@UiO-66-FA<sub>0.25</sub> (CM) and 26.7% *w/w* for DCA<sub>5</sub>@UiO-66-FA<sub>1</sub> (CM).

Although biotin signals are appreciable in the <sup>1</sup>H NMR spectrum of acid-digested DCA@UiO-66-Biot (CM), shown in Figure 2.31, very little incorporation of biotin was determined. The low intensity of the biotin signal at  $\delta = 1.2$  ppm and its poor definition does not allow proper analysis. However, an incorporation of < 2 mol % compared to bdc was estimated from the signal at  $\delta = 2.1$  ppm (t, 2H), which integrates accordingly to the rest of the identifiable biotin signals. DCA presence was confirmed with a 43.8% molar ratio compared to bdc.

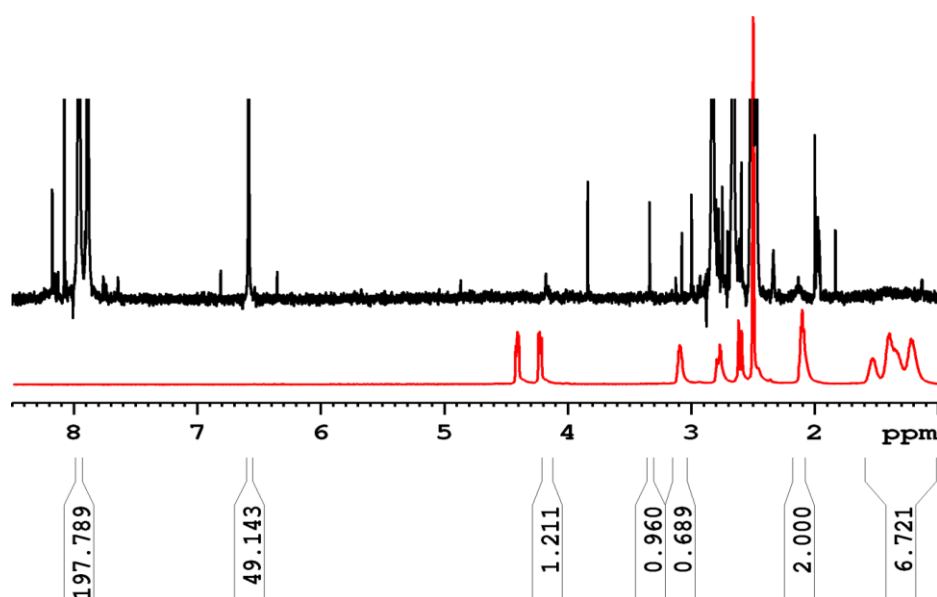


**Figure 2.31.**  $^1\text{H}$  NMR spectrum of DCA@UiO-66-Biot (CM) digested in  $\text{D}_2\text{SO}_4$  /  $\text{DMSO-}d_6$ . The resonance at  $\delta = 6.6$  ppm corresponds to the  $\text{HOOCCHCl}_2$  proton in DCA.

TGA profiles of the DCA modulated samples (Figure 2.32) show the appearance of a new decomposition step attributed to DCA decomposition. In general, it can be observed that DCA folic acid co-modulated samples have a considerably smaller metal residue than when UiO-66 synthesis is only modulated with DCA, and the DCA content measured by TGA correlates closely to that measured by ICP-MS (Table 2.4). In fact, when the DCA:FA ratio is 5:1, and higher incorporation of folic acid is determined by  $^1\text{H}$  NMR spectroscopy, the degradation profile has a more gradual character, in agreement with results found for previously synthesised folic acid containing UiO-66 samples (Section 2.3.2). The fact that DCA decomposes at a higher temperature (250–350 °C) than the one reported in the literature (194 °C) indicates that DCA is attached to UiO-66 structure,<sup>52</sup> possibly on the surface (outer and inner due to its small size) and in the defect sites.

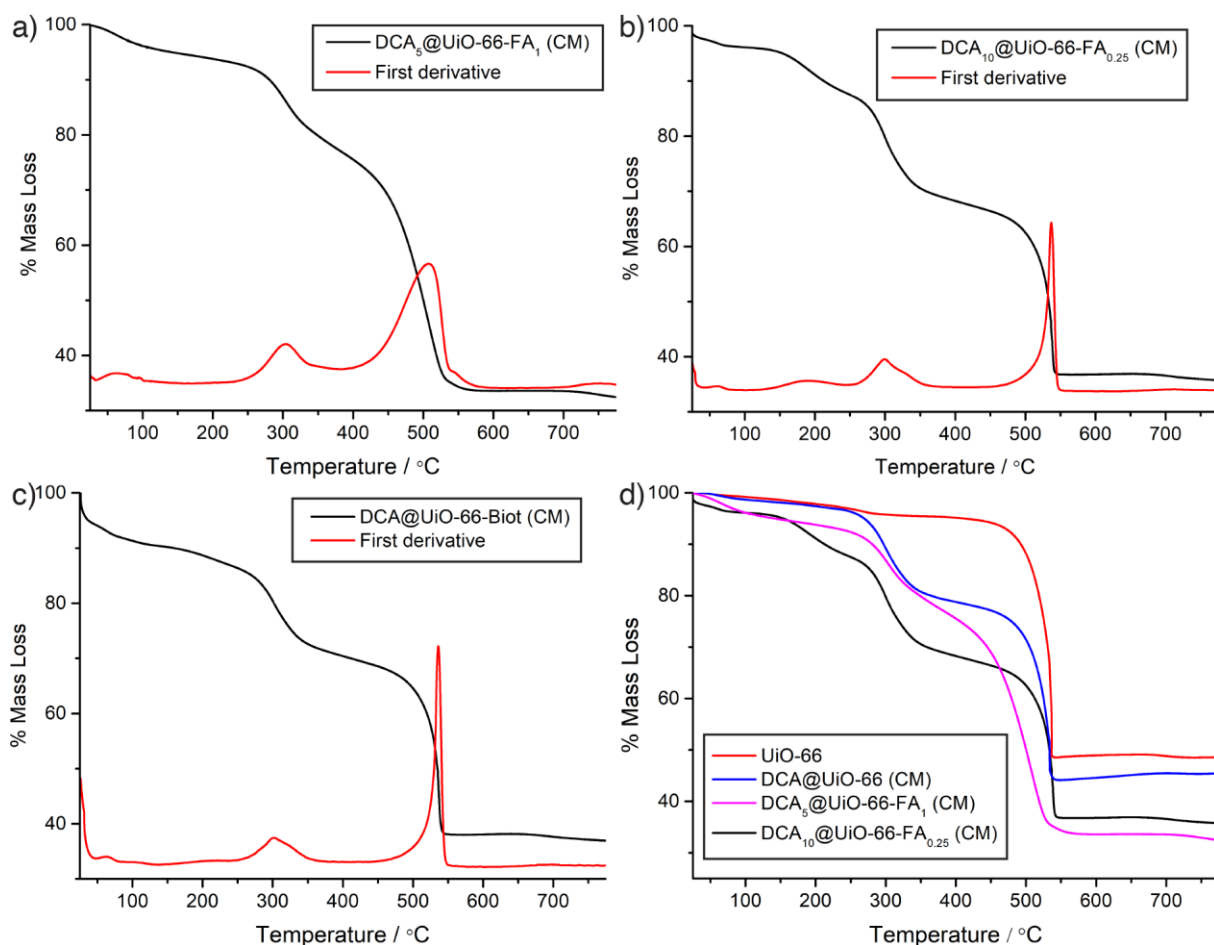


**Figure 2.32.** TGA profiles of a)  $\text{DCA}_5@UiO-66-FA_1$  (CM), b)  $\text{DCA}_{10}@UiO-66-FA_{0.25}$  (CM) and c)  $\text{DCA}@UiO-66-Biot$  (CM). d) Comparison of the DCA-loaded UiO-66 samples with and without folic acid, with empty UiO-66.

**Table 2.4.** TGA residues and DCA loading values from TGA and ICP-MS for the DCA-loaded, surface modified samples.

Sample	TGA residue at 800°C (% w/w)	DCA content (TGA / ICP) % w/w
$\text{DCA}_{10}@UiO-66-FA_{0.25}$ (CM)	35.8	19.6 / 18.9
$\text{DCA}_5@UiO-66-FA_1$ (CM)	32.9	12.1 / 11.8
$\text{DCA}@UiO-66-Biot$ (CM)	38.1	19.0 / 20.7

Nitrogen adsorption isotherms (Figure 2.33) found the samples synthesised using 10 equivalents of DCA to be highly porous, with surface areas of  $1661 \text{ m}^2\text{g}^{-1}$  and  $1357 \text{ m}^2\text{g}^{-1}$  for folic acid and biotin NMOFs respectively. These findings, together with TGA and FT-IR results, unequivocally confirm that DCA and the functionalised modulators are attached to available zirconium positions of UiO-66. In agreement with the nitrogen uptake of UiO-66-FA (CM), when the DCA:FA ratio is reduced to enhance folic acid incorporation, a lower surface area,

close to that reported for Zr-fumarate,<sup>32</sup> is obtained, although the pore volume is similar to the one reported for UiO-66.

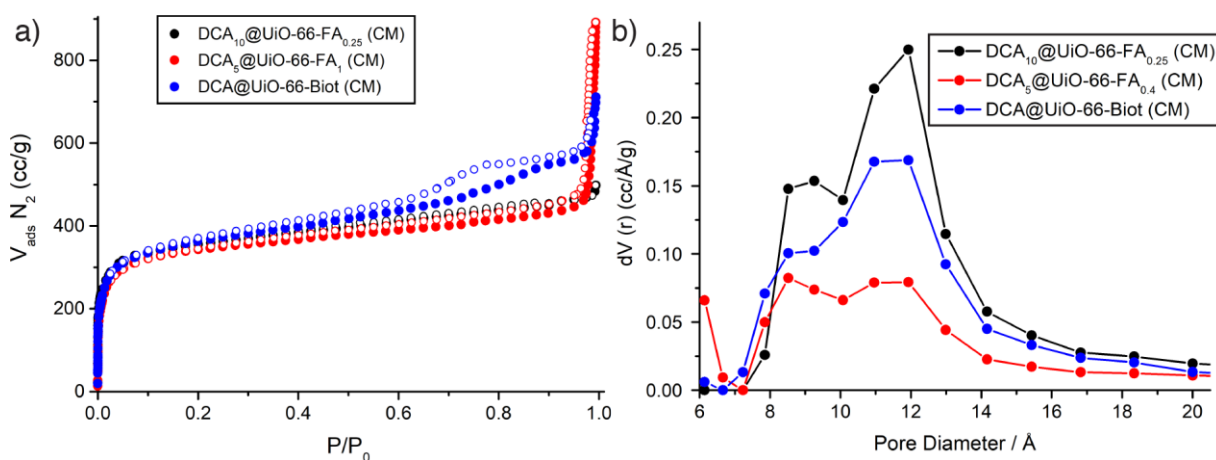


**Figure 2.33.** a)  $N_2$  adsorption isotherms (77 K) of the DCA-loaded, co-modulated MOFs. Closed symbols for adsorption, empty symbols for desorption. b) Pore size distributions calculated from the isotherms.

**DCA<sub>10</sub>@UiO-66-FA<sub>0.25</sub> (CM):**  $S_{BET} = 1661 \text{ m}^2\text{g}^{-1}$ ; pore volume =  $0.943 \text{ ccg}^{-1}$

**DCA<sub>5</sub>@UiO-66-FA<sub>1</sub> (CM):**  $S_{BET} = 844 \text{ m}^2\text{g}^{-1}$ ; pore volume =  $0.485 \text{ ccg}^{-1}$

**DCA@UiO-66-Biot (CM):**  $S_{BET} = 1357 \text{ m}^2\text{g}^{-1}$ ; pore volume =  $0.859 \text{ ccg}^{-1}$

The isotherms when adding 10 equivalents of DCA present different features depending on if folic acid or biotin are also added to the synthesis, highlighting once more the important role that the modulator plays during synthesis. DCA<sub>5</sub>@UiO-66-FA<sub>1</sub> presents a second uptake 0.92  $P/P_0$ , characteristic of filling inter-particle voids, while DCA@UiO-66-Biot exhibits a hysteresis between 0.86 and 0.52  $P/P_0$ , characteristic of mesoporous samples. The high degree of defects could be a consequence of DCA and biotin incorporation, leading to absence of linkers or even metal clusters.

The pore volumes of the samples synthesised with 10 equivalents of DCA are remarkably higher than UiO-66 ( $0.5 \text{ ccg}^{-1}$ ), being  $0.943 \text{ ccg}^{-1}$  and  $0.859 \text{ ccg}^{-1}$  for folic acid and biotin respectively. The pore size distribution shows distorted pores compared to UiO-66 (8 Å and 11 Å). The pores of the three samples are similar in size, showing two major peaks with no clear definition. This is once again due to defects induced during synthesis when incorporating modulators to UiO-66 structure.

SEM imaging shows that when UiO-66 is modulated using both DCA and biotin as modulators, small crystallites of  $166 \pm 22$  nm are obtained for the synthetic conditions used (Figure 2.34).

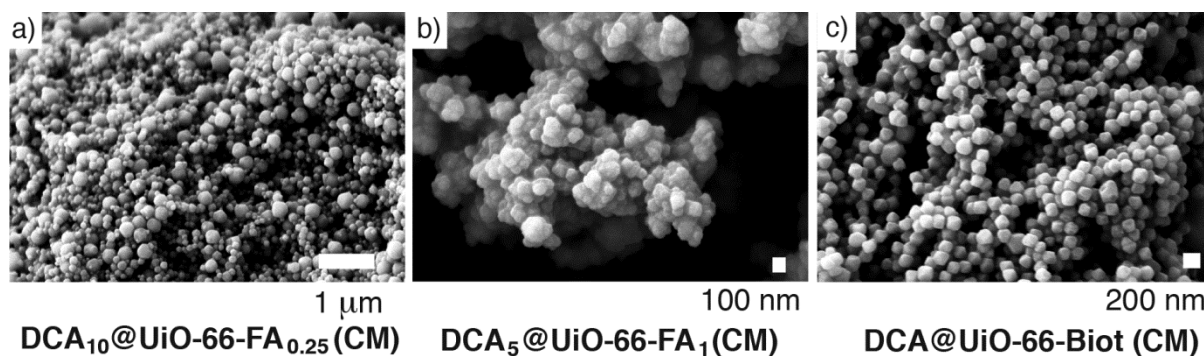


**Figure 2.34.** SEM images of a)  $\text{DCA}_{10}@UiO-66-FA_{0.25}$  (CM), b)  $\text{DCA}_5@UiO-66-FA_1$  (CM), and c)  $\text{DCA}@UiO-66-Biot$  (CM).

A decrease of particle size was observed when the ratio of DCA to folic acid was adjusted, from  $158 \pm 23$  nm to  $91 \pm 29$  nm for  $\text{DCA}_{10}@UiO-66-FA_{0.25}$  and  $\text{DCA}_5@UiO-66-FA_1$  respectively. This could be a consequence of folic acid acting as capping agent and therefore inhibiting crystal growth, yielding smaller nanoparticles.

To summarise, DCA modulation yields in highly defected, colloidal stable nanoparticles with high DCA content. Through extensive characterisation, it has been proven that DCA gets attached to the unsaturated metal cluster nodes during synthesis. Due to its low  $pK_a$ , DCA gets highly incorporated into the MOF structure, even in the presence of other functionalised modulators. The synthetic protocols are versatile and offer many options to create highly specialised drug-containing surface-functionalised MOFs in one synthetic step, being able to tune MOF content and particle size through modulators ratio adjustment.

## 2.4. DCA Modulated Synthesis of the UiO Family of Isorecticular MOFs

Due to these encouraging results, and in order to study the cytotoxicity of UiO type DCA@MOFs based on functionalised and extended linkers (Chapter 5), the DCA modulation protocol was applied to the UiO series of isorecticular MOFs, shown in Figure 2.35.

DCA@MOFs synthesis was performed following the former coordination modulation protocol, using a 1:1 ratio of  $ZrCl_4$  and linker and adding 10 equivalents of DCA to the syntheses, together with 1 equivalent of HCl.

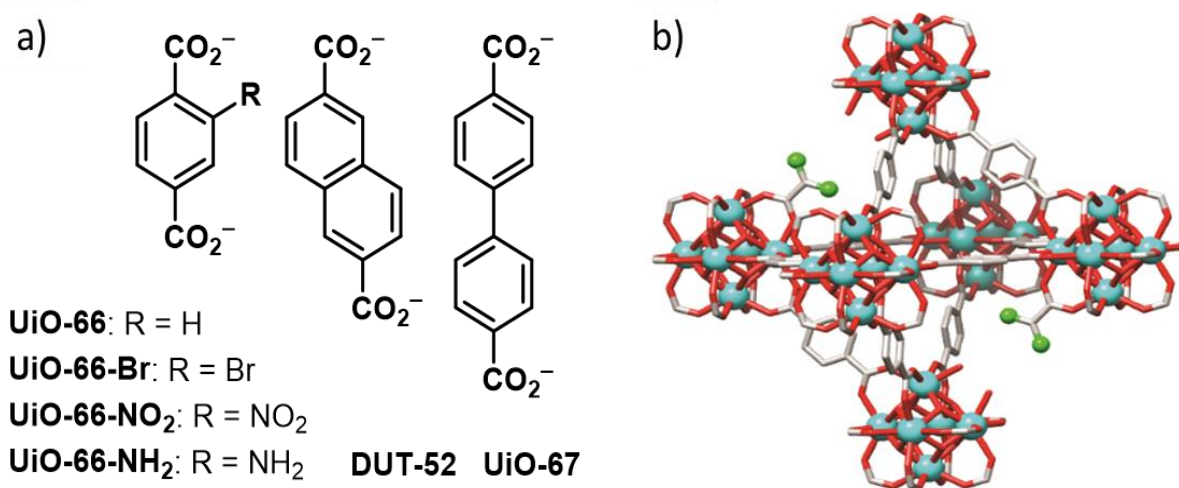


**Figure 2.35.** a) Structures of linkers used in the preparation of Zr MOFs. b) Schematic of UiO-66 with DCA capping defects.

SEM imaging (Figure 2.36) showed the DCA@UiO-66 derivate MOFs to be around 75-150 nm in diameter, with particle size distributions (Figure 2.37) showing that DCA@UiO-66 and DCA@ UiO-66-NH<sub>2</sub> are slightly smaller than DCA@UiO-66-Br and DCA@UiO-66-NO<sub>2</sub>. On the other hand, DUT-52 and DCA@UiO-67 formed microcrystals, and will not be discussed during this thesis. Particle size data is presented in Table 2.5.

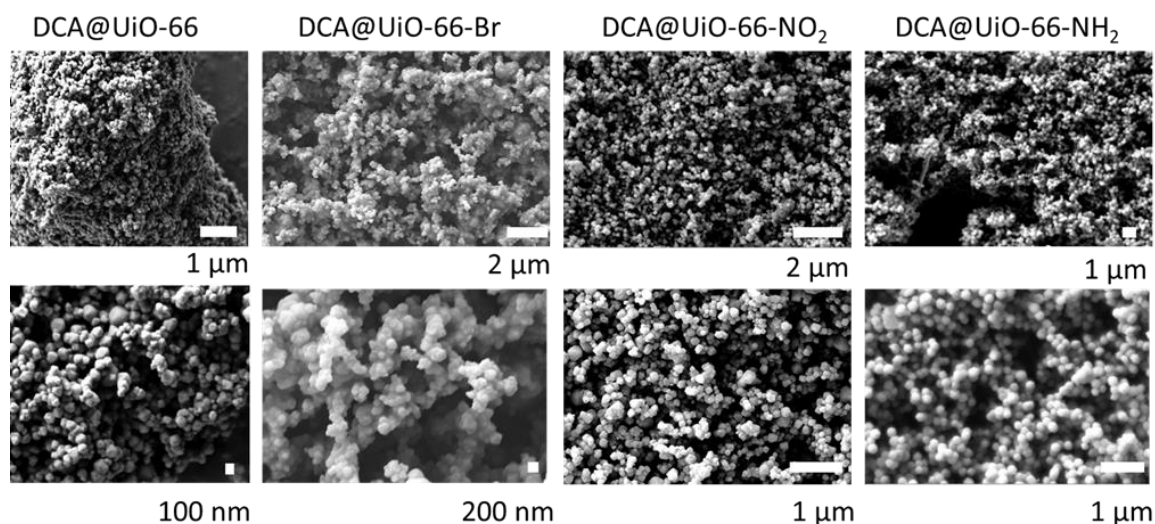


**Figure 2.36.** SEM images of DCA@UiO-66, DCA@UiO-66-Br, DCA@UiO-66-NO<sub>2</sub> and DCA@UiO-66-NH<sub>2</sub>

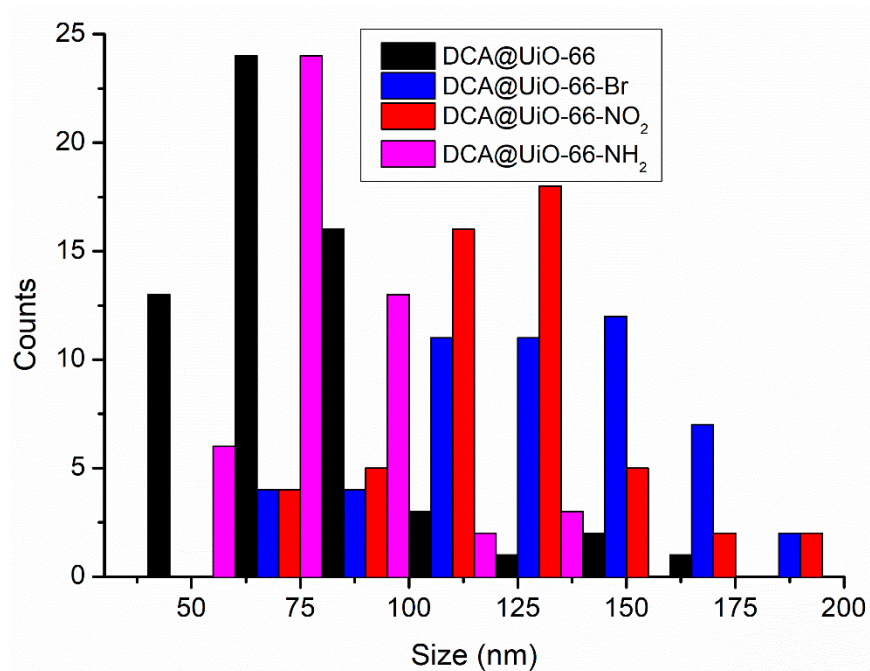


**Figure 2.37.** Particle size distribution histogram for the larger DCA-loaded terephthalate MOF samples.

PXRD patterns (Figure 2.38) show highly crystalline and phase pure MOFs with the UiO-66 topology.

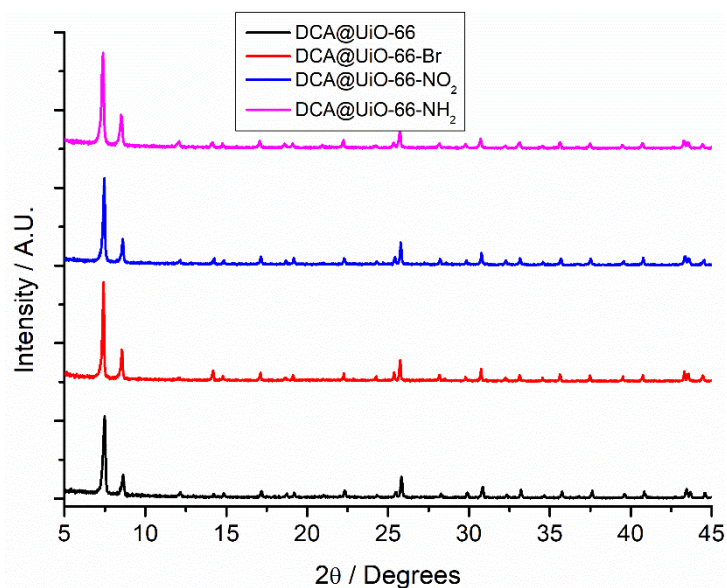


**Figure 2.38.** Stacked PXRD patterns of the larger DCA@UiO-66 MOFs.

The samples' porosity was analysed by N<sub>2</sub> adsorption and desorption measurements (Figure 2.39a), which ultimately confirmed DCA incorporation through binding to the Zr<sub>6</sub> clusters, as the samples present higher BET surface areas and pore volumes (Table 2.5) than those previously reported in the literature for pristine materials.<sup>41</sup> The pore size distributions show defective pores (Figure 2.39b), again as a consequence of DCA attachment and defect induction.

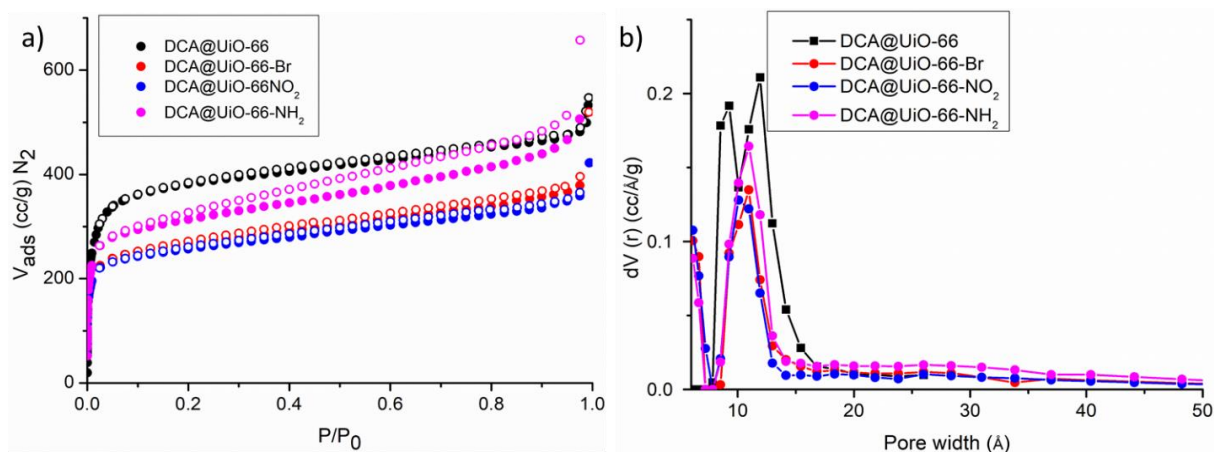


**Figure 2.39.** a) Comparison of N<sub>2</sub> uptake isotherms (77 K) for larger DCA-loaded UiO-66 MOF samples. Filled symbols indicate adsorption, empty symbols desorption. b) Pore size distributions, calculated from the N<sub>2</sub> uptake isotherms, for larger DCA-loaded UiO-66 MOFs, showing the expected pores for UiO-66 samples but with some larger, defect-based pores. N<sub>2</sub> on carbon at 77 K, slit pore, QSDFT, equilibrium model.

<sup>1</sup>H NMR spectra of the acid digested samples again show high DCA incorporation (ca. 30 mol % compared to linker), while TGA analysis enabled quantification of DCA loading (ca. 250–

375°C) and an estimation of the structural composition. A comparison of the TGA traces for the four DCA@UiO-66 derivative MOFs with an empty UiO-66 MOF can be found in Figure 2.40. The estimated DCA content in weight percent is given in Table 2.5.

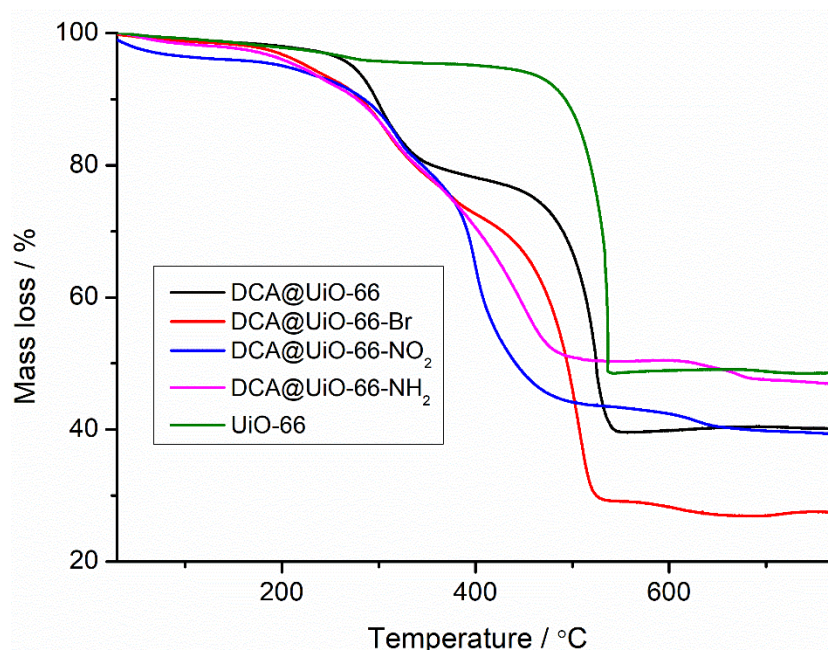


**Figure 2.40.** Comparison of the TGA profiles of the DCA@UiO-66 MOFs with empty UiO-66.

The experimental DCA and linker mass losses were compared to those calculated for theoretical model structures where DCA replaces linkers, in each case being close to the theoretical structure  $[\text{Zr}_6\text{O}_4(\text{OH})_4(\text{L})_4(\text{DCA})_2(\text{OH})_2]_n$ , indicating defective structures

**Table 2.5.** Pertinent physical properties of the larger DCA-loaded terephthalate MOFs

Sample	Size / nm	% DCA w/w	BET SA / $\text{m}^2\text{g}^{-1}$	Pore volume / $\text{ccg}^{-1}$
DCA@UiO-66	$77 \pm 24$	17.2	1510	0.76
DCA@UiO-66-Br	$131 \pm 30$	16.7	1016	0.56
DCA@UiO-66-NO <sub>2</sub>	$121 \pm 27$	16.2	985	0.52
DCA@UiO-66-NH <sub>2</sub>	$81 \pm 26$	16.9	1189	0.83

To promote cytosolic release through passive diffusion, the previous DCA modulated synthetic conditions were tuned with the aim of obtaining smaller, DCA-loaded nanoparticles (< 20 nm) of the UiO family of Zr<sub>6</sub> MOFs.

Solvothermal reaction of ZrOCl<sub>2</sub>, which has a more similar structure to the Zr<sub>6</sub> SBUs, with 2.5 eq of linker, to promote nucleation, and 18.2 eq of dichloroacetic acid yields solids whose

PXRD patterns (Figure 2.41) show Bragg peaks characteristic of the UiO-66 topology.<sup>26, 41</sup> When terephthalate linkers are used, the diffraction patterns have broad, low intensity peaks, suggesting small and defective particles, consequence of DCA attachment to the  $Zr_6$  clusters in place of linkers.

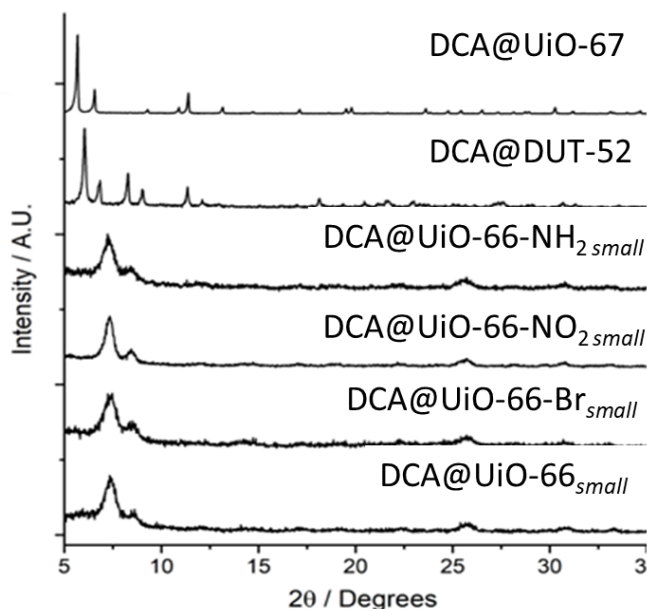


**Figure 2.41.** Stacked PXRD patterns of DCA@MOFs.

SEM imaging was used to study the morphology and size of the NMOFs, showing that while the DCA@UiO-66<sub>small</sub> derivatives are indeed small nanoparticles (Figures 2.42) of slightly different sizes depending on the linker, DCA@DUT-52 and DCA@UiO-67 are composed of bigger nanoparticles (Figure 2.43). The particle size distributions are shown in Figure 2.44, and the average particle sizes and standard deviations are given in Table 2.6.

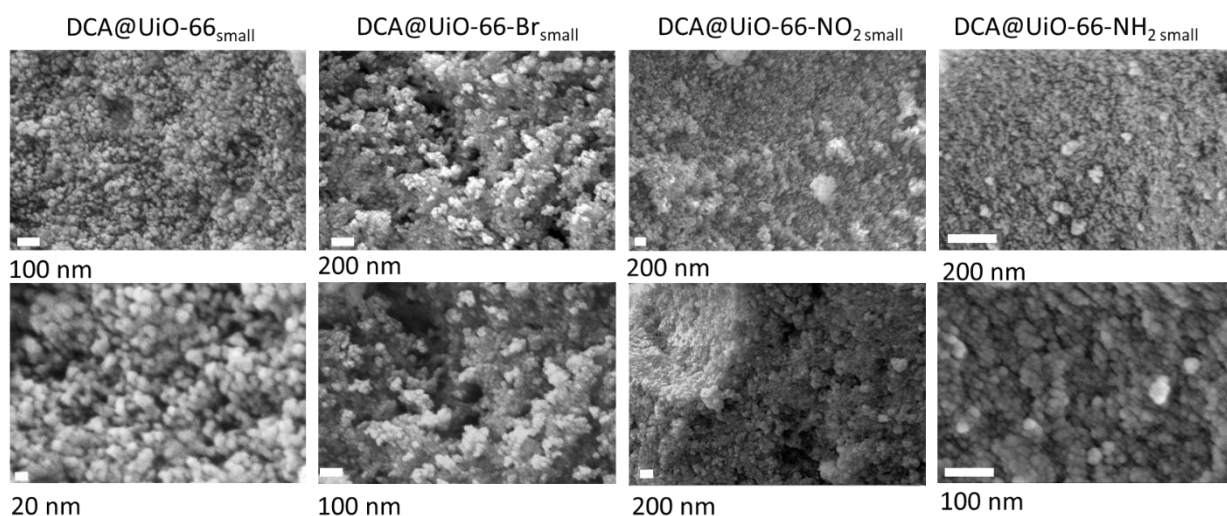


**Figure 2.42.** SEM images DCA@UiO-66<sub>small</sub> derivative MOFs.

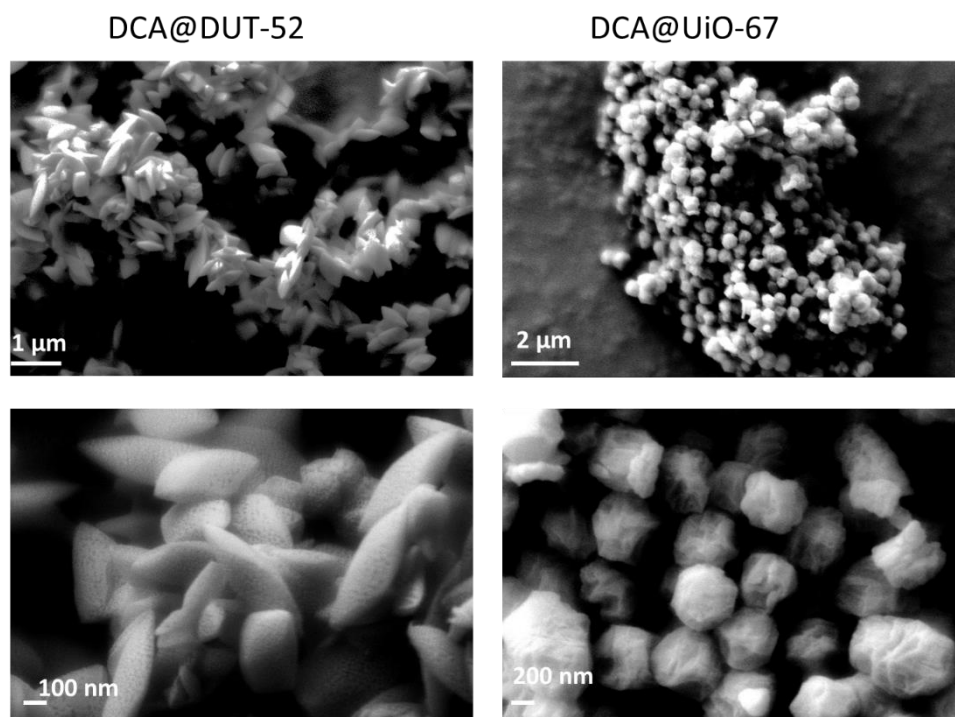


**Figure 2.43.** SEM images of a) DCA@DUT-52 and b) DCA@UiO-67.

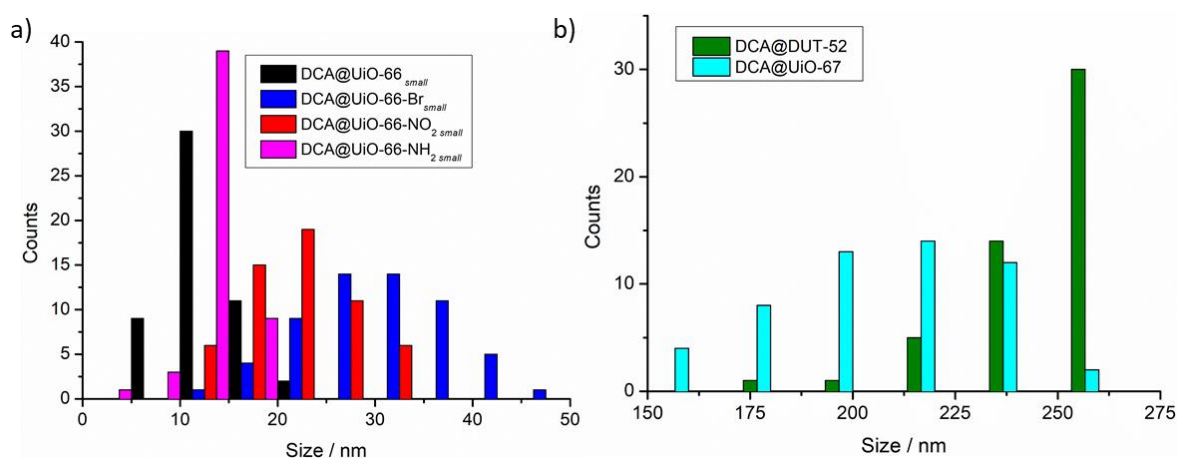


**Figure 2.44.** a) Particle size distribution histogram for DCA@UiO-66<sub>small</sub> samples. b) Particle size distribution histogram for DCA@DUT-52 and DCA@UiO-67.

The porosity of the samples was determined by N<sub>2</sub> sorption/desorption isotherms. The four terephthalate MOFs present type IV isotherms (Figure 2.45) with H2 hysteresis loops, which are typical of interconnected networks of pores with different size and shape and suggest highly defective structures.<sup>53</sup> The fact that the hysteresis closes before 0.9 P/P<sub>0</sub> in all cases, in contrast to H3 hysteresis loops, which are typical of aggregates of particles, strongly suggests that the hierarchical porosity is a consequence of attachment of DCA modulators

and resulting missing linker and cluster defects, although some contribution of inter-particle space should also be considered.

Comparison of the  $N_2$  uptake isotherms (Figure 2.46) with those of DCA@DUT-52 and DCA@UiO-67 shows that while the uptakes in the micropore region for the small samples are lower than typical UiO-66 materials,<sup>41</sup> the defectivity induces pore volumes similar to DCA@UiO-67, ranging from 0.8 to 1.2 ccg<sup>-1</sup> as a consequence of the additional, defect-induced mesoporosity. This difference is also borne out in the pore size distributions (Figure 2.47) which show well defined micropores of expected size for DCA@DUT-52 and DCA@UiO-67 but remarkably bigger pores in the case of DCA@UiO-66 *small* samples, consequence of their mesoporosity. The BET surface areas and pore volumes are given in Table 2.6.

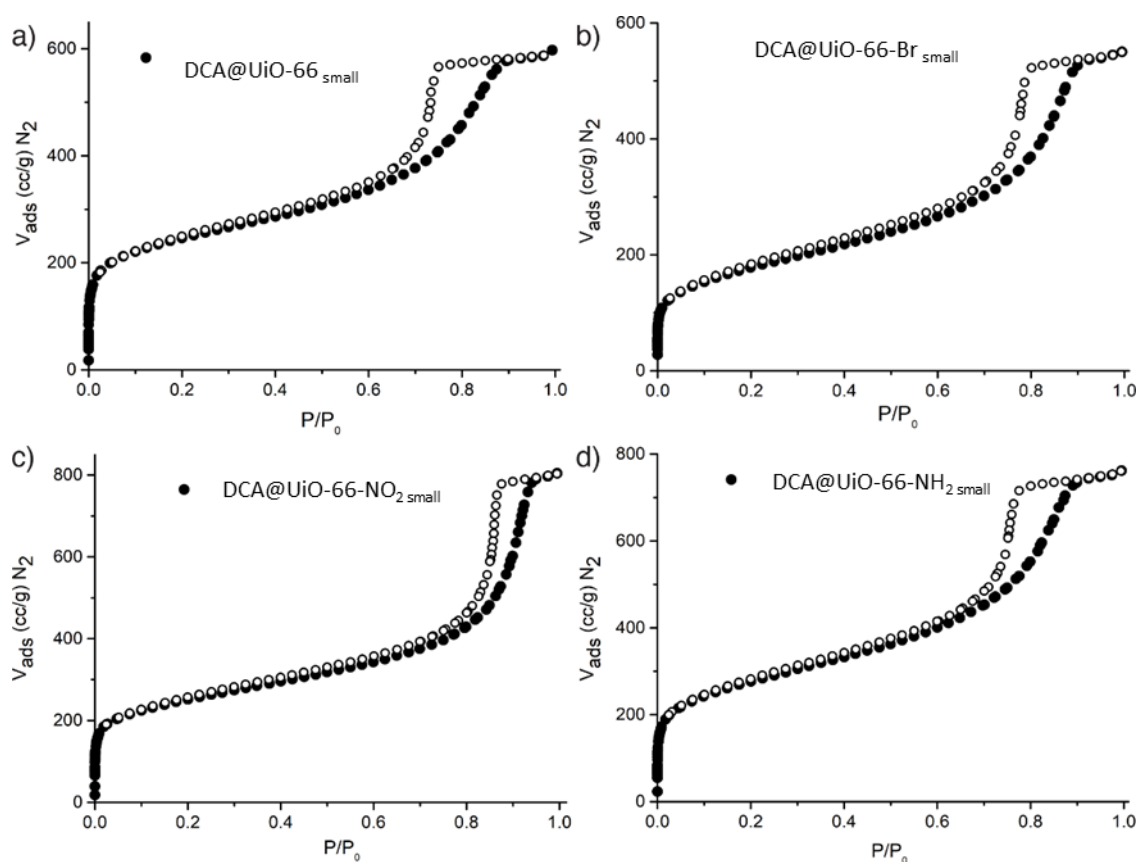


**Figure 2.45.**  $N_2$  uptake isotherms (77 K) for a) DCA@UiO-66 *small*, b) DCA@UiO-66-Br *small*, c) DCA@UiO-66-NO<sub>2</sub> *small*, and d) DCA@UiO-66-NH<sub>2</sub> *small*. Filled symbols indicate adsorption, empty symbols desorption.

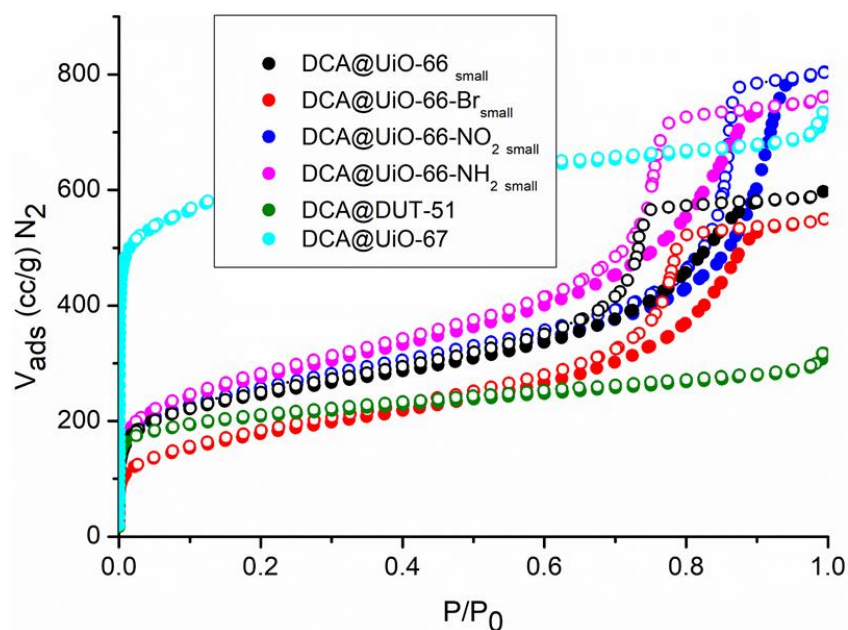


**Figure 2.46.** Comparison of  $N_2$  uptake isotherms (77 K) for all the MOFs synthesised using the  $ZrOCl_2$  protocol. Filled symbols indicate adsorption, empty symbols desorption.

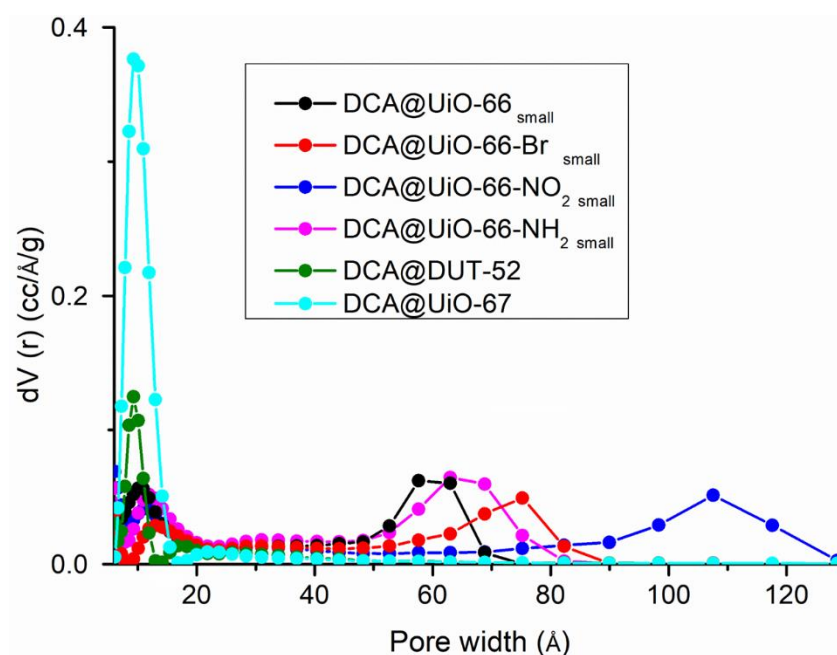


**Figure 2.47.** Pore size distributions, calculated from the  $N_2$  uptake isotherms, of the MOFs synthesised by the  $ZrOCl_2$  protocol, showing the mesopores of the defective  $DCA@UiO-66_{small}$  derivative MOFs.  $N_2$  on carbon at 77 K, slit pore, QSDFT, equilibrium model.

$^1H$  Nuclear magnetic resonance (NMR) spectra of acid-digested samples of the  $DCA@MOFs$  ( $D_2SO_4 / DMSO-d_6$ ) show significant quantities of DCA in all cases. The  $^1H$  NMR spectrum for digested  $DCA@UiO-66_{small}$  is shown as an exemplar in Figure 2.48, compared to  $DCA@UiO-66$  (ca.100 nm). The resonance at  $\delta = \sim 6.5$  ppm corresponds to the  $-CCl_2H$  proton of DCA, and it can be observed that the smaller and more defective derivative has higher DCA content.

It is not possible to quantitatively determine DCA loading values from the NMR spectra alone, as the exact composition of the MOF will depend on defectivity and the replacement of MOF linkers with capping DCA molecules. However, estimating the molar ratio of DCA compared to the ligand gives a qualitative assessment of the extent of DCA incorporation (Table 2.6).

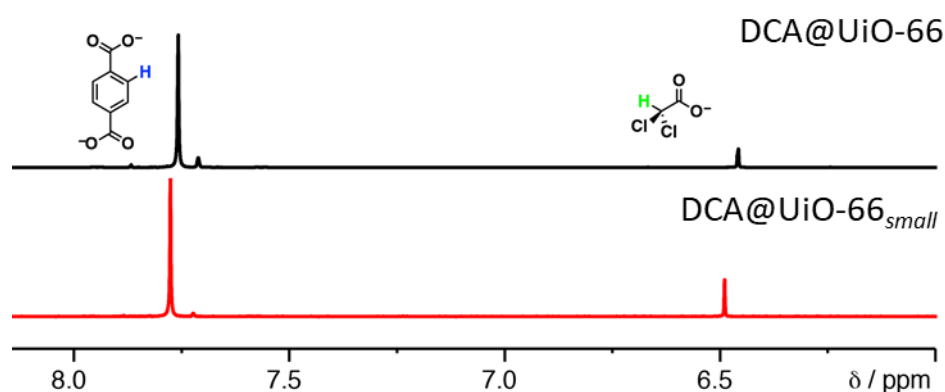


**Figure 2.48:** Partial stacked  $^1\text{H}$  NMR spectra ( $\text{D}_2\text{SO}_4 / \text{DMSO-}d_6$ ) of digested  $\text{DCA@UiO-66}_{small}$  (red) and  $\text{DCA@UiO-66}$  (black), showing the higher relative intensity of DCA for the smaller analogue MOF.

**Table 2.6.** Pertinent physical characteristics of the  $\text{DCA@MOFs}$  synthesised using the  $\text{ZrOCl}_2$  procedure

Sample	Size / nm	DCA mol % to Linker	% DCA w/w	BET SA / $\text{m}^2\text{g}^{-1}$	Pore volume / $\text{ccg}^{-1}$
<b><math>\text{DCA@UiO-66}_{small}</math></b>	$12.8 \pm 3.6$	30.3	26.2	891	0.87
<b><math>\text{DCA@UiO-66-Br}_{small}</math></b>	$30.2 \pm 7.9$	34.6	19.3	639	0.81
<b><math>\text{DCA@UiO-66-NO}_2_{small}</math></b>	$21.7 \pm 5.3$	34.5	21.5	901	1.12
<b><math>\text{DCA@UiO-66-NH}_2_{small}</math></b>	$12.5 \pm 2.9$	45.5	26.4	990	1.21
<b><math>\text{DCA@DUT-52}</math></b>	$232 \pm 30$	34.1	14.1	764	0.42
<b><math>\text{DCA@UiO-67}</math></b>	$196 \pm 32$	18.6	6.6	2241	0.99

Thermogravimetric analysis (TGA) of the  $\text{DCA@MOFs}$  shows significant mass loss events from 250–375 °C compared to pristine materials (Figure 2.49), allowing quantification of DCA content (Table 2.6).

DCA mass loss events within the MOF occur at a higher temperature than free DCA thermal decomposition (198°C),<sup>52</sup> as a consequence of its attachment to the Zr clusters. Mass loss events occurring before 225 °C are characteristic of DMF incorporation and water loss from the structure,<sup>44</sup> which is observed for both empty and DCA-containing MOFs, more notably for empty MOFs, as DMF coming from the synthetic process can get incorporated to the  $\text{Zr}_6$ , as well as formic acid from DMF hydrolysis during the reaction.<sup>37</sup> However, DCA mass loss

events from 250–375 °C can be easily identified in the trace and the first derivative, allowing DCA content to be quantified.

The experimental DCA and linker mass loss correlate well with the theoretical composition  $[\text{Zr}_6\text{O}_4(\text{OH})_4(\text{L})_3(\text{DCA})_3(\text{OH})_3]_n$  in the case of the DCA-loaded terephthalate MOFs, while DCA@DUT-52 is closer to  $[\text{Zr}_6\text{O}_4(\text{OH})_4(\text{L})_4(\text{DCA})_2(\text{OH})_2]_n$  and DCA@UiO-67 to  $[\text{Zr}_6\text{O}_4(\text{OH})_4(\text{L})_5(\text{DCA})_1(\text{OH})_1]_n$ , meaning that the terephthalate derivatives are considerably more defective, as was also suggested by PXRD and  $\text{N}_2$  adsorption analyses.

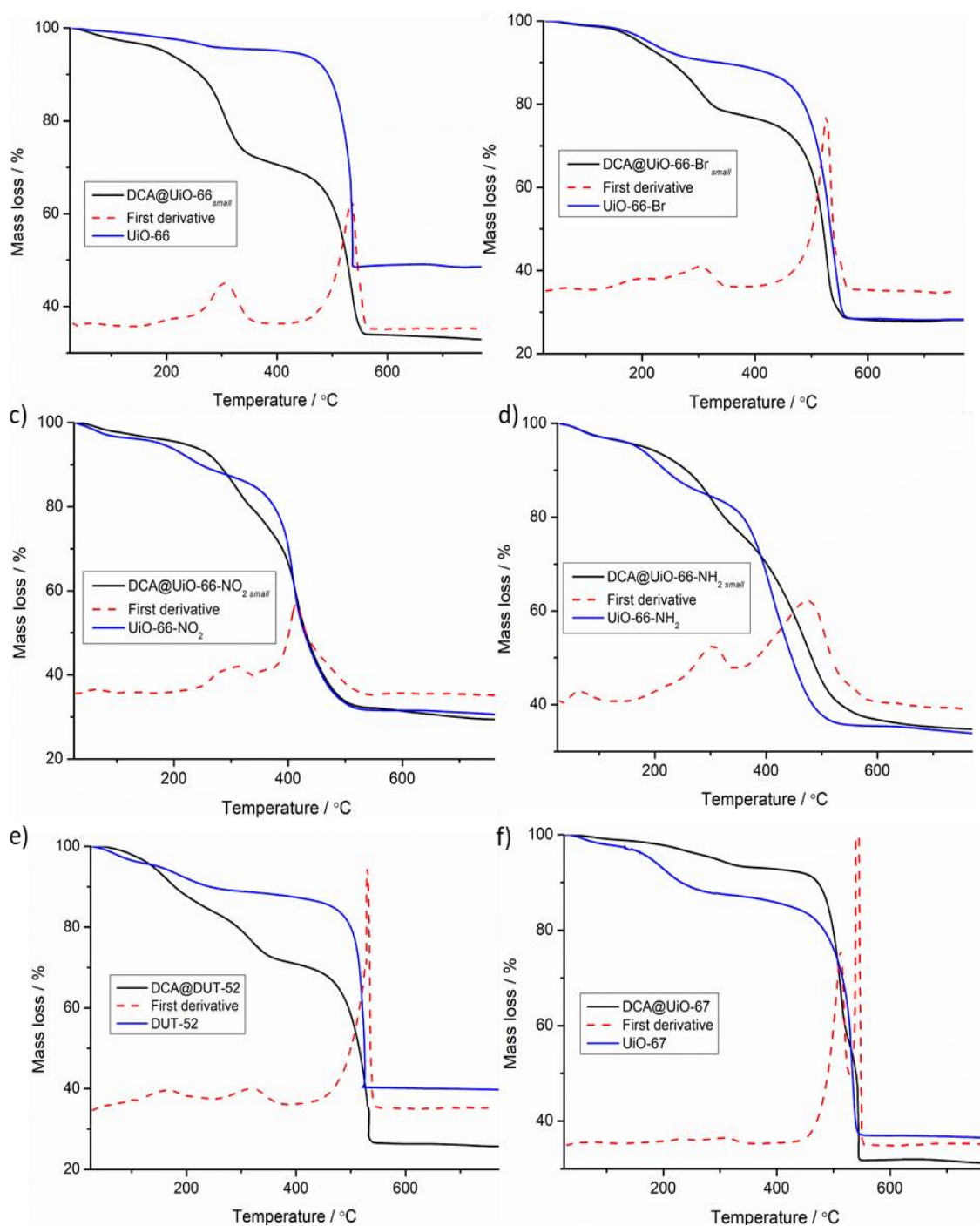


**Figure 2.49.** TGA traces in air of DCA loaded MOFs compared to empty MOFs

The particle size, aggregation and colloidal dispersion of the MOFs in water were measured by dynamic light scattering (DLS). The profiles for the small terephthalate nanoparticles are shown in Figure 2.50.

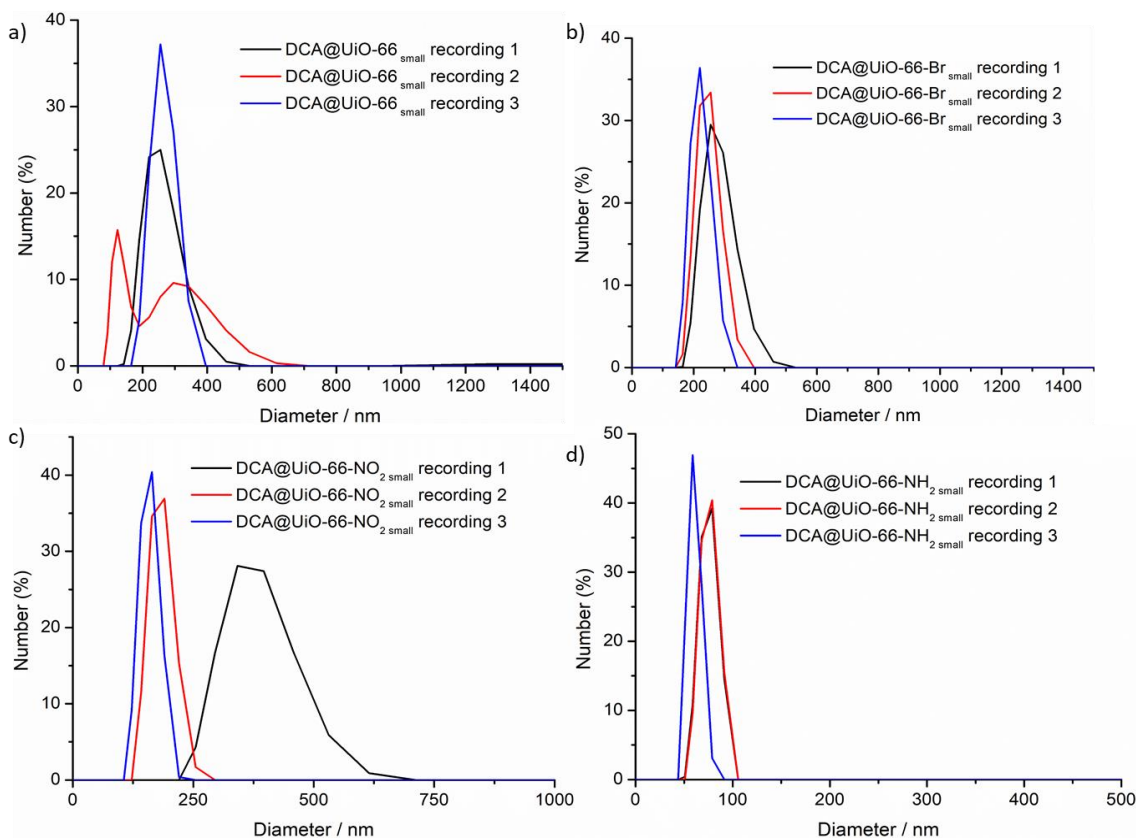


**Figure 2.50.** DLS profiles in water for DCA@UiO-66 *small* derivative MOFs.

The samples show a small degree of aggregation, except for DCA@UiO-66-NH<sub>2</sub> *small* which shows very little aggregation, likely due to positive charge on the pendant amino groups of L4 resulting in interparticle repulsion.<sup>54</sup> The DLS profiles for DCA@DUT-52 and DCA@UiO-67 are shown in Figure 2.51, and also show only a small degree of aggregation.

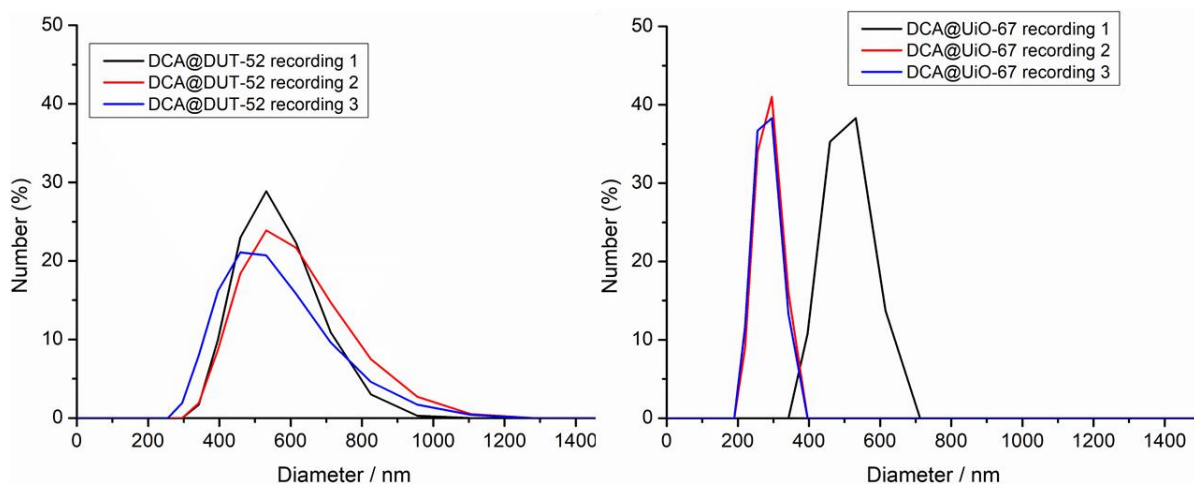


**Figure 2.51.** DLS profiles in water for a) DCA@DUT-52 and b) DCA@UiO-67.

Comparison of all samples (Figure 2.52) shows the difference in behaviour of the smaller and larger samples.

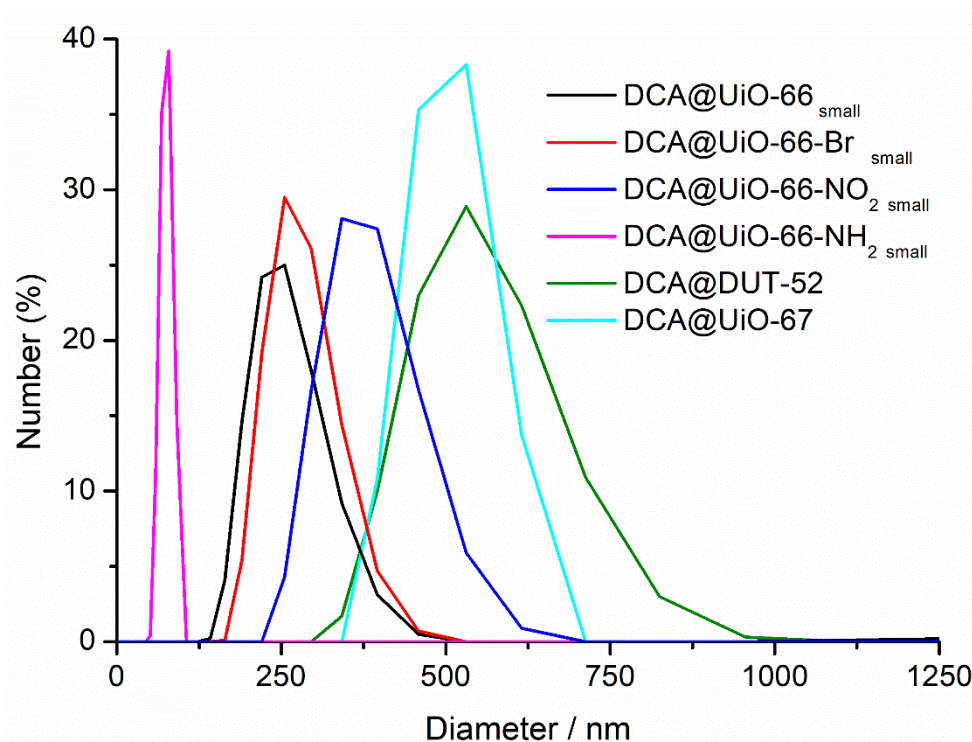


**Figure 2.52.** Comparison of the first recordings in the DLS experiments for aqueous suspensions of all the MOFs synthesised using the  $ZrOCl_2$  protocol.

It is expected that in biological systems, formation of a protein corona will limit aggregation further.<sup>27, 41, 55-57</sup> To examine this, DLS experiments were carried out on the samples that showed some aggregation – the smaller terephthalate MOFs as well as DCA@DUT-52 and DCA@UiO-67 – when dispersed in phosphate buffered saline (PBS, pH = 7.4) that had been “spiked” with 2% w/w bovine serum albumin (BSA), to mimic biological conditions. All samples showed less aggregation and improved colloidal stability, and are compared with the analogous experiments in water in Figures 2.53 and 2.54. The smaller samples stabilised to around 100-150 nm aggregates, while DCA@UiO-66-NH<sub>2</sub><sub>small</sub> appeared to be monodisperse and correlated well with particle sizes determined by SEM. The amino functionality of L4 is expected to be protonated under these conditions, and so form a highly stable corona with the negatively charged BSA. The larger particles also formed stable dispersions close to the particle sizes determined by SEM, indicating that the MOFs will not be significantly aggregated during *in vitro* cytotoxicity studies.

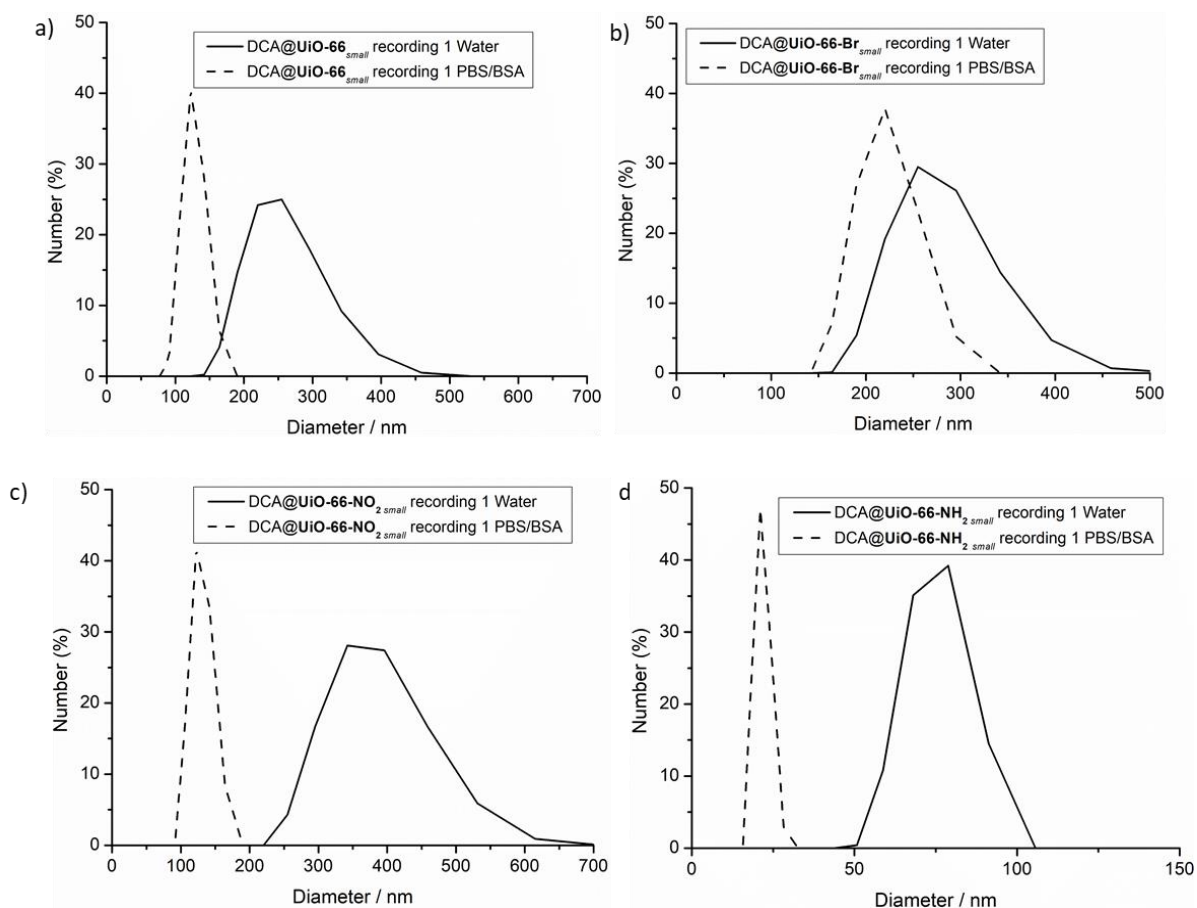


**Figure 2.53.** Comparison of the DLS profiles collected in water with those in 2% w/w BSA in PBS for a) DCA@UiO-66<sub>small</sub>, b) DCA@UiO-66-Br<sub>small</sub>, c) DCA@UiO-66-NO<sub>2</sub><sub>small</sub>, and d) DCA@UiO-66-NH<sub>2</sub><sub>small</sub>.

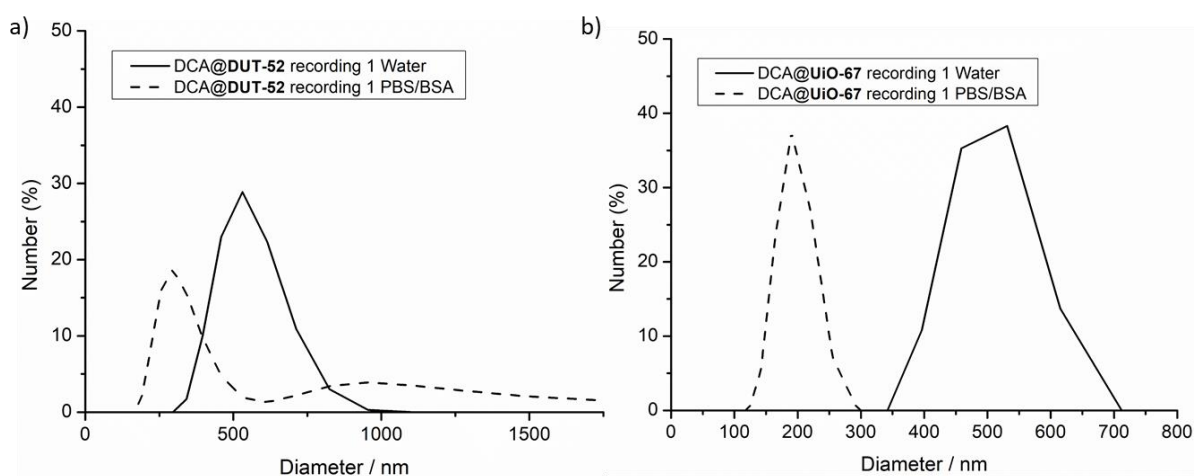


**Figure 2.54.** Comparison of the DLS profiles collected in water with those in 2% w/w BSA in PBS for a) DCA@DUT-52 and b) DCA@UiO-67.

The larger DCA-loaded terephthalate MOFs were also well-dispersed in water, with only minor aggregation, showing size distributions (Figure 2.55) close to those determined by SEM.

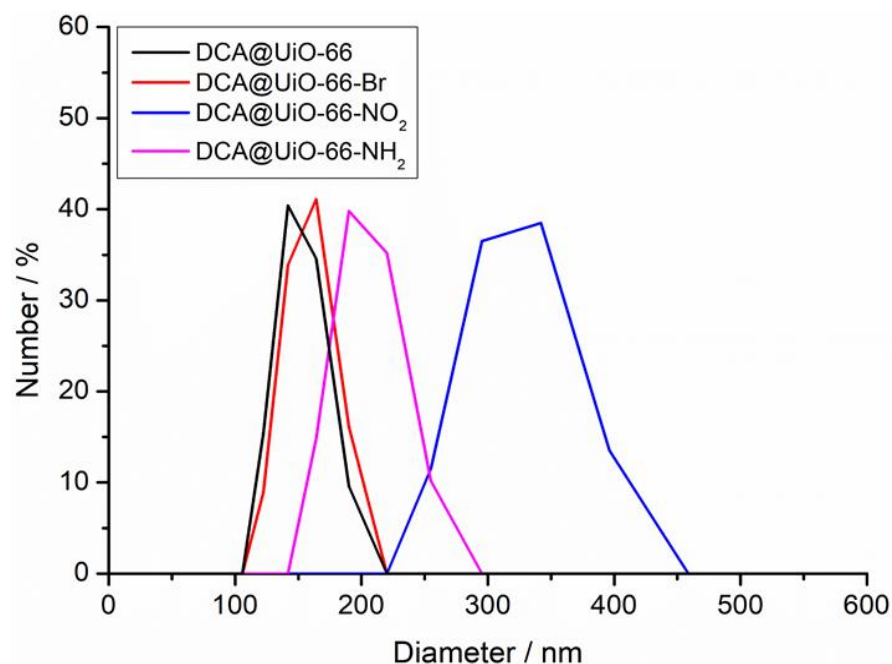


**Figure 2.55.** Comparison of the first recordings in the DLS experiments for aqueous suspensions of the larger DCA-loaded terephthalate MOFs of bigger size.

It has been reported that DCA enhances the cytotoxic activity of anticancer drugs such as 5-fluorouracil (5-FU) while reducing cancer cells resistance towards them. As such, the smaller, DCA-loaded Zr-terephthalate samples, along with DCA@DUT-52 and DCA@UiO-67, were postsynthetically loaded with 5-FU to generate multimodal DDSs.

<sup>1</sup>H NMR spectra of acid digested samples showed that DCA was still present after loading, but only very low intensity signals were observed for 5-FU, indicating low loading. Additionally, due to the very low content of 5-FU, its FT-IR vibration bands are masked by the MOF signals in the FT-IR spectra of the 5-FU@DCA@MOF samples, and characteristic vibration bands of DCA can still clearly be observed in the spectra.

Thermogravimetric analysis cannot distinguish between loaded DCA and 5-FU, although it suggests some loss of DCA during 5-FU loading for the small terephthalate MOFs. The loading of 5-FU, shown in Table 2.7, was calculated by UV-Vis spectroscopy, and found to range from 1.5–4.3% w/w (Figure 2.54).

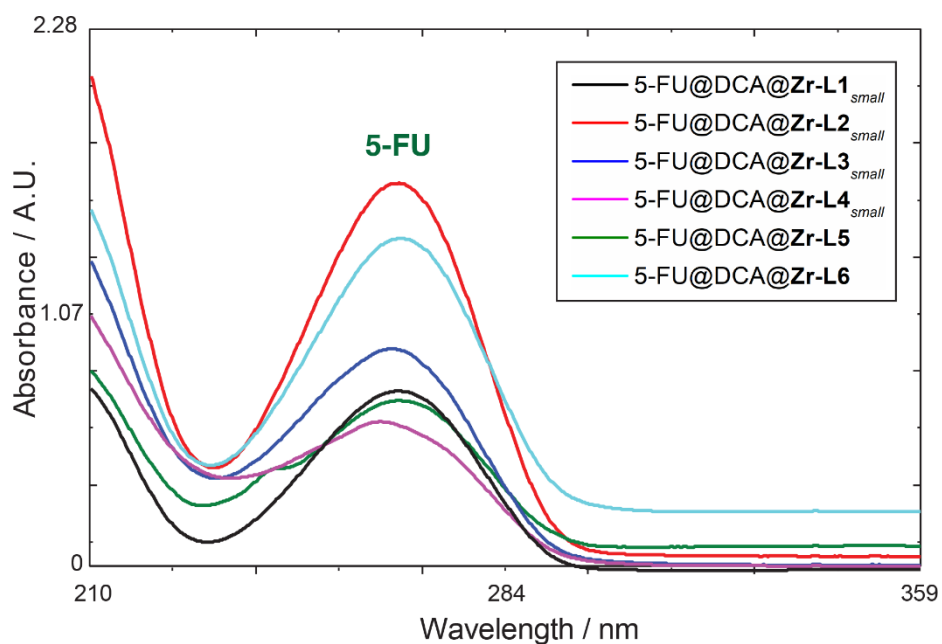


**Figure 2.54.** Release of 5-FU into methanol from the 5-FU@DCA@MOFs followed by UV/Vis spectroscopy to allow determination of 5-FU loading. Note that base line value was subtracted from the absorbance value.

Knowing the loading of 5-FU in the MOFs, it is therefore possible to estimate the DCA loading using the TGA traces, if it is assumed that the mass loss in the temperature region (250–375 °C) corresponds to thermal decomposition of both DCA and 5-FU, and therefore deduct the 5-FU content, as determined by UV/Vis spectroscopy, from the total (Table 2.7). The terephthalate-based MOFs lose significant quantities of DCA during 5-FU loading, but still retain respectable, clinically relevant contents.

**Table 2.7.** Estimation of DCA loading in the 5-FU@DCA@NMOFs by a combination of TGA analysis and UV/Vis spectroscopy. <sup>a</sup>Values in brackets are DCA loadings determined for the samples prior to 5-FU loading for comparison.

Sample	% 5-FU	% TGA	% DCA <sup>a</sup>
5-FU@DCA@UiO-66 <sub>small</sub>	1.9	24.1	22.3 (26.2)
5-FU@DCA@UiO-66-Br <sub>small</sub>	3.8	16.9	13.1 (19.3)
5-FU@DCA@UiO-66-NO <sub>2</sub> <sub>small</sub>	4.3	13.0	8.7 (21.5)
5-FU@DCA@ UiO-66-NH <sub>2</sub> <sub>small</sub>	2.4	15.0	12.6 (26.4)
5-FU@DCA@DUT-52	1.5	17.0	15.5 (14.1)
5-FU@DCA@UiO-67	2.5	9.6	7.1 (6.6)

## 2.5. Conclusions and Future Work

In conclusion, it has been shown that carboxylate modulators can be attached to the Zr positions (at outer surface and defect sites) of UiO-66 during its synthesis, yielding crystalline, phase pure, highly porous nanoparticles, as a consequence of the defects that modulators attachment induces.<sup>37</sup> The scope of modulators used during this study confirms the versatility of the protocol, being able to introduce functionalised *p*-benzoic acid and more complex modulators (i.e folic acid and biotin) to the NMOF structure during synthesis. Additionally, the resultant MOFs had the adequate particle size for drug delivery (<200 nm), and this surface functionalisation protocol could be applied to other areas such as gas capture or storage.

The use of carboxylate-containing drug molecules as modulators for synthesis of UiO-66 nanoparticles - in this study the PDK inhibitor dichloroacetic acid (DCA) - has been shown to be an efficient methodology to ensure high cargo loading at defect sites in one-pot syntheses. DCA modulation in particular generates colloiddally-stable nanoparticles with high DCA-loading values that are amenable to further functionalisation without compromising porosity. Additionally, the low  $pK_a$  of DCA ensures its high incorporation, even in the presence of other functionalised modulators, allowing the synthesis of highly specialised drug-containing surface-functionalised MOFs in one synthetic step.

DCA modulation also served as a size-control protocol, as the DCA@UiO-66 derivative MOFs synthesised under the  $ZrCl_4$  conditions had homogeneous size distributions of ca. 100 nm, while the ones synthesised under the  $ZrOCl_2$  conditions had particle sizes of ca. 20 nm. It has been observed that, under the same  $ZrCl_4$  and  $ZrOCl_2$  synthetic conditions, electron-rich terephthalates yield in relatively smaller sizes (ca. 80 and 10 nm) than electron-poor terephthalates (ca. 125 and 30 nm), while extended linkers (more hydrophobic) form micro and nanocrystals of ca.200 nm. Due to the defects that DCA attachment induces, the high porosity of the NMOFs has been used to store a second drug (5-FU) for combined treatments.

The materials presented during this chapter will be used in the subsequent chapters. For example, UiO-66-L1 and UiO-66-L2 will be used as platforms for postsynthetic modifications during Chapter 3, where the properties of all the surface-functionalised MOFs will be studied and compared with their precursors and bare MOFs synthesised under acetic acid modulated conditions. Calcein loading and postsynthetic modification of UiO-66-L1 and UiO-66-L2 (in which L2 is introduced postsynthetically) will be performed during Chapter 4, and the calcein-loaded MOFs will be further used to study the effect of surface chemistry on their cellular internalisation fate and routes, while postsynthetic modification of the DCA analogues and the evaluation of the cytotoxicity of all the DCA-containing MOFs will be studied in Chapter 5.

## 2.6. Experimental

### 2.6.1. General Experimental Remarks

**Powder X-Ray Diffraction (PXRD):** PXRD measurements were carried out at 298 K using a PANalytical X'Pert PRO diffractometer ( $\lambda(\text{CuK}\alpha) = 1.4505 \text{ \AA}$ ) on a mounted bracket sample stage. Data were collected over the range 5–45°. (University of Glasgow)

**Thermogravimetric Analysis (TGA):** Measurements were carried out using a TA Instruments Q500 Thermogravimetric Analyser. Measurements were collected from room temperature to 800 °C with a heating rate of 10 °C / min under an air atmosphere. (University of Glasgow)

**Nuclear Magnetic Resonance Spectroscopy (NMR):** NMR spectra were recorded on either a Bruker AVIII 400 MHz spectrometer or a Bruker AVI 500 MHz spectrometer and referenced to residual solvent peaks. (University of Glasgow)

**Gas Uptake:** N<sub>2</sub> adsorption isotherms were carried out at 77 K on a Quantachrome Autosorb iQ gas sorption analyser. Samples were degassed under vacuum at 120 °C for 20 h using the internal turbo pump. BET surface areas were calculated from the isotherms using the Micropore BET Assistant in the Quantachrome ASiQwin operating software. (University of Glasgow)

**Pore-Size Distribution:** Pore size distributions were calculated using the N<sub>2</sub> at 77 K on carbon (slit pore, QSDFT, equilibrium model) calculation model within the Quantachrome ASiQwin operating software. (University of Glasgow)

**UV-Vis Spectroscopy:** UV-vis spectra were recorded using a Shimadzu UV-1800; analysis was carried out using the software UVProve. (University of Glasgow)

**Scanning Electron Microscopy (SEM):** The powder samples were coated with Pd for 50 seconds using Polaron SC7640 sputter coater and imaged using a Carl Zeiss Sigma Variable Pressure Analytical SEM with Oxford Microanalysis. Particle size distribution was analysed manually using ImageJ software. (University of Glasgow)

**Fourier Transform Infrared Spectroscopy:** IR spectra of solids were collected using a Shimadzu Fourier Transform Infrared Spectrometer, FTIR-8400S, fitted with a Diamond ATR unit. (University of Glasgow)

**Dynamic Light Scattering:** Colloidal analysis was performed by Dynamic Light Scattering (DLS) with a Zetasizer Nano ZS potential analyser equipped with Non-Invasive Backscatter optics (NIBS) and a 50 mW laser at 633 nm. (University of Glasgow)

**ESIMS:** Electrospray Ionisation Mass Spectrometry was carried out on solution samples injected into a Bruker MicroTOFq spectrometer. (University of Glasgow).

### 2.6.2. Materials and Synthesis

All reagents unless otherwise stated were obtained from commercial sources and were used without further purification. The modulators L1 and L2 were synthesised by literature procedures, and the synthesis of UiO-66 –  $[\text{Zr}_6\text{O}_4(\text{OH})_4(\text{C}_8\text{H}_4\text{O}_4)_x]_n$  – was adapted from a literature procedure.<sup>42</sup>

#### ***p*-Azidomethyl benzoic acid (L1)**

The commercially available 4-(bromomethyl)benzoic acid (5 g, 23.27 mmol, 1.0 eq) was dissolved in *N,N*-dimethylformamide, DMF, (150 ml) in a round 250 ml bottom flask. Sodium azide (3.8 g, 58.18 mmol, 2.5 eq) was added dropwise. The reaction mixture was heated at 50 °C for 24 hours. The solvent was evaporated under vacuum. Following the literature procedure, *p*-azidomethyl benzoic acid (3.91 g, 22.1 mmol, 95%) was obtained pure as a white solid.<sup>58</sup>

**<sup>1</sup>H NMR** (500 MHz, CDCl<sub>3</sub>) δ 4.48 (s, 2 H), 7.46 (d, *J* = 8.4 Hz, 2H), 8.16 (d, *J* = 8.3 Hz, 2H);  
**<sup>13</sup>CNMR** (126 MHz, CDCl<sub>3</sub>) δ 53.41, 128.7, 130.62, 130.91, 141.04, 167.51.

The azide band (2130 cm<sup>-1</sup>) was identified by IR, and compared with the starting material.

**ESI-MS:** calculated for C<sub>8</sub>H<sub>6</sub>N<sub>3</sub>O<sub>2</sub> *m/z* = 176.0466; found *m/z* = 176.0455.

#### ***p*-Propargyloxy benzoic acid (L2)**

To a solution of methyl 4-hydroxybenzoate (5 g, 33 mmol, 1.0 eq) in acetonitrile (40 mL), K<sub>2</sub>CO<sub>3</sub> (6.64 g, 49.5 mmol, 1.5 eq) was added. The mixture was heated to 50 °C for 30 min followed by dropwise addition of propargyl bromide (80% in toluene, 4.9 g, 3.53 ml, 33 mmol, 1 eq). The mixture was allowed to react at the same temperature during 16 hours. Solvent was evaporated, the remaining liquid was quenched with water and extracted with chloroform (4 x 15 ml). The organic layers were combined and washed with water (2 x 10 ml) and brine (2 x 10 ml). Pure methyl *p*-propargyloxybenzoate was obtained as a white solid (8.11 g, 32 mmol, 97%).<sup>59</sup>

**<sup>1</sup>H NMR** (500 MHz, CDCl<sub>3</sub>) δ: 2.54 (t, *J* = 2.5 Hz, 1H), 3.88 (s, 3H), 4.74 (d, *J* = 2.5 Hz, 2H), 6.99 (d, *J* = 8.5 Hz, 2H), 8.00 (d, *J* = 9.0 Hz, 2H); **<sup>13</sup>C NMR** (126 MHz, CDCl<sub>3</sub>) δ: 51.86, 55.78, 76.05, 77.79, 114.51, 123.42, 131.50, 161.11, and 166.64.

Methyl *p*-propargyloxybenzoate (8 g, 32 mmol) was dissolved in a mixture of THF (45 ml) and MeOH (22.5 ml), an aqueous solution of NaOH 40% weight (25 ml) was added and the reaction mixture allowed to reflux for two hours. After cooling down, the organic solvents were distilled under vacuum yielding a clear solution, which was acidified with 6 M aqueous HCl. A white precipitate separated, was filtered and washed with abundant water, yielding after drying under vacuum pure *p*-propargyloxybenzoic acid (6.43 g, 27 mmol, 87.6%).<sup>59</sup>

**<sup>1</sup>H NMR** (500 MHz, CDCl<sub>3</sub>) δ: 3.57 (t, *J* = 2.4 Hz, 1H), 4.86 (d, *J* = 2.4 Hz, 2H), 7.04 (d, *J* = 9.0 Hz, 2H), 7.88 (d, *J* = 9.0 Hz, 2H), 12.41 (s, 1H); **<sup>13</sup>C NMR** (126 MHz, CDCl<sub>3</sub>) δ: 39.91, 56.05, 79.02, 79.14, 115.04, 124.11, 131.67, and 161.13.

**ESI-MS:** calculated for C<sub>10</sub>H<sub>7</sub>O<sub>3</sub> *m/z* = 175.0401; found *m/z* = 175.0399.

### UiO-66 Syntheses

UiO-66 was synthesised by adaptation of a literature procedure to include different modulators as follows.<sup>42</sup> For all samples, after cooling the reaction mixture, particles were collected by centrifugation (4500 rpm, 15 minutes), and washed (sonication centrifugation cycles) with fresh DMF (x1) and MeOH (x3). The NMOFs were dried for at least 24 hours under vacuum before analysis. For SEM, the samples were prepared as low concentration dispersions of nanoparticles in MeOH, which were allowed to dry in the oven at 60 °C for 5 minutes.

#### UiO-66 (Unmodulated)

1,4-Benzenedicarboxylic acid (bdc) (448 mg, 2.7 mmol) was dissolved in 30 ml of DMF. In a separate vial, the metal precursor, zirconium chloride (629 mg, 2.7 mmol) was dissolved in 30 ml of DMF. Both solutions were sonicated until complete dissolution and mixed together in a 100 ml jar. The solution was heated to 120 °C for 24 hours yielding UiO-66 nanoparticles.

#### UiO-66-AcOH (Modulated with acetic acid)

UiO-66 particles were modulated using the same procedure.<sup>42</sup> Acetic acid (4.2 ml, 7% volume) was added after mixing both precursors solutions. The sample is named UiO-66-AcOH.

#### UiO-66-L1 and UiO-66-L2 (Modulated with L1 or L2)

1,4-Benzenedicarboxylic acid (448 mg, 2.7 mmol) plus one, three or five equivalents of modulator (L1 or L2), compared to metal precursor, were dissolved in 30 ml of DMF. In a separate vial, the metal precursor, zirconium chloride (629 mg, 2.7 mmol) was dissolved in 30

ml of DMF. Both solutions were sonicated until complete dissolution and mixed together. Subsequently, acetic acid (4.2 ml, 7% volume) was added. The solution was heated to 120 °C for 24 hours yielding UiO-66 nanoparticles.

#### **Synthesis of Folic Acid and Biotin Modulated UiO-66**

1,4-Benzenedicarboxylic acid (150 mg, 0.9 mmol) plus modulator, either biotin (100 mg, 0.41 mmol, 0.45 equivalents compared to metal precursor) or folic acid (100mg, 0.23 mmol, 0.25 equivalents compared to metal precursor), were dissolved in 10 mL of DMF. In a separate vial, the metal precursor, zirconium chloride (210 mg, 0.9 mmol) was dissolved in 10 mL of DMF. Both solutions were sonicated until complete dissolution and mixed together. Subsequently, acetic acid (1.4 mL, 7% v/v) was added when necessary. The solution was heated to 120 °C for 24 h yielding UiO-66 nanoparticles.

#### **Synthesis of Dichloroacetic Acid (DCA) Modulated UiO-66**

DCA@UiO-66 synthesis was performed following the former coordination modulation protocol, adding 10 equivalents of DCA instead of AcOH (7% volume) to the syntheses, together with 1 equivalent of HCl. In the case of DCA@UiO-66-L1 and DCA@UiO-66-L2, equivalents of the modulator in question (L1 or L2) were dissolved together with the linker in DMF.

#### **Co-Modulated Synthesis of DCA-Loaded, Surface Modified UiO-66**

For the synthesis of DCA<sub>10</sub>@UiO-66-FA<sub>0.25</sub> (CM), DCA<sub>5</sub>@UiO-66-FA<sub>1</sub> (CM) and DCA@UiO-66-Biot (CM) the former coordination modulation protocol was slightly modified, dissolving folic acid (FA, 0.25 or 1 equivalents compared to metal precursor) or biotin (0.4 equivalents compared to metal precursor) together with 1 equivalent of the linker in DMF. After mixing both precursor solutions, DCA (5 or 10 equivalents) was added. After gently mixing, the solution was placed in the oven at 120 °C for 24 h.

## DCA Modulated Synthesis of UiO Family of Zr MOFs

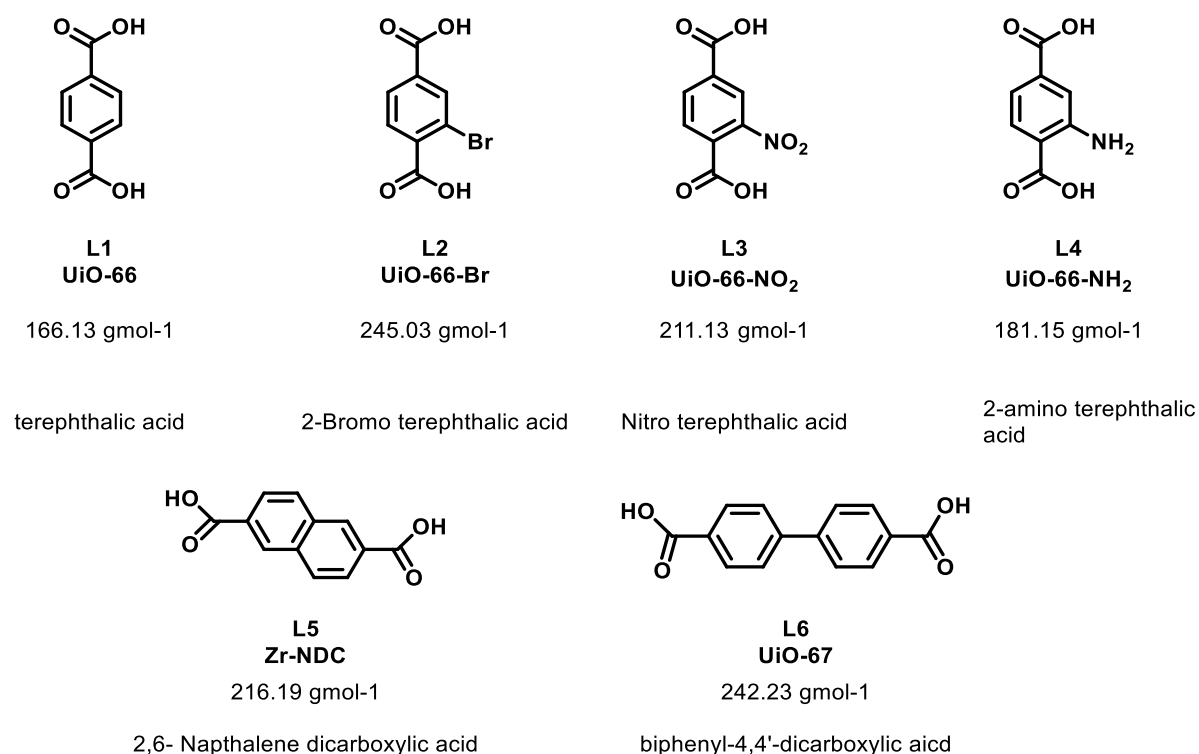


**Figure 2.55.** Linker of the UiO family of Zr MOFs synthesised in this thesis.

In separate vials, zirconyl chloride octahydrate (213 mg, 0.66 mmol, 1 equivalent) and the linker in case, (1.65 mmol, 2.5 equivalents), shown in Figure 2.55, were dissolved in 25 mL of DMF. After mixing both precursor solutions, dichloroacetic acid (DCA) (1 mL, 5 mmol, 18.75 equivalents compared to metal) was added to the reaction mixture, which after gently stirring, was placed in the oven at 120°C during 24h.

After cooling down, the powders were collected by centrifugation, and washed with DMF (X2) and MeOH (X3) through dispersion centrifugation cycles.

The resultant NMOFs were dried under vacuum at least 24 hours before analysis.

### Synthesis DCA@UiO-66 Derivatives of Bigger Size

DCA@UiO-66 derivatives synthesis was performed following the former coordination modulation protocol, using 1 to 1 ratio of ZrCl<sub>4</sub> and linker, adding 10 equivalents of DCA instead to the syntheses, together with 1 equivalent of HCl. After 24 hours, the reaction mixtures were cooled to room temperature and the NMOFs were collected with centrifugation and washed with DMF (x1) and MeOH (x3).

**5-FU Loadings:**

40 mg of the DCA@NMOF in question were sonicated during 15 minutes in a 5-FU solution ( $3 \text{ mg mL}^{-1}$  in MeOH), and then the dispersion was stirred during 3 hours at room temperature. The 5-FU@DCA@NMOFs were collected by centrifugation and washed with MeOH (x3) through dispersion centrifugation cycles to ensure no residual 5-FU was present on the surfaces of the particles. The resultant NMOFs were dried under vacuum at least 24 hours before analysis.

**5-FU UV-Vis Determination:**

Around 2.5 mg of samples were dispersed in 5 mL of MeOH and sonicated for 2 minutes in order to promote 5-FU release, followed by 30 minutes stirring at room temperature. The supernatant was collected by centrifugation, and a UV/Vis spectrum measured from  $\lambda = 200\text{-}500 \text{ nm}$ . The 5-FU content ( $\lambda_{\text{max}} = 266 \text{ nm}$ ) in weight percent was calculated against a previously calculated calibration curve (note that the base line value was subtracted from the absorbance value). Additionally, absorbance measurements of the linkers in MeOH were performed, confirming minor or no linker leakage from the MOFs that did not affect 5-FU determination.

The calculations were performed using the exact mass of each MOF added. The samples were dispersed again and the measurements were repeated 2 hours after to ensure that 5-FU release was completed.

## 2.7 References

1. P. Horcajada, C. Serre, M. Vallet-Regí, M. Sebban, F. Taulelle and G. Férey, *Angewandte Chemie*, 2006, **45**, 5974-5978.
2. A. Ray Chowdhuri, D. Bhattacharya and S. K. Sahu, *Dalton Transactions*, 2016, **45**, 2963-2973.
3. J. D. Rocca, D. Liu and W. Lin, *Accounts of Chemical Research*, 2011, **44**, 957-968.
4. R. J. Marshall and R. S. Forgan, *European Journal of Inorganic Chemistry*, 2016, **2016**, 4310-4331.
5. R. J. Marshall, S. L. Griffin, C. Wilson and R. S. Forgan, *Chemistry – A European Journal*, 2016, **22**, 4870-4877.
6. R. J. Marshall, T. Richards, C. L. Hobday, C. F. Murphie, C. Wilson, S. A. Moggach, T. D. Bennett and R. S. Forgan, *Dalton Transactions*, 2016, **45**, 4132-4135.
7. S. M. Cohen, *Chemical Reviews*, 2012, **112**, 970-1000.
8. S. J. Garibay and S. M. Cohen, *Chemical Communications*, 2010, **46**, 7700-7702.
9. M. Kim, J. F. Cahill, H. Fei, K. A. Prather and S. M. Cohen, *Journal of the American Chemical Society*, 2012, **134**, 18082-18088.
10. K. K. Tanabe, Z. Wang and S. M. Cohen, *Journal of the American Chemical Society*, 2008, **130**, 8508-8517.
11. Z. Wang and S. M. Cohen, *Chemical Society Reviews*, 2009, **38**, 1315-1329.
12. S. Liu, L. Zhai, C. Li, Y. Li, X. Guo, Y. Zhao and C. Wu, *ACS Applied Materials and Interfaces*, 2014, **6**, 5404-5412.
13. R. Makiura, S. Motoyama, Y. Umemura, H. Yamanaka, O. Sakata and H. Kitagawa, *Nature Materials*, 2010, **9**, 565-571.
14. C. V. McGuire and R. S. Forgan, *Chemical Communications*, 2015, **51**, 5199-5217.
15. Z. Rao, K. Feng, B. Tang and P. Wu, *ACS Applied Materials and Interfaces*, 2017, **9**, 2594-2605.
16. T. Rijnaarts, R. Mejia-Ariza, R. J. M. Egberink, W. van Roosmalen and J. Huskens, *Chemistry – A European Journal*, 2015, **21**, 10296-10301.
17. A. Zimpel, T. Preiß, R. Röder, H. Engelke, M. Ingris, M. Peller, J. O. Rädler, E. Wagner, T. Bein, U. Lächelt and S. Wuttke, *Chemistry of Materials*, 2016, **28**, 3318-3326.
18. I. Canton and G. Battaglia, *Chemical Society Reviews*, 2012, **41**, 2718-2739.
19. H. Gao, W. Shi and L. B. Freund, *Proceedings of the National Academy of Sciences of the United States of America*, 2005, **102**, 9469-9474.
20. A. L. Kiss and E. Botos, *Journal of Cellular and Molecular Medicine*, 2009, **13**, 1228-1237.
21. N. Oh and J. H. Park, *International Journal of Nanomedicine*, 2014, **9**, 51-63.
22. J. Rejman, V. Oberle, I. S. Zuhorn and D. Hoekstra, *The Biochemical journal*, 2004, **377**, 159-169.
23. L. Treuel, X. Jiang and G. U. Nienhaus, *Journal of the Royal Society Interface*, 2013, **10**, 20120939.
24. K. Yin Win and S.-S. Feng, *Biomaterials*, 2005, **26**, 2713-2722.
25. A. M. Bannunah, D. Vllasaliu, J. Lord and S. Stolnik, *Molecular Pharmaceutics*, 2014, **11**, 4363-4373.
26. J. H. Cavka, S. Jakobsen, U. Olsbye, N. Guillou, C. Lamberti, S. Bordiga and K. P. Lillerud, *Journal of the American Chemical Society*, 2008, **130**, 13850-13851.

27. C. Orellana-Tavra, S. Haddad, R. J. Marshall, I. Abánades Lázaro, G. Boix, I. Imaz, D. Maspoch, R. S. Forgan and D. Fairen-Jimenez, *ACS Applied Materials and Interfaces*, 2017, **9**, 35516-35525.
28. H. Guo, Y. Zhu, S. Wang, S. Su, L. Zhou and H. Zhang, *Chemistry of Materials*, 2012, **24**, 444-450.
29. T. Tsuruoka, S. Furukawa, Y. Takashima, K. Yoshida, S. Isoda and S. Kitagawa, *Angewandte Chemie International Edition*, 2009, **48**, 4739-4743.
30. F. Vermoortele, B. Bueken, G. Le Bars, B. Van de Voorde, M. Vandichel, K. Houthoofd, A. Vimont, M. Daturi, M. Waroquier, V. Van Speybroeck, C. Kirschhock and D. E. De Vos, *Journal of the American Chemical Society*, 2013, **135**, 11465-11468.
31. F. Wang, H. Guo, Y. Chai, Y. Li and C. Liu, *Microporous and Mesoporous Materials*, 2013, **173**, 181-188.
32. G. Wißmann, A. Schaate, S. Lilienthal, I. Bremer, A. M. Schneider and P. Behrens, *Microporous and Mesoporous Materials*, 2012, **152**, 64-70.
33. R. J. Marshall, C. L. Hobday, C. F. Murphie, S. L. Griffin, C. A. Morrison, S. A. Moggach and R. S. Forgan, *Journal of Materials Chemistry A*, 2016, **4**, 6955-6963.
34. M. R. DeStefano, T. Islamoglu, S. J. Garibay, J. T. Hupp and O. K. Farha, *Chemistry of Materials*, 2017, **29**, 1357-1361.
35. W. Morris, S. Wang, D. Cho, E. Auyeung, P. Li, O. K. Farha and C. A. Mirkin, *ACS Applied Materials and Interfaces*, 2017, **9**, 33413-33418.
36. A. Schaate, P. Roy, A. Godt, J. Lippke, F. Waltz, M. Wiebcke and P. Behrens, *Chemistry – A European Journal*, 2011, **17**, 6643-6651.
37. G. C. Shearer, S. Chavan, S. Bordiga, S. Svelle, U. Olsbye and K. P. Lillerud, *Chemistry of Materials*, 2016, **28**, 3749-3761.
38. D. Chen, D. Yang, C. A. Dougherty, W. Lu, H. Wu, X. He and T. Cai, M.E. Van Dort, B.D. Ross, H. Hong, *ACS Nano*, 2017, **11**, 4315-4327.
39. C. Orellana-Tavra, E. F. Baxter, T. Tian, T. D. Bennett, N. K. H. Slater, A. K. Cheetham and D. Fairen-Jimenez, *Chemical Communications*, 2015, **51**, 13878-13881.
40. C. Orellana-Tavra, S. A. Mercado and D. Fairen-Jimenez, *Advanced Healthcare Materials*, 2016, **5**, 2261-2270.
41. C. Orellana-Tavra, R. J. Marshall, E. F. Baxter, I. Abánades. Lázaro, A. Tao, A. K. Cheetham, R. S. Forgan and D. Fairen-Jimenez, *Journal of Materials Chemistry B*, 2016, **4**, 7697-7707.
42. H. Wu, Y. S. Chua, V. Krungleviciute, M. Tyagi, P. Chen, T. Yildirim and W. Zhou, *Journal of the American Chemical Society*, 2013, **135**, 10525-10532.
43. C. A. Trickett, K. J. Gagnon, S. Lee, F. Gándara, H.-B. Bürgi and O. M. Yaghi, *Angewandte Chemie*, 2015, **54**, 11162-11167.
44. M. J. Katz, Z. J. Brown, Y. J. Colon, P. W. Siu, K. A. Scheidt, R. Q. Snurr, J. T. Hupp and O. K. Farha, *Chemical Communications*, 2013, **49**, 9449-9451.
45. M. J. Cliffe, W. Wan, X. Zou, P. A. Chater, A. K. Kleppe, M. G. Tucker, H. Wilhelm, N. P. Funnell, F. X. Coudert and A. L. Goodwin, *Nature Communications*, 2014, **5**, 4176.
46. S. Bonnet, S. L. Archer, J. Allalunis-Turner, A. Haromy, C. Beaulieu, R. Thompson, C. T. Lee, G. D. Lopaschuk, L. Puttagunta, S. Bonnet, G. Harry, K. Hashimoto, C. J. Porter, M. A. Andrade, B. Thebaud and E. D. Michelakis, *Cancer Cell*, 2007, **11**, 37-51.
47. E. D. Michelakis, G. Sutendra, P. Dromparis, L. Webster, A. Haromy, E. Niven, C. Maguire, T. L. Gammer, J. R. Mackey, D. Fulton, B. Abdulkarim, M. S. McMurtry and K. C. Petruk, *Science Translational Medicine*, 2010, **2**, 31ra34.

48. E. D. Michelakis, L. Webster and J. R. Mackey, *British Journal of Cancer*, 2008, **99**, 989-994.
49. J.-w. Kim, I. Tchernyshyov, G. L. Semenza and C. V. Dang, *Cell Metabolism*, 2006, **3**, 177-185.
50. C. W. Lu, S. C. Lin, C. W. Chien, S. C. Lin, C. T. Lee, B. W. Lin, J. C. Lee and S. J. Tsai, *The American Journal of Pathology*, 2011, **179**, 1405-1414.
51. C. Trapella, R. Voltan, E. Melloni, V. Tisato, C. Celeghini, S. Bianco, A. Fantinati, S. Salvadori, R. Guerrini, P. Secchiero and G. Zauli, *Journal of Medicinal Chemistry*, 2016, **59**, 147-156.
52. D. R. Lide, *CRC Press, Handbook of Chemistry and Physics*, Taylor & Francis, Boca Raton, 2005, **86**, 3-150.
53. F. Rouquerol, J. Rouquerol and K. Sing, in *Adsorption by Powders and Porous Solids*, Academic Press, London, 1999, pp. 191-217.
54. S. K.D., *Handbook of Nanophysics: Functional Nanomaterials*, CRC Press, Boca Raton, FL, 2010.
55. E. Bellido, M. Guillevic, T. Hidalgo, M. J. Santander-Ortega, C. Serre and P. Horcajada, *Langmuir*, 2014, **30**, 5911-5920.
56. E. Bellido, T. Hidalgo, M. V. Lozano, M. Guillevic, R. Simón-Vázquez, M. J. Santander-Ortega, Á. González-Fernández, C. Serre, M. J. Alonso and P. Horcajada, *Advanced Healthcare Materials*, 2015, **4**, 1246-1257.
57. S. Sene, M. T. Marcos-Almaraz, N. Menguy, J. Scola, J. Volatron, R. Rouland, J.-M. Grenèche, S. Miraux, C. Menet, N. Guillou, F. Gazeau, C. Serre, P. Horcajada and N. Steunou, *Chem*, 2017, **3**, 303-322.
58. M. Wrobel, J. Aubé and B. König, *Beilstein Journal of Organic Chemistry*, 2012, **8**, 1027-1036.
59. S. Pandey, B. Kolli, S. P. Mishra and A. B. Samui, *Journal of Polymer Science Part A: Polymer Chemistry*, 2012, **50**, 1205-1215.

## Chapter 3

# UiO-66 Postsynthetic Surface Modifications

This Chapter is adapted in part from the following publications:

“Selective Surface PEGylation of UiO-66 Nanoparticles for Enhanced Stability, Cell Uptake and pH Responsive Drug Delivery”

*Chem*, **2017**, 2, 561–578. (DOI: 10.1016/j.chempr.2017.02.005.)

**I. Abánades Lázaro**, S. Haddad, S. Sacca, C. Orellana-Tavra, D. Fairen-Jimenez and R. S. Forgan

“Mechanistic Investigation into the Selective Anticancer Cytotoxicity and Immune System Response of Surface Functionalised, Dichloroacetate-Loaded, UiO-66 Nanoparticles”

*ACS Appl. Mater. Interfaces*, **2018**, 10, 6, 5255-5268 (DOI: 10.1021/acsami.7b17756)

**I. Abánades Lázaro**, S. Haddad, J. Rodrigo-Muñoz, C. Orellana-Tavra, V. del Pozo, D. Fairen-Jimenez, and Ross S. Forgan

“Enhancing Anticancer Cytotoxicity through Bimodal Drug Delivery from Ultrasmall Zr MOF Nanoparticles”

*Chem. Commun.*, **2018**, 54, 2792-2795. (DOI: 10.1039/C7CC09739E)

**I. Abánades Lázaro**, S. Abánades Lázaro and R. S. Forgan.

**Table of Contents**

<b>Chapter 3</b> .....	102
Table of Contents .....	103
3.1 Introduction.....	104
3.2 Aims .....	105
3.3 UiO-66 Surface Functionalisation.....	107
3.3.1 UiO-66-L1 and Ui-66-L2 Postsynthetic Covalent Surface ModificationS.....	107
3.3.1.1. Alkyl-Modified UiO-66: Proof-of-Concept Surface Modifications .....	107
3.3.1.2. UiO-66-L1 Postsynthetic Covalent PEGylation .....	111
3.3.1.3. UiO-66-L1 and UiO-66-L2 Postsynthetic Covalent Polymeric Coating.....	116
3.3.2. Postsynthetic Surface Coordination of UiO-66-L1 .....	122
3.4. The Effect of UiO-66 Surface Chemistry on its Colloidal Dispersion .....	128
3.5. The Effect of Surface Chemistry in UiO-66 Degradation Kinetics.....	140
3.6 Conclusions .....	146
3.7 Experimental.....	147
3.8 References .....	150

### 3.1 Introduction

Developing versatile and reproducible MOFs surface functionalisation protocols is crucial for their application in healthcare, particularly in anticancer drug delivery, as surface modifications can both enhance stability and dispersion in biological media, while decreasing the immune system recognition and providing the possibility of directing the DDS to damaged tissue through targeting.

Coatings with different polymers have decreased immune system recognition and accumulation in the liver of DDSs, with promising *in vitro* and *in vivo* results in anticancer therapy.<sup>1, 2</sup> For example, spherical polystyrene nanoparticles with covalently bound poly(ethylene glycol) chains on their surface were less sequestered by the liver than uncoated ones, and a correlation was found between the PEG surface density and their blood half-life, improving their stability under physiological conditions.<sup>3</sup> PEG chains have also been bound to the surface of chemically cross-linked albumin nanospheres, reducing significantly their uptake by cell culture macrophages.<sup>4</sup> Incorporation of polymers onto the external surfaces of NMOFs has been suggested as a route to enhanced stability and effective application in drug delivery.<sup>5, 6</sup> In addition, MOFs have been targeted to cancer cells by attaching different targeting units to their surface, reducing their non-specific distribution.<sup>7, 8</sup>

The Lewis acid character of MOFs' metal centres offers the possibility of coordinating nucleophiles to the coordinatively unsaturated metal sites available on the outer surface of NMOFs,<sup>9, 10</sup> and several polymer coatings, including oligonucleotides, have been added to the surfaces of MOFs by coordination to the metal clusters through one of the polymers' ends.<sup>11-13</sup> The well-known surface ligand exchange (SLE) protocol – postsynthetically exchanging surface ligands for desired functionality – is also based on coordination chemistry.<sup>14-20</sup> Postsynthetic covalent modifications, performed on functionalised organic linkers, have been widely used in biological applications of NMOFs.<sup>21-23</sup> Additionally, unsaturated carboxylic acid groups present on the MOF surface can also be exploited for postsynthetic covalent surface modifications.<sup>24</sup> For example, a green fluorescent protein was coupled to surface carboxylate groups of different MOFs using a carbodiimide-mediated reaction,<sup>25</sup> and then the protocol was applied to couple PEG5000-NH<sub>2</sub> and Stp-10C,<sup>5</sup> a derived oligoamino amide with proton-sponge features. However, the low reactivity of the organic linker's carboxylates hinders the application of this protocol, resulting in very low surface coatings (1-2% w/w).

Silica coating has been widely used to increase MOFs' water stability, to induce slow release, and to attach surface reagents through the siloxane groups.<sup>26, 27</sup> Although this approach can dramatically enhance some MOFs properties, drawbacks exist in the fact that the silica coating can block pore access, and that some silica nanoparticles have been found to be toxic.<sup>28-30</sup>

### 3.2 Aims

The need to find a rationalisation between the intrinsic characteristics of NMOFs, such as surface chemistry, and their therapeutic efficacy is inherently clear, providing if so the possibility of reducing early-stage animal testing through effective MOF engineering while maximizing the potential application of MOFs as DDSs.

Thus, the different ways of functionalising the outer surface of UiO-66 nanoparticles will be explored, in order to characterise the effect of surface chemistry and coating mode on properties such as physiological stability and colloidal dispersion. Through thoughtful choice of surface reagents with different characteristics – hydrophilic or hydrophobic, targeting agents, negatively charged, positively charged or neutral – this thesis ultimately attempts to rationalise the effect of surface chemistry of UiO-66 on HeLa cell internalisation pathways (Chapter 4), therapeutic efficiency, selectivity of cytotoxicity (targeting) and *in vitro* immune response (Chapter 5).

Different surface modification protocols will be assessed: (i) postsynthetic surface ligand exchange (PS), and (ii) click modulation, wherein functionalised modulators, previously introduced to UiO-66 structure during its synthetic process (Chapter 2), are covalently modified (Figure 3.1a). Different surface reagents (Figure 3.1b) which possess various coordinating groups – vitamin B<sub>9</sub> folic acid (FA)<sup>31</sup>, vitamin B<sub>7</sub> biotin (Biot)<sup>32</sup>, and a negatively charged anticoagulant, heparin (Hep)<sup>33</sup> – that are well known to play different biological roles, have been selected to be coordinated to UiO-66 surfaces postsynthetically. The carboxylic acid functionalities of both folic acid and biotin allowed their direct incorporation during modulated syntheses, which was detailed in Chapter two, and thus the colloidal dispersion and physiological stability of both postsynthetically coated and modulated FA and Biot samples will be compared in order to gain insights into the different surface modification protocols effect on MOFs properties.

The functionalities of *p*-azidomethylbenzoic acid (L1) and *p*-propargyloxybenzoic acid (L2), previously introduced to UiO-66 structure during its synthetic process in Chapter 2, will be used as a platform for postsynthetic surface modifications based on click chemistry during this chapter.

Proof-of-concept postsynthetic surface modifications by Copper(I)-Catalyzed Azide-Alkyne Cycloaddition (CuAAC) will be performed between the modulated MOFs (UiO-66-L1 and UiO-66-L2) and 1-dodecyne and 1-azidodecane respectively. Additionally, the amphiphilic propargyl-terminated poly(ethylene glycol) (PEG  $M_n = 500$  and 2000), the hydrophobic propargyl-terminated poly-L-lactide (PolyLact,  $M_n = 2000$ ) and the hydrophilic azide-terminated poly-*N*-isopropylacrylamide (PNIPAM,  $M_n = 15000$ ) have been selected as

protecting polymers to click to UiO-66-L1 and UiO-66-L2 surface, but in this study, UiO-66-L2 is prepared by surface ligand exchange from UiO-66-L1, and not through coordination modulation, in order to maintain appropriate particle size for further endocytosis studies (Chapter 4) and cytotoxicity assessment (Chapter 5). Thus, the properties that different surface coatings provide to UiO-66 and the potential and reproducibility of different protocols to introduce different functionalities will be evaluated.

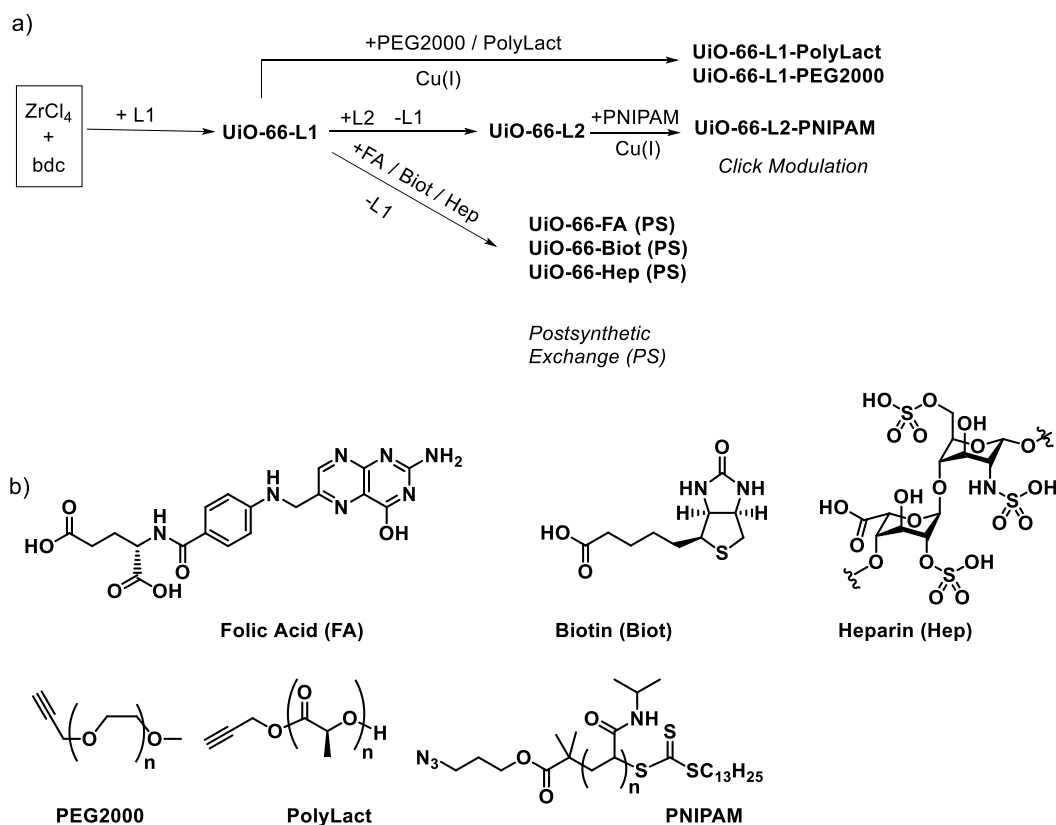


**Figure 3.1** a) Synthetic scheme for the surface modified MOFs, highlighting MOFs obtained through postsynthetic exchange (PS) and click modulation. b) Chemical structures of the surface functionality attached to the MOFs by SLE. (top) and by (CuAAC) (bottom).

### 3.3 UiO-66 Surface Functionalisations

#### 3.3.1 UiO-66-L1 and UiO-66-L2 Postsynthetic Covalent Surface Modifications

At first, proof-of-concept postsynthetic surface modifications will be performed between the modulated MOFs (UiO-66-L1 and UiO-66-L2) and 1-dodecyne and 1-azidododecane respectively. Then, surface modifications for drug delivery applications will be performed using propargyl-terminated PEG, propargyl-terminated PolyLact and azide-terminated poly-N-PNIPAM as surface reagents.

##### 3.3.1.1. Alkyl-Modified UiO-66: Proof-of-Concept Surface Modifications

After confirming, in Chapter 2, that the functionalised modulators are incorporated into the MOF structure, postsynthetic modification by Copper(I)-Catalyzed Azide-Alkyne Cycloaddition (CuAAC) was attempted. Various catalysts were tested, including CuI and a mixture of CuSO<sub>4</sub> and sodium ascorbate, resulting in loss of the sample crystallinity each time. An efficient and economic approach, using CuI and 2 equiv of acetic acid and DIPEA each as an *in situ* stabilising ligand for Cu(I),<sup>34</sup> was tolerated by the MOF structure, as confirmed by PXRD, and allowed further functionalisation of the NMOFs.

Proof-of-concept reactions using this catalyst were carried out between UiO-66-L1 and 1-dodecyne (Figure 3.2a), as well as between UiO-66-L2 and 1-azidododecane. Sample integrity throughout the process was confirmed by PXRD (Figure 3.2b).

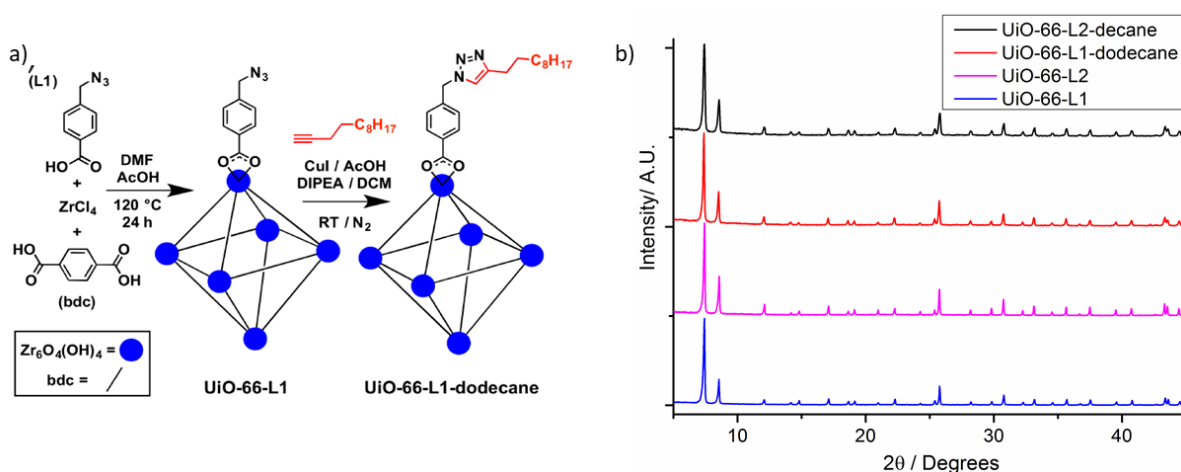


**Figure 3.2.** a) Schematic of the click modulation protocol in the preparation of UiO-66-L1-dodecane. b). Stacked PXRD profiles of UiO-66-L1 and UiO-66-L2 before and after surface alkylation.

<sup>1</sup>H NMR spectra of acid digested samples of UiO-66-L1-dodecane and UiO-66-L2-decane suggested significant conversions of the modulators into the respective triazole products; while the low modulator content makes analysis difficult, additional aromatic signals are

present alongside peaks for the alkyl groups. Full conversion would not be expected, as some modulators will be located at inaccessible internal defect sites rather than on the particle surface. High-resolution electrospray ionisation mass spectrometry (HRESI-MS) analysis of the digested MOFs (Section 3.7) showed peaks for the products of the CuAAC reaction between modulators and surface functionality as follows:

**UiO-66-L1-dodecane.** Calc  $C_{20}H_{30}N_3O_2$   $[M+H]^+$ :  $m/z = 344.2333$ ; found:  $m/z = 344.2319$ .

**UiO-66-L2-decane.** Calc  $C_{20}H_{28}N_3O_3$   $[M-H]^-$ :  $m/z = 358.2136$ ; found:  $m/z = 358.2131$ .

The conversion of the functional groups of the modulators was monitored by FTIR spectroscopy, including comparison of the spectra of the surface modified NMOFs with pristine samples where the modulator had been reacted with the respective surface component in solution (Figure 3.3). The low overall content of modulator in the samples means the signals are quite weak. For UiO-66-L1-dodecane, the  $N_3$  signal ( $\sim 2100\text{ cm}^{-1}$ ) of L1 decreases considerably upon reaction, while the C-H region ( $2700\text{-}3000\text{ cm}^{-1}$ ) shows signals for the surface alkyl unit. In the IR spectrum of UiO-66-L2-decane, the signal around  $3250\text{ cm}^{-1}$  for the acetylene functionality of L2 is lost, and again new signals appear in the C-H region ( $2700\text{-}3000\text{ cm}^{-1}$ ). Unfortunately, the signals expected for the triazole unit are masked by peaks from UiO-66 itself.

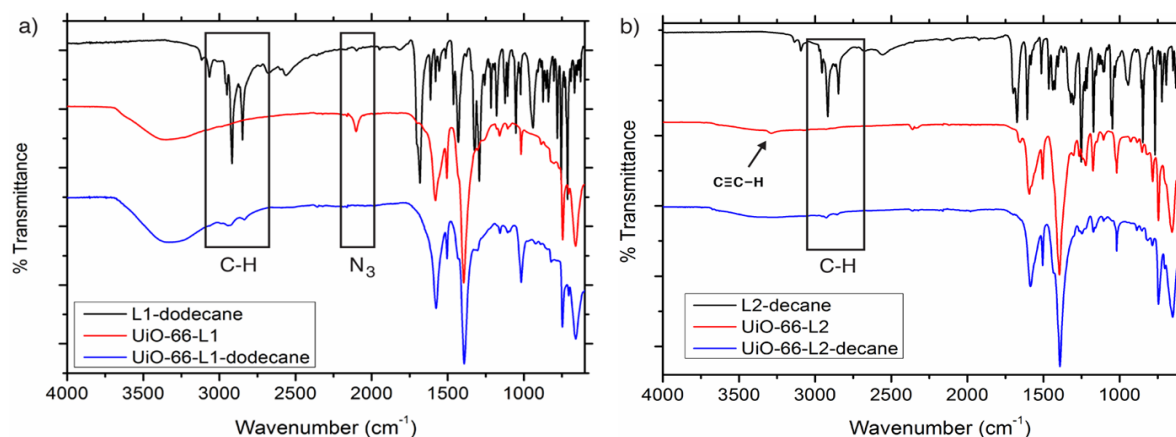


**Figure 3.3.** FTIR spectra comparing a) UiO-66-L1 before and after reaction with 1-dodecane, as well as the product of the CuAAC reaction between L1 and 1-dodecane, and b) UiO-66-L2 before and after reaction with azidodecane, as well as the product of the CuAAC reaction between L2 and azidodecane. Stacked IR spectra showing the disappearance of the azide stretch and appearance of C-H signals after the CuAAC surface reaction has taken place on UiO-66-L1.

$N_2$  adsorption isotherms measured at 77 K (Figure 3.4) confirmed that the porosity of the samples after functionalisation with alkyl chains were both maintained, with surface areas slightly decreasing -  $1168 \text{ m}^2\text{g}^{-1}$  for UiO-66-L1-dodecane and  $1262 \text{ m}^2\text{g}^{-1}$  for UiO-66-L2-decane - compared to their precursors, UiO-66-L1 ( $1565 \text{ m}^2\text{g}^{-1}$ ) and UiO-66-L2 ( $1420 \text{ m}^2\text{g}^{-1}$ ). Surface functionalisation with alkyl chains increases the mass of the particles, and so a decrease in gravimetric surface area is expected. The pore volumes are  $0.623 \text{ ccg}^{-1}$  and  $0.587 \text{ ccg}^{-1}$  for UiO-66-L1-dodecane and UiO-66-L2-decane respectively.

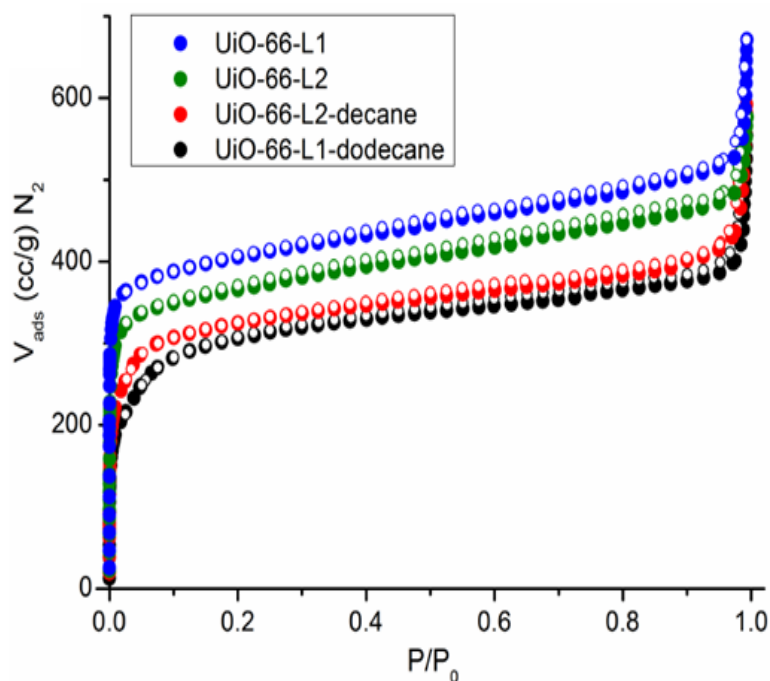


**Figure 3.4.**  $N_2$  adsorption isotherms (77 K) of the MOFs, showing a decrease in gravimetric uptake as additional mass is incorporated onto their surfaces. Closed symbols represent adsorption, empty symbols desorption.

Thermogravimetric analysis was used to investigate the incorporation of surface functionality. For UiO-66-L1-dodecane, additional mass loss events are obvious in the TGA traces recorded in air (Figure 3.5a) and under nitrogen (Figure 3.5b). These mass loss events occur at temperatures higher than the decomposition of the isolated product of the CuAAC reaction between L1 and dodecane, indicating covalent attachment to the NMOF, and a surface functionality component of around 10% *w/w*.

Similar TGA analysis was carried out on UiO-66-L2 and its functionalised analogue UiO-66-L2-decane. In both the TGA traces recorded in air (Figure 3.6a) and under nitrogen (Figure 3.6b), there is a high temperature mass loss event corresponding to covalently attached surface functionality, with a weight content of around 10% *w/w*.

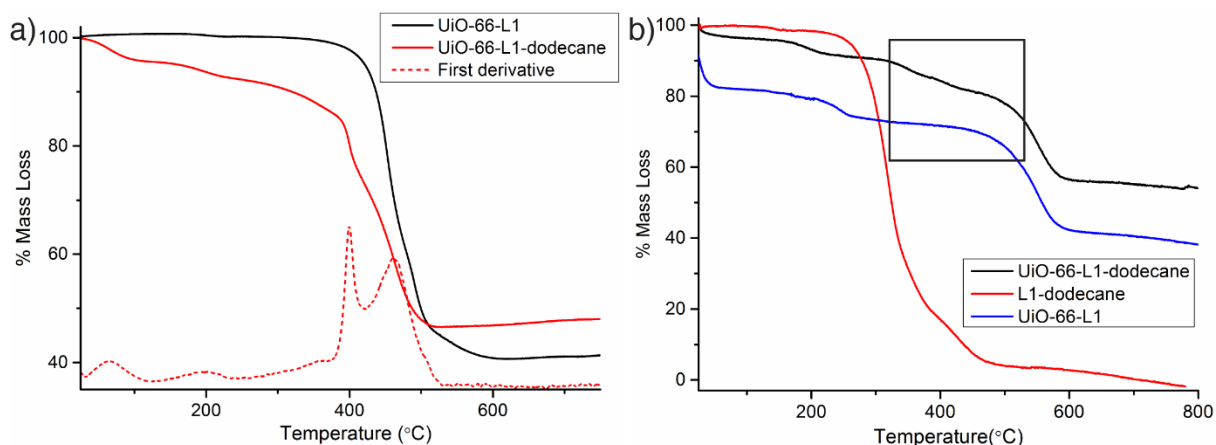


**Figure 3.5.** a) Comparison of TGA traces in air of UiO-66-L1 before and after reaction with 1-dodecyne. b) Comparison of TGA traces in nitrogen of the MOFs as well as the isolated “clicked” material L1-dodecane.

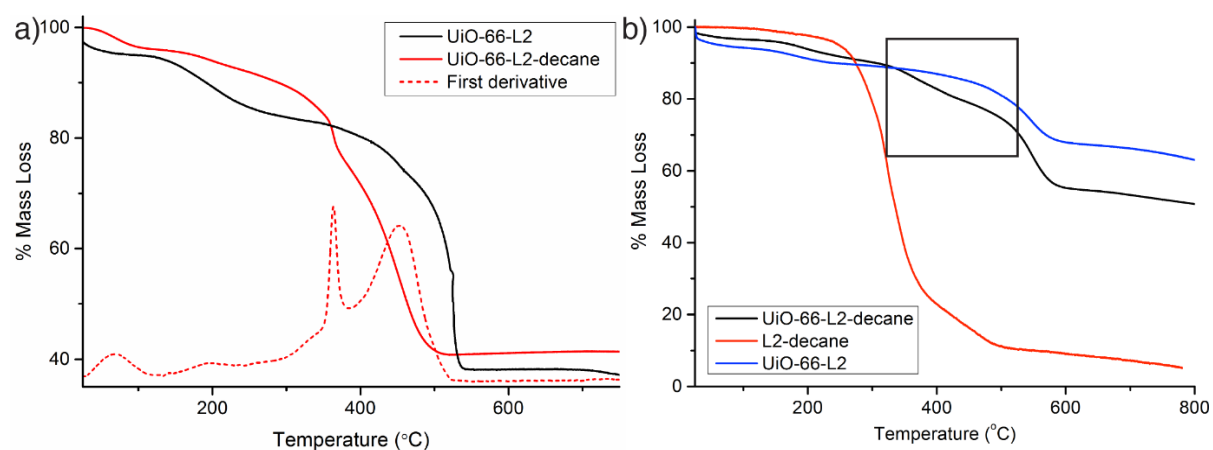


**Figure 3.6.** a) Comparison of TGA traces in air of UiO-66-L2 before and after reaction with 1-azidodecane. b) Comparison of TGA traces in nitrogen of the MOFs as well as the isolated “clicked” material L2-decane.

SEM imaging was used to examine the morphology and size of the NMOFs after surface modification. In both cases, it can be seen that particle size and morphology is retained after the click modulation protocol (Figure 3.7).

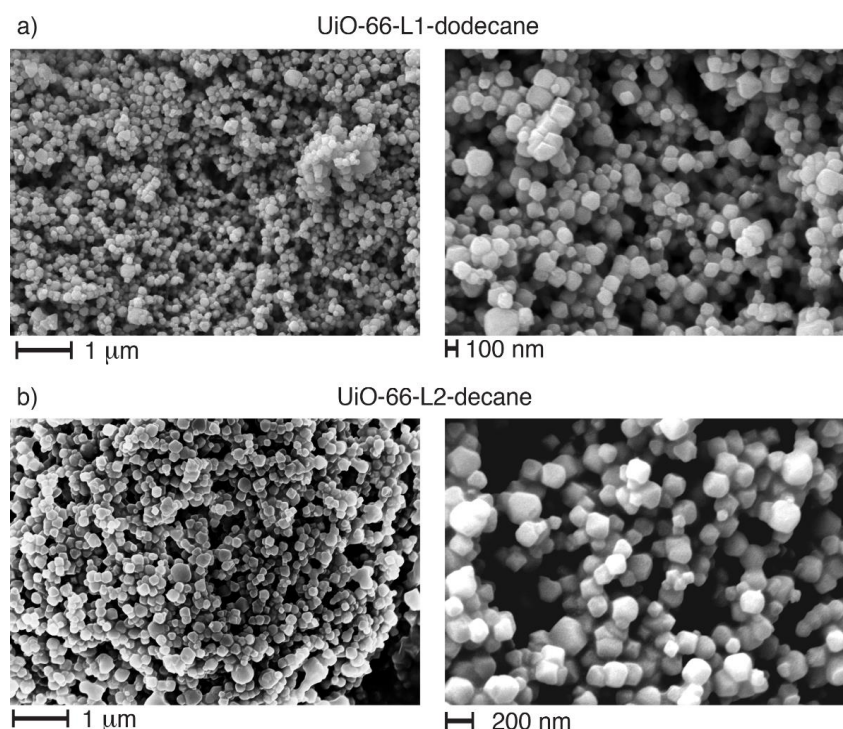


**Figure 3.7.** SEM images of a) UiO-66-L1-dodecane and b) UiO-66-L2-decane.

The full conjunction of the characterisation data proves that postsynthetic covalent modification (CuAAC) occurs only on the outer surface, and that the modulators (L1 and L2) introduced during synthesis are suitable platforms for postsynthetic surface modifications.

### 3.3.1.2. UiO-66-L1 Postsynthetic Covalent PEGylation

For drug delivery purposes, poly(ethylene glycol) chains (PEG) were chosen for UiO-66 coatings as they present an amphiphilic behaviour which resembles that of human cellular membranes.<sup>1</sup> Furthermore, other nanoparticulate DDS have shown a decrease in their immune system recognition upon PEGylation compared to bare nanoparticles.<sup>2, 3</sup> This is because the flexible and rapidly changing structure of the PEG, makes it difficult for the immune system to model an antibody around it. UiO-66-L1 was chosen for modification with propargyl-functionalised poly(ethylene glycol) chains of two different sizes, PEG550 ( $M_n = 550$ ) and PEG2000 ( $M_n = 2000$ ), as it exhibits the appropriate size for drug delivery.

PXRD analysis showed that the PEGylated NMOFs retained their crystallinity (Figure 3.8a).

Full  $^1\text{H}$  NMR spectroscopic analysis of the acid digested products, UiO-66-L1-PEG550 and UiO-66-L1-PEG2000, is difficult due to the intensity of the polymer signals. However, a control experiment - stirring PEG2000-propargyl or PEG550-propargyl with UiO-66-L1 but without

catalyst - revealed that, without Cu(I) catalyst, no polymer was present in the sample at all, confirming that covalent linkage is required for the PEG to remain attached to the MOF.

Thermogravimetric analysis, shown in Figure 3.8b, confirms the incorporation of the PEG units and strongly indicates that covalent attachment is required for their incorporation, as no mass loss events corresponding to PEG units are seen in control samples where the MOFs are simply soaked in PEG solutions without a catalyst for the CuAAC conjugation protocol. The level of PEG incorporation was estimated to be 21.7% w/w and 23.1% w/w, for UiO-66-L1-PEG550 and UiO-66-L1-PEG2000, respectively.

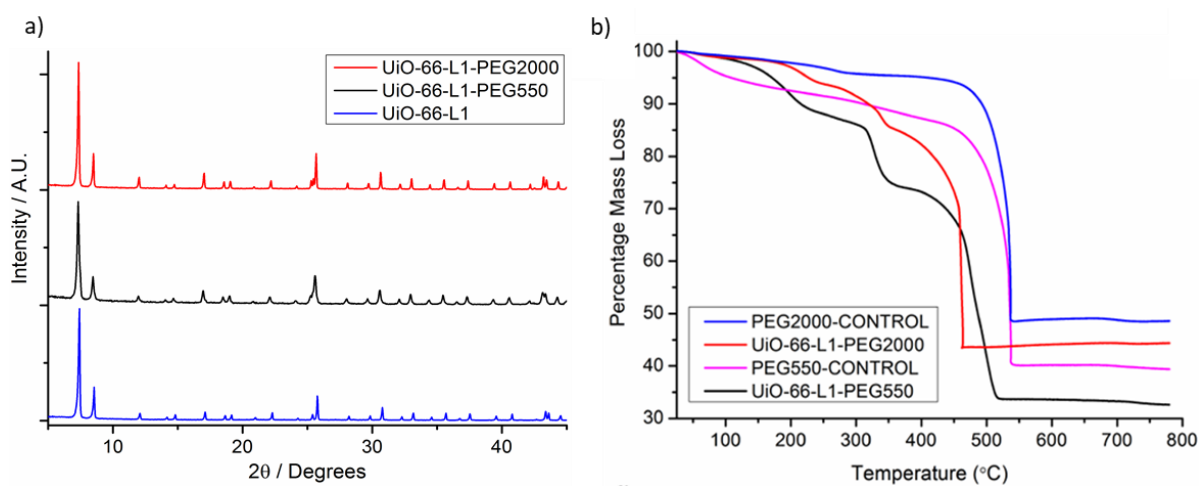


**Figure 3.8.** a) Stacked PXRD patterns of UiO-66-L1 and its PEGylated derivatives. B) TGA profiles of UiO-66-L1-PEG550 and UiO-66-L1-PEG2000 compared with control samples of UiO-66-L1 that had been exposed to propargyl-functionalised PEGs without any Cu(I) catalyst.

Whilst a series of peaks corresponding to covalently modified PEG550 (the molecules of different chain lengths are present in the starting material) are clearly visible in the HRESI-MS mass spectrum of UiO-66-L1-PEG550 (Figure 3.9), it was not possible to ionise the larger PEG2000 chains by ESIMS or MALDI-TOF. This was common to the precursors and to the digested MOFs.

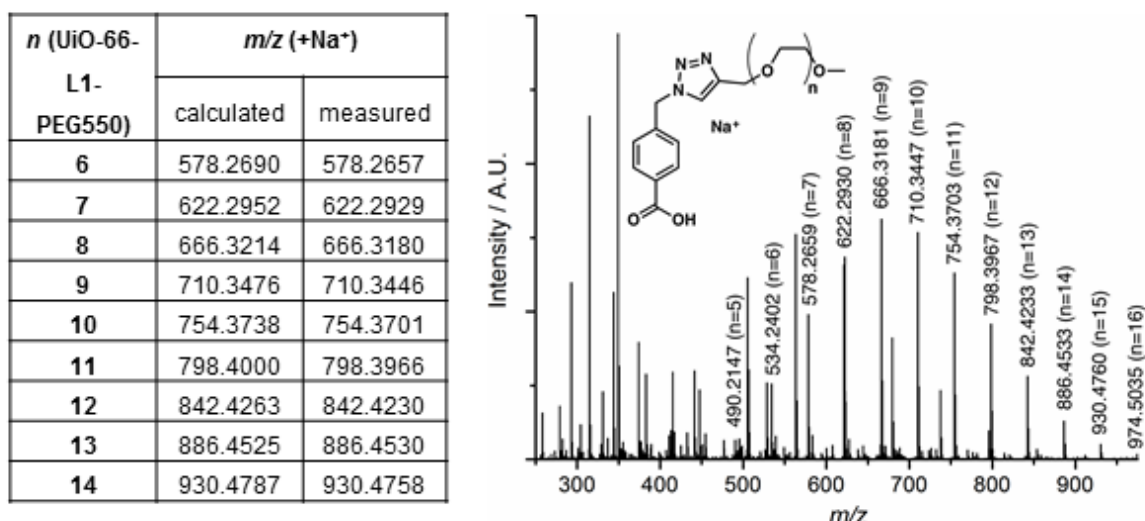


**Figure 3.9.** ESIMS of digested UiO-66-L1-PEG550 and a table of observed peaks for covalently modified PEG chains of different lengths.

FTIR spectra were collected to monitor the functional group conversion and incorporation of the PEG units to UiO-66-L1. For both UiO-66-L1-PEG550 (Figure 3.10a) and UiO-66-L1-PEG2000 (Figure 3.10b), there is a noticeable decrease in intensity of the azide signal around 2300  $\text{cm}^{-1}$ , indicating conversion of the surface L1 units, and signals for the C-H functionality of the PEG chains are observed.

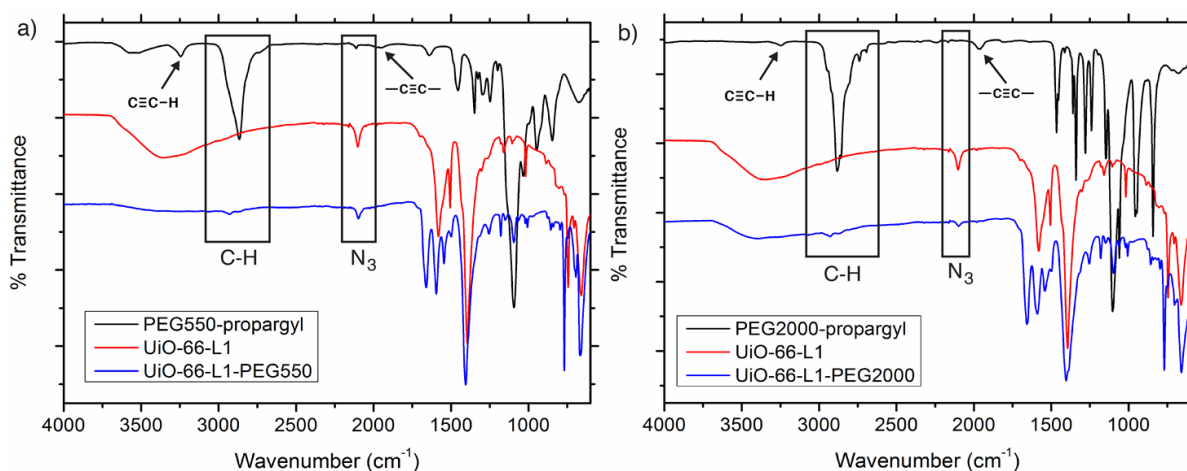


**Figure 3.10.** FTIR spectra comparing a) UiO-66-L1-PEG550 with the two starting materials used in its synthesis, and b) UiO-66-L2-PEG2000 with the two starting materials used in its preparation.

A decrease in  $\text{N}_2$  uptake upon PEGylation was observed, with BET surface areas of 865  $\text{m}^2\text{g}^{-1}$  for UiO-66-L1-PEG550 and 521  $\text{m}^2\text{g}^{-1}$  for UiO-66-L1-PEG2000 the consequence of the incorporated mass of the PEG chains (Figure 3.11). The pore size distribution of UiO-66-L1-PEG550 corresponds with that reported for UiO-66, but in the case of UiO-66-L1-PEG2000,

the adsorption and desorption isotherms reveal a Type IV isotherm, typical of mesoporous materials, but with no closure point. In the case of nitrogen adsorption at 77 K the lower closure point is usually located around  $p/p_0 \sim 0.42$ , and any hysteresis recorded below this point has been attributed to irreversible changes such as swelling of the adsorbent or surface impurities.<sup>35</sup> A similar, phenomenon has been found by Farha *et al.* upon UiO-66 functionalisation with the phospholipid DOPA, although to a lesser degree.<sup>11</sup> The fact that PEG2000 chains are considerably bigger in size than DOPA explains why it is more pronounced in this case.

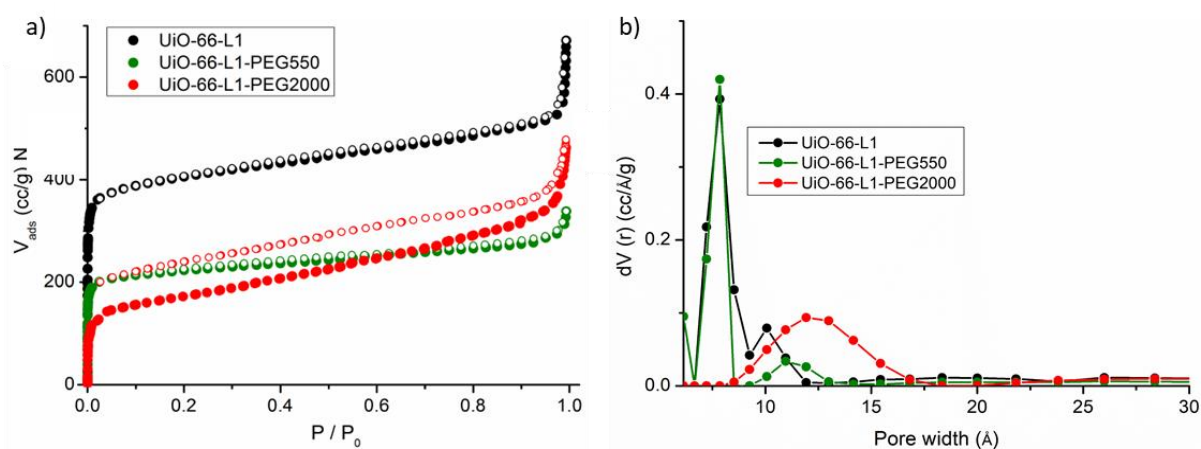


**Figure: 3.11)** N<sub>2</sub> uptake isotherms (77 K) of the PEGylated MOFs compared to their precursor UiO-66-L1. Closed symbols represent adsorption, empty symbols desorption. B) Pore size distributions of the PEGylated MOFs compared to their precursor UiO-66-L1.

Interestingly, the physical effects on nanoparticle morphology can be observed by SEM imaging (Figure 3.12). As the chain length of the surface functionality increases, the particles become more rounded in shape with less defined edges and vertices, as their surface features become dominated by the bulk of their capping polymers rather than the underlying MOF crystal structure.

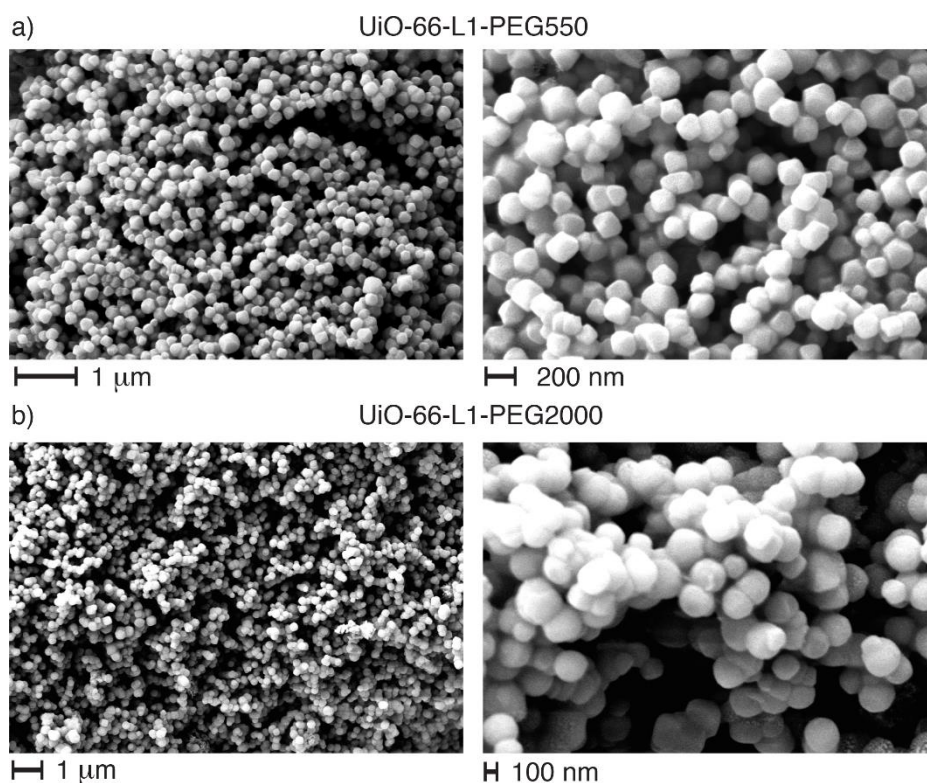


**Figure 3.11.** SEM images of a) UiO-66-L1-PEG550 and b) UiO-66-L1-PEG2000.

The particle size distributions before and after PEGylation were analysed manually using the ImageJ software package (Figure 3.12). The average size of precursor UiO-66-L1 particles was found to be  $146.6 \pm 29.3$  nm, which increased upon PEGylation to  $160.2 \pm 26.9$  nm for UiO-66-L1-PEG550 and to  $172.9 \pm 36.8$  nm for UiO-66-L1-PEG2000. This size increase is consistent with the increasing size of the surface polymer chains being installed on the nanoparticles' surfaces, but the magnitude of the size change may be affected by the accompanying change in morphology from octahedral to roughly spherical particles upon surface modification.

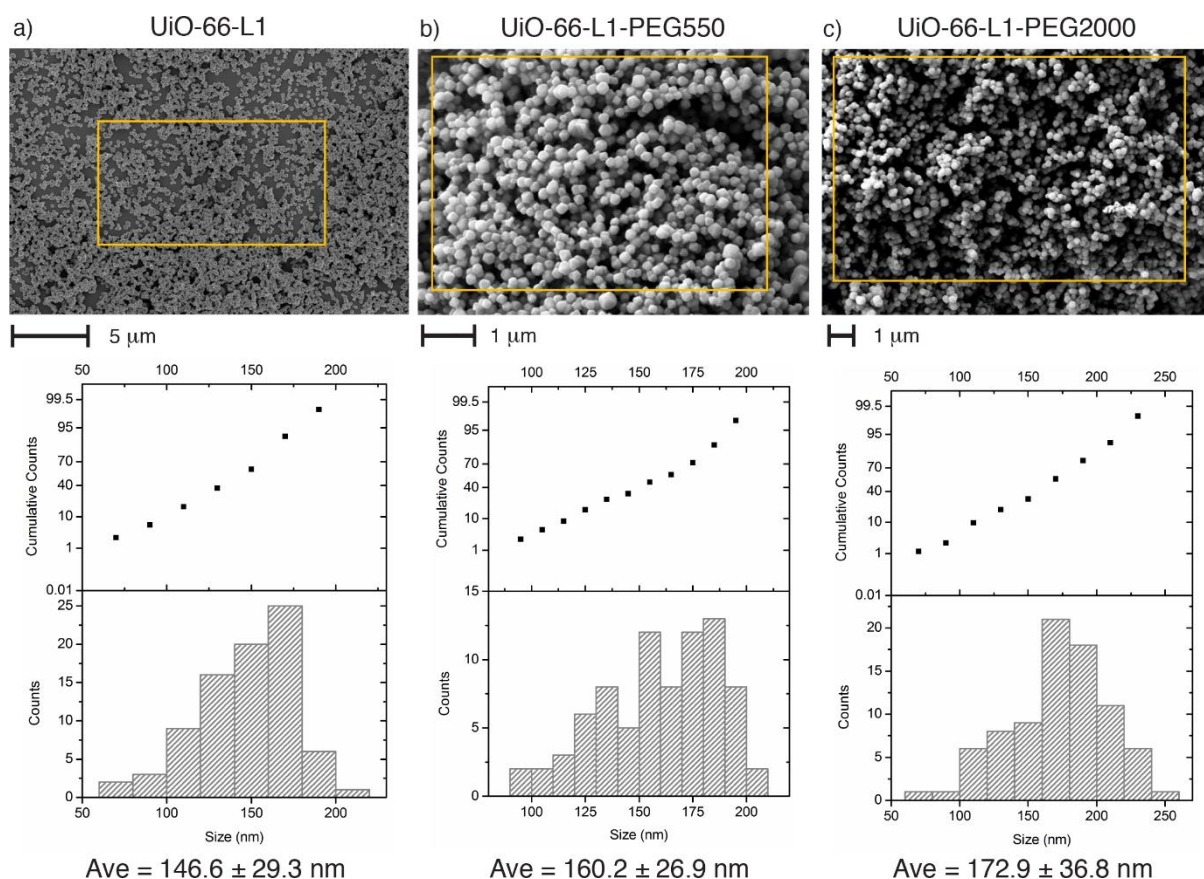


**Figure 3.12.** Particle size analysis from SEM micrographs for a) UiO-66-L1, b) UiO-66-L1-PEG550, and c) UiO-66-L1-PEG2000.

### 3.3.1.3. UiO-66-L1 and UiO-66-L2 Postsynthetic Covalent Polymeric Coating

After confirming successful surface functionalisation using the modulators' (L1 and L2) azide and propargyl functionalities to covalently attach alkyl and PEG chains to UiO-66 surface, poly-L-lactide and poly-*N*-isopropylacrylamide were chosen as additional protecting polymers. Poly-L-Lactide is biocompatible and hydrophobic,<sup>36</sup> which should boost its cell internalisation<sup>37</sup> and biocompatibility, while poly-*N*-isopropylacrylamide has a thermoresponsive behaviour, which should be retained and embodied on the coated MOF drug release kinetics.<sup>6</sup>

Surface ligand exchange was performed on UiO-66-L1 to exchange L1 with L2 on the particle surface and to retain particle size, to form UiO-66-L2. Acid-digested <sup>1</sup>H NMR spectra (in D<sub>2</sub>SO<sub>4</sub>/ DMSO-*d*<sub>6</sub>) of UiO-66-L1 (Figure 3.13, bottom) confirmed the reproducibility of the synthetic protocol to introduce L1 during synthesis, with a 14.6% molar ratio compared to the linker in UiO-66 structure, in great agreement with previous results. After surface ligand exchange of L1 for L2, the <sup>1</sup>H NMR spectrum of acid digested UiO-66-L2 (Figure 3.13, top) showed disappearance of resonances assigned to L1 and appearance of signals for L2 with

a 27.0% molar ratio compared to the bdc linker. Minor traces of L1, probably present in the core of UiO-66-L1, are still present in the  $^1\text{H}$  NMR spectrum, but the low intensity ( $\sim 2\%$  molar ratio to bdc) hinders their analysis.

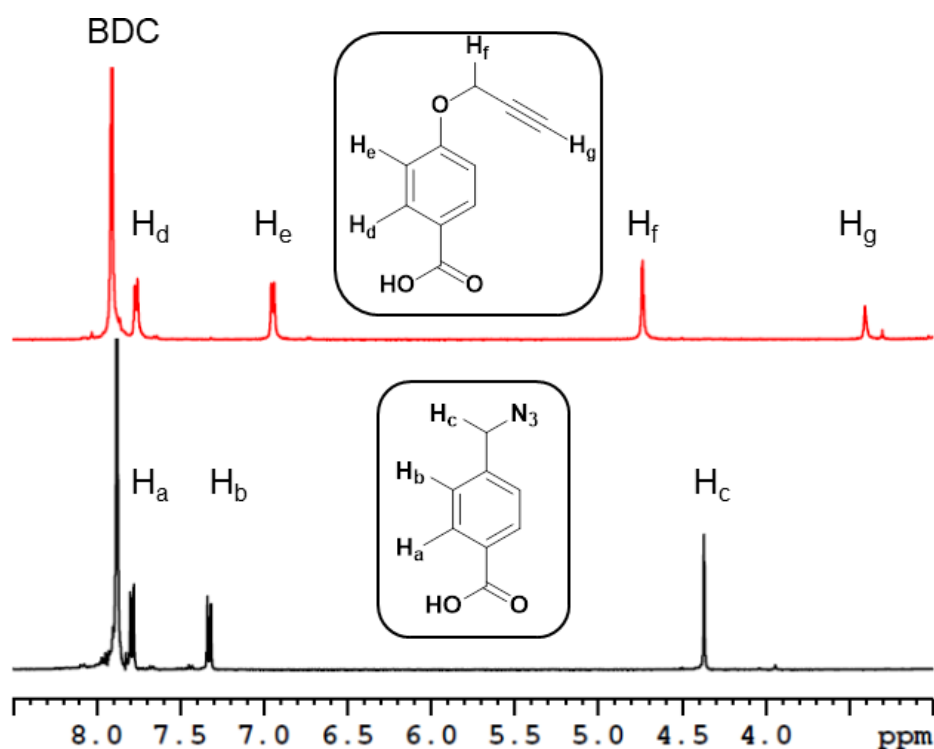


**Figure 3.13.** Stacked partial  $^1\text{H}$  NMR spectra of acid digested ( $\text{D}_2\text{SO}_4 / \text{DMSO}-d_6$ ) samples of UiO-66-L1 (bottom) and UiO-66-L2 (top), prepared from the former.

Postsynthetic covalent modifications were performed following our CuAAC protocol. UiO-66-L1 was reacted with propargyl-terminated poly-L-lactide (PolyLact,  $M_n = 2000$  Da), while UiO-66-L2 was reacted with azide terminated poly-*N*-isopropylacrylamide (PNIPAM,  $M_n = 15000$  Da), yielding UiO-66-L1-PolyLact and UiO-66-L2-PNIPAM, respectively. Analysis of the postsynthetically modified UiO-66 samples by PXRD showed that their crystallinity is not affected by the postsynthetic surface functionalisation processes.

The polymeric nature of poly-L-lactide and PNIPAM also hinders the analysis of UiO-66-L1-PolyLact and UiO-66-L2-PNIPAM by  $^1\text{H}$  NMR spectroscopy, but again the presence of polymeric signals can be observed in both cases.

Thermogravimetric analysis (TGA) of the surface-modified samples was compared with their precursors (either UiO-66-L1 or UiO-66-L2) and with authentic samples of the commercial surface reagents (Figure 3.14) prior to attachment in order to identify their characteristic features, based on which the surface moiety content can be estimated. However, due to the different, and in some case gradual, degradation profiles of most surface reagents, their exact determination is difficult.

Degradation profiles more complex than UiO-66-L1 and UiO-66-L2 were observed for the polymer coated samples prepared by click modulation. In the case of UiO-66-L1-PolyLact, the MOF structure decomposes at a lower temperature than its precursor UiO-66-L1, as a consequence of the earlier degradation of the polymer. The fact that the polymer decomposition after attachment is more gradual, and starts at a higher temperature than the free reagent, indicates that it is covalently attached. Propargyl-terminated poly-L-lactide decomposes between 225-400 °C, and the 10% w/w mass loss from UiO-66-L1-PolyLact in this temperature region is in concordance with the difference in metal residue compared to its precursor UiO-66-L1, suggesting approximately 10% w/w incorporation of the polymer.

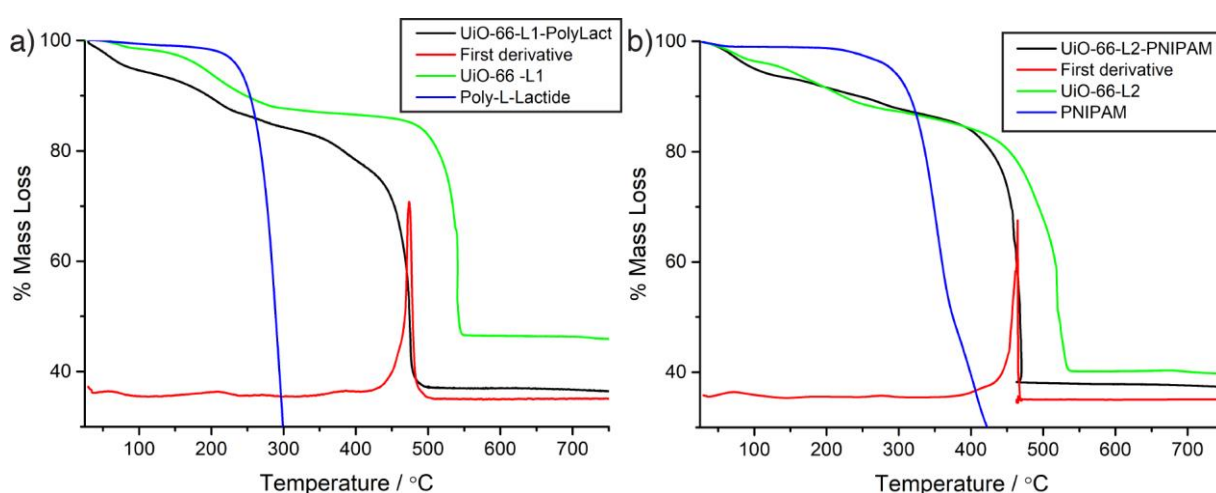


**Figure 3.14.** TGA traces of covalently surface modified MOFs compared with the surface functionality and the starting material for a) UiO-66-L1-PolyLact, and b) UiO-66-L2-PNIPAM.

Similarly, when UiO-66-L2 is reacted with PNIPAM, as the polymer itself degrades at a lower temperature than the MOF, UiO-66-L2-PNIPAM thermally degrades at lower temperature than UiO-66-L2. Gradual mass loss from the polymer to the linker decomposition temperatures corresponds to a 3% w/w mass loss, similar to the difference of metal residue to the precursor sample.

Control samples, in which either UiO-66-L1 or UiO-66-L2 were stirred under the previous CuAAC protocol conditions with the surface reagents but without the presence of the CuI catalyst, showed no major difference in the thermal stability of their structure or extra mass loss (Figure 3.15). A minor decrease in the metal residue of the samples was observed as a consequence of solvent incorporation during the process. Additionally,  $^1\text{H}$  NMR spectra of the control samples showed no presence of polymeric signals. These findings together confirm that the polymers are covalently attached to UiO-66-L1-PolyLact and UiO-66-L2-PNIPAM rather than simply adsorbed on the outer particle surfaces.

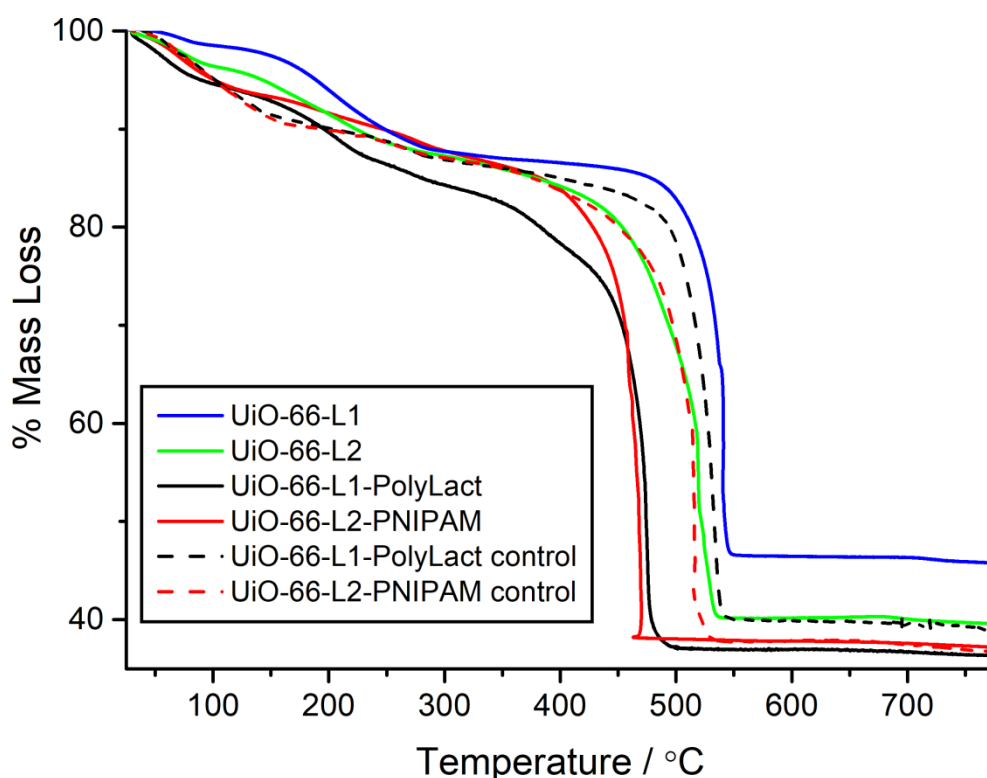


**Figure 3.15.** TGA traces of the polymer-coated samples compared to the starting materials and control reactions, where no catalyst for the CuAAC reaction has been added, to confirm that the polymers are covalently attached to the MOF.

Additionally, the propargyl band of poly-L-lactide and the azide band of UiO-66-L1 are missing in the UiO-66-L1-PolyLact spectrum, suggesting covalent reaction (Figure 3.16). Unfortunately, other signals of the different moieties are masked by UiO-66 peaks and the IR spectrum of UiO-66-L2-PNIPAM is inconclusive.

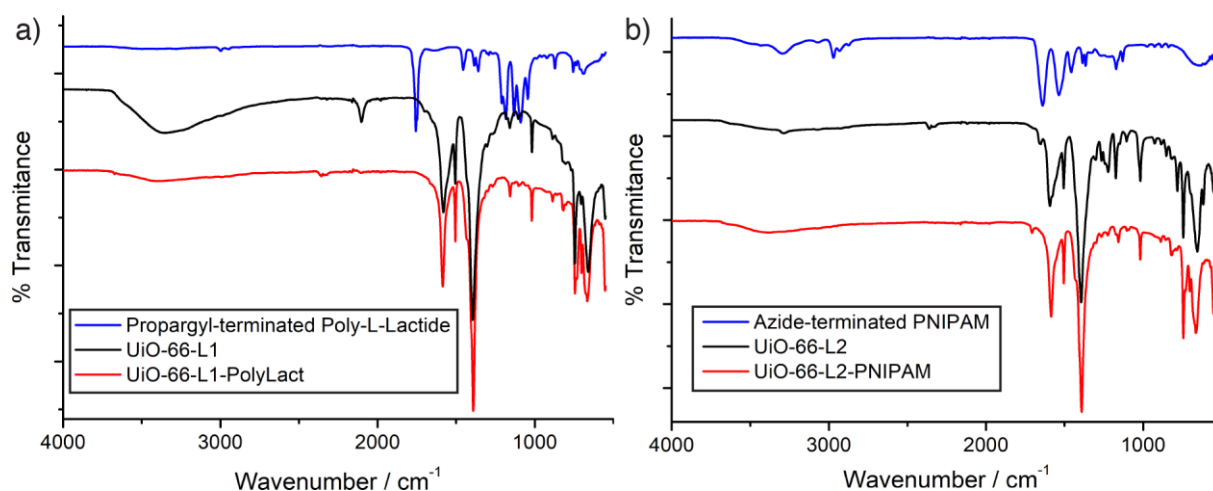


**Figure 3.16.** FT-IR spectra of the click modulated MOFs compared to the starting material and the surface functionality, for a) UiO-66-L1-PolyLact, and b) UiO-66-L2-PNIPAM.

In order to analyse the porosity of the samples upon postsynthetic surface modification,  $N_2$  adsorption and desorption isotherms were collected at 77 K (Figure 3.17). Only a small decrease in porosity after surface ligand exchange, in agreement with the moderately higher ligand content, was observed for UiO-66-L2, from  $1591 \text{ m}^2\text{g}^{-1}$  for its precursor UiO-66-L1 to  $1349 \text{ m}^2\text{g}^{-1}$ . It is still slightly more porous than non-defective UiO-66, confirming that L2 is attached to the surface and defect sites rather than stored in the pores. The isotherms of the surface modified samples showed retention of porosity and decreases in gravimetric surface areas, consistent with the addition of mass, with surface areas of  $1129 \text{ m}^2\text{g}^{-1}$  and  $1030 \text{ m}^2\text{g}^{-1}$  and pore volumes  $0.640 \text{ ccg}^{-1}$  and  $0.578 \text{ ccg}^{-1}$  for UiO-66-L1-PolyLact and UiO-66-L2-PNIPAM respectively.

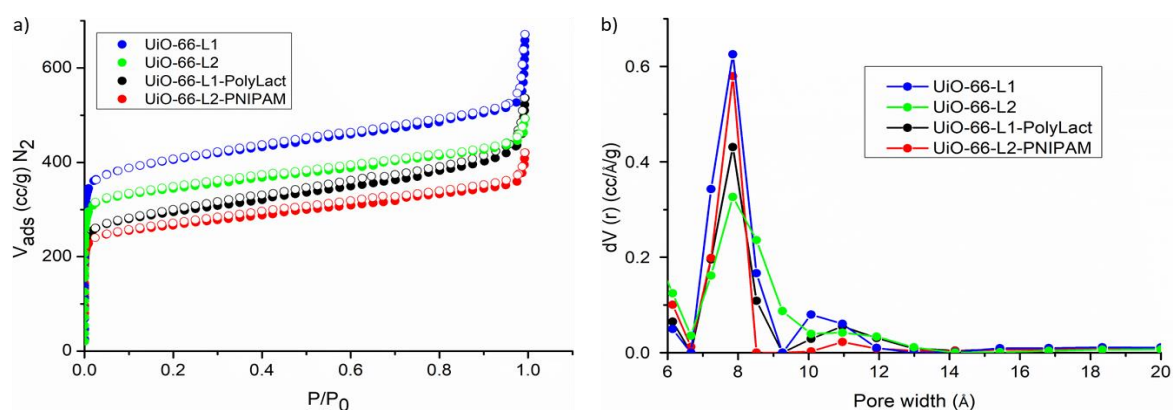


**Figure 3.17.** a)  $N_2$  adsorption isotherms (77 K) of the postsynthetically surface modified MOFs. Closed symbols for adsorption, empty symbols for desorption. b) Pore size distributions calculated from the isotherms.

SEM imaging was used to study the morphology of the NMOFs upon surface modification. Compared to the precursors UiO-66-L1 and UiO-66-L2 (Figure 3.18), the covalently-modified samples are in general more rounded in shape as a consequence of surface modifications with large polymer chains (Figure 3.19). This effect is more remarkable for UiO-66-L2-PNIPAM, due to the bigger size of PNIPAM.

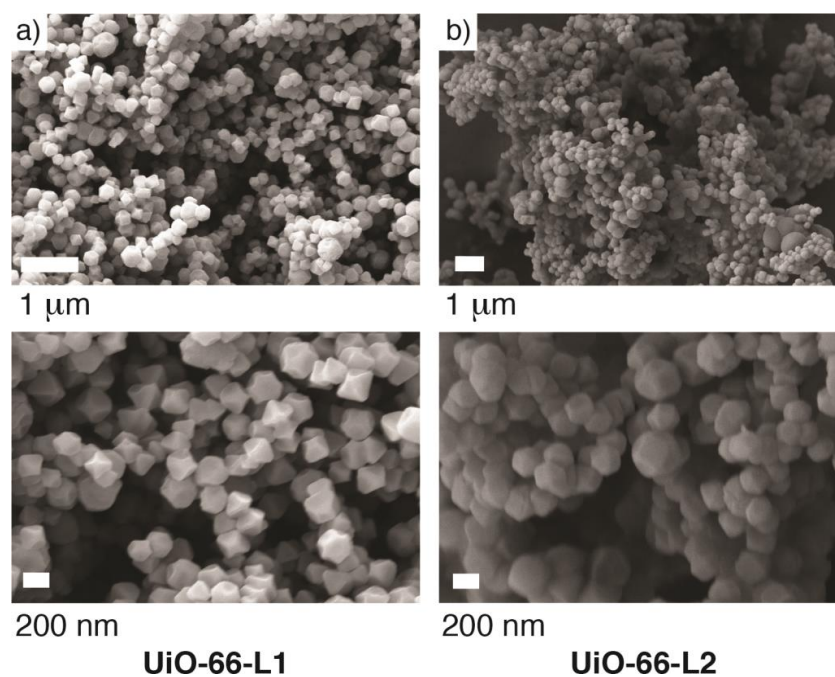


**Figure 3.18.** SEM images at different magnification of a) UiO-66-L1, and b) UiO-66-L2.

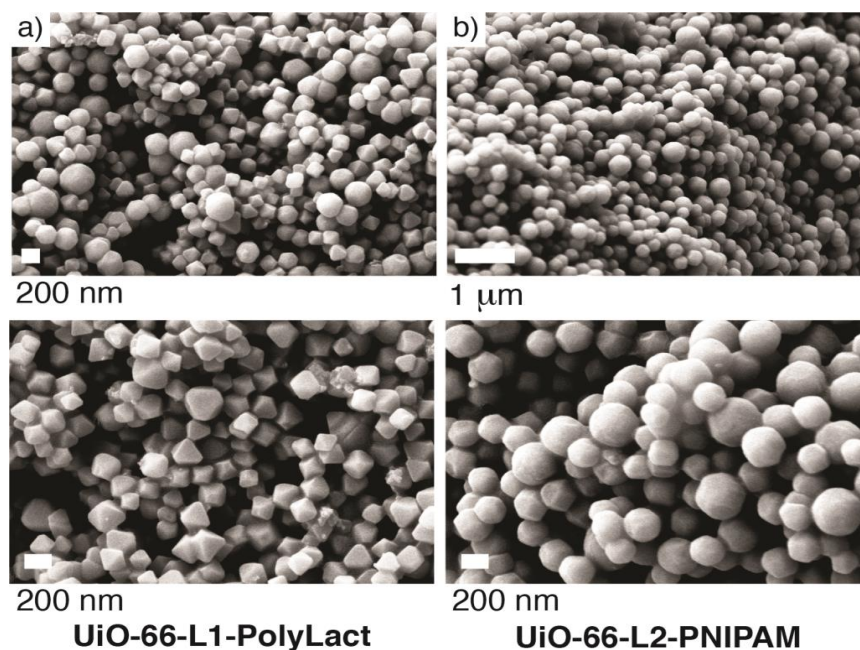


**Figure 3.19.** SEM images at different magnification of a) UiO-66-L1-PolyLact, and b) UiO-66-L2-PNIPAM.

A size increase from  $143 \pm 31$  nm and  $142 \pm 14$  nm for UiO-66-L1 and UiO-66-L2 respectively, to  $177 \pm 25$  nm and  $177 \pm 24$  nm from UiO-66-L1-PolyLact and UiO-66-L2-PNIPAM respectively was found as a consequence of surface coating. A comparison of the particle size histograms is given in Figure 3.20.

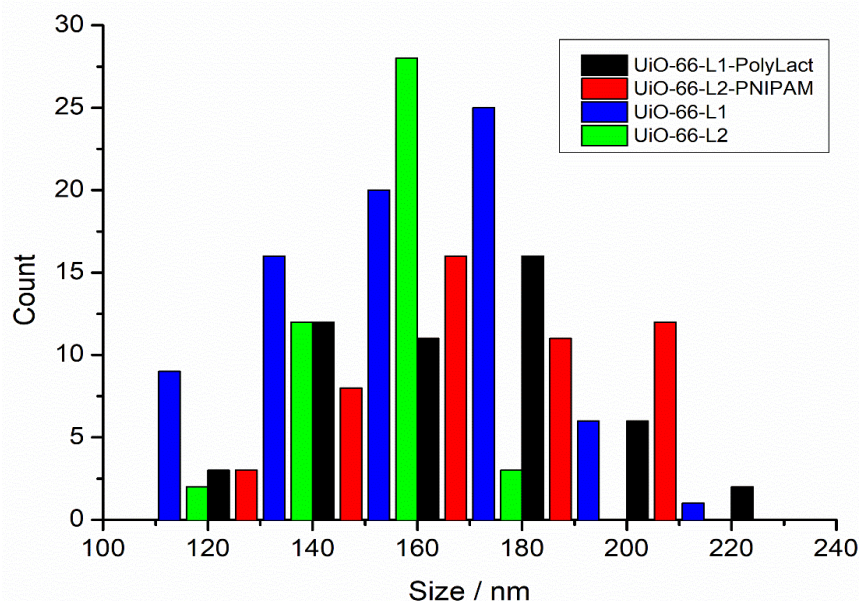


**Figure 3.20.** Comparison of particle size histograms for PolyLact and PNIPAM coated samples and their precursors.

These results prove that covalent postsynthetic surface modification can be performed using L1 and L2 as surface reagents, and that click modulation protocol is versatile and reproducible.

### 3.3.2. Postsynthetic Surface Coordination of UiO-66-L1

Postsynthetic modifications based on coordination chemistry – surface ligand exchange<sup>17</sup> – were performed on UiO-66-L1 using heparin, biotin, or folic acid as the reactants. The resultant materials are designated UiO-66-Hep (PS), UiO-66-Biot (PS) and UiO-66-FA (PS) to denote the postsynthetic functionalisation protocol.

The <sup>1</sup>H NMR spectrum of acid digested UiO-66-FA (PS) (Figure 3.21) showed the presence of some of the characteristic folic acid resonances. Some of the signals are again not present, possibly due to coordination of folic acid to the metals in solution or through deuterium exchange, and others exhibit very weak intensity (See appendix for full folic acid acidified and heated <sup>1</sup>H NMR characterisation). Analyses were consistent, showing similar folic acid contents of approximate 40 mol % compared to bdc. The content of folic acid in UiO-66-FA (PS) sample was found to be 23.6% (w/w), as determined by UV-Vis.

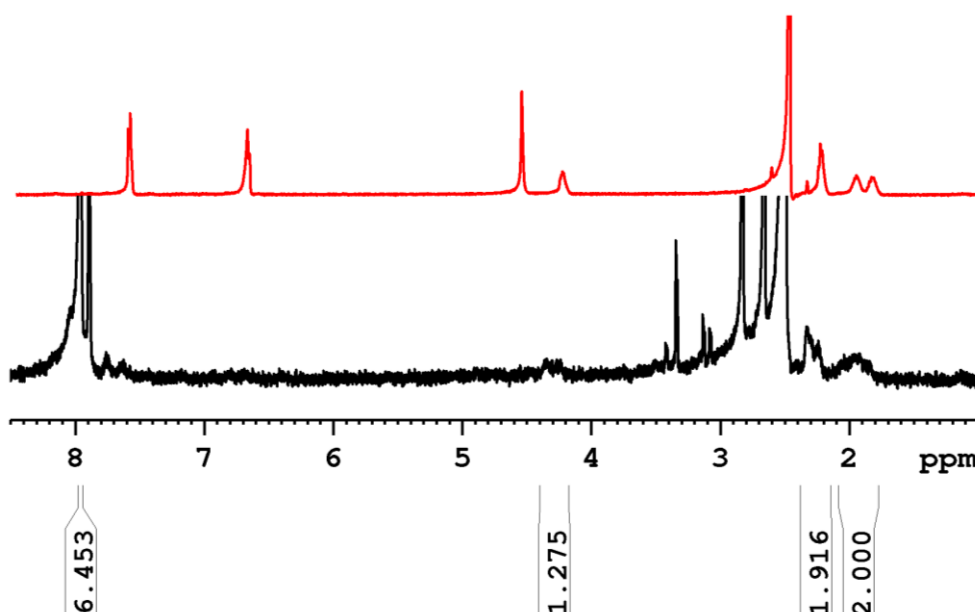


**Figure 3.21.** Stacked partial  $^1\text{H}$  NMR spectra of UiO-66-FA (PS), bottom, and folic acid, top, in  $\text{D}_2\text{SO}_4/\text{DMSO-}d_6$ .

The  $^1\text{H}$  NMR spectrum of acid-digested UiO-66-Biot (PS) shows the presence of characteristic biotin signals (Figure 3.22). However, their low intensity compared to the linker in UiO-66 hinders analysis, with an estimation of  $\sim 10$  mol % incorporation of biotin on the surface of UiO-66-Biot (PS) (See appendix for full biotin acidified  $^1\text{H}$ NMR characterisation).

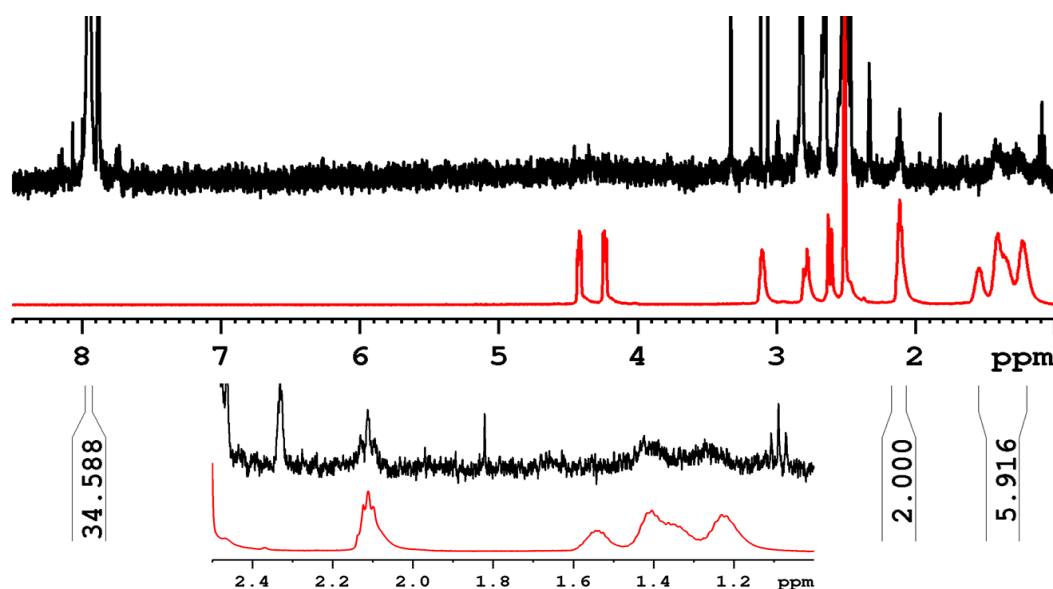


**Figure 3.22.** Stacked partial  $^1\text{H}$  NMR spectra of UiO-66-Biot (PS), top, and biotin, bottom, in  $\text{D}_2\text{SO}_4/\text{DMSO-}d_6$ . The inset highlights the characteristic alkyl region.

The characterisation of UiO-66-Hep (PS) by  $^1\text{H}$  NMR spectroscopy was complicated as a consequence of the polymeric nature of heparin itself. In general for all the samples

postsynthetically modified using coordination chemistry – UiO-66-FA (PS), UiO-66-Biot (PS) and UiO-66-Hep (PS) – it can be observed that signals assigned to the L1 modulator present in the precursor UiO-66-L1 have disappeared, presumably as a consequence of the exchange of the different functionality on the surface. The presence of the surface functionality is confirmed but full quantification is difficult as a consequence of low signal intensity compared to bdc and the possibility of missing linker defects.

Additional mass loss events are noticeable in the samples functionalised by postsynthetic exchange that can be ascribed to the surface functionality (Figure 3.23). The multi-step thermal degradation profile of heparin itself hinders the analysis of UiO-66-Hep (PS) by TGA, although the presence of heparin is clearly noticeable. The major new mass loss (235-420 °C) corresponds to 27.7% w/w of the sample, while the difference between the final residues compared with the precursor UiO-66-L1 is 16.4% w/w, confirming an increase in mass of the surface functionality even though L1 is lost from the precursor. However, heparin itself does not totally decompose, leaving a residue of ca. 37%. The fact that the main heparin decomposition step occurs in a more gradual manner for UiO-66-Hep (PS) than for free heparin indicates that heparin is attached to the UiO-66 structure, but quantification of the mass fraction of heparin is difficult.

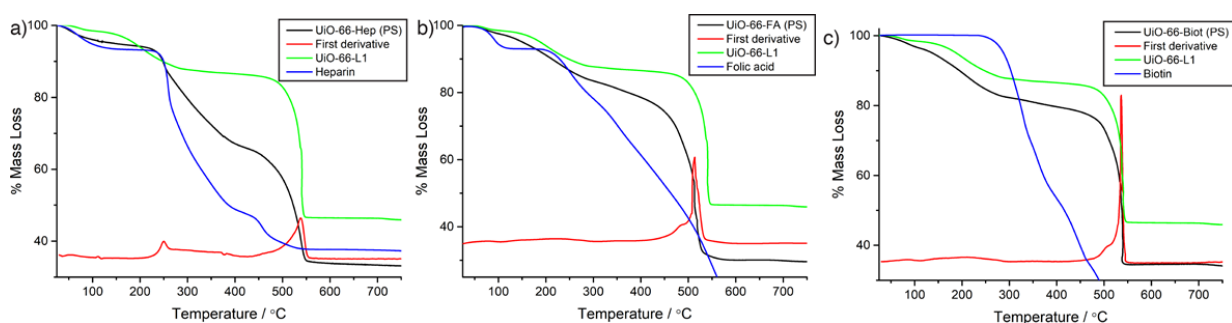


**Figure 3.23.** TGA traces of postsynthetically surface modified MOFs compared with the surface functionality and the starting material, UiO-66-L1, for a) UiO-66-Hep (PS), b) UiO-66-FA (PS), and c) UiO-66-Biot (PS).

Folic acid also degrades gradually with temperature, changing therefore the degradation profile of UiO-66-FA (PS), and making quantification of the folic acid content by mass difficult. The gradual degradation from 120-450 °C corresponds to a mass loss of 29.0%, while the difference in metal residues to a 16.7%. Although there is also a big difference in the TGA residue of the UiO-66-Biot (PS) and the precursor UiO-66-L1 (12% w/w), no notable additional features were observed in its degradation profile. Since biotin is clearly present in the acid-digested  $^1\text{H}$  NMR spectrum, it can be concluded that it decomposes together with the bdc linker between 300-400 °C.

With the combination of  $^1\text{H}$  NMR spectroscopy and TGA, it can be concluded that the different surface reagents are present on the surfaces of UiO-66. In some cases, the degradation of the surface reagents occurs at higher temperatures than the free reagents, strongly suggesting attachment. Additionally, displacement of surface-attached L1 suggests the same.

Minor changes in FT-IR spectra of the surface functionalised samples were observed (Figure 3.24). In agreement with the  $^1\text{H}$  NMR spectra, the azide band present in UiO-66-L1 at ca.  $2100\text{ cm}^{-1}$  is no longer present in the IR spectra of UiO-66-FA (PS), UiO-66-Hep (PS) and UiO-66-Biot (PS).

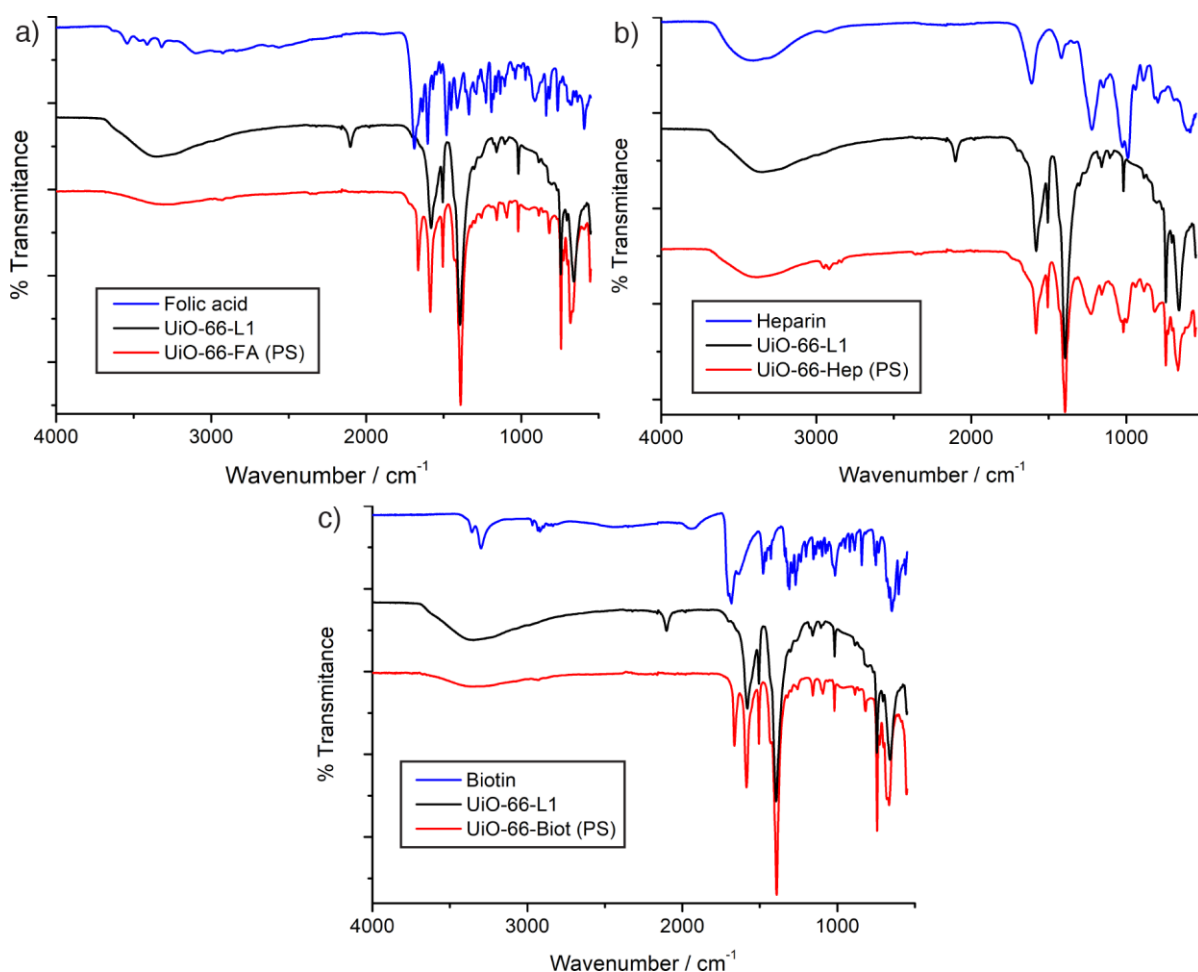


**Figure 3.24.** FT-IR spectra of the postsynthetically surface modified MOFs compared to the starting material, UiO-66-L1, and the surface functionality, for a) UiO-66-FA (PS), b) UiO-66-Hep (PS), and c) UiO-66-Biot (PS).

New IR bands, characteristics from heparin, are clearly present in the FT-IR spectrum of UiO-66-Hep (PS). The bands at  $1020\text{ cm}^{-1}$  are assigned to heparin sulfates, which are slightly

shifted when compared to free heparin, as a consequence of coordination to the zirconium positions rather than electrostatic interaction.

In order to analyse the porosity of the samples upon postsynthetic surface modification,  $N_2$  adsorption and desorption isotherms were collected at 77 K (Figure 3.25), showing decreases in surface area consistent with the addition of mass. Compared to their precursor UiO-66-L1 ( $S_{BET} = 1591 \text{ m}^2\text{g}^{-1}$ ; pore volume =  $0.791 \text{ ccg}^{-1}$ ), a considerable decrease in porosity is observed, with surface areas of  $891 \text{ m}^2\text{g}^{-1}$ ,  $879 \text{ m}^2\text{g}^{-1}$  and  $949 \text{ m}^2\text{g}^{-1}$ , and pore volumes of  $0.453 \text{ ccg}^{-1}$ ,  $0.499 \text{ ccg}^{-1}$  and  $0.496 \text{ ccg}^{-1}$  for UiO-66-Hep (PS), UiO-66-FA (PS) and UiO-66-Biot (PS) respectively, meaning that although the MOFs are still porous after the surface modification, their pore access might be partially blocked by the surface functionality.

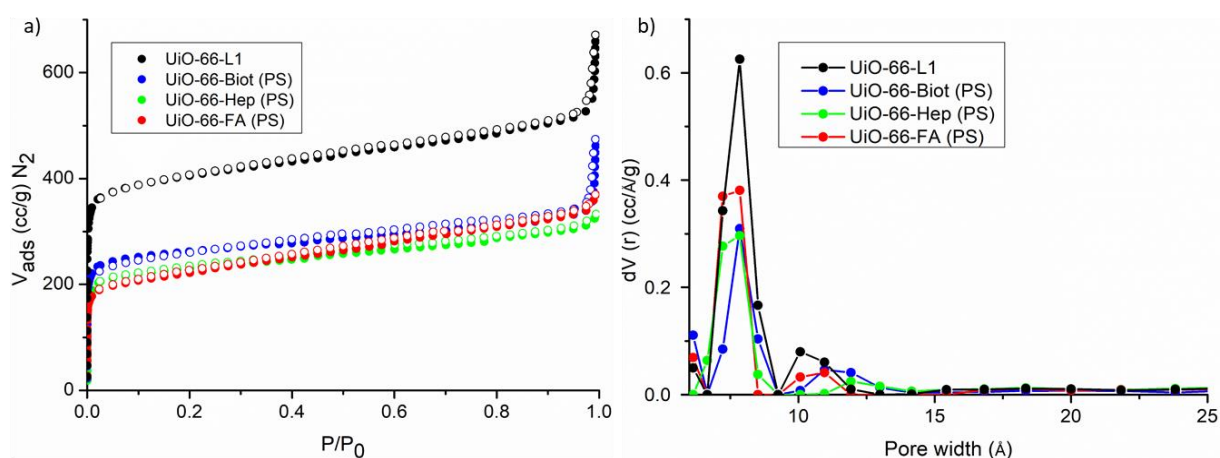


**Figure 3.25.** a)  $N_2$  adsorption isotherms (77 K) of the postsynthetically surface modified MOFs. Closed symbols for adsorption, empty symbols for desorption. b) Pore size distributions calculated from the isotherms.

Accordingly to the TGA profiles, the samples with the smallest surface areas correspond to those samples with lowest metal residue, and therefore have a greater mass content of the surface functionality. In other words, the decrease in gravimetric surface area is consistent with the amount of extra mass added to the NMOF. Additionally, the pore volumes and the pore size distributions of all the samples are similar to UiO-66, unequivocally confirming that functionalisation occurs on UiO-66 surface, not by blocking pores.

SEM imaging was used to study the morphology of the NMOFs upon surface modification (Figure 3.26), showing a slightly increase in particle size, together with a change in morphology. UiO-66-FA (PS), UiO-66-Biot (PS) and UiO-66-Hep (PS) particle sizes analysed by imageJ are  $168 \pm 26 \text{ nm}$ ,  $155 \pm 34 \text{ nm}$  and  $175 \pm 17 \text{ nm}$  respectively (Figure 3.27).

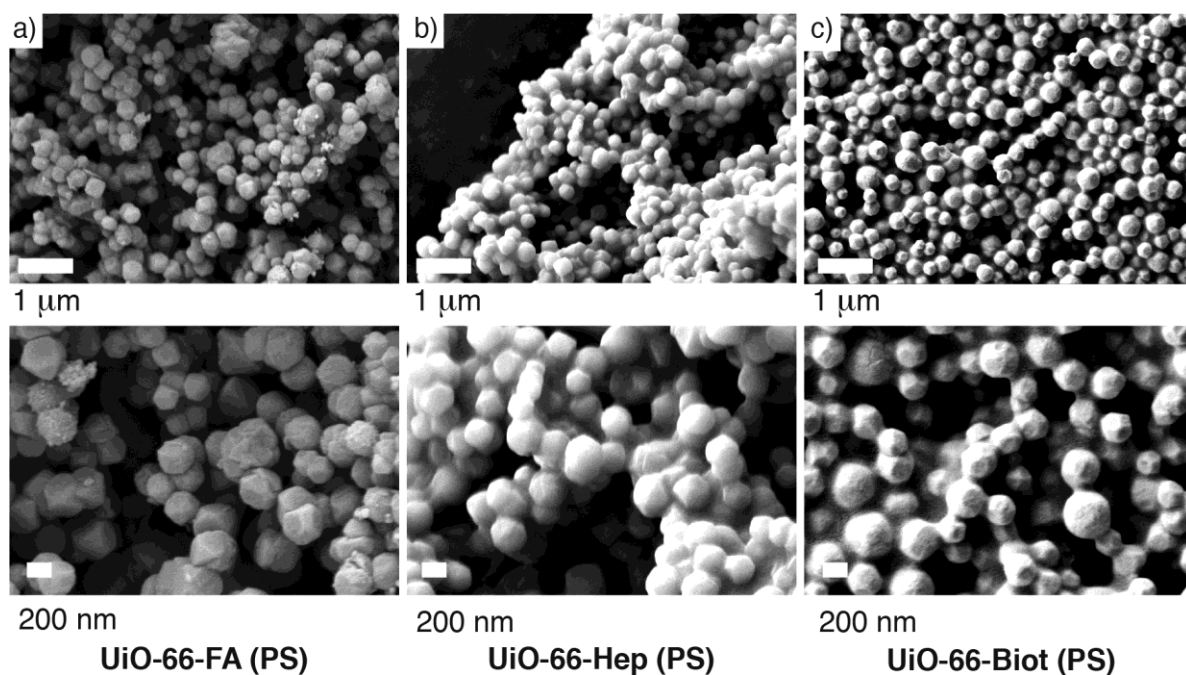


**Figure 3.26.** SEM images at different magnification of a) UiO-66-FA (PS), b) UiO-66-Hep (PS), and c) UiO-66-Biot (PS).

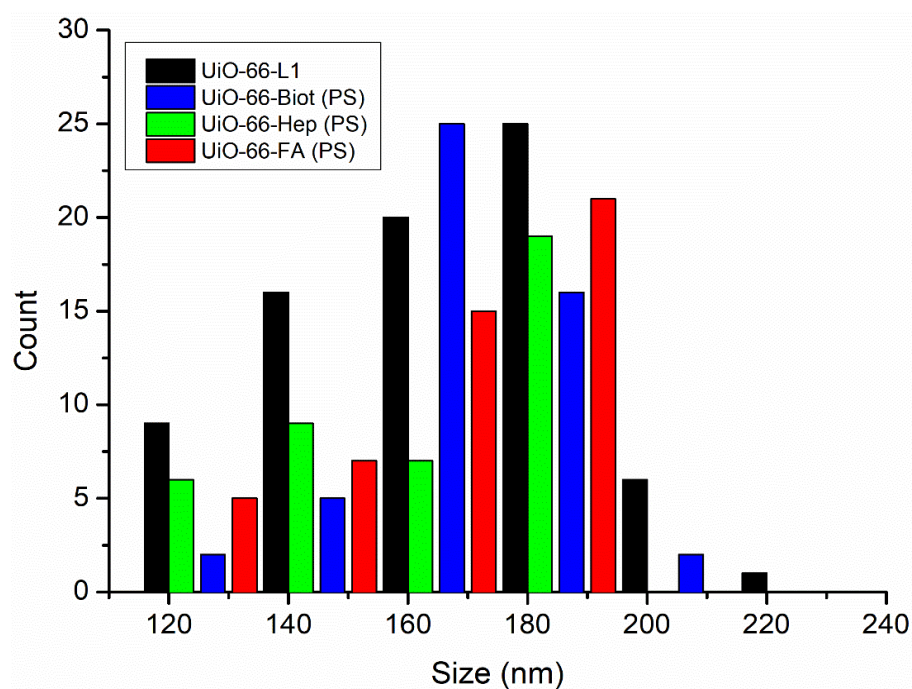


**Figure 3.27.** Comparison of particle size histograms for the surface modified samples through postsynthetic coordination and their precursor.

When UiO-66-FA is dispersed in MeOH, there is some randomly allocated material interlacing the NMOFs (Figure 3.28), presumably as a consequence of the detachment of folic acid during the sample preparation process. The sample does not have this material when the preparation

avoids dispersion. This indicates that folic acid coating might not be so stable, and it is partially released during the sample dispersion.

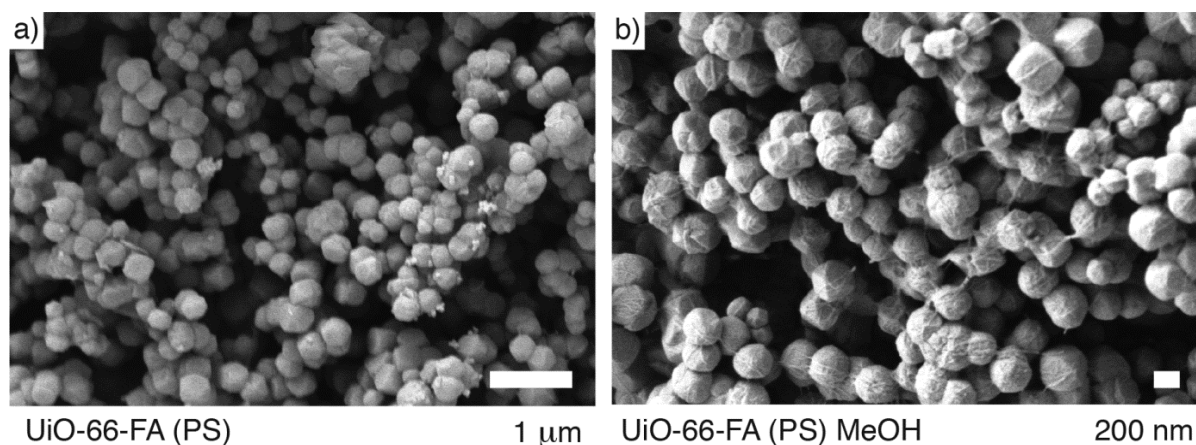


**Figure 3.28.** SEM images of UiO-66-FA (PS) a) non-dispersed, and b) dispersed with methanol.

To summarise, coordination chemistry has been successfully utilised to introduce both folic acid, biotin and heparin to UiO-66-L1 outer surface postsynthetically, showing attached modulator L1 displacement. However, a more pronounced decrease in porosity, compared to samples functionalised during synthesis (coordination modulation) or by the click modulation protocol, was observed. This could be a consequence of major outer surface coverage and partial pore window blockage; as coordination modulation induces the creation of defects through the overall attachment of modulator to the inner and outer available Zr clusters, and the postsynthetic modification of these modulators occurs only in the outer surface due to size selectivity and to steric hindrance for the CuACC catalyst formation. Coordination chemistry offers a wide variety of possibilities to be explored for surface modifications.

### 3.4. The Effect of UiO-66 Surface Chemistry on its Colloidal Dispersion

In order to study the effect on MOF colloidal dispersion upon surface chemistry and coating mode, dynamic light scattering (DLS) measurements were performed before and after surface coating- either through coordination modulation, detailed in Chapter 2, or through postsynthetic modification, detailed during this chapter- and compared to samples synthesised under conventional AcOH modulated conditions.

Particle size and aggregation in solution was measured on dispersions of 250 μg of MOF per mL of dispersant (i.e MeOH, water or PBS 10x). Three consecutive recordings, each consisting on 14 runs, were performed with a waiting time of 1 minute, and no stirring was provided during the analysis.

UiO-66-L1 and UiO-66-L2 aggregate in MeOH as a consequence of their hydrophilic surfaces, but the aggregation is however more pronounced for UiO-66-AcOH (Figure 3.29). A smaller degree of aggregation was found for UiO-66-L1, which exhibits stable colloidal dispersions with an average size of  $\sim 300$  nm, while UiO-66-L2 aggregates further during the course of the experiment, from around 500-1000 nm, and shows a second population with a smaller degree of aggregation. This may be a result of their hydrophilic surfaces.

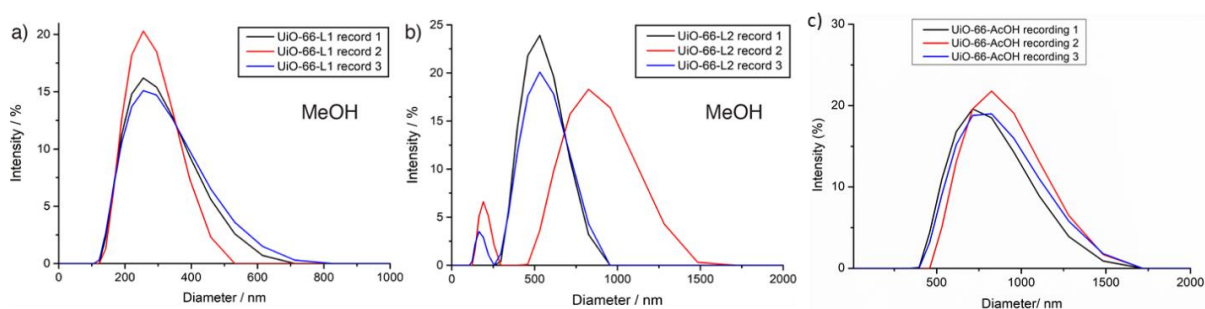


**Figure 3.29.** DLS profiles in methanol of a) UiO-66-L1 and b) UiO-66-L2 (Synthesised by SLE on UiO-66-L1), c) UiO-66-AcOH

The effect of surface PEGylation is clear. The PEGylated samples show much smaller size in solution, with average diameters around 150 nm correlating well with SEM data, suggesting well dispersed particles with no aggregation as a consequence of their PEG surfaces (Figure 3.30).

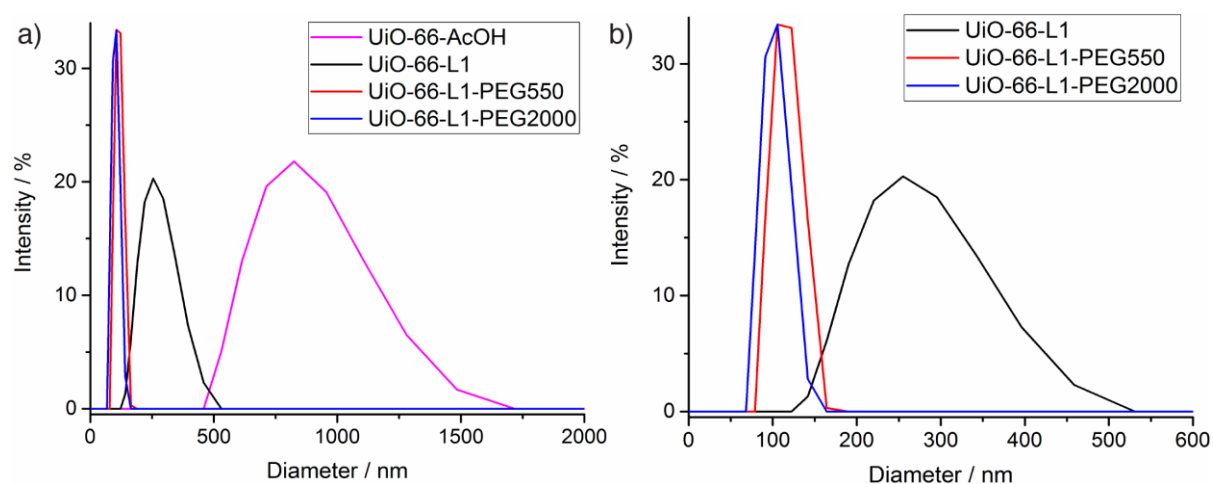


**Figure 3.30.** a) Dynamic light scattering (DLS) measurements of UiO-66 samples in methanol. b) Zoom in on DLS data for smaller particle sizes.

When the surfaces of the NMOFs are modified through postsynthetic covalent attachment of polymers (poly-L-lactide or PNIPAM) the average hydrodynamic diameter of the functionalised samples also decreases compared to their precursors (Figure 3.31). The biggest improvement is in the case of UiO-66-L1-PolyLact, which shows a particle size close to the one determined by SEM. UiO-66-L2-PNIPAM is initially monodisperse but aggregates during the course of the experiment.

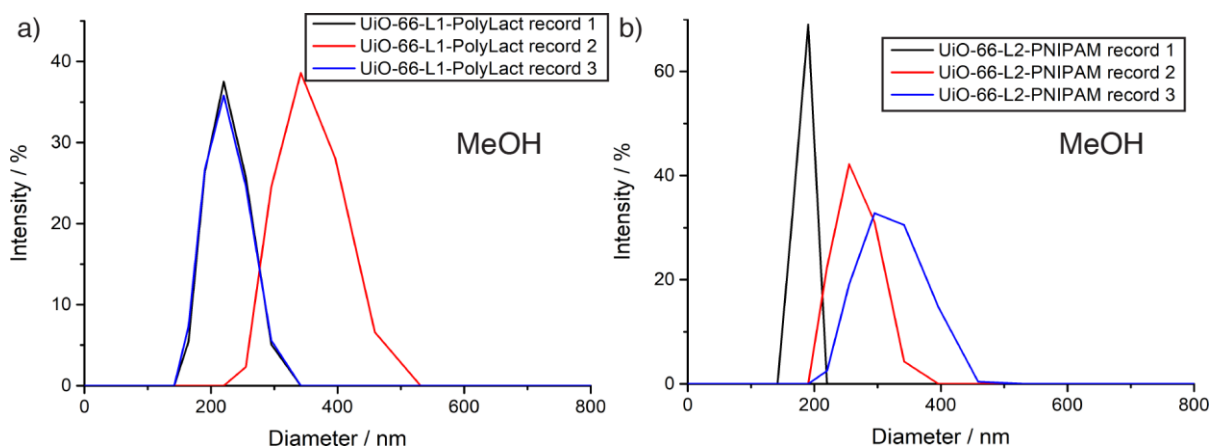


**Figure 3.31.** DLS profiles in methanol of a) UiO-66-L1-PolyLact, and b) UiO-66-L2-PINIPAM.

No drastic improvement was found for the samples postsynthetically modified using the surface ligand exchange protocol (Figure 3.32). In fact, UiO-66-Hep (PS) exhibited a higher degree of aggregation in methanol compared to its precursor UiO-66-L1. The decreasing diameter of UiO-66-Hep (PS) during the course of the experiment suggests precipitation or digestion of the MOFs as surface heparin detaches. On the other hand, UiO-66-FA (PS) and UiO-66-Biot (PS) have an average hydrodynamic diameter similar to their precursor in MeOH. While UiO-66-FA (PS) exhibits stable colloidal dispersions with no aggregation during the experiment, UiO-66-Biot (PS) further aggregates during the last recording.

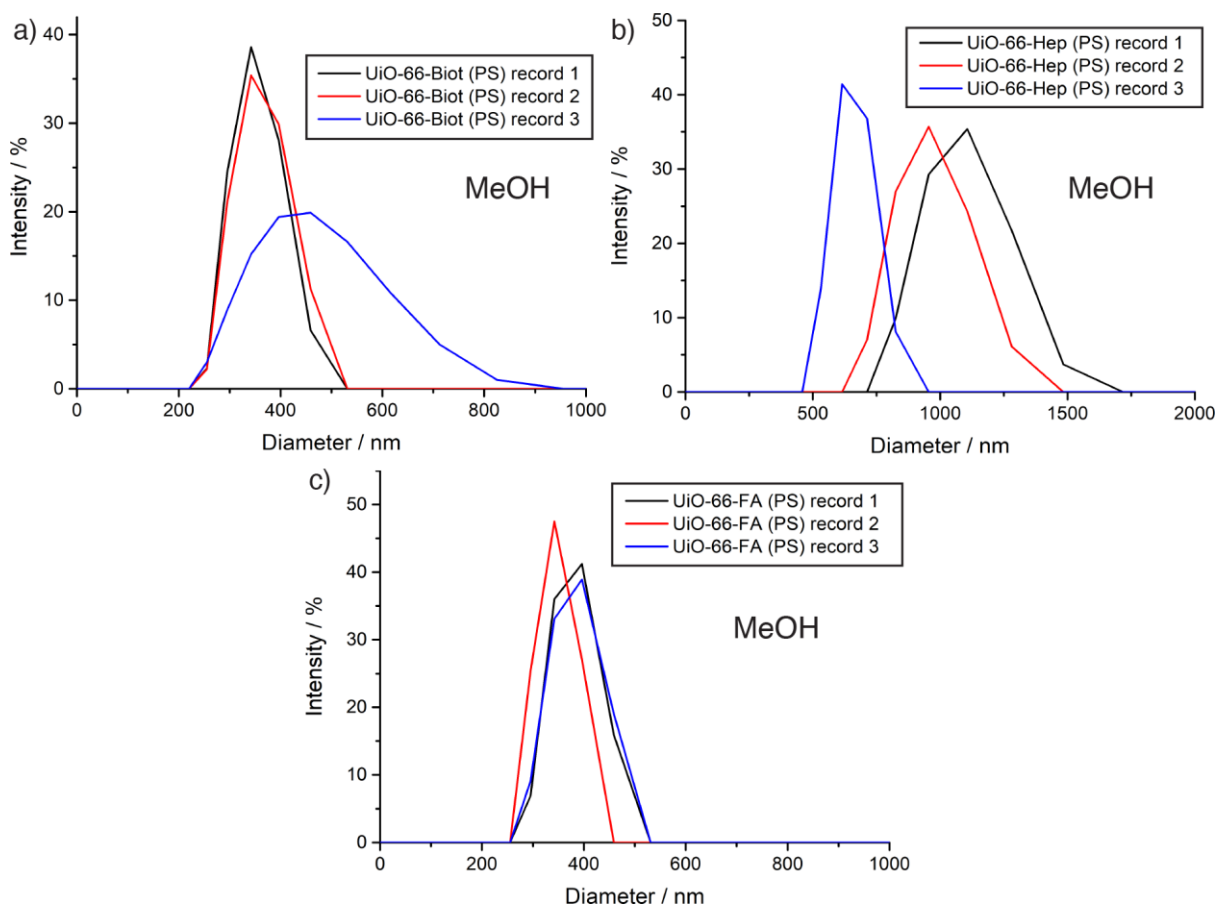


**Figure 3.32.** DLS profiles in methanol of a) UiO-66-Biot (PS), b) UiO-66-Hep (PS) and c) UiO-66-FA (PS).

The differences in the particle sizes in the surface functionalised samples (FA and Biot) prepared by coordination modulation during Chapter 2 when acetic acid is used as co-modulator is reflected in their DLS profiles (Figure 3.33). For example, UiO-66-FA (CM) forms stable aggregates with an average size of approximately 200-400 nm in MeOH, while UiO-66-FA-AcOH (CM) forms bigger aggregates (500-900 nm) that further aggregate to a size of 750-1750 nm during the course of the experiment. In contrast, UiO-66-Biot-AcOH (PS) forms smaller aggregates than UiO-66-Biot (CM), which shows significant aggregation to around 4000 nm. UiO-66-Biot (CM) forms intergrown crystals, as observed by SEM. Thus, its DLS profile in MeOH shows two populations, one with average size 400 nm, possible single crystals, and other highly polydisperse (1500-6500 nm) corresponding to intergrown crystals. UiO-66-Biot-AcOH (CM), which was identified as monodisperse crystallites of about 200 nm in size, dispersed better in MeOH, with minor aggregation over the experiment.

These results, combined with the particle size distributions from SEM, led to only take forward UiO-66-FA (CM) and UiO-66-Biot-AcOH (CM) for further experiments.

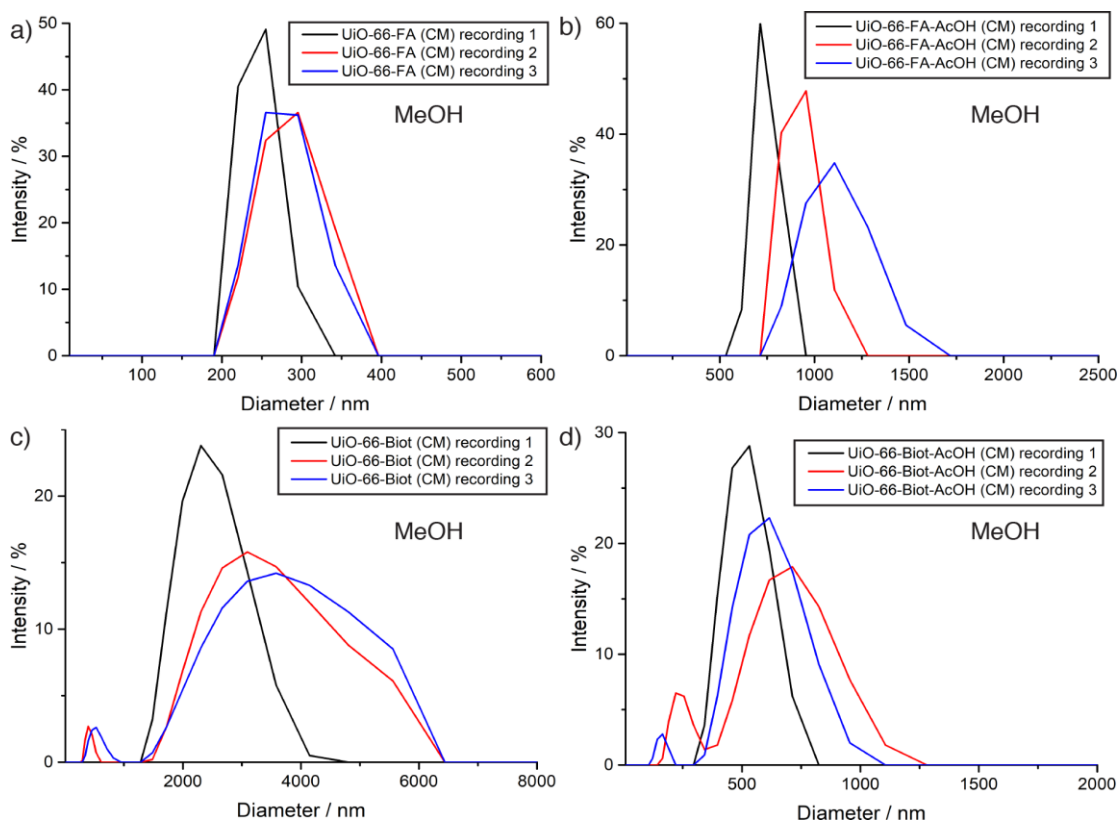


**Figure 3.33.** DLS profiles in methanol of a) UiO-66-FA (CM), b) UiO-66-FA-AcOH (CM), c) UiO-66-Biot (CM), and d) UiO-66-Biot-AcOH (CM).

When comparing the first recording of the different samples (Figure 3.34), apart from UiO-66-Hep (PS), it can be seen that the postsynthetically surface functionalised particles are in general better dispersed than their precursors in MeOH, with more homogeneous distributions, especially for the samples covalently modified with polymers. The samples prepared by coordination modulation show similar or slightly greater aggregation than UiO-66 (AcOH).

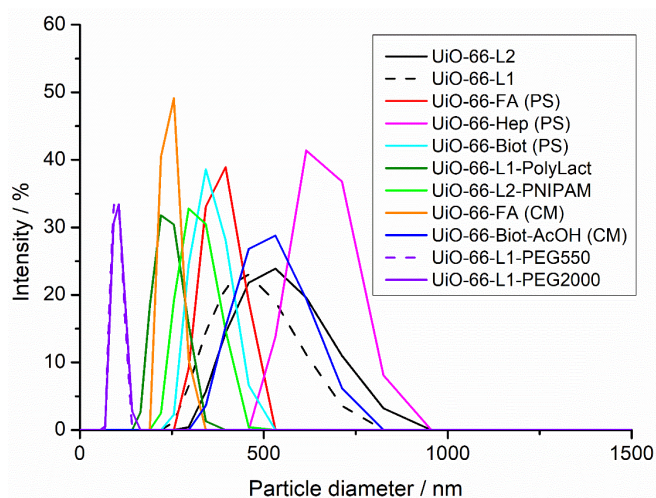


**Figure 3.34.** Comparison of DLS profiles in methanol of all samples.

DLS measurements were also carried out in water, but stable dispersions of the precursors UiO-66-L1 and UiO-66-L2 were difficult to generate. Initial aggregates of around 2500 nm in size were obtained for UiO-66-L1 followed by rapid further aggregation and precipitation, resulting in no signal populations (Figure 3.35). This slightly improved after surface ligand exchange with L2, which presented two different populations. The first had an average size of 500 nm and the second around 5000 nm, increasing in intensity during the course of the experiment as a consequence of aggregation.

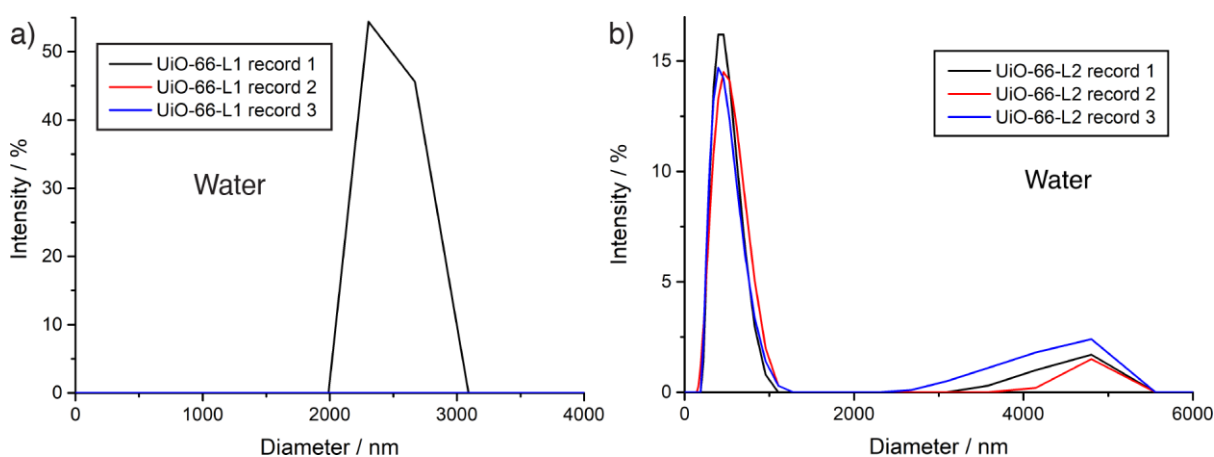


**Figure 3.35.** DLS profiles in water of a) UiO-66-L1, and b) UiO-66-L2.

The PEGylated samples showed much less aggregation, in particular UiO-66-L1-PEG2000, which has a much larger surface corona of water-compatible PEG chains and so stabilises small aggregates around 500 nm in size (Figure 3.36).

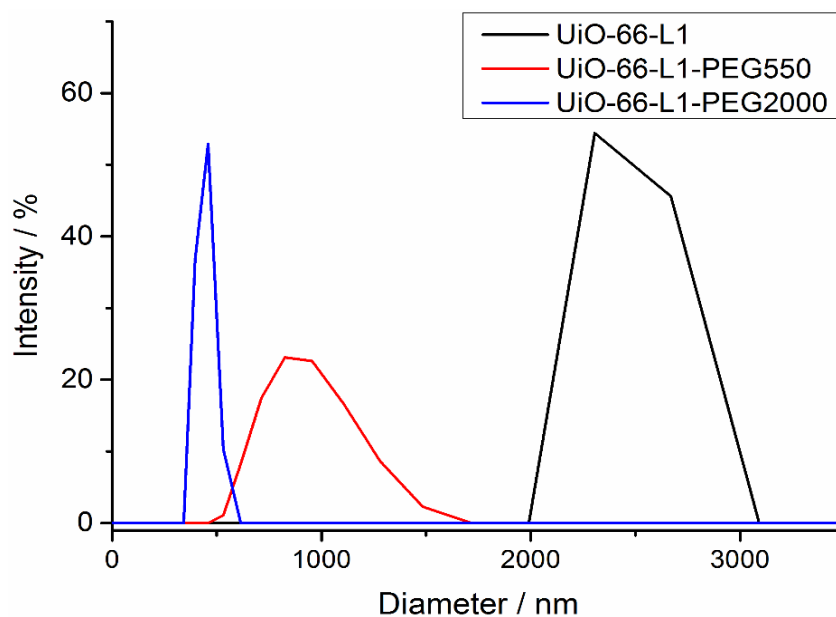


**Figure 3.36.** Dynamic light scattering measurements of UiO-66 samples in water.

During repeated DLS experiments run over 10 minutes, it was observed that UiO-66-L1-PEG2000 gradually aggregated (Figure 3.37), from particles around 250 nm to around 500 nm in diameter. Aggregates of UiO-66-L1-PEG550 across a broad size range around 1000 nm had, in contrast, stabilised rapidly prior to measurement, again indicating the significant effect of larger PEG chains on hydrodynamic behaviour of the UiO-66 nanoparticles.

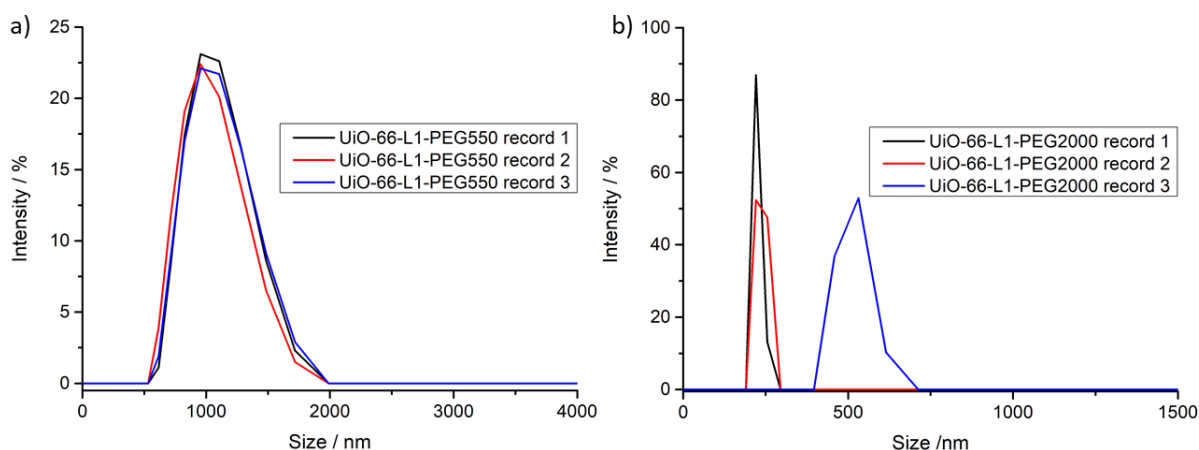


**Figure 3.37.** Time dependent aggregation observed during DLS measurements for a) UiO-66-L1-PEG550, and b) UiO-66-L1-PEG2000.

Coating the NMOFs with other polymers enhanced their colloidal dispersion properties in water (Figure 3.38). Initial colloidal dispersions with size close to the one determined by SEM were obtained, followed by strong aggregation in the case of UiO-66-L2-PNIPAM. UiO-66-L1-PolyLact was successfully dispersed and remained stable until the last measurement, where a second population appeared.

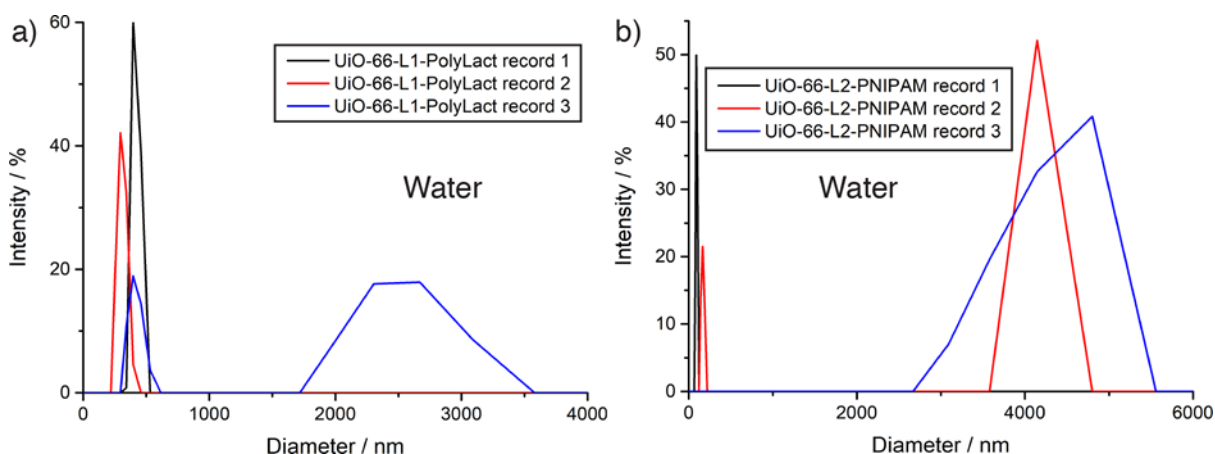


**Figure 3.38.** DLS profiles in water of a) UiO-66-L1-PolyLact, and b) UiO-66-L2-PNIPAM.

Minor improvements in the colloidal dispersion and stability in water were found for the postsynthetically-coated folic acid and biotin samples (Figure 3.39).

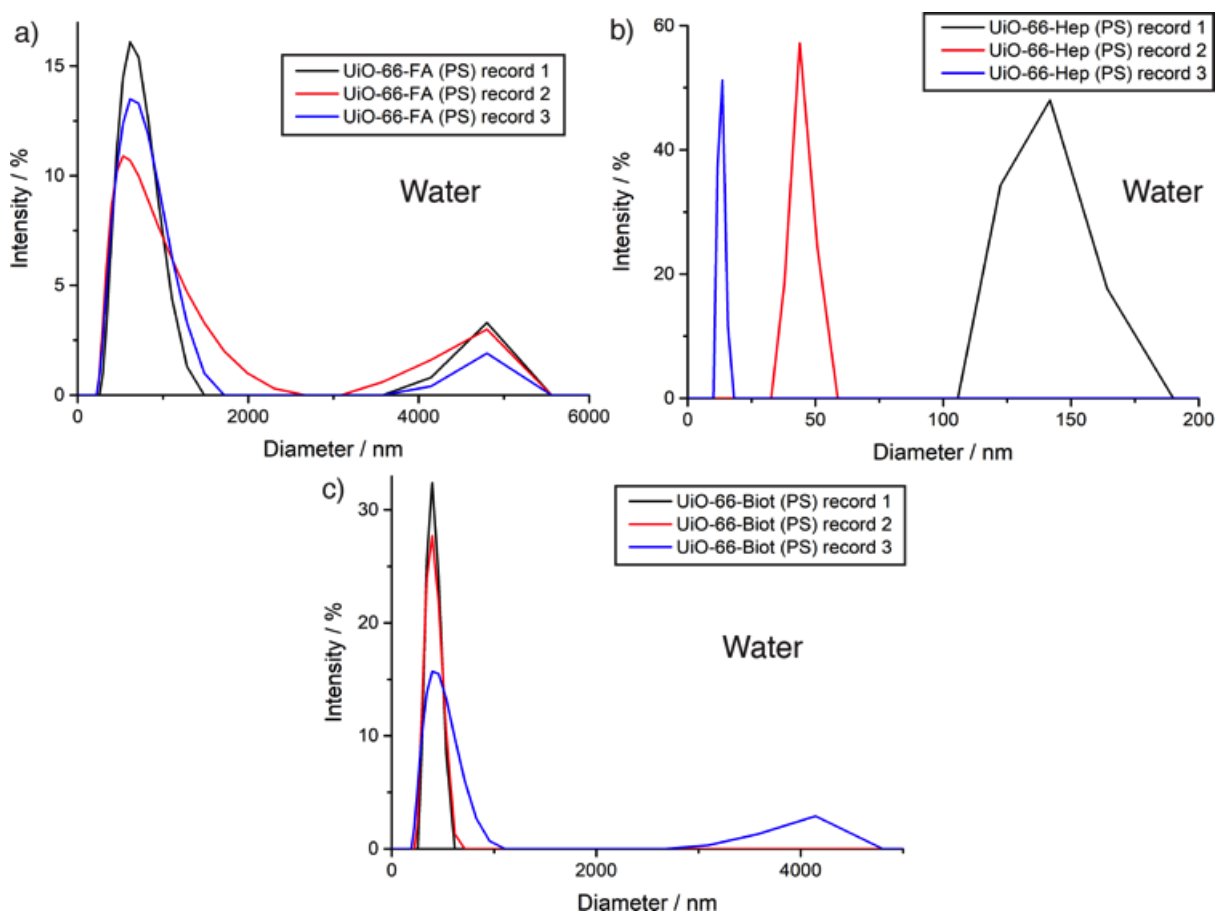


**Figure 3.39.** DLS profiles in water of a) UiO-66-FA (PS), b) UiO-66-Hep (PS), and c) UiO-66-Biot (PS).

Although UiO-66-FA (PS) also exhibits two different populations, no major aggregation or precipitation were found during the course of the experiment. UiO-66-Biot (PS) forms stable aggregates of 300 nm approximately during the first two recordings, but a second population of 4000 nm appeared due to aggregation during the third run. Once again, colloidal dispersion and stability were worst after heparin surface modification, as the sample precipitates during the course of the experiment, and a decreasing in size is observed due to sedimentation. It is likely the DLS response in the second and third runs is that of heparin (<50 nm) rather than the MOF.

Aggregation of both modulated samples in water was observed during the course of the experiment (Figure 3.40). Initially, small UiO-66-FA (CM) particles formed colloidal dispersions of 200 nm in size and further aggregated to around 1000 nm for the last recording, as did the larger UiO-66-Biot-AcOH (CM) samples, which formed initial aggregates of around 500 nm. However, more stable colloidal dispersions that unfunctionalised UiO-66 were formed.

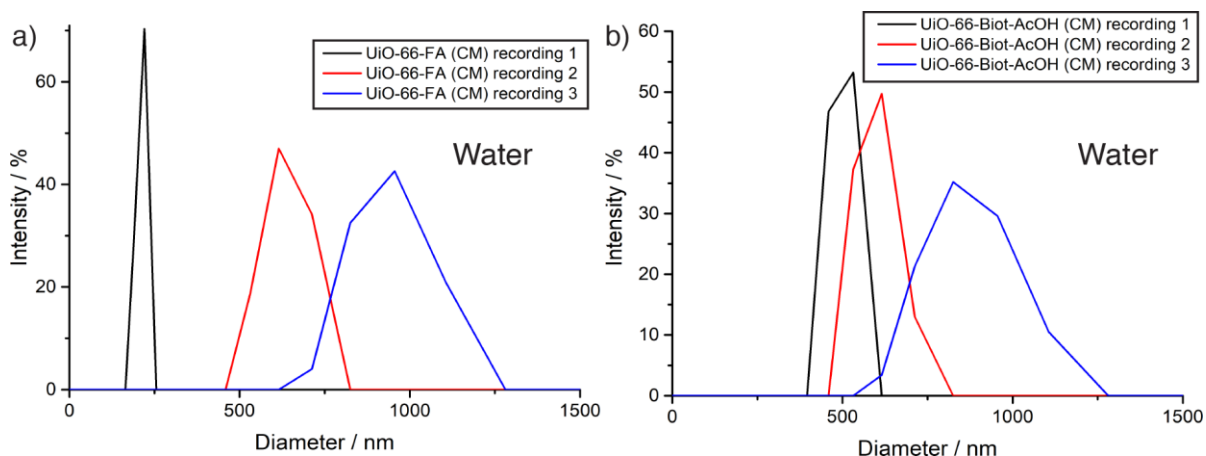


**Figure 3.40.** DLS profiles in water of a) UiO-66-FA (CM), and b) UiO-66-Biot-AcOH (CM).

Comparing all the samples (Figure 3.41), a similar trend is observed. In all cases, surface modification initially improves particle dispersity in water compared to precursor samples, but aggregation over the course of the experiments is an issue.

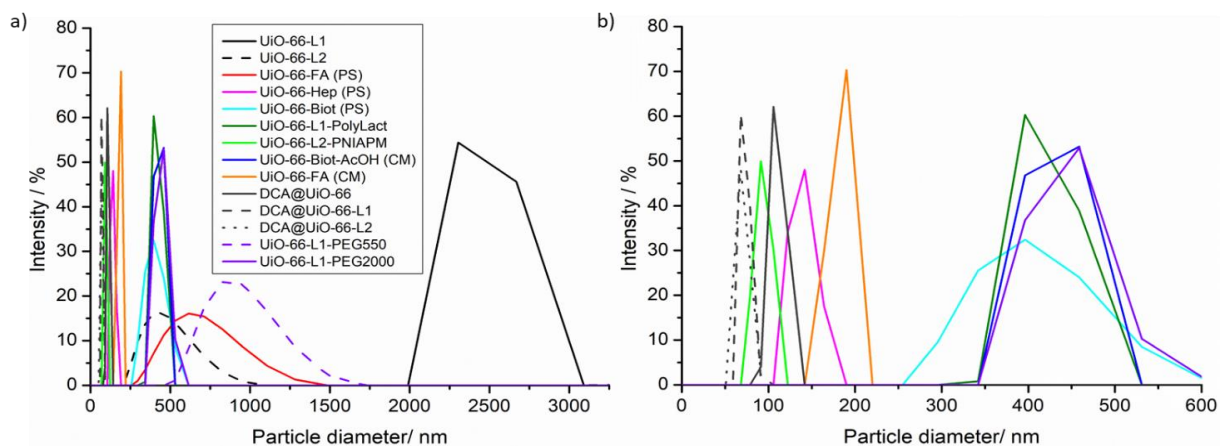


**Figure 3.41.** Comparison of DLS profiles in water of all samples.

DLS measurements were also carried in phosphate buffered saline (PBS), but it was again found difficult to generate stable dispersions of UiO-66-L1 and UiO-66-L2, as aggregation and precipitation during the course of the experiment were observed. In initial recordings, aggregates around 2000-4000 nm in size were found (Figure 3.42).

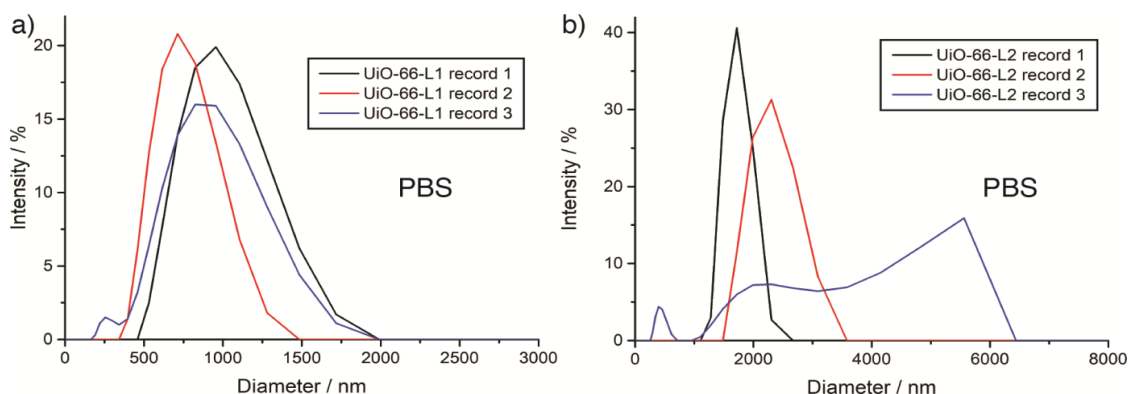


**Figure 3.42.** DLS profiles in PBS of a) UiO-66-L1, and b) UiO-66-L2.

On the other hand, stable colloidal dispersions of the postsynthetically surface functionalised nanoparticles, with different degrees of aggregation, were obtained in PBS (Figure 3.43). UiO-66-FA (PS) forms aggregates of around 750 nm, which do not considerably aggregate further during the course of the experiment. Similar behaviour is seen for the other samples functionalised through the postsynthetic exchange protocol, with UiO-66-Hep (PS) showing a similar profile with no further aggregation with time, and UiO-66-Biot (PS) a smaller average diameter of ~600 nm.

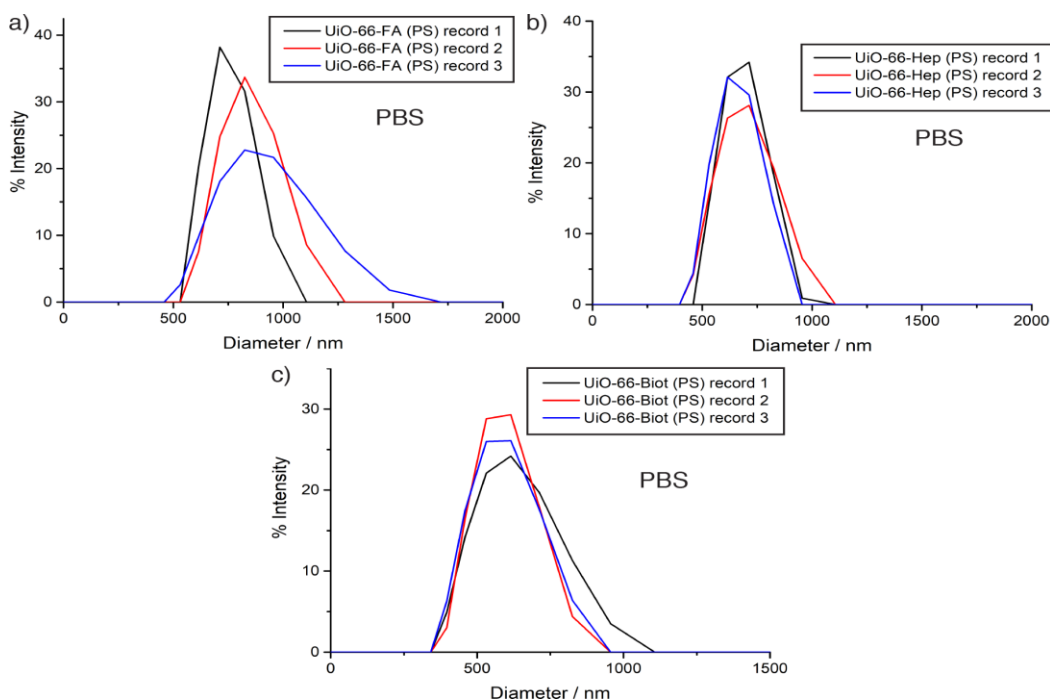


**Figure 3.43.** DLS profiles in PBS of a) UiO-66-FA (PS), b) UiO-66-Hep (PS), and c) UiO-66-Biot (PS).

In agreement with the DLS results obtained when dispersing the sample in MeOH and water, the samples functionalised using covalent click chemistry shown a considerable improvement in PBS colloidal dispersion (Figure 3.44). Although both samples form slightly bigger aggregates with time, initial recordings show particle sizes corresponding to those determined

by SEM for UiO-66-L1-PolyLact, which aggregates from 200 nm to 500 nm during the course of the experiment. In the case of UiO-66-L2-PNIPAM, slightly larger aggregates from 400 nm to 750 nm are formed during the course of the experiment.

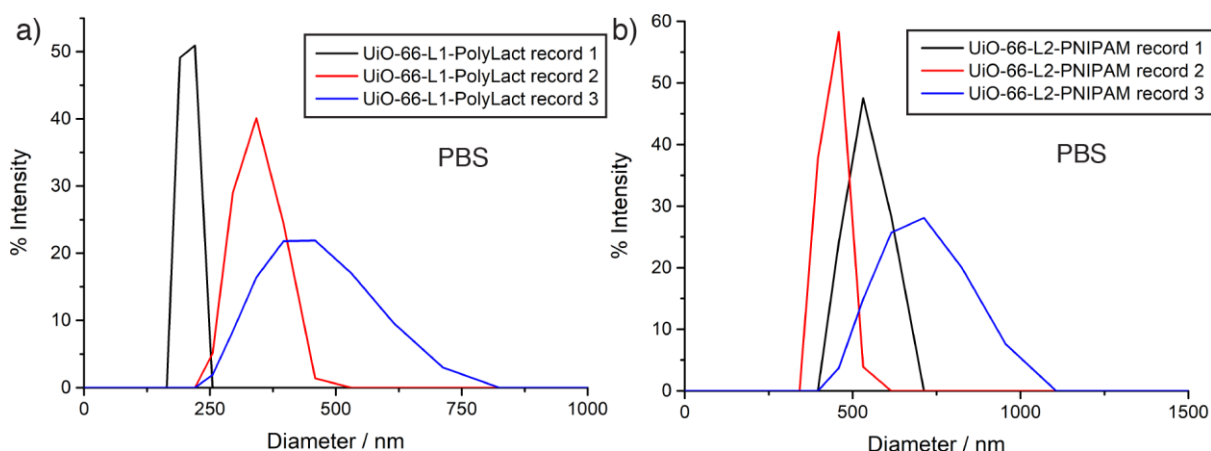


**Figure 3.44.** DLS profiles in PBS of a) UiO-66-L1-PolyLact, and b) UiO-66-L2-PNIPAM.

Similar results were found when dispersing the modulated NMOFs in PBS (Figure 3.45). During the first recording, UiO-66-FA (CM) exhibits two populations, aggregates around 500 nm and a small population very close to the size observed by SEM, which disappears for the last two recordings without further aggregation. UiO-66-Biot-AcOH (CM) forms stable aggregates of 1000 nm average size

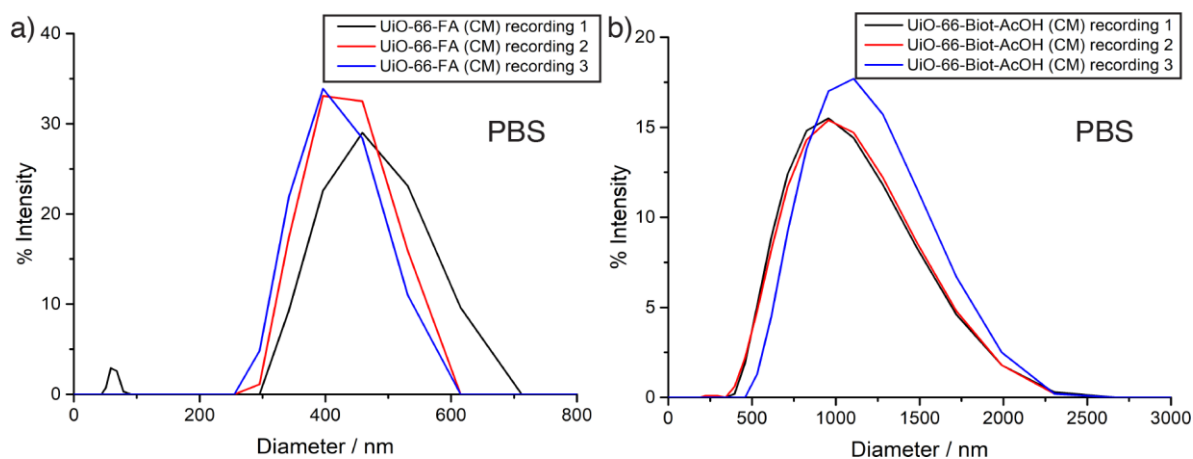


**Figure 3.45.** DLS profiles in PBS of a) UiO-66-FA (CM), and b) UiO-66-Biot-AcOH (CM).

Comparing the first recordings of the functionalised samples and their precursors in PBS, the effect on colloidal dispersion based on surface chemistry is clearly noticeable, especially when using our previously reported ‘click modulation protocol’ to covalently attach polymers to UiO-66 surface (Figure 3.46). In all cases, surface modification improves dispersity and reduces aggregation.

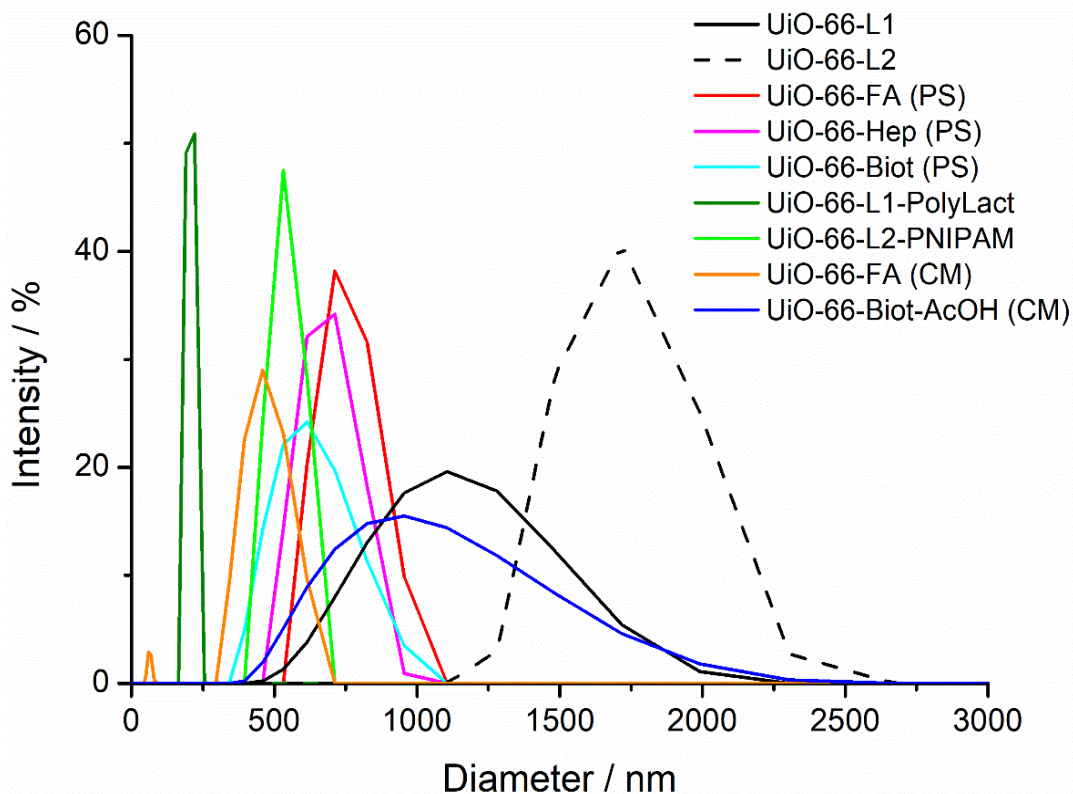


**Figure 3.46.** Comparison of DLS profiles in PBS of all samples.

The results suggest that surface modification enhances the stability and dispersion of NMOFs for drug delivery. However, the presence of different proteins, sugars and different moieties in the blood current that are known to be adsorbed onto the surfaces of NMOF will definitely have an effect on their colloidal stability and dispersion *in vivo*.<sup>38-40</sup> In fact, it has been reported that NMOF aggregation is strongly decreased in growth media.<sup>41-43</sup> During Chapter 2, the effect of adding BSA to PBS confirmed the further colloidal stability of MOFs in the presence of proteins due to the formation of a protein corona. It is important to consider that no stirring is provided during the course of the experiment, while the blood current is dynamic in its nature. Although here it is shown how to improve those properties through surface functionalisations, especially coating UiO-66 with polymers by the “click modulation” protocol, the colloidal stability of the NMOFs *in vivo* conditions is still difficult to predict. However, it is important to point out that the samples synthesised previously under the DCA modulated conditions (Chapter 2) are colloidal stable in water and PBS, showing size distributions in great agreement with SEM, without aggregation during the course of the experiment. These samples are the ones which will be used as DDSs, as they contain a high loading of the the PDK inhibitor dichloroacetate, and surface modification is expected to further enhance their dispersion.

### 3.5. The Effect of Surface Chemistry in UiO-66 Degradation Kinetics

To be an efficient injectable treatment, the nanocarrier should be stable at the first stages of the treatment, ideally not being degraded in extracellular conditions (i.e. blood, pH 7.4) in order to avoid renal clearance of the drug, yet not persistent enough to be accumulated over longer treatment periods. The nature of the metal-linker coordination bonds in MOFs ensures total degradation of the structure at sufficiently acidic pH ranges due to linker protonation, but strongly coordinating molecules, such as phosphates, are also able to displace the linkers in the structure at extracellular pH.<sup>44, 45</sup> Whilst the rapid degradation of MOFs under physiological conditions ensures no accumulation of the carrier after it has reached its target and released the drug, their instability towards phosphates, which are present in the blood, typically hinders NMOFs bioapplications due to fast release kinetics.<sup>46</sup> If the initial degradation could be slowed down while maintaining their final clearance, NMOFs therapeutic efficiency will be enhanced. Several approaches, such as amorphisation<sup>42, 47, 48</sup> or silica coating,<sup>26</sup> among others, have been studied to improve their stability towards phosphates.

To obtain the degradation profile of the different UiO-66 nanoparticles, around 10 mg of sample were dispersed in a dialysis bag with 10 ml of phosphate buffered saline (PBS) at pH 7.4, and dialysed against 100 ml of PBS (10x) under magnetic stirring at room temperature. The release of the bdc linker, indicative of degradation, was measured by UV-Vis spectroscopy. The quantity of bdc (% w/w) present in the different UiO-66 samples was calculated based on the TGA measurements.

A calibration curve of bdc in PBS pH 7.4 was performed ( $\lambda_{\text{max}} = 241 \text{ nm}$ ) and shown in Figure 3.47a. Solutions of bdc and L1 of the same concentration were measured revealing a maximum absorbance peak at 234 nm for L1 with a very similar extinction coefficient to bdc. When the absorbance of a solution of both bdc and L1 (1:1) was measured, a maximum peak absorbing at 238 nm was determined with a very similar extinction coefficient to bdc on its own (Figure 3.47b).

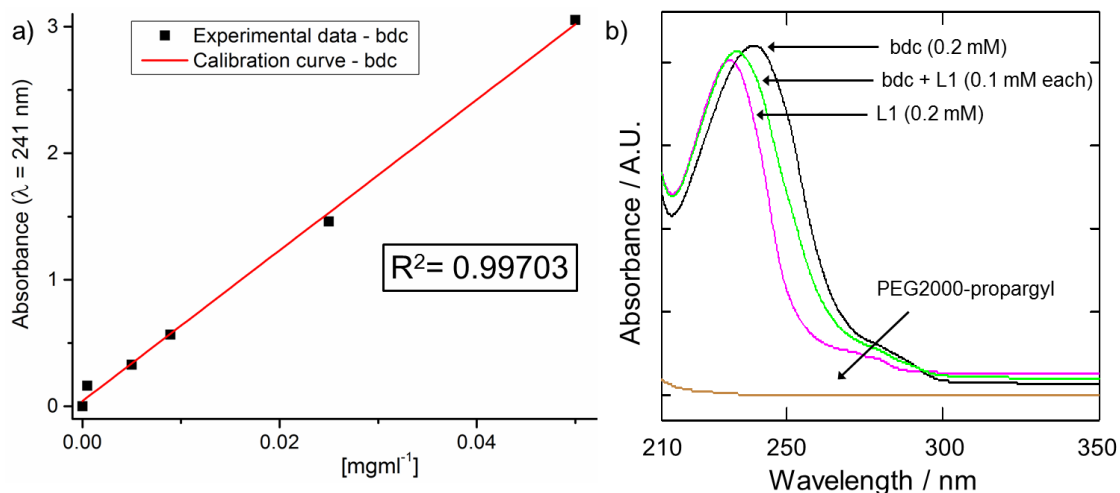


**Figure 3.47.** a) Calibration curve of bdc absorbance at  $\lambda = 241 \text{ nm}$  in PBS at pH 7.4. b) UV-Vis spectra of PEG2000-propargyl (brown), L1 (pink), bdc (black), and a mixture of L1 and bdc (green).

Due to the overlapping absorbance of L1 and bdc, the fact that the presence of L1 does not affect the bdc absorbance, and as the quantity of L1 present in sample (determined by  $^1\text{H}$  NMR) is very small compared to bdc, the bdc calibration curve in Figure 3.47a was used.

Each measurement was taken *in situ* (from 210 nm to 330 nm) and the liquid was introduced back to the dialysis media before prior measurement. Each experiment was performed separately 3 times to determine the standard deviation and each calculation was performed with the exact mass of NMOF added. Non-linear fittings of the degradation profiles are given in the appendix.

At first, comparison of the postsynthetically surface modified UiO-66 degradation profiles with their precursor UiO-66-L1 (Figure 3.48) shows the presence of an induction period, with variations depending on the surface reagent, as a consequence of the protection that the surface coating provides. Although a general enhancement in stability towards phosphate degradation were observed for all samples, after 2.5 h UiO-66-Hep (PS) has a faster degradation rate than its precursor, suggesting rapid loss of the surface polymer.

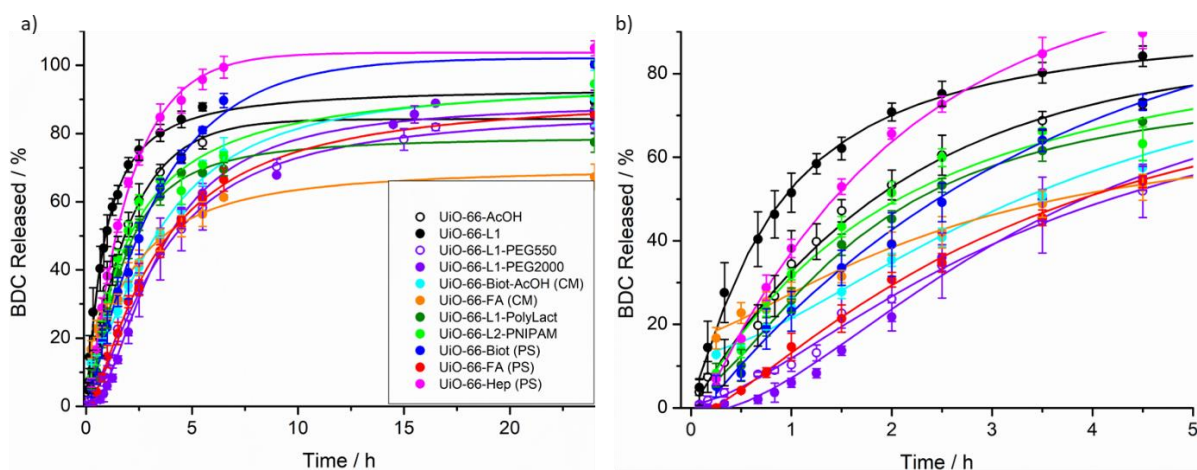


**Figure 3.48.** Comparison of the degradation profiles in PBS of surface coated and uncoated UiO-66. a) during 24 hours, b) during 5 hours, highlighting the induction period of the surface coated samples. Error bars represent the standard deviation from triplicate experiments.

Significant differences were noted for PEGylated samples compared to uncoated samples, and are plotted in Figure 3.49. There is a clear enhancement in stability for the PEGylated samples, which also degrade with a different kinetic profile (sigmoidal vs exponential), indicating that polymeric coating protects the MOFs surface from degradation.

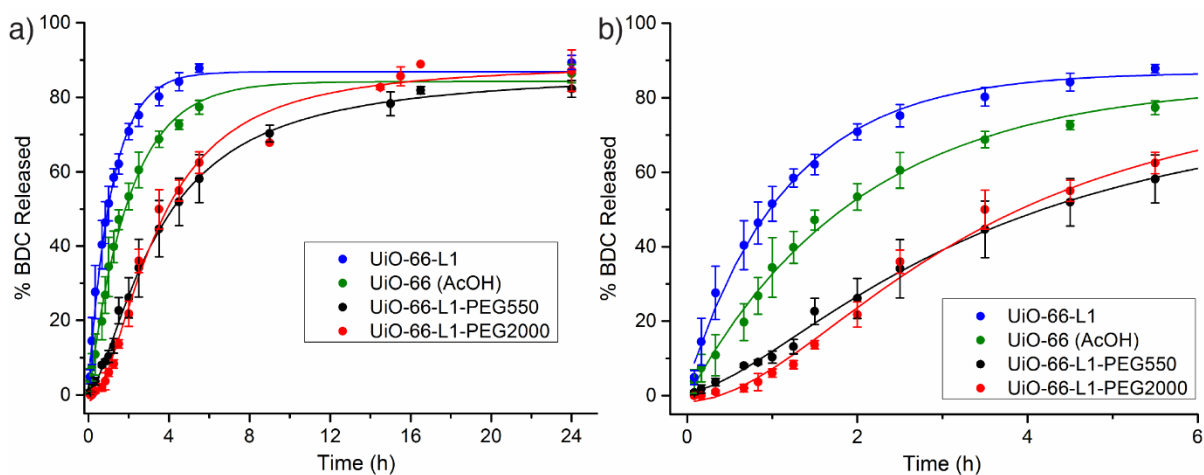


**Figure 3.49.** a) Degradation profiles of coated and uncoated UiO-66 nanoparticles in PBS pH 7.4, with b) an inset of the early time period. Error bars denote standard deviations from triplicate experiments.

The effect of exposure of the UiO-66 nanoparticles to PBS buffer on their crystallinity was investigated by powder X-ray diffraction. In the general procedure, 20 mg of the UiO-66 nanoparticles were dispersed in PBS buffer (pH 7.4, 20 ml) by sonication (5 minutes), and stirred for different contact times. Then, the nanoparticles were collected by centrifugation and

washed with fresh water. After being dried for 24 h under vacuum, their crystallinity was analysed by PXRD (Figure 3.50).

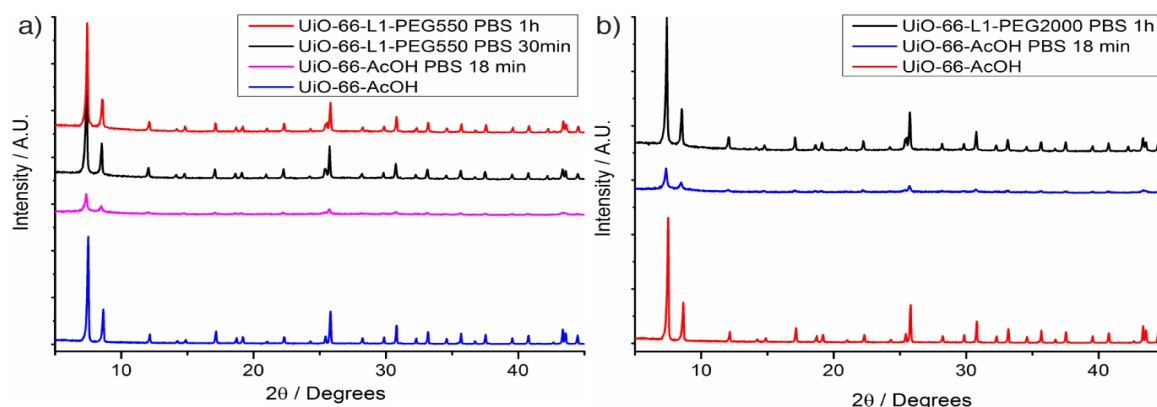


**Figure 3.50.** Stacked PXRD patterns of UiO-66 samples after different contact times with PBS buffer for a) UiO-66-L1-PEG550 and b) UiO-66-L1-PEG2000.

The samples clearly exhibit different stabilities under the experimental conditions, with uncoated UiO-66 samples rapidly losing crystallinity, while the PEGylated samples remain highly crystalline after an hour.

Similar features are observed for the postsynthetic covalent modifications with poly-L-Lactide and PNIPAM, which exhibit a sigmoidal profile versus the exponential profile of UiO-66-L1 (Figure 3.51). The importance of these findings resides in the fact that after 1 h UiO-66-L1 has released the 55% *w/w* of its linker in the structure, while UiO-66-L1-PolyLact has only released the 27% *w/w* and UiO-66-L2-PNIPAM the 30% *w/w*, yet the degradation of the three samples is very close after 24 h.

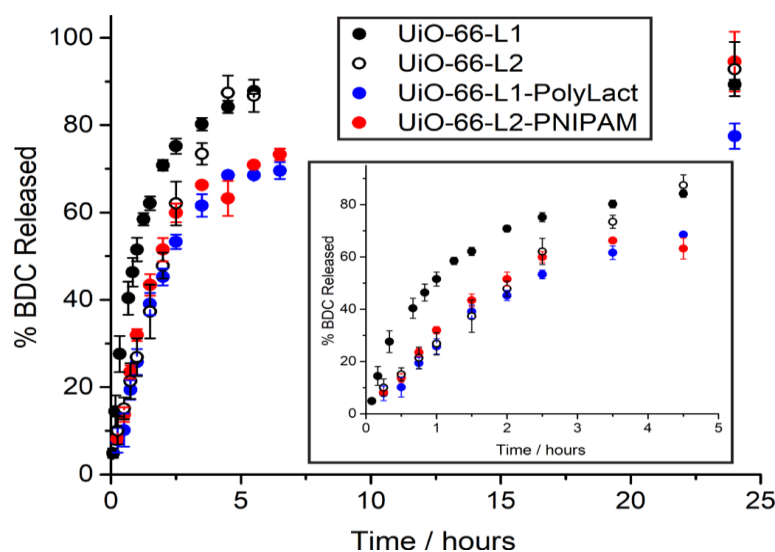


**Figure 3.51.** BDC release profiles measured by UV/vis spectroscopy of the click modulated, polymer coated UiO-66 samples. Error bars represent the standard deviation from triplicate experiments.

Comparing the degradation of the postsynthetically coordinated and modulated folic acid and biotin containing samples (Figure 3.52), different trends can be also observed based on the mode of surface modification.

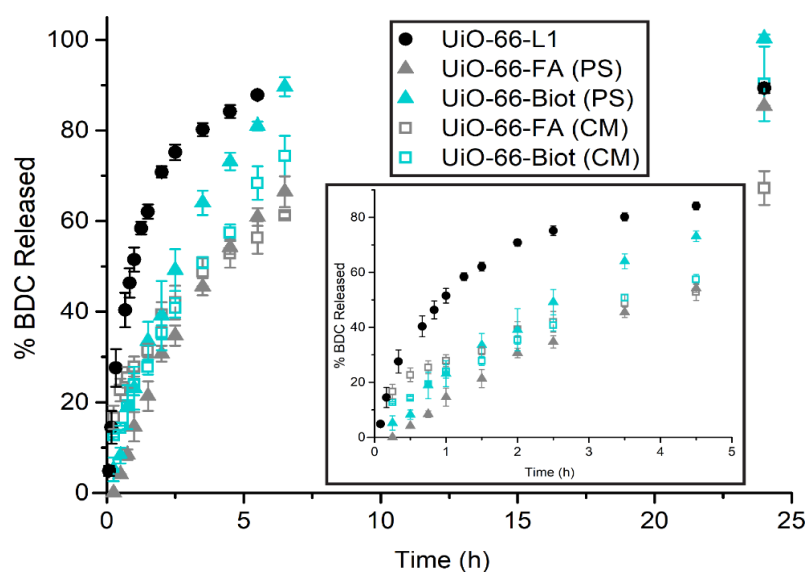


**Figure 3.52.** BDC release profiles measured by UV/vis spectroscopy of the UiO-66 samples surface modified during coordination modulation. Error bars represent the standard deviation from triplicate experiments.

An initial induction period plays an important role for all the coated samples, but is more noticeable for the postsynthetic modifications, with no bdc release for UiO-66-FA (PS) after 15 minutes. In general, even if the stabilisation is higher at the beginning of the experiment for the postsynthetically coordinated samples, presumably due to complete zirconium coordination that hinders phosphate attack, after a short period of time the degradation rate becomes faster than for the modulated samples. In fact, after only 45 minutes UiO-66-Biot (PS) has released a similar amount of linker to UiO-66-Biot (CM) (ca. 25% each versus 55% for UiO-66-L1). In the case of UiO-66-FA (PS) it takes a longer period, 3.5 h to reach a similar degradation to UiO-66-FA (CM).

Folic acid release can also be tracked by UV-vis spectroscopy during the course of the experiment (Figure 3.53). It is important to take into account that we previously determined a 23.6% w/w and 13.6% w/w of folic acid for UiO-66-FA (PS) and (CM) respectively. In both cases folic acid releases faster than the linker of the structure and with a similar profile, suggesting it is located on or near the particle surface.

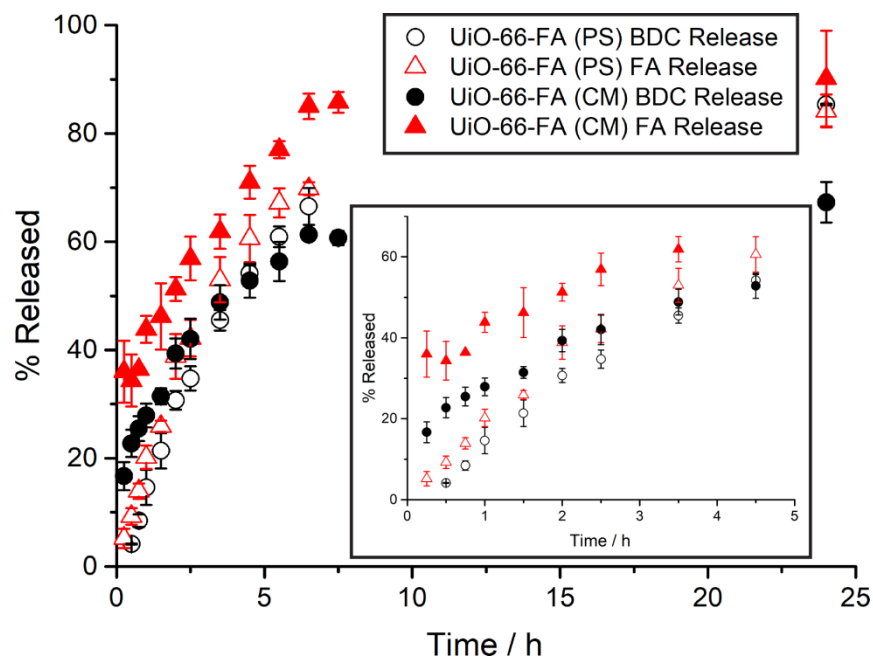


**Figure 3.53.** Comparison of BDC and folic acid release profiles measured by UV/vis spectroscopy of the folic acid coated UiO-66 samples. Error bars represent the standard deviation from triplicate experiments.

The conjunction of these results suggest that although initial enhancement of UiO-66 stability towards phosphates can be achieved by surface functionalisations, the choice of surface coating also plays an important role, both through the affinity of the coordination groups to the Zirconium positions and through the coating interaction with the aqueous media (i.e the highly water soluble heparin is less stable after 2.5 h). The mode of coating also plays an important role, as samples synthesised by coordination modulation are initially less stable than samples modified through postsynthetic coordination with the same surface reagents, possibly due to partial pore blockage, hindering the Zr positions from phosphate attack to higher extent. The click modulation protocol, in which polymers (i.e PEG, PolyLact and PNIPAM) coat UiO-66 surface is also a successful tool to enhance MOF stability, more remarkably for the PEGylated samples. Importantly, similar degrees of degradation to the uncoated samples are obtained after 24 hours, indicating that although initial drug release should be decreased, accumulation in the body due to higher stability should not be an issue.

### 3.6 Conclusions

In conclusion, a number of different functionalities have been assessed to UiO-66 surface, and different surface modification protocols – coordination modulation, postsynthetic exchange, and covalent click modulation – have been studied for the surface functionalisation of UiO-66 nanoparticles for use in drug delivery.

Postsynthetic surface modifications on UiO-66-L1 based on coordination chemistry have been performed using L2, folic acid, biotin and heparin as surface reagents, showing L1 displacement and surface reagent attachment to the available zirconium positions. Proof-of-concept CuAAC covalent modifications between UiO-66-L1 and 1-dodecyne, and between UiO-66-L2 and 1-azidodecane, have proven functionalisation occurs only on the outer surface, and the ‘click modulation’ protocol has been further applied to covalently attach PEG (Mw= 500 and 2000), Poly-L-Lactide (Mw= 2000) and PNIPAM (Mw 15000) chains to the outer surface of UiO-66 using modulators L1 and L2 as surface modification platforms.

Importantly, in nearly all cases, surface functionalisation enhances properties such as colloidal dispersion and stability towards phosphate-induced degradation compared to bare UiO-66, to a different extent depending on the surface reagent and on the coating mode. For example, the heparin coated MOF performed poorly in colloidal stability, and its degradation kinetics were only improved over a few hours, while PEGylated, and other polymer-coated MOFs, in contrast were colloidally-stable and their degradation was highly improved, with induction times of an hour during which almost no degradation occurred. It has been noted that in general, covalent postsynthetic polymer coating with PEG, PolyLact and PNIPAM though the click modulation protocol provides higher colloidal stability than postsynthetic modifications based on coordination chemistry.

Postsynthetically coating of UiO-66 with biotin and folic acid initially enhanced the stability of the MOF to a higher extent than when the same functionalities are introduced during synthesis by coordination modulation, possibly as a consequence of partial pore blockage when the coating is performed postsynthetically, hindering the external and internal surface from phosphate attack to a higher extent. However, after induction times of few hours, the samples prepared through coordination modulation have slower degradation kinetics than their postsynthetic analogues.

The surface modification protocols detailed during this chapter will be also applied to postsynthetically functionalise UiO-66 surface after loading of a fluorescent molecule (Calcein) during Chapter 4. The calcein-loaded MOFs will be used to investigate HeLa cervical cancer cells internalisation of the bare and surface-coated MOFs, using confocal microscopy and flow

cytometry, with ultimate aim of finding correlation between UiO-66 surface chemistry, cell internalisation pathways and therapeutic activity.

The use of carboxylate-containing drug molecules as modulators for synthesis of UiO-66 nanoparticles, in this study the anticancer metabolic target dichloroacetic acid, was studied during Chapter 2. DCA modulation in particular generates colloiddally-stable nanoparticles with high DCA-loading values, for which postsynthetic surface modifications will be illustrated during Chapter 5, following the protocols investigated during this chapter, in order to study the effect of surface chemistry on therapeutic activity and anticancer selectivity.

### 3.7 Experimental

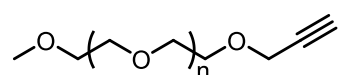
All reagents unless otherwise stated were obtained from commercial sources and were used without further purification.

#### 1-Azidodecane

1-Bromodecane (4 g, 0.018 mol, 1 eq) was dissolved in DMF (50 ml). Then, sodium azide (2.39 g, 0.036 mol, 2 eq) was added dropwise, and the mixture was allowed to react at 50°C overnight. After the solvent was evaporated, the remaining mixture was poured into water (100 ml) and extracted with DCM (3x 25 ml). The organic phase was further washed with water (2x 15 ml). The product was obtained pure as a slightly yellow oil (3.2 g, 97 % yield), whose spectroscopic data matched that found in the literature.<sup>49</sup>

**<sup>1</sup>H NMR** (400 MHz, DMSO)  $\delta$  0.86 (t,  $J$  = 6.9 Hz, 3H), 1.36 – 1.19 (m, 14H), 1.58 – 1.45 (m, 2H), 3.31 (t,  $J$  = 6.9 Hz, 2H); **<sup>13</sup>C NMR** (101 MHz, DMSO)  $\delta$  14.38, 22.55, 26.60, 28.70, 28.99, 29.13, 29.37, 29.38, 31.64, 51.10.

#### PEG550-propargyl



In a typical PEG550-propargyl synthesis ( $n = 11$ ), 1 eq (2 g, 3.64 mmol) of PEG550 methyl ether is dissolved in 50 ml anhydrous tetrahydrofuran (THF) under nitrogen. After that, 1.5 eq (236 mg, 5.46 mmol) of 60% NaH in mineral oil, and 1.5 eq (0.96 ml, 5.46 mmol) of propargyl bromide, are added. The solution is stirred overnight at room temperature. The resulting mixture is then filtrated and evaporated under vacuum. A clear, brown oil is obtained (1.225 g, 2.125 mmol, 59%).<sup>50</sup>

**<sup>1</sup>H NMR:** (500 MHz, DMSO)  $\delta$  3.25 (s, 3H), 3.47 – 3.40 (m, 4H), 3.54 – 3.48 (m, 44H), 3.68 (t,  $J$  = 1.8 Hz 1H), 4.15 (d,  $J$  = 2.4 Hz, 2H); **<sup>13</sup>C NMR:** (101 MHz, DMSO)  $\delta$  57.95, 58.51, 68.98, 70.25 (high intensity, polymeric chain), 71.75, 77.51, 80.79.

Note that triplet at 3.68 appears close the the polymer chain and determination is difficult.

**ESIMS:** calculated for  $C_4H_5O(C_2H_4O)_n C_2H_5O$ ,  $M+Na^+$  ( $n = 6$ )  $m/z = 401.2151$ ; found  $m/z = 401.2160$ , (found from  $n=6$  to  $n=17$ ).

### PEG2000-propargyl

In a typical PEG2000-propargyl synthesis ( $n = 44$ ), 1 eq (2 g, 1 mmol) of PEG2000 methyl ether is dissolved in 100 ml anhydrous tetrahydrofuran (THF) under nitrogen. After that, 1.5 eq (65 mg, 1.5 mmol) of 60% NaH in mineral oil, and 1.5 eq (0.25 ml, 1.5 mmol) of propargyl bromide, are added. The solution is stirred overnight at room temperature. The resulting mixture is then filtered and evaporated under vacuum. A white, hard powder is obtained (993 mg, 0.51 mmol, 51%).<sup>50</sup>

**<sup>1</sup>H NMR** (500 MHz, DMSO)  $\delta$  3.25 (s, 3H), 3.46 – 3.41 (m, 4H), 3.52 (s, 88H), 3.68 (t,  $J = 1.8$  Hz 1H), 4.15 (d,  $J = 2.4$  Hz, 2H); **<sup>13</sup>C NMR:** (101 MHz, DMSO)  $\delta$  57.95, 58.51, 68.98, 69.97, 70.05, 70.25 (high intensity, polymeric chain), 70.65, 71.75, 77.52, 80.79.

Note that triplet at 3.68 appears close to the polymer chain and determination is difficult.

No ionisation was observed in ESIMS, IR showed a stretch at  $\bar{\nu} = 2883$   $cm^{-1}$ , which is representative of the alkyne functionality.

### L1-dodecyne

1-Dodecyne (1.98 mmol, 327 mg, 1.2 equivalents) was dissolved in DCM (50 ml), DiPEA (4 mol%, 138  $\mu$ l), AcOH (4 mol%, 45  $\mu$ l) and CuI (2 mol%, 7.5 mg) were added, and the mixture stirred 15 minutes under nitrogen. Then, *p*-azidomethylbenzoic acid (L1) (1.65 mmol, 291 mg, 1 equivalent) was added to the reaction mixture, which was allowed to react overnight at room temperature under nitrogen atmosphere. Then, the reaction solvent was washed with water (3 x 15 ml) with an aqueous EDTA solution (2 x 15 ml) and with water (2 x 15 ml). Pure product was obtained as a white powder after evaporation of the organic solvent.

**<sup>1</sup>H NMR** (400 MHz, DMSO)  $\delta$  0.85 (t,  $J = 6.8$  Hz, 3H), 1.34 – 1.12 (m, 14H), 1.65 – 1.46 (m, 2H), 2.60 (t,  $J = 7.5$  Hz, 2H), 5.64 (s, 2H), 7.35 (d,  $J = 8.2$  Hz, 2H), 8.11 – 7.79 (m, 3H), 13.02 (s, 1H); **<sup>13</sup>C NMR** (101 MHz, DMSO)  $\delta$  14.40, 22.55, 25.43, 28.99, 29.15, 29.20, 29.35, 29.42, 31.74, 31.78, 52.65, 122.75, 128.26, 130.12, 130.18, 130.85, 141.57, 147.75.

### L2-decane

1-Azidodecane (2.5 mmol, 461 mg, 1.2 equivalents) was dissolved in DCM (50 ml), DiPEA (4 mol%, 146  $\mu$ l), AcOH (4 mol%, 48  $\mu$ l) and CuI (2 mol, 8.0 mg) were added, and the mixture stirred 15 minutes under nitrogen. Then, p-propargyloxybenzoic acid (L2) (2.1 mmol, 500 mg, 1 equivalent) was added to the reaction mixture, which was allowed to react overnight at room temperature under nitrogen atmosphere. Then, the reaction solvent was washed with water (3 x 15 ml) with an aqueous EDTA solution (2 x 15 ml) and with water (2 x 15 ml). Pure product was obtained as a white–yellowish powder after evaporation of the organic solvent.  $^1\text{H NMR}$  (400 MHz, DMSO)  $\delta$  12.63 (s, 1H), 8.25 (s, 1H), 7.89 (d,  $J = 8.7$  Hz, 2H), 7.12 (d,  $J = 8.7$  Hz, 2H), 5.22 (s, 2H), 4.36 (t,  $J = 7.1$  Hz, 2H), 1.92 – 1.65 (m, 2H), 1.23 (s, 14H), 0.85 (t,  $J = 6.9$  Hz, 3H);  $^{13}\text{C NMR}$  (101 MHz, DMSO)  $\delta$  204.59, 194.88, 162.04, 161.77, 131.71, 114.93, 49.85, 31.78, 31.73, 29.35, 29.32, 29.30, 29.10, 28.97, 28.82, 28.69, 26.26, 22.57, 14.41.

### Postsynthetic Surface Coordination of UiO-66-L1

In a typical postsynthetic surface coordination, UiO-66-L1 (250 mg) was dispersed by sonication in a solution of MeOH/Water (50 mL) containing 150 mg of the surface reagent in question during 20 minutes and stirred overnight. The NMOF was collected by centrifugation and washed by centrifugation with water (x2), acetone (x1), and methanol (x3).

### UiO-66-L2 Synthesis

UiO-66-L1 (300 mg) was dispersed in methanol (50 mL). Separately, a solution of L2 (300 mg) in methanol (50 mL) containing triethylamine (TEA, 0.3 mL) in order to extract the proton of L2 carboxylic acid and therefore favour the surface ligand exchange was prepared. As L2 is added in great excess compared to the amount of L1 present on UiO-66-L1 surface, it is expected to favour L2 incorporation over L1. Both solutions were mixed, sonicated for 15 minutes and heated to 60°C overnight. After cooling down and centrifugation, UiO-66-L2 was washed with MeOH (x5) and dried by centrifugation in order to remove unreacted materials.

### Postsynthetic Covalent Surface Modification of UiO-66-L1 and UiO-66-L2

In a typical CuAAC reaction performed on the modified MOF, 200 mg of the MOF in question, in this example UiO-66-L1, was placed in a 100 mL two neck round bottom flask. The MOF nanoparticles were dispersed in DCM (40 mL) by sonication (10 minutes). The solvent was bubbled with  $\text{N}_2$ , diisopropylethylamine (DiPEA, 304  $\mu$ L, 0.053 mmol, 4 mol %) was added, then acetic acid (92  $\mu$ L, 0.053 mmol, 4 mol %) was added, CuI (5 mg, 0.0264 mmol, 2 mol %) was added, and the mixture was stirred for 5 min under an  $\text{N}_2$  atmosphere. Propargyl-terminated Poly-L-Lactide, or the alternative surface reagent, was added dropwise. The

mixture was allowed to react for 24 h at room temperature under nitrogen. The precipitate was collected by centrifugation and washed with DCM (x2) and methanol (x3).

### **High-Resolution Electrospray Ionisation Mass Spectrometry (HRESI-MS) Sample Preparation**

NMOF samples were digested in an acidic aqueous solution, which was subsequently extracted with DCM. The organic phase was washed several times with an aqueous solution of Na<sub>2</sub>EDTA in order to remove the metals present in solution. The organic phase was then evaporated and dissolved in a 1:1 mixture of MeOH and MeCN.

### **Folic acid and Calcein Determination**

2 mg of sample was dispersed by sonication, heated in 10 mL of phosphate buffered saline (PBS) at pH = 7.4, and the dispersion was stirred for 48 h. The remaining precipitate was collected by centrifugation prior to folic acid or calcein absorbance measurement in PBS against a previously calculated calibration curve.

### **Dynamic Light Scattering (DLS) Measurements**

In a scintillation vial, dispersions with a concentration of 250 µg of MOF per mL of dispersant were prepared by sonication over 5 min prior to the measurement of each sample. Three recordings, consisting of 14 runs each, were performed consecutively at 37°C on the same sample for each measurement, at approximately 15 minute intervals. The waiting time between recordings was 5 seconds. No stirring was provided during the course of the experiment.

## **3.8 References**

1. J. L. Perry, K. G. Reuter, M. P. Kai, K. P. Herlihy, S. W. Jones, J. C. Luft, M. Napier, J. E. Bear and J. M. DeSimone, *Nano Letters*, 2012, **12**, 5304-5310.
2. J. Xie, C. Xu, N. Kohler, Y. Hou and S. Sun, *Advanced Materials*, 2007, **19**, 3163-3166.
3. R. Gref, A. Domb, P. Quellec, T. Blunk, R. H. Müller, J. M. Verbavatz and R. Langer, *Advanced Drug Delivery Reviews*, 2012, **64**, 316-326.
4. A. M. Torche, P. Le Corre, E. Albina, A. Jestin and R. Le Verge, *Journal of Drug Targeting*, 2000, **7**, 343-354.
5. A. Zimpel, T. Preiß, R. Röder, H. Engelke, M. Ingris, M. Peller, J. O. Rädler, E. Wagner, T. Bein, U. Lächelt and S. Wuttke, *Chemistry of Materials*, 2016, **28**, 3318-3326.
6. S. Nagata, K. Kokado and K. Sada, *Chemical Communications*, 2015, **51**, 8614-8617.

7. K. M. L. Taylor-Pashow, J. D. Rocca, Z. Xie, S. Tran and W. Lin, *Journal of the American Chemical Society*, 2009, **131**, 14261-14263.
8. G. Férey, C. Serre, C. Mellot-Draznieks, F. Millange, S. Surblé, J. Dutour and I. Margiolaki, *Angewandte Chemie*, 2004, **43**, 6296-6301.
9. X. Zhu, J. Gu, Y. Wang, B. Li, Y. Li, W. Zhao and J. Shi, *Chemical Communications*, 2014, **50**, 8779-8782.
10. R. Röder, T. Preiß, P. Hirschle, B. Steinborn, A. Zimpel, M. Höhn, J. O. Rädler, T. Bein, E. Wagner, S. Wuttke and U. Lächelt, *Journal of the American Chemical Society*, 2017, **139**, 2359-2368.
11. S. Wang, W. Morris, Y. Liu, C. M. McGuirk, Y. Zhou, J. T. Hupp, O. K. Farha and C. A. Mirkin, *Angewandte Chemie*, 2015, **54**, 14738-14742.
12. S. Liu, L. Zhai, C. Li, Y. Li, X. Guo, Y. Zhao and C. Wu, *ACS Applied Materials and Interfaces*, 2014, **6**, 5404-5412.
13. S. Wang, C. M. McGuirk, M. B. Ross, S. Wang, P. Chen, H. Xing, Y. Liu and C. A. Mirkin, *Journal of the American Chemical Society*, 2017, **139**, 9827-9830.
14. A. F. Gross, E. Sherman, S. L. Mahoney and J. J. Vajo, *The Journal of Physical Chemistry A*, 2013, **117**, 3771-3776.
15. M. Kondo, S. Furukawa, K. Hirai and S. Kitagawa, *Angewandte Chemie*, 2010, **49**, 5327-5330.
16. J. Park, Z. U. Wang, L.-B. Sun, Y.-P. Chen and H.-C. Zhou, *Journal of the American Chemical Society*, 2012, **134**, 20110-20116.
17. M. Kim, J. F. Cahill, H. Fei, K. A. Prather and S. M. Cohen, *Journal of the American Chemical Society*, 2012, **134**, 18082-18088.
18. T. Li, M. T. Kozlowski, E. A. Doud, M. N. Blakely and N. L. Rosi, *Journal of the American Chemical Society*, 2013, **135**, 11688-11691.
19. N. Yanai and S. Granick, *Angewandte Chemie*, 2012, **51**, 5638-5641.
20. X. Liu, Y. Li, Y. Ban, Y. Peng, H. Jin, H. Bux, L. Xu, J. Caro and W. Yang, *Chemical Communications*, 2013, **49**, 9140-9142.
21. W. Morris, W. E. Briley, E. Auyeung, M. D. Cabezas and C. A. Mirkin, *Journal of the American Chemical Society*, 2014, **136**, 7261-7264.
22. X. Gao, M. Zhai, W. Guan, J. Liu, Z. Liu and A. Damirin, *ACS Applied Materials and Interfaces*, 2017, **9**, 3455-3462.
23. S. J. Garibay and S. M. Cohen, *Chemical communications*, 2010, **46**, 7700-7702.
24. L.-L. Tan, N. Song, S. X.-A. Zhang, H. Li, B. Wang and Y.-W. Yang, *Journal of Materials Chemistry B*, 2016, **4**, 135-140.
25. S. Jung, Y. Kim, S. J. Kim, T. H. Kwon, S. Huh and S. Park, *Chemical Communications*, 2011, **47**, 2904-2906.
26. D. Peer, J. M. Karp, S. Hong, O. C. Farokhzad, R. Margalit and R. Langer, *Nature Nanotechnology*, 2007, **2**, 751-760.
27. W. J. Rieter, K. M. L. Taylor and W. Lin, *Journal of the American Chemical Society*, 2007, **129**, 9852-9853.
28. J. Lu, M. Liong, Z. Li, J. I. Zink and F. Tamanoi, *Small*, 2010, **6**, 1794-1805.
29. E.-J. Park and K. Park, *Toxicology Letters*, 2009, **184**, 18-25.
30. Y. Yu, Y. Li, W. Wang, M. Jin, Z. Du, Y. Li, J. Duan, Y. Yu and Z. Sun, *PLoS One*, 2013, **8**, e61346.
31. J. M. Scott, *The Proceedings of the Nutrition Society*, 1999, **58**, 441-448.

32. J. Zemleni and D. Mock, *The Journal of Nutritional Biochemistry*, 1999, **10**, 128-138.
33. J. Hirsh, T. E. Warkentin, S. G. Shaughnessy, S. S. Anand, J. L. Halperin, R. Raschke, C. Granger, E. M. Ohman and J. E. Dalen, *Chest*, 2001, **119**, 64-94.
34. C. Shao, X. Wang, Q. Zhang, S. Luo, J. Zhao and Y. Hu, *The Journal of organic chemistry*, 2011, **76**, 6832-6836.
35. F. Rouquerol, J. Rouquerol and K. Sing, in *Adsorption by Powders and Porous Solids*, Academic Press, London, 1999, 191-217.
36. A. A. Ignatius and L. E. Claes, *Biomaterials*, 1996, **17**, 831-839.
37. K. Yin Win and S.-S. Feng, *Biomaterials*, 2005, **26**, 2713-2722.
38. E. Bellido, M. Guillevic, T. Hidalgo, M. J. Santander-Ortega, C. Serre and P. Horcajada, *Langmuir*, 2014, **30**, 5911-5920.
39. E. Bellido, T. Hidalgo, M. V. Lozano, M. Guillevic, R. Simón-Vázquez, M. J. Santander-Ortega, Á. González-Fernández, C. Serre, M. J. Alonso and P. Horcajada, *Advanced Healthcare Materials*, 2015, **4**, 1246-1257.
40. S. Sene, M. T. Marcos-Almaraz, N. Menguy, J. Scola, J. Volatron, R. Rouland, J.-M. Grenèche, S. Miraux, C. Menet, N. Guillou, F. Gazeau, C. Serre, P. Horcajada and N. Steunou, *Chem*, 2017, **3**, 303-322.
41. C. Orellana-Tavra, S. Haddad, R. J. Marshall, I. Abánades Lázaro, G. Boix, I. Imaz, D. Maspoch, R. S. Forgan and D. Fairen-Jimenez, *ACS Applied Materials and Interfaces*, 2017, **9**, 35516-35525.
42. C. Orellana-Tavra, R. J. Marshall, E. F. Baxter, I. A. Lazaro, A. Tao, A. K. Cheetham, R. S. Forgan and D. Fairen-Jimenez, *Journal of Materials Chemistry B*, 2016, **4**, 7697-7707.
43. J. Yang, X. Chen, Y. Li, Q. Zhuang, P. Liu and J. Gu, *Chemistry of Materials*, 2017, **29**, 4580-4589.
44. K. A. Cychoz and A. J. Matzger, *Langmuir*, 2010, **26**, 17198-17202.
45. J. B. DeCoste, G. W. Peterson, H. Jasuja, T. G. Glover, Y.-G. Huang and K. S. Walton, *Journal of Materials Chemistry A*, 2013, **1**, 5642-5650.
46. X. Huang and C. S. Brazel, *Journal of Controlled Release*, 2001, **73**, 121-136.
47. C. Orellana-Tavra, E. F. Baxter, T. Tian, T. D. Bennett, N. K. H. Slater, A. K. Cheetham and D. Fairen-Jimenez, *Chemical Communications*, 2015, **51**, 13878-13881.
48. M. H. Teplensky, M. Fantham, P. Li, T. C. Wang, J. P. Mehta, L. J. Young, P. Z. Moghadam, J. T. Hupp, O. K. Farha, C. F. Kaminski and D. Fairen-Jimenez, *Journal of the American Chemical Society*, 2017, **139**, 7522-7532.
49. M. H. Ryu, J. W. Choi, H. J. Kim, N. Park and B. K. Cho, *Angewandte Chemie*, 2011, **50**, 5737-5740.
50. X. P. He, Y. L. Zeng, Y. Zang, J. Li, R. A. Field and G.-R. Chen, *Carbohydrate Research*, 2016, **429**, 1-22.

## Chapter 4

# Tuning the Endocytosis Pathways of UiO-66 by Surface Modifications

This Chapter is adapted in part from the following publications:

“Zirconium Metal-Organic Frameworks in Drug Delivery and Biomedicine”

Submitted

**I. Abánades Lázaro** and R. S. Forgan

“Selective Surface PEGylation of UiO-66 Nanoparticles for Enhanced Stability, Cell Uptake and pH Responsive Drug Delivery”

*Chem*, **2017**, 2, 561–578. (DOI: 10.1016/j.chempr.2017.02.005.)

**I. Abánades Lázaro**, S. Haddad, S. Sacca, C. Orellana-Tavra, D. Fairen-Jimenez and R. S. Forgan

“Mechanistic Investigation into the Selective Anticancer Cytotoxicity and Immune System Response of Surface Functionalised, Dichloroacetate-Loaded, UiO-66 Nanoparticles”

*ACS Appl. Mater. Interfaces*, **2018**, 10, 6, 5255-5268 (DOI: 10.1021/acsami.7b17756)

**I. Abánades Lázaro**, S. Haddad, J. Rodrigo-Muñoz, C. Orellana-Tavra, V. del Pozo, D. Fairen-Jimenez, and Ross S. Forgan

## Table of Contents

<b>Chapter 4</b> .....	153
Table of Contents .....	154
4.1 Introduction to Cellular Internalisation .....	155
4.1.1. Cellular Internalisation of MOFs .....	157
4.2 Aims .....	164
4.3. Postsynthetic Surface Functionalisation of Calcein-Loaded Samples .....	165
4.4 The Effect of PEG Coating on UiO-66 Calcein Release Kinetics.....	169
4.5 Endocytosis Efficacy of MOFs .....	173
4.6 Endocytosis Routes of MOFs .....	175
4.7 Confocal Fluorescence Microscopy .....	181
4.8 Conclusions .....	184
4.9 Experimental.....	186
4.10 References .....	188

## 4.1 Introduction to Cellular Internalisation

To be efficient DDSs, MOFs should be easily internalised by the cells that are intended to be treated and able to release their cargo in intracellular conditions. Importantly, the DDS should avoid immune system recognition, and thus not be internalised by immune system cells such as macrophages.<sup>1, 2</sup> Nanoparticle uptake by cells depends on many factors, including size, morphology and surface chemistry among others,<sup>3-8</sup> and attempts have been made to enhance uptake and also control the endocytosis mechanisms of MOFs.<sup>9, 10</sup>

Generally, molecules enter cells by passive diffusion, whereas nanoparticles are generally internalised by cells through active transport (energy-dependent) such as endocytosis. However, if small enough (< 20 nm), nanoparticles can also be internalized by passive diffusion.<sup>7, 11</sup>

Endocytosis can be categorised into phagocytosis (i.e. “cell eating”) and pinocytosis (i.e. “cell drinking”).<sup>5, 12, 13</sup> Phagocytosis refers to the process of engulfing large particles and is carried out by macrophages and neutrophils whereas pinocytosis refers to the internalization of molecules and small particles in the fluid phase and is carried out by all eukaryotic cells, and includes clathrin-mediated, caveolae-mediated, non-mediated endocytosis, and macropinocytosis among other routes (Figure 4.1).<sup>5</sup>

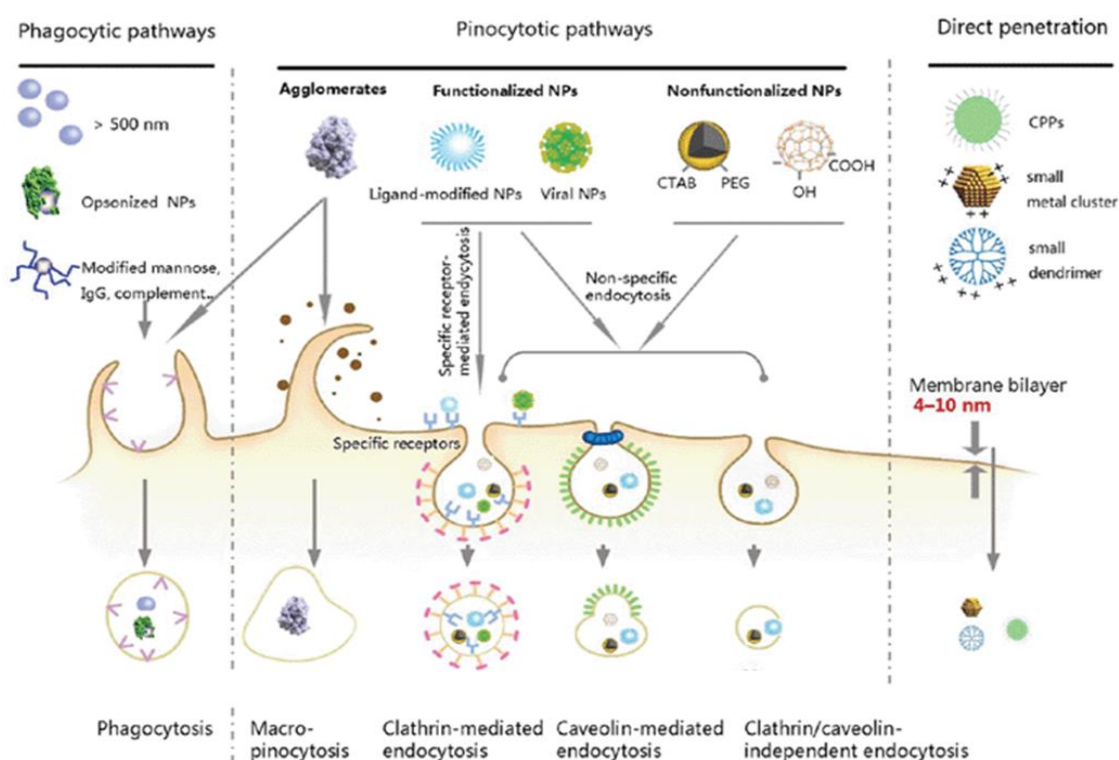


**Figure 4.1.** Representation of cell internalisation pathways.<sup>5</sup>

Clathrin-mediated endocytosis is the most understood endocytosis pathway and is used by all known eukaryotic cells, where receptors on the cell surface recognize the cargo and then internalize it into protein- (clathrin) coated vesicles, called early endosomes.<sup>14-16</sup> These early endosomes then mature into late endosomes and finally fuse with lysosomes, causing the degradation of the DDS along with its loaded cargo, thus voiding its therapeutic effect. Caveolae-mediated endocytosis is associated with the formation of lipid raft-enriched flask shape invaginations coated with caveolin.<sup>17, 18</sup> Particles internalized via caveolae-mediated endocytosis can be delivered to different locations in the cell. For instance, the formed vesicles can fuse with early endosomes and then with lysosomes for further degradation as in the case of clathrin-mediated endocytosis, but more interestingly, the internalized particles can also escape the early endosome, by the alternative formation of a pH neutral compartment called caveosome that will release its content to the cytosol in a more efficient way, avoiding lysosomal degradation (Figure 4.2). Thus, DDS internalised by caveole-mediated endocytosis are more likely to be therapeutically efficient than those internalised by the clathrin-mediated route as consequence of the faster cytosolic release, allowing cargo to reach the cells' organelles in a more effective way.<sup>8, 17</sup>

Macropinocytosis is a non-selective process in which cells uptake large quantities of fluids. Finally, in clathrin and caveolae-independent endocytosis- which is found in almost all cell types- particles are internalized non-specifically via vesicles.<sup>19</sup>

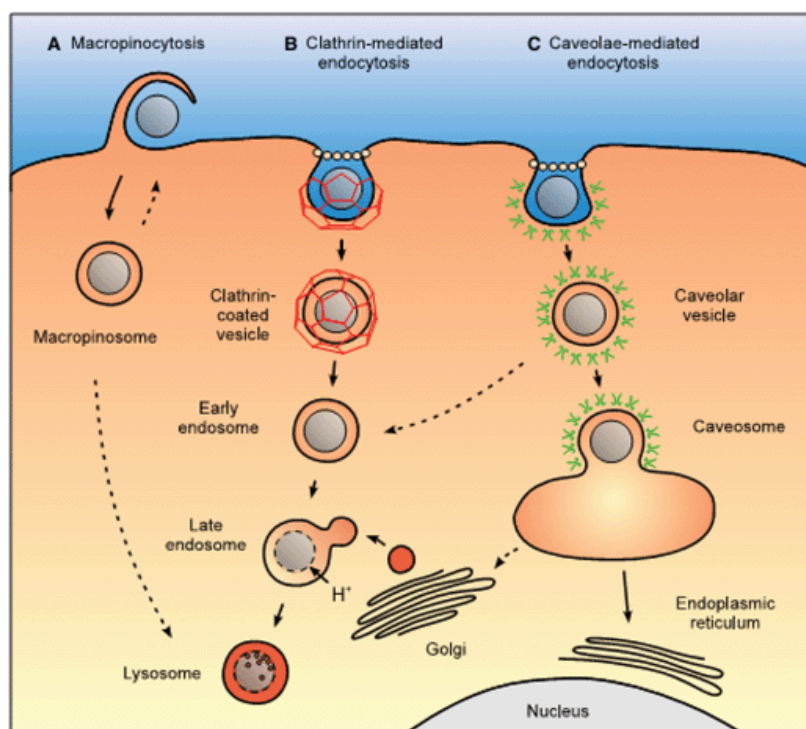


**Figure 4.2.** Routes of cellular internalisation and subsequent intracellular localisation.<sup>8</sup>

#### 4.1.1. Cellular Internalisation of MOFs

For MOFs, fluorescent linkers, cargo molecules or fluorescent active metal clusters are usually used to monitor endocytosis through confocal microscopy and fluorescence-activated cell sorting (FACS).

Xie and co-workers investigated the internalisation of UiO-66 coated with carboxyl-functionalised diiodo-substituted BODIPY (UiO-PDT) by B16F10 mouse melanoma cells for different incubation times (0.5, 2 and 4 hours) using FACS, and compared it with the mean fluorescence intensity when cells were incubated with the same concentration of free linker ( $I_2$ -BDP), which exhibits characteristic fluorescence.<sup>20</sup> A dose-response behaviour for the uptake of both was found, which was higher at 2 hours incubation time in the case of UiO-PDT (1.5 fold increase). By confocal fluorescence microscopy it was observed that the red fluorescence was mainly located in the cytoplasm of B16F10 cells for both cases. Although the authors did not investigate the endocytosis routes of internalisation, these results could be a consequence of either MOF internalisation through the caveolae-mediated route, MOF degradation allowing linker internalisation through passive uptake during the course of the experiment, or a conjunction of both.

Internalisation of UiO-66 coated with fluorescent molecules of flavin mononucleotide (UiO-66-FMN) by HepG2 human liver carcinoma cells has been investigated after 4 and 12 hours incubation time, finding that after 4 hours more than 80% of the cell population have high fluorescent mean intensity, while after 12 hours only a slightly increase is found.<sup>21</sup> These results indicate that UiO-66-FMN cell uptake occurs rapidly during the first 4 hours, after which the cell uptake rate decreases. Through confocal microscopy, high green fluorescence in the cells cytoplasm was observed.

Zhou and co-workers investigated HeLa human cervical cancer cells uptake of a porphyrinic MOF (PCN-224) by varying particle size (Figure 4.3), with the aim to enhance internalisation and cytotoxicity through passive targeting,<sup>22</sup> based on the fact that nanoparticles accumulate in cancer tissue due to the EPR effect.<sup>23</sup> Confocal microscopy showed that the NMOF was co-localised with the lysosomes and mitochondria, while no nucleus co-localisation was found (Figure 4.3a). Note that further studies, such as mitochondria isolation and content determination by ICP-MS, should be performed to unequivocally confirm mitochondria co-localisation. The authors analysed the zirconium content by ICP-MS of digested cells, which were incubated with samples of the MOF of varying size (30, 60, 90, 140, and 190 nm) over different times (0-40 hours). The highest cell uptake was found for nanoparticles of 90 nm diameter, and generally reached a plateau after 12 hours of incubation (Figure 4.3b and c).<sup>22</sup>

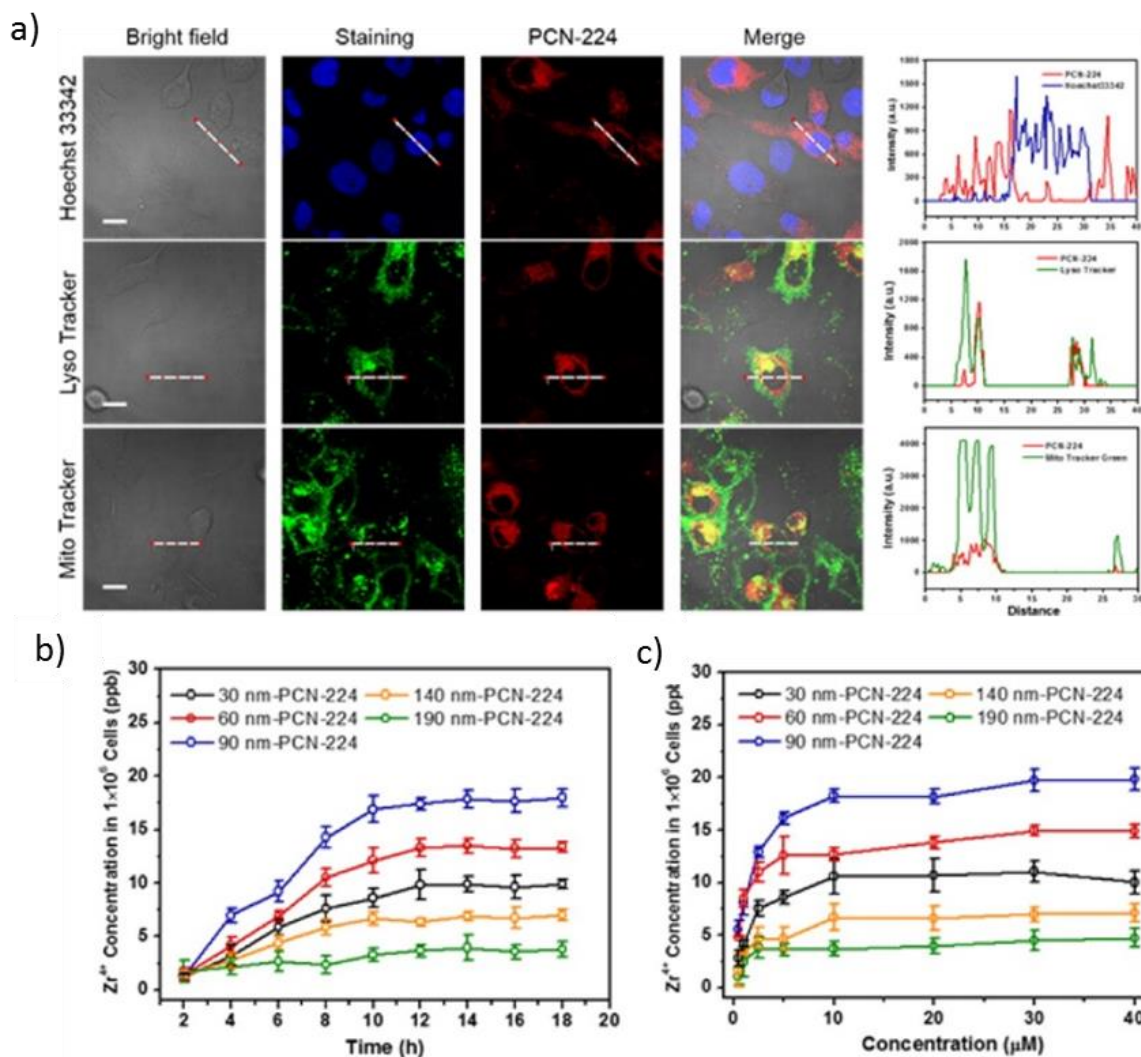


**Figure 4.3** a) Subcellular localization of PCN-224 nanoparticles by staining with organelle markers, Hoechst 33342, Lyso Tracker, and Mito Tracker green. b) Cellular uptake of PCN-224 samples with different sizes at various incubation time. Concentration = 20 μM. (c) Cellular uptake of different sized PCN-224 nanoparticles at various concentrations. Incubation time = 24 h. Data are based on ICP analysis of the Zr concentration internalized into HeLa cells. Data are means ± s.d. ( $N = 3$ ).<sup>22</sup>

Endosomal escape is a key feature for efficient siRNA delivery. Lin and co-workers performed co-localisation studies of siRNA@UiO-66 with human ovarian cancer SKOV-3 cells using confocal laser assisted microscopy, demonstrating siRNA and lysosome separation after 2 hours of incubation time.<sup>24</sup> The authors postulate that when siRNA@UiO gets entrapped in the endosomes, the presence of high endogenous phosphate concentration, and the acidic pH of those will result in structure degradation, and zirconium ions will disrupt the endosome structure, thus facilitating siRNA release. The authors did not study the endocytosis routes of cell internalisation, for in which the NMOF is internalised through caveolae-mediated route,<sup>17</sup> could also escape endosome by forming a caveosome that will release its cargo to the cytosol.

SiRNA uptake was remarkably higher (11 fold increase) when it was attached to the NMOF structure compared to free siRNA (Figure 4.4 a and b).<sup>24</sup>

Surface modification has been used to enhance endocytosis efficiency and tune the cell uptake routes of MOFs. Mirkin et al incubated DNA-modified UiO-66 with HeLa cells for 24 hours, with fluorescent Tamra functionality on the DNA showing that conjugation to the MOF resulted in enhanced uptake of the DNA sequence (Figure 4.4 c and d).<sup>25</sup> ICP-MS analysis of the zirconium content of the cells when incubated with the bare MOFs or DNA-functionalised MOFs, showed enhanced uptake for the UiO-66-DNA conjugates compared to the bare MOF, which was more remarkable for 19 nm sized nanoparticles than for 14 nm nanoparticles.

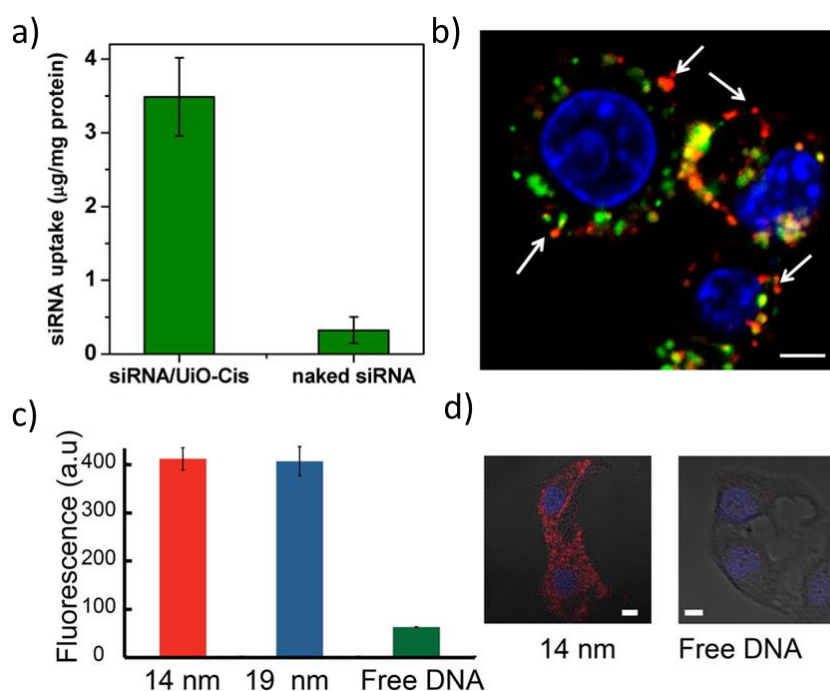


**Figure 4.4.** (a) siRNA/UiO-Cis significantly increase (by >11-fold) the siRNA uptake amount compared to naked siRNA ( $n = 3$ ). (b) siRNA (TAMRA-labeled, red) successfully escaped from endosomes as evidenced by the separation of green and red fluorescence (white arrows). Endosome/lysosome and nuclei were stained with LysoTracker Green and DAPI, respectively. Bar represents 5 µm.<sup>24</sup> (c) Cell uptake by flow cytometry of DNA-modified UiO-66. (d) Confocal microscopy of cells treated with 14 nm MOF nanoparticle–DNA conjugates and with free DNA. Scale bar = 10 µm.<sup>25</sup>

In 2016, Fairen-Jimenez et al first reported the study of internalisation of calcein-loaded UiO-66 by HeLa cells.<sup>10</sup> The authors loaded the MOFs with calcein, a fluorescent molecule not able to efficiently cross the cell membrane by itself, in order to track the MOFs internalisation routes by FACS, and utilised inhibitors to suppress the various endocytosis routes, including nystatin<sup>26</sup> as a caveolae-mediated inhibitor, chlorpromazine<sup>27</sup> and sucrose<sup>28</sup> as clathrin-mediated inhibitors and rottlerin as macropinocytosis inhibitor.<sup>29</sup> It is important to consider that

sucrose also inhibits non-mediated endocytosis routes. cal@UiO-66 cell uptake was drastically decreased when cells were incubated with the MOFs at 4 °C compared to 37 °C, confirming that cell internalisation occurs predominantly by active transport. The authors observed that UiO-66 generally undergoes cell internalisation through clathrin-mediated endocytosis, with minor contributions of the macropinocytosis process. Only a minor contribution of the caveolae route was found when the size of the particles was increased from 150 nm to 260 nm.<sup>10</sup> The authors performed fluorescence co-localisation studies in which they observed a lower degree of lysosome-MOF co-localisation for the bigger nanoparticles, correlating well with the proposed endocytosis routes.

Fairen-Jimenez and co-workers further studied HeLa cells internalisation routes of the UiO isorecticular series of Zr MOFs- including UiO-66 and its bromo, nitro and amino derivatives, Zr-naphthalene and UiO-67- indicating the effect of linker substitution, and thus external surface chemistry presented by the particles, together with particle size, on endocytosis efficiency and routes.<sup>9</sup>

At first, a study of cal@UiO-66 internalisation efficacy and routes, based on particle size (50, 75, 92, 260 and 652 nm), revealed that UiO-66 MOFs with a size of 50 nm are the most efficiently internalised, and the only which its uptake is not inhibited by chlorpromazine, meaning that its internalisation does not occur by clathrin-mediated endocytosis. As only significant inhibition was found by sucrose, the results suggests that 50 nm UiO-66 is mainly internalised by non-mediated endocytosis. The bigger MOFs, on the other hand, are internalised by clathrin-mediated endocytosis (ca.60 % inhibition) with only minor contribution of the caveolae-mediated route (ca. 20 % decrease in uptake).<sup>9</sup>

Functionalised MOFs with more polar surfaces, such as UiO-66-NO<sub>2</sub>, were taken up by HeLa cells in greater quantities, as determined by FACS using calcein-loaded nanoparticles. These more polar MOFs were predominantly internalised by clathrin-mediated endocytosis, in contrast to less polar, unfunctionalised materials (e.g. Zr-naphthalene and UiO-67), which had lower overall uptake, but primarily by caveolae-mediated endocytosis.<sup>9</sup>

Fairen-Jimenez et al reported the HeLa cell internalisation routes of NU-1000 and compared it to amorphised NU-901.<sup>30</sup> Whilst pristine, calcein loaded NU-1000 was taken up primarily by clathrin-mediated routes, with potentially a small contribution by caveolae-mediated uptake, the amorphised sample showed a more significant decrease in cellular fluorescence when incubated with nystatin but also with chlorpromazine, suggesting caveolae-mediated uptake with some contribution from clathrin-mediated endocytosis. The authors also visualised cell internalisation and intracellular location of the MOFs using structured illumination microscopy

(SIM), finding the NMOFs to be located mainly at vesicles. They observed that NMOFs start to be internalised after one hour, increasing the uptake gradually up to 24 hours.

PCN-223 is the only zirconium MOF to date for which its intracellular bio-stability has been measured.<sup>31</sup> The authors incubated HeLa and human hepatocarcinoma SMMC-7721 cells with bare nanoPCN-223, PCN-223-PBLs and TCPP, the linker of the NMOF structure, which is itself fluorescent and thus allows tracking of MOFs inside the cells. Passive uptake of free TCPP lead to low, well-distributed red fluorescence confined to the cytoplasm, while when cells were incubated with solutions of the bare MOF, only traces of nanoPCN-223 were observed as well-defined dots in the lysosomal locations inside the cells. Free TCPP located uniformly in the cell could also be observed, indicating possible degradation of the MOF sample in growth media. In contrast, they found that PBLs-coated nanoPCN-223 is only located in the lysosomes with no evidence of released TCPP in the cytoplasm. FACS showed that although TCPP undergoes passive diffusion into the cell and the mean fluorescence intensity is similar to bare nanoPCN-223, after coating with PBLs the cell uptake efficiently is enhanced ca. 1.7 fold within the first 4 hours of incubation, as no increase in fluorescence was found after longer incubation times of 12 and 24 hours.<sup>31</sup>

Targeting peptides have also been utilised to enhance MOF uptake by particular cell lines. DOX@UiO-66-Py-PGA-PEG-F3 (where the fluorescence of doxorubicin serves to track NMOFs location inside the cell) internalisation by human breast adenocarcinoma MCA-MB-231 cells was found to be remarkably higher than DOX@UiO-66-Py-PGA-PEG, as determined by flow cytometry measurements and confocal microscopy (Figure 4.5).<sup>32</sup> This is so because MCA-MB-231 cells over express the nucleolin receptor (n+), which is targeted by the F3 peptide attached to the MOF. In contrast, both targeted and non-targeted NMOFs were internalised considerably less by L929 mouse fibroblast cells, which do not over express the nucleolin receptor (n-).<sup>33</sup> DOX fluorescence was mainly located in the cytoplasm, with some co-localisation in the lysosome when FITC-modified MOFs were examined. The authors observed that DOX@UiO-66-Py-PGA-PEG-F3 internalisation plateau occurs within the first 0.25 h of incubation, in which a similar amount of internalised MOF and MOF binding to the cells surface was found. It was found that once internalised, during the next 24 hours 30% of the NMOF can be externalised by cells through exocytosis processes.<sup>32</sup>

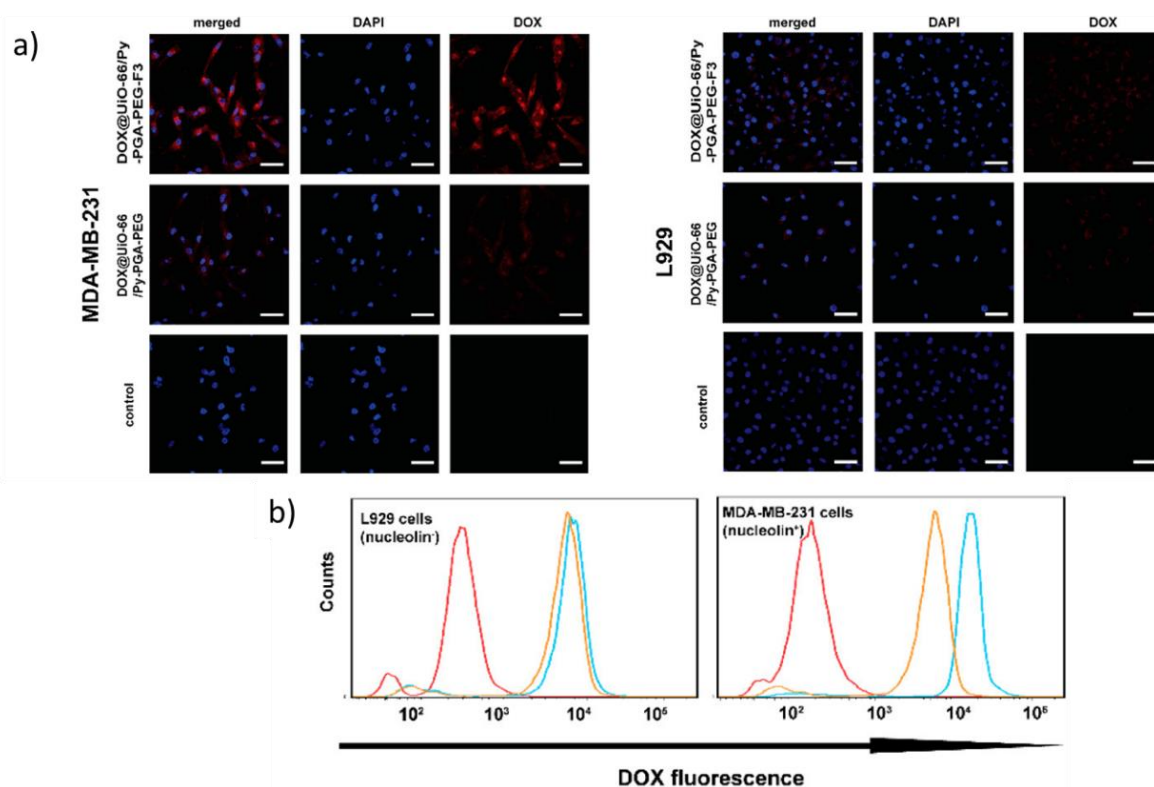


**Figure 4.5.** *In vitro* evaluation of UiO-66/Py-PGA-PEG conjugates. (a) Representative confocal fluorescence microscopy images of MDA-MB-231 (nucleolin<sup>+</sup>) and L929 cells (nucleolin<sup>-</sup>) incubated with DOX@UiO-66/Py-PGA-PEG-F3 and DOX@UiO-66/Py-PGA-PEG (both containing 50  $\mu\text{g}/\text{mL}$  of DOX). Scale bar: 20  $\mu\text{m}$ . (b) Flow cytometry analysis of DOX@UiO-66/Py-PGA-PEG-F3 (blue) and DOX@UiO-66/Py-PGA-PEG (orange) in MDA-MB-231 and L929 cells (incubation time: 0.5 h).<sup>32</sup>

HeLa cells internalisation of Zr-fum coated with various fluorescent peptides through imidazole his-tag coordination has been reported, and it is illustrated in Figure 4.6.<sup>34</sup> The authors also investigated the cellular uptake of model peptides and proteins attached to Zr-fumarate and compare it to the uptake of the free moiety. For example, they observed a 20 fold increase in the mean cell internal fluorescence of HeLa cells when incubated with Zr-fum-H<sub>6</sub>CF compared to when cells were incubated with a solution of the same concentration of free peptide in growth media, highlighting the efficiency of Zr-fum to internalise biomolecules not able to do it efficiently by themselves. A 30-fold increase in cell internalisation was found for the peptide H<sub>6</sub>-GFP when it was attached to Zr-fumarate. They investigated the use of multifunctional Zr-fumarate to simultaneously internalise two peptides, H<sub>6</sub>-GFP and H<sub>6</sub>-Tf\* (a transferrin modified peptide). Co-localisation of both peptides was observed by confocal microscopy, whereas in contrast to free H<sub>6</sub>-GFT, H<sub>6</sub>-Tf\* can be internalised by HeLa cells, as those over express the transferring receptor. However, when attached to Zr-fum, its uptake increased 5 times.

The endocytosis pathways of Zr-fum-H<sub>6</sub>-GFP were studied.<sup>34</sup> The cells were pre-incubated during 30 minutes with different concentration of the various inhibitors – In this case amiloride

to suppress macropinocytosis, genistein to inhibit caveolae-mediated endocytosis, and chlorpromazine to inhibit clathrin-mediated uptake – and then incubated with the NMOFs during 2 hours. They found that the peptide-coated NMOFs are mainly internalised by macropinocytosis, although minor contributions of the caveolae-mediated route is also observed. In general, higher levels of inhibition were found when cells were pre-treated with higher concentration of the inhibitors.

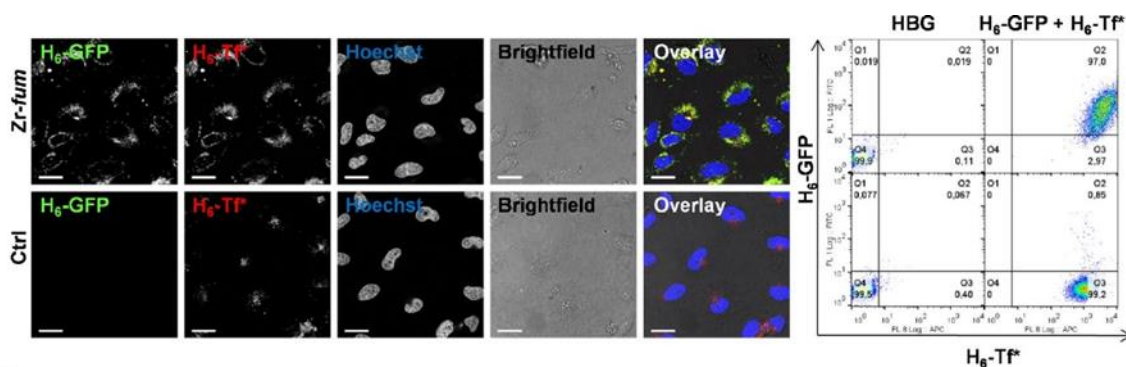


**Figure 4.6.** Simultaneous cellular uptake of fluorescent proteins H<sub>6</sub>-GFP and H<sub>6</sub>-Tf\* mediated by Zr-fum NPs. (a) Cellular uptake of Zr-fum/H<sub>6</sub>-GFP+H<sub>6</sub>-Tf\* (upper row) or control without MOF NPs (lower row). CLSM left to right: green fluorescence of H<sub>6</sub>-GFP, red fluorescence of H<sub>6</sub>-Tf\*, nuclear staining with Hoechst dye, brightfield picture, overlay of all four channels, yellow color indicates colocalization of H<sub>6</sub>-GFP and H<sub>6</sub>-Tf\*. Flow cytometry analysis: HBG (left) or H<sub>6</sub>-GFP + H<sub>6</sub>-Tf\* (right) with Zr-fum MOF NPs (upper row) or Ctrl without MOF NPs (lower row). Scale bar: 25 µm.<sup>34</sup>

Uptake by immune cells is also of great importance when considering an *in vivo* treatment,<sup>1,2</sup> but examples of MOF internalisation by macrophages in the literature are quite rare, and further work is clearly needed to understand this process and enhance NMOFs potential as DDS. Considering the amount of work into studying and enhancing cell internalisation of Zr MOFs by endocytosis processes, there is also very little research into determining and understanding the exocytosis processes, which may also play an important role in their therapeutic efficiency. The exocytosis of other nanoparticulate materials has been studied *in vitro*, and shown that it tends to occur over longer incubation times, especially if removing the nanoparticles present in the incubation media.<sup>35</sup> Being able to extend the time that the nanoparticles are present inside cells, or suppressing exocytosis processes while enhancing endocytosis processes, could be of vital importance to enhance therapeutic effect.

## 4.2 Aims

Understanding the effect of surface chemistry of MOFs on their cell internalisation routes and efficacy is imperative for their development as efficient DDSs, as it is strictly related with their therapeutic efficiency, providing insights that might reduce early-stage animal testing, while enhancing their efficacy.

In order to further study cancer cells internalisation of coated and uncoated UiO-66, both UiO-66-L1 and UiO-66-L2 will be postsynthetically loaded with calcein, a fluorescent molecule, and the former postsynthetic surface modification protocols described during Chapter 3 will be applied to the calcein loaded MOFs. Calcein has been selected as molecular probe for MOFs internalisation, due to the fact that its hydrophilic nature hinders its cellular internalisation unless it is loaded into a DDS. Thus, if calcein is released in growth media during the course of the experiment, false positives in cell internalisation will not be observed.

Calcein release from the bare and PEGylated MOFs will be investigated at pH 7.4 and pH 5.5, in order to study calcein release kinetics from the MOF in simulated extracellular conditions (pH 7.4) and intracellular conditions (pH 5.5). Particularly, extracellular pH (i.e blood current) is 7.4, while healthy and cancerous cells intracellular pH is around 6.8 and 5.5 respectively.

The cellular internalisation efficacy of bare and coated calcein-loaded UiO-66 MOFs- with PEG chains of different sizes, PolyLactide, PNIPAM, Heparin, Biotin and Folic acid- will be analysed by FACS and compared to the uptake of a solution of free calcein, with the ultimate aim of determining more desirable coatings to enhance cell internalisation, as a way of indirect cancer targeting, due to the fact that nanoparticles accumulate in cancerous over healthy tissue due to the EPR effect.

The effect of surface coating on endocytosis routes will be studied by FACS using inhibitors for certain routes. DDS internalised through caveolae-mediated endocytosis have been proven to be more efficient to deliver their cargo to the cellular organelles, and thus can be more therapeutically active.<sup>17</sup> Additionally, the contribution of active and inactive transport will be studied by incubating HeLa cells with MOFs at 37°C and at 4°C, where the metabolic activity is attenuated. The findings described during this chapter will be related to the therapeutic efficacy of the MOFs during Chapter 5.

Cellular internalisation of cal@UiO-66-L1, cal@UiO-66-L1-PEG550 and cal@UiO-66-L1-PEG2000 will be also studied by confocal microscopy, in order to visually determine the cellular integrity of the cells after MOFs internalisation and the MOFs location inside the cells.

### 4.3. Postsynthetic Surface Functionalisation of Calcein-Loaded Samples

Calcein was selected as a fluorescent molecule to track the NMOFs inside cells, in order to study endocytosis fates and pathways (Sections 4.5 and 4.6). Calcein's hydrophilicity does not allow it to efficiently cross the cell membrane, and thus intracellular cytoplasmic fluorescence is significantly increased when calcein is incorporated into a carrier.<sup>9</sup> UiO-66-L1 and UiO-66-L2 were postsynthetically loaded with calcein by soaking the MOFs in a calcein solution in methanol (Section 4.9), and their surfaces subsequently modified either using the click modulation method or postsynthetic external surface ligand exchange (PS) (Figure 4.7), ensuring all samples were of similar particle size as they originated from one batch of UiO-66-L1.

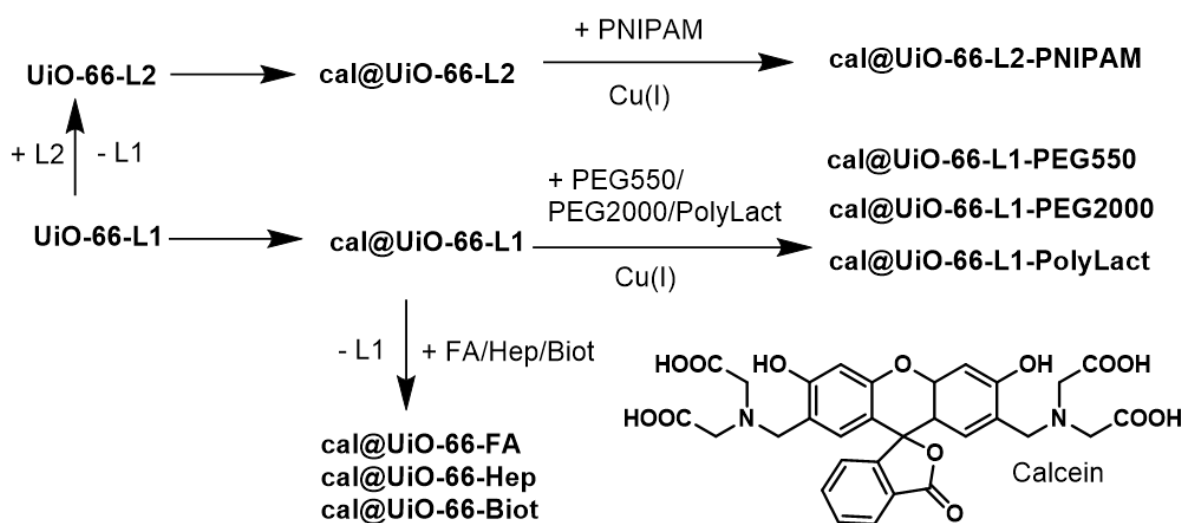


**Figure 4.7.** Synthesis of calcein-loaded, surface modified MOFs obtained through postsynthetic exchange (PS) and click modulation.

The samples retained their crystallinity after calcein loading and subsequent surface modification, as confirmed by PXRD.<sup>36, 37</sup>

Figure 4.8 shows the thermal decomposition of cal@UiO-66-L1 compared to free calcein, UiO-66-L1 and UiO-66-AcOH. For cal@UiO-66-L1, the absence of a significant calcein decomposition step at 200 °C, together with its bigger size compared to the pore cavity, suggests that calcein is attached to the zirconium clusters present in the surface and defect sites through its carboxylic acid groups. The multi-step degradation profile makes quantitative calcein content analysis by TGA difficult, however, it is clearly present.

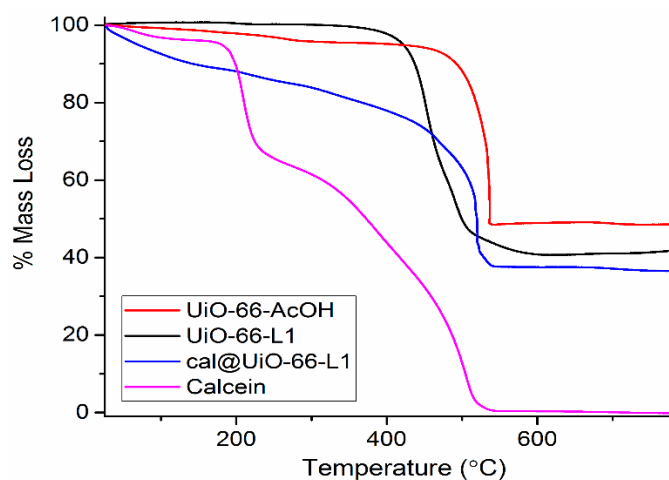


**Figure 4.8.** TGA profiles of cal@UiO-66-L1 in air and its comparison with UiO-66-AcOH, UiO-66-L1 and calcein.

Adsorption isotherms ( $N_2$ , 77 K) were used to investigate the mode of calcein incorporation, showing only a minor decrease in surface area and pore volume from  $S_{BET}=1565 \text{ m}^2\text{g}^{-1}$  and pore volume =  $0.762 \text{ ccg}^{-1}$  for UiO-66-L1 to  $S_{BET} = 1002 \text{ m}^2\text{g}^{-1}$  and pore volume =  $0.469 \text{ ccg}^{-1}$  for cal@UiO-66-L1, indicating that the majority of the calcein is attached to the outer surface and defect sites of the MOFs rather than being stored in the pores. The azide band characteristic of L1 was still present in the FT-IR spectra, confirming the presence of the modulator after the loading process.

As previously, full characterisation of the samples confirmed the surface moieties' attachment to the calcein-loaded NMOFs' surface, and calcein loading was measured by UV/Vis spectroscopy of all acid-digested samples (Table 4.1).

**Table 4.1.** Calcein loadings of the surface modified MOFs, determined by UV-Vis spectroscopy.

Sample	Calcein Loading (UV-Vis, % w/w)
cal@UiO-66-L1	17.9
cal@UiO-66-L1-PEG550	13.1
cal@UiO-66-L1-PEG2000	10.3
cal@UiO-66-L1-PolyLact	6.9
cal@UiO-66-L2-PNIPAM	8.0
cal@UiO-66-FA (PS)	9.8
cal@UiO-66-Hep (PS)	13.0
cal@UiO-66-Biot (PS)	12.8

An illustrative example of TGA analysis of cal@UiO-66-L1-PEG550 and cal@UiO-66-L1-PEG2000 is shown in Figure 4.9, where the appearance of a new degradation step at the reported degradation temperature of PEG confirms that the PEGylation has been successful. As the thermal degradation of calcein and PEG occur across the same temperature ranges, it is not possible to determine exact contents of either functionality by TGA.

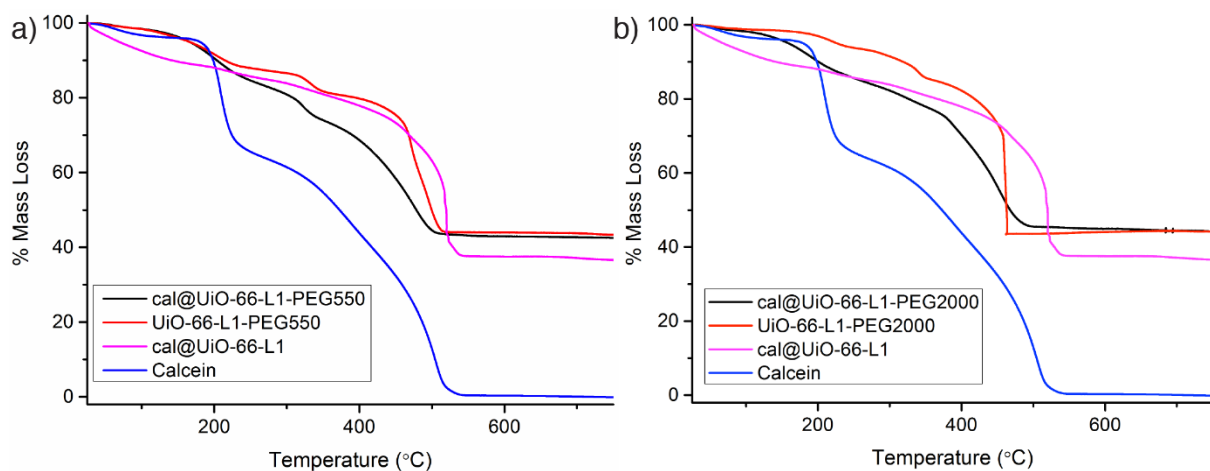


**Figure 4.9.** a) TGA traces of cal@UiO-66-L1-PEG550 in air and its comparison with cal@UiO-66-L1, UiO-66-L1-PEG550, and calcein. b) TGA traces of cal@UiO-66-L1-PEG2000 in air and its comparison with cal@UiO-66-L1, UiO-66-L1-PEG2000 and calcein.

Similarly, the TGA profiles of the postsynthetically coated, calcein loaded samples (PolyLact, PNIPAM, Folic acid, Biotin and Heparin) show decomposition steps characteristic of the surface reagents, while their characteristic vibration bands could also be observed by FT-IR, and the MOFs prepared by postsynthetic exchange on cal@UiO-66-L1 showed disappearance of the azide stretch of L1 (Figure 4.10).<sup>36, 37</sup>

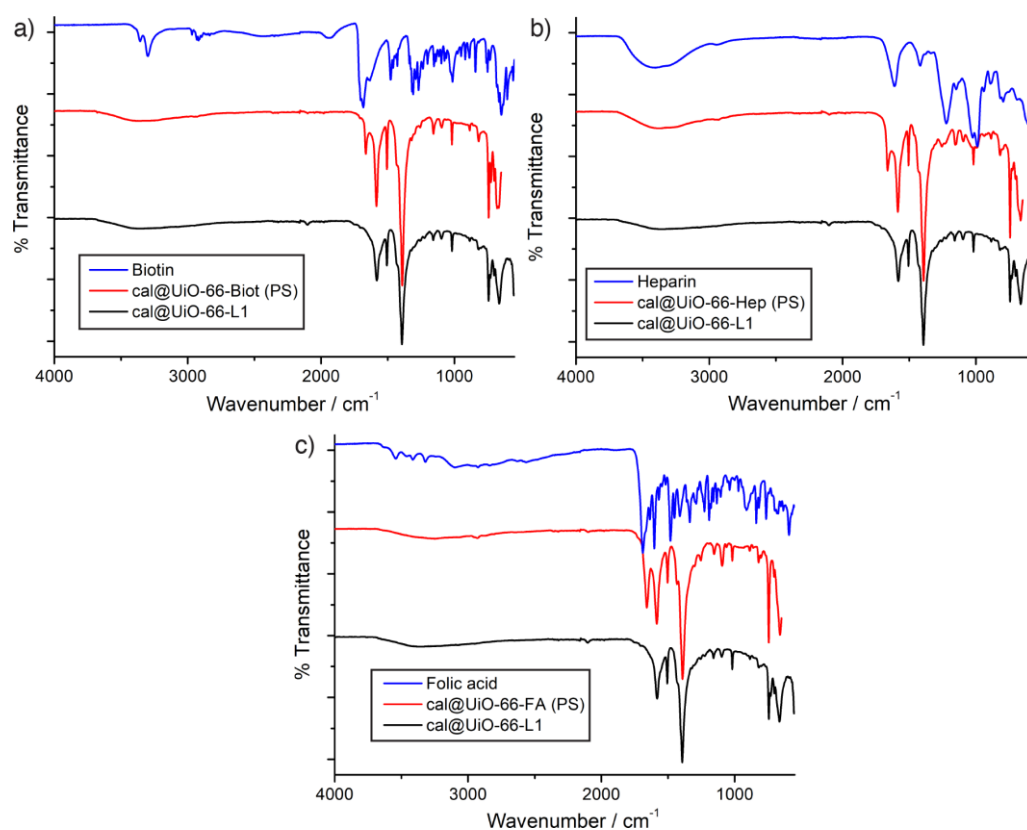


**Figure 4.10.** FT-IR spectra of calcein-loaded MOFs prepared by ligand exchange, compared to the precursor and the surface functionality, for a) cal@UiO-66-Biot (PS), b) cal@UiO-66-Hep (PS), and c) cal@UiO-66-FA (PS).

Nitrogen adsorption and desorption isotherms confirmed that the porosity of the samples is retained after surface functionalisation, and an example of the PEGylated samples is shown in Figure 4.11, which shows a similar decrease in porosity, in concert with surface mass addition, to the analogous empty samples described during Chapter 3.<sup>36, 37</sup>

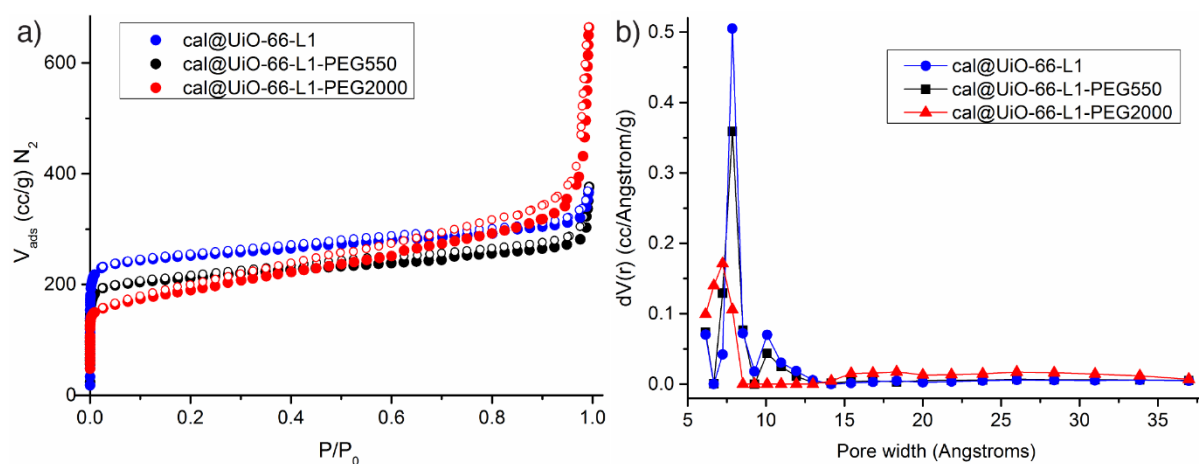


**Figure 4.11.** a) Adsorption and desorption isotherms ( $N_2$ , 77 K) of calcein loaded UiO-66 samples. Filled symbols represent adsorption, empty symbols represent desorption. b) Pore size distribution (slit pore,  $N_2$  at 77 K on carbon, QSDFT equilibrium model) of the calcein loaded UiO-66 samples.

#### 4.4 The Effect of PEG Coating on UiO-66 Calcein Release Kinetics

Due to the higher degree of initial stabilisation of UiO-66-L1-PEG550 and UiO-66-L1-PEG2000 towards phosphates compared to their precursor (see Chapter 3), drug release kinetics were further studied for this two samples and UiO-66-L1. Monitoring release at different pH values is important, given that extracellular pH is  $\sim 7.4$ , intracellular pH is  $\sim 6.8$ , and the intracellular pH of cancer cells is close to 5.5,<sup>38, 39</sup> providing a potential mechanism for targeted drug delivery.

In a typical calcein release experiment, between 5 and 10 mg of NMOF were dispersed in a dialysis bag with 10 ml of PBS (required pH), and dialysed against 100 ml of PBS (same pH) under magnetic stirring at room temperature. A full UV-Vis spectrum (210-550 nm) was performed for each measurement, which was taken in situ, and the liquid was added back to the dialysis media prior to the next measurement. Characteristic peaks for calcein absorbance were analysed against previously calculated calibration curves for calcein in PBS at pH 7.4 and 5.5 ( $\lambda_{\max} = 498$  and 452 nm respectively). For each experiment, calculations were performed with the exact mass of NMOF added. The release of calcein from both PEGylated and uncoated samples was affected by the pH, however, the release at pH 7.4 was drastically decreased for the PEGylated samples compared to their precursor cal@UiO-66-L1, which releases in contrast its full calcein cargo after 2 days, with an initial burst released of ca.40 % after 2 hours.. Both cal@UiO-66-L1-PEG550 and cal@UiO-66-L1-PEG2000 initially release calcein slowly at pH 7.4 and do not release more than  $\sim 30\%$  of their total cargo after 5 days. In contrast, they rapidly release ca 80% of cargo within an hour at pH 5.5, and release nearly the full amount in pH 5.5 after 2 days (Figure 4.12a).

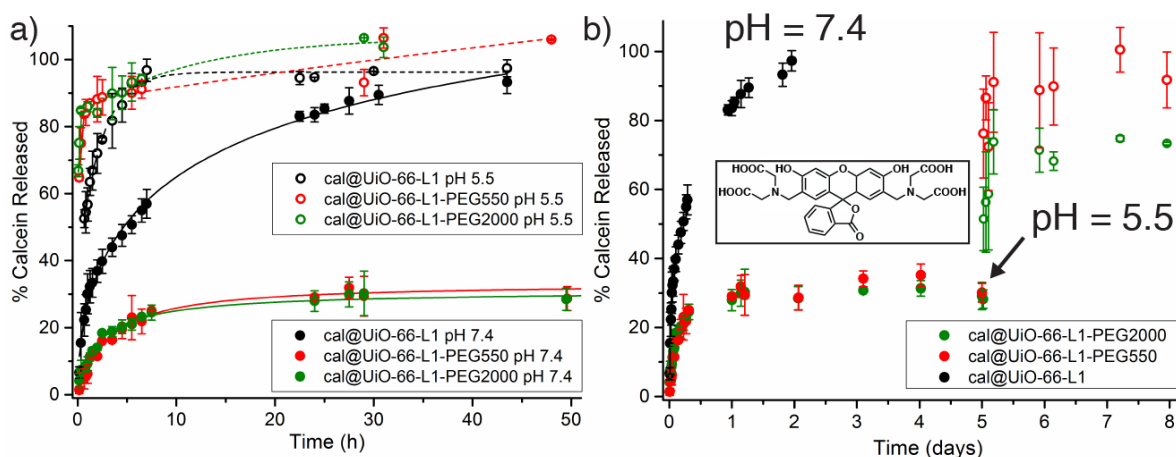


**Figure 4.12.** a) Calcein release profiles from cal@UiO-66-L1, cal@UiO-66-L1-PEG550 and cal@UiO-66-L1-PEG2000 in PBS at pH = 7.4 and pH = 5.5. b) pH-responsive release of calcein from the PEGylated MOFs. Inset: chemical structure of calcein. Error bars denote standard deviations from triplicate experiments. Release kinetic profile fittings are given in the appendix.

If this behaviour can be retained *in vivo*, PEGylated UiO-66 samples could be expected to store the majority of cargo in extracellular conditions, avoiding the non-selective distribution of therapeutics, while being able to release it once it has reached its target. The stimuli-responsive release of calcein from the PEGylated MOFs was therefore assessed by a similar experiment, where the pH of the PBS solution was adjusted from 7.4 to 5.5 after 5 days (Figure 4.12b). An immediate, rapid release of calcein was observed, with slightly less calcein released from UiO-66-L1-PEG2000 than the analogue with the shorter chain. Nonetheless, this result is highly promising for drug delivery applications, should the particles be efficiently internalised by cells.

To gain further insight into the mechanism of release, samples of the MOFs were subjected to simulated release conditions at pH 7.4; cal@UiO-66-L1 after 1 day and cal@UiO-66-L1-PEG2000 after 2 days. The amount of calcein released from both individual experiments determined by UV-Vis spectroscopy - 67.5% from cal@UiO-66-L1 and 42.7% from cal@UiO-66-L1-PEG2000 - is in concordance with the release profiles.

Both samples showed a decrease in crystallinity by PXRD after calcein release, although the characteristic UiO-66 reflection peaks could be determined (Figure 3.13), meaning that the core of the materials remains crystalline.

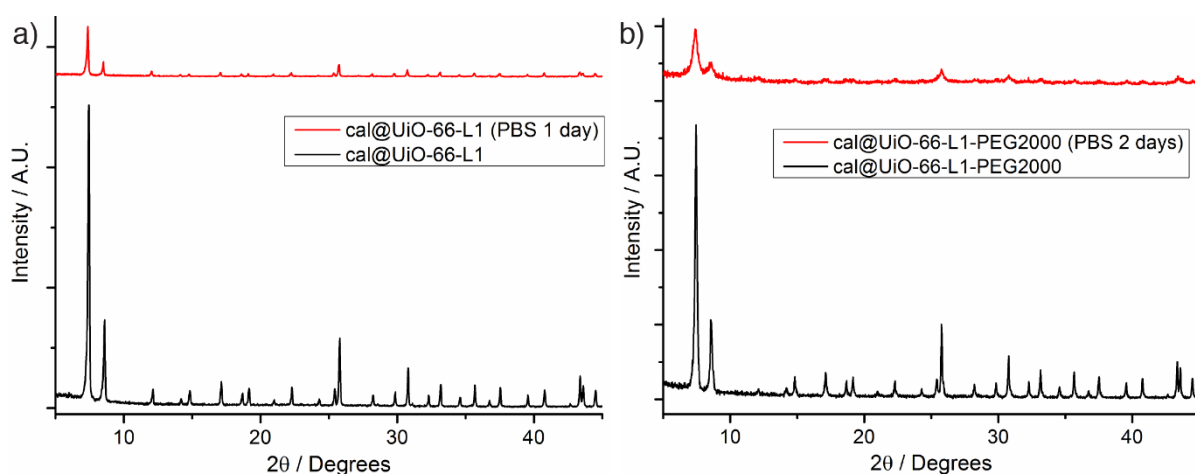


**Figure 4.13.** Stacked PXRD patterns of NMOFs before and after simulated release conditions.

TGA analysis showed the disappearance of the PEG moiety from cal@UiO-66-L1-PEG2000, and an increase on the metal residue for both samples (Figure 4.13), suggesting some degradation.

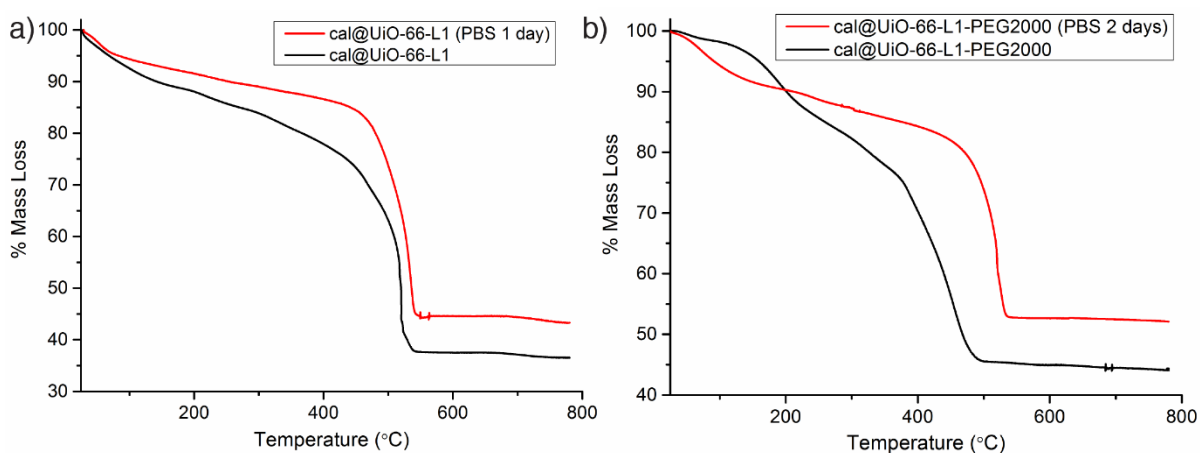


**Figure 4.13.** TGA traces in air of a) cal@UiO-66-L1 and b) cal@UiO-66-L1-PEG2000, before and after release.

Both samples remain porous, with an increase in surface area of cal@UiO-66-L1 (from  $S_{\text{BET}} = 1002$  to  $1155 \text{ m}^2\text{g}^{-1}$ ) resulting from release of significant amounts of calcein mass, and a slight decrease in the surface area of cal@UiO-66-L1-PEG2000 (from  $S_{\text{BET}} = 683$  to  $554 \text{ m}^2\text{g}^{-1}$ ) possibly due to pore blocking or incorporated additional mass, such as phosphates (Figure 4.14).

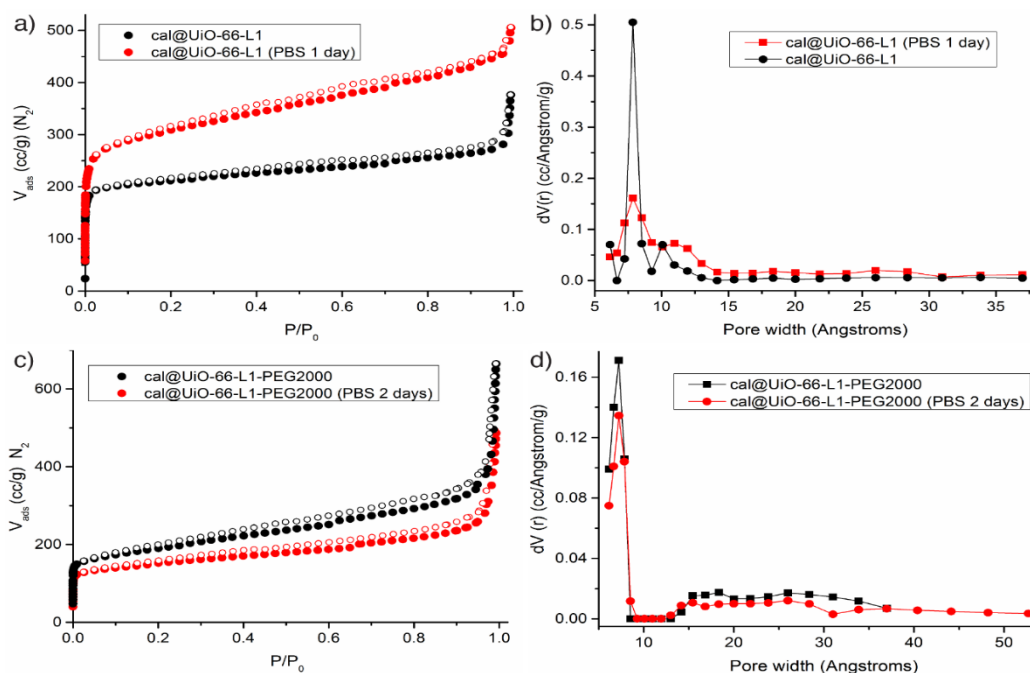


**Figure 4.14.** a)  $\text{N}_2$  adsorption isotherm (77 K) for cal@UiO-66-L1 after 1 day in PBS compared to the pristine material, alongside b) the calculated pore size distributions (slit pore,  $\text{N}_2$  at 77 K on carbon, QSDFT equilibrium model). c)  $\text{N}_2$  adsorption isotherm (77 K) for cal@UiO-66-L1-PEG2000 after 2 days in PBS compared to the pristine material, alongside d) the calculated pore size distributions (slit pore,  $\text{N}_2$  at 77 K on carbon, QSDFT equilibrium model).

It is hypothesized that, at pH 7.4, the phosphates present in PBS attack the zirconium positions<sup>40</sup> displacing the surface ligands and the calcein. When UiO-66 is not PEGylated, the MOF is much more accessible (both internally and externally) and therefore so are the zirconium clusters, enabling a faster exchange between phosphates and ligands, modulators and calcein. On the other hand, for surface modified cal@UiO-66-L1-PEG2000, the phosphates must diffuse through the PEG coating before reaching the MOF. A corona of coordinating phosphates could be then formed, obstructing the MOF and hindering further phosphate attack to release remaining calcein molecules. Indeed, FT-IR spectra of cal@UiO-66-L1-PEG2000 after 1 day in PBS at pH 7.4 showed more significant signals for phosphates (at  $\sim 1000\text{ cm}^{-1}$ ) than in the case of cal@UiO-66-L1 under the same conditions, suggesting the PEG coating induces a corona build-up while unmodified UiO-66 simply undergoes surface exchange for the first stages of release (Figure 4.15). When the pH is more acidic, the carboxylate units of bdc ligands, surface functionality and calcein are easier to protonate, and therefore MOF degradation and calcein release is much more pronounced.

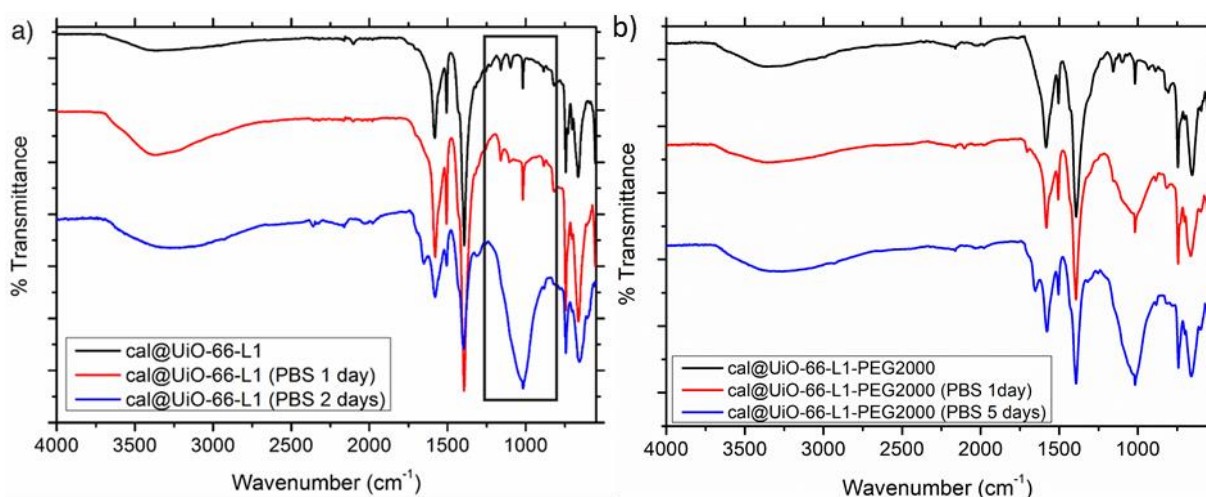


**Figure 4.15.** Stacked FTIR spectra of a) cal@UiO-66-L1 compared to the sample after 1 and 2 days simulated release conditions, and b) cal@UiO-66-L1-PEG2000 compared to the sample after 1 and 5 days simulated release conditions.

#### 4.5 Endocytosis Efficacy of MOFs

As all the cal@NMOF samples were prepared from the same base batch, it is expected that variations are caused by changes in external surface chemistry, not particle size, in concert with previous work which shows particle size has only minor effect until sizes >500 nm are reached.<sup>9</sup>

The endocytosis efficiency was calculated by incubating cervix cancer HeLa cells with 0.5 mgmL<sup>-1</sup> of NMOF in growth media (See section 4.9), and adjusting the cells' cytoplasmic fluorescence with the weight percent of calcein determined for each NMOF (Table 4.2). The data are expressed as mean and standard error of five replicates (n = 5), and the cytoplasmic fluorescence has been normalised taking cal@UiO-66-L1 as 100% (Figure 4.16). In addition, the cells were also incubated with a solution of free calcein in media with the same concentration reached with cal@UiO-66-L1 incubation, proving that due to its hydrophilic nature, calcein is not efficiency internalised by cells without a carrier.

**Table 4.2.** Calcein loadings of the surface modified MOFs, determined by UV-Vis spectroscopy, and their subsequent endocytosis efficiencies for HeLa cells normalised to cal@UiO-66-L1.

Sample	Calcein Loading (UV-Vis, % w/w)	Endocytosis Efficiency %
cal@UiO-66-L1	17.9	100
cal@UiO-66-L1-PEG550	13.1	149 ± 2
cal@UiO-66-L1-PEG2000	10.3	116 ± 1
cal@UiO-66-L1-PolyLact	6.9	141 ± 2
cal@UiO-66-L2-PNIPAM	8.0	150 ± 1
cal@UiO-66-FA (PS)	9.8	184 ± 2
cal@UiO-66-Hep (PS)	13.0	171 ± 3
cal@UiO-66-Biot (PS)	12.8	37 ± 1

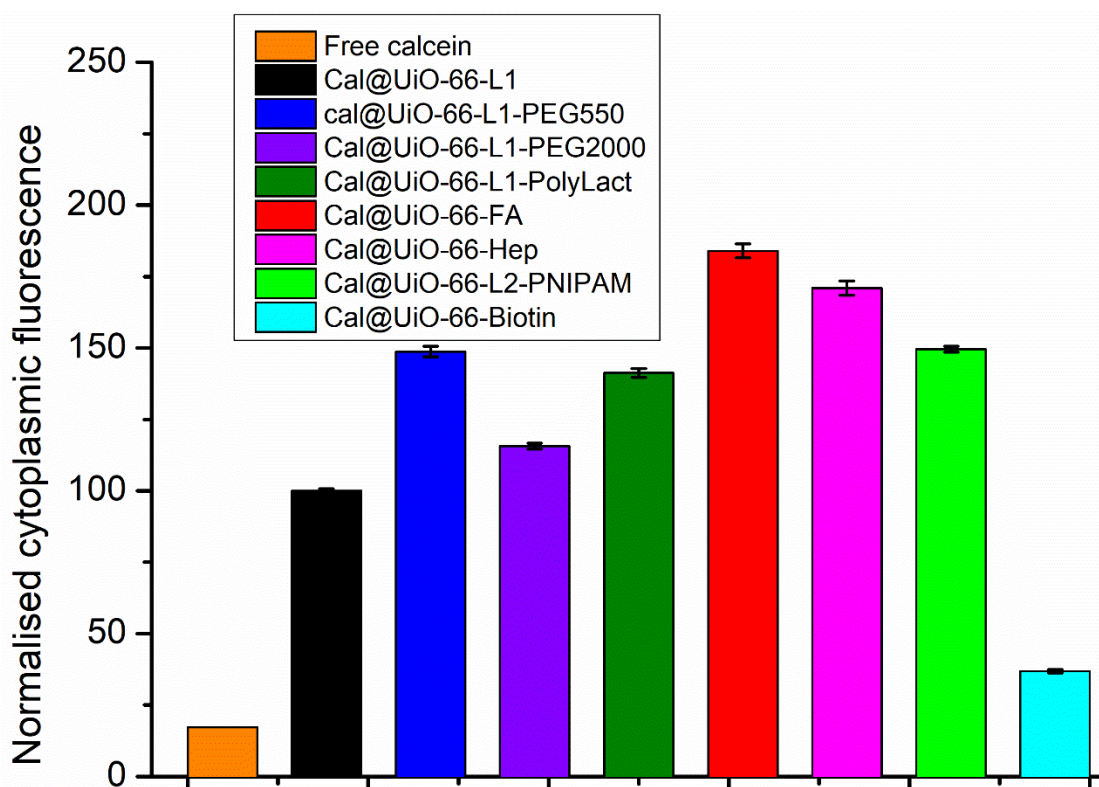


**Figure 4.16.** Endocytosis efficiency of calcein-loaded MOFs for the HeLa cell line, normalised to cal@UiO-66-L1. Error bars represent the standard deviation of 5 measurements.

In general, cal@UiO-66 uptake is highly efficient compared to free calcein (6-10 fold increase), proving the validity of NMOFs as carriers to internalise cargo not able to efficiently cross the cell membrane by themselves. cal@UiO-66-Biot (PS) was, however, poorly internalised by HeLa cells compared to cal@UiO-66-L1, with very close efficiency ( $37 \pm 1\%$ ) to free calcein ( $17 \pm 1\%$ ) showing that biotin coating might not be desirable to enhance NMOF cell internalisation, although biotin could be used as a platform for further postsynthetic modifications, such as N-alkylation.

cal@UiO-66-FA (PS) had the highest internalisation, followed by cal@UiO-66-Hep (PS), cal@UiO-66-L2-PNIPAM, cal@UiO-66-L1-PEG2000, cal@UiO-66-L1-Poly-Lact and cal@UiO-66-L1-PEG550 (Table 4.2).

HeLa, and other cancerous cells, are known to over express the folate receptor (FR) on their surface,<sup>41-43</sup> and therefore the folate present on the surface of cal@UiO-66-FA (PS) could bind to the FR, providing a mode of targeting and enhanced internalisation of the NMOF. Similarly, some cancer cells overexpress receptors to which heparin can bind.<sup>44</sup>

Although NPs passively accumulate in cancer tissue *in vivo* due to the EPR effect,<sup>23</sup> increasing the endocytosis efficiency is clearly one way to increase their therapeutic efficiency. However,

targeting units, such as folate, can be used to enhance the uptake of MOFs in cancer cells without compromising healthy cells. Additionally, the mechanism of cell internalisation is important if the MOFs are to avoid degradation in the lysosome before releasing their therapeutic cargo.

#### 4.6 Endocytosis Routes of MOFs

To monitor the endocytosis routes by which the different MOFs are internalised by HeLa cells, a series of pharmacological inhibitors was employed.<sup>10</sup> Chlorpromazine<sup>27</sup> and sucrose<sup>28</sup> were used to inhibit clathrin-mediated pathways<sup>16</sup> although it is important to consider that sucrose can additionally inhibit some non-mediated endocytosis processes. Nystatin<sup>26</sup> was used as an inhibitor of caveolae-mediated endocytosis<sup>17</sup> and rottlerin<sup>29</sup> was used to inhibit macropinocytosis.<sup>19</sup> If uptake is found to be lower when a certain inhibitor is used, this indicates the particular route being inhibited is significant in internalising the nanoparticles.

As positive controls for the inhibitors, tracers known to follow each pathway were used: transferrin<sup>45</sup> and ceramide<sup>46</sup> for clathrin- and caveolae-mediated pathways respectively, and dextran<sup>47</sup> for macropinocytosis. Cells were incubated with each inhibitor for 30 minutes and then for 90 minutes together with the NMOF (Section 4.9), confirming the inhibition of the specific routes (Figure 4.17). It should be noted that inhibition of one route may allow other routes to be utilised, and so significant decreases may not always be observed.

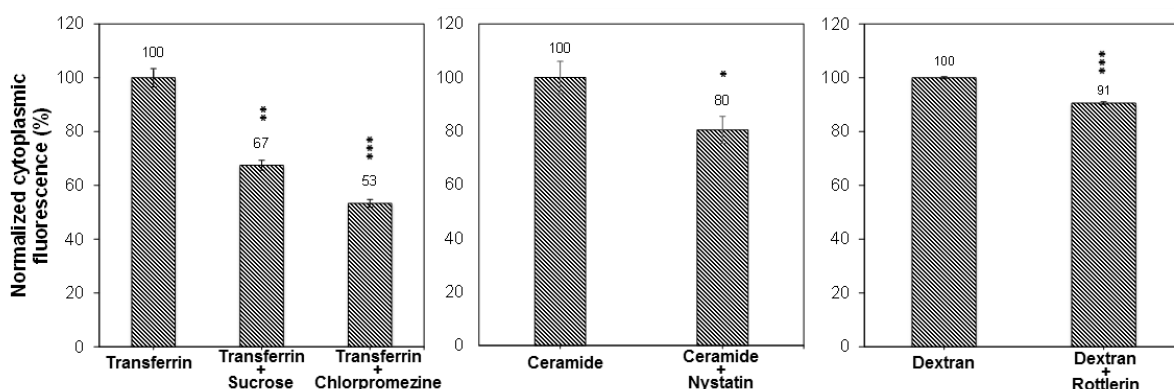


**Figure 4.17.** FACS of the positive controls of desired endocytosis routes, showing statistical difference for the concentration of tracers used. Error bars represent the standard deviation of 3 measurements.

Cell internalisation studies without the use of inhibitors were performed at 37 °C, to which the inhibited uptakes were normalised to, and at 4 °C, in order to attenuate energy-dependent internalisation. When cells were incubated at 4 °C cell internalisation of the NMOFs decreased by 50-85% compared to the control at 37 °C (Figure 4.18). However, the difference in cytoplasmic fluorescence of the HeLa cells after incubation with cal@UiO-66-Biot (PS), which was the less efficiently internalised MOF, at 37 °C and 4 °C is not as remarkable as for all

other NMOFs, only decreasing by 28%. Indeed, apart from cal@UiO-66-Biot and cal@UiO-66-L1-PolyLact, the decrease in cells' internal fluorescence is more remarkable for the surface coated samples than for cal@UiO-66-L1.

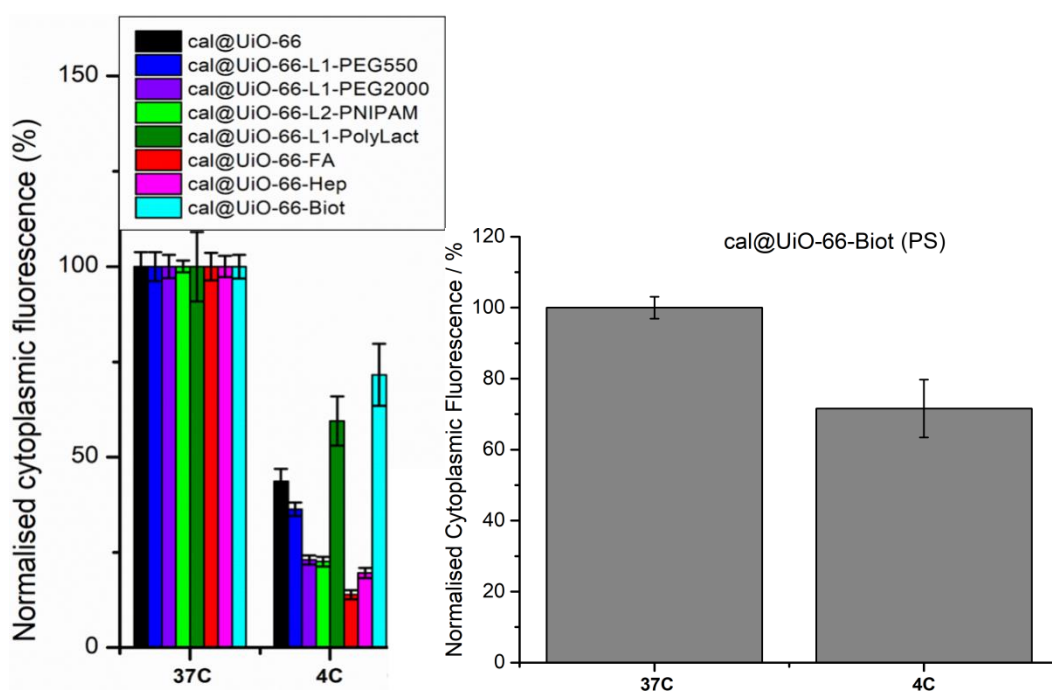


**Figure 4.18.** Endocytosis efficiency of cal@MOFs at 37 °C and 4 °C with no inhibitors. 4°C internalisation indicates non-active transport contribution. Error bars represent the standard deviation of 5 measurements.

At 4 °C most cellular functions are attenuated, and therefore active transport, such as endocytosis, is highly decreased. These results indicate that cal@UiO-66-Biot (PS) is not significantly internalised by active transport, explaining why the endocytosis efficiency is remarkably decreased when compared to unfunctionalised UiO-66. Therefore, biotin coated materials might not be especially effective as DDSs, although biotin functionalities could provide a platform for further postsynthetic modifications that might increase the NMOFs efficiency. As no efficient internalisation is observed, no further experiments were carried out with this sample.

It has been previously reported that naked UiO-66 nanoparticles generally enter HeLa cells through clathrin-mediated endocytosis, ultimately resulting in lysosome storage, reducing their potential therapeutic efficiency.<sup>9, 10</sup> The uptake of cal@UiO-66-L1 after exposure to the clathrin-mediated inhibitors, sucrose and chlorpromazine, was reduced to  $\sim 27 \pm 1\%$  and  $37 \pm 5\%$  respectively, whereas exposure to nystatin had no effect ( $\sim 107 \pm 7\%$ ), revealing that the unfunctionalised MOF is not internalised through the caveolae-mediated route, while pre-incubation with rottlerin decreased its uptake to  $\sim 79 \pm 6\%$  (Figure 4.19).

PEG chains have an amphiphilic character that resembles that of the cell membrane, which should be assessed to the PEGylated MOF surface, while cal@UiO-66, in contrast, has a hydrophilic surface. Hence, PEGylation might tune their internalisation pathways.

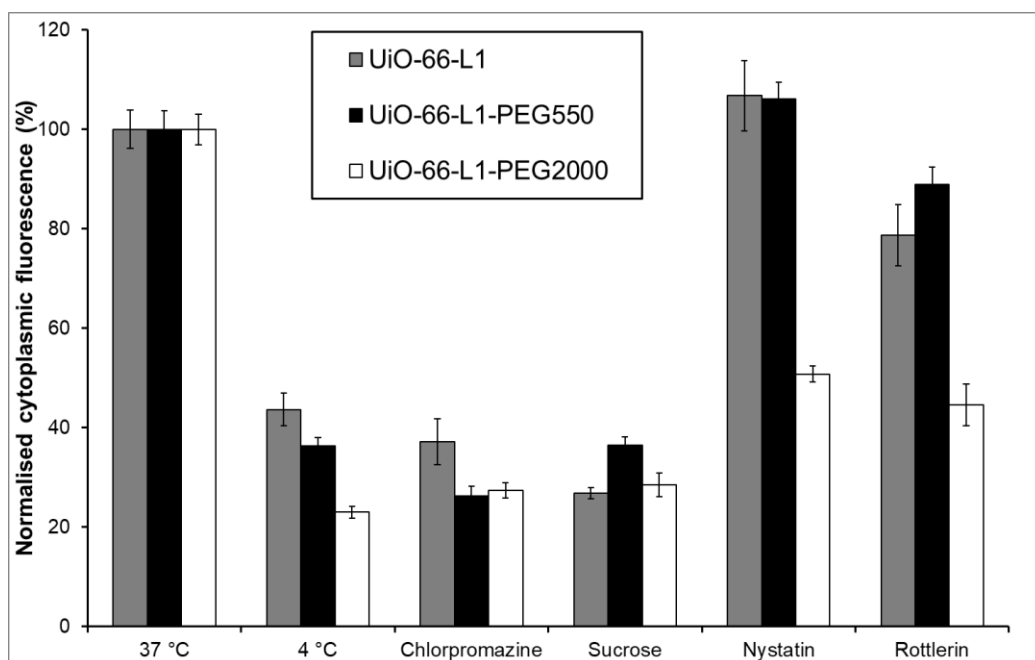


**Figure 4.19.** Normalised internal fluorescence, obtained through FACS, of HeLa cells after the uptake of cal@UiO-66-L1, cal@UiO-66-L1-PEG550, and cal@UiO-66-L1-PEG2000 in the presence and absence of the pharmacological endocytosis inhibitors. Error bars represent the standard deviation of 5 measurements.

On the one hand, the PEG550 coating did not affect the routes of endocytosis with values similar to cal@UiO-66-L1. For example, the uptake after exposure to sucrose and chlorpromazine decreased to  $\sim 36 \pm 2\%$  and  $26 \pm 2\%$  respectively, whereas there was no reduction in uptake upon exposure to nystatin ( $\sim 106 \pm 3\%$ ), and rottlerin slightly decreased the uptake to  $\sim 89 \pm 4\%$  (Figure 4.10). On the other hand, significant changes in cell internalisation routes were found upon PEG2000 coating. Exposing the cells to sucrose and chlorpromazine decreased cal@UiO-66-L1-PEG2000 uptake to  $\sim 28 \pm 2\%$  and  $27 \pm 2\%$  respectively, but more importantly, with nystatin and rottlerin the uptake was reduced to  $\sim 51 \pm 2\%$  and  $45 \pm 4\%$ , respectively, showing cal@UiO-66-L1-PEG2000 is partially internalised through macropinocytosis and more importantly, through caveolae-mediated endocytosis (Figure 4.10), suggesting that its therapeutic efficiency might be enhanced compared to uncoated MOF.

This indicates that the UiO-66 internalisation pathway is significantly affected by the functionality attached to its surface, with the longer PEG chains ( $M_w \sim 2000$ ) allowing the NMOFs to partially avoid lysosomal degradation, possibly due to its amphiphilic nature, which

is thought to be more compatible with the caveolae-mediated route. In addition, part of the cellular trafficking of all three MOFs occurs through macropinocytosis, as the uptake is affected by the presence of rottlerin. However, macropinocytosis is a non-selective process allowing the internalisation of large quantities of material, independent of its constitution. Although this route contribution could be a consequence of aggregation of nanoparticles, the contribution to cal@UiO-66-L1-PEG2000 internalisation is greater than for cal@UiO-66-L1-PEG550 and cal@UiO-66-L1, while the later exhibit a higher degree of aggregation, as determined by DLS measurements (See Chapter 3).

Folate receptors have been reported to often be located within caveolae invaginations.<sup>43, 48</sup> cal@UiO-66-FA (PS) uptake decreased to  $62 \pm 2\%$  when HeLa cells were incubated with nystatin, indicating caveolae-mediated internalisation, while no significant inhibition was found when incubated with chlorpromazine ( $96 \pm 3\%$ ), meaning that the MOF is not internalised by clathrin-mediated endocytosis, and only a minor effect ( $81 \pm 5\%$ ) was observed when rottlerin was inhibiting macropinocytosis pathways. Sucrose significantly decreased cal@UiO-66-FA (PS) uptake to  $36 \pm 4\%$ , meaning that folate coating not only provides a way of cancer targeting, but also alters cancer cell endocytosis selection pathways from clathrin-mediated to both caveolae-mediated and non-mediated endocytosis (Figure 4.20). These results suggest that drug loaded UiO-66-FA samples have potential to be efficient therapeutic DDSs, as they could potentially escape the early endosomes, avoiding lysosome storage and being released to the cytosol to reach target organelles.

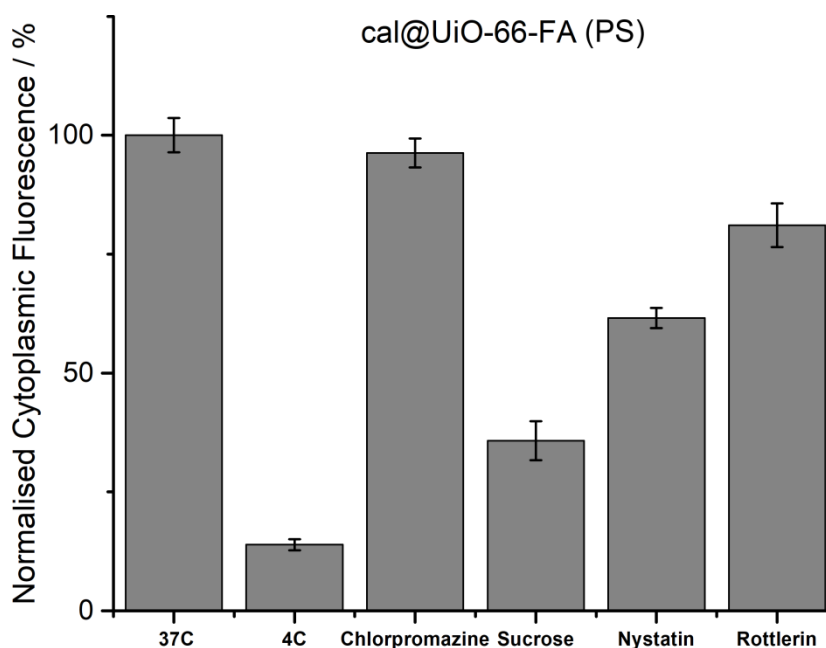


**Figure 4.20.** Endocytosis efficiency of cal@UiO-66-FA (PS) in the presence of different inhibitors normalised to the efficiency observed at 37 °C with no inhibitor. Error bars represent the standard deviation of 5 measurements.

The endocytosis pathways of cal@UiO-66-Hep (PS) show differences compared cal@UiO-66 (Figure 4.21). Exposing HeLa cells to nystatin decreased cal@UiO-66-Hep (PS) cell internalisation to values of  $60 \pm 1\%$ , showing that the heparin coated MOF is also partially internalised by caveolae-mediated endocytosis. However, in contrast to cal@UiO-66-FA (PS), clathrin-mediated routes also play a role in HeLa cell internalisation of cal@UiO-66-Hep (PS), as normalised cell cytoplasmic fluorescence decreases to values of  $70 \pm 2\%$ , while inhibiting macropinocytosis decreases the MOF normalised uptake to  $83 \pm 3\%$ . Additionally, sucrose also decreased its cell internalisation to values of  $41 \pm 4\%$ .

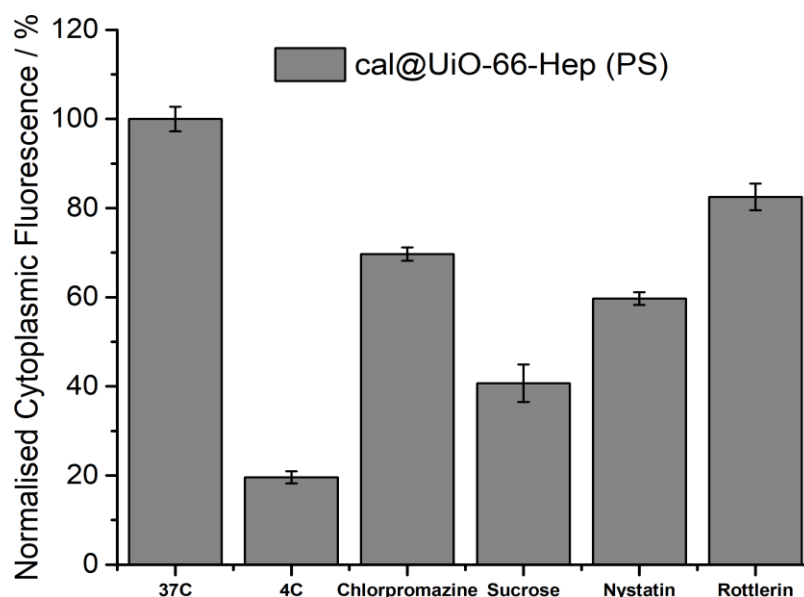


**Figure 4.21.** Endocytosis efficiency of cal@UiO-66-Hep (PS) in the presence of different inhibitors, normalised to the efficiency observed at 37 °C with no inhibitor. Error bars represent the standard deviation of 5 measurements.

In the cases of cal@UiO-66-L1-PolyLact and cal@UiO-66-L2-PNIPAM, cell internalisation decreased when inhibiting with sucrose ( $50 \pm 5\%$  and  $54 \pm 1\%$ , respectively), while no significant decrease was found when inhibiting clathrin-mediated ( $84 \pm 11\%$  and  $105 \pm 5\%$  respectively) or caveolae-mediated routes ( $106 \pm 13\%$  and  $103 \pm 4\%$  respectively), and only minor macropinocytosis attributions upon PNIPAM coating ( $80 \pm 4\%$ ). Surprisingly, even though cal@UiO-66-L1-PolyLact uptake is more efficient than for cla@UiO-66-L1, its uptake at 4 °C is not as low as for the other surface functionalised NMOFs, indicating that cell internalisation does not occur exclusively by active transport. These results suggest that these polymer-coated samples are mainly internalised by non-mediated endocytosis processes, with a significant contribution for cal@UiO-66-L1-PolyLact from energy independent processes. (Figure 4.22).

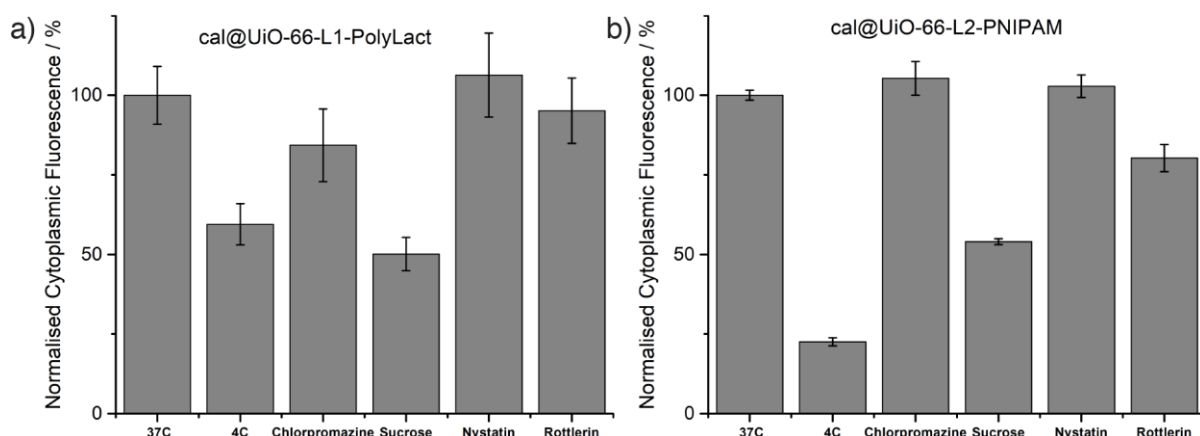


**Figure 4.22.** Endocytosis efficiency of a) cal@UiO-66-L1-PolyLact, and b) UiO-66-L2-PNIPAM, in the presence of different inhibitors, normalised to the efficiency observed at 37 °C with no inhibitor. Error bars represent the standard deviation of 5 measurements.

Comparing the uptake routes of functionalised samples together (Figure 4.23), some features are notable. In general, cell uptake through clathrin-mediated endocytosis (inhibited by chlorpromazine), which was the major route for cal@UiO-66-L1, cal@UiO-66-L1-PEG550, and contributes partially to cal@UiO-66-L1-PEG2000 internalisation, has remarkably decreased to similar levels upon all the other coatings. Nearly all samples show some inhibition by rottlerin, most significantly for cal@UiO-66-L1-PEG2000, suggesting some contribution from macropinocytosis, apart from cal@UiO-66-L1-PolyLact, which has greater levels of non-active transport. Inhibition by nystatin, which indicates caveolae-mediated uptake and should be favourable for drug delivery, is observed for cal@UiO-66-FA (PS), cal@UiO-66-Hep (PS) and for cal@UiO-66-L1-PEG2000.

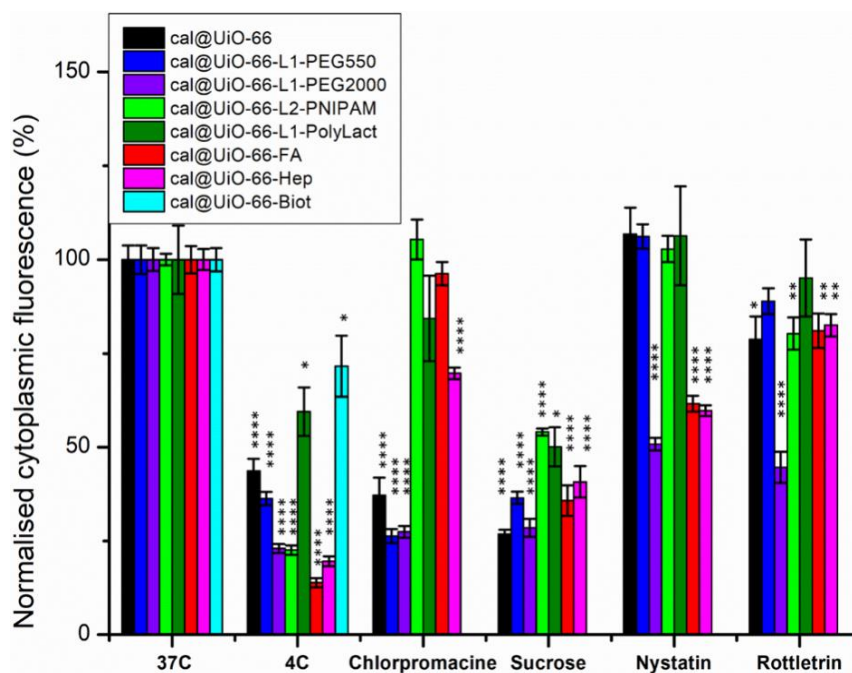


**Figure 4.23.** Endocytosis efficiencies of the calcein-loaded MOFs for the HeLa cell line when incubated with various inhibitors. The statistical significance was determined by ordinary one-way ANOVA and is indicated on the part b): \* =  $P \leq 0.05$  \*\* =  $P \leq 0.01$  \*\*\* =  $P \leq 0.001$  \*\*\*\* =  $P \leq 0.0001$ . Error bars represent the standard deviation of 5 replicates.

#### 4.7 Confocal Fluorescence Microscopy

Confocal fluorescence microscopy has been used to confirm successful internalisation of the MOF nanoparticles by HeLa cells and their subsequent intracellular calcein release. On the one hand, calcein cannot cross the cell membrane alone, on the other hand, it self-quenches, and so the green fluorescence is only observed upon release of calcein from the internalised NMOF.

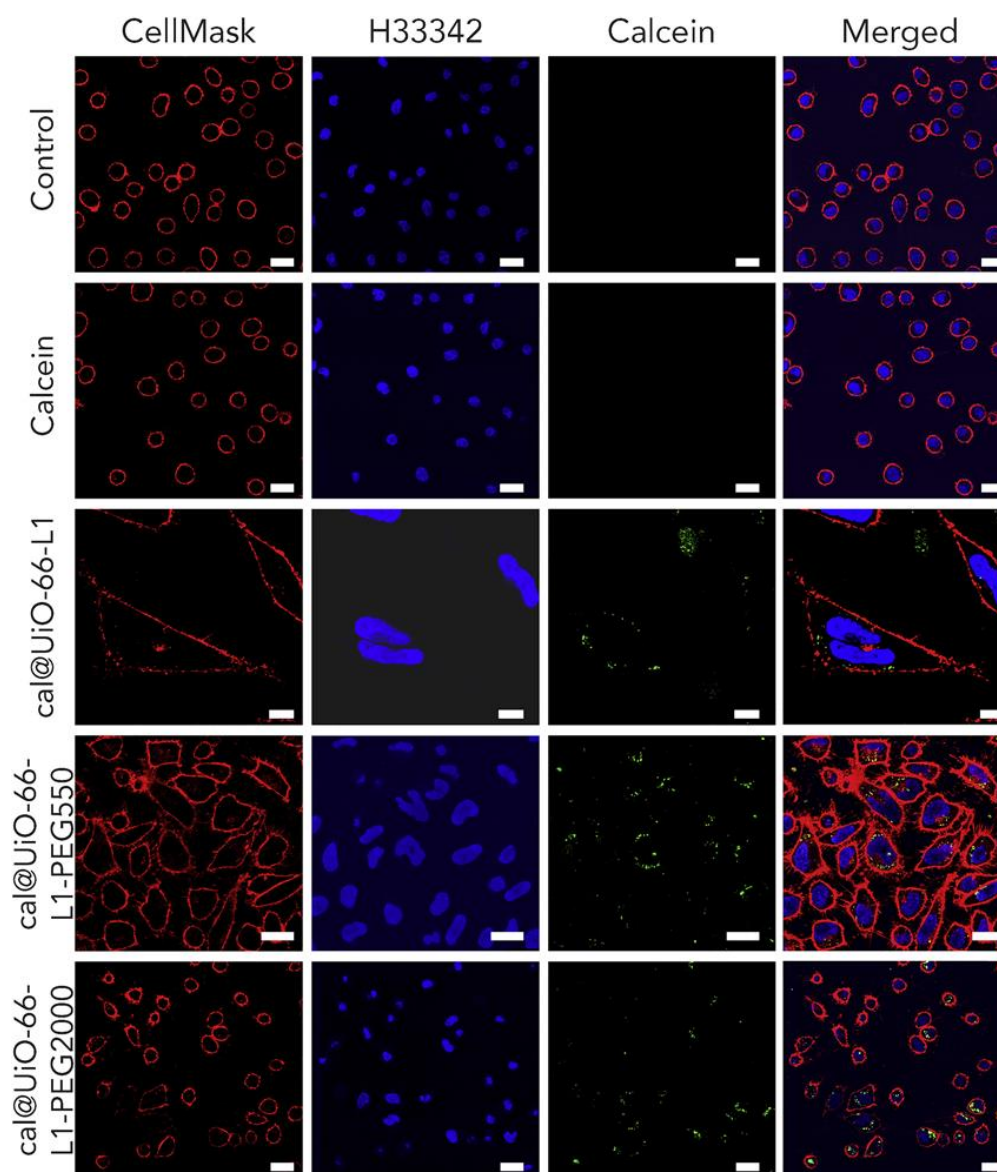


**Figure 4.24.** Confocal microscopy images of HeLa cells incubated with different materials, from top to bottom: control; free calcein; cal@UiO-66-L1; cal@UiO-66-L1-PEG550; cal@UiO-66-L1-PEG2000. Cells were subsequently stained with Hoechst 33342 (5  $\mu\text{g}/\text{mL}$ ) and CellMask™ Orange (1X). Scale bar represents 25  $\mu\text{m}$  in all images except for cal@UiO-66-L1, in which it represents 10  $\mu\text{m}$ . Performed by S. Haddad.

Figure 4.24 shows the confocal microscopy images of HeLa cells incubated during 2 hours with, from top to bottom: nothing (control); free calcein; cal@UiO-66-L1; cal@UiO-66-L1-PEG550; cal@UiO-66-L1-PEG2000. Hoechst 33342 (H33342) and CellMask were used to stain the nucleus and the membrane of the cells, respectively. CellMask acts as a viability control, probing the cell membrane integrity, and shows that the MOFs are inside the cells. The effectiveness of calcein as a probe is demonstrated by the fact that free calcein is not taken up by cells - the control cells and those incubated with free calcein show no green signal

- in concert with previous reports.<sup>9</sup> As calcein self-quenches, any green fluorescence within cells comes from released calcein from internalised MOF materials. Therefore, it is visually proven that cal@UiO-66-L1, cal@UiO-66-L1-PEG550 and cal@UiO-66-L1-PEG2000 all transport and deliver calcein into HeLa cells.

Laser confocal microscopy was also used to qualitatively determine the degree of co-localisation between the calcein-loaded NMOF particles (green) and the lysosomes (red), using LysoTracker®-Deep red (Figure 4.25).<sup>10</sup> After 2 hours of incubation, a high level of co-localisation was found for all three MOFs, as FACS confirmed that clathrin-mediated uptake takes place in all NMOFs. However, in the case of cal@UiO-66-L1-PEG2000, a higher degree of localised light green particles outside the lysosomes can also be observed, suggesting altered uptake mechanisms. Despite the fact that the release profiles determined that PEGylated UiO-66 samples only release ~15% of calcein at pH 7.4 after 2 hours of exposure (See section 4.4), the green fluorescence is clearly visible outside the lysosome, suggesting a proportion of cal@UiO-66-L1-PEG2000 is internalised by a different uptake mechanism (in the more acidic lysosome 85% of calcein would be expected to be released in pH 5.5 at the same exposure time).

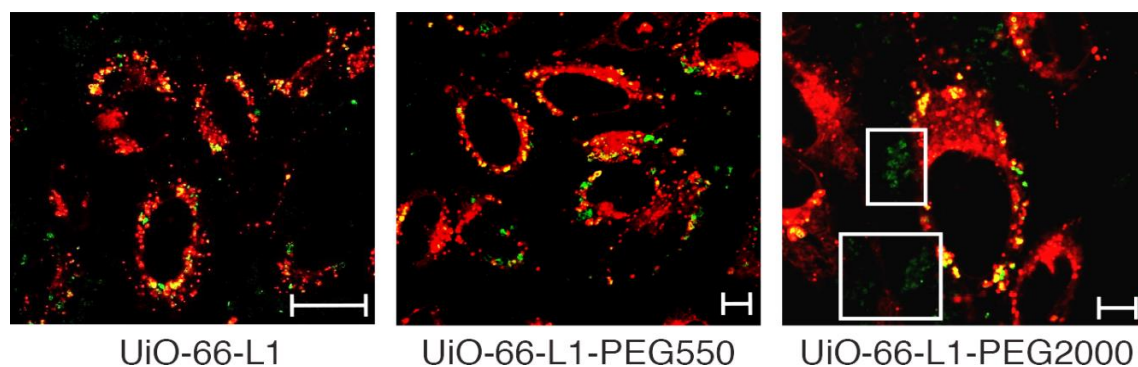


**Figure 4.25.** Confocal fluorescence microscopy images of NMOF uptake into HeLa cells using a lysotracker (red) to stain the lysosome and showing calcein internalisation (green). Non-lysosomal calcein is highlighted in white boxes for UiO-66-L1-PEG2000. Scale bars represent 25  $\mu\text{m}$ , 10  $\mu\text{m}$  and 7.5  $\mu\text{m}$ , from left to right. Performed by S. Haddad.

In summary, these results shown that UiO-66 and functionalised analogues are efficiently internalised, and demonstrate the power of surface functionalisation in MOFs cellular internalisation efficacy and pathways, which can be tuned from clathrin-mediated to caveolae-mediated endocytosis, the second being more desirable for DDSs to be efficient, as facilitates early endosome escape and subsequent cytosolic release.

## 4.8 Conclusions

In order to study MOFs' cancer cells internalisation, a fluorescent molecule (calcein) has been loaded into UiO-66-L1 and UiO-66-L2, which have been further postsynthetically modified following the protocols detailed in Chapter 3, confirming the orthogonality of the postsynthetic surface modifications with cargo loading.

Calcein release from bare UiO-66-L1, UiO-66-L1-PEG550 and UiO-66-L1-PEG2000 has been studied in PBS at pH 7.4 and 5.5. The release kinetics were drastically reduced at pH 7.4 for the PEGylated MOFs (ca. 10% w/w linker release after 1 hour versus 52% w/w for cal@UiO-66-L1), while they were maintained at pH 5.5 (total release in 10 hours), as the nature of the MOFs' metal-linker coordination bond enhances their degradation at more acidic pH. The PEGylated MOFs did not release further cargo (ca. 30% w/w) after approximately 10 hours in PBS at pH 7.4, whereas the non-PEGylated MOF released all its cargo after 2 days. More importantly, stimuli-responsive release was achieved by changing the pH of the release media of the PEGylated MOFs from 7.4 to 5.5 during the course of the experiments. This phenomena has been explained by the formation of a phosphate corona at pH 7.4, which hinders further calcein release from the PEG-coated MOFs, which partially protonates under acidic pH and breaks down

The ability of surface functionalised and bare UiO-66 to be internalised by cells through active transport, such as endocytosis, and to deliver its cargo has been proved both by FACS and confocal microscopy. Loading the MOFs with calcein enables the monitoring of their internalisation by cells, as compared to free calcein, cells have a 6-fold increase in internal fluorescence after treatment with cal@UiO-66-L1, a consequence of free calcein's poor internalisation due to its hydrophilic nature. The cellular uptake of cal@UiO-66-L1 has been enhanced by almost all surface functionalisations, apart from the biotin coated sample, which was poorly internalised (ca. 37 %) compared to its precursor bare sample, with almost no internalisation through active-transport. Due to the over expression of the folate receptor by HeLa cervix cancer cells, cal@UiO-66-FA internalisation was twice as effective when compared to the bare precursor MOF.

Surface modifications have proven to alter the endocytosis routes of uptake. Although cal@UiO-66 and cal@UiO-66-L1 are mainly internalised through clathrin-mediated endocytosis, with partial contribution of macropinocytosis, different uptake routes are found depending on the surface coating. While cal@UiO-66-L1-PEG550 internalisation does not differ significantly from its precursor, caveolae-mediated endocytosis is significant in the uptake of cal@UiO-66-L1-PEG2000, whose uptake was inhibited by ca. 40% by nystatin,

meaning that the amphiphilic character of the PEG chains favour the caveolae-mediated route only when the PEG chains are long enough. Clathrin-mediated endocytosis and macropinocytosis have been also assessed as important routes of internalisation for both PEGylated MOFs, with a higher degree of macropinocytosis contribution upon longer PEG chains.

As the folate receptors are often located within caveolae invaginations, cal@UiO-66-FA was also internalised through the caveolae-mediated route, with no contribution of clathrin-mediated endocytosis. Thus, folic acid coating not only targets cancer cells and enhanced the cellular internalisation of MOFs, it also tunes their internalisation to more desired pathways. Heparin is on the other hand internalised by both clathrin and caveolae-mediated endocytosis, with minor contribution upon macropinocytosis.

Samples coated with the polymers Poly-L-lactide and PNIPAM were not internalised through caveolae or clathrin-mediated endocytosis, with only minor contribution of the macropinocytosis route upon PNIPAM coating. The high degree of inhibition by sucrose, known to inhibit also non-mediated uptake routes, indicates that non-mediated endocytic processes are the major routes of internalisation of these MOFs, with a high degree of non-active transport in the case of cal@UiO-66-L1-PolyLact.

With these results in mind, the cytotoxicity of the samples will be studied in Chapter 5. The bare and surface functionalised materials, empty and drug-loaded, will be incubated with HeLa cells, and the viability of these will be measured, with the aim of understanding the effect of the endocytosis routes in their therapeutic activity.

## 4.9 Experimental

### 4.9.1 General Experimental remarks

**Flow Cytometry:** Measurements were carried out using Cytex DXP8 analyser cytometer; BLU mode (laser)-FLU1 (fluorescence detector). The analysis was done using FlowJo and Prism softwares. (University of Cambridge)

**Confocal Microscopy:** Measurements were carried out using Leica TCS SP5 confocal microscope. The microscope was equipped with 405 diode, argon and HeNe lasers. Leica LAS AF software was used to analyse the images. (University of Cambridge)

### 4.9.2 Protocols

#### Calcein Loading of UiO-66-L1 and UiO-66-L2

300 mg of UiO-66-L1 or 150 mg UiO-66-L2 were dispersed by sonication (15 minutes) in 150 mL or 75 mL of a methanolic solution of calcein ( $10 \text{ mg mL}^{-1}$ ) respectively, and stirred at room temperature for 48 hours. The solid was collected by centrifugation (4500 rpm, 20 min), and submitted to dispersion centrifugation cycles with fresh methanol until the supernatant solution remained colorless (around 5 times). The calcein loaded materials were obtained as a bright orange powder.

#### Postsynthetic Modifications of Calcein Loaded MOFs

Surface modification of cal@UiO-66-L1 and cal@UiO-66-L2 followed the previous protocols for surface ligand exchange and covalent modification than during Chapter 3, as per Figure 4.7.

#### Calcein Release Experiments

The pH of the release media was adjusted from 7.4 to 5.5 during the course of the experiment by adding 50  $\mu\text{L}$  of concentrated HCl to the 100 ml of PBS pH 7.4 placed in contact with the dialysis bag, in order to obtain pH 5.5. The quantity of concentrated HCl need to change the pH of the dialysis media was determined previous to the experiment.

#### Simulated Calcein Release

To simulate release conditions on a larger scale, 50 mg samples of the calcein-loaded NMOFs were dispersed in 50 ml of PBS pH 7.4, which was stirred at room temperature for 2 days in the case of cal@UiO-66-L1-PEG2000 and for 1 day for cal@UiO-66-L1. Then, the NMOF was collected by centrifugation (4500 rpm, 15 minutes), and washed with water 3 times. The NMOFs were dried for 24 hours under vacuum before further analysis.

### **Flow Cytometry Assays (FACS)**

In all the FACS experiments, HeLa cells were seeded in a Cellstar 24-well plate at a density of  $5 \times 10^4$  cells/well and incubated for 48 h at 37 °C with 5% CO<sub>2</sub> in complete medium.

### **Endocytosis Efficiency**

The endocytosis efficiency of the calcein loaded MOFs was measured by fluorescence assisted cell sorting (FACS) using the HeLa cell line. After 48 h of cell growth, the cells were washed with PBS and incubated with a solution of the NMOF in question in media for 2 h. Then, the media of each well was aspirated and the wells were washed extensively (PBS x 3) to remove non-internalised MOF or incubation conditions. The cells were then harvested by adding 0.1 mL of trypsin and incubated for 5 min at 37 °C with 5% CO<sub>2</sub>. The cells were recovered by centrifugation (5 min at 1200 rpm) and re-suspended in 100 µL of cDMEM without phenol red. Finally the samples were measured in a Cytex DXP8 analyser cytometer within 30 min. The analysis of the data was done using FlowJo and Prism software.

### **Positive Control of Endocytosis Routes**

After cell growing for 48 h, each well containing cells was washed with PBS and pre-treated with sucrose ( $102.7 \text{ mgmL}^{-1}$ , 0.3 M), chlorpromazine ( $31.9 \text{ µgmL}^{-1}$ , 100 µM), nystatin ( $250 \text{ µgmL}^{-1}$ ), and rottlerin ( $2.6 \text{ µgmL}^{-1}$ , 5 µM) for 30 min at 37 °C. Subsequently, endocytosis tracers (transferrin-AlexaFluor-633,  $25 \text{ µgmL}^{-1}$ ; BODIPY TR-ceramide,  $3.5 \text{ µgmL}^{-1}$ ; and Texas Red-dextran-10 kDa,  $0.5 \text{ mgmL}^{-1}$ ) known to specifically go through the clathrin, caveolae, and macropinocytosis pathways respectively, were added and incubated for another 1.5 h. After each treatment, the medium of each well was aspirated and the wells were washed extensively to remove all the conditions. The cells were then harvested by adding 0.1 mL of trypsin and incubated for 5 min at 37 °C with 5% CO<sub>2</sub>. Cells were recovered by centrifugation (5 min at 1200 rpm) and re-suspended in 100 µL of complete medium without phenol red. Finally the samples were measured in a Cytex DXP8 analyser cytometer within 30 min. The analysis of the data was done using FlowJo and Prism software.

### **Inhibition Studies of Endocytosis Routes**

After culturing for 48 h, each well containing cells was washed with PBS and pre-treated with either sucrose ( $102.7 \text{ mgmL}^{-1}$ , 0.3 M), chlorpromazine ( $31.9 \text{ µgmL}^{-1}$ , 100 µM), nystatin ( $250 \text{ µgmL}^{-1}$ ), or rottlerin ( $2.6 \text{ µgmL}^{-1}$ , 5 µM) for 30 min at 37 °C. Then, the different NMOFs ( $0.5 \text{ mgmL}^{-1}$  in growth media) were added and incubated for another 1.5 h. Subsequently, following the general procedure, the samples were measured by flow cytometry.

### Confocal Microscopy

For all the co-localization experiments, HeLa cells were seeded in a NUNC™ imaging four-well plate at a density of  $1.11 \times 10^5$  cell/mL and incubated for 24 h at 37 °C with 5% CO<sub>2</sub> in cDMEM. At the end of the incubation period the four-well plate was placed on a Leica TCS SP5 confocal microscope to be imaged. The microscope was equipped with 405 diode, argon and HeNe lasers. Leica LAS AF software was used to analyse the images.

The cells were then washed with PBS and incubated with 0.5 mg/mL of UiO-66-L1, UiO-66-L1-PEG550, or UiO-66-L1-PEG2000, along with LysoTracker®-Deep red for 2 h at 37 °C with 5% CO<sub>2</sub> in cDMEM. Subsequently, the cells were washed with PBS to remove the conditions, with trypan blue (0.4%) to quench any external fluorescence, and again three times with PBS. Finally, fresh media without phenol red was added to each sample.

### 4.10 References

1. M. A. Dobrovolskaia and S. E. McNeil, *Nature Nanotechnology*, 2007, **2**, 469-478.
2. P. R. Taylor, L. Martinez-Pomares, M. Stacey, H. H. Lin, G. D. Brown and S. Gordon, *Annual Review of Immunology*, 2005, **23**, 901-944.
3. I. Canton and G. Battaglia, *Chemical Society Reviews*, 2012, **41**, 2718-2739.
4. M. Gonzalez-Gaitan and H. Stenmark, *Cell*, 2003, **115**, 513-521.
5. T.-G. Iversen, T. Skotland and K. Sandvig, *Nano Today*, 2011, **6**, 176-185.
6. J. Rejman, V. Oberle, I. S. Zuhorn and D. Hoekstra, *The Biochemical Journal*, 2004, **377**, 159-169.
7. K. Yin Win and S.-S. Feng, *Biomaterials*, 2005, **26**, 2713-2722.
8. Z. Mao, X. Zhou and C. Gao, *Biomaterials Science*, 2013, **1**, 896-911.
9. C. Orellana-Tavra, S. Haddad, R. J. Marshall, I. Abánades Lázaro, G. Boix, I. Imaz, D. Maspoch, R. S. Forgan and D. Fairen-Jimenez, *ACS Applied Materials and Interfaces*, 2017, **9**, 35516-35525.
10. C. Orellana-Tavra, S. A. Mercado and D. Fairen-Jimenez, *Advanced Healthcare Materials*, 2016, **5**, 2261-2270.
11. A. M. Bannunah, D. Vilasaliu, J. Lord and S. Stolnik, *Molecular Pharmaceutics*, 2014, **11**, 4363-4373.
12. S. Bolte and F. P. Cordelières, *Journal of Microscopy*, 2006, **224**, 213-232.
13. T. Wang, J. Bai, X. Jiang and G. U. Nienhaus, *ACS Nano*, 2012, **6**, 1251-1259.
14. O. Harush-Frenkel, N. Debotton, S. Benita and Y. Altschuler, *Biochemical and Biophysical Research Communications*, 2007, **353**, 26-32.
15. S. Mayor and R. E. Pagano, *Nature Reviews. Molecular Cell Biology*, 2007, **8**, 603-612.
16. H. T. McMahon and E. Boucrot, *Nature Reviews. Molecular Cell Biology*, 2011, **12**, 517-533.
17. A. L. Kiss and E. Botos, *Journal of Cellular and Molecular Medicine*, 2009, **13**, 1228-1237.
18. J. Shin and S. N. Abraham, *Immunology*, 2001, **102**, 2-7.
19. J. P. Lim and P. A. Gleeson, *Immunology and Cell Biology*, 2011, **89**, 836-843.

20. W. Wang, L. Wang, Z. Li and Z. Xie, *Chemical Communications*, 2016, **52**, 5402-5405.
21. X. Zhu, J. Gu, Y. Wang, B. Li, Y. Li, W. Zhao and J. Shi, *Chemical Communications*, 2014, **50**, 8779-8782.
22. J. Park, Q. Jiang, D. Feng, L. Mao and H.-C. Zhou, *Journal of the American Chemical Society*, 2016, **138**, 3518-3525.
23. K. Greish, *Methods in Molecular Biology*, 2010, **624**, 25-37.
24. C. He, K. Lu, D. Liu and W. Lin, *Journal of the American Chemical Society*, 2014, **136**, 5181-5184.
25. W. Morris, W. E. Briley, E. Auyeung, M. D. Cabezas and C. A. Mirkin, *Journal of the American Chemical Society*, 2014, **136**, 7261-7264.
26. Y. Chen, S. Wang, X. Lu, H. Zhang, Y. Fu and Y. Luo, *Blood*, 2011, **117**, 6392-6403.
27. D. Vercauteren, R. E. Vandenbroucke, A. T. Jones, J. Rejman, J. Demeester, S. C. De Smedt, N. N. Sanders and K. Braeckmans, *Molecular Therapy : The Journal of the American Society of Gene Therapy*, 2010, **18**, 561-569.
28. T. J. Tuthill, E. Groppelli, J. M. Hogle and D. J. Rowlands, *Current topics in Microbiology and Immunology*, 2010, **343**, 43-89.
29. K. Sarkar, M. J. Kruhlak, S. L. Erlandsen and S. Shaw, *Immunology*, 2005, **116**, 513-524.
30. M. H. Teplensky, M. Fantham, P. Li, T. C. Wang, J. P. Mehta, L. J. Young, P. Z. Moghadam, J. T. Hupp, O. K. Farha, C. F. Kaminski and D. Fairen-Jimenez, *Journal of the American Chemical Society*, 2017, **139**, 7522-7532.
31. J. Yang, X. Chen, Y. Li, Q. Zhuang, P. Liu and J. Gu, *Chemistry of Materials*, 2017, **29**, 4580-4589.
32. D. Chen, D. Yang, C. A. Dougherty, W. Lu, H. Wu, X. He, T. Cai, M. E. Van Dort, B. D. Ross and H. Hong, *ACS Nano*, 2017, **11**, 4315-4327.
33. E. J. Joo, G. B. ten Dam, T. H. van Kuppevelt, T. Toida, R. J. Linhardt and Y. S. Kim, *Glycobiology*, 2005, **15**, 1-9.
34. R. Röder, T. Preiß, P. Hirschle, B. Steinborn, A. Zimpel, M. Höhn, J. O. Rädler, T. Bein, E. Wagner, S. Wuttke and U. Lächelt, *Journal of the American Chemical Society*, 2017, **139**, 2359-2368.
35. N. Oh and J. H. Park, *International Journal of Nanomedicine*, 2014, **9**, 51-63.
36. I. Abánades Lázaro, S. Haddad, J. M. Rodrigo-Muñoz, C. Orellana-Tavra, V. del Pozo, D. Fairen-Jimenez and R. S. Forgan, *ACS Applied Materials and Interfaces*, 2018, **10**, 5255-5268.
37. I. Abánades Lázaro, S. Haddad, S. Sacca, C. Orellana-Tavra, D. Fairen-Jimenez and R. S. Forgan, *Chem*, 2017, **2**, 561-578.
38. C. Deutsch, J. S. Taylor and D. F. Wilson, *Proceedings of the National Academy of Sciences of the United States of America*, 1982, **79**, 7944-7948.
39. R. A. Cairns, I. S. Harris and T. W. Mak, *Nature Reviews Cancer*, 2011, **11**, 85-95.
40. J. B. DeCoste, G. W. Peterson, H. Jasuja, T. G. Glover, Y.-g. Huang and K. S. Walton, *Journal of Materials Chemistry A*, 2013, **1**, 5642-5650.
41. C. Chen, J. Ke, X. E. Zhou, W. Yi, J. S. Brunzelle, J. Li, E.-L. Yong, H. E. Xu and K. Melcher, *Nature*, 2013, **500**, 486-489.
42. I. R. Vlahov and C. P. Leamon, *Bioconjugate Chemistry*, 2012, **23**, 1357-1369.
43. G. L. Zwicke, G. A. Mansoori and C. J. Jeffery, *Nano Reviews*, 2012, **3**, 18496.
44. J. Hirsh, T. E. Warkentin, S. G. Shaughnessy, S. S. Anand, J. L. Halperin, R. Raschke, C. Granger, E. M. Ohman and J. E. Dalen, *Chest*, 2001, **119**, 64S-94S.
45. C. R. Hopkins and I. S. Trowbridge, *Journal of Cell Biology*, 1983, **97**, 508-521.

46. C. S. Chen, A. G. Rosenwald and R. E. Pagano, *The Journal of Biological Chemistry*, 1995, **270**, 13291-13297.
47. M. Makarow, *The Embo Journal*, 1985, **4**, 1861-1866.
48. G. A. Mansoori, K. S. Brandenburg and A. Shakeri-Zadeh, *Cancers*, 2010, **2**, 1911-1928.

## Chapter 5

# Study of Therapeutic Efficiency and Human Immune Response of Zirconium MOFs

This Chapter is adapted in part from the following publication:

“Zirconium Metal-Organic Frameworks in Drug Delivery and Biomedicine”

Submitted

**I. Abánades Lázaro** and R. S. Forgan

“Selective Surface PEGylation of UiO-66 Nanoparticles for Enhanced Stability, Cell Uptake and pH Responsive Drug Delivery”

*Chem*, **2017**, 2, 561–578. (DOI: 10.1016/j.chempr.2017.02.005.)

**I. Abánades Lázaro**, S. Haddad, S. Sacca, C. Orellana-Tavra, D. Fairen-Jimenez and R. S. Forgan

“Mechanistic Investigation into the Selective Anticancer Cytotoxicity and Immune System Response of Surface Functionalised, Dichloroacetate-Loaded, UiO-66 Nanoparticles”

*ACS Appl. Mater. Interfaces*, **2018**, 10, 6, 5255-5268 (DOI: 10.1021/acsami.7b17756)

**I. Abánades Lázaro**, S. Haddad, J. Rodrigo-Muñoz, C. Orellana-Tavra, V. del Pozo, D. Fairen-Jimenez, and Ross S. Forgan

“Enhancing Anticancer Cytotoxicity through Bimodal Drug Delivery from Ultrasmall Zr MOF Nanoparticles”

*Chem. Commun.*, **2018**, 54, 2792-2795. (DOI: 10.1039/C7CC09739E)

**I. Abánades Lázaro**, S. Abánades Lázaro and R. S. Forgan.

**Table of Contents**

<b>Chapter 5</b> .....	191
Table of Contents .....	192
5.1 Introduction.....	193
5.1.1 <i>In vitro</i> Studies of MOFs.....	193
5.1.2 <i>In vivo</i> Studies of MOFs .....	201
5.1.3 Dichloroacetate, a Metabolic Target.....	203
5.2 Aims .....	205
5.3 Therapeutic Efficiency of the DCA@UiO family .....	207
5.3.1 Therapeutic Efficiency of DCA@MOFs .....	207
5.3.2. Therapeutic Efficiency of 5-FU@DCA@MOFs .....	212
5.4. Postsynthetic Surface Functionalisation of DCA-Loaded Samples.....	216
5.5. Therapeutic efficacy of DCA-Loaded, Surface Modified UiO-66.....	222
5.5.1 MOFs Cytotoxicity Towards HeLa Cervix Cancer Cells .....	222
5.5.2. Cytotoxicity Against MCF-7 and HEK293 .....	228
5.5.3. Cytotoxicity of Free Dichloroacetate .....	232
5.6. Immune System Response Towards Surface Modified UiO-66.....	233
5.6.1. Endocytosis Efficiency Towards J774 Macrophage Cells .....	234
5.6.2. Cytotoxicity Against J774 and PBL Cells .....	235
5.6.3. Reactive Oxygen Species Generation in J774 and PBL Cells .....	237
5.7 Conclusions .....	239
5.8 Experimental.....	242
5.9 Refereces .....	244

## 5.1 Introduction

### 5.1.1 *In vitro* Studies of MOFs

The therapeutic efficiency of any DDS is strictly correlated to its ability to cross the cell membrane and successfully deliver the drug to the various cell compartments.<sup>1,2</sup> As described in Chapter 4, both cell internalisation rates and routes are of crucial importance for efficient drug delivery, as well as low toxicity and the ability to deliver active cargo into cells. Typically, *in vitro* cell proliferation experiments, such as MTS and MTT assays after incubation of cells with the DDSs, are used as key initial evaluators of the effect of factors such as surface modification and drug loading. A summary of the most relevant *in vitro* studies carried out with MOFs is given in table 5.1.

During Chapter 1, the biocompatibility of bare Zr MOFs, such as UiO-66 (IC<sub>50</sub> of 1.50 ± 0.15 mg/mL after 24 hours of exposure),<sup>3, 4</sup> PCN-223, ZJU-800<sup>5</sup> or Zr-fumarate,<sup>6</sup> was discussed. This biocompatibility and their high storages capacities mean many examples of Zr MOFs *in vitro* and *in vivo* anticancer activity are emerging in the literature.<sup>7-9</sup>

The efficiency of therapeutic cargo delivery into cells can be monitored *in vitro*, by comparing cell proliferation in the presence of drug loaded MOF with that of the free drug and the empty MOF. The therapeutic efficiency of UiO-66-AL, coated on its inner and outer surface with the drug Alendronate, was tested in human liver carcinoma HepG2 cells (Figure 5.1a) and human breast cancer MCF-7 cells (Figure 5.1b) using the MTT protocol.<sup>10</sup> The authors found that after 24 hours of incubation, the free drug had a higher effect than the loaded NMOFs, while after 48 hours, incubation with UiO-66-AL decreased cell viability to a slightly higher extent than when cells were treated with a solution of the same free drug concentration. These results could indicate slow uptake of the MOF or particles reaching different intracellular locations after different time periods, but it is also important to consider that if the NMOF itself degrades during the incubation time, the free drug subsequently present in the growth media could then be internalised through passive diffusion and thus inhibit cancer cell growth.

**Table 5.1:** Summary of in vitro studies carried out using Zirconium MOFs as DDs

MOF	Drug Loading	Cell line	Results
UiO-66	n/a	HeLa (human cervical cancer)	IC <sub>50</sub> = 1.50 ± 0.15 mg/mL of NMOF <sup>3,4</sup>
PCN-223 nanoPCN-223@ DOPC/DOPC	n/a	SMMC-7721 (human hepatocellular carcinoma) HeLa	Biocompatibility of empty MOF (0-50 µM based on linker TCPP) <sup>11</sup>
UiO-66-AL	Alendronate (AL) 51.4 % w/w	MCF-7 human breast carcinoma HepG2 human liver carcinoma	Higher efficacy than free drug for 48 h incubation time <sup>10</sup>
UiO-PDT	PDT based on linker I2-BODYPI	B16F10 mouse melanoma CT26 murine colon carcinoma C26 mouse colon carcinoma	No dark cytotoxicity (0.625 mg/mL of NMOF) Similar cytotoxicity to free linker under UV light <sup>12</sup> IC <sub>50</sub> = 0.70 µg/mL IC <sub>50</sub> = 1.15 µg/mL IC <sub>50</sub> = 0.51 µg/mL
PCN-224 PCN-224-FA	PDT based on linker	HeLa (over express FR) A549 human lung carcinoma (no FR over expression)	No cytotoxicity in dark 2 fold increase compared to free linker and more efficiency upon FA coating only for HeLa cells <sup>13</sup>
NU-1000 NU-091	α-CH (ca. 81 % w/w)	HeLa	Higher cytotoxicity than the free drug <sup>14</sup>
UiO family	α-CH (ca. 30 w/w %)	HeLa	Cytotoxicity accordingly with endocytosis routes of internalisation <sup>4,15</sup>
Zr <sub>80</sub> UiO-66-py-PGA-PEG-F3 <sup>16</sup>	DOX (50 % w/w)	MDA-MB-231 triple negative breast cancer L929 fibroblast	F3 functionalised samples higher cytotoxicity in cancer cells than non F3 targeted MOF (nucleolin targeting) Low L929 cell internalisation <sup>16</sup>
SiRNA-UiO-Cis	Cisplatin (12.3 % w/w)	SKOV-3 human ovarian cancer (cis-platin resistance) MCF-7, H460 human lung carcinoma and A2780 human ovarian carcinoma (cis-platin sensitive)	Co-delivery cis-platin and siRNA to overcome cis-platin resistance. Lower IC <sub>50</sub> values than free cis-platin when cis-platin resistant cells are incubated with siRNA- SiRNA-UiO-Cis more effective than UiO-Cis For cis-platin sensitive cell lines UiO-Cis and siRNA-UiO-Cis had similar cytotoxic effect. <sup>17</sup>
DOX@UiO-68-N3-DNA conjugates	DOX 52.8 Mmol DOX./ gram of NMOF.	MDA-MB-231 Breast adenocarcinoma MFC-10A breast epithelial cells	Time-dependant apoptosis studies Empty MOFs no cytotoxicity in both cell lines Nucleolin targeting MOF slightly higher cytotoxicity than non-targeted. DOX loaded MOFs higher cytotoxicity in cancer cells <sup>18</sup>
DOX@Fe <sub>3</sub> O <sub>4</sub> @UiO-66-NH <sub>2</sub>	DOX	HeLa 3T3 Mouse fibroblast	Empty MOF no cytotoxic up to 0.5 mg/mL Ca. 60 % cancer cells death upon treatment with 0.02 mg/mL of DOX loaded MOF, while 3T3 cells proliferation is not affected up to 0.5 mg/mL of loaded MOF. <sup>19</sup>
Zr-fum-H <sub>6</sub> -Tags	Pro-apoptosis peptides	HeLa	Higher cytotoxicity than free peptides due to higher fate of cell internalisation <sup>6</sup>

The biocompatibility of UiO-PDT, UiO-66 surface-modified with I2-BODIPY (I2-BDP), was investigated for mouse colon carcinoma C26 cells, murine colon carcinoma CT26 cells, and B16F10 mouse melanoma cells, with no induced cytotoxicity when cells were incubated for 24 h with concentrations up to  $1 \text{ mgmL}^{-1}$ .<sup>12</sup> As UiO-PDT can generate singlet oxygen ( $^1\text{O}_2$ ) under UV-light irradiation with similar efficiencies to I2-BDP (the free linker), the *in vitro* phototoxicity of UiO-66-PDT ( $0\text{-}0.625 \text{ mgmL}^{-1}$ ) was assessed using the MTT assay with CT26, C26 and B16F10 cells (Figure 5.1c). The authors observed that free I2-BDP has  $\text{IC}_{50}$  levels  $>15 \text{ }\mu\text{gmL}^{-1}$  in the dark, which decreases to  $\text{IC}_{50} < 0.8 \text{ }\mu\text{gmL}^{-1}$  when irradiated at a power density of  $80 \text{ mW cm}^{-2}$  for 10 min for the studied cell lines. UiO-PDT has similar cytotoxicity values to free I2-BDP under UV irradiation, with  $\text{IC}_{50}$  values of 0.70, 1.15 and  $0.51 \text{ }\mu\text{gmL}^{-1}$  for B16F10, CT26 and C26 cells in turn (Figure 5.1d), despite the higher cell internalisation of UiO-66-PDT compared to I2-BDP (1.5 fold), as determined by FACS.<sup>12</sup> The fact that I2-BDP can potentially undergo passive diffusion and thus be located in the cytoplasm rather than in vesicles, might be the reason why there is not a more pronounced cytotoxic effect when cells are incubated UiO-PDT, together with the fact that free linker has a slightly better ability to generate singlet oxygen.

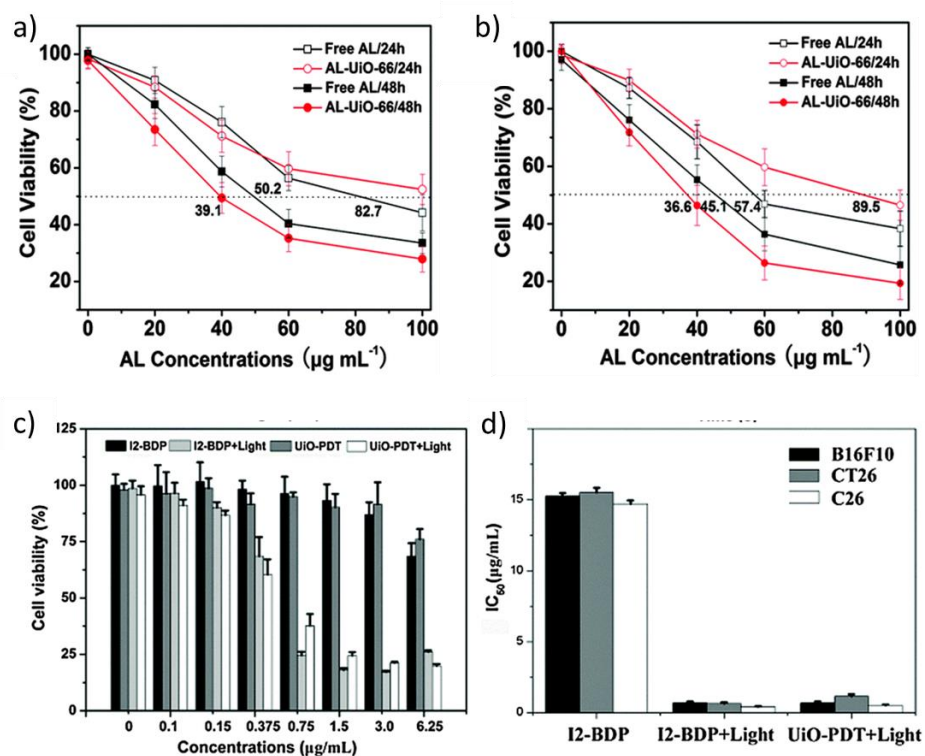


**Figure 5.1.** Cell viabilities of (a) HepG2 and (b) MCF-7 cells incubated with free AL and AL-UiO-66 at different concentrations for 24 and 48 h.<sup>10</sup> (c) *In vitro* cytotoxicities of free I2-BDP and UiO-PDT nanocrystals against B16F10 cells before and after being irradiated with visible light at a power density of  $80 \text{ mW cm}^{-2}$  for 10 minutes. (d) Half maximal inhibitory concentration ( $\text{IC}_{50}$ ) of I2-BDP and UiO-PDT with and without light irradiation against B16F10 cells.<sup>12</sup>

The potential of five PCN-224 samples of different particle sizes as PDT devices was also tested on HeLa cells, and therapeutic efficiency was consistent with the cell uptake results.<sup>13</sup> PCN-224 is a porphyrinic-based Zr MOF, which is also PDT active. Particles of 90 nm size, which were the most efficiently internalised size fraction, were also the most cytotoxic under light irradiation, with a 2 fold increase in cytotoxicity compared to free linker, while no remarkable effect on cell proliferation was found in dark. HeLa cells overexpress the folate receptor,<sup>20-22</sup> and thus coating the MOF with folic acid (PCN-224-FA) resulted in an enhancement of its therapeutic efficiency in comparison to the unmodified MOF. A control experiment, in which folate receptor negative negative cells (human lung carcinoma A549 cells) were treated with PCN-224-FA and bare PCN-224 was performed, showing no enhancement in either cell internalisation or PDT efficacy upon folate coating.<sup>13</sup>

$\alpha$ -Cyano-4-hydroxycinnamic acid ( $\alpha$ -CHC) has been proposed as an anticancer drug, and has been loaded postsynthetically into the pores of Zr MOFs.<sup>4</sup> An investigation of the delivery of  $\alpha$ -CHC into HeLa cells by UiO-66 series MOFs showed that cell proliferation was dependent on the endocytosis pathways of the MOFs.<sup>15</sup> As UiO-66 is internalised through clathrin-mediated endocytosis,  $\alpha$ -CHC@UiO-66 (31% w/w  $\alpha$ -CHC loading) did not have a negative effect on HeLa cells after incubation for 24 hours, but as UiO-67 partially undergoes caveolae-mediated endocytosis, incubation with  $\alpha$ -CHC@UiO-67 (20% w/w  $\alpha$ -CHC loading, 0.25-1 mgmL<sup>-1</sup>) decreased cell proliferation to < 70% for the concentrations studied, while the empty MOF was non-cytotoxic.<sup>4</sup> Due to the larger porosities of NU-1000 and NU-901,  $\alpha$ -CHC loadings of up to 81% w/w have been reached.<sup>14</sup> The therapeutic effect in HeLa cells of  $\alpha$ -CHC loaded NU-1000 and NU-901 before and after amorphisation through temperature treatment was studied using the MTS assay and compared to a control in which the cells were incubated with a solution of the same concentration of free drug (Figure 5.2).

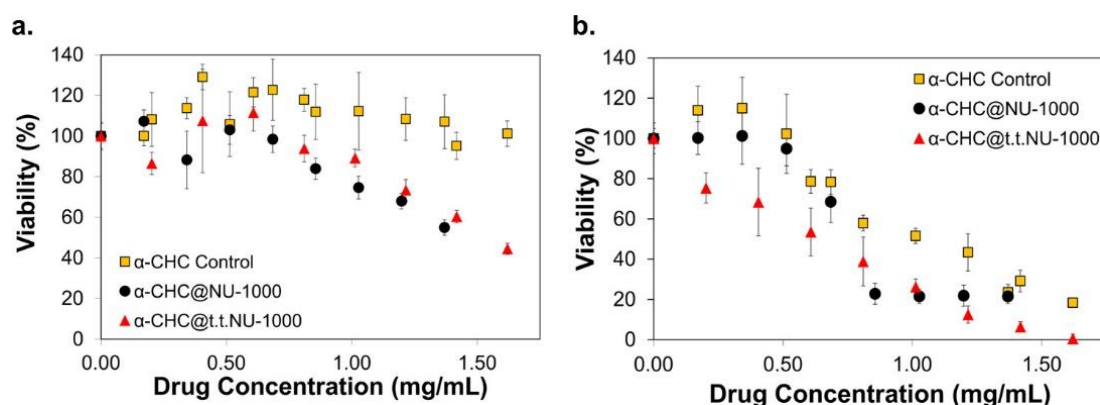


**Figure 5.2.** MTS Assays measuring enzymatic metabolic activity for  $\alpha$ -CHC-loaded NU-1000 in both crystalline and temperature treated complexes for (a) 11 h and (b) 48 h of in vitro incubation. The free drug control,  $\alpha$ -CHC, is shown incubated for both time points in yellow. Samples were run in minimum of four replicates. Standard errors are shown for each given concentration.<sup>14</sup>

Although both  $\alpha$ -CHC@NU-1000 and  $\alpha$ -CHC@tt-NU-1000 induce higher cell cytotoxicity than the free drug after 11 hours incubation, there is no significant difference between pristine and amorphised MOF (Figure 5.2a). The enhancement in cytotoxicity compared to the free drug could be a consequence of its greater internalisation when loaded in the DDS compared to passive diffusion, and to the internalisation of the MOF through caveolae-mediated endocytosis, enabling endosomal escape. After 48 hours of incubation time a notable difference upon temperature treatment was found, especially for lower concentrations of the temperature-treated NU-1000 (Figure 5.2b). While the free drug and  $\alpha$ -CHC@NU-1000 did not induce any cytotoxicity up to  $0.6 \text{ mgmL}^{-1}$  drug concentration, cell viability decreased to ca. 80% for  $0.2 \text{ mgmL}^{-1}$   $\alpha$ -CHC loaded in thermally treated NU-1000, while  $\alpha$ -CHC@tt-NU-1000 killed all cells at a drug concentration of  $1.60 \text{ mgmL}^{-1}$  of drug. Similar behaviour is observed for  $\alpha$ -CHC@NU-901 and  $\alpha$ -CHC@tt-NU-901, which have the same effect on HeLa cell viability after 11 hours of incubation, again showing considerably more cytotoxicity than the free drug, while after 48 hours of treatment, the efficacy of the thermally treated sample difference is more pronounced at lower concentrations. However, the loaded-MOF concentration necessary to reach the drug concentration stated during the experiment are quite high (around  $2 \text{ mgmL}^{-1}$  for the maximum concentrations), while the authors only studied the cytotoxicity of empty NU-1000 after 24 hours of incubation at concentrations up to  $1.6 \text{ mgmL}^{-1}$ , being non-cytotoxic, and no cytotoxic values of NU-901 are reported.<sup>14</sup>

The effect of empty and DOX loaded core-shell  $\text{Fe}_3\text{O}_4@\text{UiO}-66\text{-NH}_2$  on HeLa cells growth was investigated using the MTT assay. While empty MOF did not induce cytotoxicity even at concentrations of  $0.5 \text{ mgmL}^{-1}$  of MOF (Figure 5.3a), HeLa cells growth was significantly affected upon treatment with  $\text{DOX}@\text{Fe}_3\text{O}_4@\text{UiO}-66\text{-NH}_2$ , which induced 60% cell death when treated with a solution of MOF containing  $0.02 \text{ mg/mL}$  of DOX during 24 hours.<sup>19</sup> The NMOF possessed similar anti-cancer activity to DOX when incubation time was 24 hours, which was enhanced after 48 hours (Figure 5.3b). Noteworthy, the loaded NMOF did not affect considerably mouse fibroblast 3T3 cells for concentrations up to  $0.5 \text{ mg/mL}$  of NMOF, showing no negative effects on normal cells (Figure 5.3c).

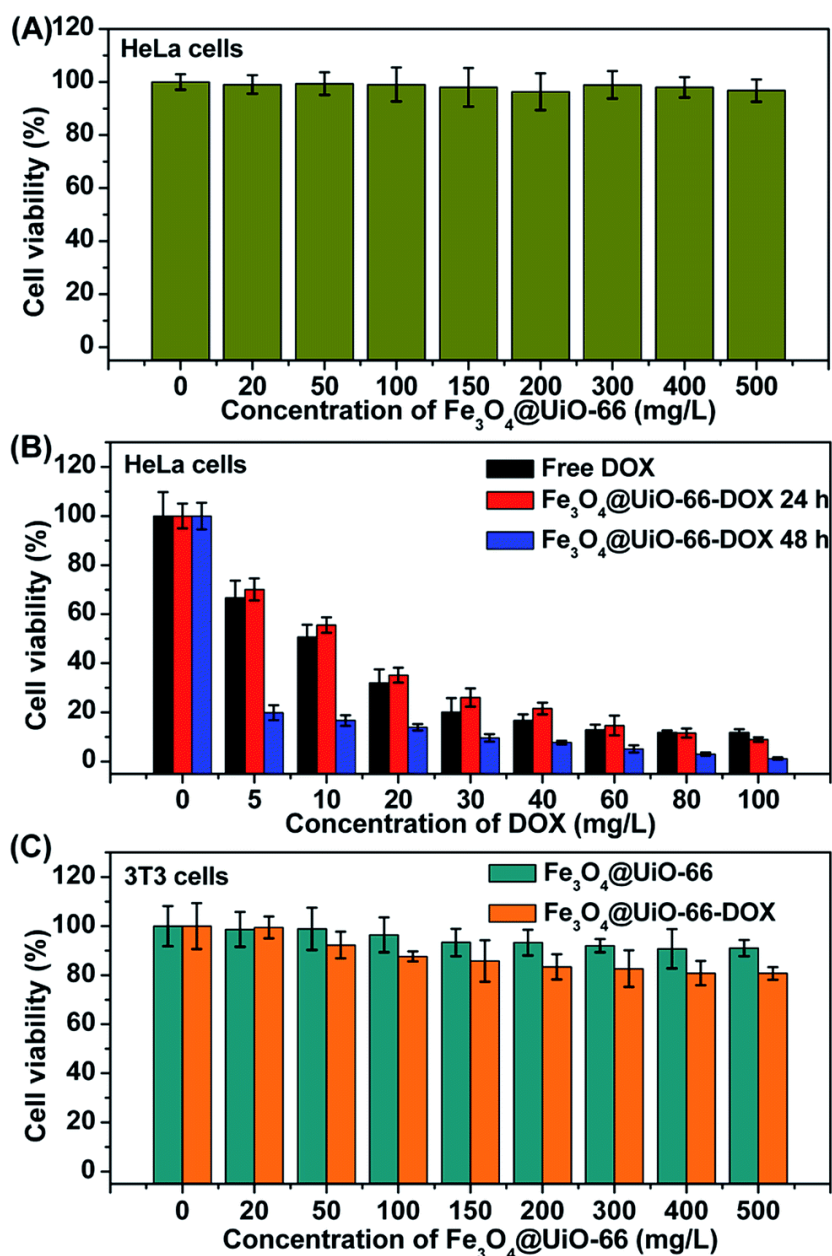


**Figure 5.3.** (a) Cell viability of HeLa cells after incubation with different concentrations of  $\text{Fe}_3\text{O}_4@\text{UiO}-66$ . (b) Cell viability of HeLa cells after incubation with free DOX and  $\text{Fe}_3\text{O}_4@\text{UiO}-66$ -DOX for 24 h or 48 h at the same concentration of DOX. (c) Cell viability of 3T3 cells after incubation with  $\text{Fe}_3\text{O}_4@\text{UiO}-66$  and  $\text{Fe}_3\text{O}_4@\text{UiO}-66$ -DOX for 24 h at the same concentration of  $\text{Fe}_3\text{O}_4@\text{UiO}-66$ .<sup>19</sup>

The potential of Zr-fumarate as a delivery vector for biomolecules was investigated by attaching various pro-apoptotic peptides (Bak, Bad, KLK) and a cytochrome c protein (CytC), which due to their membrane impermeability are not able to efficiently cross the cells membrane by themselves, to the NMOF surface using His-tags.<sup>6</sup> A decrease in HeLa cell viability when treated with the peptide-modified NMOFs was considered a consequence of efficient cytosolic release of the attached peptides. The authors compared the effect on cells growth to those obtained when incubating cells with free peptide or naked Zr-fumarate during

the same period of time. The peptide or protein conjugated MOFs induced remarkably higher cytotoxicity (ca. 40% cells viability) compared with the free peptide (ca. 90%), while naked MOF did not exhibit any cytotoxicity, confirming the intracellular delivery of the peptides by the MOF.<sup>6</sup>

Lin and co-workers investigated siRNA transfection efficiency mediated by siRNA-UiO-Cis, which possess loaded-cisplatin and attached siRNA through phosphates, in SKOV-3 ovarian cancer cells, which have cis-platin resistance.<sup>17</sup> By siRNA delivery, the authors aimed to inhibit three genes (surviving, Bcl-2 and P-gp) in order to overcome cis-platin resistance. ELISA assays showed that while when cisplatin resistant cells were incubated with UiO-66-Cis together with a pool of siRNA or with siRNA specific to inhibit certain genes, induced potent gene silencing, while free siRNAs on their own did not have the same effect (Figure 5.4a). These results correlated with the therapeutic effect, as when SKOV-3 cisplatin resistant cells were incubated with either UiO-Cis or free cis-platin plus a pool of siRNA, a similar cytotoxic effect to the free drug on its own ( $IC_{50} = 53.9 \pm 4.7$ ,  $53.2 \pm 4.4$  and  $45.1 \pm 7.0$   $\mu$ M cis-platin for free cis-platin, UiO-Cis and free cis-platin/pool siRNA respectively) was observed, whereas when were cells incubated with UiO-Cis/pool siRNA or free cis-platin/siRNA-UiO remarkably lower  $IC_{50}$  values ( $4.7 \pm 1.8$  and  $6.6 \pm 0.3$   $\mu$ M cis-platin respectively) were found (Figure 5.4b). Importantly, no cytotoxicity was found for siRNA-UiO, confirming that it is the co-delivery of siRNA and cis-platin what induces KOV-3 cells cytotoxicity.<sup>17</sup>

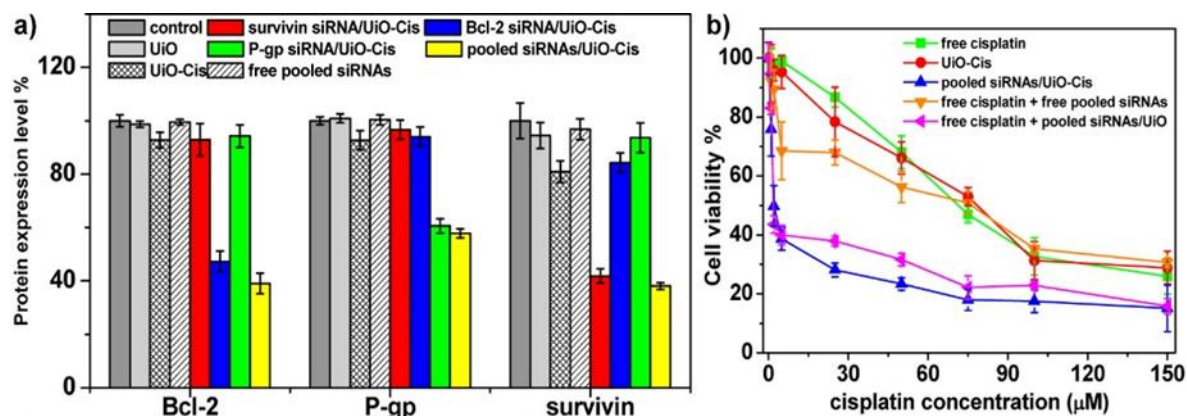


**Figure 5.4.** In vitro gene silencing efficiency and anticancer efficacy. (a) siRNA/UiO-Cis-mediated efficient gene silencing in SKOV-3 cells at a 30 nM siRNA dose. Silencing efficiency was expressed as percentage values of control group treated with PBS. (b) SKOV-3 cells were incubated with free cisplatin, UiO-Cis, pooled siRNAs/UiO-Cis, free cisplatin plus free pooled siRNAs, and free cisplatin plus pooled siRNAs/UiO at different concentrations for 72 h, and then the cytotoxicity was determined by MTS assay.<sup>17</sup>

Experiments using cis-platin sensitive cell lines, such as human ovarian carcinoma A2780, human breast carcinoma MCF-7 and human lung carcinoma H460 cells, demonstrated that both UiO-Cis and siRNA-UiO-Cis had similar levels of cytotoxicity, strongly suggesting that siRNA and cis-platin co-delivery using UiO-68 as a DDS could overcome cis-platin resistance of certain cancer cells through the combined effect of therapeutics and MDR-gene silencing. Through Annexin V conjugate staining and DNA ladder assays, siRNA-UiO-Cis cytotoxicity was proved to occur due to induced apoptosis rather than necrosis.<sup>17</sup>

*In vitro* tumour targeting using the F3 nucleolin targeting peptide was investigated with <sup>89</sup>Zr-UiO-66-py-PGA-PEG-F<sub>3</sub> against both the MDA-MB-231 triple-negative breast cancer cells, which over express the nucleolin receptor (n+), and L929 fibroblasts, which do not (n-).<sup>16</sup> <sup>89</sup>Zr-UiO-66-py-PGA-PEG-F<sub>3</sub> is surface-modified with surface PEG and targeting F3 peptide chains introduced through  $\pi$ - $\pi$  stacking. The empty MOF did not affect MDA-MB-231 cell growth in concentration range (0-50  $\mu\text{g mL}^{-1}$ ), and the doxorubicin loaded targeted MOF decreased MDA-MB-231 cell viability to a greater extent than an analogue without the F3 peptide, as a consequence of enhanced MOF internalisation through targeting receptor-mediated endocytosis.<sup>16</sup>

The cytotoxicity of various doxorubicin loaded UiO-68-N<sub>3</sub>-DNA conjugates has also been assessed against MDA-MB-231 cells by measurement of time-dependent apoptosis.<sup>18</sup> The empty NMOFs induced less than 20% cell death after 42 hours, while the DOX-loaded MOF functionalised with a cytosine-rich DNA sequence induced around 50% of cell apoptosis for the same incubation time. Addition of the AS1411 aptamer, which binds to the nucleolin receptor (overexpressed on the surface of cancer cells) to the doxorubicin-loaded MOF induced 100% of cell death for the same incubation time, again as a consequence of targeting.

Cell apoptosis was found to be a function of time, with different slopes depending of the NMOF. Cytotoxicity of the NMOFs was investigated in both MFC-10A breast epithelial cells and MDA-MB-231 breast cancer cells after incubation with the NMOF during 6 hours, followed by cells washing and further three and five days of incubation, showing no remarkable cytotoxicity for the empty MOFs in any cell line. The difference between the two surface-functionalised NMOFs was not remarkable. While C-rich DNA sequences reduced cell proliferation to levels of ca. 65 %, the extra nucleolin receptor on the NMOF surface reduced cell proliferation to levels of ca. 55% after 72 hours of incubation time. When the NMOF was surface functionalised with Mg<sup>2+</sup>-dependent DNAzyme subunit separate by ATP-aptamer sequences, empty MOF did not induce cell death on any of the two cell lines, while DOX loaded MOF decreased cell viability of breast cancer cells to ca. 70% after 3 days and ca. 60 % after 5 days, while not affecting the growth of healthy breast cells.<sup>18</sup>

### 5.1.2 *In vivo* Studies of MOFs

*In vivo* studies have also been performed using Zr-based MOFs as DDSs. For example, the distribution and clearance profile of Zr<sup>89</sup>UiO-66 up to 120 hours post-injection was investigated *in vivo* using PET. The health of the mice was monitored after treatment of medium doses (10 mg/kg) and high doses (50 mg/kg) of Zr<sup>89</sup>UiO-66-Py-PGA-PEG, finding no side effects or acute, medium or chronic toxicity. PET scans of MDA-MB-231 tumours were taken at point times of 0.5, 2, 20, 24, 48, 72, 96 and 120 hours.<sup>16</sup>

The circulation half-life of Zr<sup>89</sup>-UiO-66-Py-PGA-PEG was determined through serial blood sampling method, being 118.8 min, indicating that the PEG surface density achieved by  $\pi$ - $\pi$  interactions might not be high enough to prolong circulation times. Zr<sup>89</sup>-UiO-66-Py-PGA-PEG-F<sub>3</sub> tumour uptake was found to be higher at all the time points than Zr<sup>89</sup>-UiO-66-Py-PGA-PEG as a consequence of the targeting peptide F<sub>3</sub>. However, after a maximum uptake around 2 hours after injection, MOF accumulation in tumour tissue gradually decreases with time. The MOFs were found to be highly accumulated in the liver and spleen, with no major decrease over time. In order to study F<sub>3</sub> targeting properties, the NMOFs were administered together with a nucleolin blocking dose (10 mg/kg) five minutes before Zr<sup>89</sup>-UiO-66-Py-PGA-PEG-F<sub>3</sub>, causing tumour uptake reduction and thus confirming that targeting through F<sub>3</sub> peptide is one of the reasons why tumour uptake is slightly enhanced, while liver and spleen accumulation were not affected. The MOFs have slow clearance from the liver, while no radioactivity deposition was found in the bone or kidney. Tumour-muscle contrast was found to be efficient and as high as  $76.3 \pm 3.9$  at 2 hours post-injection, while  $19.6 \pm 5.4$  after 120 hours.<sup>16</sup> The DOX@UiO-66-Py-PGA-PEG and DOX@UiO-66-Py-PGA-PEG-F<sub>3</sub> *in vivo* DOX release was studied by *ex vivo* fluorescence imaging, showing a 4-fold increase DOX signal in tumour upon F<sub>3</sub> peptide targeting.<sup>16</sup>

The potential of Fe<sub>3</sub>O<sub>4</sub>@UiO-66-NH<sub>2</sub> core-shell composites as MRI contrast agents was also evaluated *in vivo*.<sup>19</sup> Previously, magnetic resonance (MR) images of HeLa cells treated with different concentration of Fe<sub>3</sub>O<sub>4</sub>@UiO-66-NH<sub>2</sub> were performed in order to gain insights into the T2-weighted images obtained during *in vivo* treatment (Figure 5.5a). Bio distribution and toxicology studies were performed *in vivo* to evaluate potential toxic effects, and thus T2-weighted images of the Kummung mice were taken 1, 7, 14 and 30 days after injection (Figure 5.5b). Since no darkening effect was found in the urinary bladder, while high darkening with time-recovery signal was observed in the liver, Fe<sub>3</sub>O<sub>4</sub>@UiO-66-NH<sub>2</sub> seems to be excreted from the liver rather than from the kidney. Remarkable signal darkening was found in the liver 10 min post-injection, and after 1 hour in the tumour, which remarkably increased for 9 hours post-injection time (Figure 5.5c), thus confirming NMOFs accumulation in tumour tissue after prolonged times. The biodistribution of the core-shell MOFs was determined *ex vivo* in

specimens after 1, 7 and 30 days of injection by ICP-MS determination of the iron and zirconium levels of the different digested organs. In concordance with T2-weighted images, high accumulation of Zr and Fe was found in the liver and spleen. The levels decreased with prolonged times, reaching similar levels to untreated control after 30 days. However, the iron content in the liver was slightly higher than the untreated mice after 30 days. The body weight and growth of mice was found not to be affected when treated with  $\text{Fe}_3\text{O}_4@\text{UiO}-66\text{-NH}_2$ , and blood analysis was consistent with the untreated control. In general, it was proved that  $\text{Fe}_3\text{O}_4@\text{UiO}-66\text{-NH}_2$  is relatively safe for *in vivo* treatments. The anti-cancer therapeutic effect of the core-shell MOFs was measured *in vivo* towards HeLa bearing tumour mice. While tumours in control mice growth quickly, mice treated with  $\text{DOX}@\text{Fe}_3\text{O}_4@\text{UiO}-66\text{-NH}_2$  showed tumour growth inhibition with a 4 fold decrease in weight. The tumour growth was monitored *in vivo* through MRI. Darkening effect was observed in the tumour area, thus indicating passive accumulation in the tumour (Figure 5.5c).<sup>19</sup>

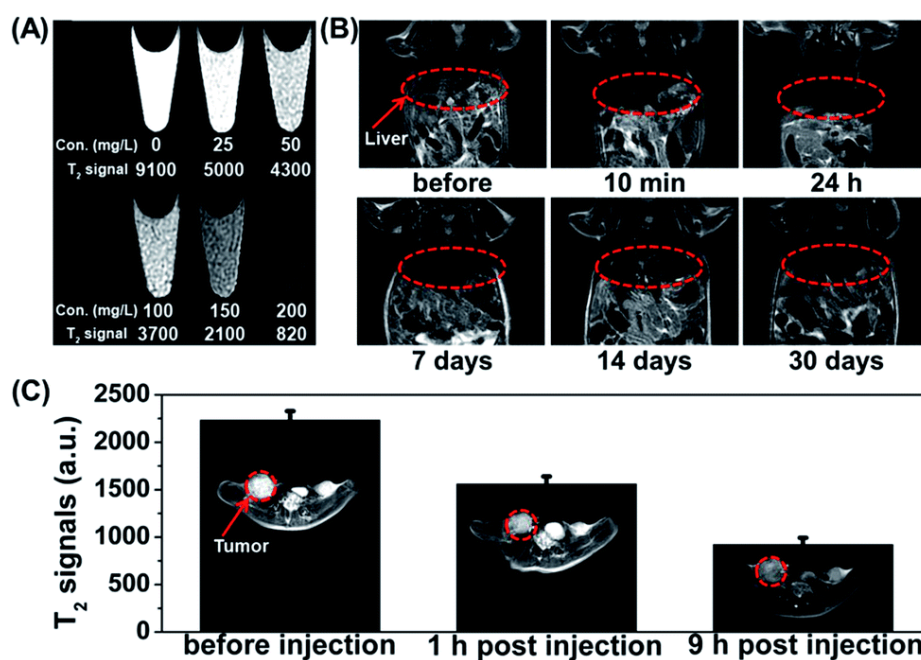


**Figure 5.5.** (a) MR images of HeLa cells after incubation with different concentrations (0, 25, 50, 100, 150 and 200 mg L<sup>-1</sup>) of  $\text{Fe}_3\text{O}_4@\text{UiO}-66\text{-NH}_2$  for 24 h. (b) T2-weighted MR images of the Kunming mouse before and after intravenous injection of  $\text{Fe}_3\text{O}_4@\text{UiO}-66\text{-NH}_2$  at different time points (liver region marked by red cycles). (c) T2-weighted MR images and T2-MR signals of tumor on HeLa-tumor bearing mice before injection, 1 h and 9 h post injection of  $\text{Fe}_3\text{O}_4@\text{UiO}-66\text{-NH}_2$  intravenously (tumor region marked by red cycles).<sup>19</sup>

Accumulation in the liver and spleen is often a consequence of high macrophage recognition and uptake. Therefore developing surface functionalisations that avoid macrophage recognition, while enhancing cancer cells uptake through targeting units might be an alternative to overcome accumulation in the body. Additionally, surface modifications that

ensure adequate colloidal dispersion and ideal drug release kinetics under extracellular conditions, while fast surface detachment and consequent degradation under intracellular conditions might be an alternative to overcome accumulation issues.

### 5.1.3 Dichloroacetate, a Metabolic Target

Dichloroacetate (DCA) is a pyruvate dehydrogenase kinase (PDK) inhibitor which has been investigated for over 40 years for the treatment of mitochondrial disorders such as lactic acidosis.<sup>23-26</sup> PDK is one of the main enzymes responsible for promoting glycolysis over glucose oxidation in cancer cells, as it can inhibit pyruvate dehydrogenase (PDH), an enzyme that converts pyruvate to acetylCoA.<sup>27-29</sup> Once glucose has been transformed to pyruvate, instead of being decarboxylated to form acetylCoA and entering the Krebs cycle in the mitochondria, pyruvate is alternatively transformed to lactate in the cytosol of cancer cells,<sup>30, 31</sup> allowing them to grow in hypoxic conditions (low presence of oxygen) and resist apoptosis.<sup>32-34</sup> DCA shifts cancer cells metabolism from glycolysis back to glucose oxidation by PDH re-activation, decreasing the mitochondrial membrane hyperpolarisation and activating Kv channels, thus unlocking cancer cells from a state of apoptosis resistance without affecting growth of healthy cells.<sup>35-39</sup>

Although DCA is not currently under clinical use as an anticancer drug, due to its ability to target glycolysis it has been studied as a potential metabolic cancer therapy since 2007,<sup>38, 40</sup> with several clinical trials showing significant tumour remission without healthy cells damage, low side effects and toxicity, and safe chronic use.<sup>35, 37, 39, 41, 42</sup> However, due to its ability to cross the brain membrane barrier, chronic exposure to very high DCA doses can result in reversible peripheral neuropathy.<sup>43</sup>

The hydrophilic nature of DCA means it does not efficiently cross the cell membrane,<sup>44</sup> with limited ability to reach its target mitochondria, and thus free DCA displays low cytotoxicity, with IC<sub>50</sub> values in the milimolar range, three orders of magnitude higher than anticancer drugs such as cisplatin.<sup>45</sup> DCA is rapidly cleared out from the blood stream, with initial half-life times of about an hour,<sup>25</sup> leading to poor efficacy and targeting when the drug is injected alone.<sup>39, 45</sup> Nevertheless, cancer cells have shown remarkably lower resistance factors to DCA compared to cisplatin and other anticancer therapeutics (Figure 5.6),<sup>45</sup> which is a notable drawback for anticancer therapy.

For example, oxaliplatin, a prodrug of cisplatin with FDA approval,<sup>46</sup> modified with DCA axial ligands (Figure 5.6) displayed enhanced anticancer activity in cisplatin sensitive and resistant cancer cells lines compared to cisplatin and oxaliplatin.<sup>45</sup> After 72 hours of incubation with MCF-7 cisplatin resistant breast cancer cells, oxaliplatin had IC<sub>50</sub> doses of  $19 \pm 1 \mu\text{M}$ , while the oxaliplatin DCA conjugates had IC<sub>50</sub> doses of  $1.6 \pm 0.2 \mu\text{M}$ . Importantly, the resistant factor

was also lowered from 6.7 to 1. The authors found that when oxaliplatin was incubated with free DCA there was no significant decrease in the  $IC_{50}$  dose, possibly as a consequence of poor internalisation of DCA on its own.<sup>45</sup>

Polymeric nanoparticulate encapsulation of a cisplatin prodrug containing DCA axial ligands (mitaplatin) in poly(D,L-Lactic-co-glycolic acid)-block-poly(ethylene glycol) (PLGA-PEG) has been performed and evaluated *in vivo*, showing that encapsulation increases circulation times while reduces accumulation in the kidneys, with controlled release of mitaplatin overtime compared to free mitaplatin, thus enhancing its long-term anticancer efficacy.<sup>47</sup>

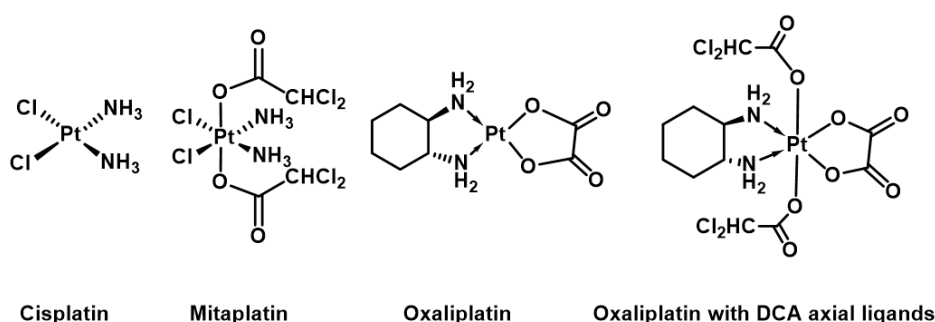


**Figure 5.6.** Cisplatin and its prodrugs: Mitaplatin, a derivate of cisplatin containing DCA axial ligands<sup>47</sup> oxaliplatin, a produg of cisplatin, and a derivate of oxaliplatin with DCA axial ligands.<sup>45</sup>

DCA is known to enhance the potency of the thymidylate synthase inhibitor 5-FU effects,<sup>48, 49</sup> and thus its  $IC_{50}$  dose towards HCT116 colon cancer cells was also reduced from  $18 \pm 2 \mu\text{M}$  to  $14 \pm 2 \mu\text{M}$  when 2 mM of DCA was incubated together with 5-FU.<sup>49</sup> A dose-dependent synergic effect of 5-FU and DCA has been reported for colorectal cancer cells, for which DCA enhanced  $IC_{50}$  doses and 5-FU antiproliferational effects due to apoptosis induction through inactivation of cancer cells glycolysis, shifting the metabolism of pyruvate back to glucose oxidation in the mitochondria.<sup>48</sup> However, the doses of DCA needed to achieve this effect are again quite high due to its poor cellular internalisation.

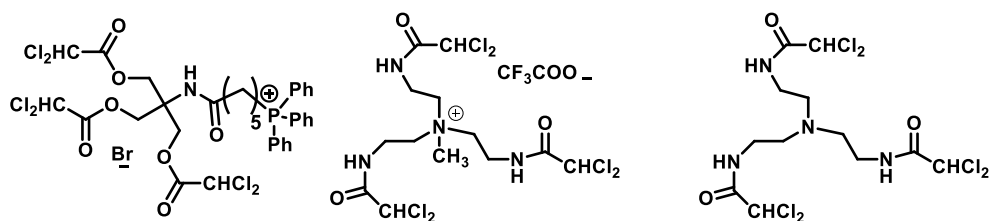


**Figure 5.7.** DCA prodrugs designed to target mitochondria: compounds backboned with phosphonium or ammonium salts and tertiary amine scaffolds.<sup>44</sup>

Due to the high membrane potential across the mitochondrial inner membrane (negative inside), positively charged molecules, such as phosphonium or ammonium salts, are often used to target mitochondrial internalisation.<sup>50-52</sup> Hence, DCA prodrugs, containing compounds

backboned with phosphonium or ammonium salts and tertiary amine scaffolds (Figure 5.7), have been evaluated with the aim of developing DCA analogues with enhanced mitochondria targeting effects.<sup>44</sup> The authors analysed the anticancer activity of the new DCA-loaded compounds, as well as the cytotoxicity of their non-loaded backbones, towards a panel of leukaemia cell lines, finding a 30 fold increase on its activity when attached to the amino scaffold, while the scaffold on its own was non-cytotoxic.<sup>44</sup>

DCA was chosen as the object of the study due to the fact that its cytotoxic effect will only be observed if MOFs are able to deliver cargo into the cytosol and subsequently reach the mitochondria. This allows experimental confirmation that therapeutically active DCA-loaded MOF nanoparticles have been successfully internalised, and by specific endocytosis mechanisms that result in the DDS being localised in the cytosol rather than lysosomes. As such, DCA is an excellent mechanistic probe for the therapeutic efficiency and cellular internalisation of NMOFs, while its less problematic side-effects, together with the lower cancer cells resistance towards it, compared to other anticancer drugs, make it a potential therapeutic candidate if it can be efficiently delivered.

## 5.2 Aims

The ultimate aim of this Chapter is to find rationalisation between the surface chemistry, the endocytosis efficiency and routes of Zr MOFs and their therapeutic efficacy, with the ultimate goal of providing insights that might reduce early-stage animal testing by the design of suitable MOF structures for drug delivery applications for which their routes of internalisation and therapeutic efficacy could be predicted.

From a chemical point of view, the lower  $pK_a$  value (1.36) of dichloroacetic acid means considerable amounts can be attached to UiO-66 Zr positions at defect sites during synthesis as described during Chapter 2, even in the presence of other functionalised modulators. Additionally, this concept of defect loading of drugs that act as modulators in synthesis could be applied to any therapeutic molecule containing carboxylate groups, such as doxorubicin.

The therapeutic efficacy of the UiO family of isorecticular DCA@MOFs, whose syntheses were described during Chapter 2, to deliver the anticancer metabolic target DCA will be studied in MCF-7 breast cancer cells in order to gain insights into the effect of both particle size and surface chemistry on therapeutic activity. As such, the bigger DCA@UiO-66 derivate MOFs (ca. 100 nm) will be compared with DCA@DUT-52 and DCA@UiO-67 due to their similar size. Later, the cytotoxicity of the bigger DCA@UiO-66 derivate MOFs will be compared with their smaller analogues (< 20 nm), to investigate if these small nanoparticles can be internalised

by passive diffusion, thus avoiding lysosome storage and reaching the cytosol in a more effective manner.<sup>53, 54</sup>

On the one hand the DCA@UiO-66 derivative MOFs possess different pendant functional groups in their linkers, and consequently different surface chemistry. On the other hand DCA@DUT-52 and DCA@UiO-67 linkers are more hydrophobic, enabling the determination of hydrophobicity on anti-cancer therapeutic efficacy. Importantly, the endocytosis routes of this family of MOFs have been reported, and while the UiO-66 derivatives are mainly internalised through clathrin-mediated endocytosis, the caveolae-mediated endocytosis plays a more important role on the internalisation of DUT-52 and UiO-67.

Since it has been shown during Chapter 2 that introducing DCA during synthesis as a modulator results in highly porous MOFs,<sup>55</sup> whose porosity can be used to store a second drug (in this case 5-FU),<sup>56</sup> the ability of the smaller Zr-terephthalate derivate MOFs and the bigger DUT-52 and UiO-67 MOFs to delivery two drugs (DCA and 5-FU) in tandem will also be investigated during this chapter and compared to the anticancer effect of both free drugs separately and incubated together with MCF-7 cells to determine if there could be a synergic effect on the co-delivery of 5-FU and DCA.<sup>48, 49</sup>

The postsynthetic surface modification protocols detailed during Chapter 3<sup>55, 57</sup> will be applied to the DCA@UiO-66 MOFs synthesised by coordination modulation during Chapter 2 in order to investigate the anti-cancer therapeutic activity depending on the MOF surface coating (Folic acid, Biotin, Heparin, PEG, Poly-L-Lactide and PNIPAM). Hence, the cytotoxicity of empty and loaded bare and surface functionalised UiO-66 will be investigated at first using the HeLa cervical cancer cell line, for which the endocytosis efficacy and routes of these calcein-loaded MOFs was investigated during Chapter 4, aiming to find a correlation between their surface chemistry, endocytosis fate and routes, and final therapeutic effect.

The most promising surface functionalised candidates will be then tested against a series of both cancerous and healthy cells lines to assess their anti-cancer selectivity and possibly side effects towards healthy cells. Evaluation of the *in vitro* immune response towards these MOFs will be also investigated, including uptake, cytotoxicity and reactive oxygen species production, using both macrophages and lymphocytes isolated from the blood of human donors, which might provide a possible idea of their *in vivo* performance without animal testing.

### 5.3 Therapeutic Efficiency of the DCA@UiO family

The therapeutic efficacy of the DCA@MOFs of the UiO family of different particle sizes, described during Chapter 2, is studied towards MCF-7 breast cancer cells in order to find insights into the effect of both particle size and surface chemistry. The particle size, determined by SEM, and the DCA content, determined by TGA, of the different MOFs are given in Table 5.2. Additionally, as the small DCA@UiO-66 derivatives, as well as DCA@DUT-52 and DCA@UiO-67, were postsynthetically loaded with 5-FU, the 5-FU loadings, determined by UV-Vis, together with the DCA content after 5-FU loading, determined by TGA, are also given in Table 5.2

**Table 5.2.** Particle size and DCA content of the DCA@MOFs of the UiO family.

Sample	Size / nm	% DCA w/w <sup>a</sup>	% 5-FU
DCA@UiO-66	77 ± 24	17.2	
DCA@UiO-66-Br	131 ± 30	16.7	
DCA@UiO-66-NO <sub>2</sub>	121 ± 27	16.2	
DCA@UiO-66-NH <sub>2</sub>	81 ± 26	16.9	
DCA@UiO-66 <i>small</i>	12.8 ± 3.6	26.2 (22.3)	1.9
DCA@UiO-66-Br <i>small</i>	30.2 ± 7.9	19.3 (13.1)	3.8
DCA@UiO-66-NO <sub>2</sub> <i>small</i>	21.7 ± 5.3	21.5 (8.7)	4.3
DCA@UiO-66-NH <sub>2</sub> <i>small</i>	12.5 ± 2.9	26.4 (12.6)	2.4
DCA@DUT-52	232 ± 30	14.1 (15.5)	1.5
DCA@UiO-67	196 ± 32	6.6 (7.1)	2.5

<sup>A</sup> DCA loadings in brackets correspond to the DCA content after 5-FU loading

#### 5.3.1 Therapeutic Efficiency of DCA@MOFs

The cytotoxicity of the DCA@MOFs of the UiO family, described during Chapter 2, and free DCA (in the form of sodium dichloroacetate, NaDCA) was measured against MCF-7 breast carcinoma cells using the MTS assay.

The MTS assay for NaDCA is shown in Figure 5.8, and confirms that DCA has little effect on cell proliferation. A dose-responsive cytotoxicity is evident, but only at very high concentrations, with 40.6 ± 18.2% viability after incubation with 9 mgmL<sup>-1</sup> of NaDCA, in great agreement with literature reports. The maximum dose of DCA delivered by the DCA@MOFs will be 0.264 mgmL<sup>-1</sup> when cells are incubated with a solution of 1mgmL<sup>-1</sup> of DCA@UiO-66-

$\text{NH}_2$  *small*, which has a DCA loading of 26.4% *w/w*. After incubation with  $0.5 \text{ mgmL}^{-1}$  NaDCA, the viability of MCF-7 cells is  $99.9 \pm 26.0\%$ , and it has been previously reported that the empty MOFs are none toxic,<sup>3,4</sup> thus, any cytotoxicity comes from enhanced delivery of DCA into the MCF-7 cells by the MOF nanoparticles.

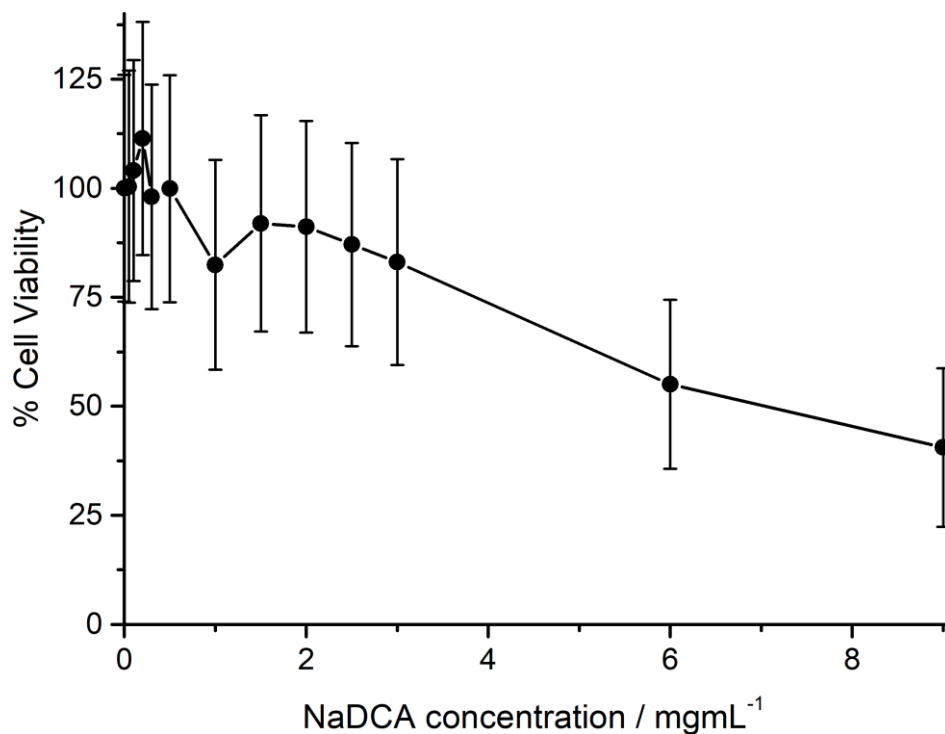


**Figure 5.8.** Viability, as measured by MTS proliferation assay, of MCF-7 cells when incubated with different concentrations of sodium dichloroacetate for 72 h. Error bars represent the standard deviation from triplicate experiments.

To examine the effect of ligand functionality and hydrophobicity the cytotoxicities of the larger DCA-containing terephthalate derivatives (ca. 70-130 nm) were compared with DCA@DUT-52 and DCA@UiO-67 (ca. 200 nm), and plotted against MOF concentration (Figure 5.9) and DCA concentration (Figure 5.10). DCA@DUT-52 and DCA@UiO-67 are the most therapeutically active, decreasing MCF-7 viabilities to around 35% when delivering  $<0.1 \text{ mgmL}^{-1}$  of DCA. These results correlate well with the enhanced cytotoxicity towards HeLa cancer cells of UiO-67 when delivering the anti-cancer drug  $\alpha$ -cyano-4-hydroxycinnamic acid,<sup>4, 15</sup> likely as a consequence of the preference of DUT-52 and UiO-67 for caveolae-mediated endocytosis promoting efficient cytosolic cargo release,<sup>15</sup> rather than size, as empty analogous MOF samples of varying size were found to not be cytotoxic towards HeLa cells.<sup>4</sup>

DCA@UiO-66, in contrast, shows no cytotoxicity towards MCF-7, likely due to clathrin-mediated endocytosis leading to lysosome localisation.<sup>15, 58, 59</sup> DCA@UiO-66-Br and DCA@UiO-66-NO<sub>2</sub> only reduce proliferation to  $61 \pm 16\%$  and  $81 \pm 15\%$ , respectively, at the highest delivered DCA concentrations, while the enhanced therapeutic effect of DCA@UiO-66-NH<sub>2</sub>, with cell viabilities similar to DCA@DUT-52, could be a result of the positive surface charge of protonated amino units in the 2-amino terephthalate enhancing internalisation efficiency.<sup>60, 61</sup>

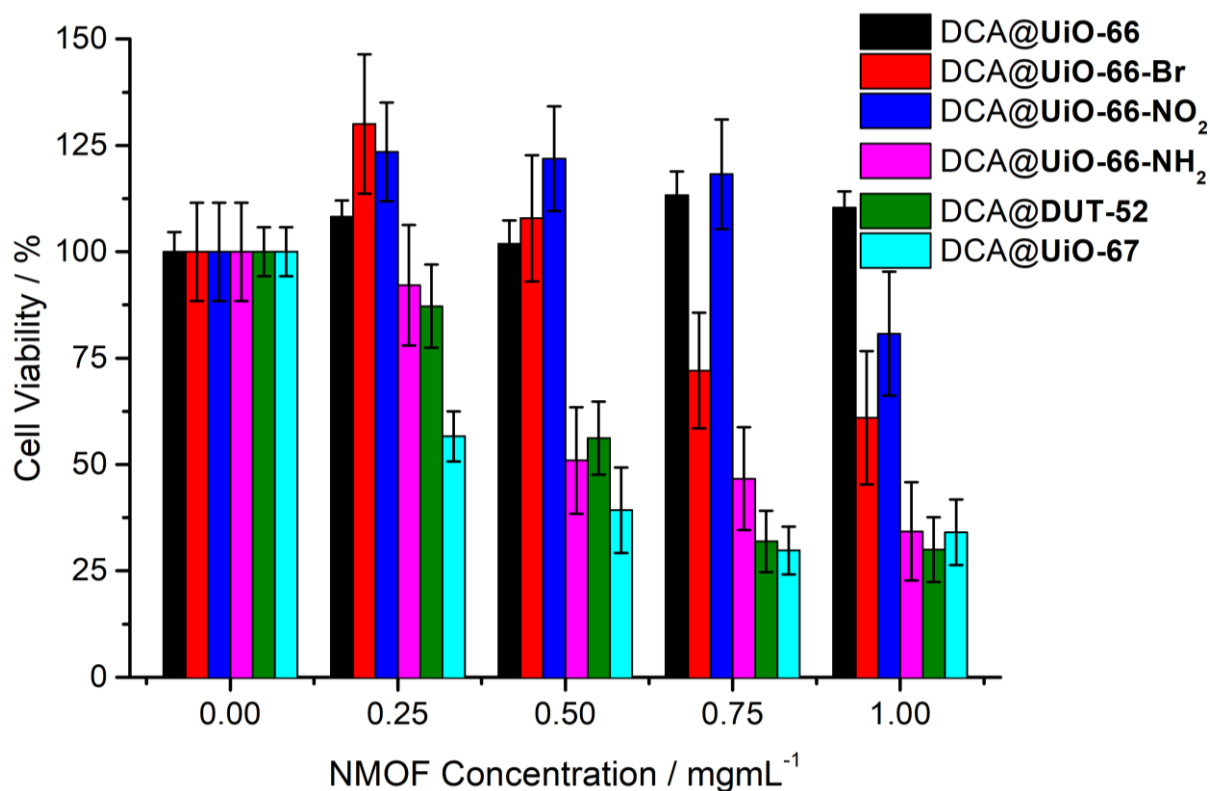


**Figure 5.9.** Viability, as measured by MTS proliferation assay, of MCF-7 cells when incubated with different concentrations of the larger DCA@MOF nanoparticles for 72 h. Error bars represent the standard deviation from triplicate experiments.

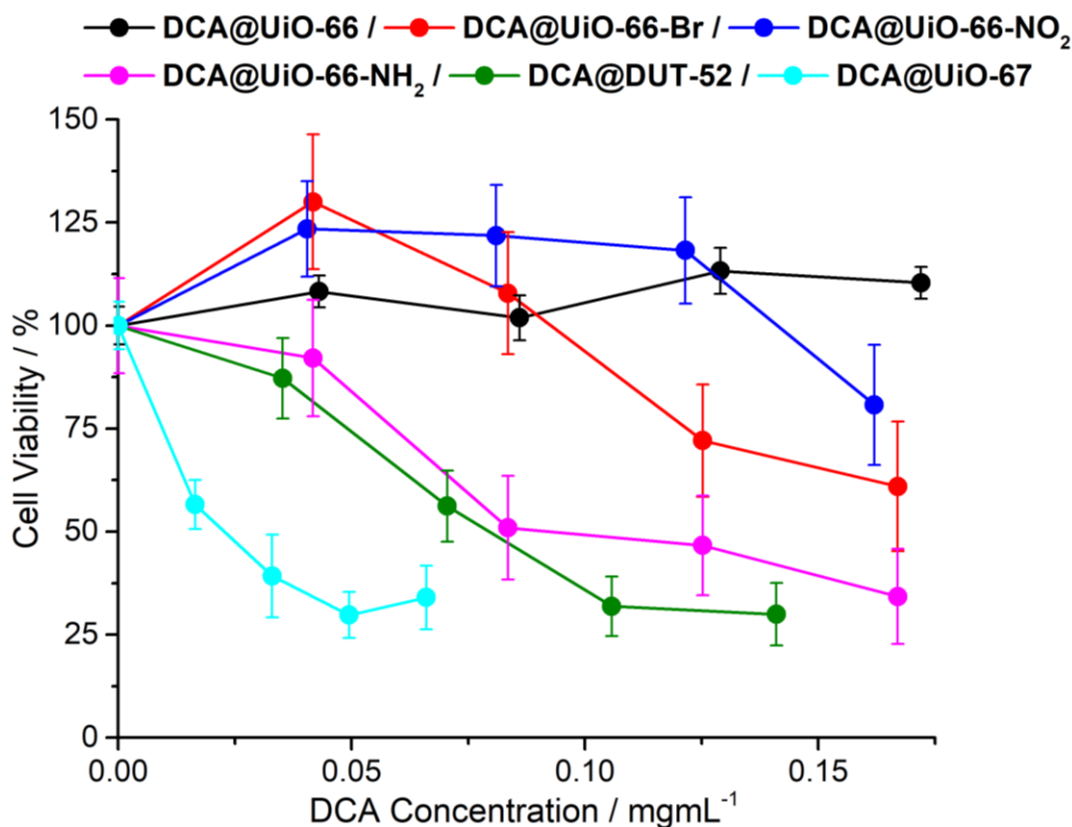


**Figure 5.10.** Viability, as measured by MTS proliferation assay, of MCF-7 cells when incubated with different concentrations of the larger DCA@MOF nanoparticles for 72 h, based on the DCA concentrations reached by their respective loadings. Error bars represent the standard deviation from triplicate experiments.

The effect of particle size was assessed by comparing the cytotoxicities of the DCA@UiO-66<sub>small</sub> derivatives (~20 nm) towards MCF-7 cells with their larger analogues (~100 nm). Figure 5.11 shows a comparison of MCF-7 cell proliferation on incubation with the small and large terephthalate MOFs, plotted against MOF concentration, and the analogous chart plotted against DCA concentration is given in Figure 5.12.

Generally the smaller nanoparticles showed enhanced cytotoxicity when plotted against DCA concentration, suggesting enhanced internalisation and cell uptake by passive diffusion resulting in cytosolic release.<sup>54</sup> Figure 5.12 shows the more pronounced cytotoxicity of DCA@UiO-66-NO<sub>2</sub><sub>small</sub> compared to its larger analogue, which shows no appreciable deleterious effects, with similar trends observed for DCA@UiO-66<sub>small</sub> and DCA@UiO-66-Br<sub>small</sub>. Only DCA@UiO-66-NH<sub>2</sub><sub>small</sub> (ca 13 nm) was less efficient than its larger analogue DCA@UiO-66-NH<sub>2</sub> (ca 86 nm), but both samples still reduced cell proliferation, again likely due to their surfaces having significant positive charge.<sup>60, 61</sup>

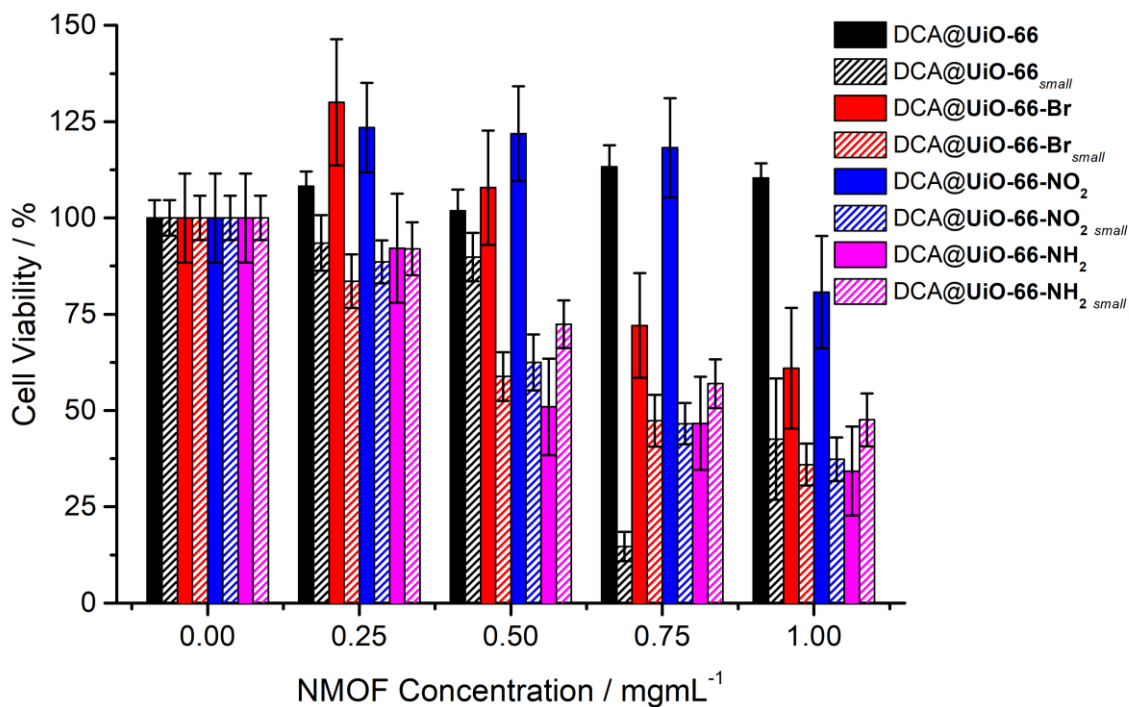


**Figure 5.11.** Comparison of the viability, as measured by MTS proliferation assay, of MCF-7 cells when incubated with different concentrations of the DCA-loaded terephthalate MOF nanoparticles of different sizes for 72 h. Error bars represent the standard deviation from triplicate experiments.

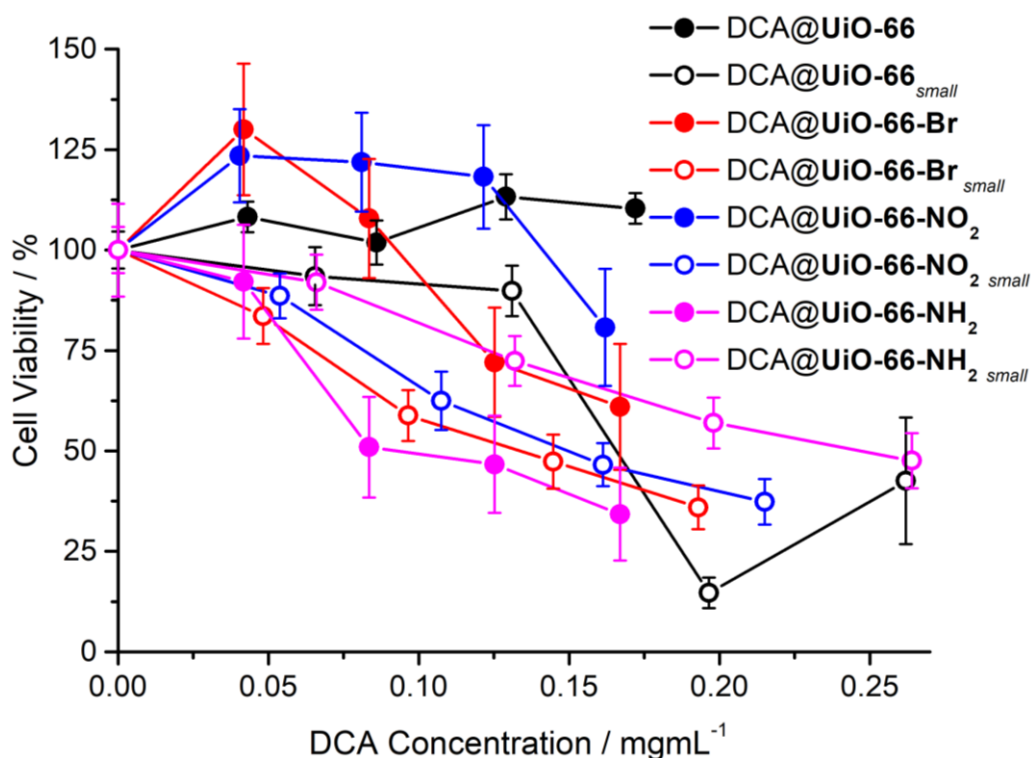


**Figure 5.12.** Comparison of the viability, as measured by MTS proliferation assay, of MCF-7 cells when incubated with different concentrations of the DCA-loaded terephthalate MOF nanoparticles of different sizes for 72 h, plotted against DCA concentration of the DDSs rather than MOF concentration. Error bars represent the standard deviation from triplicate experiments.

It has been reported that the functionalised UiO-66 derivative MOFs are mainly internalised through clathrin-mediated endocytosis by HeLa cervix cancer cells, and hence stored in the lysosomes, which hinders their ability to release their cargo into the cytosol.<sup>15</sup> These results indicate that although surface chemistry plays a more important role than particle size, the therapeutic activity of the MOFs can be enhanced by particle size reduction, possibly as a consequence of partial internalisation through passive diffusion, enabling the smaller MOFs to directly reach the cancer cells cytosol, and releasing their cargo in a more effective manner.

### 5.3.2. Therapeutic Efficiency of 5-FU@DCA@MOFs

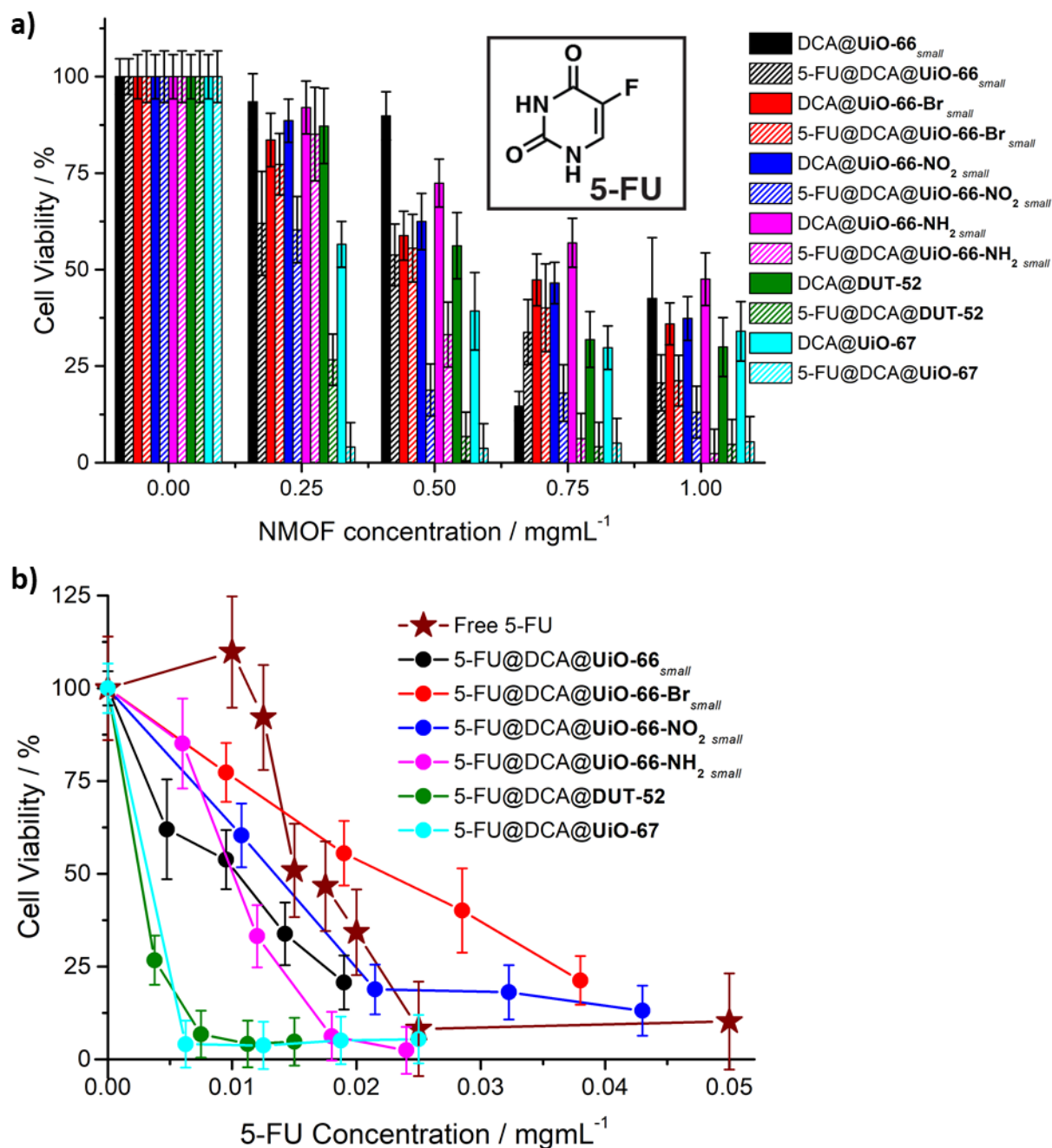
5-FU acts as a thymidylate synthase (TS) inhibitor, and thus needs to reach the nucleus of cancer cells to be effective,<sup>62</sup> while DCA inhibits pyruvate kinase and hence acts in the mitochondria.<sup>38</sup> As such, the efficacy of both drugs depends on localisation in the cytosol after uptake, and so successful delivery of both drugs into the cytosol of cancer cells by one DDS may result in enhancement of therapeutic activity.

Importantly, although 5-FU is a well-known and used anticancer therapeutic, its cytotoxic effects are an issue to many patients, gastrointestinal toxicity being one of the most commonly observed side effects. Hence, dosing is often limited by safety, while its activity is moderate at low doses.<sup>62</sup> Additionally, many cancer cells are developing resistance towards 5-FU, which is itself problematic.<sup>63, 64</sup> Although it has been reported that DCA enhances 5-FU activity through a dose-dependent synergistic effect, the DCA doses needed to induce this effect are still considerably high.<sup>48, 49</sup>

The MTS cell viability assays for MCF-7 cells incubated with 5-FU@DCA@MOFs, whose syntheses are described during Chapter 2, were performed following the same protocol as for the DCA@MOFs, in parallel to enable better comparison of the cytotoxic results. Additionally, the MTS assay was carried out against free 5-FU to determine its therapeutic efficiency, also in parallel. The results are plotted in Figure 5.13a against MOF concentration and compared to their precursor DCA@MOF, and in Figure 5.13b against 5-FU concentration and compared to the free drug.

Free 5-FU has significant cytotoxicity under these conditions, presumably after uptake into the MCF-7 cells by passive diffusion. The 5-FU loadings in the 5-FU@DCA@MOFs mean that individual MTS assay experiments under the same conditions and MOF concentrations as in the Section 5.3.1 will result in delivery of very low quantities of 5-FU (see Figure 5.13b). The 5-FU concentrations achieved by the 5-FU@DCA@MOFs dispersed in growth media are in

the range of non-cytotoxic and cytotoxic free 5-FU concentrations, which allows determination of any enhancement in cytotoxicity compared to free 5-FU.



The enhanced cytotoxicity of all the 5-FU@DCA@MOFs towards MCF-7 cells compared to their DCA@MOF precursors, despite the decrease in DCA content determined after 5-FU loading, is clearly observed when cell proliferation is plotted against MOF concentration (Figure 5.13a) suggesting successful intracellular delivery of 5-FU. Of the smaller MOF species, 5-FU@DCA@UiO-66<sub>small</sub> exhibits a more significant dose-response effect than its precursor, decreasing cell viability with concentration down to  $21 \pm 7\%$  at  $1 \text{ mgmL}^{-1}$ . The cytotoxicity of 5-FU@DCA@UiO-66-Br<sub>small</sub> increases only slightly compared to its precursor, whereas 5-FU@DCA@UiO-66-NO<sub>2small</sub> and 5-FU@DCA@UiO-66-NH<sub>2small</sub> have more notable enhancements, with cell viabilities of  $19 \pm 7\%$  and  $33 \pm 8\%$ , respectively, when MCF-7 cells were incubated with  $0.5 \text{ mgmL}^{-1}$  of the MOFs. The most effective of the DCA@MOFs, DCA@DUT-52 and DCA@UiO-67, also showed further enhancements in cytotoxicity towards MCF-7 cells when loaded with 5-FU; cell viability drastically decreases to values of  $7 \pm 6\%$  and  $4 \pm 6\%$  when cells were incubated with just  $0.5 \text{ mgmL}^{-1}$  of 5-FU@DCA@DUT-52 and 5-FU@DCA@UiO-67, respectively.

Free 5-FU itself also has significant dose-responsive cytotoxic behaviour (Figure 5.13b), with an  $\text{IC}_{50}$  of  $0.015 \pm 0.001 \text{ mgmL}^{-1}$ , but plotting cytotoxicity of the 5-FU@DCA@MOF samples against 5-FU concentration shows they have a greater effect than the free drug at lower concentrations, which might be a consequence of more efficient or faster internalisation, or a synergistic effect of DCA and 5-FU delivered in tandem, in great agreement with literature reports.<sup>48, 49</sup>

At higher concentrations 5-FU@DCA@UiO-66<sub>small</sub> and 5-FU@DCA@UiO-66-NH<sub>2small</sub> continue to exhibit greater cytotoxic effects than the free drug, while 5-FU@DCA@UiO-66-NO<sub>2small</sub> has no notable enhancement and 5-FU@DCA@UiO-66-Br<sub>small</sub> has a poorer performance than free 5-FU. Again, the larger samples, 5-FU@DCA@DUT-52 and 5-FU@DCA@UiO-67 have the most pronounced cytotoxic effects, significantly enhancing the efficacy of free 5-FU and killing nearly all cells at all measured concentrations, suggesting that it is the surface chemistry of the MOFs that influences cellular uptake, and thus cytotoxicity, to a greater extent than particle size.

Control experiments were carried out to assess the enhancement in cytotoxicity when 5-FU and DCA are delivered in a bimodal fashion by the Zr MOFs. MTS assays on a new batch of MCF-7 cells were carried out in the presence of (i) free 5-FU, (ii) free 5-FU spiked with  $0.1 \text{ mgmL}^{-1}$  NaDCA, and (iii) free 5-FU spiked with  $0.2 \text{ mgmL}^{-1}$  NaDCA. The addition of NaDCA was designed to mimic the concentrations of DCA delivered by the 5-FU@DCA@MOFs; the results are shown in Figure 5.14, and are the same within experimental error, showing that no enhancement of 5-FU cytotoxicity occurs when administered with free DCA at the given doses,

which is presumably a consequence of the fact that DCA cannot efficiently cross the cell membrane without a suitable DDS.

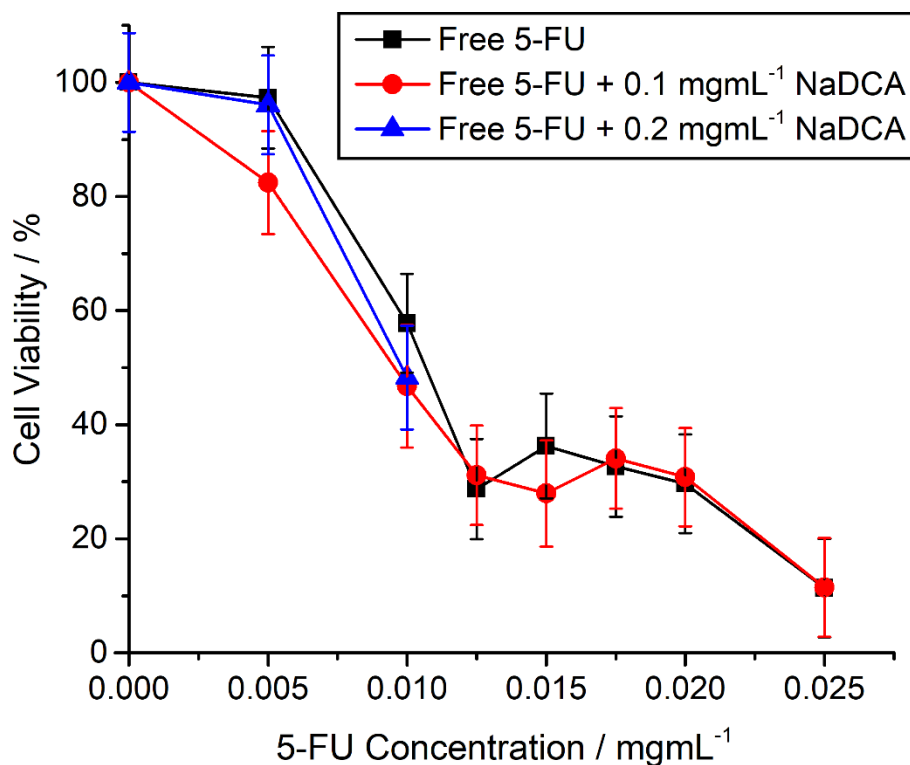


**Figure 5.14.** Comparison of the viability, as measured by MTS proliferation assay, of MCF-7 cells when incubated with different concentrations of 5-fluoruracil, spiked with different concentrations of NaDCA, for 72 h. Error bars represent the standard deviation from triplicate experiments.

Slightly different cytotoxicities of free 5-FU towards MCF-7 cells were observed at low 5-FU concentrations when compared to the data previously collected, presumably as a consequence of these additional MTS assays being carried out on a completely new batch of MCF-7 cells. When the average cell proliferation values from these two independent MTS assays are plotted against the cell proliferation values previously determined for the 5-FU@DCA@MOFs (Figure 5.15), the trends showed in Figure 5.13b are still evident, and the conclusions and hypotheses made do not change. These experiments show that, when comparing absolute values from MTS cell proliferation assays, it is important to collect data from assays run concurrently on the same batch of cells to ensure experimental error is reduced. The data presented in Figure 5.13 come from assays carried out on the same batch of cells in parallel, which should give a better comparison.

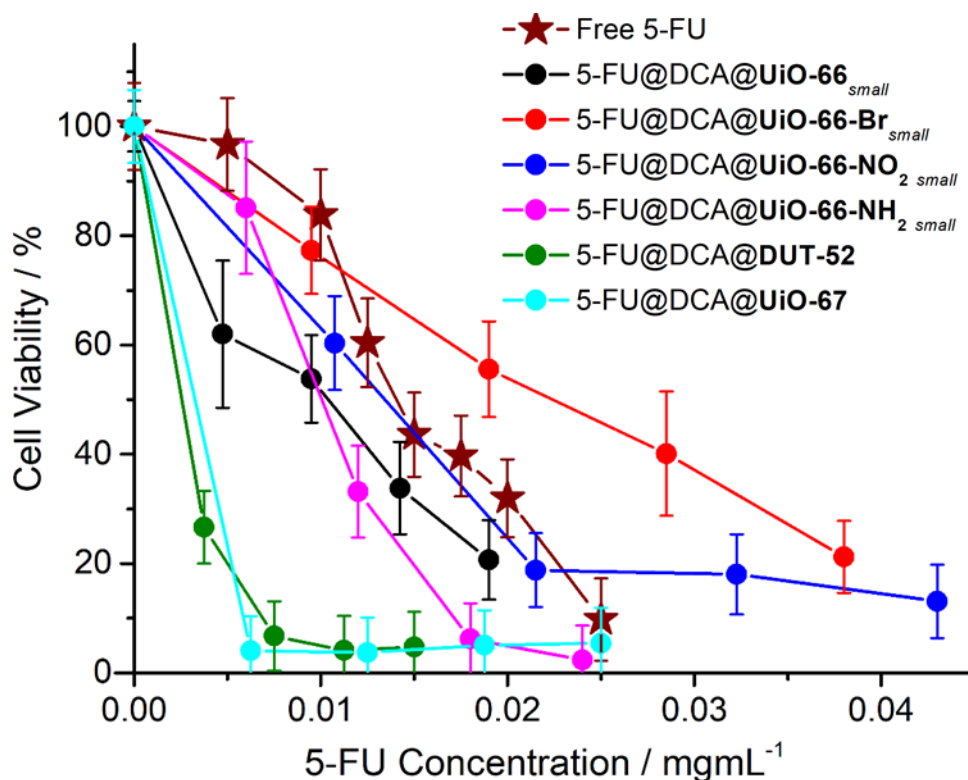


**Figure 5.15.** Comparison of MTS cell proliferation assays of 5-FU@DCA@MOFs plotted against 5-FU concentration compared to a value for free 5-FU that is the average of two separate sets of assays carried out at different times on different batches of MCF-7. Error bars represent the standard deviation from triplicate experiments.

The results show that although therapeutic efficiency can be enhanced by particle size reduction, possibly as a consequence of passive diffusion or higher internalisation rates, surface chemistry plays a more important role than particle size in therapeutic efficacy. This observation is in great agreement with reported endocytosis routes of internalisation,<sup>15, 58</sup> showing that DUT-52 and UiO-67, for which the caveolae-mediated route plays a more important role in their internalisation, are more therapeutically active than the terephthalate derivative MOFs, which are mainly internalised through clathrin-mediated endocytosis, and hence stored in the lysosomes before reaching their target.

#### 5.4. Postsynthetic Surface Functionalisation of DCA-Loaded Samples

Since it has been proven during Section 5.3 that surface chemistry plays a more important role than particle size in MOFs therapeutic activity, DCA@UiO-66 was chosen as the object of further study of postsynthetic modifications in order to avoid surface chemistry variability due to functional groups present on its surface. The fact that DCA@UiO-66 has poor anticancer performance when its size is ca. 77 nm, not being therapeutically active, enables determination of therapeutic enhancement after postsynthetic surface modifications.

Moreover, UiO-66 is amenable to functionalisation and it is the most porous MOF of the Zr-terephthalate derivatives.

During Chapter 2 the validity of the coordination modulation protocol to introduce a small molecule with high metabolic anticancer activity, dichloroacetate (DCA), as a modulator that is attached to UiO-66 metal nodes during synthesis was proven.<sup>55, 56</sup> Importantly, the attachment of DCA throughout the MOF ensures it is not lost on postsynthetic modification.<sup>57</sup> Post-synthetic surface modifications (Figure 5.16) were performed under the same conditions as in Chapter 3 and in Chapter 4, and full characterisation proved the surface moieties attachment without major DCA leakage from the NMOF structure.<sup>55, 57</sup>

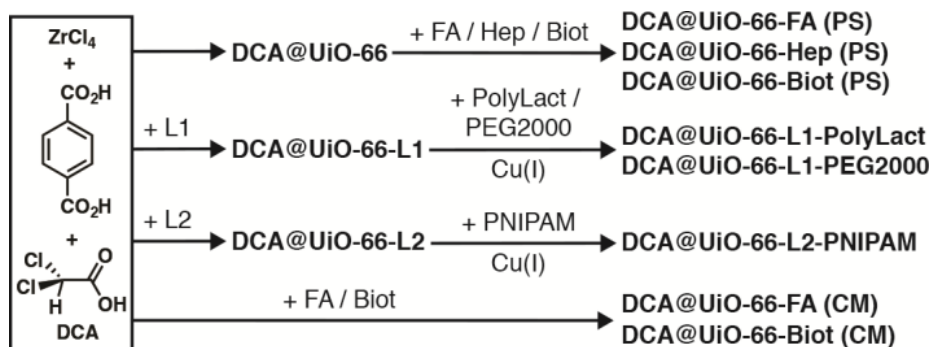


**Figure 5.16.** Synthesis of DCA-loaded, surface modified MOFs obtained through coordination modulation (CM), click modulation, and postsynthetic exchange (PS).

Surface modification of DCA@UiO-66 by postsynthetic exchange was carried out with heparin, folic acid and biotin, while the click modulation protocol was used to attach the polymers to the surfaces of the modulated samples DCA@UiO-66-L1 and DCA@UiO-66-L2 (Figure 5.16). The samples retained their crystallinity upon the postsynthetic surface modifications, as confirmed by PXRD.

The  $^1\text{H}$  NMR spectra of digested samples of the postsynthetically modified DCA@UiO-66-FA (PS) and DCA@UiO-66-Biot (PS) showed high incorporation of both surface reagents. Through analysis of the  $^1\text{H}$  NMR spectrum of acid-digested DCA@UiO-66-FA (PS) (Figure 5.17), the DCA content in the sample was estimated to be 25.9 mol % compared to bdc, slightly lower than the precursor sample DCA@UiO-66, for which a 35.2 mol % of DCA was estimated. Interestingly, even though the amount of washes after the postsynthetic modification was considerable, a 24.5% molar ratio of folic acid to bdc was found, while the mass quantity of folic acid determined by UV-Vis spectroscopy was 17.9% w/w.

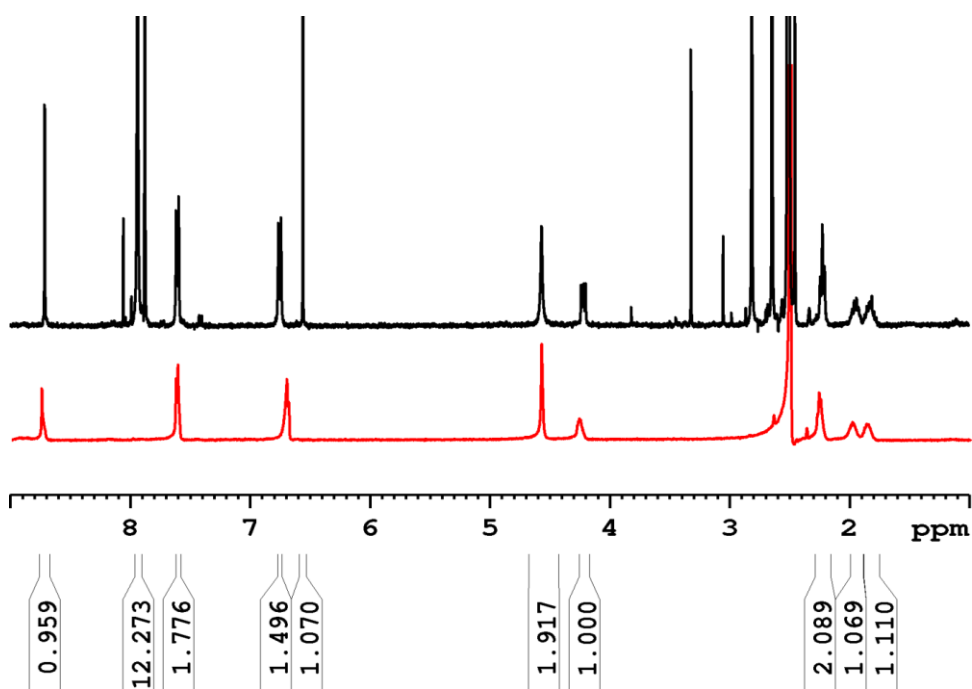


**Figure 5.17.** <sup>1</sup>H NMR spectrum of DCA@UiO-66-FA (PS) digested in D<sub>2</sub>SO<sub>4</sub> / DMSO-*d*<sub>6</sub> (top) compared to the spectrum of folic acid.

A similar phenomenon occurs in the case of DCA@UiO-66-Biot (PS), where DCA content decreased upon biotin coating, from 35.2% to 19.0% molar ratio, suggesting DCA on the surfaces of the MOFs can be exchanged (Figure 5.18), and that due to the high defectivity of the DCA@MOFs, more metal nodes could be exposed and hence the coordination of the surface reagents is higher than in Chapter 3.

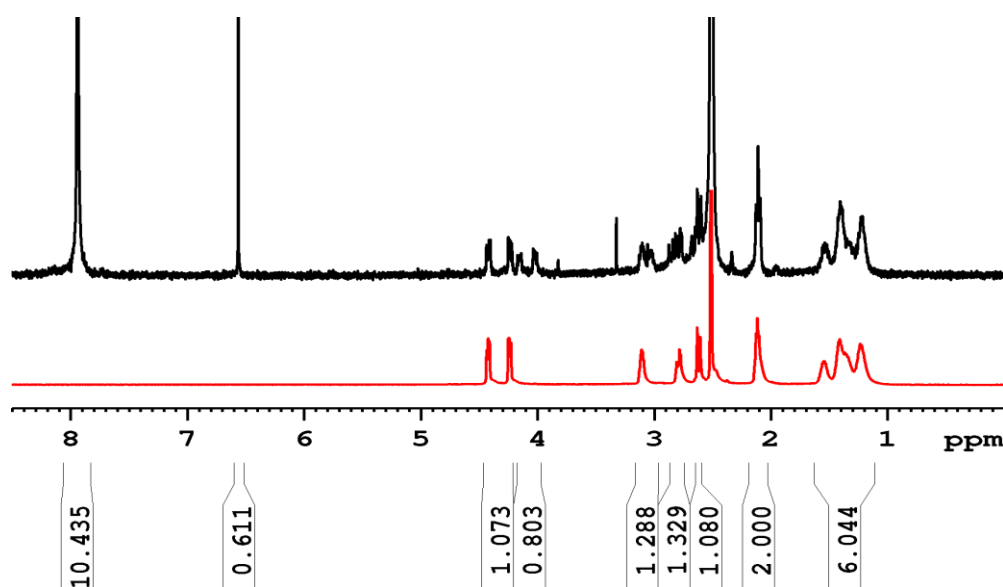


**Figure 5.18.** <sup>1</sup>H NMR spectrum of DCA@UiO-66-Biot (PS) digested in D<sub>2</sub>SO<sub>4</sub> / DMSO-*d*<sub>6</sub> (top) compared to the spectrum of biotin.

$^1\text{H}$  NMR spectra of digests of the samples containing polymers (DCA@UiO-66-Hep (PS), DCA@UiO-66-L1-PEG2000, DCA@UiO-66-L1-PolyLact and DCA@UiO-66-L2-PNIPAM) were complex and did not give useful information about the surface moieties, but showed the presence of resonances for the polymers.

Thermogravimetric analysis of the postsynthetically coated, DCA-loaded samples confirmed the presence of DCA and of the surface reagents. The TGA profile of DCA@UiO-66-FA (PS) profile shows a more gradual degradation profile than its precursor and a lower metal content, consistent with the high incorporation of folic acid observed by  $^1\text{H}$  NMR spectroscopy. In the case of DCA@UiO-66-Biot (PS), again a higher amount of organic matter is present in the structure compared to its precursor, and the decomposition step attributed to DCA starts at a slightly higher temperature and in a more gradual manner, presumably as a consequence of the decomposition of biotin molecules coating the surface. As the major heparin decomposition step occurs at a similar temperature to DCA, for DCA@UiO-66-Hep (PS) the DCA content cannot be accurately determined by TGA (Figure 5.19).

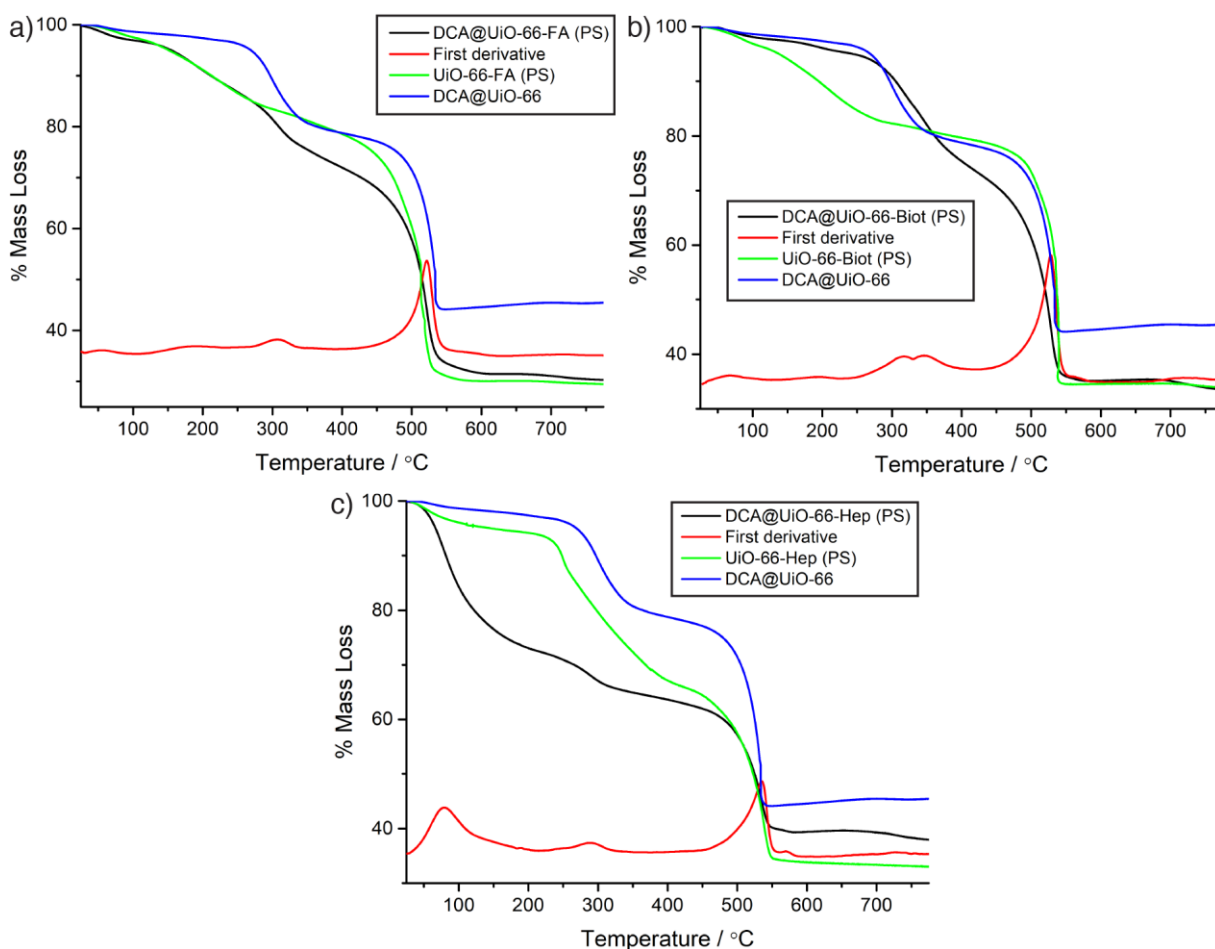


**Figure 5.19.** TGA profiles of DCA-loaded, surface modified MOFs compared to the empty modified MOF and DCA@UiO-66 for a) DCA@UiO-66-FA (PS), b) DCA@UiO-66-Biot (PS), and c) DCA@UiO-66-Hep (PS).

While TGA analysis confirmed the presence of the PEG functionality in DCA-UiO-66-L1-PEG2000, the mass loss events for DCA and the PEG chains occurred simultaneously (Figure 5.20a), precluding calculation of DCA loading, and so the ICP-MS methodology was used.

In agreement with previous covalent surface modifications performed during Chapter 3, DCA@UiO-66-L1-PolyLact exhibits a lower thermal stability than its precursor DCA@UiO-66-L1, as confirmed by its TGA profile (Figure 5.20b). A similar DCA decomposition step, although at a slightly higher temperature, is observed after the surface modification, while the metal residue is slightly higher than the precursor, possibly due to partial DCA detachment during the postsynthetic modification or solvent trapped in the precursor. In the same way, the structure of DCA@UiO-66-L2-PNIPAM is less thermally stable, with a slightly higher metal residue, than its precursor (Figure 5.20c).

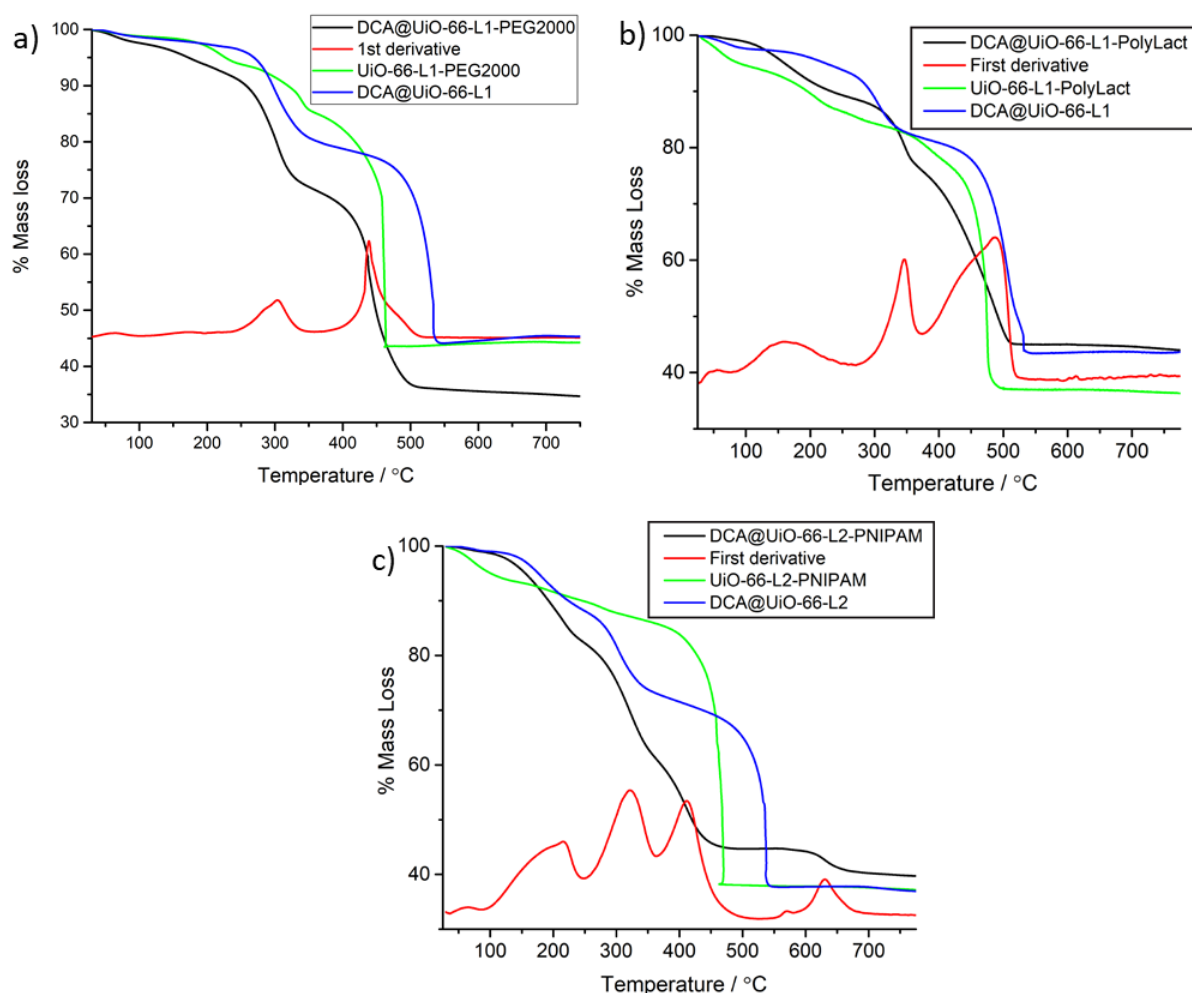


**Figure 5.20.** TGA profiles of DCA-loaded, click modulated MOFs compared to the empty modified MOF and the DCA-loaded precursor for a) DCA@UiO-66-L1-PEG2000 b) DCA@UiO-66-L1-PolyLact, and c) DCA@UiO-66-L2-PNIPAM.

TGA clearly shows the presence of DCA in all the materials, and analysis of the traces allowed estimation of DCA content for all samples except DCA@UiO-66-Hep (PS), DCA@UiO-66-L1-PEG2000 and DCA@UiO-66-L2-PNIPAM, as DCA decomposition coincided with other mass loss events. The values correlate well with those measured by inductively coupled plasma mass spectrometry (ICP-MS) determination of chloride content (Table 5.2). A gradual decrease in DCA loading occurring as the mass of the surface functionality increased was observed, as would be expected. The TGA values are likely slightly higher due to other mass loss events occurring alongside the DCA thermal decomposition.

SEM images of the samples showed an increase in size of all nanoparticles after surface functionalisation, but all were in the appropriate size range for drug delivery.<sup>55, 57</sup> The particle size distributions are presented in Table 5.2.

Additionally, the DCA loading and particle size of the co-modulated samples with DCA and either folic acid or biotin, which syntheses and characterisation was described during Chapter 2, are also given in Table 5.2, as their therapeutic efficacy will also be studied and compared with the postsynthetically modified samples during this chapter.

**Table 5.2.** Particle sizes, determined by SEM, and DCA loadings, determined independently by TGA and ICP-MS, of the surface modified MOFs and their precursors.

Sample	SEM Particle Size (nm)	DCA (TGA, % w/w)	DCA (ICP-MS, % w/w)
DCA@UiO-66	77 ± 24	17.0	16.9
DCA@UiO-66-L1	100 ± 15	15.9	15.5
DCA@UiO-66-L2	77 ± 11	18.7	18.9
DCA@UiO-66-L1-PEG2000	130 ± 29	n/a <sup>a</sup>	12.1
DCA@UiO-66-L1-PolyLact	138 ± 27	9.0	7.6
DCA@UiO-66-L2-PNIPAM	159 ± 21	n/a <sup>a</sup>	3.2
DCA@UiO-66-FA (PS)	146 ± 38	15.8	13.3
DCA@UiO-66-Biot (PS)	130 ± 33	15.6	9.4
DCA@UiO-66-Hep (PS)	133 ± 33	n/a <sup>a</sup>	5.1
DCA <sub>10</sub> @UiO-66-FA <sub>0.25</sub> (CM)	158 ± 23	19.6	18.9
DCA <sub>5</sub> @UiO-66-FA <sub>1</sub> (CM)	91 ± 29	12.1	11.8
DCA@UiO-66-Biot (CM)	166 ± 22	19.0	20.7

<sup>a</sup>Could not be calculated due to overlapping thermal decomposition events.

### 5.5. Therapeutic efficacy of DCA-Loaded, Surface Modified UiO-66

To investigate the consequences of surface coating on the therapeutic efficacy of the surface functionalised NMOFs (synthesized either through coordination modulation, detailed in Chapter 2, or through postsynthetic modification, described during this Chapter) the cytotoxicity of the materials against three different cell lines – HeLa (cervical cancer), MCF-7 (breast carcinoma) and HEK293 (healthy kidney) – was analysed by the MTS assay.

#### 5.5.1 MOFs Cytotoxicity Towards HeLa Cervix Cancer Cells

At first, the cytotoxicity of the modulators L1 and L2 was investigated using the MTS assay. UiO-66 itself, and its components, have previously been found to be non-toxic using this methodology.<sup>3, 4</sup> No decrease in cell viability was observed up to 1 mgmL<sup>-1</sup> concentration of either of the modulators (Figure 5.21), confirming that they are non-toxic towards HeLa cells.

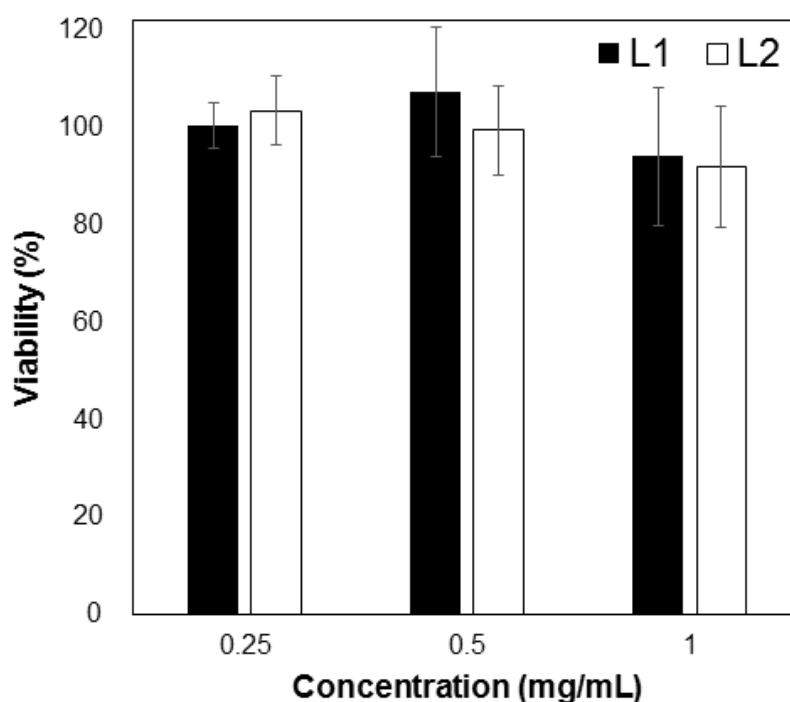


**Figure 5.21.** Metabolic activity of HeLa cells after 72 h of exposure to L1 and L2, measured by MTS assay. Error bars represent the standard deviation from five experiments.

Then, HeLa cells proliferation when incubated with the empty surface functionalised NMOFs, synthesised and characterised either during Chapter 2 (CM) or during Chapter 3 (PS), for 72 h was investigated, finding that only UiO-66-L2-PNIPAM was cytotoxic for concentrations above 0.25 mgmL<sup>-1</sup>, while incubation with other coated UiO-66 samples enhanced HeLa cells proliferation with a dose-response pattern, presumably as a consequence of the incorporation of the NMOFs' organic components into their metabolic cycle (Figure 5.22).

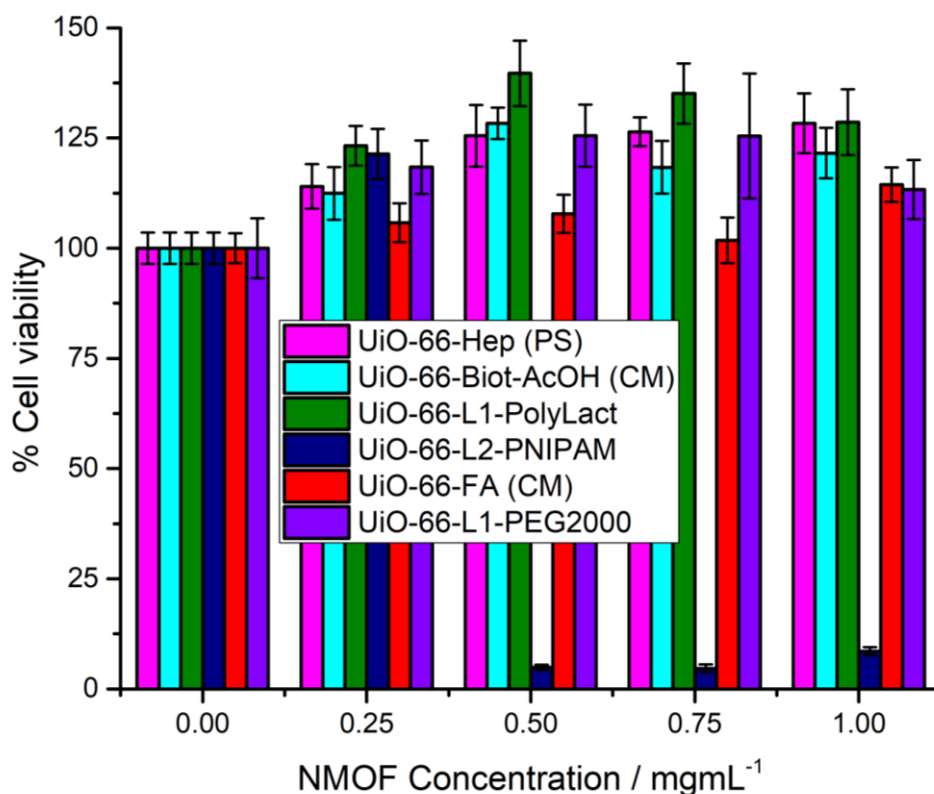


**Figure 5.22.** Viability, as measured by MTS assay, of HeLa cells incubated with different concentrations of empty, surface modified MOFs for 72 h. Error bars represent the standard deviation from five experiments.

Once the cytotoxicity of the empty samples was assessed, proving their validity as carriers, their therapeutic effect when loaded with DCA was analysed. DCA containing folic acid surface-functionalised materials, either introduced during synthesis using the coordination modulation protocol, or postsynthetically using coordination chemistry, were incubated with HeLa cells for 24 and 72 h.

Folic acid has high binding affinity for folate receptor (FR) proteins – glycosylphosphatidylinositol anchored cell surface receptors – which are known to be over expressed on the cell membrane of most cancerous cells.<sup>20-22, 65</sup> Folic acid is involved in nucleotide synthesis and in the metabolic maintenance of 1C-pathways in all living cells,<sup>66</sup> while its high binding affinity for FR has been widely used for targeting drug delivery, to enhance FR-mediated endocytosis.<sup>22, 65, 67-71</sup> However, the level of expression of FR in healthy cells is minimal when compared to malignant cells, such as ovarian endometrial, lung, cervical, breast, colorectal, kidney, and brain carcinomas among others, although FR is also overexpressed in activated macrophages.<sup>72, 73</sup>

Although unfunctionalised DCA@UiO-66 does not decrease HeLa cell proliferation ( $128 \pm 5\%$  cell viability at a concentration of  $1 \text{ mgmL}^{-1}$  after 72 hours of incubation), likely as a

consequence of inefficient cytosolic release after clathrin-mediated internalisation,<sup>15</sup> after 24 h of incubation (Figure 5.23a), only the NMOFs synthesised using the coordination modulation protocol start to induce cytotoxicity. On the other hand, for 72 h of incubation (Figure 5.23b), all the DCA folic acid coated NMOFs exhibit some degree of cytotoxicity, and once again the postsynthetically modified sample is less therapeutically efficient, with  $74 \pm 4\%$  cell viability at a NMOF concentration of  $1 \text{ mgmL}^{-1}$ . Between the two samples synthesised by the one-pot coordination modulation protocol, the one with higher folic acid content,  $\text{DCA}_5@\text{UiO-66-FA}_1$  (CM), rather than the highest DCA content  $\text{DCA}_{10}@\text{UiO-66-FA}_{0.25}$  (CM), is more efficient, killing  $85 \pm 3\%$  of the cells at concentrations of  $0.25 \text{ mgmL}^{-1}$  and killing all cells when incubated with  $1 \text{ mgmL}^{-1}$  of NMOF in growth media.  $\text{DCA}_{10}@\text{UiO-66-FA}_{0.25}$  (CM) starts to reduce cell proliferation at  $0.75 \text{ mgmL}^{-1}$  ( $85 \pm 3\%$  cell viability) and only kills  $52 \pm 5\%$  of cells at  $1 \text{ mgmL}^{-1}$ , despite containing more DCA ( $\sim 19\%$  w/w) than  $\text{DCA}_5@\text{UiO-66-FA}_1$  (CM) ( $\sim 12\%$  w/w).

Clearly the mode of external surface attachment of folate is key to therapeutic activity: the most cytotoxic folate-coated MOF has the lowest drug content. The enhanced cytotoxicity may be due to folate coating enhancing endocytosis efficiency possibly due to the extra amount being internalised by FR-mediated endocytosis, and promoting caveolae-mediated endocytosis,<sup>22, 69</sup> as described during Chapter 4 for the calcein-loaded folic acid-coated MOF. These findings highlight the importance and correlation of endocytosis efficiency and pathways with therapeutic efficiency.

The postsynthetically coated MOF will have the bulk of the folic acid on the nanoparticle external surface, while the NMOFs prepared by coordination modulation may have folate throughout the nanoparticles in defect sites, enhancing the targeting properties even after the onset of degradation. Cytotoxicity of free NaDCA towards HeLa was later found to be negligible until cells were incubated with concentrations  $>4 \text{ mgmL}^{-1}$  (Section 5.5.3) confirming that effective delivery of DCA into cells by the DDSs is occurring, with a greater than 300 fold enhancement in cytotoxicity compared to the free drug when DCA is transported into HeLa cells by  $\text{DCA}_5@\text{UiO-66-FA}_1$  (CM).

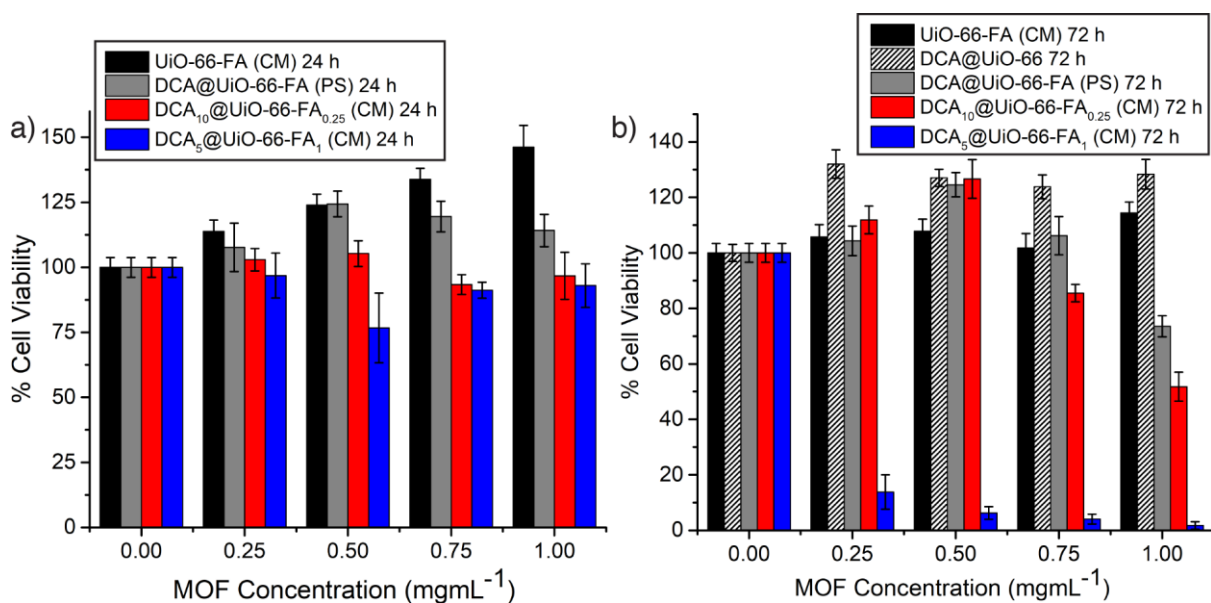


**Figure 5.23.** Cytotoxicities of empty and DCA-loaded folic acid coated MOFs against HeLa cells as measured by MTS assay after a) 24 h of incubation and b) 72 h of incubation. Error bars represent the standard deviation from five experiments.

It has been reported that the uptake of unfunctionalised UiO-66 by HeLa cells does not remarkably vary when size is the only variable.<sup>15</sup> While the smaller size of DCA<sub>5</sub>@UiO-66-FA<sub>1</sub> (CM) might enhance its efficiency, it is postulated that the effect is minor, especially when we observe that DCA<sub>10</sub>@UiO-66-FA<sub>0.25</sub> (CM) and DCA@UiO-66-FA (PS) have similar sizes (Section 5.4) and very different therapeutic effects. Additionally, it was proven that surface chemistry plays a more important role than particle size on anticancer therapeutic activity in related Zr MOFs during Section 5.3.<sup>56</sup> It is likely that the postsynthetic (PS) coating is less stable than when folate is introduced during the synthetic process (CM), thus partially being released during the incubation time – as observed by SEM during Chapter 3 – therefore decreasing its efficiency. Free folic acid can bind to FR, and therefore decreases the availability of those receptors to bind to the folic acid coated NMOFs, decreasing their uptake efficiency.<sup>20, 22</sup>

DCA@UiO-66-L1-PEG2000, which is also internalised through the caveolae-mediated route, is more toxic than the unfunctionalised DCA@UiO-66 derivatives after 72 hours of incubation (Figure 5.24), presumably because of enhanced lysosome-escaping capabilities<sup>59</sup> and stability, although to a lesser extent than the targeted folic acid MOF.

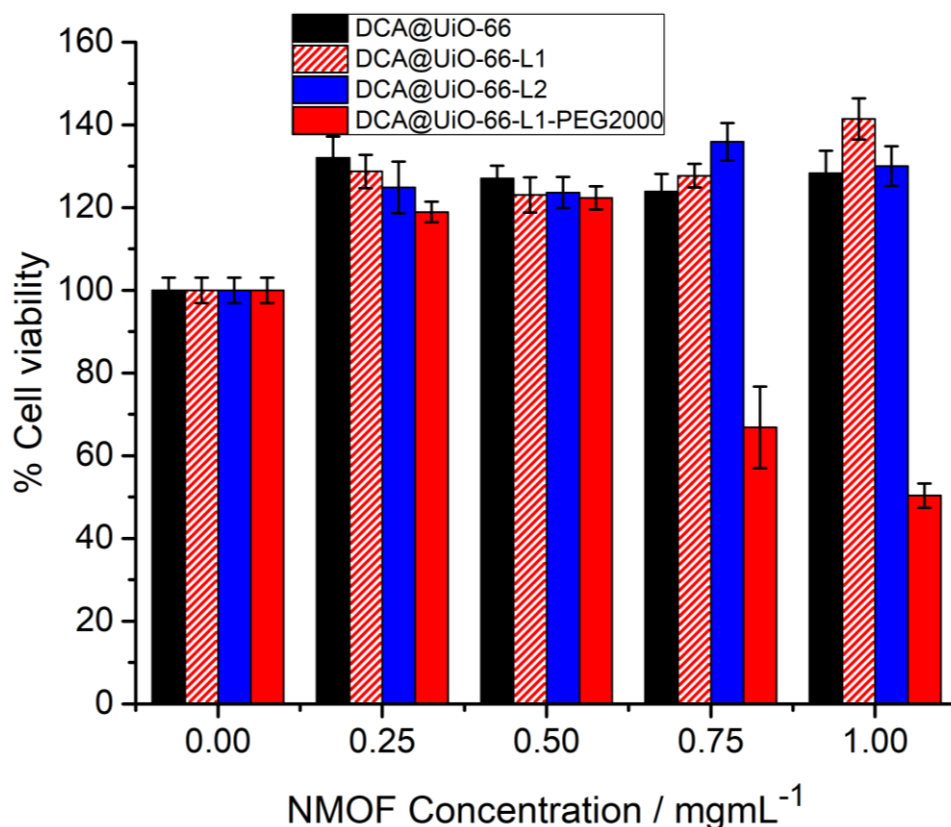


**Figure 5.24.** Cytotoxicities of DCA-loaded bare and PEGylated MOFs against HeLa cells as measured by MTS assay after 72 h of incubation. Error bars represent the standard deviation from five experiments.

Interestingly, DCA@UiO-66-L1-PolyLact produced a similar effect on HeLa cell growth regardless of the incubation time (24 or 72 hours), which could be indicative of its significant internalisation by energy-independent endocytosis,<sup>1</sup> determined during Chapter 4, while empty UiO-66-L1-PolyLact did not show any toxicity. Inhibition of cell growth starts to be observed when incubated with 0.75 mgmL<sup>-1</sup> of DCA-loaded MOF for 24 h or 72 h (85 ± 3% cell viability), while it kills almost all HeLa cells at 1 mgmL<sup>-1</sup> (Figure 5.25a).

Although the empty UiO-66-L2-PNIPAM was already found to be cytotoxic at concentrations of 0.5 mgmL<sup>-1</sup> and above, DCA loading enhanced its cytotoxic effects, with DCA@UiO-66-L2-PNIPAM killing all HeLa cells at the NMOF concentration of 0.25 mgmL<sup>-1</sup> (Figure 5.25b). These MOFs undergo HeLa cells internalisation primarily through non-mediated endocytosis, in contrast to the unfunctionalised MOFs, which are mainly internalised through clathrin-mediated endocytosis.

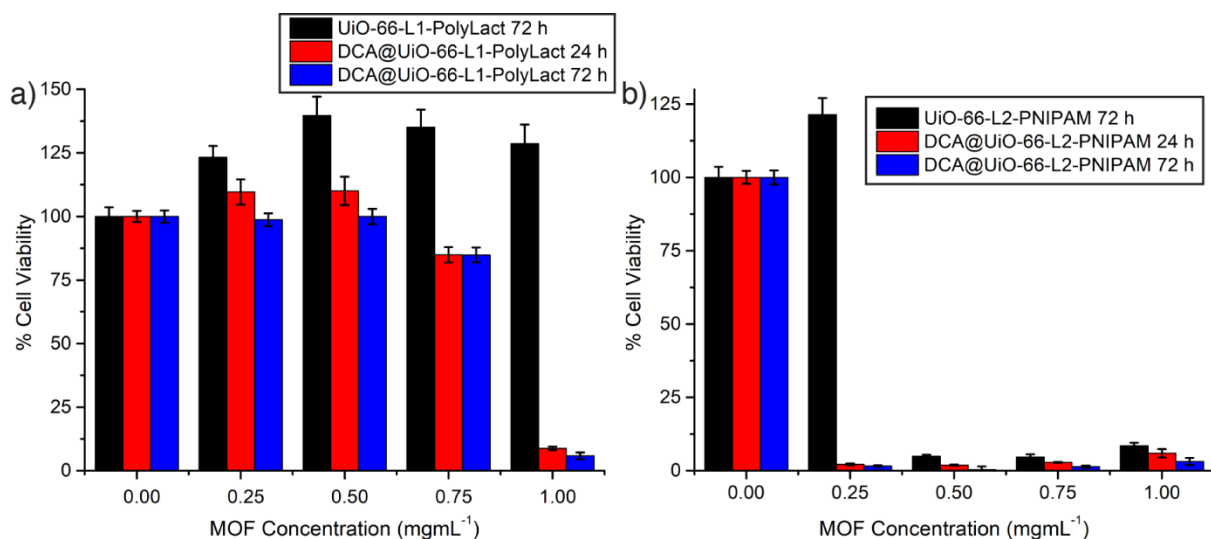


**Figure 5.25.** Cytotoxicities against HeLa cells as measured by MTS assay, for a) empty and DCA-loaded UiO-66-L1-PolyLact, and b) empty and DCA-loaded UiO-66-L2-PNIPAM. Error bars represent the standard deviation from five experiments.

In concert with the fact that the biotin-coated sample is the least efficiently internalised NMOF with almost no active transport, DCA@UiO-66-Biot samples (both prepared by coordination modulation and postsynthetically) do not exhibit any cytotoxicity for 72 h of incubation in any of the cases (Figure 5.26).

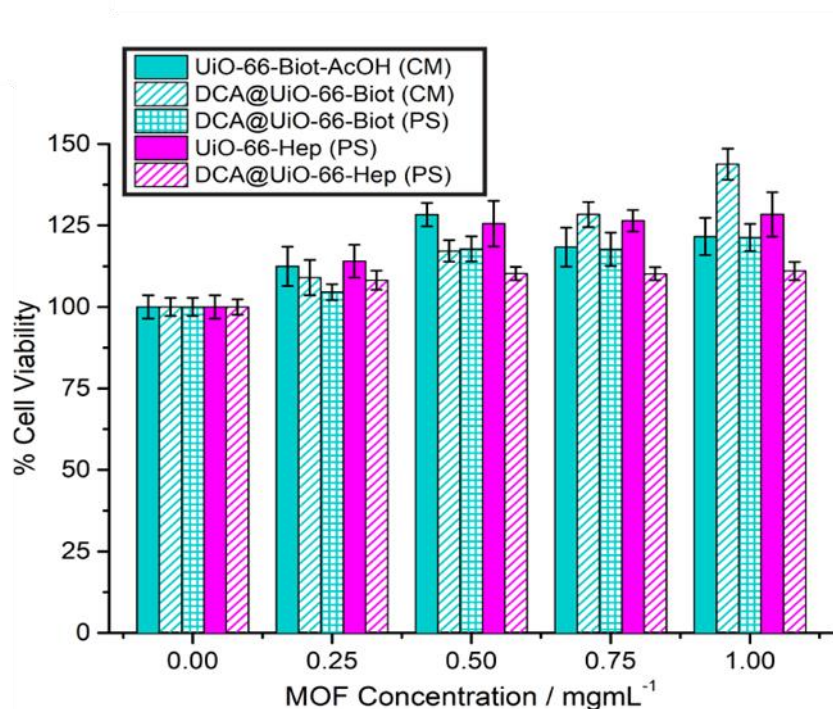


**Figure 5.26.** HeLa cytotoxicity of empty and DCA-loaded heparin and biotin modified samples. Error bars represent the standard deviation from five experiments.

In contrast to folate coated and PEGylated NMOFs, although it was observed that the caveolae-mediated endocytosis is enhanced after heparin coating when compared to naked UiO-66, DCA@UiO-66-Hep (PS) also does not exhibit any cytotoxicity towards HeLa cells even after of 72 h of incubation. UiO-66-Hep (PS) showed undesirable degradation kinetics and colloidal stability when compared to UiO-66-L1 precursor samples, as described during Chapter 3, and so may not be suitably stable. Additionally, heparin is known to bind to several growth factors, and can activate their signalling cascades.<sup>74-76</sup> For example, the growth of three different colon cancer cell lines has been reported to be stimulated upon heparin addition,<sup>77</sup> which could explain why no cytotoxicity is observed in this case. This underlines the importance of also studying other variables, such as the cell processes in which the surface coating, or even the NPs components, are involved.

### 5.5.2. Cytotoxicity Against MCF-7 and HEK293

Based on the cell viability results obtained using the HeLa cervical cancer cell line, it was decided to further investigate the *in vitro* anticancer selectivity of the most effective NMOFs against other cell lines. The cytotoxicities of DCA<sub>5</sub>@UiO-66-FA<sub>1</sub>, DCA@UiO-66-L1-PEG2000, DCA@UiO-66-L1-PolyLact and DCA@UiO-66-L2-PNIPAM were measured against the breast carcinoma cell line MCF-7 using the MTS assay, and compared with DCA@UiO-66. Following the protocol detailed for HeLa cells, cells were incubated with different concentrations of the NMOFs for 72 h, with three replicates for each concentration (n = 3). In order to study the effect of the therapeutically active materials in non-cancerous cells, cell proliferation was also studied in human embryonic kidney cells (HEK293) in parallel following the former MTS protocol. The incubation time was 72 h, with n = 3. Ideally, in order to be an efficient therapeutic agent, the DCA@NMOFs should not significantly decrease healthy cell proliferation. Since DCA reprograms the mitochondria of cancer cells to normal functions and restores their apoptosis, it may be expected that there shouldn't be an effect in healthy cells.<sup>37, 38, 40</sup>

It was noted that the results had large errors, and it was thought that washing away excess MOF with PBS after incubation may have been washing away cells that were not well adhered to the plate. To investigate this, the experiments were repeated with only one PBS wash to remove excess MOF after the 72 h incubation stage of the MTS protocol and the results compared in Figures 5.27 and 5.28.

Comparing the results obtained for each cell line by both MTS methodologies, one can observe that in general smaller errors are obtained when the number of PBS washes is reduced and the cell proliferation is higher, which indeed suggests that cells are being washed away during the PBS washing stage, as controls in which empty wells are seeded with

dispersions of MOF in growth media did not have a higher absorbance than controls with only media, meaning that MOF adherence to the plate was not giving false positive errors.

In the case of MCF-7 it can be observed that similar cell proliferations levels were obtained for DCA@UiO-66 and DCA@UiO-66-L1-PolyLact. However, MCF-7 cell proliferation changed for the samples that were assessed as cytotoxic, DCA<sub>5</sub>@UiO-66-FA<sub>1</sub> and DCA@UiO-66-L2-PNIPAM, which were “less” cytotoxic when the number of washes was reduced. On the other hand, DCA@UiO-66-L1-PEG2000 cytotoxicity is slightly enhanced when MCF-7 cells are only washed once (Figure 5.27).

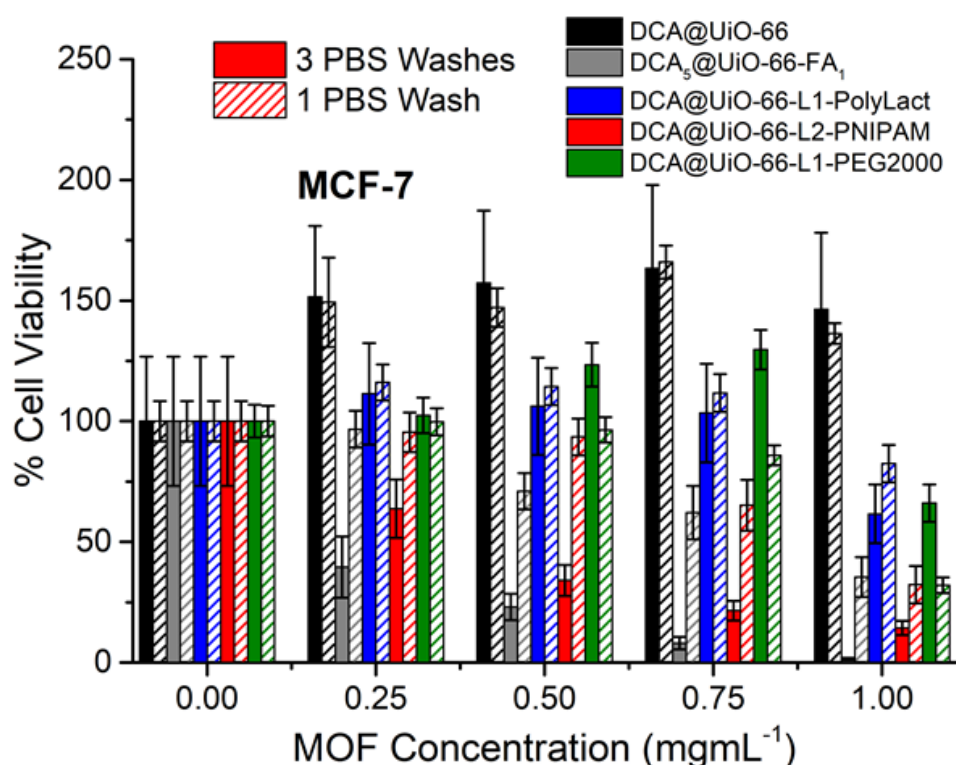


**Figure 5.27.** Effect of PBS washing on cytotoxicity as measured by MTS assay for the DCA-loaded MOFs against MCF-7 cells. Error bars represent the standard deviation from triplicate experiments.

A similar trend occurs for HEK293 cell proliferation, as generally smaller errors were obtained when reducing the number of PBS washes. Again, a larger difference between the values obtained from both approaches was found for DCA@UiO-66-L2-PNIPAM, especially at lower concentrations. For a concentration of 1 mgmL<sup>-1</sup> of DCA@NMOFs the values obtained were very close for both methods, with slightly higher proliferations when the cells were washed only once, apart from DCA@UiO-66-L1-PEG2000, which was again more cytotoxic when cells were only being washed once (Figure 5.28). DCA@UiO-66 exhibits enhanced cell proliferation in general, particularly at higher concentrations.

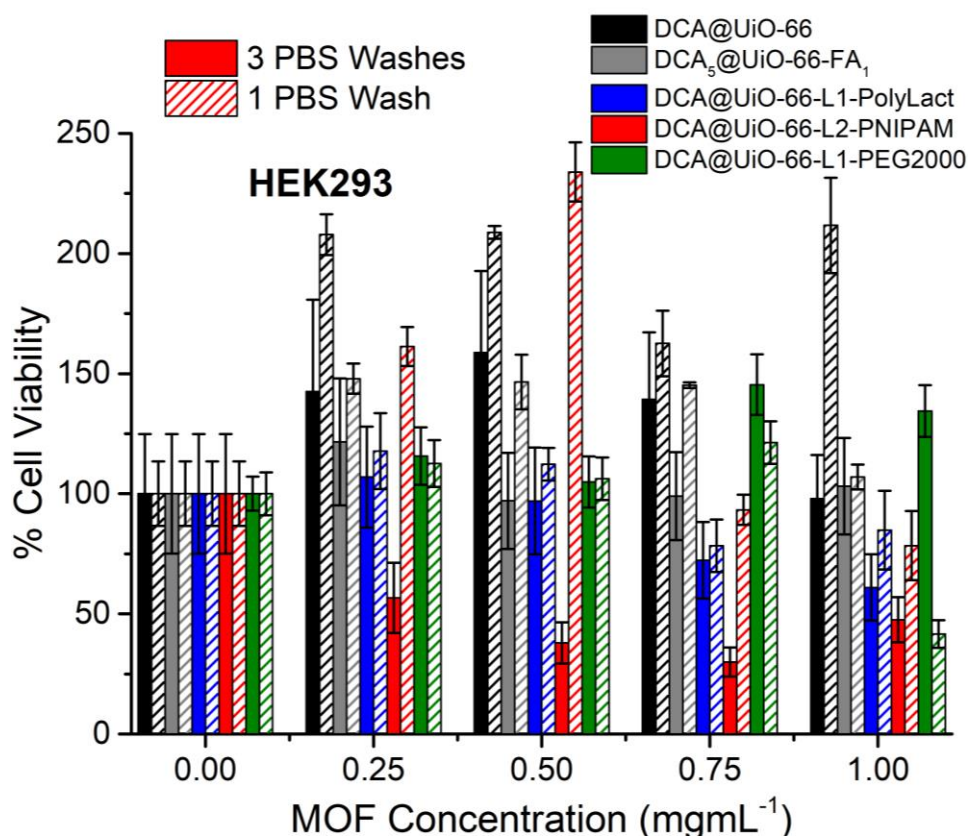


**Figure 5.28.** Effect of PBS washing on cytotoxicity as measured by MTS assay for the DCA-loaded MOFs against HEK293 cells. Error bars represent the standard deviation from triplicate experiments.

In general it can be observed that the cell proliferation with both HEK293 and MCF7 cells when incubated with DCA@UiO-66 – which already enhanced cell proliferation when washing 3 times – is slightly enhanced, and although it has the highest DCA content, no negative effect against MCF- and HEK293 cells was found, with  $136 \pm 4\%$  and  $212 \pm 20\%$  cell proliferation after 72 h of incubation with a solution of  $1 \text{ mgmL}^{-1}$  of MOF compared to untreated controls.

As a general trend observed for all the experiments, no matter the number of washes, DCA@UiO-66-FA is not cytotoxic for healthy HEK293 cells while it is for cancerous MCF7 cells, and DCA@UiO-66-L1-PolyLact has similar levels of cytotoxicity for both cell lines, which was slightly reduced with the second approach. It is clear that the values obtained with only one PBS wash are more representative of actual cytotoxicity for MCF-7 and HEK293, and so these are used for comparison with the HeLa cell data (Figure 5.29), in order to assess the selectivity of cytotoxicity.

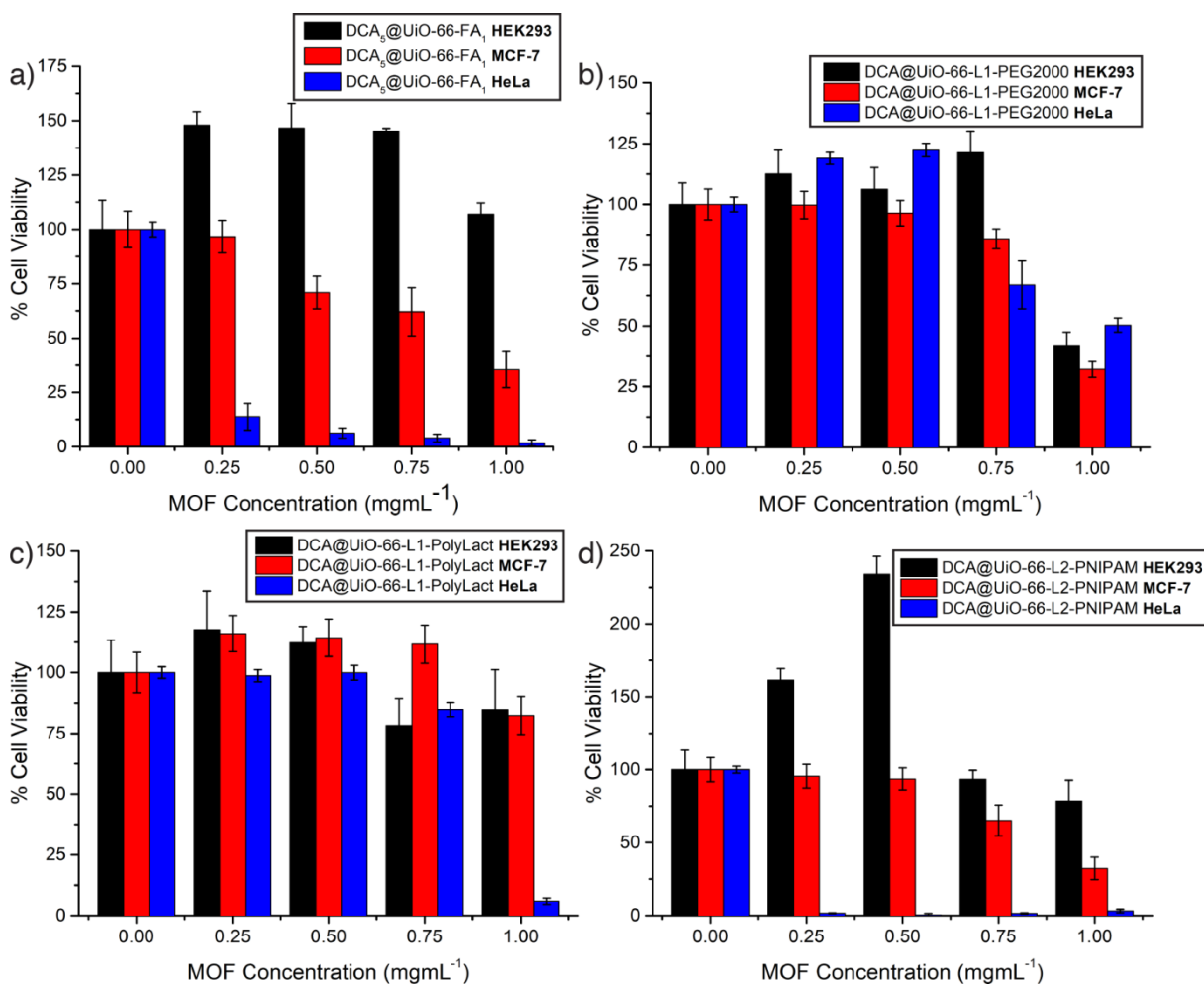


**Figure 5.29.** Cytotoxicities against HEK293, MCF-7, and HeLa cells assessed by MTS assay for a)  $\text{DCA}_5@UiO-66-FA_1$  (CM), b)  $\text{DCA}@UiO-66-L1-PEG2000$ , c)  $\text{DCA}@UiO-66-L1-PolyLact$ , and d)  $\text{DCA}@UiO-66-L2-PNIPAM$ . Error bars represent the standard deviation from triplicate experiments.

These results strongly indicate that  $\text{DCA}_5@UiO-66-FA_1$  (CM) is the most efficient and safe drug delivery vehicle, especially when comparing the cell proliferation trends of the three different cell lines, FR(+) HeLa and MCF7,<sup>65</sup> and FR(-) HEK293,<sup>20</sup> highlighting the effective folic acid targeting strategy (Figure 5.29a). The dose-responsive curve towards MCF-7 cells showed a similar trend to the HeLa experiment, although with slightly lower efficacy;  $71 \pm 8\%$  cell viability at a concentration of  $0.5 \text{ mgmL}^{-1}$  and  $35 \pm 8\%$  for a concentration of  $1 \text{ mgmL}^{-1}$ . More importantly, after 72 h of incubation with HEK293 cells, proliferation was not reduced in the presence of  $\text{DCA}_5@UiO-66-FA_1$  (CM) at any concentration, with  $107 \pm 5\%$  cell viability at the NMOF concentration of  $1 \text{ mgmL}^{-1}$ . These results suggest that folate induces cancer cell-targeting, as HeLa cells have a higher FR overexpression than MCF-7,<sup>65</sup> and thus therapeutic efficacy in HeLa is more pronounced. On the other hand, HEK293 has been reported to have normal levels of expression of the FR,<sup>20</sup> and thus no effect is observed on their cell proliferation possibly as a consequence of poor internalisation and/or a lack of metabolic effect of DCA on

healthy cells. It is also important to consider that free dichloroacetate was not cytotoxic to either MCF-7 or HEK293 cells at the concentrations delivered by the NMOFs (Figure 5.30), confirming the efficient delivery of DCA into the cells by the MOF DDSs.

In general, DCA@UiO-66-L1-PEG2000 does not exhibit any selectivity of cytotoxicity for higher concentrations, with similar cytotoxic values for the three cell lines (Figure 5.29b). DCA@UiO-66-L1-PEG2000 induced some cytotoxicity to MCF-7 cells, with a  $32 \pm 3\%$  cell viability when cells were incubated with  $1 \text{ mg mL}^{-1}$  of MOF, similar to the cell viability reported for HeLa cells ( $50 \pm 3\%$ ) at the same concentration. However, some unwanted cytotoxicity of DCA@UiO-66-L1-PEG2000 was observed against HEK293 ( $42 \pm 6\%$  viability) at the highest concentration of  $1 \text{ mg mL}^{-1}$ .

Interestingly, DCA@UiO-66-L1-PolyLact and DCA@UiO-66-L2-PNIPAM were less cytotoxic towards MCF-7 and HEK293 than HeLa cells (Figures 5.29c and 5.29d). DCA@UiO-66-L1-PolyLact is only cytotoxic in cancer cells at higher concentrations, more significant for HeLa cells ( $6 \pm 1\%$  cell viability at  $1 \text{ mg mL}^{-1}$ ) than for MCF-7 cells ( $82 \pm 8\%$  cell viability at  $1 \text{ mg mL}^{-1}$ ). However, cell proliferation in HEK293 cells is also reduced, although not significantly ( $85 \pm 16\%$  cell viability at  $1 \text{ mg mL}^{-1}$ ). Therefore, if accumulated in the body during an *in vivo* treatment, it might induce healthy tissue damage. DCA@UiO-66-L2-PNIPAM, which already exhibits high cytotoxicity even empty in HeLa cells for concentrations of  $0.50 \text{ mg mL}^{-1}$  and higher, was remarkably less cytotoxic for MCF7 and HEK293 (cell viability  $32 \pm 8\%$  and  $78 \pm 14\%$  when treated with  $1 \text{ mg mL}^{-1}$  of MOF respectively). Its use might be safe if in low concentrations, but cytotoxicity towards healthy HEK293 kidney cells for higher concentrations might be a concern.

### 5.5.3. Cytotoxicity of Free Dichloroacetate

The therapeutic effect of dichloroacetate alone against HeLa, MCF-7 and, HEK293 was also investigated by MTS assay, using the same protocol as for the DCA-loaded MOFs but incubating the cells with different concentrations of sodium dichloroacetate (NaDCA) for 72 h. The results (Figure 5.30) show that dichloroacetate does not induce significant toxicity when it is not loaded into a drug delivery vehicle. The results are similar for all cell lines, with  $IC_{50}$  values around  $9 \text{ mg mL}^{-1}$ . Even at the highest concentration of  $1 \text{ mg mL}^{-1}$  of DCA<sub>5</sub>@UiO-66-FA<sub>1</sub>, only  $\sim 0.12 \text{ mg mL}^{-1}$  of DCA is delivered and the result is the death of over 50% MCF-7 cancer cells, while more than 85 % of HeLa cells die when incubated with only  $0.25 \text{ mg mL}^{-1}$  of MOF (ca.  $0.03 \text{ mg mL}^{-1}$  of DCA). Thus, it is clear that encapsulation within the MOFs enhances cytotoxicity of DCA by a factor of  $>75$  for MCF-7 cells and  $>350$  for HeLa cells, considerably higher than for other DCA prodrugs, while no cytotoxicity is found towards HEK293 non-cancerous kidney cells.

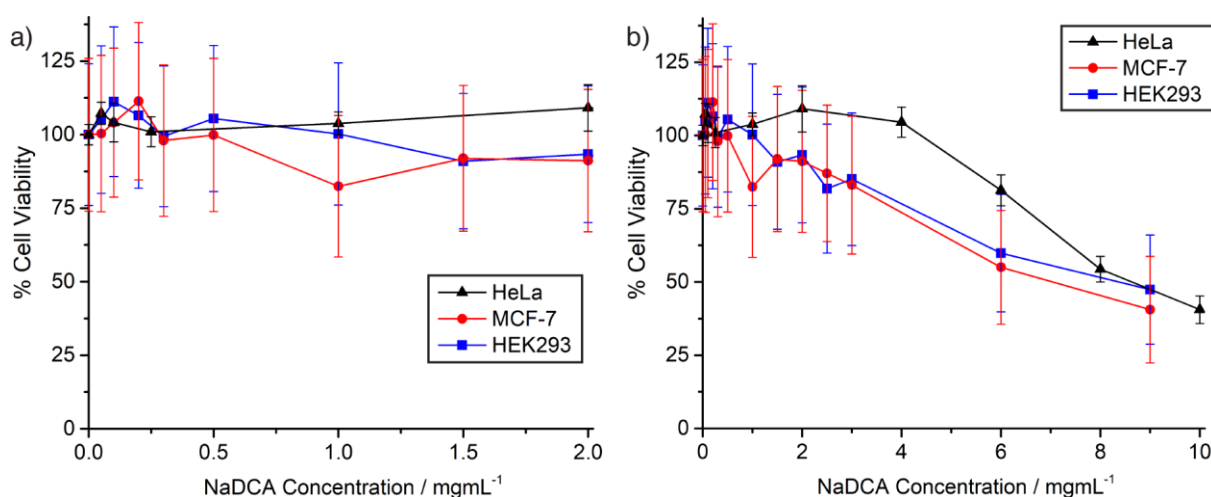


**Figure 5.30.** Cytotoxicity against HeLa, HEK293, and MCF-7 cell lines of sodium dichloroacetate at a) low, and b) high concentrations of NaDCA. Error bars represent the standard deviation from triplicate experiments.

It can also be observed, that the higher DCA loading is around 20 w/w %, and as such, when cells are incubated with 1 mgmL<sup>-1</sup> of MOF (maximum dose), only a DCA concentration of ca. 0.20 mgmL<sup>-1</sup> is reached, which is non-cytotoxic towards any of the tested cell lines without the presence of a carrier. Hence, it is clear that incorporating DCA into MOFs as DDSs enhance its effect on cancer cells (with over a 50 fold increase for HeLa cells in all cases) when the appropriate coating is provided to the MOF surface, related with cellular internalisation efficacy and routes, as bare DCA@UiO-66 was non-cytotoxic towards any of the three cell lines.

## 5.6. Immune System Response Towards Surface Modified UiO-66

The immune response toward exogenous materials plays a crucial role in any treatment efficacy; DDSs will not be efficient if they are cleared out of the blood stream by macrophages, or if they stimulate/suppress immune response or induce tissue damage.<sup>78, 79</sup> Macrophages uptake efficiency, cytotoxicity, and Reactive Oxygen Species (ROS) production by macrophages and peripheral blood lymphocytes (PBLs) are of importance when considering the efficiency of a drug vehicle, but only few studies have assessed these issues so far with MOFs.<sup>80-82</sup> Importantly, they can provide further insights into possible treatment efficiency without resorting to early stage animal testing. As such, cytotoxicity of the NMOFs was assessed against the J774 mouse monocyte macrophage cell line and also human peripheral blood lymphocytes (PBLs) isolated from the blood of three donors. The generation of ROS by

these cells in the presence of the MOFs was also assessed by the 2',7'-dichlorodihydrofluorescein diacetate (H2DC-FDA) fluorescent probe.

### 5.6.1. Endocytosis Efficiency Towards J774 Macrophage Cells

Initially, the uptake of the calcein-loaded MOFs by the J774 macrophage cells was monitored by flow cytometry, to confirm that internalisation occurs and help rationalise any cytotoxicity. The ratio of the mean fluorescence intensity (MFI) between cells cultured with  $0.25 \text{ mgmL}^{-1}$  of MOFs and cultured with medium alone was analysed to determine the cells integrity and uptake ratio for each MOF in triplicate, normalised to cal@UiO-66-L1 to determine the effect of surface chemistry (Figure 5.31).

Normalised cell fluorescence showed that only PEGylation decreases macrophage uptake, to levels of  $80 \pm 4\%$  compared to cal@UiO-66-L1, which tallies well with observations that PEGylation of nanoparticles decreases macrophage recognition.<sup>83, 84</sup> cal@UiO-66-FA (PS) was the most efficiently internalised NMOF, with values of  $189 \pm 15\%$  – expected, as activated macrophages are known to overexpress the folate receptor<sup>72, 73</sup> – followed by cal@UiO-66-L2-PNIPAM with  $176 \pm 9\%$  cell internalisation and cal@UiO-66-L1-PolyLact with  $155 \pm 7\%$  macrophage uptake efficiency, correlating well with the endocytosis efficiency experiments on the MOFs entering HeLa cells, described during Chapter 4.

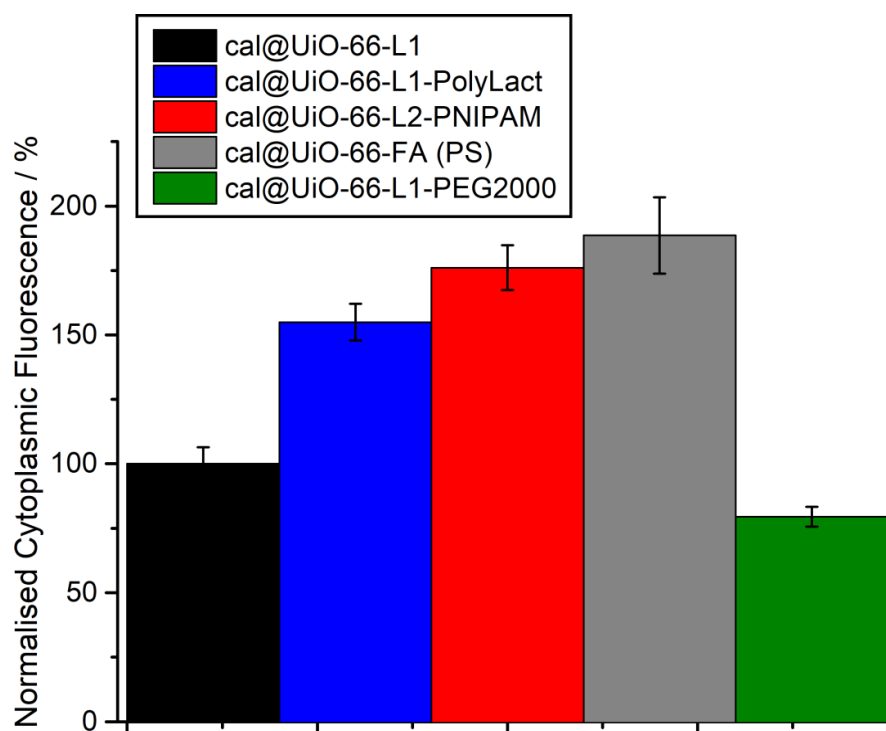


**Figure 5.31.** Endocytosis efficiency (J774 cell line) of the surface-modified, calcein loaded MOFs normalised to cal@UiO-66-L1. Error bars represent the standard deviation from triplicate experiments.

### 5.6.2. Cytotoxicity Against J774 and PBL Cells

To measure cell proliferation in the macrophage cell line J774 or in PBLs isolated from the blood of donors, the cell proliferation kit I MTT (Roche), based on the cleavage of the tetrazolium salt 3-(4,5-dimethylthiazol-2-yl)-2,5-diphenyltetrazolium bromide, was used.

J774 cells were incubated with nanoparticles (0.1, 0.25 and 0.5  $\text{mgmL}^{-1}$ ) for 24 h. PBLs MTT assay was performed similarly but the incubation time with nanoparticles was 48 h, meaning that the final incubation time of MOFs with macrophages was 48 hours and with PBLs 72 hours (See Section 5.8). Results were expressed as mean  $\pm$  standard error of the mean of triplicates. The average of the absorbance obtained for each concentration of each nanoparticle was compared with untreated cells.

In parallel, the cytotoxicity of empty surface-functionalised MOFs and  $\text{DCA}_5@UiO-66-FA_1$ ,  $\text{DCA}@UiO-66-L1-PolyLact$  and  $\text{DCA}@UiO-66-L2-PNIPAM$  was studied for both J774 macrophages and PBLs. No cytotoxicity was observed when incubating J774 cells with either UiO-66-FA (CM) or  $\text{DCA}_5@UiO-66-FA_1$  (CM), despite the fact that, in contrast to the folate receptor negative HEK293 healthy cell line, activated macrophages overexpress the folate receptor.<sup>72, 73</sup> In fact, cell proliferation was slightly enhanced ( $128 \pm 10\%$  and  $142 \pm 11\%$ , respectively) at a NMOF concentration of 0.5  $\text{mgmL}^{-1}$  (Figure 5.32a).

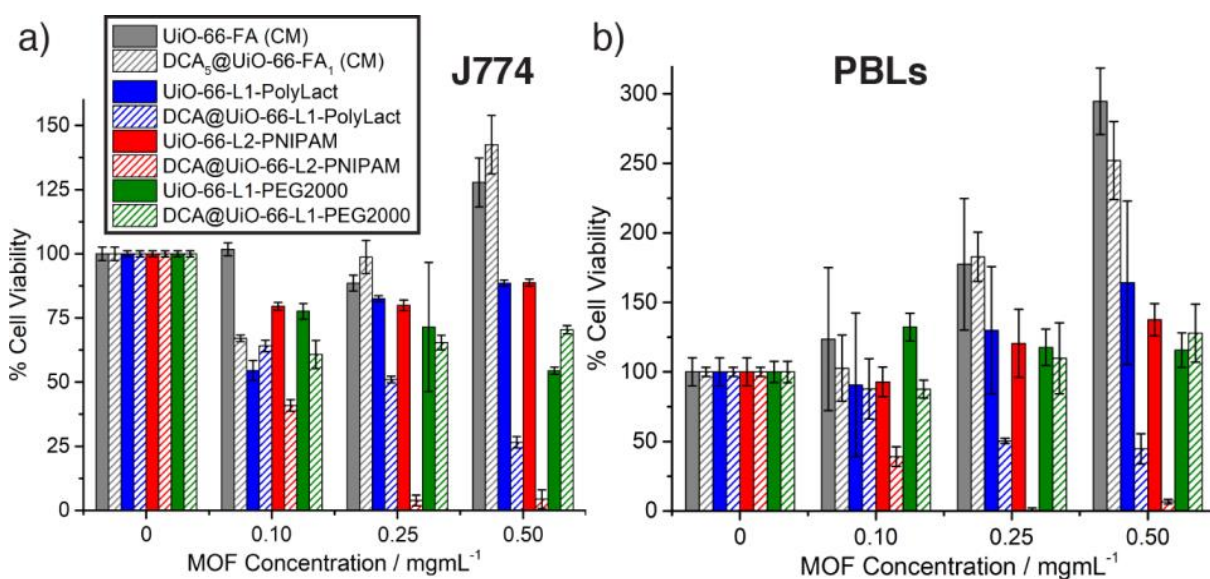


**Figure 5.32.** Cytotoxicity of empty and DCA-loaded UiO-66 samples against a) J774 macrophage cells and b) a pool of peripheral blood lymphocytes from three human donors. The key for part a) also applies in part b). Error bars represent the standard deviation from triplicate experiments.

UiO-66-L1-PEG2000 and  $\text{DCA}@UiO-66-L1-PEG2000$  materials decreased macrophages cell proliferation to levels of  $54 \pm 1\%$  and  $70 \pm 2\%$ , respectively, at 0.5  $\text{mgmL}^{-1}$ , showing that the

DCA-containing anticancer MOF was more well tolerated at higher concentrations than the empty carrier.

Cytotoxicity assays showed that UiO-66-L1-PolyLact and UiO-66-L2-PNIPAM were well tolerated by J774 macrophages (both having  $89 \pm 1\%$  cell viability at  $0.5 \text{ mgmL}^{-1}$ ), despite empty UiO-66-L2-PNIPAM having proven to be highly cytotoxic for HeLa cells. DCA@UiO-66-L1-PolyLact and DCA@UiO-66-L2-PNIPAM killed almost all cells, despite the reports that DCA does not affect healthy cells. Cell viability values of  $27 \pm 2\%$  and  $4 \pm 4\%$ , respectively, were induced by incubation with  $0.5 \text{ mgmL}^{-1}$  NMOF (Figure 5.32a). The results suggest that the surface functionalities, together with DCA, might have some synergistic effect on metabolic activity.

As detailed in Section 5.1.2, DCA inhibits the pyruvate dehydrogenase kinase (PDK), which is overexpressed in cancer cells, shifting their metabolism from glycolysis back to glucose oxidation.<sup>25, 36, 38</sup> High lactate levels are characteristic of metabolism through glycolysis, as PDK in cancer cells inhibits pyruvate dehydrogenase (PDH), the enzyme responsible for converting pyruvate to acetylCoA, which further enters the Krebs cycle in the mitochondria during glucose oxidation, and alternatively, pyruvate is transformed to lactate in the cytosol of cancer cells.<sup>32, 33</sup> Hence, as lactate is covering the surface of DCA@UiO-66-L1-PolyLact, upon internalisation, higher lactate levels could be found in the cytosol of macrophages, and together with DCA induce unwanted cytotoxicity, as the empty UiO-66-L1-PolyLact was non-cytotoxic. This hypothesis would however require further investigation.

The peripheral blood lymphocyte cytotoxicity (PBLs) assays were performed with a pool of PBLs from three different human donors (Figure 5.32b). It is important to remark that PBLs, isolated from human donors, provide a way of *in vitro* analysis close to *in vivo* conditions without animal testing. Each NMOF concentration was incubated in triplicate ( $n = 3$ ), and the experiment was performed twice to ensure reproducibility of the results (Figure 5.33). The results obtained in both independent studies showed similar cell proliferation trends when PBLs were incubated with the NMOFs in question, with DCA<sub>5</sub>@UiO-66-FA<sub>1</sub> and DCA@UiO-66-L1-PEG2000 being the only DCA-loaded MOFs not to negatively affect cell proliferation.

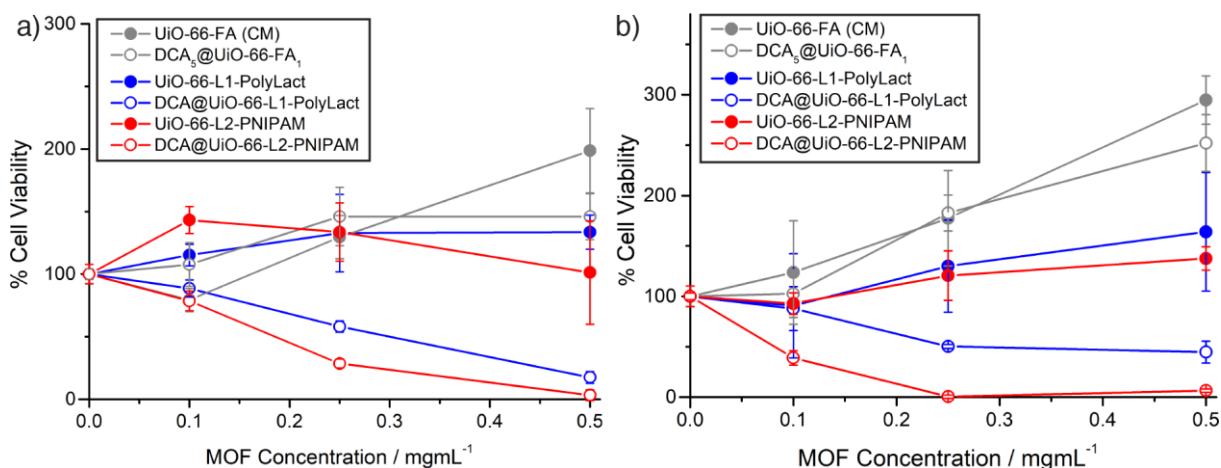


**Figure 5.33.** Cell viabilities of PBLs in the presence of different concentrations of the surface modified MOFs with and without DCA. a) and b) are two replicates with two different pools of PBLs extracted from human blood at different times. Error bars represent the standard deviation from triplicate experiments.

Incubation of PBLs with UiO-66-FA (CM) or  $\text{DCA}_5@UiO-66-FA_1$  for 72 hours yielded similar results to when the same MOFs were incubated with J744 macrophages, obtaining enhanced, dose-responsive cell proliferation by MTT assay for two independent experiments (Figure 5.33) which showed similar trends. Viabilities of  $295 \pm 24\%$  and  $199 \pm 34\%$  for empty UiO-66-FA (CM) and  $252 \pm 28\%$  and  $146 \pm 18\%$  for  $\text{DCA}_5@UiO-66-FA_1$  (CM) were found at  $0.5 \text{ mgmL}^{-1}$  incubation. UiO-66-L1-PolyLact and UiO-66-L2-PNIPAM, did not induce PBLs cell death at  $0.5 \text{ mgmL}^{-1}$  ( $164 \pm 59\%$  and  $134 \pm 14\%$  viability for the former;  $138 \pm 12\%$  and  $101 \pm 41\%$  viability for the latter), while incubation with  $\text{DCA}@UiO-66-L1-PolyLact$  and  $\text{DCA}@UiO-66-L2-PNIPAM$  under the same conditions reduced cell viability to values of  $45 \pm 11\%$  and  $17 \pm 5\%$  for the former, and  $7 \pm 2\%$  and  $3 \pm 4\%$  for the latter. These are major issues that may preclude the use of the DCA-containing polymer-coated samples *in vivo*.

In contrast, UiO-66-L1-PEG2000 and  $\text{DCA}@UiO-66-L1-PEG2000$  induced PBL cell proliferation from a single pool to levels of  $116 \pm 12\%$  and  $128 \pm 21\%$  compared to untreated cells at a concentration of  $0.5 \text{ mgmL}^{-1}$ . Whilst the response of the J774 cells and the HEK293 cells to  $\text{DCA}@UiO-66-L1-PEG2000$  could be problematic, the selectivity of the cytotoxicity of folate targeted, DCA loaded,  $\text{DCA}_5@UiO-66-FA_1$  (CM) nanoparticles is very promising, killing almost all cancer cells whilst not negatively affecting the proliferation of any healthy cells.

### 5.6.3. Reactive Oxygen Species Generation in J774 and PBL Cells

Reactive oxygen species (ROS) production was investigated to gain insights into the cytotoxic effects of the NMOFs and to assess induction of oxidative stress (Figure 5.34 and 5.35).<sup>85, 86</sup> J774 macrophage cells and PBLs were incubated with different doses of the NMOFs over 2

h, followed by incubation with the intracellular fluorescent probe H2DC-FDA in order to track ROS production by flow cytometry.

In agreement with the cell proliferation results obtained by MTT assay, DCA@UiO-66-L2-PNIPAM induced the highest ROS production in J774 cells, with a 5.5 fold increase at a NMOF concentration of  $0.5 \text{ mg mL}^{-1}$  a possible reason for the significant cytotoxicity, while the non-cytotoxic empty UiO-66-L2-PNIPAM only induced a 1.4 fold increase in ROS production at the same concentration. Whilst empty UiO-66-L1-PolyLact did not induce significant cytotoxicity in the J774 cell lines, higher ROS production was found when incubating macrophages with the empty sample (3.2 fold increase) compared to DCA@UiO-66-L1-PolyLact (1.9 fold increase), which is more cytotoxic. Similarly, incubating J774 macrophages with UiO-66-L1-PEG2000 induced a slightly higher ROS production (2 fold increase) than incubation with DCA@UiO-66-L1-PEG2000 (1.5 fold increase) for the same concentration. UiO-66-FA (CM) did not induce significant ROS production, with a 1.2 fold increase when incubating macrophages with a  $0.5 \text{ mg mL}^{-1}$  concentration of NMOF, while DCA<sub>5</sub>@UiO-66-FA<sub>1</sub> (CM) did induce ROS production with a 2.8 fold increase, although MTT assays showed cell proliferation was enhanced in all cases, suggesting that ROS production is not a major source of cytotoxicity for these particular MOFs (Figure 5.34).

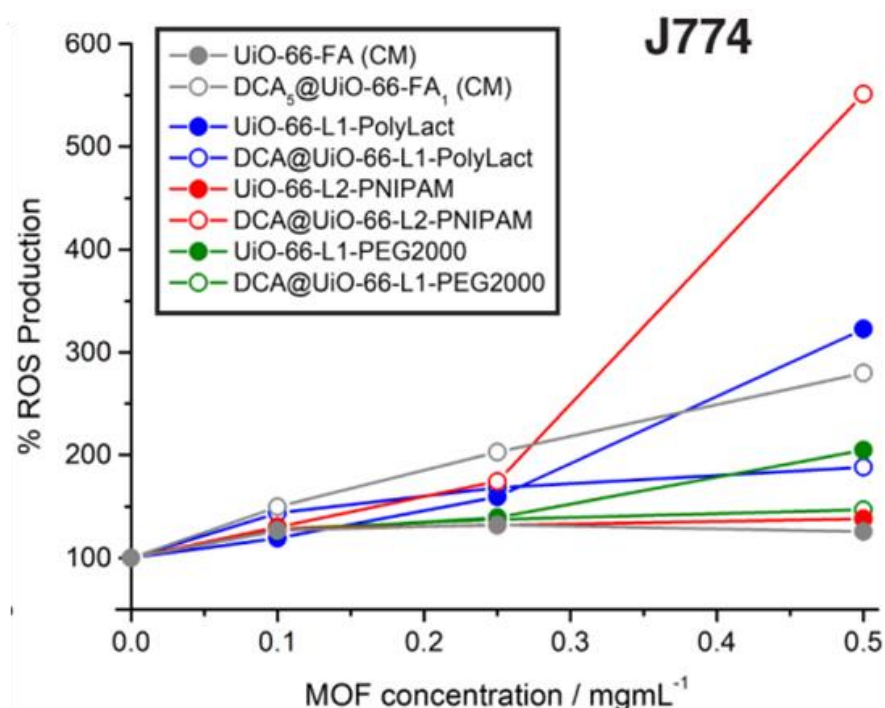


**Figure 5.34.** Reactive oxygen species generation by J774 macrophage cells in the presence of empty and DCA-loaded UiO-66 samples.

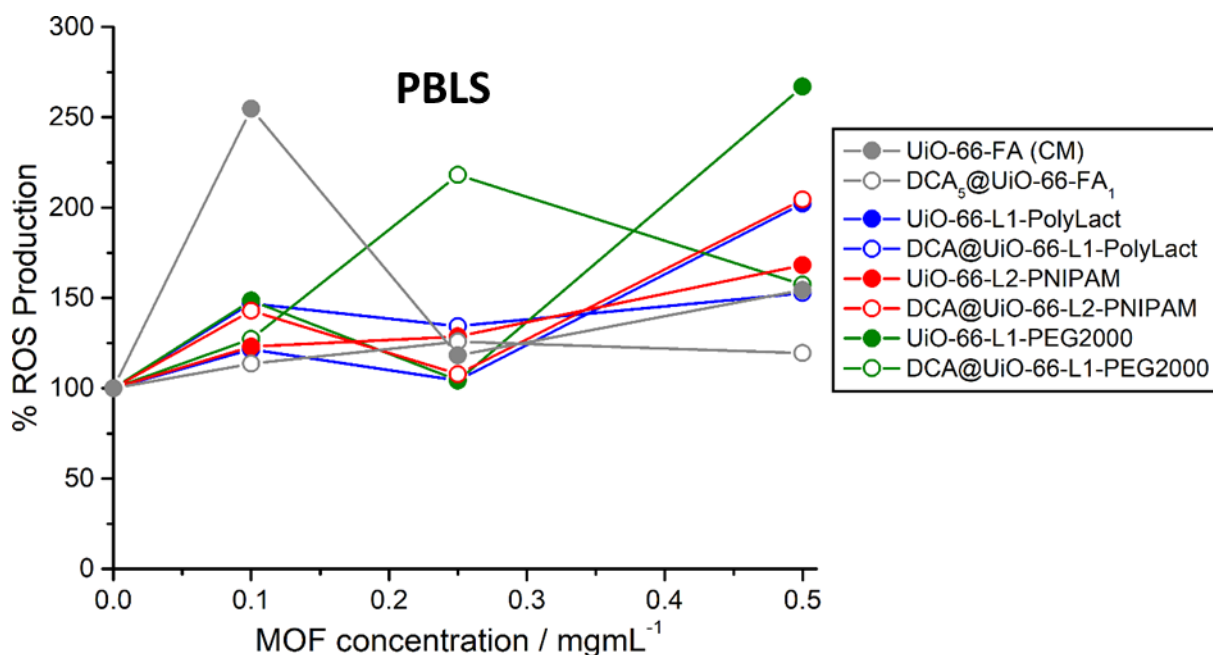


**Figure 5.35.** Reactive oxygen species (ROS) generation in PBLs when incubated with surface modified MOFs.

ROS production in PBLs was also monitored (Figure 5.35) with no discernible trends, although DCA<sub>5</sub>@UiO-66-FA<sub>1</sub> was again well tolerated. These results suggest that while higher concentrations MOFs can induce some ROS production, it does not seem to result in cytotoxicity towards these healthy cells. It is also important to note that concentrations of DCA-loaded NMOFs lower than 0.5 mgmL<sup>-1</sup> did not induce considerable ROS production, despite being therapeutically active towards cancer cell lines.

## 5.7 Conclusions

During Chapter 2 it was shown that incorporation of DCA at defects sites during the modulated synthesis of Zr MOFs of UiO family offers (i) particle size control in the assembly of highly defective ~20 nm nanoparticles of hierarchically porous materials, (ii) high loading (15–25% w/w) of the anticancer probe molecule DCA, and (iii) porous MOFs into which further medicinal cargo (5-FU in this case) can be loaded.

During this Chapter, the therapeutic activity of the UiO family of Zr-MOFs - including UiO-66 (Zr-terephthalate) and its bromo, nitro and amino derivatives, DUT-52 (Zr-Naphthalene dicarboxylate) and UiO-67 (Zr-biphenyldicarboxylate) – which have been proven to be non-cytotoxic when empty up to 1 mgmL<sup>-1</sup>,<sup>4</sup> has been studied towards MFC-7 breast cancer cells, in order to rationalise their activity with their reported endocytosis routes of internalisation.<sup>15</sup> In this way, both particle size and surface chemistry were studied.

On the whole, the smaller (~20 nm) DCA-terephthalate particles exhibit greater cytotoxicity towards MCF-7 cancer cells than their larger (~100 nm) analogues; possibly due to partial internalisation of the smaller MOFs through passive diffusion, which allows DCA release directly into the cytosol to enhance its therapeutic effects. However, the surface chemistry of the MOFs has a greater effect, with DCA@DUT-52 and DCA@UiO-67 being the most therapeutically efficient MOFs, despite their bigger size. These results are in agreement with a recent study on endocytosis mechanisms, which shows that the Zr-terephthalate MOFs are mainly internalised by clathrin-mediated endocytosis, hence being stored in the lysosomes before releasing their cargo, while the DUT-52 and UiO-67 are partially internalised through the caveolae-mediated route, hence being potentially able to escape the early endosome, releasing their cargo into the cytosol in a more effective manner. Here it is shown that although surface chemistry plays a more important role than particle size, possibly as a consequence of the cellular internalisation routes, an enhancement in therapeutic activity can be achieved by particle size reduction, potentially allowing the MOFs to partially undergo cellular internalisation by passive diffusion. When MTS data for MOFs of comparable size is plotted against the maximum DCA concentration delivered for each MOF concentration, it can be observed that the best DDS is UiO-67, followed by DUT-52, which has similar activity to UiO-66-NH<sub>2</sub>, presumably due to its positively charged surface, which enhances cellular internalisation, followed by the bromo and nitro derivative, while unfunctionalised UiO-66 of ca. 77 nm does not induce any cytotoxicity.

Concurrent delivery of two drugs from the 5-FU@DCA@MOFs further enhances cytotoxicity compared to precursor DCA@MOFs and both free drugs. Delivery of multiple drugs from one DDS has the potential to overcome issues with resistance and poor efficacy, and is enabled by utilisation of different loading protocols; defect-loading of cargo into Zr MOFs during synthesis is possible for any carboxylic acid containing drug.

Postsynthetic surface functionalisations, using folic acid, biotin, heparin, PEG, Poly-L-Lactide and PNIPAM, have been performed on DCA@UiO-66, and it has been proven to be also compatible with all the surface modification protocols during this chapter without mayor DCA leakage. Extensive *in vitro* studies of empty, and especially DCA-loaded materials, have shown that folic acid coated MOFs exhibit selective cytotoxicity towards HeLa (cervical) and MCF-7 (breast cancer) cells, without adversely affecting proliferation of healthy kidney (HEK293), macrophage (J774) and PBL cells, possibly due to the over expression of the folate receptor on the surfaces of cancer cells and a preference for desirable caveolae-mediated endocytosis. The method of folic acid coating is vital – incorporation of folic acid and DCA in a one-pot, modulated synthesis produced significantly more active MOFs than postsynthetically coating MOFs with folic acid. Hence, the therapeutic efficiency of free DCA

was drastically improved, with a >350 fold increase in selective cytotoxicity observed when loaded into DCA<sub>5</sub>@UiO-66-FA<sub>1</sub> (CM), while uncoated DCA@UiO-66 did not produce any negative effect on the various cell lines.

The polymer-coated, DCA loaded MOFs prepared by click modulation also showed therapeutic potential, decreasing proliferation of the cancerous cell lines, but each had drawbacks. Both DCA@UiO-66-L1-PolyLact and DCA@UiO-66-L2-PNIPAM induced death in J774 macrophage cells and human lymphocytes – key components of the immune system – with the latter stimulating significant ROS production in J774 cells. While DCA@UiO-66-L1-PEG2000 was tolerated well by the immune system cells, as would be expected, it induced some cytotoxicity in healthy kidney cells at high concentrations, suggesting *in vivo* accumulation in healthy tissue might induce damage.

These results demonstrate the power of surface functionalisation and importance of cell internalisation pathways in the application of MOFs for drug delivery. The potential of DCA<sub>5</sub>@UiO-66-FA<sub>1</sub> for use as a selective anticancer DDS for *in vivo* localised treatment is apparent, particularly given the use of the metabolic probe DCA as a modulator during synthesis resulting in a drug-loaded nanoparticle that is still porous and can be loaded with a second drug for synergistic multimodal therapy. The work also highlights the broad *in vitro* experimental toolkit available to provide information on cellular uptake, endocytosis mechanisms, immune response and cytotoxicity prior to any *in vivo* treatment, thus reducing the need for early stage animal testing and acting according to the three Rs: reduction, refinement and replacement.

## 5.8 Experimental

### 5.8.1. General Experimental Remarks

**Flow Cytometry (Immune System Response):** Measurements were performed using BD FACS Canto II. The analysis was done using Infinicyt and Prism softwares (Instituto de Investigación Sanitaria Fundación Jiménez Díaz, Spain).

### 5.8.2 DCA@UiO-66 Surface Modifications

#### Postsynthetic Modifications of DCA Loaded MOFs

Surface modification of DCA@UiO-66, DCA@UiO-66-L1 and DCA@UiO-66-L2 followed the previous protocols for surface ligand exchange and covalent modification reported in Chapter 3, as per Figure 5.16. Surface modifications based on coordination chemistry were performed on DCA@UiO-66 (Folic acid, biotin and heparin), while surface modifications based on covalent chemistry were performed on DCA@UiO-66-L1 (Poly-L-Lactide and PEG) and on DCA@UiO-66-L2 (PNIPAM).

### 5.8.3 *In vitro* Protocols

#### 5.8.3.1 Cell Culture

**HeLa cervical cancer cell line** was maintained at 37 °C with 5% CO<sub>2</sub> in high rich glucose (4500 mg/L) Dulbecco's modified Eagle's Medium (DMEM) with phenol red supplemented with 10% (v/v) Fetal Bovine Serum (FBS), 2 mM L-glutamine, 100 units/mL penicillin and 100 µg/mL streptomycin. This was named complete DMEM (cDMEM). The cells were passaged three times a week (at 75-80% of confluence) at a density of 2.8 x 10<sup>4</sup> cell/cm<sup>2</sup>. (University of Cambridge)

**MCF-7 breast cancer cells** and **HEK293 human embryonic kidney cells** were maintained at 37 °C with 5% CO<sub>2</sub> in high rich glucose (4500 mgL<sup>-1</sup>) Dulbecco's modified Eagle's Medium (DMEM) with phenol red supplemented with 10% (v/v) Fetal Bovine Serum (FBS), 2 mM L-glutamine, 100 unitsmL<sup>-1</sup> penicillin and 100 µg mL<sup>-1</sup> streptomycin. This was named complete DMEM (cDMEM). The cells were passaged once or twice a week (at 75-80% of confluence) at a density of 2.8 x 10<sup>4</sup> cell/cm<sup>2</sup>. (University of Glasgow)

**J774 mouse monocyte-macrophage cell line** was cultured in RPMI-1640 medium supplemented with 0.1 mM nonessential amino acids, 100 U/mL penicillin, 100 µg/mL streptomycin, 10 mM HEPES, 2 mM L-glutamine, and 10% (v/v) fetal bovine serum and

passed twice a week (at 75-80% of confluence) at a density of  $2.8 \times 10^4$  cell $\text{cm}^{-2}$ . (Fundación Jiménez Díaz, Spain)

**Human peripheral blood lymphocytes (PBLs)** were isolated by gradient centrifugation on Lymphoprep from the blood of three donors. After washes in RPMI 1640, the PBMCs were resuspended in completed RPMI supplemented as described above and were employed to analyze reactive oxygen species and for MTT assays. The culture cells were maintained at 37 °C in a 5% CO<sub>2</sub> atmosphere. (Fundación Jiménez Díaz, Spain)

### 5.8.3.2. Cytotoxicity essays

#### MTS

The day before the experiment, cells were seeded into a 96 well plate at a density of  $10 \times 10^3$  cells per well (100  $\mu\text{L}$ ). Prior to the treatments, cells were washed twice with PBS twice. The MOFs were suspended in cDMEM by sonication at different concentrations, added to the cells and incubated – with 5 or 3 replicates for each MOF concentration and 8 replicates for media without cells and for untreated cells – for 24 h or 72 h at 37 °C with 5% CO<sub>2</sub>. To measure the toxicity, the cells were washed three times or one time with phosphate buffered saline (PBS), the media was replaced with 100  $\mu\text{L}$  of fresh culture media containing 20  $\mu\text{L}$  of MTS/phenazinemethosulfate (in a proportion 20:1) solution, and the plate was incubated for 1 h at 37 °C with 5% CO<sub>2</sub>. The plates were read at 490 nm by UV/vis spectrophotometry.

#### MTT

J774 cells at  $4 \times 10^4$  (100  $\mu\text{l}$ ) and  $1 \times 10^5$  PBLs (100  $\mu\text{l}$ ) were cultured with different doses of NMOFs previously suspended in RPMI 1640 complete medium. J774 cells were incubated with nanoparticles for 24 h and PBLs for 48 hours. After that, 3-(4,5-dimethylthiazol-2-yl)-2,5-diphenyltetrazolium bromide (MTT) reagent (10  $\mu\text{l}$ ) per well was added. After 4 h of incubation in 5% CO<sub>2</sub> at 37 °C with MTT reagent, 100  $\mu\text{l}$  of MTT solubilisation buffer were added, followed by overnight incubation. Finally absorbance ( $\lambda = 570$  nm) was measured in a TECAN Infinite F200.

### 5.8.3.3 Macrophage Uptake

$5 \times 10^5$  J774 cells per well were cultured with the different cal@NMOFs at 0.25 mg $\text{mL}^{-1}$  concentration for 2 h in 5% CO<sub>2</sub> and 37 °C. Cells were recollected, washed with PBS and resuspended in FACS Flow and analysed by flow cytometry.

### 5.8.3.4 Reactive Oxygen Species (ROS) Production

Five hundred thousand ( $5 \times 10^5$ ) J774 cells (or PBLs) were cultured with the NMOFs at different doses in RPMI complete medium without phenol red for 2 h in 5% CO<sub>2</sub> at 37 °C. Then, 500  $\mu\text{l}$  of PBS and 0.25  $\mu\text{l}$  of the intracellular fluorescent probe H<sub>2</sub>DC-FDA (20 mM

probe, 5 mM final concentration) were added. After incubation, cells were recollected and washed with PBS. Cells were resuspended in FACS Flow and analysed by flow cytometry in a BD FACS Canto II flow cytometer, analysing the intracellular probe fluorescence. The ratio of the mean fluorescence intensity (MFI) between cells cultured with nanoparticles and cells cultured with medium alone was analysed.

## 5.9 Refereces

1. I. Canton and G. Battaglia, *Chemical Society Reviews*, 2012, **41**, 2718-2739.
2. J. Rejman, V. Oberle, I. S. Zuhorn and D. Hoekstra, *The Biochemical Journal*, 2004, **377**, 159-169.
3. C. Orellana-Tavra, E. F. Baxter, T. Tian, T. D. Bennett, N. K. H. Slater, A. K. Cheetham and D. Fairen-Jimenez, *Chemical Communications*, 2015, **51**, 13878-13881.
4. C. Orellana-Tavra, R. J. Marshall, E. F. Baxter, I. A. Lazaro, A. Tao, A. K. Cheetham, R. S. Forgan and D. Fairen-Jimenez, *Journal of Materials Chemistry B*, 2016, **4**, 7697-7707.
5. K. Jiang, L. Zhang, Q. Hu, D. Zhao, T. Xia, W. Lin, Y. Yang, Y. Cui, Y. Yang and G. Qian, *Journal of Materials Chemistry B*, 2016, **4**, 6398-6401.
6. R. Röder, T. Preiß, P. Hirschle, B. Steinborn, A. Zimpel, M. Höhn, J. O. Rädler, T. Bein, E. Wagner, S. Wuttke and U. Lächelt, *Journal of the American Chemical Society*, 2017, **139**, 2359-2368.
7. S. Beg, M. Rahman, A. Jain, S. Saini, P. Midoux, C. Pichon, F. J. Ahmad and S. Akhter, *Drug Discovery Today*, 2017, **22**, 625-637.
8. J. D. Rocca, D. Liu and W. Lin, *Accounts of Chemical Research*, 2011, **44**, 957-968.
9. J. Wu, J. W. Xu, W. C. Liu, S. Z. Yang, M. M. Luo, Y. Y. Han, J. Q. Liu and S. R. Batten, *Inorganic Chemistry Communications*, 2016, **71**, 32-34.
10. X. Zhu, J. Gu, Y. Wang, B. Li, Y. Li, W. Zhao and J. Shi, *Chemical Communications*, 2014, **50**, 8779-8782.
11. J. Yang, X. Chen, Y. Li, Q. Zhuang, P. Liu and J. Gu, *Chemistry of Materials*, 2017, **29**, 4580-4589.
12. W. Wang, L. Wang, Z. Li and Z. Xie, *Chemical Communications*, 2016, **52**, 5402-5405.
13. J. Park, Q. Jiang, D. Feng, L. Mao and H.-C. Zhou, *Journal of the American Chemical Society*, 2016, **138**, 3518-3525.
14. M. H. Teplensky, M. Fantham, P. Li, T. C. Wang, J. P. Mehta, L. J. Young, P. Z. Moghadam, J. T. Hupp, O. K. Farha, C. F. Kaminski and D. Fairen-Jimenez, *Journal of the American Chemical Society*, 2017, **139**, 7522-7532.
15. C. Orellana-Tavra, S. Haddad, R. J. Marshall, I. Abánades Lázaro, G. Boix, I. Imaz, D. Maspoch, R. S. Forgan and D. Fairen-Jimenez, *ACS Applied Materials and Interfaces*, 2017, **9**, 35516-35525.
16. D. Chen, D. Yang, C. A. Dougherty, W. Lu, H. Wu, X. He, T. Cai, M. E. Van Dort, B. D. Ross and H. Hong, *ACS Nano*, 2017, **11**, 4315-4327.
17. C. He, K. Lu, D. Liu and W. Lin, *Journal of the American Chemical Society*, 2014, **136**, 5181-5184.
18. W.-H. Chen, X. Yu, A. Ceconello, S. Yang Sung, R. Nechushtai and I. Willner, *Chemical Science*, 2017, **8**, 5769-5780.

19. H. X. Zhao, Q. Zou, S. K. Sun, C. Yu, X. Zhang, R. J. Li and Y. Y. Fu, *Chemical Science*, 2016, **7**, 5294-5301.
20. C. Chen, J. Ke, X. E. Zhou, W. Yi, J. S. Brunzelle, J. Li, E.-L. Yong, H. E. Xu and K. Melcher, *Nature*, 2013, **500**, 486-489.
21. D. Feng, Y. Song, W. Shi, X. Li and H. Ma, *Analytical Chemistry*, 2013, **85**, 6530-6535.
22. G. L. Zwicke, G. A. Mansoori and C. J. Jeffery, *Nano Reviews*, 2012, **3**, 18496.
23. P. W. Stacpoole, L. R. Gilbert, R. E. Neiberger, P. R. Carney, E. Valenstein, D. W. Theriaque and J. J. Shuster, *Pediatrics*, 2008, **121**, e1223-e1228.
24. P. W. Stacpoole, D. S. Kerr, C. Barnes, S. T. Bunch, P. R. Carney, E. M. Fennell, N. M. Felitsyn, R. L. Gilmore, M. Greer, G. N. Henderson, A. D. Hutson, R. E. Neiberger, R. G. O'Brien, L. A. Perkins, R. G. Quisling, A. L. Shroads, J. J. Shuster, J. H. Silverstein, D. W. Theriaque and E. Valenstein, *Pediatrics*, 2006, **117**, 1519-1531.
25. P. W. Stacpoole, N. V. Nagaraja and A. D. Hutson, *Journal of Clinical Pharmacology*, 2003, **43**, 683-691.
26. P. W. Stacpoole, E. C. Wright, T. G. Baumgartner, R. M. Bersin, S. Buchalter, S. H. Curry, C. A. Duncan, E. M. Harman, G. N. Henderson, S. Jenkinson, J. M. Lachin, A. Lorenz, S. H. Schneider, J. H. Siegel, W. R. Summer, D. Thompson, C. L. Wolfe, B. Zorovich, and the DCA-Lactic Acidosis Study Group, *The New England Journal of Medicine*, 1992, **327**, 1564-1569.
27. J.-w. Kim, I. Tchernyshyov, G. L. Semenza and C. V. Dang, *Cell Metabolism*, 2006, **3**, 177-185.
28. C. W. Lu, S. C. Lin, C. W. Chien, S. C. Lin, C. T. Lee, B. W. Lin, J. C. Lee and S. J. Tsai, *The American Journal of Pathology*, 2011, **179**, 1405-1414.
29. S. J. Yeaman, E. T. Hutcheson, T. E. Roche, F. H. Pettit, J. R. Brown, L. J. Reed, D. C. Watson and G. H. Dixon, *Biochemistry*, 1978, **17**, 2364-2370.
30. C. Sebastián, Bernadette M. M. Zwaans, Dafne M. Silberman, M. Gymrek, A. Goren, L. Zhong, O. Ram, J. Truelove, Alexander R. Guimaraes, D. Toiber, C. Cosentino, Joel K. Greenson, Alasdair I. MacDonald, L. McGlynn, F. Maxwell, J. Edwards, S. Giacosa, E. Guccione, R. Weissleder, Bradley E. Bernstein, A. Regev, Paul G. Shiels, David B. Lombard and R. Mostoslavsky, *Cell*, 2012, **151**, 1185-1199.
31. J. Favier, J.-J. Brière, N. Burnichon, J. Rivière, L. Vescovo, P. Benit, I. Giscos-Douriez, A. De Reyniès, J. Bertherat, C. Badoual, F. Tissier, L. Amar, R. Libé, P.-F. Plouin, X. Jeunemaitre, P. Rustin and A.-P. Gimenez-Roqueplo, *PLoS One*, 2009, **4**, e7094.
32. R. A. Cairns, I. S. Harris and T. W. Mak, *Nature Reviews Cancer*, 2011, **11**, 85-95.
33. P. P. Hsu and D. M. Sabatini, *Cell*, 2008, **134**, 703-707.
34. G. Kroemer and J. Pouyssegur, *Cancer Cell*, 2008, **13**, 472-482.
35. A. Anemone, L. Consolino, L. Conti, F. Reineri, F. Cavallo, S. Aime and D. L. Longo, *International Journal of Oncology*, 2017, **51**, 498-506.
36. D. Heshe, S. Hoogestraat, C. Brauckmann, U. Karst, J. Boos and C. Lanvers-Kaminsky, *Cancer Chemotherapy and Pharmacology*, 2011, **67**, 647-655.
37. E. D. Michelakis, G. Sutendra, P. Dromparis, L. Webster, A. Haromy, E. Niven, C. Maguire, T. L. Gammer, J. R. Mackey, D. Fulton, B. Abdulkarim, M. S. McMurtry and K. C. Petruk, *Science Translational Medicine*, 2010, **2**, 31ra34.
38. E. D. Michelakis, L. Webster and J. R. Mackey, *Br. J. Cancer*, 2008, **99**, 989-994.
39. J. Y. Wong, G. S. Huggins, M. Debidda, N. C. Munshi and I. De Vivo, *Gynecologic Oncology*, 2008, **109**, 394-402.
40. S. Bonnet, S. L. Archer, J. Allalunis-Turner, A. Haromy, C. Beaulieu, R. Thompson, C. T. Lee, G. D. Lopaschuk, L. Puttagunta, S. Bonnet, G. Harry, K. Hashimoto, C. J.

- Porter, M. A. Andrade, B. Thebaud and E. D. Michelakis, *Cancer Cell*, 2007, **11**, 37-51.
41. E. M. Dunbar, B. S. Coats, A. L. Shroads, T. Langae, A. Lew, J. R. Forder, J. J. Shuster, D. A. Wagner and P. W. Stacpoole, *Investigational New Drugs*, 2014, **32**, 452-464.
42. A. Khan, D. Andrews, J. Shainhouse and A. C. Blackburn, *World Journal of Clinical Oncology*, 2017, **8**, 371-377.
43. P. W. Stacpoole, G. N. Henderson, Z. Yan and M. O. James, *Environmental Health Perspectives*, 1998, **106**, 989-994.
44. C. Trapella, R. Voltan, E. Melloni, V. Tisato, C. Celeghini, S. Bianco, A. Fantinati, S. Salvadori, R. Guerrini, P. Secchiero and G. Zauli, *Journal of Medicinal Chemistry*, 2016, **59**, 147-156.
45. J. Zajac, H. Kostrhunova, V. Novohradsky, O. Vrana, R. Raveendran, D. Gibson, J. Kasparikova and V. Brabec, *Journal of Inorganic Biochemistry*, 2016, **156**, 89-97.
46. P. M. Hoff, E. D. Saad, F. Costa, A. K. Coutinho, R. Caponero, G. Prolla and R. C. Gansl, *Clinical Colorectal Cancer*, 2012, **11**, 93-100.
47. T. C. Johnstone, N. Kulak, E. M. Pridgen, O. C. Farokhzad, R. Langer and S. J. Lippard, *ACS Nano*, 2013, **7**, 5675-5683.
48. J. Tong, G. Xie, J. He, J. Li, F. Pan and H. Liang, *Journal of Biomedicine and Biotechnology*, 2011, **2011**, 740564.
49. Y. Xuan, H. Hur, I.-H. Ham, J. Yun, J.-Y. Lee, W. Shim, Y. B. Kim, G. Lee, S.-U. Han and Y. K. Cho, *Experimental Cell Research*, 2014, **321**, 219-230.
50. L. Galluzzi, N. Larochette, N. Zamzami and G. Kroemer, *Oncogene*, 2006, **25**, 4812-4830.
51. M.-C. Frantz and P. Wipf, *Environmental and Molecular Mutagenesis*, 2010, **51**, 462-475.
52. M. P. Murphy and R. A. Smith, *Annual Review of Pharmacology and Toxicology*, 2007, **47**, 629-656.
53. L. Shang, K. Nienhaus and G. U. Nienhaus, *Journal of Nanobiotechnology*, 2014, **12**, 5-16.
54. L. Treuel, X. Jiang and G. U. Nienhaus, *Journal of the Royal Society Interface*, 2013, **10**, 20120939.
55. I. Abánades Lázaro, S. Haddad, J. M. Rodrigo-Muñoz, C. Orellana-Tavra, V. del Pozo, D. Fairen-Jimenez and R. S. Forgan, *ACS Applied Materials and Interfaces*, 2018, **10**, 5255-5268.
56. I. Abanades Lazaro, S. Abanades Lazaro and R. S. Forgan, *Chemical Communications*, 2018, **54**, 2792-2795.
57. I. Abánades Lázaro, S. Haddad, S. Sacca, C. Orellana-Tavra, D. Fairen-Jimenez and R. S. Forgan, *Chem*, 2017, **2**, 561-578.
58. C. Orellana-Tavra, S. A. Mercado and D. Fairen-Jimenez, *Advanced Healthcare Materials*, 2016, **5**, 2261-2270.
59. A. L. Kiss and E. Botos, *Journal of Cellular and Molecular Medicine*, 2009, **13**, 1228-1237.
60. A. M. Bannunah, D. Vilasaliu, J. Lord and S. Stolnik, *Molecular Pharmaceutics*, 2014, **11**, 4363-4373.
61. K. Yin Win and S.-S. Feng, *Biomaterials*, 2005, **26**, 2713-2722.
62. J. L. Grem, *Seminars in Radiation Oncology*, 1997, **7**, 249-259.

63. H. Akhdar, P. Loyer, C. Rauch, A. Corlu, A. Guillouzo and F. Morel, *European Journal of Cancer*, 2009, **45**, 2219-2227.
64. R. M. Mader, M. Müller and G. G. Steger, *General Pharmacology: The Vascular System*, 1998, **31**, 661-666.
65. J. Sudimack and R. J. Lee, *Advanced Drug Delivery Reviews*, 2000, **41**, 147-162.
66. J. M. Scott, *The Proceedings of the Nutrition Society*, 1999, **58**, 441-448.
67. I. R. Vlahov and C. P. Leamon, *Bioconjugate Chemistry*, 2012, **23**, 1357-1369.
68. H. Chen, R. Ahn, J. Van den Bossche, D. H. Thompson and T. V. O'Halloran, *Molecular Cancer Therapeutics*, 2009, **8**, 1955-1963.
69. G. A. Mansoori, K. S. Brandenburg and A. Shakeri-Zadeh, *Cancers*, 2010, **2**, 1911-1928.
70. J. M. Saul, A. Annapragada, J. V. Natarajan and R. V. Bellamkonda, *Journal of Controlled Release*, 2003, **92**, 49-67.
71. L. Yang, M. Liu, K. Huang, X. Ai, C. Li, J. Ma, T. Jin and X. Liu, *Applied Surface Science*, 2017, **392**, 189-195.
72. C. M. Paulos, M. J. Turk, G. J. Breur and P. S. Low, *Advanced Drug Delivery Reviews*, 2004, **56**, 1205-1217.
73. B. Varghese, E. Vlashi, W. Xia, W. Ayala Lopez, C. M. Paulos, J. Reddy, L. C. Xu and P. S. Low, *Molecular Pharmaceutics*, 2014, **11**, 3609-3616.
74. Z. Fen, M. S. Dhadly, M. Yoshizumi, R. J. Hilker, T. Quertermous, R. L. Eddy, T. B. Shows and M. E. Lee, *Biochemistry*, 1993, **32**, 7932-7938.
75. J. Hirsh, T. E. Warkentin, S. G. Shaughnessy, S. S. Anand, J. L. Halperin, R. Raschke, C. Granger, E. M. Ohman and J. E. Dalen, *Chest*, 2001, **119**, 64S-94S.
76. J. Lin, L. Hutchinson, S. M. Gaston, G. Raab and M. R. Freeman, *The Journal of Biological Chemistry*, 2001, **276**, 30127-30132.
77. G. Chatzinikolaou, D. Nikitovic, A. Asimakopoulou, A. Tsatsakis, N. K. Karamanos and G. N. Tzanakakis, *International Union of Biochemistry and Molecular Biology Life*, 2008, **60**, 333-340.
78. M. A. Dobrovolskaia and S. E. McNeil, *Nature Nanotechnology*, 2007, **2**, 469-478.
79. P. R. Taylor, L. Martinez-Pomares, M. Stacey, H. H. Lin, G. D. Brown and S. Gordon, *Annual Review of Immunology*, 2005, **23**, 901-944.
80. Y. Zhang, C. Liu, F. Wang, Z. Liu, J. Ren and X. Qu, *Chemical Communications*, 2017, **53**, 1840-1843.
81. E. Bellido, T. Hidalgo, M. V. Lozano, M. Guillevic, R. Simón-Vázquez, M. J. Santander-Ortega, Á. González-Fernández, C. Serre, M. J. Alonso and P. Horcajada, *Advanced Healthcare Materials*, 2015, **4**, 1246-1257.
82. K. Lu, C. He and W. Lin, *Journal of the American Chemical Society*, 2015, **137**, 7600-7603.
83. J. L. Perry, K. G. Reuter, M. P. Kai, K. P. Herlihy, S. W. Jones, J. C. Luft, M. Napier, J. E. Bear and J. M. DeSimone, *Nano Letters*, 2012, **12**, 5304-5310.
84. J. Xie, C. Xu, N. Kohler, Y. Hou and S. Sun, *Advanced Materials*, 2007, **19**, 3163-3166.
85. E. Birben, U. M. Sahiner, C. Sackesen, S. Erzurum and O. Kalayci, *The World Allergy Organization journal*, 2012, **5**, 9-19.
86. E.-J. Park and K. Park, *Toxicology Letters*, 2009, **184**, 18-25.

# Chapter 6

## Conclusions

**This Chapter is adapted in part from the following publications:**

“Selective Surface PEGylation of UiO-66 Nanoparticles for Enhanced Stability, Cell Uptake and pH Responsive Drug Delivery”

*Chem*, **2017**, 2, 561–578. (DOI: 10.1016/j.chempr.2017.02.005.)

**I. Abánades Lázaro**, S. Haddad, S. Sacca, C. Orellana-Tavra, D. Fairen-Jimenez and R. S. Forgan

“Mechanistic Investigation into the Selective Anticancer Cytotoxicity and Immune System Response of SurfaceFunctionalised, Dichloroacetate-Loaded, UiO-66 Nanoparticles”

*ACS Appl. Mater. Interfaces*, **2018**, 10, 6, 5255-5268 (DOI: 10.1021/acsami.7b17756)

**I. Abánades Lázaro**, S. Haddad, J. Rodrigo-Muñoz, C. Orellana-Tavra, V. del Pozo, D. Fairen-Jimenez, and Ross S. Forgan

“Enhancing Anticancer Cytotoxicity through Bimodal Drug Delivery from Ultrasmall Zr MOF Nanoparticles”

*Chem. Commun.*, **2018**, 54, 2792-2795. (DOI: 10.1039/C7CC09739E)

**I. Abánades Lázaro**, S. Abánades Lázaro and R. S. Forgan.

**Table of Contents**

**Chapter 6**..... 248  
Table of Contents ..... 249  
6.1 Conclusions ..... 250  
6.2 References ..... 258

## 6.1 Conclusions

The main aims of each chapter of this thesis are outlined below

### Chapter 2:

- Develop versatile and reproducible protocols for the one-pot synthesis of surface-functionalised UiO-66, drug-containing UiO-66 and surface-functionalised drug-containing UiO-66, with the appropriate size for drug delivery, through coordination modulation.
- Apply the UiO-66 drug modulated synthetises to the UiO family of isorecticular MOFs (Zr- BDC and bromo, nitro and amino derivatives, Zr-NDC and Zr-BPDC), obtaining two sets of drug@nanoMOFs, one with a size of ca 100 nm and other smaller than 20 nm), and use the MOFs porosity to load a second drug.

### Chapter 3:

- Use the functionalities of the p-benzoic acid functionalised modulators, introduced to UiO-66 surface as modulators during Chapter 2, to postsynthetically attach various polymers (e.g PEG, Poly-L-Lactide and PNIPAM) to UiO-66 surface through copper-catalysed azide-alkyne cycloaddition (click modulation protocol).
- Use coordination chemistry to postsynthetically coat UiO-66 surface with the modulators introduced to UiO-66 surface during synthesis in Chapter 2.
- Ultimately study the colloidal dispersion and stability towards phosphates of the bare and surface functionalised MOFs in order to gain insights into the effect of surface chemistry and coating mode (either by coordination modulation, covalent or coordination chemistry) on MOFs physical properties.

### Chapter 4:

- Apply the postsynthetic surface modification protocols detailed in Chapter 3 to calcein-loaded analogue UiO-66 samples.
- Study the effect of PEGylation towards drug release kinetics.
- Study the effect of surface chemistry on the MOFs internalisation efficacy and routes by HeLa cervical cancer cells.

### Chapter 5:

- Study the anticancer performance (towards MCF-7 breast cancer cells) of the DCA@MOFs of the UiO isorecticular series, detailed in Chapter 2, as a function of particle size and surface chemistry.

- Investigate the anticancer performance of 5-FU@DCA@UiO MOFs and compare it with their precursor DCA@MOFs and both free drugs, incubated with MCF-7 cells on their own or together, in order to understand the effect of the dual-drug MOFs.
- Apply the former postsynthetic surface functionalisation protocols, detailed in Chapter 3, to the DCA@UiO-66 modulated samples, synthesised during Chapter 2.
- Assess the biocompatibility of the bare and surface functionalised MOFs on HeLa cervix cancer cells.
- Investigate the therapeutic effect of all DCA-loaded, bare and surface functionalised, UiO-66 MOFs, aiming to find a correlation with the endocytosis routes of internalisation determined during Chapter 4 and the physical properties studied for the empty analogues from Chapter 3.
- Assess the anticancer selectivity of the most promising MOF candidates towards a series of healthy and cancerous cells lines and study the effect of those empty and drug-loaded MOFs in macrophages and lymphocytes proliferation and ROS production.

On the whole, all the aims have been successfully achieved, ultimately providing insights into the effect of MOFs surface chemistry on their physical properties, cellular routes of internalisation and therapeutic efficacy.

During Chapter 2 it was shown that carboxylate modulators can be attached to UiO-66 surface and defect sites during synthesis, hence resulting in surface-functionalised drug-containing MOFs by a simple, versatile and reproducible one-pot protocol. The scope of modulators used during this study (*p*-functionalised benzoic acid derivatives, folic acid, biotin and DCA) has proven the versatility of the protocol to introduce simple or more complex functionalised modulators to UiO-66 structure, resulting in highly crystalline, porous MOFs with the appropriate size for *in vitro* experiments.

Importantly, it has been shown that the degree of modulator incorporation is  $pK_a$  dependent,<sup>1</sup> as, for example, the anticancer metabolic target DCA ( $pK_a$  1.4) is significantly incorporated into the structure (ca. 20% *w/w*) while AcOH ( $pK_a$  4.8) does not significantly incorporate. Folic acid and biotin incorporation is also in great agreement with their respective  $pK_a$  (3.5 and 4.5 for folic acid and biotin respectively). In concordance, the porosity of the modulated samples is remarkably boosted, with surface areas of ca. 1550  $m^2g^{-1}$  for DCA@UiO-66 vs 1200  $m^2g^{-1}$  for ideal UiO-66.<sup>2</sup> The degree of defects that DCA modulation induces has been estimated by TGA, showing that approximately 2 linkers are missing on the structure, being replaced by DCA, which results in a high surface charge, and consequently well-dispersed MOFs in aqueous solvents, overcoming one of the most relevant drawbacks for MOFs applications in

drug delivery.<sup>3,4</sup> The low  $pK_a$  of DCA ensures high incorporation even in the presence of other functionalised modulators, and the incorporation of both DCA and functionalised modulator has been controlled by tuning the ratio of both. DCA modulation also serves as a size control protocol, resulting in homogeneous distributions between 70 and 150 nm regardless of the functionalised co-modulator. The one-pot synthesis of multi-drug and multi-functionalised MOFs is currently under investigation, in which multiple functionalised carboxylate modulators (e.g protecting and targeting units) and multiple carboxylate and phosphate containing drugs are introduced as UiO-66 modulators during synthesis. Future work will involve the refinement of the protocols and the study of their therapeutic performance.

The DCA modulation protocol has been successfully applied to the UiO family of isorecticular MOFs, for which two different conditions have resulted in two sets of MOFs of different sizes, enabling the size and surface dependent study of their cytotoxicity during Chapter 5. The Zr-terephthalate derivative MOFs synthesised under DCA modulated conditions using  $ZrCl_4$  as the metal precursor ultimately result in homogenous MOFs of ca. 100 nm, while when  $ZrOCl_2$  is used as the metal precursor, together with an excess of linker, ultrasmall MOFs (10-30 nm) are obtained, which are scarce in the literature.

A general trend, in which terephthalate linkers with electron withdrawing groups ( $NO_2$  and Br) result in slightly bigger MOFs than terephthalate linkers with electron donating groups ( $NH_2$ ) and regular terephthalate, has been found for both synthetic conditions, possibly as a consequence of the reduced electron density of the carboxylate groups when electron withdrawing groups are present in the structure, which, in comparison, slows down the nucleation process. More hydrophobic linkers, such as NDC and BPDC, result in microcrystals when  $ZrCl_4$  is the metal precursor and nanoparticles of ca. 200 nm when  $ZrOCl_2$  is the metal precursor. For the second synthetic conditions, a new phase of Zr-NDC has been found, for which the particles have an ovoid structure, together with new reflection peaks in the PXRD pattern. This new phase is under current examination in a coordination modulation investigation of Zr-NDC using various DCA concentrations, temperatures and other co-modulators with the ultimate aim of obtaining single crystals for structure characterisation.

In general, and in contrast to analogous MOFs synthesised by AcOH modulation, the DCA modulated MOFs of the UiO family are well dispersed in water and in PBS spiked with BSA. Although small MOFs usually aggregate more in aqueous solvents than bigger analogues,<sup>5</sup> the ultrasmall DCA@MOFs are well-dispersed in water, and the effect of the presence of proteins in the dispersant, such as bovine serum albumin, has been proven to further enhance MOFs colloidal stability through the formation of a protein corona.<sup>6-8</sup>

The induction of defects under the  $ZrOCl_2$  DCA modulated conditions is remarkable, yielding in mesoporous Zr-terephthalate derivative MOFs, and since DCA is attached to the  $Zr_6$  nodes, the remaining porosity has been used to successfully load a second drug - the well-known anticancer drug 5-fluorouracil - into the small Zr-terephthalate MOFs and into Zr-NDC and Zr-BPDC.

During Chapter 3, a series of surface functionalities – Folic acid, biotin, heparin, PEG, Poly-L-Lactide and PNIPAM - have been attached postsynthetically to UiO-66 surface for drug delivery purposes. The first three reagents have been coordinated to the  $Zr_6$  nodes, while the last three have been covalently attached to the p-functionalised benzoic acid modulators introduced to UiO-66 during Chapter 2, together with other proof-of-concept modifications. The postsynthetic covalent modifications have been confirmed by ESI-MS, among other characterisation techniques, while the surface reagents introduced by coordination have been proven to be attached to the  $Zr_6$  clusters, in both cases without major pore blockage.

The colloidal stability of the MOFs in aqueous solvents has been improved in nearly all cases upon surface modification, apart from heparin, more significantly in the case of the polymeric coatings through click chemistry, for which size profiles are in great agreement with SEM particle size. Similarly, the stability of the MOFs towards phosphate attack has also been improved, with induction periods of a few hours in which almost no degradation occurs, but reaching similar levels of degradation after 24 h, indicating that although the burst release of the drug could be potentially avoided for the first stages of circulation, similar degradation to uncoated MOFs should occur for longer stages of treatment. Hence, their accumulation, which is one of the major drawbacks of silica coating and of other DDSs,<sup>9, 10</sup> should not be enhanced. Once again, the polymeric coatings effect was more significant, with a higher degree of initial stability. Different degradation profiles for the folic acid and biotin coated samples were found depending on the coating mode (coordination modulation and postsynthetic). Although a higher degree of stabilisation was found for the postsynthetic samples at first stages - with almost no degradation during the first hour possibly due to partial window blockage when the coating is performed postsynthetically, as determined by  $N_2$  uptake experiments - after a few hours the samples synthesised by coordination modulation were more stable than the ones synthesised postsynthetically. The folate-coated samples degradation profile is embodied in both cases by folic acid release from the structure, indicating that in the case of the modulated sample, a considerable amount of coordinated folic acid is present throughout the internal structure.

The postsynthetic modification protocols have been proven to be compatible with cargo loading, as during Chapter 4 a fluorescent molecule, calcein, was loaded into the MOFs prior

to the surface modifications, which were successfully performed without major calcein leakage. Calcein, which possesses carboxylates in its structure, was proven to be attached to the Zr clusters at defect sites, partially blocking the pore windows, which ensures compatibility with surface modifications. Hence, the set of calcein-loaded surface modified UiO-66 enabled the study of the endocytosis routes of internalisation by HeLa cells, but also the simulated drug release profiles.

As the PEGylated MOFs were found to have the highest degree of the stabilisation towards phosphates, their release kinetics were studied in PBS at pH 7.4 and pH 5.5 and compared to the precursor sample. A pH dependent release profile was found in all cases, a consequence of the lability of the metal-linker bond under acidic conditions, due to partial linker protonation. The release kinetics at pH 7.4 were drastically slowed down upon PEGylation, only releasing ca. 30 % after 1 day, and releasing no more cargo for up to 5 days, while the uncoated sample released its full cargo after 2 days. By changing the pH of the release media during the course of the experiment the full cargo of the PEGylated samples was further released, which is highly desirable for an anticancer DDSs. Through characterisation of the samples under simulated release conditions it was found that the enhancement upon PEGylation at pH 7.4 was a consequence of the in-situ formation of a phosphate corona hindering further cargo release, which was protonated under acidic conditions, thus enabling stimuli-responsive cargo release.

MOFs internalisation by HeLa cells was found to be surface chemistry dependent. Surface coating improved MOFs internalisation in all cases with exception of the biotin-coated sample, which was poorly internalised when compared to the uncoated sample, with similar levels of internalisation to free calcein. Due to the over expression of the folate receptor on HeLa cells<sup>11</sup> surface, the folate-coated sample was the most efficiently internalised with a ca. 180 % internalisation compared to the uncoated sample. In great agreement with reports of the UiO family of isorecticular MOFs HeLa cells internalisation, cal@UiO-66 was mainly internalised by clathrin-mediated endocytosis, which ultimately results in lysosome storage, with no contribution of the caveolae-mediated route. Certain surface coatings, such as PEGylation (only for the longer chains), folate and heparin, tune cal@UiO-66 internalisation from clathrin to caveolae-mediated endocytosis, potentially enabling cargo release into the cytosol in a more effective manner, while the poly-L-Lactide and PNIPAM coated MOFs are mainly internalised through non-mediated endocytosis. Partial uptake by the clathrin-mediated route was still significant for the PEGylated and heparin-coated samples, whereas no inhibition was found upon folate, Poly-L-Lactide and PNIPAM coatings. Macropinocytosis plays a role in all the MOFs internalisation, with exception of Poly-L-Lactide coating, which was partially internalised by inactive transport.

During Chapter 5, an extensive investigation of the therapeutic activity of DCA@MOFs on MCF-7 breast cancer cells was performed, with the ultimate aim of obtaining insights of the effect of particle size and surface chemistry, finding a correlation with the reported routes of cellular internalisation.<sup>5</sup> Cytotoxic studies of the DCA@UiO-66 (Zr-BDC) derivative MOFs of size ca. 100 nm were compared to DCA@DUT-52 (Zr-NDC) and DCA@UiO-67 (Zr-BPDC), of size ca. 200 nm. In great agreement with cellular internalisation reports, which showed no caveolae-mediated contribution to UiO-66 cellular internalisation, DCA@UiO-66 had no cytotoxic effect. Only a minor contribution of the caveolae-mediated route (ca. 20% inhibition) was reported for UiO-66 bromo, nitro and amino derivative MOFs, and although they were found to be more efficiently internalised than DUT-52 and UiO-67, the caveolae-mediated route played a more important role for the last two. Only minor cytotoxic effects were found for DCA@UiO-66-Br and DCA@UiO-66-NO<sub>2</sub>, whereas DCA@DUT-52 and DCA@UiO-67 were the most therapeutically efficient MOFs despite their lower DCA content. DCA@UiO-66-NH<sub>2</sub> therapeutic efficacy was considerable, possibly as a consequence of the positive charge of the pendant amino groups under physiological conditions.

It is important to remark, that although the reported routes of cellular internalisation were performed on calcein-loaded analogue MOFs synthesised using other modulated conditions (generally AcOH and benzoic acid), and such, may have less favourable performance in colloidal stability in PBS, and for HeLa cervix cancer instead of MCF-7 cancer cells, the trends in therapeutic efficacy of the DCA@MOFs correlate well with the reported caveolae-mediated contribution upon internalisation.<sup>5</sup> Additionally, the size-dependence internalisation routes of cal@UiO-66 (AcOH modulated) have also been reported, finding the smaller MOF (ca. 50 nm) to be the most efficiently internalised and the only one not to undergo clathrin-mediated endocytosis, indicating significant contribution of non-mediated routes.<sup>5</sup> For bigger sizes, internalisation was found not to be size-dependent, with major contributions of clathrin-mediated endocytosis and macropinocytosis in all cases.

Examples of ultras-small UiO-66 nanoparticles are scarce in the literature. This thesis has shown that DCA@UiO-66 therapeutic effect is enhanced by particle size reduction, as the analogous MOF of size ca. 13 nm was therapeutically efficient despite the sample ca. 100 nm being non-cytotoxic up to 1 mgmL<sup>-1</sup>. Apart from DCA@UiO-66-NH<sub>2</sub>, which already decreased MCF-7 cells proliferation when particle size was ca. 100 nm, all the small DCA@UiO-66 derivative MOFs were more efficient than their bigger analogues, presumably as a consequence of possible passive diffusion through the cell membrane. However, when analysing the cell proliferation data for the small DCA@UiO-66 derivatives as a function of the maximum DCA concentration reached upon MOF incubation, and comparing it to DCA@DUT-52 and DCA@UiO-67, the fact that surface chemistry plays a more important role than particle

size is evident. DCA@UiO-67 is the most efficient MOF, followed by DCA@DUT-52 and DCA@UiO-66-NH<sub>2</sub>.

Similar trends in MCF-7 cells proliferation were found upon incubation with 5-FU@DCA@MOFs, which were significantly more active than their DCA precursor MOFs. Comparison of their effect on cells proliferation (against maximum 5-FU concentration reached) to free 5-FU, showed surface chemistry dependence, following similar trends to the DCA precursors: 5-FU@DCA@UiO-67 and 5-FU@DCA@DUT-52 were the most cytotoxic, followed by 5-FU@DCA@UiO-66<sub>small</sub> and 5-FU@DCA@UiO-66-NH<sub>2</sub> <sub>small</sub>, all of them significantly more active than 5-FU, whereas 5-FU@DCA@UiO-66-NO<sub>2</sub> <sub>small</sub> effect in cell proliferation was similar to 5-FU, and 5-FU@DCA@UiO-66-Br performance was worse than the free drug. The UiO-66 derivative MOFs with electron withdrawing groups (Br, NO<sub>2</sub>) were significantly bigger (ca. 30 nm) than UiO-66 and UiO-66-NH<sub>2</sub> (ca. 13 nm), which are more likely to undergo passive internalisation. The effect of 5-FU incubation together with free DCA was studied for concentrations in the range of those reached by the MOFs, finding no enhancement in the IC<sub>50</sub> dose in comparison to free 5-FU. Importantly, although it has been reported that DCA enhances the effect of 5-FU on cancer cells,<sup>12, 13</sup> the DCA doses required to reach the synergic effect are at least one order of magnitude higher than the maximum dose reached if the MOFs release their full cargo.

A new project to study the MCF-7 cellular internalisation rates and dose-uptake by FACS is currently underway, using calcein-loaded analogues of ca. 100 nm and 200 nm in size, and future work will be performed to study the cellular internalisation of smaller analogues both by FACS (quantitatively) and by confocal microscopy, in order to assess the intracellular location of the MOFs at different incubation times to gain insights into the design of MOFs for high therapeutic efficacy. In addition, selectivity towards non-cancerous cells lines will be studied.

The surface modification protocols detailed during Chapter 3, were successfully applied to the DCA@UiO-66 modulated samples synthesised during Chapter 2, proving that DCA modulation is compatible with postsynthetic surface modifications without major DCA leakage. All the surface functionalised MOFs - apart from UiO-66-L2-PNIPAM, which was cytotoxic for concentration of 0.5 mgmL<sup>-1</sup> and above - were proven to be biocompatible upon incubation with HeLa cells for concentrations up to 1 mgmL<sup>-1</sup>.<sup>14</sup> Their therapeutic effect, when loaded with DCA, was again in great agreement with their routes of internalisation. As cal@UiO-66 was mainly internalised through the clathrin-mediated route, DCA@UiO-66 was non-cytotoxic for concentrations up to 1 mgmL<sup>-1</sup>, and since the calcein-loaded biotin-coated sample was not efficiently internalised, none of the DCA-containing biotin-coated samples were cytotoxic. PEGylation, on the other hand, enhanced DCA cytotoxicity (which only had effects on HeLa

cells proliferation for concentrations higher than 3 mgmL<sup>-1</sup>) with a >70 fold increase, in agreement with the partial internalisation of this sample through caveolae-mediated endocytosis. Between the folate-coated samples, different trends in cytotoxicity were found depending on the folate content and mode of coating; in all cases the samples synthesised by coordination modulation were more efficient than the sample coated postsynthetically. This is likely to be a consequence of the presence of folates in the inner surface of the modulated samples, for which if degradation occurs during the incubation time, targeting is still taking place through folate attached to SBUs in the MOF core. In between the two samples synthesised by coordination modulation, the one with the highest folate content was the most therapeutically active despite having a slightly lower DCA content, enhancing the IC<sub>50</sub> of DCA with a >350 fold increase.

Despite cal@UiO-66-Heparin being found to undergo HeLa cells internalisation partially by the caveolae-mediated route, the DCA-loaded analogue did not induce HeLa cells cytotoxicity. Heparin is known to bind to several cell growth receptors and activate their signalling cascades,<sup>15-17</sup> which together with the poorer performance of the empty analogue, UiO-66-Hep (PS), in colloidal dispersion and stability towards phosphates, may explain why there was not an enhancement in therapeutic performance compared to its precursor DCA@UiO-66.

Although no contribution of the caveole-mediated route was found for cal@UiO-66-L1-PolyLact and cal@UiO-66-L2-PNIPAM, internalisation of these samples mainly occurred by non-mediated routes, with no clathrin-mediated contribution. Thus, DCA@UiO-66-L1-PolyLact decreased HeLa cells proliferation for high concentrations, while DCA@UiO-66-L2-PNIPAM killed almost all cells at 0.25 mgmL<sup>-1</sup>.

The anticancer selectivity was investigated for the most promising candidates, DCA@UiO-66-L1-PEG2000, DCA@UiO-66-L1-PolyLact, DCA@UiO-66-L2-PNIPAM and DCA<sub>5</sub>@UiO-66-FA<sub>1</sub>. The DCA-loaded materials were tested against MCF-7 breast cancer cells, HEK293 embryonic cells, J744 macrophages and lymphocytes, while the empty analogues were also tested against macrophages and lymphocytes. DCA@UiO-66 did not affect MCF-7 and HEK293 cells proliferation negatively. Although some concerns over cytotoxicity were found towards HEK293 human embryonic kidney cells for DCA@UiO-66-L1-PEG2000, with a similar decrease in cells proliferation compared to HeLa and MCF-7 breast cancer cells (ca. 50 % for 1 mgmL<sup>-1</sup>), macrophages cells proliferation only decreased to ca. 70 %, while no negative effect was found to lymphocytes.

DCA@UiO-66-L2-PNIPAM was selective towards HeLa and MCF-7 breast cancer cells for lower concentrations, while DCA@UiO-66-L1-PolyLact was more cytotoxic to HeLa cells than for HEK293 and MCF-7, the last two having a similar degree of proliferation (ca. 80 %) upon

incubation with 1 mgmL<sup>-1</sup> of MOF. Although the empty analogues were not remarkably cytotoxic towards macrophages and lymphocytes, so were the DCA-loaded analogues.

DCA<sub>5</sub>@UiO-66-FA<sub>1</sub> was selective towards HeLa and MCF-7 cancer cells, with an effect on cells proliferation in great agreement with reports on the overexpression of the folate receptors in the cell membrane of both cells,<sup>18</sup> while no negative effect on HEK293, macrophages or lymphocyte cells proliferation was found.

These results provide mechanistic insight into the design and functionalisation of MOFs for drug delivery, and demonstrate the power of surface functionalisation and importance of cell internalisation pathways in the application of MOFs for drug delivery. The potential of DCA<sub>5</sub>@UiO-66-FA<sub>1</sub> for use as a selective anticancer DDS for *in vivo* localised treatment is apparent, particularly given the use of the metabolic probe DCA as a modulator during synthesis resulting in a drug-loaded nanoparticle that is still porous and could be loaded with a second drug for synergistic multimodal therapy. The work also highlights the broad *in vitro* experimental toolkit available to provide information on cellular uptake, endocytosis mechanisms, immune response and cytotoxicity prior to any *in vivo* treatment, thus reducing the need for early stage animal testing and acting according to the three Rs: reduction, refinement and replacement.

## 6.2 References

1. G. C. Shearer, S. Chavan, S. Bordiga, S. Svelle, U. Olsbye and K. P. Lillerud, *Chemistry of Materials*, 2016, **28**, 3749-3761.
2. J. H. Cavka, S. Jakobsen, U. Olsbye, N. Guillou, C. Lamberti, S. Bordiga and K. P. Lillerud, *Journal of the American Chemical Society*, 2008, **130**, 13850-13851.
3. Z. Mao, X. Zhou and C. Gao, *Biomaterials Science*, 2013, **1**, 896-911.
4. W. Morris, S. Wang, D. Cho, E. Auyeung, P. Li, O. K. Farha and C. A. Mirkin, *ACS Applied Materials and Interfaces*, 2017, **9**, 33413-33418.
5. C. Orellana-Tavra, S. Haddad, R. J. Marshall, I. Abánades Lázaro, G. Boix, I. Imaz, D. MasPOCH, R. S. Forgan and D. Fairen-Jimenez, *ACS Applied Materials and Interfaces*, 2017, **9**, 35516-35525.
6. E. Bellido, M. Guillevic, T. Hidalgo, M. J. Santander-Ortega, C. Serre and P. Horcajada, *Langmuir*, 2014, **30**, 5911-5920.
7. E. Bellido, T. Hidalgo, M. V. Lozano, M. Guillevic, R. Simón-Vázquez, M. J. Santander-Ortega, Á. González-Fernández, C. Serre, M. J. Alonso and P. Horcajada, *Advanced Healthcare Materials*, 2015, **4**, 1246-1257.
8. S. Sene, M. T. Marcos-Almaraz, N. Menguy, J. Scola, J. Volatron, R. Rouland, J.-M. Grenèche, S. Miraux, C. Menet, N. Guillou, F. Gazeau, C. Serre, P. Horcajada and N. Steunou, *Chem*, 2017, **3**, 303-322.
9. G. Jarockyte, E. Daugelaite, M. Stasys, U. Statkute, V. Poderys, T.-C. Tseng, S.-H. Hsu, V. Karabanovas and R. Rotomskis, *International Journal of Molecular Sciences*, 2016, **17**, 1193.

10. J. Lu, M. Liong, Z. Li, J. I. Zink and F. Tamanoi, *Small*, 2010, **6**, 1794-1805.
11. J. Sudimack and R. J. Lee, *Advanced Drug Delivery Reviews*, 2000, **41**, 147-162.
12. J. Tong, G. Xie, J. He, J. Li, F. Pan and H. Liang, *Journal of Biomedicine and Biotechnology*, 2011, **2011**, 740564.
13. Y. Xuan, H. Hur, I.-H. Ham, J. Yun, J.-Y. Lee, W. Shim, Y. B. Kim, G. Lee, S.-U. Han and Y. K. Cho, *Experimental Cell Research*, 2014, **321**, 219-230.
14. C. Orellana-Tavra, R. J. Marshall, E. F. Baxter, I. A. Lazaro, A. Tao, A. K. Cheetham, R. S. Forgan and D. Fairen-Jimenez, *Journal of Materials Chemistry B*, 2016, **4**, 7697-7707.
15. G. Chatzinikolaou, D. Nikitovic, A. Asimakopoulou, A. Tsatsakis, N. K. Karamanos and G. N. Tzanakakis, *International Union of Biochemistry and Molecular Biology Life*, 2008, **60**, 333-340.
16. Z. Fen, M. S. Dhadly, M. Yoshizumi, R. J. Hilkert, T. Quertermous, R. L. Eddy, T. B. Shows and M. E. Lee, *Biochemistry*, 1993, **32**, 7932-7938.
17. J. Lin, L. Hutchinson, S. M. Gaston, G. Raab and M. R. Freeman, *The Journal of Biological Chemistry*, 2001, **276**, 30127-30132.
18. D. Feng, Y. Song, W. Shi, X. Li and H. Ma, *Analytical Chemistry*, 2013, **85**, 6530-6535.

# Chapter 7

# Appendix

**Table of Contents**

<b>Chapter 7</b> .....	260
Table of Contents.....	261
7.1 Modulators' <sup>1</sup> HNMR.....	262
7.2 Kinetic Fitting of Degradation Profiles.....	265
7.3 Kinetic Fitting of Calcein Release Profiles .....	267

## 7.1 Modulators' $^1\text{H}$ NMR

$^1\text{H}$  NMR spectra of authentic samples of the commercially available surface reagents were collected in order to identify their characteristic signals and to compare them with the  $^1\text{H}$  NMR spectra of the surface-modified NMOFs digested in  $\text{D}_2\text{SO}_4 / \text{DMSO-}d_6$ .  $^1\text{H}$  NMR spectra in acidified  $\text{DMSO-}d_6$  were also obtained in order to identify changes upon acidification with  $\text{D}_2\text{SO}_4$  and upon acidification and heating, procedure used to digest the MOFs for their  $^1\text{H}$ NMR analysis. The  $^1\text{H}$  NMR spectra of folic acid in  $\text{DMSO-}d_6$  and acidified  $\text{DMSO-}d_6$  are shown in Figure 7.1. The amino and amido resonances disappear upon acidification, presumably due to exchange with the deuterated acid, but the other resonances show no significant shifts.

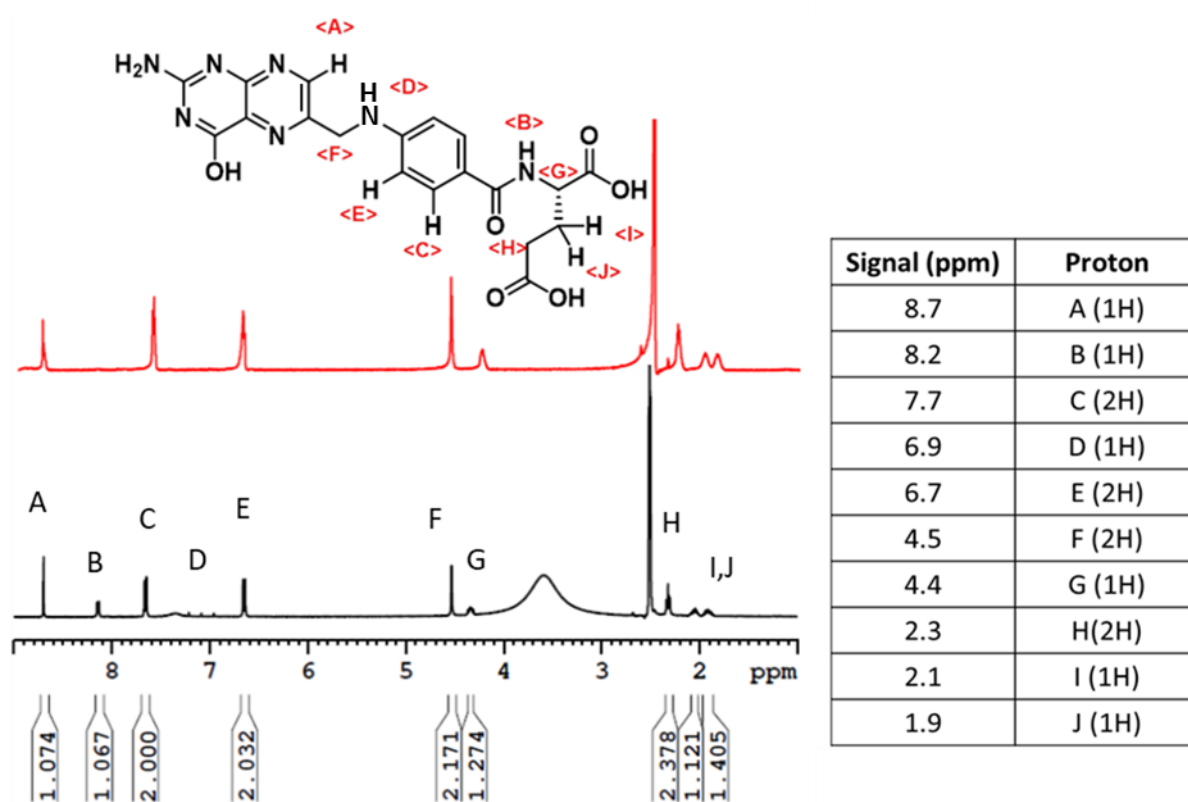


**Figure 7.1.** Stacked partial  $^1\text{H}$  NMR spectra of folic acid in  $\text{DMSO-}d_6$  (bottom) and acidified  $\text{DMSO-}d_6$  (top), with signal assignment.

On the other hand, upon acidification and heating, shifting in the signals are observed, together with changes in the integration ratio of the signals (Figure 7.2).

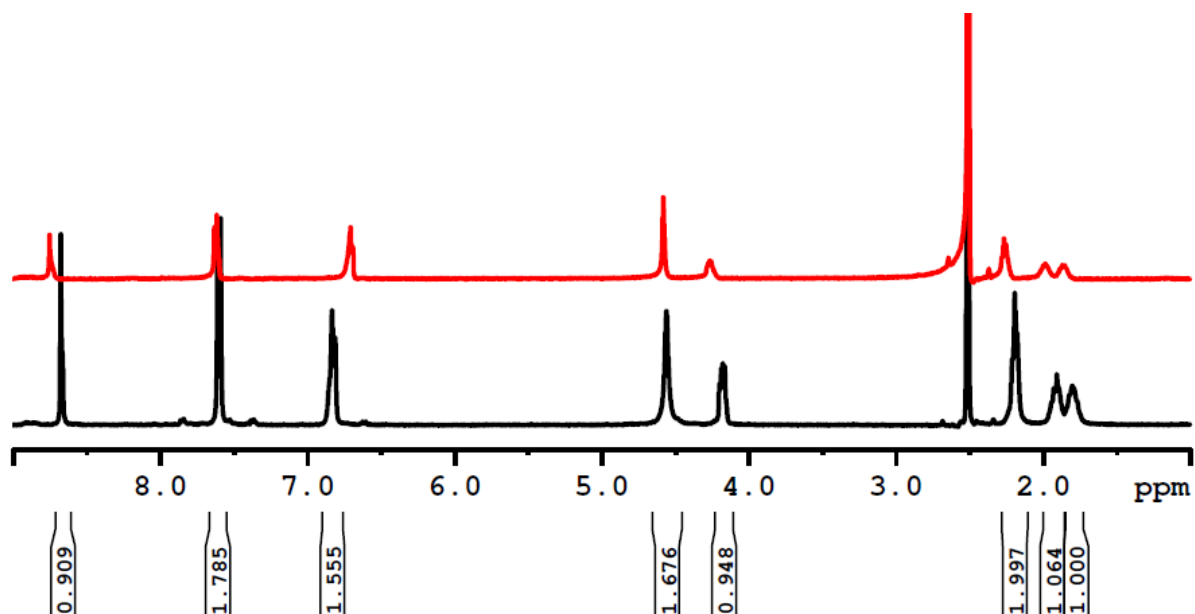


**Figure 7.2:** Stacked partial  $^1\text{H}$  NMR spectra of folic acid in acidified  $\text{DMSO}-d_6$  (top), and in acidified  $\text{DMSO}-d_6$  after heating, showing signals shifting and changes in the signals' integration.

In Figure 7.3, a representation of pH effect on folic acid is shown, which explains why resonance signal shifting is more remarkable in signals F and A, which correspond to the closer protons to the protonated nitrogen. Additionally, proton exchange with deuterium can occur, thus changing the integration ratio.

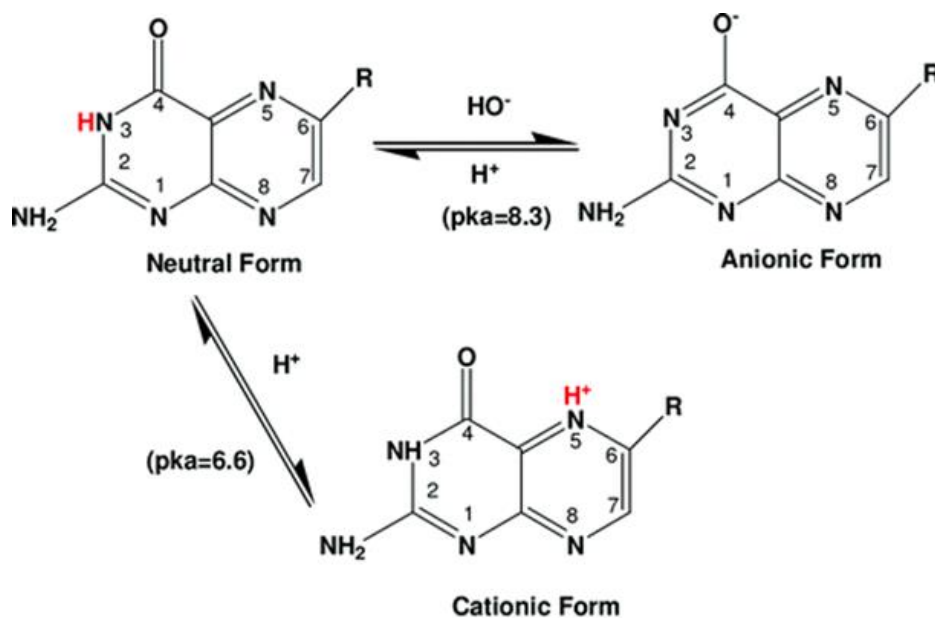


**Figure 7.3:** The effect of pH on folic acid structure, showing protonation of N5.

Hence, it is explained why in the MOFs' acidified  $^1\text{H}$ NMR not all folic acid signals are observed, and why in some cases multiple signals, coming from the multiple species in solution are observed, as both acidification and heating are provided. Additionally, due to the presence of different species in solution, due to acidification, heating, and Zr presence – metals such as zirconium can coordinate to folic acid and form complexes in solution - different sets of signals are expected to be observed.

By comparing the intensity of the resonances of the surface moieties with the aromatic resonance of the bdc linker in UiO-66, the molar ratio of the different moieties compared to the linker can be estimated. Integration based on the alkyl signals (H, I, J) is consistent, and so their integration ratio was used for folic acid estimation in the MOFs digests.

The  $^1\text{H}$  NMR spectra of commercially available biotin in  $\text{DMSO}-d_6$  (Figure 7.4, bottom) showed shifting of the signals and disappearance of resonances for exchangeable N-H protons upon acidification (Figure 7.4, top). Apart from the N-H protons, all the characteristic signals were observed in the MOFs digested  $^1\text{H}$ NMR spectra.

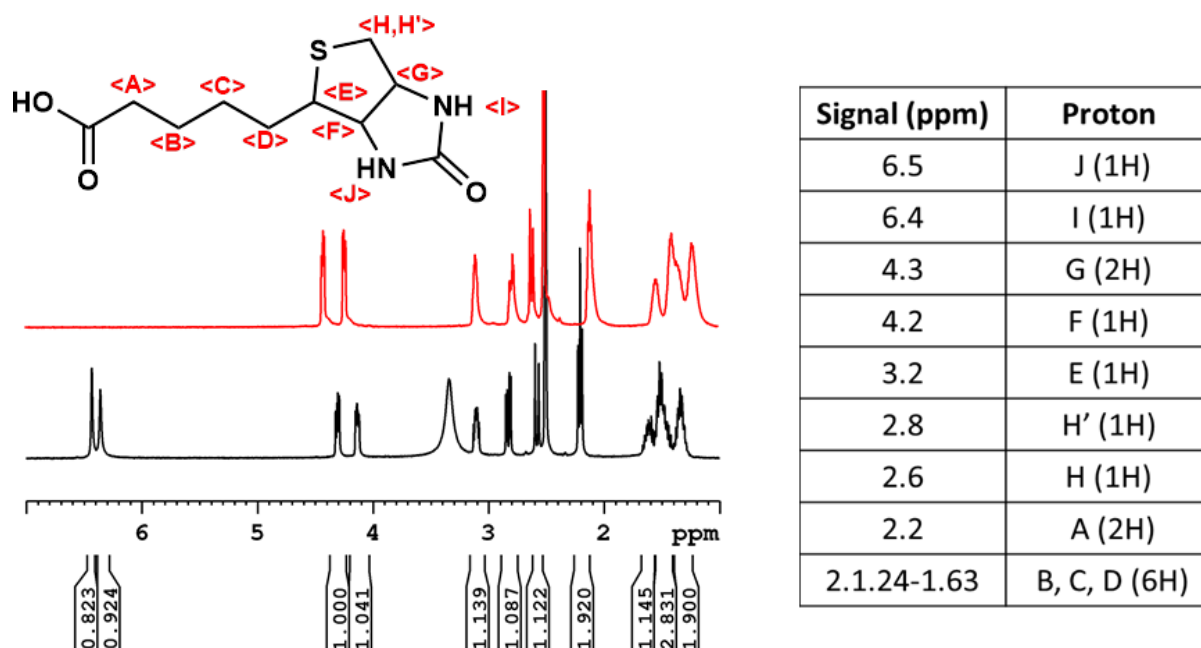


**Figure 7.4.** Stacked partial  $^1\text{H}$  NMR spectra of biotin in  $\text{DMSO}-d_6$  (bottom) and acidified  $\text{DMSO}-d_6$  (top), with signal assignment.

## 7.2 Kinetic Fitting of Degradation Profiles

The kinetic profiles for the degradation of the samples were determined by curve fitting utilising Microcal Origin software, and are shown in Table 7.1.

**Table 7.1.** Kinetic profiles of the samples' degradation.

NMOF	Degradation equation	R <sup>2</sup>
UiO-66-AcOH	% bdc released = $84.24 - 84.75 e^{t/2.01}$	R <sup>2</sup> = 0.9942
UiO-66-L1	% bdc released = $86.863 - 83.831 e^{t/1.90}$	R <sup>2</sup> = 0.9935
UiO-66-L1-PEG550	% bdc released = $0.72 + 86.50 (t^{0.08}/(1.16+t^{0.08}))$	R <sup>2</sup> = 0.9977
UiO-66-L1-PEG2000	% bdc released = $-1.64 + 89.07 (t^{1.84}/(9.2853+t^{1.84}))$	R <sup>2</sup> = 0.9908
UiO-66-L1-PolyLact	% bdc released = $3.31 + (75.82)(t^{1.64}/(2.36 + t^{1.64}))$	R <sup>2</sup> = 0.9959
UiO-66-L2-PNIPAM	% bdc released = $96.66 (t^{1.11}/2.08 + t^{1.11})$	R <sup>2</sup> = 0.9798
UiO-66-Biot (PS)	% bdc released = $102.15 - 79.45t$	R <sup>2</sup> = 0.9953
UiO-66-FA (PS)	% bdc released = $-2.41 + 94.05 (t^{1.36} / (5.03+ t^{1.36}))$	R <sup>2</sup> = 0.9983
UiO-66-Hep (PS)	% bdc released = $103.73 - 66.31t$	R <sup>2</sup> = 0.9984
UiO-66-FA (CM)	% bdc released = $12.69 + (82.12) (t^{1.63}/(8.38 + t^{1.63}))$	R <sup>2</sup> = 0.9937
UiO-66-Biot-AcOH (CM)	% bdc released = $16.73 + (53.34) (t^{1.45} / (3.99 + t^{1.45}))$	R <sup>2</sup> = 0.9913
UiO-66-FA (PS)	% FA released = $84.01 - 64.28t$	R <sup>2</sup> = 0.9937
UiO-66-FA (CM)	% FA released = $(-71.64) / (1+e^{(t-2.08)} / 1.82t) + 87.12)$	R <sup>2</sup> = 0.9913

The uncoated samples, UiO-66-AcOH and UiO-66-L1, exhibit exponential degradation profiles:  $y = y_0 + A_1 e^{x/t_1}$ . In contrast, the PEGylated samples exhibit sigmoidal degradation profiles:  $y = \text{start} + (\text{end} - \text{start})(x^n/(k^n + x^n))$ , clearly indicating a different initial degradation mechanism. UiO-66-L1-PolyLact and UiO-66-L2-PNIPAM also present sigmoidal degradation profiles, with  $y = \text{start} + (\text{end} - \text{start})(x^n/(k^n + x^n))$  and  $y = V_{\text{max}} (X^n/K^n + X^n)$  equations respectively. In contrast, UiO-66-Hep (PS) and UiO-66-Biot (PS) exhibit exponential degradation profiles, although following a different equation ( $y = a - bc^x$ ) than their precursor UiO-66-L1, while UiO-66-FA (PS) degradation profiles are sigmoidal ( $y = \text{start} + (\text{end} - \text{start})(x^n/(k^n + x^n))$ ).

Similar profiles occur for the biotin and folic acid modulated samples, which follow  $y = \text{start} + (\text{end} - \text{start})(x^n/(k^n + x^n))$  sigmoidal degradation kinetics. The release of bdc from the folic acid coated samples (both postsynthetically coated and modulated) follow similar degradation

profiles, but for UiO-66-Biot-AcOH (CM), the profile is markedly different from the exponential degradation profile of UiO-66-Biot (PS).

Folic acid release occurs in both cases at a higher rate than bdc release. The differences in folic acid release from the modulated and postsynthetically modified UiO-66 are noticeable in their kinetics, being exponential ( $y = a - bc^x$ ) for the UiO-66-FA (PS) sample and sigmoidal ( $y = (A_1 - A_2) / (1 + e^{(x-x_0) / d_x}) + A_2$ ) for the UiO-66-FA (CM), suggesting the coating is easier to remove from postsynthetically coordinated samples.

These results highlight the importance of surface coating to enhance UiO-66 degradation kinetics towards phosphates for initial contact times, while ensuring similar final degradation rates. The mode of coating has been proved to also play an important role, especially for the first stages of degradation. Surface modifications performed by coordination chemistry postsynthetically have a more pronounced initial effect than those where the functionality is introduced during synthesis, possibly due to the higher hindering of Zr units from phosphate attack. Surface modification based on the 'click modulation' protocol also highly enhance degradation kinetics, more remarkable for the PEG chains.

### 7.3 Kinetic Fitting of Calcein Release Profiles

The kinetic profiles of calcein release (Table 7.2) and simultaneous linker release (Table 7.3) from the calcein-loaded bare and PEGylated samples were determined by curve fitting utilising Microcal Origin software.

**Table 7.2.** pH Dependence of calcein release from cal@UiO-66-L1, cal@UiO-66-L1-PEG550 and cal@UiO-66-L1-PEG2000.

NMOF	Release equation	R <sup>2</sup>
cal@UiO-66-L1 pH 7.4	% calcein released = $158.66(t^{0.05}/1.13 + t^{0.05})$	R <sup>2</sup> = 0.99442
cal@UiO-66-L1-PEG550 pH 7.4	% Calcein Released= $33.14(t^{1.06}/0.11 + t^{1.06})$	R <sup>2</sup> = 0.97539
cal@UiO-66-L1- PEG2000 pH 7.4	% Calcein Released= $31.21(t^{0.90}/0.11 + t^{0.90})$	R <sup>2</sup> = 0.99387
cal@UiO-66-L1 pH 5.5	% calcein released = $96.33 - 59.47 e^{-t/2.26}$	R <sup>2</sup> = 0.99061
cal@UiO-66-L1-PEG550 pH 5.5	% Calcein Released= $48.94 + 38.49 (1 - e^{-t/0.31}) + 70.22(1 - e^{-t/153.72})$	R <sup>2</sup> = 0.91157
cal@UiO-66-L1- PEG2000 pH 5.5	% Calcein Released= $43.52 + 39.73 (1 - e^{-t/0.099}) + 23.44(1 - e^{-t/11.17})$	R <sup>2</sup> = 0.97093

There is a clear difference in the release profiles at pH 7.4. Although calcein release follows a sigmoidal profile  $y = V_{\max} (X^n / K^n + X^n)$  in all cases, the rate of release from cal@UiO-66-L1 is clearly higher than for the PEGylated samples, while the later also reach a plateau around 30 % release after 1 day versus total calcein release from cal@UiO-66-L1 for the same release time.

At pH 5.5, although all following exponential kinetics, the release profiles differ between bare and PEGylated samples -  $y = y_0 + A_1 e^{-x/t_1}$  for cal@UiO-66-L1 and  $y = y_0 + A_1 (1 - e^{-t/t_1}) + A_2 (1 - e^{-t/t_2})$  for the PEGylated samples - but all release their cargo after 1 day.